ROBUST NEEDLE CHANNEL PLANNING FOR PATIENT-TAILORED APPLICATOR DESIGN IN CERVICAL CANCER BRACHYTHERAPY

Robin Straathof

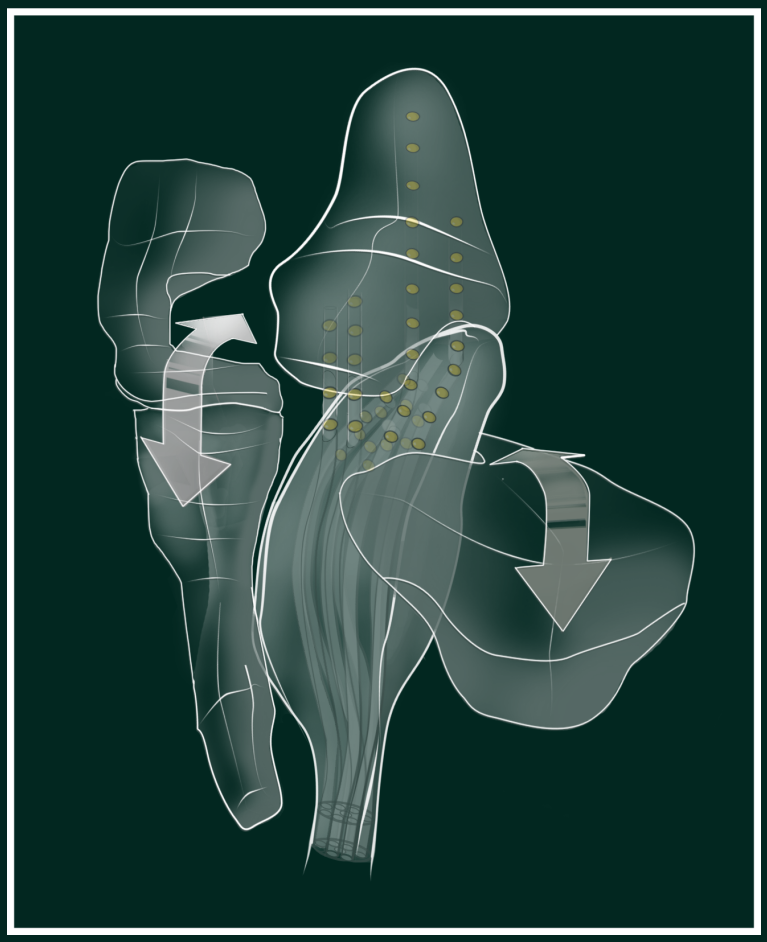

Master Thesis 2020-2021

Robust needle channel planning for patient-tailored applicator design in cervical cancer brachytherapy

Robust needle channel planning for patient-tailored applicator design in cervical cancer brachytherapy

Robin Straathof

To obtain the degree of

Master of Science
in Mechanical Engineering

at the Delft University of Technology,
Department of BioMechanical Engineering.

Student number: 4362640
Date: January 12, 2021
Thesis committee:

Prof. dr. J. Dankelman,	TU Delft, supervisor
Dr. ir. N.J.P. van de Berg,	TU Delft, supervisor
I.K.K. Kolkman-Deurloo, PhD,	Erasmus MC
Dr. J. Alonso Mora,	TU Delft
Prof. dr. C.C.L. Wang,	TU Delft

TU Delft

Abstract

Brachytherapy (BT) is an essential component in the treatment of cervical cancer as it allows for locally delivering a high dose to the tumour with minimal trauma to surrounding tissues and organs at risk (OARs). However, in advanced cervical cancer patients commercially available BT applicators are particularly ill-adapted and therefore result in suboptimal local control and frequent occurrence of substantial tissue morbidity. Additionally, cervical cancer BT is associated with large dosimetric uncertainty which has been shown to significantly impact the delivered dose and the occurrence of normal tissue complications. The clinical outcomes of treatment may be improved through combined efforts in sophisticated applicator design and robust treatment optimisation. Patient-tailored BT applicators have been introduced to improve dose conformity, but currently rely on manual indication of needle channels. Automated needle channel planning software for this purpose exists, but does not account for OAR dose constraints or uncertainty in the planning environment. Robust treatment optimisation, on the other hand, potentially improves the dose conformity of plans in the presence of uncertainty, but relies on the questionable presumption that optimisation of dwell times can fully correct for suboptimal dwell positions. In this thesis, the freedom of source placement that 3D-printed applicators allow and the principle of robust treatment optimisation are leveraged to develop robust needle channel planning software for personalised applicators. This thesis was accordingly divided into three parts.

The aims of this study were threefold. This thesis first aimed to: (i) classify and quantify dosimetric uncertainty components in cervical cancer BT, (ii) assess their impact on the clinical outcome, and (iii) cast these outcomes into a mathematical optimisation problem suited for motion planning (MP). Secondly, this thesis aimed to: (iv) develop a general tool to aid the selection process of a MP class given this heuristic problem description, and (v) use this for the selection of a robust MP class for BT. Lastly, this thesis aimed to: (vi) develop robust motion planners capable of generating needle channels in complex environments under uncertainty, and (vii) implement and evaluate their performance in a simulated patient case.

In the first part, literature was reviewed to establish the dosimetric uncertainty budget and evaluate geometric uncertainty of OARs. Inter and intra-fraction uncertainty are likely the greatest contributors to the uncertainty budget, possibly increasing the delivered dose to OARs with up to $4.0 \pm 20\%$ ($k = 1$). Using dose-response models it was established that this may realistically increase the occurrence of moderate to severe morbidity of the bladder or rectum by 1.5 and 3.7% respectively. The BT needle channel planning problem under uncertainty was accordingly defined as the problem of computing multiple feasible, non-intersecting curvature-constrained channels under probabilistic or bounded spatial uncertainty of OARs. In the second part, a tool termed motion-planning quality function deployment (MP-QFD) was developed to select a suitable motion planning class. Using the results from a pilot study among nine medical specialists, this tool substantiated the preferred choice for an incremental sampling-based motion

planning algorithm. In the last part, robust variants of sampling-based planners were introduced that are capable of computing trajectories for non-holonomic agents in environments under uncertainty. In a two-dimensional simulated patient case, it was shown that these planners were able to generate near-optimal trajectories that (probabilistically) guaranteed not exceeding OAR dose constraints. Subsequent dose-based optimisation showed that (robust) trajectory planning could theoretically yield treatment plans with improved dose conformity over those generated for conventional applicators. Due to modelling assumptions, robust motion planning did not result in improved dose conformity over a nominal motion planning approach in a worst-case scenario. Future work should therefore focus on improving our understanding of OAR movement in and during BT treatment and validating this theoretical work in a patient case series.

Acknowledgements

This Master's thesis would have not been possible without the support and guidance from many people. First and foremost, I would like to express sincere gratitude towards my supervisors. Nick, without your -sometimes daily- support I would have not been able to write this thesis. You gave me the freedom and means to explore my interests, but always kept me on track. Moreover, I particularly appreciate that you were always there to help me resolve the problems I experienced and helped me see things clearly. Your comments and the discussions we had were invaluable to improve the quality of this thesis. I can safely say that I could not have wished for a better supervisor. Jenny, I remember how nervous I was the first time that I entered your room for my internship, as I have aspired to work under your supervision since I attended your lectures. In every meeting we had since then, you were always kind and provided me with many useful suggestions and ideas. Especially, I would like to thank you for your comforting words each time I saw you. Moreover, I would like to thank all members of my thesis committee for their time and effort in reviewing this thesis.

It has been a privilege to have worked with the people of the MISIT lab over the past year. Even though I was a student, I appreciate how you made me feel like a member of this lab. I am very proud to be able to continue working in this lab to further explore the world of scientific research. I would also like to thank my fellow students whom have always supported me during my studies. Jette and Vera, I would like to thank you in particular as you have truly made my years as a student in Delft very enjoyable. I owe major thanks to my former roommates in Delft who provided a relaxed atmosphere and made Delft feel like my new home.

I would like to thank my mom and dad, for unconditionally supporting me and taking good care of me and Marvin. It is impossible to describe my gratitude towards you. Marvin, you have been a constant source of inspiration to me and I value how I could always exchange thoughts with you on study topics. Lastly, Nada, I am blessed to have you in my life. I would like to thank you for your love, continuous support and being a constant source of happiness to me. I owe you everything.

Robin Straathof
January 12, 2021
Leiden

0. Preliminaries

0.1 Nomenclature in BT

α/β	Radiosensitivity coefficient ratio
Δ	Dosimetric variation
Φ_{an}	1D anisotropy function
γ_{50}	Normalised dose-response gradient at 50% response
Λ	Dose-rate constant in water
Σ	SD of systematic error
σ	Group random error
σ_σ	SD of random error
σ_p	Overall random error
BED	Biologically effective dose
c_{ap_d}	Constraint function for the ath structure at dose calculation point p_d
d	(Nominal) Dose per fraction
$\bar{d}$	Actual dose delivered per fraction
$\dot{d}$	Dose rate
d_{p_d}	Dose to calculation point p_d
D	Total delivered dose over treatment
D_V	Dose received by at least partial volume V
EQDX	Equieffective dose
EUD	Equivalent uniform dose
F_L	2D anisotropy function
G	Repair function
G_L	Geometry function for line source
g_L	Radial dose function for line source
G_P	Geometry function for point source
L	Length of the BT source
M	Group systematic error (Mean of means)
M_a	Penalty weight for the ath structure the ath structure
M_p	Overall mean error
N	Number of fractions
$\overline{\text{NTCP}}$	Average normal tissue complication probability with uncertainty
NTCP	Normal tissue complication probability
r	Distance from a point of interest to the centre of the BT source
S_K	Air kerma strength of the BT source
TCD_{50}	Dose required for 50% response
TCP	Tumour control probability
$\overline{\text{TCP}}$	Average tumour control probability with uncertainty
V_D	Volume receiving a dose of at least D
w_{ap_d}	Penalty function for the ath structure at dose calculation point p_d

0.2 Nomenclature in MP

$\vee$	Map from Lie algebra to Real space
$\wedge$	Map from Real space to Lie algebra
exp	Exponential map
log	Logarithmic map
$\mathcal{A}$	Agent
$\mathcal{C}$	Configuration space
$\mathcal{C}_{obs}$	Set of configurations in collision
$\mathcal{E}$	Entry region
$\mathcal{I}$	Stay-in region
$\mathcal{N}$	Candidate set of dwell segments
$\mathcal{N}(\mu, P_c)$	Multivariate normal distribution with mean μ and covariance matrix P_c
$\mathcal{N}_{free}$	Set of feasible dwell segments
$\mathcal{O}$	Obstacle space
$\mathcal{S}$	Set of optimal dwell segments
$\mathcal{T}$	Tumour region
$\mathcal{U}$	Control space
$\mathcal{W}$	World
$\mathcal{X}$	State space
$\mathcal{X}_{free}$	Set of states in the free space
$\mathcal{X}_{j,t}$	jth Obstacle (OAR) at time t
$\mathcal{X}_m$	Set of planned needles
$\mathcal{X}_{obs}$	Set of states in collision
$\mathcal{Y}$	Set of dwell segments in collision
$\mathcal{Y}$	Set of non-feasible dwell segments

$\mathbb{P}$	Probability
$\mathbb{RP}^n$	Real projective space
$\mathbb{R}^n$	Euclidean space
$\mathbb{S}^n$	Spherical space
C	Cost criterion
E	List of edges
G	Graph
$I(\epsilon)$	Coverable points
L	Length of agent
$M_q(\epsilon)$	Set of dwell segments that covers point q
N	Number of samples
O	Order of complexity
P_c	Covariance matrix of the jth OAR
Q_{near}	Set of near neighbours
S_j	Bounded uncertainty set of the jth OAR
$\mathfrak{se}(2)$	Lie algebra with dimension n
$SE(n)$	Special Euclidean group with dimension n
$SO(n)$	Special orthogonal group with dimension n
V	List of vertices
X_t	Pose at time t
$X_{children}$	Set of children nodes
α_l	User weight for the lth cost function component
Δ	Trajectory-wise risk threshold
δ	Step duration
Δ_t	Stepwise risk threshold
ϵ	Dose coverage radius
η_j^c	Deterministic constraint tightening parameter for the jth obstacle
$\bar{\kappa}$	Upper bound to curvature
κ_t	Curvature at time t
ξ	Velocity twist of rigid body
$\bar{\lambda}$	Maximum step size
λ_t	Step size at time t
ψ_p	Joint tolerated risk level
ψ_s	Stepwise tolerated risk level
ρ	Distance metric
τ	Path
τ_q	Dose calculation point
$\mathbf{c}_j$	Uncertain translation of the jth OAR
$\mathbf{e}$	Edge
$\mathbf{f}_j$	Bounded displacement interval
$\mathbf{p}$	Point in Euclidean space
$\mathbf{p}/\mathbf{q}/\mathbf{x}_{samp}$	Sampled point / configuration / state
$\mathbf{q}$	Configuration
$\mathbf{q}/\mathbf{x}_{nearest}$	Nearest configuration / state according to cost metric
$\mathbf{q}/\mathbf{x}_{near}$	Nearest configuration / state according to distance metric
$\mathbf{q}/\mathbf{x}_{new}$	New configuration / state
$\mathbf{q}/\mathbf{x}_{parent}$	Parent configuration / state
$\mathbf{u}$	Control input
$\mathbf{v}$	Vertex
$\mathbf{x}_0^i$	Initial state of the ith agent
$\mathbf{x}_T^i$	Terminal state of the ith agent at time T
$\mathbf{x}_t^i$	State of the ith agent at time t
$\tilde{x}$	Trajectory
f_l	Cost function component
$r_{D,j}$	Dose constraint radius for the jth OAR
s_i	Individual dwell segment
$t_{z_p^i}$	Dwell time for dwell position z_p^i
$\bar{v}_t$	Upper bound to tangential velocity
v_t	Tangential velocity at time t
w	Width of agent
z_p^i	Dwell position in the ith source channel

0.3 Nomenclature in QFD

γ_{lj}	Correlation between lth and jth HOW
$\mathbb{H}$	Cumulative index vector
$\mathbb{U}$	Binary index vector
A_m	Technical alternative
A_i	Attractive WHAT
B_i	Basic WHAT
C_o	Competitor
d_i	Final importance of WHAT
DI_i	Dissatisfaction index
E	Technical matrix
e_{mj}	Degree of attainment of jth HOW for mth alternative
g_i	Relative importance of WHAT
H_j	Technical attribute / HOW
I_i	Indifferent WHAT

IR_i	Improvement ratio of WHAT
k	Kano category coefficient
L	Ordinal scale level
O_i	One-dimensional WHAT
R	Relationship matrix
r_{ij}	Correlation coefficient between ith WHAT and jth HOW
S	Overall user satisfaction
SI_i	Satisfaction index
T_j	Indicator function of WHAT prioritisation
W_i	User weight / WHAT
w_j	Weight of prioritisation of jth technical attribute
x_{io}	Attainment of ith WHAT of oth competitor
y_i	Degree of fulfillment of WHAT

Contents

List of Figures

List of Tables

Part I
Evaluation and specification of uncertainty in cervical cancer brachytherapy

This part provides an overview of dosimetric uncertainties and their clinical impact on brachytherapy for cervical cancer, and makes a case for the implementation of robust planning software in the development of patient-tailored brachytherapy applicators. Advances in treatment modalities leading to the development of these patient-tailored brachytherapy applicators and dose planning concepts are described in Chapter 1. Moreover, the problem of uncertainty in cervical cancer brachytherapy is introduced and current solutions explored. In Chapter 2 dosimetric uncertainty components in cervical cancer brachytherapy are structured and their magnitude and impact on the clinical outcome of patients are assessed. Geometric inter and intra-fraction uncertainty are further investigated in Chapter 3. The brachytherapy needle channel planning problem under uncertainty is then mathematically formulated in Chapter 4, which lies at the basis for the planning software developed in this thesis.

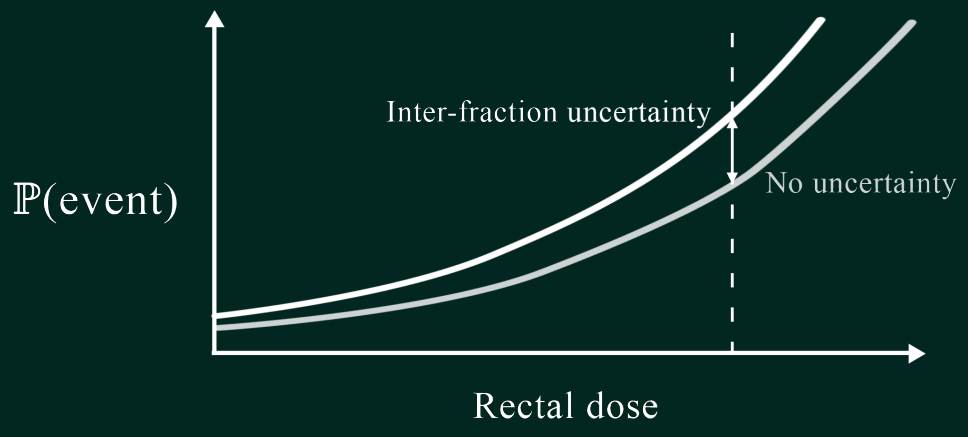

Illustration: Impact of dosimetric uncertainty on the predicted occurrence of rectal complications

1. Clinical introduction

1.1 Cervical cancer: epidemiology, diagnosis and treatment

Cancer of the cervix, or cervical cancer, is the fourth most commonly occurring form of cancer and cancer-related mortality among women worldwide, with an estimated 570,000 patients newly diagnosed and accountable for an estimated 311,365 deaths in 2018 [1]. The human papillomavirus (HPV) is the (virtually) necessary cause of cervical cancer. Advances in screening and systematic vaccination have drastically decreased the incidence and mortality of cervical cancer in particular for developed countries [2–4]. For women who develop cervical cancer, the treatment modality is among others dependent on the stage of cancer including tumour size, local extension and nodal involvement. These are typically characterised using the International Federation of Gynaecology and Obstetrics (FIGO) staging system and TNM Classification. Next to tumour related factors, the choice of treatment strategy is influenced by: (i) patient factors: including age, desire to preserve fertility, overall health, body habitus and presence of comorbidity, (ii) physician's preference or expertise, (iii) institutional traditions and (iv) resource availability amongst other factors [5].

Brachytherapy (BT) encompasses all temporary or permanent techniques of placing radiation sources in close proximity to or within the tumour. It allows for locally delivering a (additional) high cervical and para-cervical equieffective dosage to the tumour, due to the characteristic rapid absorbed-dose fall-off in the direction orthogonal to the source, which obeys an inverse square law. This would not be possible with external beam radiation therapy (EBRT) alone, without significant side effects to organs at risk (OARs) or surrounding normal tissues (Figure 1.1) [6–9]. Therefore, it is an essential component of radiotherapy and plays an important role in the treatment of cervical cancer in general. Surgery has been the standard treatment method in early stage disease (FIGO stages IA-IB1 or TMN stages T1a-T1b), although radiotherapy possibly including brachytherapy (BT) could be used in the case of unfavourable prognosis as well. Combination therapy generally involving external beam radiation therapy (EBRT) and brachytherapy with or without concurrent cisplatin chemotherapy is especially recommended for patients with locally advanced carcinomas (stages IB2-IVA or T1b2-T4) [7, 10–12].

1.2 Basic concepts in brachytherapy

This section provides a comprehensive overview of basic concepts in brachytherapy to arrive at a uniform and reliable terminology.

1.2.1 Treatment modality

Low, pulsed and high-dose-rate brachytherapy

Within brachytherapy treatment different categories can be distinguished based on the delivered dose rate. As its definitions have changed throughout time, the result of 'new' clinical insights, confusion may arise when reviewing older literature. The classification described below is somewhat arbitrary as rather than what these strict dose rate boundaries may indicate, biological effects change gradually with dose.

Definition 1.2.1. Low-dose-rate brachytherapy: *Low-dose-rate brachytherapy* (LDR-BT) has been previously defined as brachytherapy with an *absorbed dose rate* of 0.4–2 Gray per hour (Gy/h) [13], and more recently with an absorbed dose rate of <1 Gy/h [7];

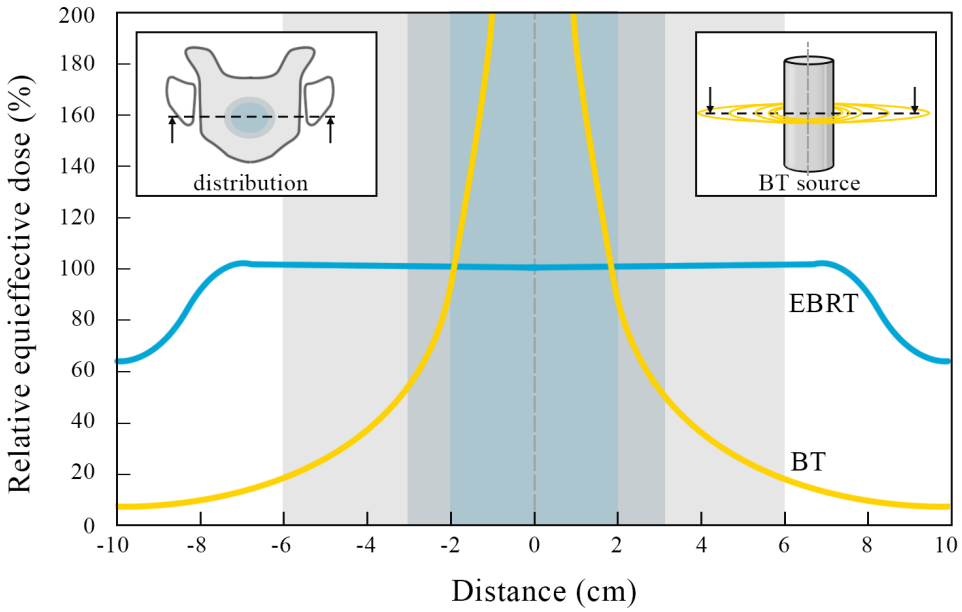

Figure 1.1: Dose distribution profiles of EBRT (blue —) and BT (gold —). The dose-distance profile orthogonal to the BT source's longitudinal direction follows an inverse square law. Therefore, the geometry function that is used to approximate the behaviour of the spatial distribution can be written as $G_p(r) = 1/r^2$, with r the distance of a point orthogonal to the source. Figure adapted from Ref. [7].

Definition 1.2.2. High-dose-rate brachytherapy: *High-dose-rate brachytherapy* (HDR-BT) is defined as brachytherapy with an *absorbed dose rate* of >12 Gy/h [7, 13];

Definition 1.2.3. Pulsed-dose-rate brachytherapy: *Pulsed-dose-rate brachytherapy* (PDR-BT) is defined as brachytherapy with a constant or varying dose per *pulse*, i.e. irradiation of a shorter duration than the time required for complete recovery of the tissue. Typically, its *absorbed dose rate* is between 0.5-1 Gy/h (with one pulse per hour) [7].

Sometimes also *medium-dose-rate (MDR)* brachytherapy is distinguished, with an hourly absorbed dose of 2-12 Gy/h [13], or 1-12 Gy/h [7]. However, its use in clinical practice is limited. Traditionally, cervical carcinoma has been treated using continuous LDR-BT, but a shift towards continuous HDR-BT and PDR-BT has occurred during the past few decades [7, 14]. Advantages of HDR-BT over LDR-BT are manifold, including shorter treatment time, less applicator movement and lower radiation exposure to hospital staff. Although clinical outcomes and toxicities are roughly similar for all techniques [14–18], for these reasons this thesis will focus on HDR-BT.

Brachytherapy dose delivery schedule

Definition 1.2.4. Fraction: A *fraction* is a continuous period of irradiation, with specified absorbed dose.

Definition 1.2.5. Application: An *application* is a single insertion of the brachytherapy applicator.

HDR brachytherapy is typically applied in the last 2-3 weeks after 5 weeks of (chemo-) radiotherapy, with both modalities optimally accounting for approximately half the resulting absorbed dose [7, 19]. A typical image-guided adaptive HDR brachytherapy schedule with curative intent includes four

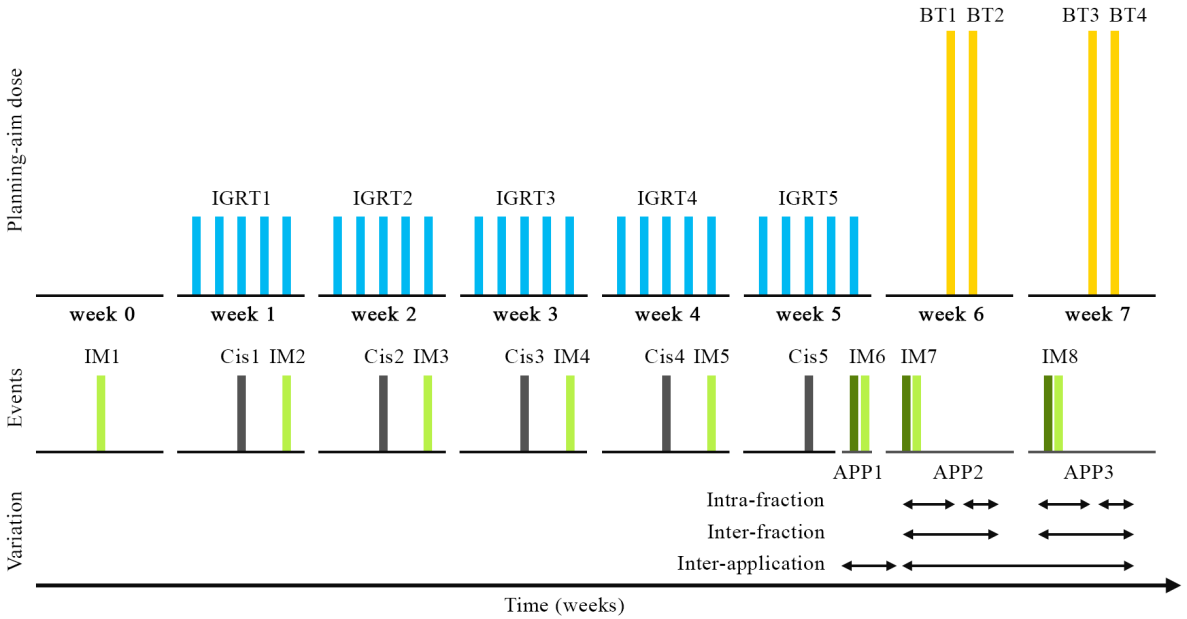

Figure 1.2: A typical treatment schedule for cervical cancer including image-guide radiotherapy (IGRT) (each blue bar representing an EBRT fractions of 2 Gy), concomitant weekly chemotherapy (each grey bar representing a course of cisplatin (Cis) 40 mg m^{-2}), and brachytherapy (each yellow bar representing a HDR brachytherapy fraction of 7 Gy). Imaging sessions and brachytherapy applicator insertions are marked with bright green and dark green bars respectively. A week prior to treatment a pre-BT image is taken with applicator *in situ* for treatment planning. Four fractions of brachytherapy are applied with two insertions where the applicator is left in place overnight. Time frames in which uncertainties could occur during treatment are marked with black arrows. Figure adapted from Ref. [7].

fractions, e.g. of 7 Gy planning-aim dose to the high risk clinical target volume each, delivered over two weeks in two applications (Figure 1.2). This is known as a *hypofractionated*, i.e. more than 2.2 Gy delivered per fraction, *accelerated*, i.e. more than 10 Gy per week, schedule.

1.2.2 Brachytherapy dose definitions and calculations

The definitions given in this subsection are obtained from the recommended reporting levels by the International Commission on Radiation Units and Measurements (ICRU) Report 89 [7].

Definition 1.2.6. Planning-aim dose: The *planning-aim dose* is the dose in Gy that is the goal for treatment and is defined prior to treatment planning.

Definition 1.2.7. Prescribed dose: The *prescribed dose* is the dose in Gy derived from the treatment planning (optimisation) process and after approval of the operating oncologist.

Definition 1.2.8. Delivered dose: The *delivered dose* is the actual dose in Gy administered to the patient during the treatment.

Definition 1.2.9. Absorbed dose: The *absorbed dose* is the planned or delivered dose in Gy to a specific area of the tissue or any other medium.

In practice, the definition of 'absorbed dose' only marginally differs from that of 'delivered dose', as absorbed dose is often used in the context of treatment planning, e.g. as in 'prescribed absorbed

dose', losing its meaning. However, the term 'absorbed' may still be used to differentiate between purely the irradiated energy and its effects. An absorbed dose may result in different biological effects or clinical outcome for a patient depending on treatment modality (including dose rate, fraction size and duration), therapeutic interventions, heterogeneities, patient-related factors, and tumour-related factors among others [7]. Therefore, a transformation of the absorbed dose to biologically (equi)effective dose is required.

Biologically effective dose (BED)

Definition 1.2.10. Biologically effective dose: The *biologically effective dose (BED)* in Gy is a predictor of the biological effect as a function of the delivered dose.

Adopted from external beam radiation therapy (EBRT), the **linear-quadratic (LQ)** model is the most commonly implemented tool for HDR brachytherapy to model the biologically effective dose (BED) for different time-dose-rate-fractionation schemes [7, 20]. Moreover, it serves an important role as a tool for calculating the *cumulative dose* from EBRT and BT. In this model, the radiosensitivity of the treated cells, i.e. BED, to changes in dose, e.g. per fraction or dose rate, is represented by the respective linear and quadratic coefficients α ($[\alpha] = \text{Gy}^{-1}$) and β ($[\beta] = \text{Gy}^{-2}$), and their ratio α/β ($[\alpha/\beta] = \text{Gy}$):

$$\text{BED}_{\alpha/\beta} = Nd\left(1 + G\frac{d}{\alpha/\beta}\right) \tag{1.1}$$

With, N the amount of fractions, d the dose per fraction in Gy, and G the repair function which is $G = 1$ for HDR-BT [21]. Typically, ratios of $\alpha/\beta = 10$ Gy for the target volume and $\alpha/\beta = 3$ Gy for organs at risk or normal tissues are assumed, as also recommended by the Gynaecological GEC-ESTRO Working Group [22]. For clarity, these ratios are indicated by a subscript for dose reporting, e.g. $\text{BED}_{\alpha/\beta=10}$. A brief overview of alternative models is given in Appendix A.2.

Equieffective dose

Definition 1.2.11. Equieffective dose: The *equieffective dose (EQDX)* is the dose in Gy that when delivered under a different condition, produces an equivalent effect or outcome as when delivered under fractions of X gray.

The **EQD2**, i.e. where the reference treatment delivers 2 Gy per fraction, is recommended and typically used for reporting [7]. This technique assumes the LQ-model to hold true, which has been more elaborately discussed in Appendix A.2. The equieffective dose at 2 Gy reference fractions is calculated via (see for a derivation Appendix A.2):

$$\text{EQD2}_{\alpha/\beta} = \frac{\text{BED}_{\alpha/\beta}}{\left(\frac{2G}{\alpha/\beta} + 1\right)} \tag{1.2}$$

The EQD2 formalism allows for the simple addition of the doses delivered by EBRT and BT to study the combined effects of both modalities.

Dose-volume parameters

Definition 1.2.12. Dose volume histogram: A *dose volume histogram (DVH)* relates the irradiated volume to the absorbed dose of that volume.

The dose volume histogram is typically used in its cumulative form, of which single parameters can be extracted to predict biological effects or treatment outcome [7]. In general, a DVH may be used as a tool for quantifying the dose level in the target volume or organs at risk, may possibly be used as an indicator for hot and cold spots, and may be the input for dose-response models [23]. The dose and volume parameters that are extracted from DVHs, are mathematically defined as:

$$D_V = \{D(v) \mid v \geq V\} \tag{1.3}$$

$$V_D = \{V(\mathcal{D}) \mid \mathcal{D} \geq D\} \tag{1.4}$$

Here, $D(v)$ marks the dose as a function of volume v and $V(\mathcal{D})$ the volume as a function of the dose $\mathcal{D}$. Simply stated, D_V is the dose in Gy received by at least a volume V, where $[V] = \%$ or cm^3. V_D is the partial volume in % or cm^3 receiving doses of at least D, which may be the absorbed dose, $EQD2$, or a percentage of a specified dose [7]. The following list of dose-volume parameters is recommended for reporting or includes often used parameters in literature [7, 22]: (i) $D_{98\%}$, $D_{90\%}$, and $D_{50\%}$ for the high risk clinical target volume, (ii) $D_{98\%}$ and $D_{90\%}$ for the intermediate risk clinical target volume, (iii) $D_{98\%}$ and $D_{90\%}$ for the gross tumour volume, and (iv) $D_{0.1cm^3}$ and D_{2cm^3} for organs at risk (e.g. bladder, rectum, and sigmoid). The main limitation of this model is that it reduces spatial dosimetric information into two-dimensional dose-volume relations [7], see also Appendix A.2.

Dose distribution calculations

Definition 1.2.13. TG-43 formalism: Dose calculations are most often performed using the American Association of Physicists in Medicine (AAPM) *TG-43 formalism* [24], enabling the calculation of a two-dimensional dose distribution around axially symmetric cylindrical sources.

The two-dimensional dose rate equation according to this formalism is the following [24]:

$$\dot{d}(r,\theta) = S_K \cdot \Lambda \cdot \frac{G_L(r,\theta)}{G_L(r_0,\theta_0)} \cdot g_L(r) \cdot F_L(r,\theta) \tag{1.5}$$

where,

- $\dot{d}(r,\theta)$ is the dose rate (in cGy h^{-1}) in water at a distance r (in cm) and polar angle θ (in rad) measured from a point of interest to the centre of the source;
- S_K is the air kerma strength of the BT source (in U = μGy m^2h^{-1} = cGy cm^2h^{-1});
- Λ is the dose-rate constant in water (in cm^{-2});
- $G_L(r,\theta)$ is the geometry function (in cm^{-2});
- $\{r_0,\theta_0\}$ are the reference distance and angle, usually 1 cm and $\pi/2$ rad respectively;
- $g_L(r)$ is the radial dose function, i.e. perpendicular to source axis (dimensionless);
- $F_L(r,\theta)$ is the 2D anisotropy function (dimensionless);

For more detailed information on these parameters and a discussion on the uncertainties thereof the reader is referred to Refs. [24, 25]. Some of these values -i.e. S_K, Λ- can directly be obtained from data sheets or treatment planning systems. The calculation of radial dose and anisotropy functions is usually based on table lookup via linear interpolation. The geometry function for a line source is the following:

$$G_L(r,\theta) = \begin{cases} \frac{\beta}{L\, r\, \sin(\theta)} & \text{if } \theta \neq 0 \\ \frac{1}{r^2 - L^2/4} & \text{if } \theta = 0 \end{cases} \tag{1.6}$$

where, L is the active length (in cm) of the line source. β is the angle (in rad) subtended to the outer points of the source from the point of interest. Although other conventions have been used to compute this angle, the following expression is the most common:

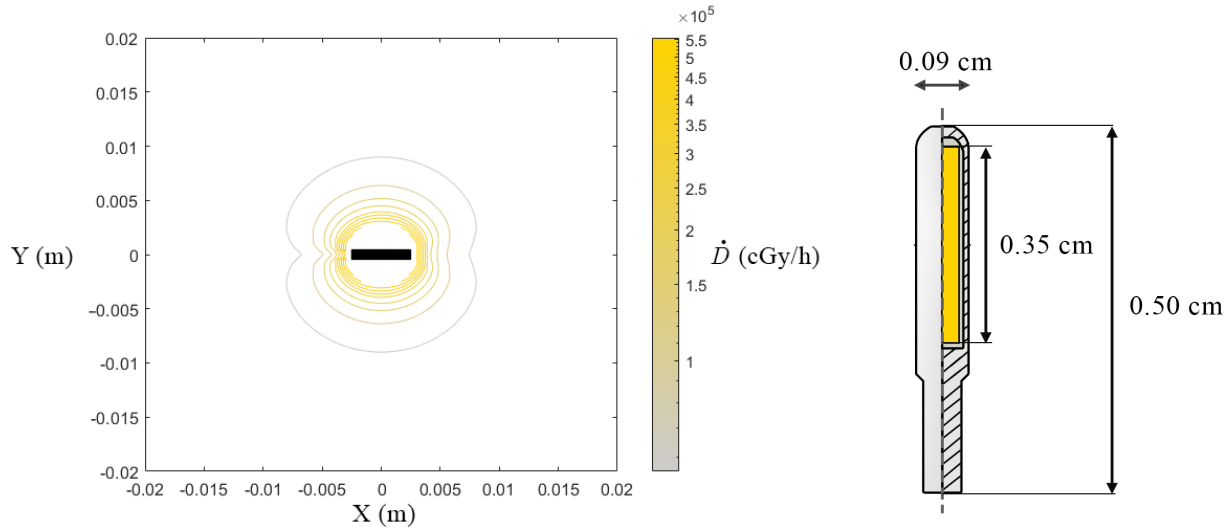

(a) Contour plot showing isodose-rate lines of the mHDR-v2 model. **(b)** mHDR-v2 source.

Figure 1.3: Spatial dosimetric distribution and geometry of the mHDR-v2 source model used in this thesis.

$$\beta = \arctan\left(\frac{r\cos(\theta) + L/2}{r\sin(\theta)}\right) - \arctan\left(\frac{r\cos(\theta) - L/2}{r\sin(\theta)}\right) \tag{1.7}$$

In this thesis the HDR microselectron v2 (mHDR-v2, Elekta, Stockholm, Sweden) ^{192}Ir model is used (Figure 1.3b), of which dose distribution data is available online [26]. The contour-plot showing the dose-rate distribution for the mHDR-v2 model, as computed with MATLAB (MATLAB R2020a, MathWorks, Natick, MA, USA) Script A.1.1, is shown in Figure 1.3a.

The isodose curves shown in Figure 1.3a illustrate the anisotropy of the dosimetric distribution, captured by the function $F_L(r, \theta)$. A separate function exists for one-dimensional point sources, which results in a radially symmetrical dose distribution.

1.2.3 Clinical outcome parameters and morbidity

Definition 1.2.14. Local control: *Local control (LC)* is the absence of progressive or recurrent disease, known as *progression free survival*, in central and non-central pelvis at a specified time from the end of treatment [27].

The local control rate is often the primary endpoint to express the efficacy of brachytherapy or other radiotherapy treatment modalities. Related endpoints are *complete remission*, *progression-free survival* for the whole pelvis, and *overall survival* and *cancer specific survival* [28]. It may seem trivial that methods that lead to higher local control rates also increase the likelihood of overall survival. Recurrent cervical cancer was for example found to be the common cause of death in a multi-institutional cohort of locally advanced cervical cancer patients treated with EBRT and BT with or without concomitant chemotherapy [29]. With the advances in the reduction of local control, distant relapses may become the predominant sites of failure [28].

Definition 1.2.15. Treatment-related morbidity: Radiation-induced morbidity, or *treatment-related morbidity*, of irradiated volumes, i.e. organs at risk or normal tissues, is a side effect of treatment.

It is common to grade the severity of morbidity using the *'Common Terminology Criteria for Adverse Events' (CTCAE)* on a five-point scale. Treatment-related morbidity of any grade is associated with user-reported impairment on the *quality of life* [30]. Any treatment strategy must therefore account for both the curative potential of the treatment modality, e.g. the local control, and the likelihood of side effects, e.g. the morbidity and quality of life [7].

1.2.4 Dose-response relationships

Definition 1.2.16. Tumour control probability: *Tumour control probability (TCP)* is formally defined as the probability that no clonogenic cell survives the treatment.

Typically, TCP models relate clinical outcome, which is predominantly local control, to the survival fraction predicted by the linear quadratic model, using *Poissonian* or *logistic modelling* [31]. Whereas the former has a more mechanistic character, the latter is on an empirical basis [32]. Moreover, the dose-response curves of logistic models tend to be more applicable to describe the heterogeneous populations, whilst the former is more suited to describe individual tumours [33, 34]. Although both are used almost equally throughout literature on the topic [31], a trend towards logistic models may be distinguished [35], and therefore only this type of model is treated.

The general form of the **logistic dose–response model** is the following:

$$P = \frac{\exp\left(a_0 + a_1 D + a_2 D d + ...\right)}{\left(1 + \exp\left(a_0 + a_1 D + a_2 D d + ...\right)\right.} \tag{1.8}$$

Here, P is the probability of an event occurring, based on the LQ-model, with D and d the total dose and dose per fraction respectively. The coefficients of this model, $a_0, a_1, ...$, are estimated by logistic regression, where the ratio a_1/a_2 is an estimate of the α/β ratio [32, 35]. This model may be parameterised in terms of the dose required for 50% response, TCD_{50}, and the normalised dose-response gradient, γ [35–37]:

$$\mathrm{TCP} = \frac{1}{\left(1 + \exp\left(4 \cdot \gamma_{50}(1 - D/\mathrm{TCD}_{50})\right)\right)} \tag{1.9}$$

Here, TCP is the tumour control probability and γ_{50} the normalised dose-response gradient at 50% response.

Definition 1.2.17. Normal tissue complication probability: *Normal tissue complication probability (NTCP)* is defined as the probability that a complication of the irradiated normal tissue occurs.

Similar to the TCP, it is assumed that this dose-response function for the NTCP can be sufficiently approximated by a sigmoidal shape, which generally provides a good fit to clinical data but does not necessarily have a mechanistic basis. In theory, the logistic model from Eq. 1.9 may therefore be used directly to calculate the NTCP and in practice this is indeed sometimes performed [35, 38]. Alternative formulations are summarised in Appendix A.2.

1.3 Advances in brachytherapy techniques and systems

1.3.1 Evolution of brachytherapy techniques

Two-dimensional approaches to brachytherapy

As introduced in the 1950s the brachytherapy dose has been historically mainly prescribed to a predefined point relative to the (intracavitary) applicator, point A, which was thought to be

an indicator of the average location of an extension of a tumour. To date, the use of point A for reporting, treatment planning and new applicator development is still common [7, 19]. The exact definition of the location of point A changed between different brachytherapy dosimetric systems. Although it has been shown that this is a fairly good representation for capturing the extension of an average carcinoma, point A dose description: (i) underestimates the absorbed dose for large tumours and overestimates that of small tumours, (ii) does not necessarily correlate with an anatomical point/structure, (iii) cannot be used for (combined) interstitial applicators, and (iv) is a poor surrogate for evaluating the dose in the time-dependent tumour volume (also known as a 4-dimensional or 4D target) throughout treatment [7, 19, 39, 40]. Dose-point calculations for organs at risk (OARs) using reference points introduced in the late 1970s and standardised in 1985 were performed based on two-dimensional (2D) orthogonal radiographs [13]. Although these reference points were later shown to correlate well with high-dosed OAR partial volumes that are linked to tissue morbidity, these possibly underestimate the doses to these partial volumes [41, 42]. Therefore, two-dimensional treatment planning approaches resulted in high local/regional relapse rates, especially for locally advanced tumours with parametrial involvement, as well as high occurrence of tissue morbidity or other complications [18].

Volume-based approaches and related concepts

With progress in advanced 3D volumetric-imaging tools, including computed tomography (CT) and the increasingly used magnetic resonance imaging (MRI), and treatment planning systems a shift towards 3D treatment planning and optimisation has taken place in recent years [7]. The development of BT target volumes, as introduced by the Gynaecological Groupe Européen de Curiethérapie and the European Society for Therapeutic Radiology and Oncology (GYN EC-ESTRO) working group, have been instrumental to support this shift towards image-guided BT (IGBT) [12, 19, 22]. The current recommended basis of treatment prescription and planning, according to International Commission on Radiation Units and Measurements (ICRU) Report 89, is the primary gross tumour volume GTV-T, which is at the initialisation of brachytherapy denoted as GTV-T_{res}. For convenience, the '-T' indicating the primary tumour is often dropped. The clinical target volume, CTV, is the region to be treated to control microscopic disease and includes the GTV_{res}, but also the whole cervix and the presumed extracervical tumour extension (see also Figure 1.4) [7]. Based on the risk of occurrence, a high risk CTV_{HR} and intermediate risk CTV_{IR} are distinguished (Figure 1.4). It is recommended that the prescribed $D_{90\%}$ of the CTV_{HR} amounts to ≥84-87 Gy $EQD2_{\alpha/\beta=10}$ to obtain high local control rates [43–47]. Additionally, a planning target volume, PTV, can be defined that includes the CTV with additional margins that account for organ motion or delivery-related inaccuracies, known as the internal margin, and geometrical uncertainty as a result of radiotherapy technique, known as the set-up margin.

Organs at risk (OARs) are a set of tissues that could suffer morbidity after irradiation and hence these should be spared during treatment. In specific, radiosensitive organs or organs closely residing to radiation sources such as the rectum, bladder, small bowel and sigmoid have been distinguished as OARs in cervical BT guidelines [7, 22, 49]. Sometimes also the vagina and ureter are considered as OARs in treatment planning. Dose volume constraints are of vital importance for OAR sparing, commonly using D_{2cm^3} ≤70 Gy $EQD2_{\alpha/\beta=3}$ for the rectum, sigmoid and bowel and D_{2cm^3} ≤90 Gy for the bladder [22]. Increasing evidence shows that to reduce the probability of morbidity for the rectum and bladder dose constraints should be lowered to D_{2cm^3} ≤65 Gy and D_{2cm^3} ≤80 Gy for these OARs respectively [50].

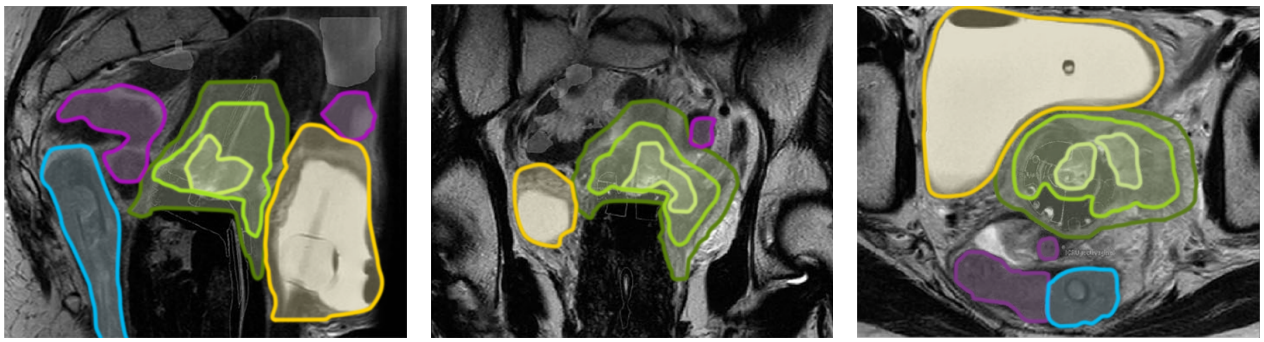

(a) Sagittal view. **(b)** Coronal view. **(c)** Transversal view.

Figure 1.4: Delineations of volumes of interest on T2-weighted MRI views: GTV_{res} (light green —), CTV_{HR} (bright green —), CTV_{IR} (dark green —), bladder (gold —), rectum (blue —), and sigmoid (purple —). Figure adapted from Ref. [48].

Adaptive brachytherapy treatment planning

Motivated by tumour volume regression, especially during the first weeks of EBRT treatment and to a minor extent during brachytherapy, and other anatomical changes such as internal organ movement, adaptive/time-dependent treatment planning has gradually been introduced [7, 19]. In image-guide adaptive BT (IGABT) the use of repeated volumetric imaging allows for dose adaptation and escalation based on tumour response, whilst conforming the dose to OARs to set constraints [19, 28, 29]. Using IGABT, several multicentre studies as well as mono-institutional studies have demonstrated that excellent local control is achievable for small and well-responding tumours, i.e. stage IB1-IIB or typically 20-50 mm in diameter, with (estimated) local control rates ranging approximately between 86-98% at 3 years [28, 29, 51–53], and 91-98% at 5 years [29, 54]. Also for locally advanced carcinomas IGABT shows promising outcomes, e.g. 77%–82% (estimated) local control at 3 years for FIGO-stage IIIB patients [28, 29, 52]. Severe tissue morbidity actuarial rates, i.e. G3-5, of OARs for IGABT after three years are nevertheless low and range between 2-12% [28, 29, 55, 56]. Both retrospective and more scarce prospective analyses indicate a major improvement in outcome for these (adaptive) volume-based approaches over conventionally used two-dimensional treatment planning methods [28, 29, 53, 57, 58].

However, in the case of even more challenging carcinomas typically characterised by: (i) high FIGO-stage (FIGO ≥IIIA), (ii) large size (diameter >50-70 mm or volume >30 cm^3), (iii) extensive (para)vaginal or parametrial involvement, and/or (iv) limited response to EBRT, the ability to achieve a high dose conformity of treatment planning alone with standard intracavitary applicators is limited. The incidence of these especially challenging carcinomas is unknown, but possibly concerns up to a coarsely estimated 20% of all patient cases treated with BT. In the study by Schmid et al. parametrial remnants were present in the majority (77%) of parametrial spaces investigated of patients with FIGO stage IIB or IIIB at the time of BT [59]. Residual tumour (GTV_{res}) was still present at BT in 45% of the cases of patients with tumours initially extending to the outer third of the parametrial space. In the study by Jastaniyah et al., residual distal disease or disease extending to the pelvic side wall was present at the time of BT in 16% of the patients staged IIB or IIIB [60]. In the case of these locally advanced or challenging carcinomas the local control rate of IGABT is slightly lower and around 75-79% at 2-3 years or 72-76% at 5 years with standard intracavitary applicators [29, 52, 57, 61, 62]. These findings must be cautiously interpreted as in these studies different treatment approaches (not all of these include adaptive planning), treatment modalities, applicator types, treatment schedules, follow-up time,

adjuvant treatment, and treatment planning related parameters such as prescription volumes or dosimetric constraints among others have been considered. Nevertheless, in a mono-institutional study the only prognostic factors significantly affecting local control in multivariate regression were tumour size, FIGO-stage and whether volume-based treatment planning was used [63].

Although IGABT limits the occurrence of severe morbidity, a high occurrence of low to moderate morbidity grades, i.e. G1-G2, is still observed with current treatment plans and modalities, including forms of vaginal morbidity (around 75% incidence of grade $\geq$1, and 22% of grade $\geq$2 at 2 years), and urinary morbidity (40% incidence of G1, and 10% incidence of G2 at 3 years) [30, 64]. The occurrence of this mild to moderate tissue morbidity should not be neglected, as it has shown to impact the patients' quality of life several years after treatment [65].

1.3.2 Evolution of brachytherapy applicators

Intracavitary applicators

Temporary intracavitary (IC) applicators (Figure 1.5a) have long been the most common tool for placing radioactive sources in proximity of the tumour and are inserted in the vaginal or uterine cavity. Several commercially available types can be distinguished including tandem and ring (T/R), tandem and ovoid (T/O) and tandem and cylinder applicators [7]. The choice of applicator is mainly dependent on the patient's anatomy and the topography of the tumour. As modelling has shown for interstitial applicators, the centrally located tandem is essential to deliver adequate dose to the central region of the tumour, to additionally provide dose to the parametria and to extend the dose superiorly to the applicator [66, 67]. In general T/O applicators likely result in higher OAR doses and larger treated volume than T/R applicators [68], but short term toxicities are found to be similar for both types [69]. However, as mentioned, the ability of these applicators to treat challenging tumours whilst sparing OARs is limited. Tumour modelling has shown that T/R applicators enable an adequate coverage for 60% of the tumours [70].

Interstitial applicators

Interstitial (IS) templates (Figure 1.5b) can guide needles that are afterloaded in a parallel or oblique direction into tumour tissue [74]. Previously, this concerned standardised templates such as the MUPIT, Syed-Neblett and more recently the Benidorm template for locally advanced carcinomas, whereas personalised interstitial templates are under development. In a recent systematic review, the local control rate, 79%, with median follow-up ranging between 14-55 months, and occurrence of G3-G4 toxicity, 12%, were found to be similar for IS templates to that of IC applicators [74]. The advantage of the higher freedom of source placement with IS templates than with commercially available IC applicators has been illustrated in computer simulation and patient studies, showing better target coverage in the parametrial, paravaginal or paraurethral regions of large advanced tumours with similar or better sparing of the OARs as long as a central tandem is still provided [66, 67, 75]. Commonly cited disadvantages of IS techniques include loss of dose conformity due to possible needle deflection or other inaccuracies in source placement, comfort of the patient during treatment as they are largely bed-bound, and the required experience for the procedure [10, 76, 77].

Hybrid intracavitary/interstitial applicators

In order to treat tumours with an unfavourable topography including parametrial extension or asymmetry by enabling greater freedom of source placement, combined intracavitary/interstitial (IC/IS) applicators have been introduced [78]. The first of this type of hybrid applicators were standard IC applicators which included holes in the ring such that needles could be inserted in a direction parallel to the tandem, e.g. the Vienna applicator [79], or ovoids, e.g. the Utrecht

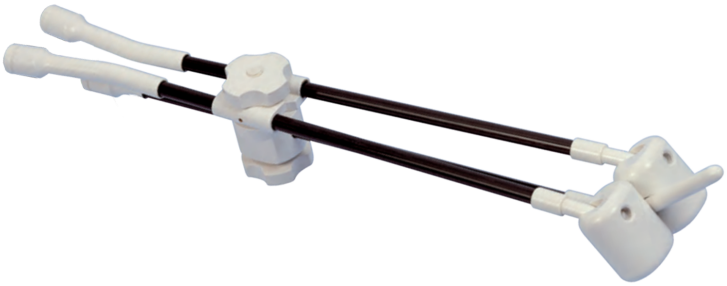

(a) Standard CT/MR tandem-ovoid IC applicator (Elekta, Stockholm, Sweden). Figure adapted from Ref. [71].

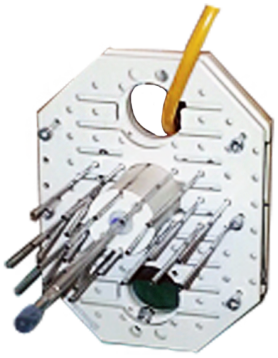

(b) Martinez Universal Perineal Interstitial Template (MUPIT, Elekta, Stockholm, Sweden). Figure adapted from Ref. [72].

(c) Utrecht IC/IS CT/MR Applicator (Elekta, Stockholm, Sweden). Figure adapted from Ref. [73].

(d) Customised 3D printed prototype IC/IS ARCHITECT applicator. Figure adapted from Ref. [48].

Figure 1.5: Developments in brachytherapy applicators for the treatment of cervical cancer.

applicator [51]. To further increase the span of the high isodose volume, oblique needle paths were later introduced in T/R or T/O applicators [80, 81]. Most of the needles are inserted through the latero-posterior positions [51, 82], which corresponds to common infiltration patterns [59, 83]. Whereas the planning-aim isodose volume of IC applicators at the height of point A typically extends to around 25 mm from the tandem, oblique needle IC/IS applicators enable extension up to 45 mm covering up the full parametrial space [7, 79, 80, 82]. With simplified computer models it has been suggested that with IS needles in a hybrid applicator the planning-aim isodose volume could be increased to sufficiently cover the target region in almost all patient cases [70, 84]. Accordingly, in challenging cases IC/IS applicators can increase the dose to the CTV-T_{HR} [51, 81, 85], and result in high local control rates (76-92% at 3 years or 72-87% at 5 years) [78, 83].

Patient-tailored applicator design

Despite that commercially available applicators are able to achieve high dose coverage of the tumour in the majority of patient cases, these still lack the adaptability to achieve high dose conformity in all patients as these are confined to positioning the BT sources in standard configurations. Therefore, recently personalised applicators have been developed. To adapt

applicators to an individual's anatomy, pioneering work was based on the vaginal mould technique [86]. Recent developments for cervical cancer BT applicators have been in the field of 3D printing (Figure 1.5d), including: (i) channelled applicators shaped to fit the vaginal cavity [48, 87–90], (ii) individualised cylindrical applicators [91, 92], (iii) customised templates for IC/IS applicators [93–95], and (iv) 3D-printed shielding [96]. The benefits of these personalised applicators include among others: (i) increased dose conformity [87, 93, 95, 97], (ii) reliable and comfortable placement without requiring vaginal packing even for patients with irregular vaults [86], (iii) improved needle guidance and minimisation of the number of needles, and (iv) adaptability to the changing anatomy throughout treatment.

The current procedure of the ARCHITECT personalised BT applicator is described in the article by Laan et al. [48], and involves: (1) imaging and segmentation of the anatomy possibly with a 'dummy' applicator in place, (2) constructing the applicators outer surface from segmentation of the vaginal vault, (3) manually indicating and interpolating needle channels, and (4) including additional structures for reconstruction or a central 'tandem' channel (Figure 1.6). The needle channel planning process is currently performed manually, and is therefore highly dependent on the oncologist's experience, is time-consuming, and might result in kinematically infeasible or non-optimal channels. Moreover, this procedure is separated from treatment planning, such that simultaneous optimisation of the applicator design and treatment plan cannot be performed. Automated needle channel planning is needed to enable optimal patient-tailored plans and is therefore crucial in the development of these personalised applicator designs.

1.4 Uncertainty in cervical cancer BT

1.4.1 Sources and magnitude of uncertainty

A general overview in which uncertainty components in brachytherapy are identified and their magnitude estimated has only recently been presented in the articles by Kirisits et al. [98], and Tanderup et al. [99], focusing on gynaecological cancer IGABT specifically.

For cervical cancer BT, total uncertainties of 12% and 21–26% ($k = 1$) in the delivered dose for a single fraction were estimated for the CTV_{HR} and OARs, respectively [98, 99]. This uncertainty budget was composed of uncertainty in: (i) source strength, (ii) dose and DVH calculation (i.e. treatment planning), (iii) dose delivery including applicator reconstruction and source positioning,

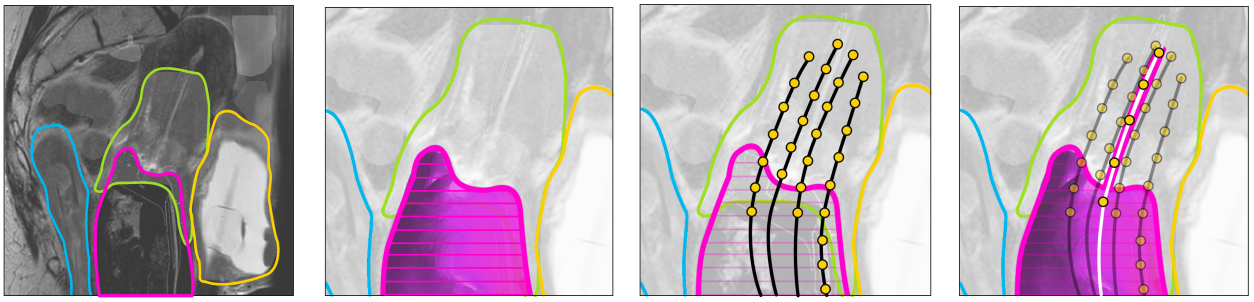

(a) Step 1: Segmentation of CTV_{HR}, OARs and vaginal cavity.

(b) Step 2: Applicator surface generation from concatenated contours.

(c) Step 3: Manual channel indication and interpolation.

(d) Step 4: Addition of other structures such as central tandem.

Figure 1.6: Process steps in generating the personalised 3D-printed ARCHITECT applicator. Shown are: CTV_{HR} (bright green —), bladder (gold —), rectum (blue —), applicator outline (pink —), source channels (black —), and sources (gold dots ●). Figure adapted from Ref. [48].

(iv) DVH addition across fractions, (v) contouring, and (vi) inter- and intra-fraction changes including applicator movement and anatomical changes. In the editorial by Tanderup et al., it was argued that the uncertainty budget of the target volume is dominated by contouring uncertainty (SD = 9%, $k = 1$), whereas the major contributors to the total dosimetric uncertainty of the OARs are intra- and inter-fraction uncertainties (SD = 20 – 25%, $k = 1$) [9]. Reduction of these dosimetric uncertainties was thought to improve clinical outcome of treatment. Therefore, Nesvacil et al. investigated the clinical impact of different types of uncertainty components and the magnitude [38]. The simulated local control of the target volume subject to the aforementioned levels of uncertainty decreased only marginally, i.e. <1%. For OARs, the clinical impact of dosimetric uncertainty on the simulated tissue complication probability may be larger, i.e. <5%, as was demonstrated for the rectum at typical prescription doses.

1.4.2 Current strategies in brachytherapy in reducing the impact of uncertainty

Several strategies to reduce the dosimetric variation in radiotherapy and brachytherapy include margin-based planning, stochastic treatment planning optimisation and robust treatment planning optimisation [100]. In radiotherapy, margin-based approaches where the clinical target volume is extended by a -often isotropic- safety margin to obtain the planning target volume are still the standard [7, 101]. However, population-based margins can be ill-suited at the individual patient level, and for that reason patient-specific or adaptive margins have been proposed [102, 103]. Whereas such an approach is suitable for radiotherapy, in brachytherapy only margins along the tandem direction of an applicator may be implemented to compensate for uncertainty due to the dose gradient [39]. Nonetheless, 3D-printed applicators, which have more freedom in the dwell position placement than conventional applicators, could possibly open up a new field in determining BT margins to partially account for uncertainty, but this is as of yet unfeasible.

Rather than 'hard' constraints that are established when using margins, several articles in radiotherapy have modelled uncertainty using an a priori known or partially known probability distribution and optimised the treatment plan, conventionally known as stochastic or probabilistic treatment planning optimisation [100]. In this type of planning, the effect of dosimetric uncertainties is directly included in the optimisation, for example by implementing probabilistic objective functions [104]. Although it has been demonstrated that such plans can achieve greater conformity, one limitation of probabilistic treatment planning optimisation is that the underlying probability distributions have to be known [100, 102]. Moreover, with stochastic programming the computation may quickly become intractable, known as the 'curse of dimensionality' which depends on the number of constraints and the formulation of the objective function [100]. A stochastic optimisation method has not yet been implemented for brachytherapy. Robust optimisation[1] is an alternative to stochastic optimisation, where rather than representing the uncertainty by a probability distribution, a set of - typically worst-case - values for the uncertainty is selected and only robustly feasible solutions are sought [100]. Although worst-case robust optimisation does not require a priori probability distributions to be known, and is generally more computationally tractable than stochastic optimisation, the solution is often overly conservative [100]. Therefore, approaches to reduce this conservatism have frequently been the topic of investigation.

[1] 'Robust' optimisation is in the definition in radiotherapy often synonymous with (possibly 'worst-case') optimisation where uncertainty parameters reside in a (non-probabilistic) bounded uncertainty set. Note that 'robust' in general means that a method is relatively unaffected by changes in parameters.

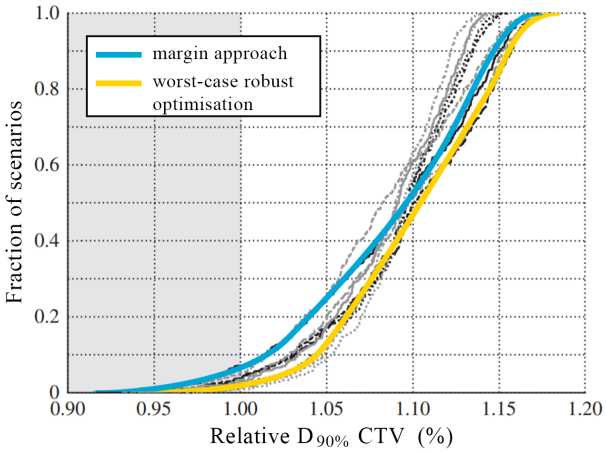

(a) Frequency of obtaining a specific planning-aim CTV dose under delineation uncertainty with either a margin approach or worst-case robust optimisation for a single patient. Figure adapted from Ref. [100].

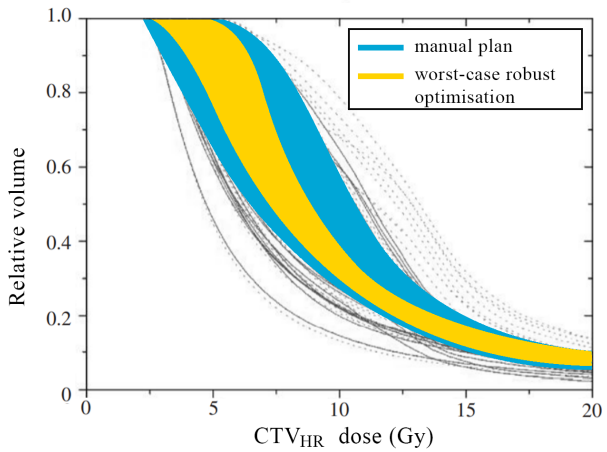

(b) Dose volume histograms for the CTV_{HR} with either a manual treatment plan or as obtained using worst-case robust optimisation. Figure adapted from Ref. [109].

Figure 1.7: Schematic illustrations of the benefits of worst-case robust treatment planning for brachytherapy over conventional treatment planning techniques in the presence of uncertainty.

As of yet, to the best of the author's knowledge, three groups have applied worst-case robust optimisation to treatment planning for brachytherapy. In the article by Balvert et al., and in the preceding work in their group done by Gorissen et al. [105], worst-case robust optimisation was used to account for delineation uncertainties in prostate brachytherapy [100]. These authors found that worst-case robust optimisation led to an improved target coverage compared with a margin approach under delineation uncertainty (Figure 1.7a), whereas the risk of overdosing the rectum was reduced [100]. In the recent manuscript by Jo et al., worst-case robust optimisation was shown to maintain a sufficient target dose with improved OAR sparing in comparison with manual or inverse optimisation plans under applicator positioning uncertainty [106]. In addition, the bandwidth of the DVH diagram decreased for the worst-case robust approach, i.e. the range of DVH variation, in comparison with manual treatment planning (Figure 1.7b). Lastly, van der Meer and colleagues performed robust multi-objective optimisation with an evolutionary algorithm to account for both catheter displacements as well as organ reconstruction uncertainty in two separate decision phases: (1) catheter position planning, and (2) dwell time planning [107, 108]. These authors showed that their algorithm, combining worst-case robust optimisation over organ reconstructions and catheter positions, was capable of replicating the optimisation front using dwell time optimisation alone, thereby illustrating the feasibility of combined/simultaneous catheter and dwell time planning.

These examples present likely evidence that robust treatment optimisation is able to lower the dosimetric and clinical impact of inter-fraction and contouring uncertainties. However, in most cases this type of treatment planning optimisation is still restricted to a finite fixed set of dwell positions, and rather is only able to modify the dwell times. In this case, the necessary precondition to enable full compensation of dosimetric uncertainty is that the placement of these dwell positions is optimal, as treatment planning itself may never be able to fully correct for non-ideal source placement [110]. For example, as illustrated by van der Meer et al. although for a few patients, treatment optimisation only considering dwell time planning may result in plans with lower conformity compared to those with optimised catheter positions [107, 108]. Moreover, these authors showed that worst-case robust

optimisation of catheters and dwell times can be used to generate realistic dosimetric plans, i.e. representative for those generated in the stage of dwell time optimisation, already in an early treatment stage [108]. Robust optimisation, in the form of worst-case optimisation or stochastic optimisation, of BT source channels may therefore be considered in the applicator development stage to enable accurate plans in the dwell-time planning phase.

1.5 Rationale for robust applicator design and treatment planning

With current commercially available BT applicators the ability to optimise the dose conformity is limited for cervical cancer patients with advanced tumours [48]. In these patients current image-guided therapy results in suboptimal local control and tissue morbidity. Additionally, despite that systematic dosimetric variation of OARs is limited to $< 5\%$, large random variations (SD = 20-30%, $k = 1$) have been shown to impact the delivered dose to OARs [98, 99, 111], and the predicted occurrence of normal tissue complications [38]. The clinical outcome of BT may be improved through more sophisticated applicator design and robust treatment optimisation. The former requires automated needle channel planning software, for which currently only non-robust variants have been introduced. The latter, although shown to be able to improve the dose conformity and robustness against the dose delivery errors, relies on the precondition that dose optimisation is fully able to correct for suboptimal dwell positions. It is likely that this is not always possible [110]. In this thesis, the freedom of source placement that 3D-printed applicators allow and the principle of robust treatment optimisation are leveraged to develop robust needle channel planning software for personalised applicators. This new type of applicators is expected to improve the dose conformity and clinical outcome of treatment.

1.6 Thesis structure

This thesis is structured in three parts reflecting the three major aims of this study:

1. **Part I:** This part provides an overview of dosimetric uncertainties, estimates their clinical impact on brachytherapy for cervical cancer, and accordingly makes a case for the implementation of robust planning software in the development of patient-tailored brachytherapy applicators. The following research questions were therefore formulated:

   (i) What are the magnitudes of individual dosimetric uncertainty components in cervical cancer BT?
   (ii) What is the impact of different types of dosimetric uncertainty on the clinical outcome of treatment?
   (iii) How can these clinical outcomes be cast into a mathematical optimisation problem suited for motion planning (MP)?

2. **Part II:** The selection of an applicable MP algorithm from the myriad of options available given this heuristic or mathematical problem formulation is generally difficult for one unfamiliar with MP. Therefore this part aims to answer the research questions:

   (iv) How can we support the decision-making process of a user in the selection of a single alternative from a set of viable alternatives given a trivial problem formulation and a set of requirements?
   (v) What robust MP algorithm class could potentially achieve the highest user satisfaction and conformance to the BT needle channel planning problem?

3. **Part III:** In the final part, several robust MP algorithms from the selected MP class are developed, implemented and evaluated for the BT needle channel planning problem under uncertainty. The following research were treated in this part:
   (vi) Which variants in the selected MP class have been introduced and how can their operating principles and implementations be leveraged to establish planners that are suitable for the MP of needle channels subject to uncertainty?
   (vii) How can we implement these MP algorithms in a simulated patient case study and what are the potential benefits of (robust) MP for patient-tailored BT applicators over conventional BT applicators?

Additionally, this thesis aims to stimulate communication between the different disciplines that are involved in brachytherapy. A uniform terminology has therefore been introduced for several of the topics, including brachytherapy (Section 1.2), uncertainty (Appendix A.3), and motion planning (Section 4.1). Used symbols throughout this thesis are shown in Section 0.1-0.3. Figures adapted from literature have been recoloured for consistency. As to encourage readers to reproduce the author's computer-generated figures, several MATLAB (MATLAB R2020a, MathWorks, Natick, MA, USA) scripts are provided in Appendix A.1.

2. The impact of uncertainties in cervical cancer BT

2.1 Background

Only in recent years the interest in the identification and analysis of uncertainties in BT burgeoned, opposed to EBRT where uncertainties have been investigated and addressed over the past several decades [99]. It may be postulated that this is the consequence of uncertainties being smaller in BT than EBRT as a result of the proximity of the sources in the former [98], and due to lesser tumour regression occurring during the course of treatment [112, 113]. However, due to the steep dose gradient in BT, even the slightest inaccuracies may lead to (clinically) significant dosimetric uncertainties [99]. Moreover, the assumption that a BT intracavitary applicator and tumour, possibly combined with the surrounding organs and normal tissues, constitute a stable system when an appropriate implant is used [114], has only recently been questioned. Lastly, in BT the dose distributions are non-uniform in the target region, and therefore are profoundly different from the ones generated by EBRT [39, 111]. Hence, considerations and approaches used for EBRT to reduce uncertainties may not be applicable to the field of BT. Therefore, this chapter provides an overview of the uncertainty components and their magnitude in the field of BT, the clinical impact of these uncertainties and strategies to reduce uncertainty in the procedure. Relevant general terminology for this chapter regarding uncertainty is for conciseness given in Appendix A.3.

2.2 Methods

2.2.1 Classifying uncertainty components in brachytherapy

Previous work in uncertainty component classification

In several works, classifications for uncertainty components in brachytherapy and radiotherapy have been provided. In the review by Kirisits et al. [98], and the related work by Tanderup et al. [99], uncertainty components were identified through expert consensus and quantified through a review of literature for brachytherapy in general and for cervix cancer IGABT respectively. In these two articles, uncertainty components were distinguished based on the steps of the brachytherapy procedure from calibration to delivery, being: (i) source strength, (ii) dose and DVH calculation (i.e. treatment planning), (iii) dose delivery including applicator reconstruction and source positioning, (iv) DVH addition across fractions, (v) contouring, and (vi) inter- and intra-fraction changes including applicator movement and anatomical changes [98, 99]. An even more elaborate example of uncertainties that may be distinguished in brachytherapy per step can be found in Table 11.5 in Ref. [115]. Although the articles by Kirisits et al. and Tanderup et al. provide clear overviews of the dosimetric uncertainty budget in brachytherapy, due to the aforementioned advances in brachytherapy, imaging, and treatment planning in recent years this review of the magnitudes of uncertainty must be updated. Additionally, only dosimetric variation as the result of random errors is considered in these two articles, possibly as dosimetric uncertainty from systematic errors was found to be of a smaller magnitude than that of random errors in a preceding multicentre study [111][1]. However there are indications that the clinical impact of systematic and random components is different [38], similar to radiotherapy for which

[1] An alternative reason might lie in terminology, as when defining uncertainty as the dispersion of measurements quantified using standard deviations, variation from systematic errors is not classified as uncertainty per se.

this has been demonstrated [35, 101]. For this purpose, next to the classification based on nature of the uncertainties, a further distinction between systematic and random components of uncertainty is proposed based on the underlying error type. This enables a calculation of the clinical impact of uncertainties, similar to the methodology used in the work by Nesvacil et al. [38], and a report by the IAEA [35]. Lastly, the development and implementation of personalised applicators additionally brings about other uncertainty considerations which are discussed in this chapter.

Some other classifications have been proposed. Nesvacil et al. distinguish between technological uncertainties, and uncertainties related to the workflow and anatomy of the patient [38]. Similarly, a joint working group differentiate accuracy requirements in numerical, physical and clinical dose delivery accuracy [116]. Although these are theoretically useful, in practice these components are intertwined and do not allow this separation [117]. A distinction between uncertainty in: (i) dosimetry, expressed in absorbed dose in Gy, EQD2 or a percentage of the dose, and (ii) geometry, typically expressed in mm, is often made in radiotherapy [35, 118]. In brachytherapy however, translating geometric errors to dosimetric impact is difficult. Although Tanderup et al. showed that applicator reconstruction uncertainty in translation in all directions and rotation in the transversal plane linearly influenced DVH parameters [119], this may not be the case when also accounting for other rotational directions for the CTV_{HR} and some other OARs [120]. Similarly, little is known about the clinical effect of these geometrical uncertainties [35]. For that reason, this work will focus on dosimetric uncertainty directly instead of deriving this from geometric uncertainty estimates.

Uncertainty from systematic and random errors

In radiotherapy, systematic errors are the errors that influence all treatment fractions of the radiotherapy course in a systematic, i.e. a similar, way, hence are often referred to as treatment preparation errors [121]. Random errors, or treatment execution errors, signify day-to-day variations or between sessions. This classification is useful, as in radiotherapy these two error components have a different effect on the absorbed dose [35, 101, 121]. In brachytherapy a similar definition is used, where systematic uncertainty -i.e. stemming from systematic errors- is of similar magnitude and direction throughout all treatment fractions, and random uncertainty -i.e. stemming from random errors- differ between fractions [98, 111]. Typically, in brachytherapy systematic and random errors are approximated as the average mean, M_p, and standard deviation (SD), σ_p, of a sample population's differences in dose or spatial location between time points, e.g. between fractions, respectively [111], in a so-called two-parameter model [122]. This is different from common practice in radiotherapy, where in a four-parameter model: (i) the group systematic error, M, is calculated via the mean of the means, i.e. mean-of-means, of individual patients' error statistics over multiple time points, (ii) SD of the systematic error due to inter-patient differences, Σ, is estimated as the standard deviation of the means of individual patients' error statistics, and (iii) the SD of the random error in between fractions, σ, is estimated from the root-mean-square (RMS) of the SDs of individual patients' statistics [101, 122][2]. Additionally, the SD of the SDs of patients' errors can be computed, σ_σ, which is a measure of the intra-fraction variability of σ [123], although in practice this cannot be estimated in this way as this requires numerous fractions per patient [124]. A two-parameter model is appropriate if used to describe the error characteristics for the entire population, whereas the four-parameter model allows for individual patient describing information [122].

[2]RMS is used as the number of measurements per patient is finite and thus a residual error persists [101].

Table 2.1: Example calculation of statistical parameters describing the random an systematic errors from a set of patient data for several fractions. MATLAB code for this calculation is given in Script A.1.5. Note that the data in this table represents geometric errors, but the calculation is the same for different types of variables. Adapted from van Herk [101].

	Patient 1		**Patient 2**		**Patient 3**			
	x (mm)	y (mm)	x (mm)	y (mm)	x (mm)	y (mm)		
Fraction 1	2	3	1	0	-2	-3		
Fraction 2	3	3	2	0	-2	-2		
Fraction 3	2	2	0	2	-1	-3		
Fraction 4	3	2	-1	1	-2	-2	**Statistics**	
Mean	2.50	2.50	0.50	0.75	-1.75	-2.5	$M_x = 0.42$	$M_y = 0.25$
							$\Sigma_x = 2.13$	$\Sigma_y = 2.54$
SD	0.58	0.58	1.29	0.96	0.50	0.58	$\text{RMS}_x = 0.87$	$\text{RMS}_y = 0.73$
							$\sigma_{\sigma,x} = 0.44$	$\sigma_{\sigma,x} = 0.22$

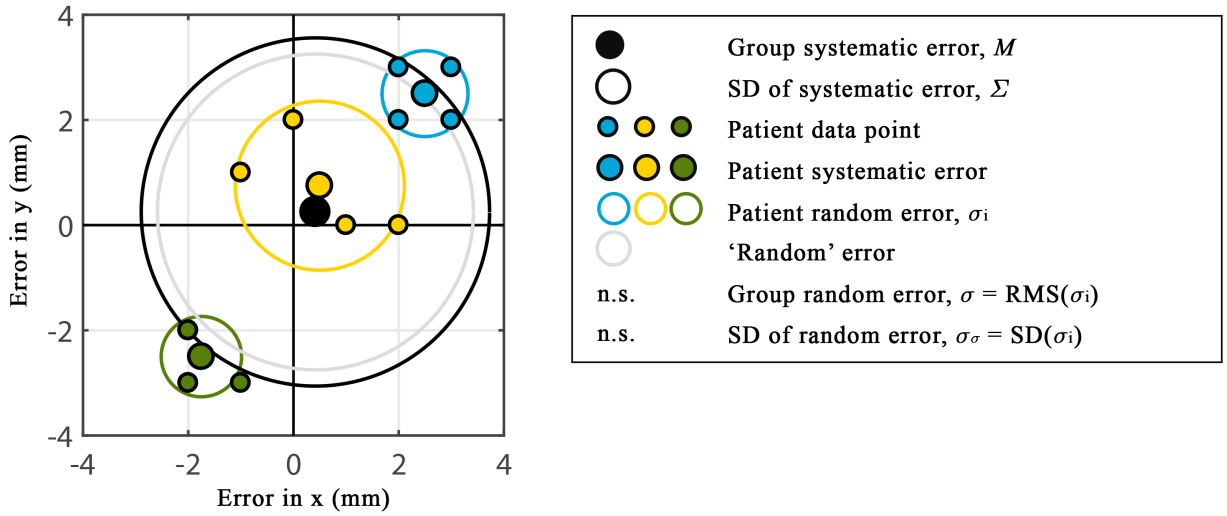

Figure 2.1: Illustration of error components from the data in Table 2.1. The MATLAB script for generating this figure is given in Script A.1.5. The group systematic error M is equivalent with the 'systematic error' in brachytherapy literature. However, this only describes the mean of the group systematic error, as the result of a consistent setup error. Due to patient heterogeneity in the sample this group systematic error is distributed with Σ. The group random error does not have a zero mean for a finite number of fractions, and is therefore described with a mean, σ, and standard deviation σ_σ. The 'random' error in brachytherapy is a measure of the total spread within the sample. Adapted from Ref. [101, 125]. n.s. = not shown.

In previous works in brachytherapy the term 'systematic uncertainty' corresponds to the effects of the group systematic error M. The 'random uncertainty' in brachytherapy literature does not have such an equivalent in radiotherapy, other than that it represents the total spread of the data. Its underlying random error is called the 'overall random error' in the remainder of this work[3]. In Figure 2.1 and Table 2.1 it is shown that by deeming the group systematic error M equivalent to the systematic error, as is done in brachytherapy literature, one neglects the presence of inter-patient differences. Indeed, in Figure 2.1 it may be seen how two of the patients (patient 1 and 3) have a significant bias as measured from the origin, but that this is cancelled out when taking the mean

[3]One may relate this overall random error to the other mentioned components via: $\sigma_p = \sqrt{\Sigma^2 + \sigma^2}$ [122].

of the three individual systematic errors. The overall random error in BT literature overestimates the spread of values around the individual patient mean. Use of the four-parameter model in BT uncertainty reporting would be helpful for improving the accuracy of treatment. Whether the four-parameter model may be used for brachytherapy, e.g. with three imaging sessions, has not been investigated properly. For example, Hellebust et al. showed the effect of repetitive imaging on the inter-fraction variation [126], where for a limited number of fractions a large residual persists, i.e. non-zero mean, dominating the random error. Such a model may possibly be only accurately applied for an arbitrarily set bound of $N \geq 4$ fractions [98].

Intra-fraction, inter-fraction and inter-application uncertainty

In radiotherapy, inter-fraction and intra-fraction uncertainty are often distinguished, whereas in brachytherapy this may be confusing as also inter-application uncertainty is acknowledged, which corresponds to the concept of inter-fraction uncertainty in radiotherapy [45]. Inter-application overall random uncertainty, as assessed based on imaging between two insertions, has been found to be of larger magnitude than intra-application uncertainty [111]. This may be explained by the difficulty in replicating the applicator's position, which significantly affects the surrounding tissues' topography [22]. Furthermore, the tumour regression in between applications may be larger than when measured between fractions [112]. Moreover, in the case of a IC/IS applicator the applicator's geometry is not reproducible between two insertions, and hence for each insertion of a IC/IS applicator it is recommended to generate a new image set and use this for treatment planning [7]. The minimisation of this type of uncertainty through a change of planning schedule has been the subject of multiple studies [79, 127–129]. In previous uncertainty budget analyses inter-application uncertainty is not included [98, 99]. For the development of patient-tailored BT applicators estimating the changes between two insertions is of importance. The applicator design is generated based on imaging of a different insertion/application than the imaging used for treatment delivery, with a dummy applicator or only gauze packing.

Proposed classification of uncertainty components

In this work rather than calculating a value representing the 'total' uncertainty, only the magnitude of individual uncertainty components is assessed. The usual model to depict the effect of uncertainty components in radiotherapy is the 'chain of radiotherapy', a serial construct which is based on the presumption that its weakest link determines the total accuracy [130, 131]. However, such an analogy does not include the complex interplay of uncertainty components, nor does it include the possibly unequal contribution of components on the clinical impact. Furthermore, uncertainty at some stages may be mitigated through correction, such as image guidance, or other strategies. Software capable of propagating uncertainty for more complicated 'what-if' scenarios has been developed for radiotherapy [115]. Uncertainty propagation models for brachytherapy do not exist as of yet.

Consider a single brachytherapy applicator insertion, with one imaging session and two delivered fractions, whereas the full brachytherapy treatment delivers four fractions over two insertions and imaging sessions (see Figure 1.2). Possible sources of dosimetric variation in chronological order of occurrence, mainly based on the works by Kirisits et al. and van Dyk et al. [98, 115], are illustrated in Figure 2.2. Although this list contains redundancy due to the interwoven character of the uncertainty components, it provides a simple basis for uncertainty analysis.

The classification of uncertainty in Figure 2.2 is based on the treatment schedule as depicted in Figure 1.2. In a fully image-guided adaptive BT approach, such as proposed by ICRU report 89

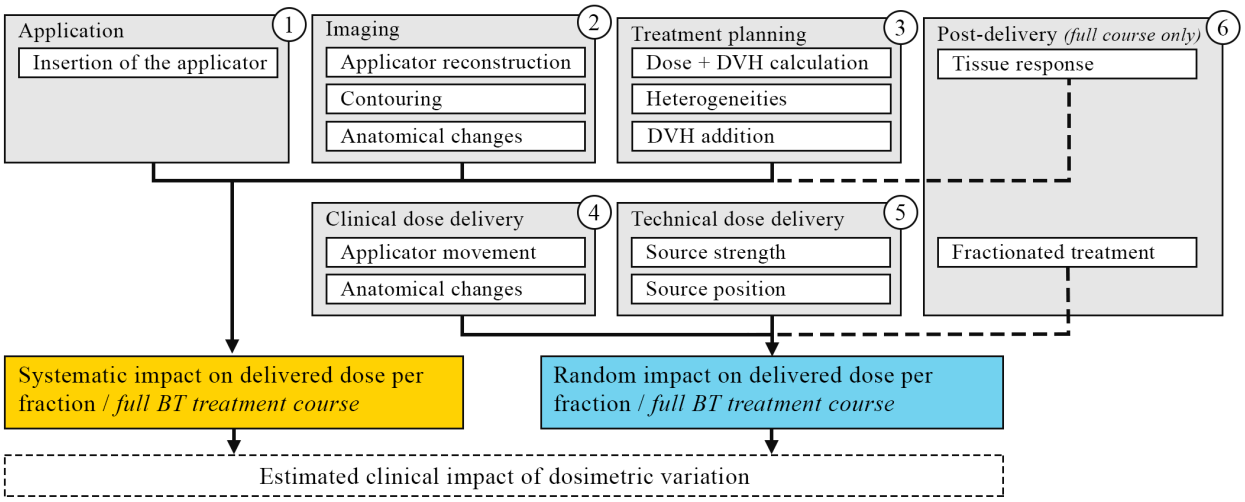

Figure 2.2: Classification of sources of variation and their components in cervical cancer brachytherapy for the treatment schedule in Figure 1.2 as used in this study. Based on previous overviews by Kirisits et al. and van Dyk et al. [98, 115].

and in several institutes practised [7], the uncertainties that are distinguished to have a systematic impact would rather be equivalent to the ones classified as having a random impact. For example, at the Erasmus MC hospital in Rotterdam the common practice is to deliver BT over three (or four) fractions spread over three weeks, each preceded with an applicator insertion and a MRI or CT imaging session. In such a schedule, for example contouring errors elicit a random impact on each fraction, opposed to a systematic impact when using one imaging session per two fractions in succession. However, the influence of random errors becomes greater when using three fractions opposed to four, i.e. by factor $\sqrt{4}/\sqrt{3}$. The effects of the treatment schedule on the delivered dose subject to uncertainty are therefore also investigated briefly in this thesis.

In this chapter uncertainty is analysed for the high-risk tumour volume ($\mathrm{CTV_{HR}}$), bladder, rectum and sigmoid. Dosimetric uncertainty in this thesis refers to the uncertainty of the $D_{90\%}$ for the tumour and D_{2cm^3} for the OARs respectively as these are standard for reporting [7]. Although the ARCHITECT applicator may allow for combined intracavitary and interstitial use, most of the analyses in this chapter focus on intracavitary applicators for the reason of data availability. Interstitial use of the applicator may be associated with greater uncertainty in the source positioning than described for intracavitary applicators, e.g. through needle deflection or errors in insertion depth [80, 81, 132]. Contrarily, a hybrid configuration is generally more stable [133].

2.2.2 Clinical impact modelling

Delivered dose and response modelling

In order to simulate the clinical impact of dosimetric uncertainty components, the models introduced in Subsection 1.2.4 are used. The implementation of other basic models has been briefly discussed in Appendix A.3.7. First, the delivered dose per fraction, $\tilde{d}$, as a function of the nominal planning-aim dose per fraction, d, and dosimetric variation, Δ may be described as:

$$\tilde{d}_{i,j} = d + \Delta_{i,j} \tag{2.1}$$

for $i = \{1, 2\}$ insertions and $j = \{1, 2\}$ fractions, assuming that the planning-aim dose per fraction is constant throughout treatment. Let us for simplicity assume that the first and second insertion

are independent, i.e. uncorrelated, events[4]. Additionally, the two fractions within an insertion are assumed to be uncorrelated events. Moreover, the systematic and random uncertainty are assumed to be normally distributed. The systematic uncertainty then persist for two subsequent fractions. Once per insertion a number is drawn from a normal distribution, with relative group mean and overall random error as defined using the two-parameter model, and is multiplied with the prescribed dose d. Due to the independence of the two insertions, the dosimetric variation due to systematic uncertainty may be expressed for each application via:

$$\Delta_{i,\text{sys}} \sim \mathcal{N}(M_p \cdot d/100, (\sigma_p \cdot d/100)^2) \tag{2.2}$$

Here, M_p is the relative group systematic error and σ_p the relative overall random error in the two-parameter model, both expressed as a percentage. Using the assumption that all fractions are uncorrelated events, the random dosimetric error would for each fraction be drawn from the normal distribution:

$$\Delta_{i,j,\text{ran}} \sim \mathcal{N}(M_p \cdot d/100, (\sigma_p \cdot d/100)^2) \tag{2.3}$$

Note that this mathematical formulation of dosimetric uncertainty uses the two-parameter model which does not include patient specific parameters.

The delivered dose from all fractions containing either a random or systematic error for a single patient is converted to EQD2 dose, the dose from 25 fractions of 1.8 Gy from EBRT are added, and the clinical impact of dosimetric uncertainty or the probability of an event, either local control or tissue morbidity, is calculated using the logit-model as described in Subsection 1.2.4. In order to establish whether an event occurs, a sample is drawn from a set containing 0 (indicating no event) and 1 (indicating that an event occurs) with the probabilities calculated in the logit-model. Next, logistic regression is applied in order to determine the curve that predicts the 'actual' dose-response relationship under uncertainty, and the curve that resembles the dose-response relationship without uncertainty. The built-in `MATLAB` function `mnrfit` is used for this purpose. Data was also fitted to Eq. 1.9 using non-linear least-square regression with `lsqcurvefit`, but both methods produced similar results (results not shown). This process is repeated to include 1,000 patients per uncertainty type. Both the mean of the resulting dose-response relationship curves and the spread of curves of individual patients are computed. A scheme illustrating the workflow is shown in Figure 2.3.

Model parameters

The radiosensitivity coefficient ratio α/β may vary for different tumour histologies or tissue types (see Appendix A.2), but in accordance with ICRU report 89 constant ratios of $\alpha/\beta = 3$ Gy for OARs and $\alpha/\beta = 10$ Gy for the CTV_{HR} throughout treatment are assumed [7]. The parameters for the logit-model are: γ_{50}, the normalised dose-response gradient at 50% response, and TCD_{50}, the dose for 50% response. In their 2016 work, Nesvacil et al. derived $\gamma_{50} = 0.47$ and $\text{TCD}_{50} = 36.0$ Gy for the CTV_{HR} from the data of a large multi-institutional patient study [38]. However, it is known that larger inter-patient variability in data will cause the overall population dose-response curve to be less steep, i.e. decreasing γ_{50}, than the case for a more stratified population [35]. Therefore, the value of γ_{50} as used by Nesvacil et al. for the CTV_{HR} dose-response relationship may result in an estimated lower clinical impact of the dosimetric uncertainty than would be at patient level or for a more stratified population. Indeed, in other studies the dose-response gradient γ_{50} was found to lie around 0.5-2.1 for cervical cancer, with a TCD_{50} of around 25-60 Gy providing a good fit to clinical data [36, 44, 134]. Values of $\gamma_{50} = 1.0$ and $\text{TCD}_{50} = 60.0$ Gy, which are in accordance with the findings by Dimopoulos et al. [44], are

[4]This is a heavy simplification, for example neglecting the possible presence of patient-specific errors.

therefore implemented as well in this study for comparison with the results obtained using $\gamma_{50} = 0.47$ and $\text{TCD}_{50} = 36.0$ Gy.

The description of the parameters involved in the prediction of tissue complications for the bladder, rectum and sigmoid from the planning-aim D_{2cm^3} using a logit NTCP model are scarce. In contrast, parameter data for other models such as the LKB probit-model [135], or the relative seriality model [136], and other treatment modalities have been well-described. Nesvacil and colleagues have used $\gamma_{50} = 2.0$ and $\text{TCD}_{50} = 110$ Gy to relate the occurrence of late rectal side effects to the D_{2cm^3} in a logit-model [38]. However, these authors did not generate dose-response relationships under uncertainty for other OARs. In order to provide a reasonable estimate of the parameters for other OARs, the logit-model in Eq. 1.9 was fitted to the probit-model with data by Burman et al. [135], such that the following approximate results are established: (i) $\gamma_{50} = 4.0$ and $\text{TCD}_{50} = 80$ Gy for the bladder, (ii) $\gamma_{50} = 3.0$ and $\text{TCD}_{50} = 80$ Gy for the rectum, and (iii) $\gamma_{50} = 2.5$ and $\text{TCD}_{50} = 55$ Gy for the sigmoid. Note that these parameters are very rough estimates and have no direct implication, e.g. incontinence or dysuria, as the data by Burman et al. were established: (i) based on expert consensus, (ii) using radiotherapy alone, (iii) when two-dimensional imaging and treatment was common, (iv) for specific (severe) end-points, and (v) mostly assuming whole organ irradiation without regarding different functional or structural organisation or the effects of hot spots. These parameters were therefore further tuned to yield more accurate dose-response relationships. With these parameters the occurrence of bladder complications was likely overestimated, such that the parameters were adjusted $\gamma_{50} = 1.5$ and $\text{TCD}_{50} = 120$ Gy for the bladder based upon the findings of Dale et al. [137]. Similarly, the use of these parameters would result in overestimating the occurrence of sigmoid bowel complications, and the parameters were adjusted to $\gamma_{50} = 2.5$ and $\text{TCD}_{50} = 150$ Gy. The resulting NTCP models and the magnitude of the NTCP at common planning-aim dose values were in line with the $\geq$G2 complication rate in cervical cancer brachytherapy studies [28, 55, 138].

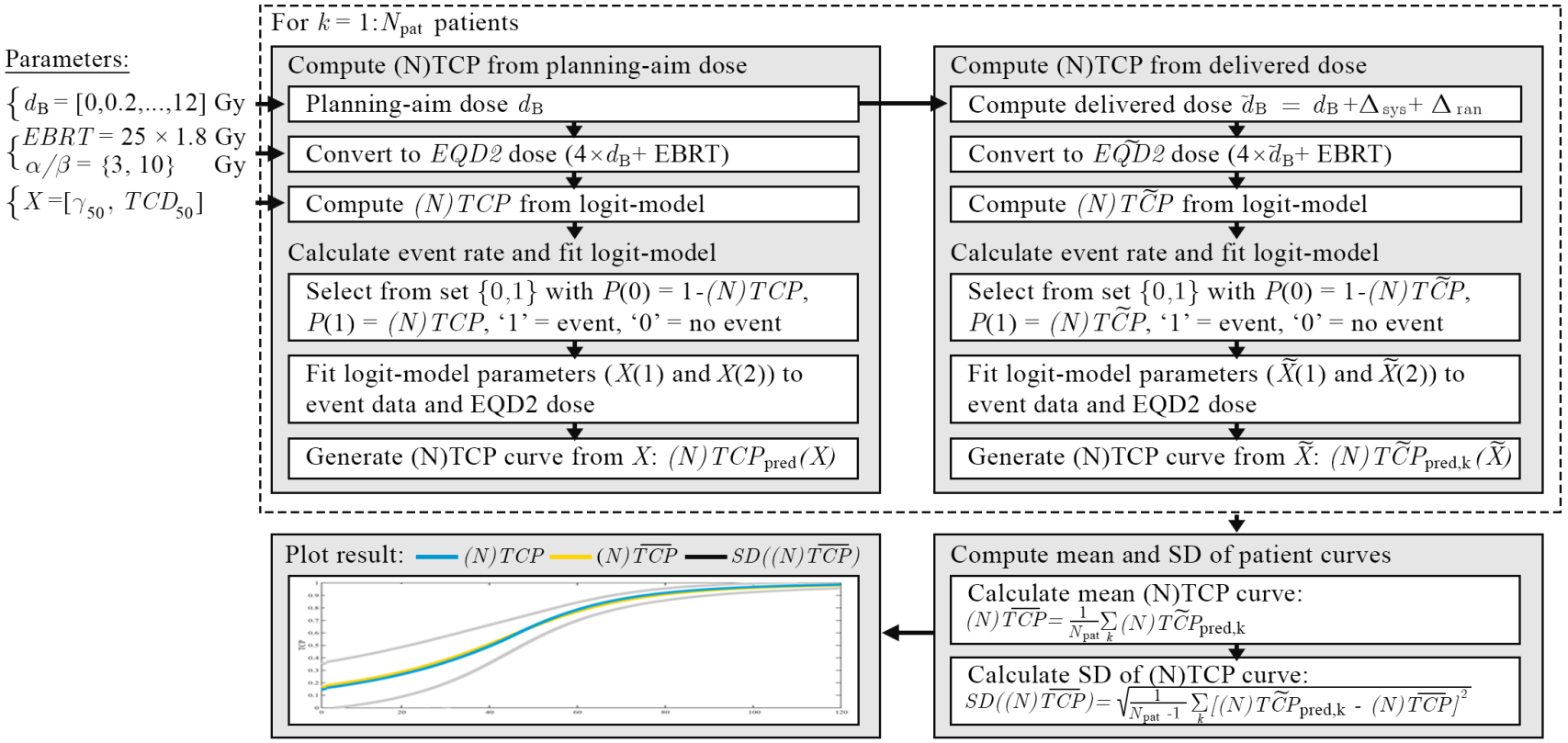

Figure 2.3: Schematic representation of the workflow for generating the dose-response relationships under uncertainty, and the reference curve without uncertainty. The accompanying MATLAB script that is used for generating these relationships can be found in Script A.1.6.

2.3 Results

2.3.1 Literature review of uncertainty components

Application: insertion of the applicator

Direct estimates of the dosimetric uncertainty associated with the reproducibility of inserting the applicator are lacking, and instead must be derived indirectly, e.g. from the differences between inter and intra-application data. That the procedure of intracavitary applicator insertion is associated with dosimetric uncertainty, may be deduced from the study by Nesvacil et al., where the overall random uncertainty was found to be greater for inter-application than for intra-application data [111], although this might be explained by other factors such as the greater time in between measurements. Both geometric variation [139–143], and resulting dosimetric variation [129, 144, 145], have been documented to occur between intracavitary applicator insertions. Placement variation between two consecutive insertions seems to be depending on: (i) the applicator type [144], although no differences between applicator types were found in the comparison by Nesvacil et al. [111], (ii) tumour size or stage [139, 146], and (iii) operator-dependent procedures and tools including the application of vaginal packing and external fixation [139, 141, 143, 144]. Jamema et al. calculated the inter-application dosimetric variation as the difference in dose between a treatment plan that is obtained from the first imaging session after the first application and applied to the second image after the second application, and the treatment plan developed specifically based on this second image [145]. The group systematic error was found to be small for the rectum and bladder D_{2cm^3} (0.6-0.9% of the planning-aim dose per BT fraction), but large for the sigmoid D_{2cm^3} (11.9%). The overall random error was found to vary between 13.1-15.1% ($k = 1$) of the planning-aim dose per BT fraction for the bladder and rectum, to 37.5% for the sigmoid ($k = 1$), likely as the sigmoid has a higher mobility than the rectum and bladder. Similar findings have been reported by Lang et al. [129], and in the multicentre comparison by Nesvacil et al. [111]. However, inter-application variation cannot be equated with the variation associated with the insertion only, as the former inherently includes organ movement effects, tumour shrinkage, and contouring uncertainty. Inter-application variation in these studies is presumably dominated by organ mobility, which has an estimated overall random uncertainty of 20-25% [99], and not by variation associated with the insertion.

It has been long known that implantation of IC applicators is frequently not ideal, which has been distinguished as an important factor for local control if no treatment optimisation is used [146–148]. Treatment optimisation however may partially be able to account for suboptimal insertion and placement of the applicator. Viswanathan et al., and Petric et al. mentioned that poor/suboptimal applicator placement cannot be corrected for using treatment optimisation alone [10, 110], but did not present direct evidence for this claim. Kissel et al. conversely noted that in their patient study suboptimal placement could be resolved in half of the patients through dosimetric optimisation and therefore did not result in lower dose to the target volume [147]. Rangarajan established no significant differences in the relevant DVH parameters if suboptimal applicator placement was adjusted to an optimal position in ten patients [68].

In the recent study by Rigaud et al. dosimetric variation due to insertion was estimated using deformable image registration, but analysis was based on a pre-planning CT without an applicator inserted (Figure 2.4) [149]. As a conservative estimate for the variation between consecutive insertions, the data from the multicentre study by Nesvacil et al. may be used [111]. This study presented the data of three centres analysing dose parameters during one applicator insertion, and three centres analysing data from subsequent applications. Assuming similar workflows for each

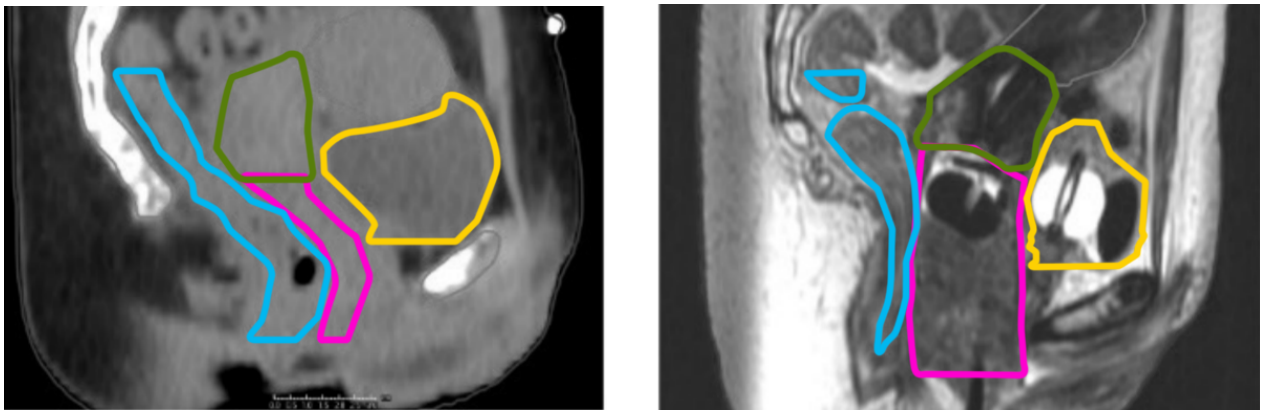

(a) Pre-BT CT without applicator. **(b)** MRI at time of BT with applicator.

Figure 2.4: CT/MR images showing the deformations induced by applicator insertion for a single patient. Between two insertions the difference in the displacement of organs would be less pronounced. Shown are: cervix (dark green —), bladder (gold —), rectum (blue —), and vaginal cavity (pink —). Figure adapted from Ref. [149].

centre, equal delivered dose in each of the fractions and no time effects -such as tumour regression- among others, one may argue that the differences between inter-application uncertainty and intra-application uncertainty are solely due to uncertainty associated with the additional insertion. This results in a relative dosimetric overall random error of 10.6%, 11.7%, 10.0% and 19.0% ($k = 1$) for the CTV_{HR}, bladder, rectum and sigmoid respectively. These random error magnitudes correspond to significant applicator shifts of several millimetres[5]. Systematic variations were in this study not found to be significantly different for inter and intra-application uncertainty [111], and hence the group systematic error is set equal to zero in this analysis. It is unknown to what extent treatment optimisation is fully able to compensate for differences of this magnitude. The effects of dosimetric variation associated with consecutive insertions are therefore modelled in a worst-case scenario where it is assumed that treatment optimisation is insufficient in compensating for this geometric variation.

After insertion of the applicator, the patient must be transferred for 3D imaging, which is included in the insertion uncertainty estimate. Previously, mean shifts of 1-5 mm have been reported for intracavitary applicators during transfer [151–153]. In a recent work, even when using external fixation, mean shifts of 1.9, 3.0, and 9.5 mm were reported in the lateral, longitudinal and anteroposterior directions respectively [154]. To simulate the corresponding dosimetric impact, the authors of this study applied 5 mm anterior virtual shifts of the applicator in treatment planning software. This decreased the rectum and sigmoid D_{2cm^3} by 19.4 and 12.2% respectively, but increased that of the bladder by 36.5%. However, in reality OARs would move with shifts of the applicator, filling the 'vacancy' left by the applicator, rendering such results unreliable [154].

Imaging: applicator reconstruction

Several uncertainty components may be distinguished within the category of imaging variation, which may be summarised under: (i) applicator reconstruction, and (ii) organ and tumour contouring. Both are dependent on several factors including the imaging modality, resolution of images, patient or applicator-related artefacts, image fusion and operator experience [155]. One may note that these two components are often included in estimates of other forms of uncertainty.

[5] For example an estimated 5-6 mm for the CTV_{HR} based on applicator displacement/dosimetric impact data [119, 150].

For example, organ motion variation may not be assessed separately from contouring variations in estimates of the inter-fraction uncertainty, whereas applicator reconstruction variation cannot be separated from treatment planning dose variation [98]. By assessing the magnitude of these imaging related uncertainties, also more accurate uncertainty estimates can be made for non-imaging related aspects.

The magnitude of reconstruction uncertainty is for BT applicators limited. The preferred imaging modality for cervical cancer BT is MRI [7, 22], due to its ability to discriminate soft tissue and its multiplanar capability [132, 155]. However, reconstruction of brachytherapy applicators is more challenging for MRI than for CT imaging due to lack of contrast in the former [119, 155]. Although the use of alternative imaging modalities for the reconstruction has been proposed, it is advisable to use the same imaging set as for the contouring [156, 157]. When basing the reconstruction of the applicator on the contrast, errors from imaging artifacts, orientation of the imaging planes and the intervals between these planes may arise [158]. In the inter-observer studies by Haack et al. whom reconstructed the applicator using the artefact signal and MR markers, and Petit et al. whom used a 3D SPGR scan, geometric reconstruction mean errors of smaller than 1 mm for both plastic and titanium applicators were measured using a 1.5 T MR scanner [159, 160]. To minimise observer dependence and other direct imaging effects, recently automatic reconstruction algorithms using library-based reconstruction have been developed for MRI, which in one study shows equivalent or lower variability than the measured inter-observer variability, and has geometric errors within one millimetre [161]. However any library-based approach requires an accurate representation of the applicator in the library, which would otherwise result in a systematic error over treatment [156]. For conventional applicators it was found that models in a common library were accurate within 0.4 mm [162]. As it may be difficult to perform verification of the accuracy of a 3D-printed applicator and its corresponding CAD-model, for now direct imaging seems to be more appropriate. In the article describing the development of the ARCHITECT patient-tailored applicator, channels were envisioned that would provide anchor points for reconstruction [48].

Another recent development is the introduction of 3.0 T scanners, which when using T2-weighted images may result in significant artefacts for titanium applicators, corresponding to geometric reconstruction errors of several millimetres [163]. For a plastic applicator, image distortions using a 3.0 T MRI scanner have been established to be well below 1 mm [164]. Additionally, geometric variability in the longitudinal direction has been associated with finite slice thickness [159], and for that reason the use of multiplanar or 3D imaging is recommended [156]. In order to establish the dosimetric consequences of these geometric variations, studies have virtually shifted applicators in treatment planning software and compared DVH parameters of shifted and nominal plans [119, 150]. For the bladder and rectum in the study by Tanderup et al., DVH parameters varied with 5–6% per mm applicator displacement in the anteroposterior direction, and for other organs this dosimetric variation was established to be around 4% per mm (see Figure 2.5) [119]. When systematic errors are avoided through quality control, the dosimetric uncertainty corresponding to applicator reconstruction uncertainty is limited to 5-10% for the CTV_{HR} and OARs [119]. Systematic errors, however, may not entirely be eliminated. Schindel et al. showed that the applicator must not displace more than 1.5 mm during reconstruction, which would otherwise result in 10% dosimetric differences in DVH parameters [150]. In the study by Berger et al., only the D_{2cm3} of the rectum was significantly affected by direct reconstruction variations, with a dose difference compared to a reference plan of 0.2 ± 0.3 Gy for a prescription dose of 7 Gy [157]. As a rough 'best-case' estimate, in this study a geometric error of 0.3 ± 0.1 mm is assumed in a general direction, in accordance with the data by van Heerden et al. for 3.0 T MR imaging for a plastic

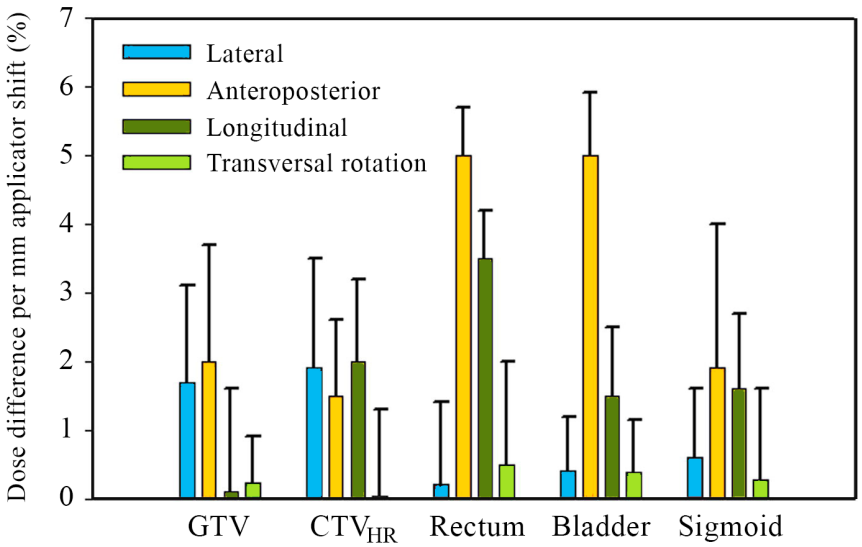

Figure 2.5: Dosimetric gradient (in % dose per mm) associated with virtual intracavitary applicator shifts for the target and several OARs in several directions. Figure adapted from Ref. [119].

applicator [164]. Using the gradient data by Tanderup et al. in Figure 2.5 [119], this corresponds to relative dosimetric variations per fraction of -0.45 ± 0.15% for the CTV$_{HR}$ $D_{90\%}$, and 1.5 ± 0.5%, 1.5 ± 0.5%, and 0.6 ± 0.2% for the bladder, rectum and sigmoid D_{2cm^3} respectively ($k = 1$). Rotations have not been considered, as generally these have a lower impact [119, 154].

Imaging: contouring of target and organs at risk

Contouring (Figure 2.6) is one of the main contributors to the uncertainty budget [99]. For that reason, several publications have addressed quantification of the variations in target and organ delineation. In the research by Petric et al., the delineations of ten experienced observers for six cases were compared on geometric properties such as the volume, volume conformity and descriptive distances to two reference delineations, based on expert consensus or using an expectation–maximisation algorithm [165]. However, this does not directly translate to dosimetric impact calculations. Therefore using the same data set, Hellebust et al. determined the dosimetric impact of inter-observer uncertainty as the mean of the relative standard deviations for DVH parameters corresponding to the delineations of the six cases [166]. For the reference contour generated based on expert consensus or the expectation–maximisation algorithm respectively, the established mean relative SDs were 9.1/10.0% for the CTV$_{HR}$, and 5.3/5.4%, 7.5/7.5%, and 11.2/11.3% for the bladder, rectum and sigmoid D_{2cm^3} ($k = 1$). Image acquisition was done using 0.2 T and 1.5 T MRI systems. Lower inter-observer conformity than in the previous studies was found in a study using 3.0 T MRI, although this might have been caused by the more complex treated cases and the larger number of participating clinicians [167]. Good concordance between observers was reported in another study using 3.0 T MRI, but the mean relative SDs were high, e.g. 27 to 28% for the CTV$_{HR}$ $D_{90\%}$ [168]. For CT-based delineation slightly higher dosimetric impact has been reported than found by Hellebust et al., likely due to the lower visibility of target and organ tissues on CT [169]. PET-CT may aid in improving the interobserver conformity [165]. Commonly recommended to minimise contouring uncertainties are adequate training and standard delineation guidelines [165]. For example, the largest inter-observer differences have been documented for the sigmoid in several reports [166, 169], indicating problems with the interpretation of this organ and marking an area of possible improvement. Indeed, several institutes were noted to deviate from Gyn GEC-ESTRO recommended delineation protocols regarding the sigmoid [158].

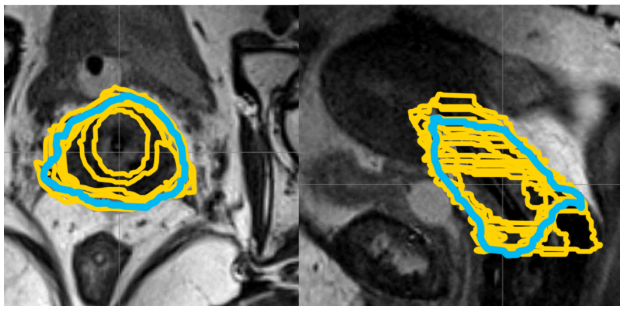

(a) Axial (left) and sagittal (right) CTV_{HR} delineation for patient case 2.

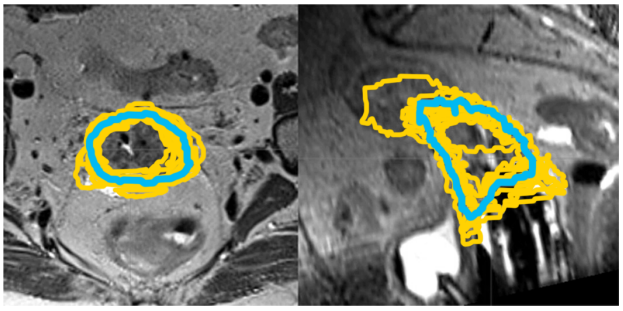

(b) Axial (left) and sagittal (right) CTV_{HR} delineation for patient case 3.

Figure 2.6: Illustration of contouring variation of the CTV_{HR} on MRI for two patient cases with individual observer's (gold —) and consensus contours (blue —). Figure adapted from Ref. [167].

Dosimetric impact of systematic errors, for example caused by the imaging modality, inaccurate delineation guidelines or procedures have not been described in literature. There are hints that for example the use of 3.0 T MRI may result in underestimation of possible residual disease whereas CT may overestimate the volume in advanced tumours with parametrial extension [167]. However, such systematic deviations must be further researched. Systematic inter-observer deviations may be inferred by comparing reference delineations from expert consensus and that by the expectation–maximisation algorithm which tries to establish the hidden true segmentation and could be used as ground truth. Those variations related to the imaging modality may be established by comparing different treatment modalities, although no gold standard is available.

Treatment planning: dose and DVH calculation

Commercial treatment planning systems (TPS) have commonly implemented the Task-group 43 (TG-43) formalism, of which best-practice uncertainties have been presented by DeWerd et al. [25]. The dosimetric uncertainty in dose calculation -composed of aspects related to source description, measurement of the dose, Monte Carlo simulations and dose interpolation- at 1 cm distance on the BT source transverse plane was evaluated to be 3.4% ($k = 1$) for high-energy sources, i.e. HDR-BT. Over time, the source description has been modified, which is reflected in updates of the total uncertainty, e.g. to 3.8% ($k = 1$) [98, 170, 171]. However, this uncertainty may be greater at smaller distances from the source or at far larger distances [98].

Several variations may be associated with the calculation of DVHs, including but not limited to: (i) volume calculation accuracy, (ii) dose calculation accuracy, (iii) resolution of the dose grid, (iv) DVH dose sampling and spatial location, and (v) DVH dose bin width [172, 173]. In a somewhat older work, Kirisits et al. reviewed seven planning systems in a phantom setup and found dosimetric differences between the TPSs of up to 12% from the mean [174]. The planning systems mainly deviated in the way the volume was constructed from the finite thickness slices, especially at the outer contours, and the resolution thereof. Nevertheless, the mean SD of the D_{2cm^3} for the phantom organs was only 1-5% ($k = 1$). The overall accuracy of DVHs generated by TPSs compared with analytic calculations has also been investigated. Gossman et al. compared TPS-generated DVHs for two types of HDR sources adjacent to a contoured cuboid structure with hand calculations [175]. The authors found an average disagreement of 0.4% between hand calculations and the TPS, ranging up to 1.0%. Nelms et al. compared two DVH calculation algorithms with analytically calculated DVHs, and found mean differences mostly within 1% [172]. The influence of increasing the amount of dose calculation points has been evaluated for prostate brachytherapy at the expense of computation time, and plans within 1% accuracy were achievable [170]. Lastly, the dose bin

width of cumulative DVHs impacts the uncertainty in dosimetric parameters, however the extent of this effect has not been properly reported. The uncertainty as the result of the aforementioned components may therefore be composed of 3.8% dosimetric deviation for the HDR dose calculation, 1% TPS volume calculation accuracy, 1% TPS dose calculation accuracy, and 1% contribution of the resolution and sampling of the dose grid, to a combined 4.2% uncertainty ($k = 1$). For an elaborate recent review of literature on the topic, the reader is referred to the work by Kanani et al. [173]. No data or indications are available on the presence of systematic variations.

Treatment planning: heterogeneities

In the TG-43 formalism several assumptions are made which may affect the dose and are classified as medium heterogeneities, among which are source shielding effects, patient tissue heterogeneities and patient anatomical boundaries or scattering effects [24, 98]. The dosimetric impact of these assumptions has been estimated for cervical cancer brachytherapy through the use of advanced model-based software, known as model-based dose calculation algorithms (MBDCA) [176–181]. Solely including the effects of a solid unshielded titanium applicator, differences with the TG-43 formalism and Acuros (Acuros BV, Varian Medical Systems, Charlotte, NC) -a grid-based Boltzmann solver (GBSS)- of less than 5% in dosimetric parameters were found [176]. For a shielded applicator, DVH parameters were found to be significantly lower for the GBBS than for the TG-43 formalism, with a mean difference of -3.4 to -6.2% for OARs [177]. Dosimetric differences between TG-43 and GBSS calculations were found to be greater for metal BT applicators (>1%) than plastic ones (∼0.5%) in a phantom study by Hofbauer et al. due to shielding effects in the former [178]. These authors reported relative dosimetric differences of –0.47 ± 0.33 % for the CTV_{HR} $D_{90\%}$, and –0.87 ± 0.25, –2.14 ± 0.63, –1.69 ± 0.81 ($k = 1$) for the D_{2cm^3} of the bladder, rectum and sigmoid respectively between model-based and conventional calculations in a patient study. Similarly, in other studies relative dosimetric differences <5% between TG-43 and MBDCAs were noted [179, 180]. In the study by Hofbauer et al. no specific effects of rectal filling or packing were found, in contrast to the study by Abe et al. where large differences (>10%) were found when the rectum was modelled to fully consist of air in a worst-case assumption to simulate rectal filling [181].

The applicator models for these computations require accurate representations of the geometry and material. Task group 186 (TG-186) has recommended that the geometry must be verified by an independent investigator, and if not available, the responsibility of verification lies with the end user [182]. However performing such a verification for each 3D-printed BT applicator is tedious. Instead, computer-aided drawing (CAD) files may be imported directly in a MBDCA, acknowledging that its validity may not be fully assured.

The TG-43 formalism results in a systematic overestimation of the doses to organs and the target. The measurements obtained by Hofbauer et al. are used in this study to estimate the biological effects of neglecting heterogeneities in the TG-43 formalism [178], assuming that the TG-43 is still used in regulatory practice.

Treatment planning: DVH addition

In order to calculate the cumulative dose to the target or organs at risk after several fractions, it is assumed that the same volume is irradiated to the highest absorbed dose in each fraction, sometimes erroneously termed as a 'worst-case assumption', but more recently as the practice of 'DVH parameter addition' (see Figure 2.7) [7, 183]. Nevertheless, the assumption that the D_{2cm^3} remains located in one part of the organ may result in an overestimation of the actual absorbed dose [98]. This is among others dependent on the mobility of the organ and the applicator. For

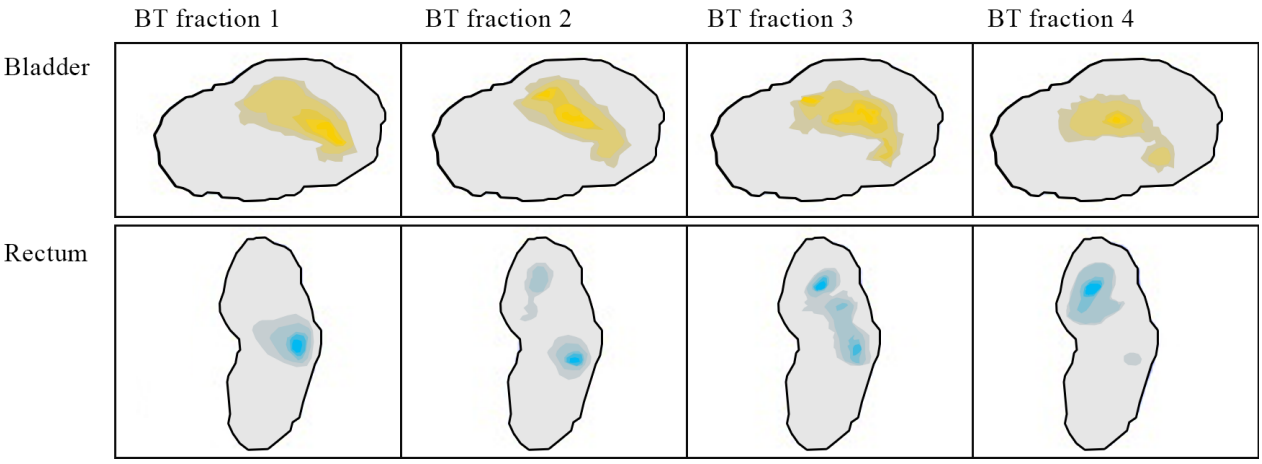

Figure 2.7: Inter-fraction variation of the spatial dose distribution of a single patient for the bladder and rectum. Contrary to the DVH parameter addition assumption, the D_{2cm^3} (brightest colour gold or blue) does not remain on the same location. Figure adapted from Ref. [185].

example in the study by Jamema et al. the overlap of D_{2cm^3} volumes between applications was >50% in the majority of patients for the more static rectum, 10-50% for the bladder, and <10% for the sigmoid [145]. Therefore for the sigmoid the validity of the DVH addition assumption was questioned. For the purpose of evaluating the variation caused by this assumption, several studies have compared the dose for a volume as calculated via DVH addition with a dose calculated for a specific volume tracked with deformable image registration (DIR) [183–187]. DVH addition was found to overestimate the D_{2cm^3} of the bladder with a mean relative difference of 1.5 ± 1.8%, with all doses calculated in EQD2, for PDR cervix cancer brachytherapy [183]. In the study by Kobayashi et al., addition of DVH parameters for an additional HDR-BT fraction was associated with a relative mean difference of 2.8 ± 8.0% and 0.7 ± 3.4% for the bladder and rectum D_{2cm^3} respectively ($k = 1$), with doses calculated in EQD2 [185]. These variations may be explained by the lack of a bladder filling protocol used in the study. Similar figures were described by Jamema et al., who reported relative EQD2 dose differences of 5.7 ± 5.7% and 1.4 ± 2.1% for the bladder and rectum D_{2cm^3} per BT fraction ($k = 1$) [188]. Note that these relative dosimetric uncertainties would likely be lower when expressed in relative absorbed dose and not in equieffective dose, but that translation of these findings is difficult due to the lack of full data in articles. Greater variation between DVH addition and DIR plans was found for the sigmoid in one study for the full BT+EBRT treatment plan [186], but in general little has been reported about the dosimetric impact of the DVH addition assumption on the sigmoid [98, 189]. For a recent overview of literature, the reader is referred to Jamema et al. [189]. It must be noted that DIR algorithms may cause additional uncertainty as deformations in cervix cancer are difficult to model, and therefore their routine use is not yet recommended [7, 189]. Still its figures give some indication of the inaccuracies associated with DVH parameter addition. The variability of the D_{2cm^3} of OARs due to the DVH assumption is in this study coarsely estimated based on relative EQD2 data.

The impact of the uniform dose assumption on the target volume is likely negligible [99], since the applicator and tumour constitute a stable system. Only one study was found in which the DVH assumption for the CTV_{HR} was evaluated. Over the full treatment dose, no significant differences between the $D_{90\%}$ of the CTV_{HR} estimated from DVH addition and DIR were documented [187]. As this topic is ill-investigated for a single BT fraction, it is for now assumed that no variations arise in the $D_{90\%}$ of the CTV_{HR} due to DVH addition.

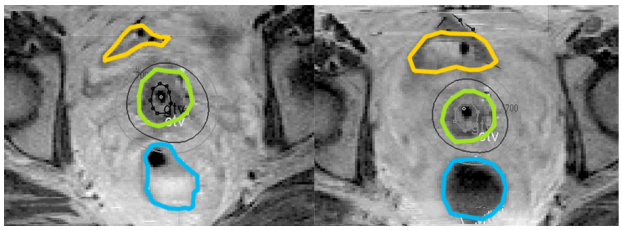

(a) Axial MRI image of fractions 1 (left) and 2 (right) for the first BT insertion.

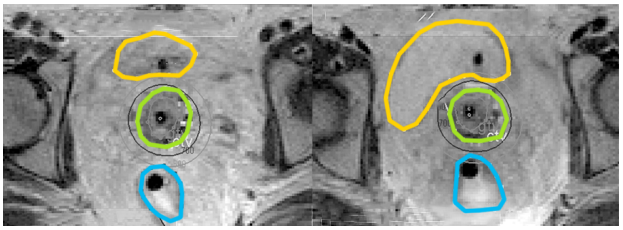

(b) Axial MRI image of fractions 1 (left) and 2 (right) for the second BT insertion.

Figure 2.8: MRI images illustrating inter-fraction anatomical variations of the CTV_{HR} (bright green —), bladder (gold —) and rectum (blue —) for a single patient. Figure adapted from Ref. [129].

Clinical dose delivery: applicator movement

Applicator movement can also be present during the treatment. The applicator and tumour constitute a relatively stable system when an appropriate implant and vaginal packing is used. Still, Tanderup et al. found a mean SD of displacement of 1.2, 1.2, and 0.9 mm in the lateral, longitudinal and anteroposterior direction respectively during PDR-BT relative to a rectum probe [190]. For intracavitary applicators without IS needle insertion, the mean displacement was found to be -0.7 ± 0.9 mm, which was significant, during HDR-BT fractions [133]. This corresponded with a dosimetric increase of 1.6 ± 2.6% per fraction for the $D_{90\%}$ of the CTV_{HR} ($k = 1$). For combined IC/IS treatment, the mean displacement was not found to be significant. Cooper et al. noted that near the tip of the tandem the displacement relative to the uterus may be greater than near the base, i.e. ring, of the applicator [191]. As no other data was found to be available describing the dosimetric impact of movement of the applicator relative to the target volume, the data by Karlsson et al. is used in this thesis [133].

Clinical dose delivery: anatomical changes

Anatomical variations, e.g. positional and volumetric changes of organs or tissue, influence the absorbed dose between insertions and fractions and also during the delivery of fractions (see Figure 2.8). Such anatomical changes that may impact DVH parameters likely originate from bladder filling status and possibly from rectal filling status [126, 192–195], patient positioning [196], and variations in vaginal gauze packing or other systems to displace OARs [197]. For simplicity, only intra-application anatomical changes are considered here, i.e. inter-fraction and intra-fraction changes. In their pooled analysis of the results of six institutions, Nesvacil and colleagues observed intra-application variation of -2.5 ± 10.8% for the CTV_{HR} $D_{90\%}$, and 1.3 ± 17.7%, 3.8 ± 20.5% and -2.3 ± 23.5% for the bladder, rectum and sigmoid D_{2cm^3} respectively ($k = 1$) [111]. These percentages do not only constitute of dosimetric differences due to anatomical changes, but also include contouring and reconstruction uncertainties. As these contribute up to around 9.5% of the random error on the CTV_{HR}, Nesvacil et al. concluded that the applicator-target is a stable system [111]. The difference between the dosimetric uncertainties for the D_{2cm^3} of the OARs and earlier stated contouring/reconstruction uncertainties is attributed to anatomical changes of the organs relative to the applicator [111]. Additionally, these individual institutes differed in the used treatment modality, protocols and applicator type, and time in between procedures among others. In one of the studies in this pooled analysis it was concluded that if a constant bladder filling was to be ensured, geometric variations between two fractions for the same insertion 16-20 hours apart are of little influence on the dose [129]. However, despite adherence to BT protocols, major dosimetric differences may occur due to shape variations [198].

It would be of interest to further decompose intra-application uncertainty into contributions of individual components that can be directly quantified, such as the movement that caused the variation. Using rigid image registration, Chakraborty et al., estimated that 47% and 19% of the variation in the rectal and bladder dose respectively could be explained by applicator movement opposed to organ movement or volumetric changes [198]. Some articles describe the centre of volume (COV) location of partial volumes relative to the applicator and relate this for example to bladder/rectal filling and packing [199, 200]. The resulting dosimetric impact of spatial uncertainty on the dose in the highest irradiated subvolumes, e.g. D_{2cm^3}, is often found to be minimal [126, 145, 199, 200]. However, dosimetric indices for small partial volumes do not have a fixed location and therefore cannot be used to accurately model the dosimetric impact of spatial uncertainty for the fully treated organ. Deformable image registration techniques have been used for more accurate dose accumulation calculations, but additionally may be used to track/predict and quantify inter-fraction organ motion and its impact. The complexity of this problem, e.g. caused by the rigid applicator and sliding between tissues [189], and the dependence on accurate delineations, implies that these motion models suffer from significant uncertainties as well.

Intra-fraction motion during cervical cancer BT has been described in multiple works [201–203]. In a study where a personalised vaginal mould was used as an applicator for PDR-BT, a significant systematic increase in the rectum was noticed, of 6% ± 5.3% in relative EQD2 dose, likely caused by rectal filling, whereas this was not the case for the bladder or the sigmoid [201]. Similarly, although intra-fraction rectal dose differences are not always found to be significant, in individual cases outliers occur where rectal dose increased [203]. Using DIR, Miyasaka et al. however found the rectal dose to become significantly lower during treatment, i.e. -2.3 ± 9.9% relative dose to D_{2cm^3} ($k = 1$), which opposes the previous findings [204]. This however may be explained by an increase in bladder filling as catheters were not consistently used, pushing the rectum in the posterior direction. Bladder filling could also explain the increase of the bladder D_{2cm^3} of 2.4 ± 8.8% ($k = 1$), which moved superiorly in this study. In another study in intrafraction variation, only the sigmoid D_{2cm^3} was influenced significantly, with relative dosimetric differences of 0.6 ± 0.6 Gy (corresponding with 8.7 ± 8.6 % for a 7 Gy fraction ($k = 1$)) [202]. This reflects the high mobility of the sigmoid, but also possibly the greater uncertainty in the contouring procedure of this organ. Although studies show mixed results, intra-fraction organ motion seems to be a large contributor to the inter-fraction variation, despite the limited time span in which these variations may occur.

Technical dose delivery: source strength

Source strength variation influences the brachytherapy treatment process from planning and up to delivery [98]. Therefore, it has been the subject of multiple studies and reviews. Task group 138 (TG-138) calculated an uncertainty in the source strength of 1.5% for a HDR source ($k = 1$) [25]. For simplicity it is assumed that all organs and the target are equally affected by this uncertainty, although these dosimetric points have a different spatial location and orientation to the source[6].

Technical dose delivery: source position

Despite the use of automatic remote afterloaders, source positioning is still subject to errors. Typically, a geometrical uncertainty of ± 1 mm ($k = 1$) is well-achievable with these afterloaders through straight applicators [205]. Recently, in a study evaluating the source positioning accuracy of an afterloader using length verification average deviations were found of less than 1 mm for

[6] In reality the dose surrounding the longitudinal axis of the source is not uniform, and variations of 2-20% have been reported [25].

several commercially available curved and straight applicators [206]. For applicators of higher curvature, such as ring applicators, these average deviations amount to 2.5-5.5 mm [98, 206]. Such high curvatures, e.g. radii of 13 mm in some ring applicators, are not achievable for interstitial needles used in 3D printed IC/IS applicators where the radius is limited to 35 mm due to friction [48], and hence deviations will likely be less[7]. Although systematic errors in the source position relative to the applicator due to afterloader inaccuracy may be decreased through quality assessment with commercial applicators [98], these errors still likely persist for highly curved applicators and result in significant point dose differences [207]. Similarly, Humer et al. simulated the impact of rotation of the loading pattern and found that differences of 2.5 mm resulted in dosimetric uncertainty <3% for the D_{2cm^3} of OARs and <2% for the $D_{90\%}$ of the $\mathrm{CTV_{HR}}$. However, as the rectum D_{2cm^3} had a larger systematic dosimetric error than the other evaluated volumes, from linear interpolation the authors concluded that dosimetric differences <2% for the target, bladder and sigmoid are possible and <5% for the rectum when containing the source positional accuracy within 2 mm as is commonly recommended [208]. Source path verification may not be feasible for each personalised applicator, such that systematic errors may persist in all of the fractions. The use of simple source verification methods prior to treatment or improvements in afterloader accuracy may aid in reducing this error. Temporal inaccuracies in source position are generally almost negligible, amounting to ≤0.5% dosimetric impact ($k = 1$) [35, 98]. Lastly differences in source orientation within the applicator may occur [98]. The channel diameter of the ARCHITECT applicator is currently 2.6 mm [48], whereas conventional hollow needles are around 2.2 mm in diameter. This play of 0.2 mm will likely not result in significant dosimetric differences.

Post-delivery: target and organ response

Time-dependent effects, including tumour and organ response, such as oedema, can influence the absorbed dose in subsequent fractions and are inherently included in inter-fraction and inter-application uncertainty estimates. For interstitial applicators, it has been established that these two factors influence needle and template displacements and deformations [77, 209]. For PDR-BT such changes have been described by Morgia et al. [210]. In their study, the tumour volume increased significantly over the brachytherapy fractions resulting in a relative reduction of the total BT+EBRT EQD2 $D_{90\%}$ dose of -6.1 ± 7.3%, and -7.5 ± 7.2% over two days. Also the estimated rectal D_{2cm^3} dose increased significantly, albeit that this may be due to rectal filling, and not necessarily oedema, which was an effect previously noticed for PDR-BT as well [201]. However, evidence for HDR brachytherapy shows that rather the tumour regresses over fractions [112, 113, 211–213], which means that in some individual cases the treatment planning must be adapted in order to ensure OAR dose constraints. Regression due to brachytherapy may not be as pronounced as described in the frequently cited study by Dimopoulos et al. who showed a regression of the target volume from 16 $\mathrm{cm^3}$ to 8 $\mathrm{cm^3}$ in four fractions, as in this case brachytherapy is initiated during EBRT treatment [112]. Rather, the treatment volume likely remains largely constant over the course of brachytherapy [113]. Therefore, despite not investigated, the dosimetric impact of possible tumour regression would likely be small.

Post-delivery: fractionated treatment

Random errors have a zero mean by definition. For this reason, for a number of fractions N, random errors within a fraction tend to level out via a factor $1/\sqrt{N}$ [35]. This implies that treatment with an increased amount of fractions is more forgiving, whereas in brachytherapy with four fractions the uncertainty from random errors is half of what has been reported previously.

[7] The effect of multiple bends in succession on the positioning accuracy is unknown, which may possible increase the positioning error.

2.3.2 Uncertainty budget for cervical cancer BT

Based on the previous literature analysis of sources of uncertainty, an uncertainty budget for cervical cancer HDR brachytherapy using an intracavitary applicator with the treatment schedule illustrated in Figure 1.2 is shown in Table 2.2. For convenience and as this table contains rough estimates, values above 1.0% were rounded to the nearest halves. All figures are expressed relative to the planning-aim absorbed dose in Gy for a single BT fraction. Both the mean and standard deviations of relative dosimetric variations are given, which is not to be confused with systematic and random uncertainty components. For example, for a source of uncertainty having a systematic impact over two fractions succeeding one imaging session, such as contouring variation, a dosimetric error which is obtained from a normal distribution, characterised by mean and SD, influences both fractions the same. In the case of an uncertainty having a random impact, the dosimetric error for each fraction individually would be drawn from a normal distribution.

As can be seen in Table 2.2, the largest individual contributors to uncertainty in the BT treatment are contouring uncertainties for the CTV_{HR} $D_{90\%}$ and anatomical changes for the OARs D_{2cm^3}. The latter follows from subtracting the SDs of contouring, reconstruction, and applicator movement uncertainties from the inter-fraction SD via the root sum of squares. For individual uncertainty components, the SDs describing the systematic or random uncertainty are in general <10% for the CTV_{HR} and <15% for the OARs ($k = 1$). However, the SD of the total uncertainty may amount up to <12% and <25% for the CTV_{HR} and OARs respectively. Of the OARs, the SD of the delivered dose to the bladder is in general the smallest, whereas the delivered dose to the sigmoid is subject to the largest uncertainty.

The largest values of the mean of dosimetric variation are found for the DVH addition assumption, which overestimates the dose to the OARs, and for inter-fraction changes, where organ motion and anatomical changes have predicted patterns throughout treatment and hence influence the dose to the CTV_{HR} and OARs systematically. Bias in the delivered dose is in general <4%.

2.3.3 Clinical impact of dosimetric uncertainty

Clinical impact at planning-aim dose

The basic model used to calculate the clinical impact of dosimetric uncertainty and generate the figures in this part, is given in Script A.1.6. For all components in Table 2.2, the: (i) event probability of the population average delivered dose with uncertainty, $(N)\overline{TCP}$, (ii) standard deviation of this population average event probability, $SD((N)\overline{TCP})$, and (iii) the error between the population average event probability and the event probability of the planning-aim dose, $(N)\overline{TCP} - (N)TCP$, at the dose constraint level[8] are given in Table 2.3.

As can be observed in Table 2.3, for the general population the error between the calculated event probability for the logit-model with and without uncertainty, i.e. the clinical impact of uncertainty components, is small at the planning-aim dose level and smaller than what may be expected from the magnitudes of the dosimetric uncertainties in Table 2.2. Local control, which is modelled to be around 94.5% without uncertainty at the planning-aim dose level, is at most decreased by 0.4 percentage points due to inter-fraction changes. The simulated occurrence of tissue morbidity is around 12.3%, 8.2%, and 0.6% for the bladder, rectum and sigmoid respectively. Inter-fraction changes, mainly anatomical changes, are the greatest contributors to variation in this predicted tissue morbidity and increase the occurrence by 1.5%, 3.7% and 0.5% respectively.

[8] These planning dose constraints are >90 Gy for CTV_{HR}, <80 Gy for bladder, <65 Gy for rectum, and <70 Gy for sigmoid [50].

Table 2.2: Uncertainty budget for a single fraction of cervical cancer HDR brachytherapy using an intracavitary applicator, with the classification from Figure 2.2. Percentages express the relative dosimetric variation to the planning-aim absorbed dose in Gy.

Uncertainty components		CTV_{HR} $D_{90\%}$		Bladder D_{2cm^3}		Rectum D_{2cm^3}		Sigmoid D_{2cm^3}	
		Mean (%)	SD (%)	Mean (%)	SD (%)	Mean (%)	SD (%)	Mean (%)	SD (%)
Systematic impact on delivered dose									
1.	Application: insertion of the applicator (including contouring and registration)[a]	0	10.5	0	11.5	0	10.0	0	19.0
2.	Imaging: reconstruction[b]	-0.5	0.2	1.5	0.5	1.5	0.5	0.6	0.2
	Imaging: contouring[c]	0	9.5	0	5.5	0	7.5	0	11.0
	Imaging: anatomical changes[d]	0	3.0	0	6.0	0	8.0	0	7.0
3.	Treatment planning: dose and DVH calculation[c]	0	4.0	0	4.0	0	4.0	0	4.0
	Treatment planning: heterogeneities[e]	-0.5	0.3	-1.0	0.3	-2.0	0.6	-1.5	0.8
	Treatment planning: DVH addition[f]	0	0	2.0	6.0	1.0	3.5	4.0	8.0
Random impact on delivered dose									
4.	Clinical dose delivery: applicator movement	1.5	2.5	0	0	0	0	0	0
	Clinical dose delivery: inter-fraction changes (including contouring, registration, tissue response, applicator movement and intra-fraction variation)[g]	-2.5	11.0	1.5	17.5	4.0	20.5	-2.5	23.5
5.	Technical dose delivery: source strength	0	1.5	0	1.5	0	1.5	0	1.5
	Technical dose delivery: source position[h]	0	2.0	0	2.0	2.0	3.0	0	2.0

[a]No data available of variability due to insertion. The random error is estimated as the difference between inter-application and intra-application data by Nesvacil et al. [111]. Systematic error is set to zero. Worst-case scenario only relevant for patient-tailored designs, when not able to compensate for geometric differences between pre-planning and at time of treatment via treatment planning.
[b]Estimated using the gradient data in % dose per mm by Tanderup et al. [119], and with a displacement of 0.3 ± 0.1 mm [164].
[c]No data available for the systematic variation.
[d]Rough estimates based on dosimetric differences between treatment plans after pre-planning and pre-treatment scans by Nomden et al. [203], and Anderson et al. [214].
[e]Assuming that the TG-43 formalism is used in the TPS and as such heterogeneities are neglected.
[f]No data available for the CTV_{HR}. Other data is coarsely estimated based on relative EQD2 differences between DVH addition and DIR-based calculation. Accuracy of DIR algorithms is limited for large deformations and displacements.
[g]Data by Nesvacil et al. [111].
[h]Assuming an error of 2 mm in source positioning for a ring applicator [208]. Systematic rectum error corresponds to 2 mm clockwise deviation of source positions.

Table 2.3: Clinical impact of the dosimetric uncertainty described in Table 2.2 for a treatment schedule illustrated in Figure 1.2. Population average event probability calculated using a logit-model with uncertainty, $(N)\overline{TCP}$, standard deviation of the event probability calculated using a logit-model with uncertainty, SD, and the error between the population average event probability from a logit-model with and without uncertainty, $(N)\overline{TCP} - (N)TCP$, are given at the planning-aim dose values[8]. All the values are given as percentages (%).

Uncertainty components	$\mathbf{CTV_{HR}}$ $\mathbf{D_{90\%}}$		Bladder $\mathbf{D_{2cm^3}}$		Rectum $\mathbf{D_{2cm^3}}$		Sigmoid $\mathbf{D_{2cm^3}}$	
	$\overline{TCP} \pm SD$	$\overline{TCP}$-TCP	$\overline{NTCP} \pm SD$	$\overline{NTCP}$-$NTCP$	$\overline{NTCP} \pm SD$	$\overline{NTCP}$-$NTCP$	$\overline{NTCP} \pm SD$	$\overline{NTCP}$-$NTCP$
Systematic impact on delivered dose								
1. Application: insertion of the applicator (including contouring and registration)	94.4±3.8	-0.3	11.9±5.3	0.6	8.9± 6.3	0.8	1.3±1.2	0.7
2. Imaging: reconstruction	94.4±3.8	-0.2	11.4±5.7	0.0	8.4±6.5	0.1	0.7±0.9	0.0
Imaging: contouring	94.4±3.7	0.1	11.3±5.5	0.0	8.5±6.6	-0.2	0.9±1.0	0.3
Imaging: anatomical changes	94.5±3.7	0.3	11.8±5.4	0.3	8.5±6.7	0.2	0.7±1.0	0.1
3. Treatment planning: dose and DVH calculation	94.4±3.8	-0.1	11.4±5.6	-0.1	8.2±6.5	-0.4	0.7±0.9	0.1
Treatment planning: heterogeneities	94.4±3.6	0.2	11.0±5.3	-0.3	7.3±5.7	-1.3	0.6±0.9	0.0
Treatment planning: DVH addition	94.3±3.8	-0.1	12.2±5.7	0.5	8.5±6.7	0.3	0.8±1.0	0.2
Random impact on delivered dose								
4. Clinical dose delivery: applicator movement	94.8±3.5	0.2	11.5±5.6	0.1	8.0±6.2	-0.1	0.7±0.9	0.1
Clinical dose delivery: inter-fraction changes (including contouring, registration, tissue response, applicator movement and intra-fraction variation)	94.0±3.8	-0.4	12.8±5.9	1.5	11.7±7.8	3.7	1.1±1.1	0.5
5. Technical dose delivery: source strength	94.7±3.6	0.2	11.5±5.5	0.0	8.4±6.4	0.5	0.6±0.8	0.0
Technical dose delivery: source position	94.6±3.8	0.2	11.4±5.5	0.3	8.4±6.7	-0.1	0.6±0.9	0.0

Interestingly, despite the large standard deviation of the error that may be associated with inserting the applicator and the contouring error, only a small clinical impact is established for these two errors, likely as these errors are cancelled out over the population and partially over two imaging sessions. Only uncertainty components with a non-zero mean in Table 2.2 seem to affect the event probabilities at planning-aim dose levels.

Effect of uncertainty components on event probability

To demonstrate how event probabilities are impacted by different magnitudes and types of uncertainty, a simulation is shown in Figure 2.9 using Script A.1.7. As can be seen, the effects of systematic and random components for the simulated population are similar as both are stochastic variables, and for individual patients the systematic or random effects level out over two insertions or over four separate fractions respectively. For a greater group mean error the slope of the dose-response curve increases, similar to what is noticed by Nesvacil et al. [38]. However, the shift of the curve for greater positive systematic uncertainty towards lower doses as denoted by the aforementioned authors was not established in this study. This may be explained by the inherent characteristics of the logistic regression used in order to derive the dose-response relationships; increasing the steepness of the dose-response curve in general has a similar effect in providing an improved fit for greater positive systematic uncertainty as shifting the dose-response curve to the left. When simulating the effects of the magnitude of the standard deviation, it can be seen that the differences between the curves at different uncertainty levels is minor, although a flattening of the curve may be seen for greater values as has been previously reported [35, 38]. This stems from the non-linearity of the LQ-model used for converting the absorbed dose to equieffective dose in 2 Gy fractions (EQD2).

Dose-response curves under uncertainty

Impact of dosimetric uncertainty on simulated local control

Dose-response curves for inter-fraction changes, as these are the main contributors to the uncertainty budget, are illustrated in Figure 2.10. Dosimetric uncertainty in brachytherapy seems to only marginally affect the local control rate for the general population at the planning-aim dose level of 90 Gy as the results from the simulation in Table 2.3 and dose-response curve in Figure 2.10a suggest. In the latter a decrease of 0.4% in local control is barely noticeable. In fact, most of the error between the TCP models with and without uncertainty seems to be the consequence of model inaccuracies such as the limited simulated population size. However, as can be observed in Figure 2.10a, the discrepancy between the dose-response curves with and without uncertainty becomes somewhat greater at lower dose prescription levels. This is caused by a slight decrease in the slope at 50% dose response (outside of the range of the graph). An additional benefit of escalating the dose to the high-risk tumour volume is therefore that the impact of dosimetric uncertainty becomes less according to this model.

Impact of dosimetric uncertainty on simulated tissue morbidity occurrence

Figure 2.10b, 2.10c, and 2.10d show the predicted tissue morbidity - dose responses with and without inter-fraction changes for the bladder, rectum and sigmoid respectively. The combination of the dose-response gradient and the dose for 50% occurrence, results in a greater predicted occurrence of tissue morbidity of the rectum at lower doses than predicted for the other two organs at risk. In combination with the large mean error in dose due to inter-fraction changes, in this model the rectum is clearly the organ that is affected most by uncertainty at the dose constraint level. In all of the OARs the inter-fraction uncertainty seems to increase the occurrence of tissue morbidity at the displayed dose ranges, which is undesired.

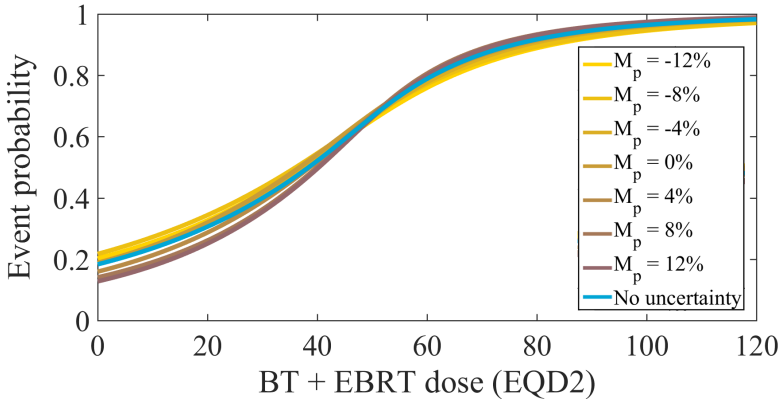

(a) Influence of the mean of systematic uncertainty components.

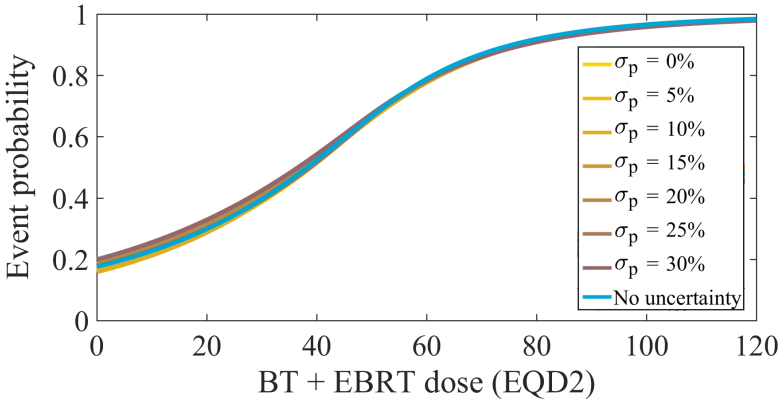

(b) Influence of the SD of systematic uncertainty components.

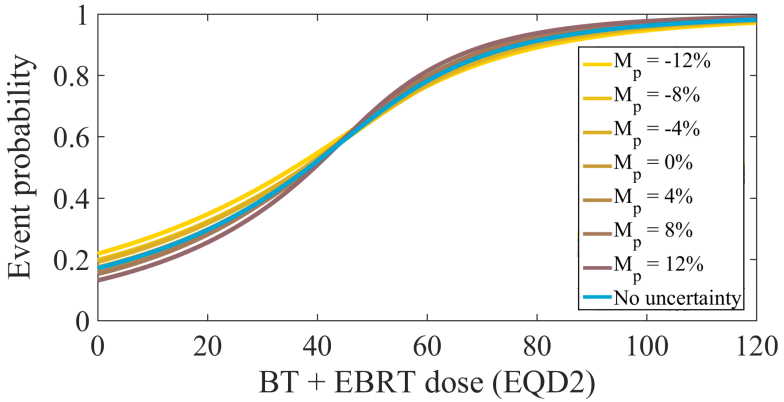

(c) Influence of the mean of random uncertainty components.

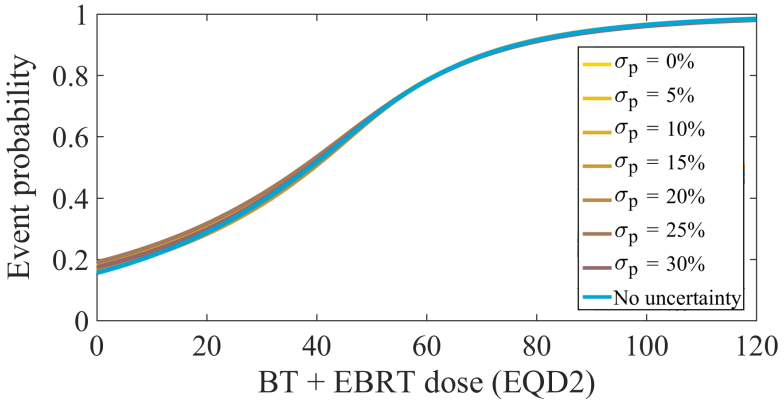

(d) Influence of the SD of random uncertainty components.

Figure 2.9: Illustrations of the influence of different types of uncertainty components and their magnitude. For the CTV_{HR} it is preferred that the event probability, or TCP at the planning-aim dose (∼90 Gy) is as high as possible. For OARs on the other hand it would be preferred that the event probability, or $NTCP$, at dose constraints (65-80 Gy) is as low as possible. Simulations performed for the CTV_{HR}, with $\gamma_{50} = 0.47$ and $TCD_{50} = 36.0$ Gy for $N_{pat} = 200$ patients per uncertainty level. `MATLAB` code is provided in Script A.1.7.

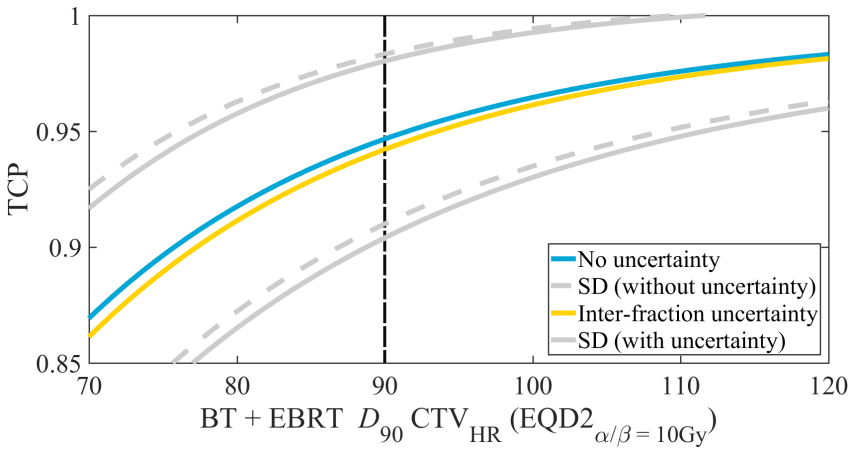

(a) Dose-response curves for the CTV_{HR}.

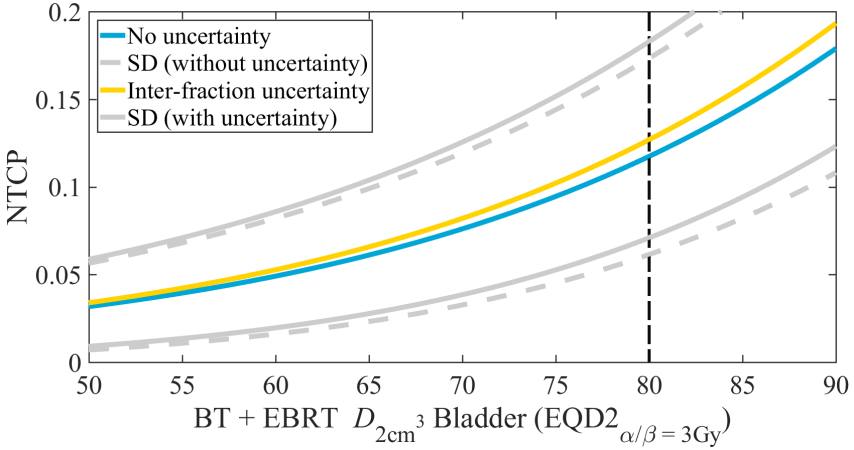

(b) Dose-response curves for the bladder.

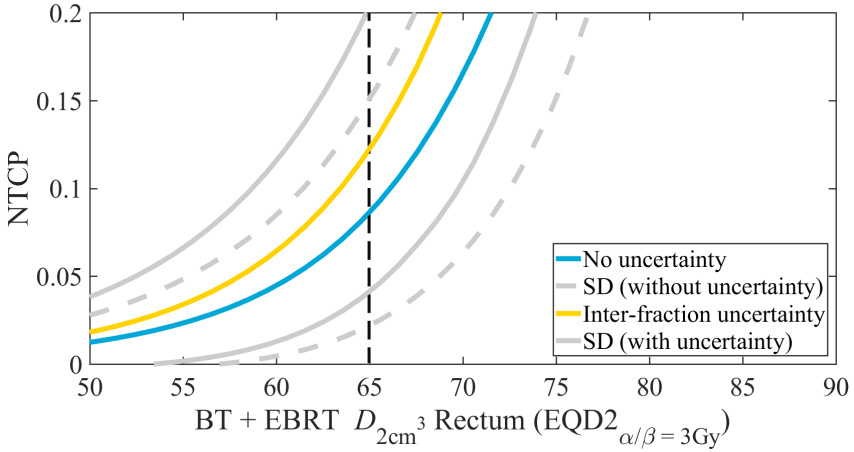

(c) Dose-response curves for the rectum.

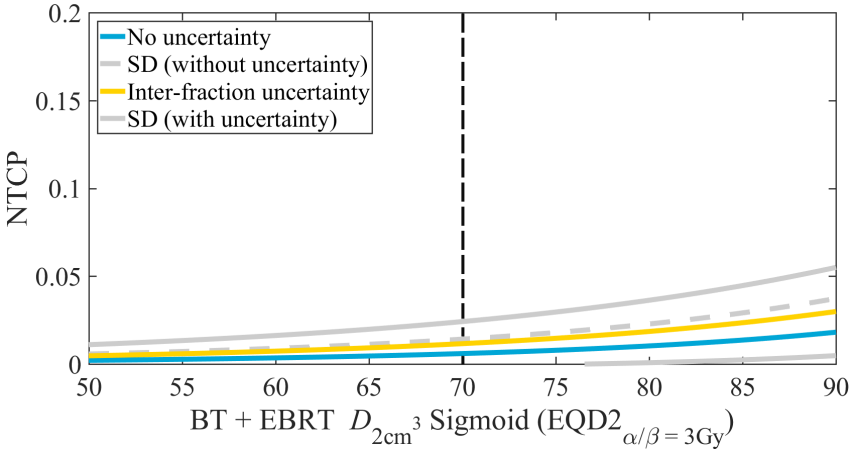

(d) Dose-response curves for the sigmoid.

Figure 2.10: Simulated dose-response curves: (i) with inter-fraction uncertainty (gold —), which is modelled as having a random impact with M_p and σ_p derived from Table 2.2, and (ii) without uncertainty (blue —) for the CTV_{HR}, bladder, rectum and sigmoid. The dotted black line (- -) indicates the planning-aim dose/dose constraints. `MATLAB` code is provided in Script A.1.6.

2.4 Discussion

The purpose of this chapter was to establish the magnitude of uncertainty components in cervical cancer BT and to assess their clinical impact on the tumour and organs at risk. First, BT literature concerning dosimetric uncertainty was reviewed and an uncertainty budget was composed. As it was complex to strictly dissect uncertainty in individual uncertainty components, major contributors -sometimes comprised of multiple sources of uncertainty- were sought and established. Due to this complex interplay of uncertainty components it was decided not to calculate the total dose uncertainty using the simple method of taking the square root of the sum of these components in quadrature, as was done in previous works [98, 99]. Moreover, the uncertainty components were quantified with the two-parameter model as per standard in BT literature instead of a four-parameter model. For individual patients, therefore, the mean error over treatment fractions will likely be larger and the standard deviation smaller.

From the example uncertainty budget with one imaging session per two brachytherapy fractions and a total of four fractions, it is clear that for individual patients the systematic dosimetric impact on the delivered dose can be substantial. For example, by basing the applicator design on a possible poor insertion and a 'snapshot' image of the patient's topographic anatomy, in a worst-case scenario where treatment optimisation cannot be used to compensate for these dosimetric differences the resulting systematic error over two fractions may detriment the dose to the tumour and increase the dose received by OARs by >10%. For this reason the applicator design should be evaluated prior to the treatment delivery, and re-evaluated after the first two BT fractions or ideally after each fraction. Nevertheless, when the clinical workflow does not permit frequent imaging the applicator design should be robust against these uncertainties over multiple fractions. Similarly, contouring uncertainties and anatomical changes during imaging are substantial, with SDs of 3-11%, and only partially cancel out over two insertions in a single patient case.

The main contributor to uncertainty in the delivered dose to the CTV_{HR} in the uncertainty budget is seemingly contouring uncertainty, as was established previously [98, 130]. For organs at risk, the main uncertainty seems to stem from inter-fraction changes and in particular organ movement or volume changes relative to the applicator, as also acknowledged in previous work [98]. Additionally, the overestimation of the dose to the organs at risk as the consequence of DVH addition may be significant, especially for the sigmoid. In general however the clinical impact of this overestimation of OAR dose is limited; it merely implies that the delivered dose to the tumour may be escalated safely without exceeding OAR dose limits. Moreover, discrepancies between different deformable image registration algorithms and their failure to model large deformations indicate that estimations of the magnitude of this error are not accurate. Systematic errors in source positioning may not be accounted for when using personalised applicators as validation for each applicator design is intractable, but in general the dosimetric effects of this type of variation are limited.

Next, the clinical impact -defined as the simulated event probability- of dosimetric uncertainty components was investigated. For the general population the clinical impact of dosimetric uncertainty for all investigated components is small at the planning-aim dose level (Table 2.3) and perhaps smaller than expected from the magnitudes of the dosimetric uncertainties in Table 2.2. Even inter-fraction changes, which have an especially unfavourable impact on the (N)TCP due to the combination of a negative (/positive) mean dosimetric uncertainty and a large SD, only show

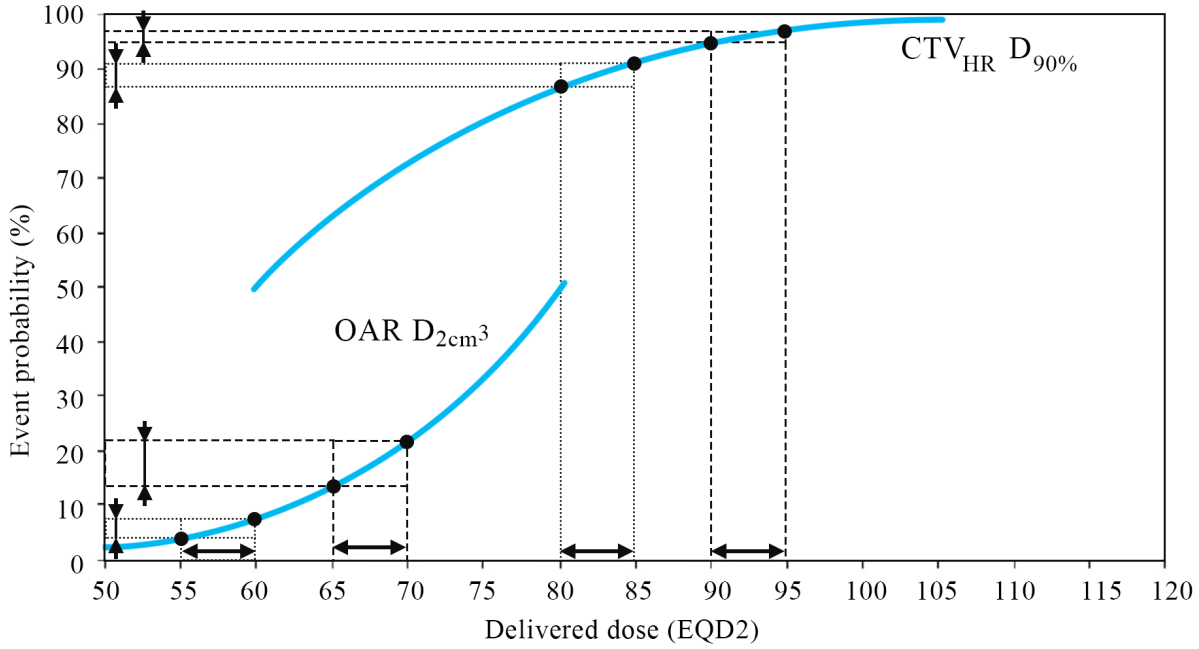

Figure 2.11: Illustration of the impact of dosimetric uncertainty of 5 Gy on the local control and morbidity tissue morbidity. At lower dose levels along the TCP curve, the impact of dosimetric uncertainty becomes greater. At higher dose levels of the NTCP curve the impact of uncertainty in the dose becomes greater. Figure adapted from Ref. [99].

a marginal effect on the (N)TCP in Table 2.3. Nesvacil et al. obtained similar results; 20% random uncertainty had negligible effects on the TCP with the same dose-response parameters as used in this study and >2–3% on the modelled NTCP of the rectum with different parameters [38]. If the simulation used in this study was re-ran with the same rectum morbidity parameters as used by Nesvacil et al. an impact of 1% was found on the NTCP for 20% random uncertainty on a single BT fraction dose. Systematic uncertainty components were in their study modelled to persist over four BT fractions, but for the overall population the results are found to be similar; in their study a 3% positive systematic bias in the dose per fraction led to an increase of the TCP by approximately 0.7%, whereas a 3% positive sytematic bias increased the NTCP of their rectum model by approximately 0.3 percentage points at planning-aim dose/dose constraint levels.

Several reasons may explain the finding that in this analysis the clinical impact of dosimetric uncertainty is small. First, as both the systematic and random uncertainty components are stochastic variables drawn from normal distributions, the dosimetric error levels out to the group mean for the simulated population and for a single patient over the amount of fractions [35]. Therefore, the clinical impact of a greater SD in the delivered dose due to random or systematic uncertainty components is minimal when evaluated for a large population. The magnitude of the mean error affects the event probability more significantly than the SD, but is <4% as reviewed in Table 2.2. Secondly, the clinical impact of dosimetric uncertainty is dependent on the dose level (Figure 2.11) [99], and planning-aim dose values are not necessarily achieved in clinical practice. For the CTV$_{HR}$ the clinical impact of uncertainty is lower at higher dose levels, such as the 90 Gy used for generating the data in Table 2.3. With a planning-aim dose to the $D_{90\%}$ of the CTV$_{HR}$ of 85, 80 or 75 Gy, the clinical impact of inter-fraction changes is determined at -0.5%, -0.6% and -0.8% respectively opposed to -0.4% for a planning-aim dose of 90 Gy. In similar fashion, in individual patients the dose levels to the OARs may exceed the dosimetric constraints, which

result in a greater impact of the dosimetric uncertainty. For example, a delivered dose of 90 Gy to the bladder -which was a previous Gyn GEC ESTRO dose constraint and is still commonly used- leads to an inter-fraction impact of 1.9% opposed to 1.5% for a dose of 80 Gy. When considering delivered doses of 75 Gy for the rectum and sigmoid, opposed to 65 and 70 Gy respectively, the impact on the simulated NTCP of inter-fraction dosimetric uncertainty increases to 9.1%, and 0.6%. Despite that the sigmoid is the most mobile organ, which is reflected in the largest SD of the inter-fraction error, the event probability does not change substantially with this error. Possibly, this is due to the negative mean inter-fraction error as obtained from the data by Nesvacil et al. [111]. Such a negative dosimetric impact on the sigmoid D_{2cm^3} is associated, for example, with bladder distension over several fractions. In some studies the data support such a conclusion [202], or do not mark a significant dosimetric bias [214]. However, also a positive mean inter-fraction error for the sigmoid has been reported [145]. Simulations with a zero mean for the sigmoid inter-fraction error did not yield any clinically different results as at the dose constraint level the predicted occurrence of tissue morbidity at the sigmoid is low in general. Although the exact implications of the tissue morbidity models are deliberately left unspecified, i.e. as not to focus on a specific type of complication, these roughly correspond to events with severity scores $\geq$G2 based on their occurrence at planning-aim doses. The frequency of lower severity side-effects is far greater and would be more susceptible to dosimetric uncertainty in absolute percentages. Lastly, although evaluated for a great number of patients, the figures in Table 2.3 are not stable and may change upon reproduction. For a greater number of simulated patients, e.g. 3,000 or 10,000, this issue still persists to some extent.

Additionally, as uncertainty components may have a more pronounced negative impact on the modelled local control and tissue morbidity than the simulation suggests, the behaviour of dose-response curves (Figure 2.10) was further investigated by altering model parameters. The parameters used in the logit-model for predicting local control were derived from a relatively heterogeneous population in a multi-centre study [111]. With an increased dose-response gradient, $\gamma_{50} = 1$, but subsequently higher dose for 50% response, $\mathrm{TCD}_{50} = 60.0$ Gy to still yield credible results in the local control, the simulation for inter-fraction changes was re-ran. This resulted in a loss of the simulated local control of 1.5%, higher than the 0.4% earlier reported. For individual patients, the effects of uncertainty deviates from this population average. In order to illustrate such patient-specific effects, the dose-response gradient γ_{50} for an individual patient can be modelled to be higher than that of the average population as has been done previously [215, 216], but this practice is inherently flawed[9] despite perhaps useful for illustration purposes. Even when condoning this practice by increasing the 'individual' patient's γ_{50} and TCD_{50}, the impact of inter-fraction uncertainty may be reduced at high planning-aim doses, e.g. 90 Gy, but drastically increase at lower dose levels, e.g. 80 Gy, such that it is difficult to draw any conclusion. Also for the NTCP-dose relationship the clinical impact of uncertainties may be different for individual patient cases than what the population model might suggest. Several authors have noticed large differences in D_{2cm^3} doses due to inter or intra-fraction changes for individual patients [202, 203, 214], reflected in the large standard deviations (20-30%) of this type of uncertainty [111]. Again however, despite that both individual and population-based dose-response models can be parameterised by the same kind of variables and can be linked, a reliable derivation of patient-specific values for these parameters is difficult. In summary, the magnitude of individual patients' data pairs, $\{\gamma_{50}, \mathrm{TCD}_{50}\}$, cannot be accurately estimated from population-based data

[9] For example, for an individual patient the theoretical dose-response relationship is a step function, which has an infinite slope and thus an individual patient's TCP cannot be obtained from clinical data.

due to inter-patient heterogeneity [217], and therefore the clinical impact of uncertainty on an individual patient may not be inferred from the presented data.

In theory, using three opposed to four BT fractions and compensating this with dose escalation to 8-10 Gy per fraction, as also performed in the Erasmus MC in Rotterdam, would increase the clinical impact of random errors as a larger residual persists. Therefore, another simulation study was carried out in which the consequence on the local control or tissue morbidity of random uncertainty with standard deviations of 12% for the target and 25% for the OARs was computed for a treatment with three fractions (MATLAB script not provided). At the planning-aim dose level of 90 Gy, it was found that this fractionation schedule resulted in no differences in simulated local control for the population in comparison with one with four fractions. This is in accordance with the negligible differences found in the study by Nesvacil et al. when the fractionation schedule is changed [38]. For this random uncertainty an increase from 3.1% to 3.3% in predicted rectal tissue morbidity was simulated for a four or three fraction treatment schedule, similar to the changes reported by Nesvacil et al. [38].

There are some limitations to the models used in this study. As argued in 1.2.4, the simplified logit-models used are not mechanistic but rather are fits to a clinical data set and have therefore limited predictive power [32]. Moreover, a uniform dose is assumed in the irradiated structures, whereas in BT the dose distribution is heterogeneous. Lastly, the dependence on the modelling parameters γ_{50}, $\mathrm{TCD}_{50}\}$, α/β may alter results, although previous studies have found that the model is robust against small variations in these values [38, 134].

2.5 Conclusions and future work

In this study dosimetric uncertainties in cervical cancer BT were reviewed and their clinical impact on the predicted local control and tissue morbidity were assessed. Inter-fraction uncertainty is likely the greatest contributor to the uncertainty budget and the dominant factor affecting the clinical impact. It is comprised mainly of dosimetric variation due to changes of the anatomy relative to the applicator and contouring uncertainty. Inter-fraction uncertainty negatively affects the delivered dose applied to the tumour volume with a relative dosimetric difference of -2.5 $\pm$ 11.0% per BT fraction ($k = 1$). The delivered dose to organs at risk may be increased with up to around 4.0 $\pm$ 20% ($k = 1$) due to this type of uncertainty. Nevertheless, the clinical impact of dosimetric uncertainty components in general is found to be limited when simulated over a large population with the simple model used in this study. The data generated in this study indicates that, when it is assured that the target region receives a high dose (>85 Gy), the probability of local control is rather robust against the reviewed uncertainties (<1.0% decrease). Also for OARs the impact of dosimetric uncertainty on the occurrence of tissue morbidity is for most types of uncertainty <1.0% for the simulated population. Inter-fraction changes are however able to substantially affect the clinical outcome for OARs. Inter-fraction changes may realistically increase the occurrence of more severe complications of the bladder or rectum by 1.5 and 3.7% respectively. Potentially, at higher absorbed doses, these changes are associated with a potential increase in occurrence of 2.0 and 9.0%. Moreover, for individual patients the effects of dosimetric uncertainty may even be more pronounced than this analysis indicates. However, the used model was not able to accurately predict these effects. For future work, it may be interesting to perturb individual patients' DVHs with dosimetric uncertainty and evaluate the effects on clinical outcome with predictive dose-response models. In particular, models that are able to account for the dose heterogeneity in BT, such as EUD-based models, are of interest for this purpose. Moreover, in order to more accurately assess the impact of dosimetric uncertainty on clinical outcome at the individual patient level and to guide quality assurance, future work could focus on characterising uncertainties with the four-parameter model.

3. Inter and intra-fraction uncertainty in cervical cancer BT

3.1 Background

Organs in the pelvic cavity naturally change their position and volume over time, partially influenced by organ filling status. Due to the steep dose gradient of BT, even the slightest geometric changes of organs with respect to the implant may lead to dosimetric deviations of around 20-25% (1 SD, including contouring variations) [99], and possibly adverse effects on the treatment outcome. In the previous chapter it was shown that inter-fraction uncertainty, in particular anatomical changes of organs relative to the BT applicator during or in between fractions, can have a significant impact on the predicted tissue morbidity of OARs. For individual patients the dosimetric differences due to inter-fraction uncertainty may even be greater [98], as pelvic organ motions seem to be patient-specific [218]. Although the high standard deviations of the dosimetric uncertainty established in the previous chapter partially indicate the unpredictable nature of the movement of organs and individual patient heterogeneity, the non-zero mean dosimetric errors also indicate general population motion patterns. Rather than that displacements or deformations are fully random, for several reasons it would make sense that organs follow directional motion patterns in the case of cervical cancer BT. First, the BT applicator (along with vaginal packing) and surrounding bony anatomy are rigid and therefore provide boundary conditions for the movement of organs [219]. Moreover, movement in the lateral directions of organs at risk is limited by broad ligaments, whereas motions in the other directions or rotations are permitted [220]. Furthermore, in the case that no strict filling/emptying protocols are used, the volume of the hollow organs may increase systematically during treatment [111]. Additionally, over the course of BT treatment, minor tumour regression may be expected [112, 113], possibly influencing the position of surrounding organs. Lastly, motion of the organs may not entirely be independent of each other, although evidence on this is mixed [220]. For example, it is mentioned that the peritoneum allows almost independent movement of the bladder, cervix-uterus, and rectum-sigmoid [221]. Supporting this finding is that in some studies only weak correlations between intra-fraction organ motions are found [204, 214]. Knowledge of the motion and volumetric patterns of organs, random or directional, can aid in determining dwell position locations robust against these changes. For this reason, a review of inter and intra-fraction geometric uncertainty is required and in this chapter presented.

Jadon et al. have systematically reviewed literature on inter and intra-fraction pelvic organ motion during EBRT [218]. However, these findings are not directly applicable to BT. First, as mentioned, the BT applicator influences the movement of the organs surrounding it. Secondly, the length of both types of treatment is different and preparation protocols, e.g. of the bladder and bowel, are used more frequently for BT [149]. More importantly, as the applicator can move several millimetres relative to bony marks, rather than expressing changes with respect to the bony anatomy as is often done for EBRT, changes of organs must be expressed relative to the applicator [7, 198]. A review that is specifically focused on inter and intra-fraction uncertainty in brachytherapy does not exist.

3.2 Materials and methods

A brief review of literature was carried out where peer-reviewed full-text articles and conference papers were sought. No restrictions relating to the publication status were applied. This review

included: (i) a systematic search using keywords related to cervical cancer, brachytherapy, OAR movement and time-span (e.g. inter-fraction), (ii) a search of articles using image registration techniques based on the recent review by Jamema et al. [189], and (iii) a manual search based on the reference lists and forward citations of these articles.

A list of exclusion criteria was developed to obtain relevant articles. As the focus of this study is on brachytherapy, other radiotherapy studies not incorporating brachytherapy were excluded. Also literature regarding brachytherapy with interstitial applicators without an intracavitary implant were excluded. The study had to report geometric variations of one or more OARs -i.e. bladder, rectum or sigmoid- and preferably these deviations had to be relative to the applicator or CTV_{HR} and not any other reference frame, e.g. bony anatomy. If volumetric changes of OARs were reported, then the article was automatically included, regardless of the reference frame selected.

3.3 Results and discussion

3.3.1 Inter-fraction changes

Ten studies were identified in this review which reported inter-fraction volumetric or positional changes for one or more OARs. The findings of these studies are summarised in Table A.1. In these studies, inter-fraction changes were measured over different applicator insertions, spanning from a single day up to a week apart. Regarding volumetric changes, all studies that catheterised the bladder, e.g. through a Foley catheter, or used a uniform bladder filling protocol did not find significant changes in the bladder volume over treatment [68, 145, 198, 210]. In the study by Hellebust et al., where no such a protocol was used, the bladder volume decreased significantly over the treatment duration, likely due to radiation-induced irritation [126]. Additional analyses summarised in Table A.3 showed that induced bladder distension is capable of these large volumetric and positional changes of OARs. Despite that a rather constant volume throughout treatment can be achieved by adhering to bladder protocols, shape changes of the bladder may still influence dosimetry [198]. Relative inter-fraction rectum variations were in some studies found to be greater than that of the bladder [126, 210], but in others not [145, 198], and may be minimised through bowel preparation [145]. Inter-fraction sigmoid volumetric changes are likely small [145], and may be attributed to contouring difficulties [166, 169].

A limited amount of studies describe inter-fraction positional changes of OARs relative to the BT applicator and no data was found regarding inter-fraction centre of mass/volume changes of full organs. Liao et al. describe centre of mass changes of the $2cm^3$ volume receiving the highest dose, which were found to be greatest for the sigmoid and less for the bladder and rectum [222], corresponding to the permitted motion freedom of these organs. However, the displacement of these highly irradiated volumes is not much of interest as these do not have fixed locations on the organs. The displacement of OARs may be several millimetres of magnitude based on the average of the distance between two contours [223]. None of the reviewed studies specified preferred directions of motion of OARs, indicating that this may well be stochastic. Inter-fraction motion patterns have been described for ICRU or other OAR points relative to bony anatomy [224–228]. The results of these studies are mixed possibly reflecting differences in clinical practice among institutes, with mean Euclidean displacements ranging anywhere from 4 to 28 mm, and limited population sizes. Nevertheless, some general observations may be done based on this data. No evidence was found that would indicate preferred motion directions of OARs, contrary to the review for radiotherapy by Jadon et al. where it was observed that lateral movement is less than the motion in other directions [218]. However, this may be explained by the presence of vaginal packing in BT treatment which

could limit anteroposterior and superoinferior motion and allow for lateral movement of OARs. The mean vector displacements of organs relative to bony anatomy found in these studies seemed to be greater, i.e. >10 mm, than those identified in studies relative to the applicator, often <10 mm. This would possibly indicate that these organs move along with the motion of the applicator, but concrete evidence for this is lacking. Moreover, the measured OAR displacements in these studies generally show large standard deviations and presence of outliers, reflecting patient heterogeneity. Lastly, due to the large dosimetric and possible clinical impact of this geometric uncertainty, it is recommended to perform image acquisition and to optimise treatment plans for each BT fraction.

3.3.2 Intra-fraction changes

Despite the relatively short duration of the delivery of a brachytherapy fraction, significant intra-fraction variations in dosimetry have been reported previously (see Subsection 2.3.1). Contrarily, little has been published on the magnitude of volumetric or positional changes of OARs during treatment delivery, and this has been summarised in Table A.2. Relatively small increases in the volume of bladder, rectum and sigmoid were reported by Simha and colleagues for treatment with a short duration and with the use of filling protocols [202]. In the study by Anderson et al. larger changes in the volume of organs occurred, but also with a longer treatment time and these changes were not found to be significant [214]. In individual patients, however, large variations in the volumetric changes were observed. Interestingly, these authors found no correlation between the treatment duration and OAR movement, noting that this would imply that "OAR movement is stochastic". However, in this article it is not described how OAR movement is assessed and this conclusion is likely drawn based upon group aggregate data. Significant intra-fraction changes in bladder and rectal volume occurred in the study by Miyasaka et al., likely as the bladder filling protocol was not used consistently [204], which stresses the importance of adhering to BT guidelines as also illustrated in Table A.3.

In the identified studies describing intra-fraction positional changes, the average variations were found to be small and below 3 mm in all directions for the bladder and rectum. Miyasaka et al. observed larger systematic changes (>3 mm) in the position of the bladder in superior-inferior direction in some individuals, likely due to the absence of bladder catheters [204]. Expansion of the rectal wall in anteroposterior direction was also observed in some individuals, likely due to the build-up of gas which may occur even after bowel preparation. Similar observations were done in other studies [201, 229]. Counteracting rectal filling may be done through rectal catheters (Figure 3.1) [203], but in general rectal filling is difficult to prevent completely and in many institutes not part of regulatory practice. Sigmoid movement was not observed to be larger than that of the bladder or rectum, nor predictable in the study by Mazeron et al. [230]. However, Phillips and colleagues found intra-fraction movement of the sigmoid to be greater than that of the bladder and rectum [231], which would correspond with the freedom of motion that the topography allows. In conclusion, intra-fraction displacement of OARs may be several millimetres of magnitude in all directions, but may assumed to be random when adhered to BT protocols and when reviewed over a large population. There are indications that in general the rectum progressively fills during treatment and systematically expands in the anteroposterior direction. For individual patients volume and positional variations may be up to an order magnitude larger, but specific motion patterns are not precisely described. Intra-fraction uncertainty is difficult to address -opposed to inter-fraction uncertainty when imaging facilities are available- and hence almost inherent to treatment. Therefore, as a first step robust applicator design could focus on determining dwell positions robustly against these intra-fraction changes.

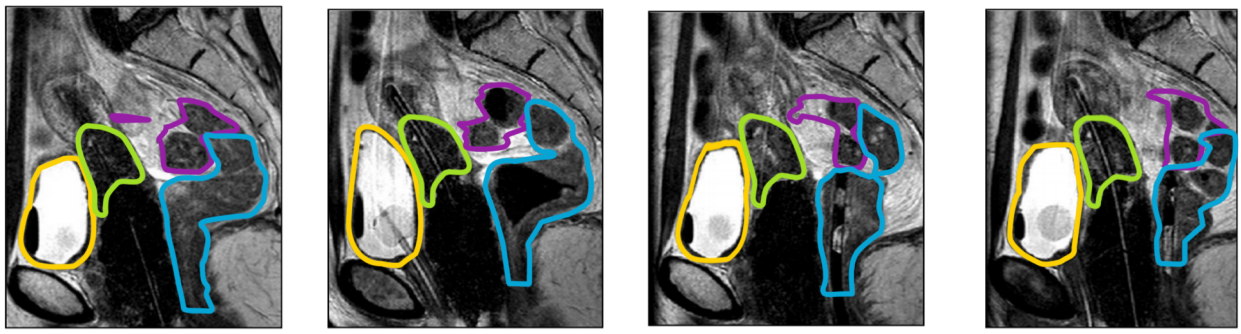

(a) MRI before treatment. **(b)** MRI after 4h prior to irradiation. **(c)** MRI after insertion of rectal catheter. **(d)** MRI post-irradiation.

Figure 3.1: MR images showing the deformations due to rectal filling occurring prior to and during treatment. When not counteracted, the rectal wall expands in anteroposterior direction and becomes more proximal to the implant. After insertion of the rectal catheter (c, just prior to irradiation), the rectum stabilises through the use of rectal catheters (d, just after irradiation). Shown are: target volume (bright green —), bladder (gold —), rectum (blue —), and sigmoid (purple —). Figure adapted from Ref. [232].

3.4 From population analysis to patient-specific planning

The motions of pelvic organs are likely patient-specific [218], reflected in the observation that intra-fraction dosimetric differences show great heterogeneity [201–203]. As such, no distinct motion patterns have been identified in the literature review and independent stochastic rigid body translations based on population data are assumed for the BT needle channel planning problem as more elaborately described in Section 4.3. However, organ motion is comprised of a series of complex interactions and deformations with a higher dimensionality, which may not be accurately reflected in these population statistical rigid motion models [233]. Therefore, the use of population-based models, e.g. from literature analysis or population analysis, to develop patient-specific robust applicators would only have limited effectiveness. The acquisition of patient-specific data, e.g. via serial images, however is time intensive and in many cases not possible. One important development to enable individualised predictions of OAR motions or deformations from population analysis is principal component analysis (PCA), which mainly has been used for prostate cancer radiotherapy [233–235], and only recently and in lesser extent for cervical cancer [236, 237]. Tilly et al. formulated a population statistical shape model (SSM) of the cervix, bladder and rectum from a set of patients from whom multiple images were obtained [237]. Seven dominating eigenmodes were needed to explain the variance in organ motions of patients. This SSM could then be tailored to an individual patient using three image series with sufficient accuracy, corresponding to obtaining two deformation vector fields per patient. Rigaud et al. also built a SSM based on a training set of patients, but generated potential anatomies for an individual patient based on a single scan [236]. From leave-one-patient-out validation again a sufficient accuracy in the prediction of motions of the cervix-uterus and bladder seems to be achieved, which translated into better dose conformity of these modelled plans in comparison with classical library-based plans. However, such algorithms have not been applied previously to cervical cancer brachytherapy, nor to more mobile organs such as the sigmoid. The modelling of these more complex situations has recently been the topic of research [238]. These algorithms currently still have limited predictive power, and must be improved further for clinical use. Ideally, a SSM would be derived from principal component analysis for cervical cancer brachytherapy, such that based on the pre-planning MRI organ motion or deformations may be predicted for individual patients such that robust patient-tailored applicators can be developed.

4. The BT needle channel planning problem under uncertainty

4.1 Terminology and concepts in motion planning

In this chapter, the BT needle channel planning problem under uncertainty is introduced, which is a typical motion planning (MP) problem. Therefore, first some basic terminology and concepts in the field of motion planning are introduced. The terminology in this section has mainly been adopted as used in the popular book by LaValle [239], and a previous unpublished literature study on the topic of motion planning under uncertainty [240].

4.1.1 Topological spaces

Configuration space

Definition 4.1.1. The **configuration space** $\mathcal{C}$ (C-space) is the set of all configurations $\mathbf{q} \in \mathcal{C}$ of a system/agent $\mathcal{A}$ in world $\mathcal{W}$ [239].

A configuration is a set of parameters which defines the position and orientation of a system. In order to describe a configuration $\mathbf{q}$, translations are represented by Cartesian coordinates with values in Euclidean space $\mathbb{R}^n$ (n indicating the dimension), and rotations are expressed in angular coordinates with values in the *special orthogonal group* $SO(n)$, which is the set of $n \times n$ rotation matrices. A rigid body in three-dimensional (3D) space ($n = 3$) which is allowed to rotate and translate is represented with the set $SE(3)$: $\mathcal{C} = \mathbb{R}^3 \times \mathbb{RP}^3$, which is a six-dimensional differentiable manifold. Such a differentiable manifold is also known as a **Lie group**. Usually, a configuration in 3D-space is parameterised with $(x, y, z)^T$ for translation, and for example Euler angles $(\phi, \theta, \psi)^T$ for rotation. In a two-dimensional world ($n = 2$) the set of configurations which can be attained by the system is expressed as $\mathcal{C} = \mathbb{R}^2 \times \mathbb{S}^1$, or $SE(2)$. This manifold is homeomorphic to $\mathbb{R}^2 \times \mathbb{RP}^2$. A system's configuration is then commonly parameterised with generalised coordinates $\mathbf{q} = (x, y, \theta)^T$. When time is explicitly incorporated as an additional dimension, the combined space is sometimes referred to as configuration-time space $\mathcal{CT}$.

State space

Definition 4.1.2. The **state space** $\mathcal{X}$ is the set of all possible states $\mathbf{x} \in \mathcal{X}$ of a system/agent $\mathcal{A}$ in world $\mathcal{W}$ [239].

A state usually encompasses the agent's configuration and velocity: $\mathbf{x} = (\mathbf{q}, \dot{\mathbf{q}})^T$. This implies that the state space is of a higher dimension than the configuration space. When time is explicitly incorporated, the combined space is sometimes referred to as state-time space $\mathcal{XT}$.

Obstacle space

Definition 4.1.3. The **obstacle space** $\mathcal{O}$ is the set of all possible configurations, then denoted as $\mathcal{C}_{obs} \subset \mathcal{C}$, or states, $\mathcal{X}_{obs} \subset \mathcal{X}$, at which the system is in intersection with obstacle region $\mathcal{O} \subset \mathcal{W}$, which is the union of individual obstacles [239].

The set of configurations or states where the agent is in collision can then mathematically be formulated respectively as $\mathcal{C}_{obs} = \{\mathbf{q} \in \mathcal{C} \mid \mathcal{A}(\mathbf{q}) \cap \mathcal{O} \neq \emptyset\}$, and $\mathcal{X}_{obs} = \{\mathbf{x} \in \mathcal{X} \mid \mathcal{A}(\mathbf{q}) \cap \mathcal{O} \neq \emptyset\}$

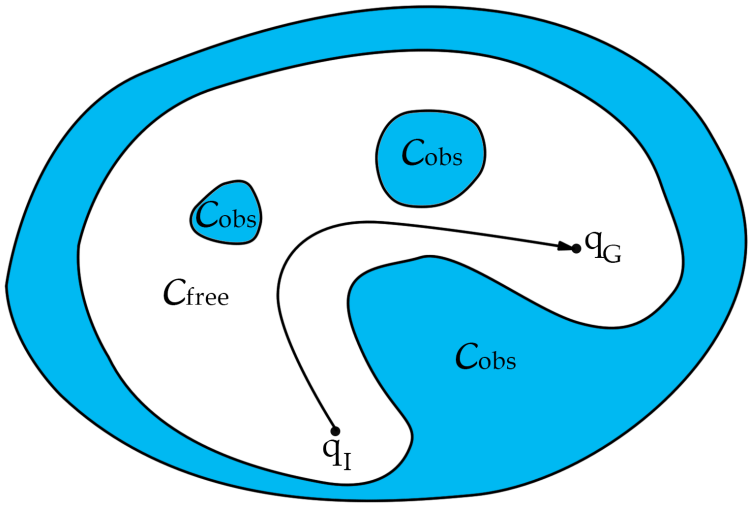

Figure 4.1: The basic path planning problem, known as the Piano mover's problem, where a collision-free path from q_I to q_G in $\mathcal{C}_{free}$ must be found. Image adapted from [239].

although other definitions of the obstacle state space are possible (e.g. inevitable collision states). Individual obstacle regions can then with slight abuse of notation be abbreviated to $\mathcal{C}_{j,t}$ or $\mathcal{X}_{j,t}$ with subscript $_t$ indicating their possible time dependence.

Free space

Definition 4.1.4. The **free space** $\mathcal{C}_{free}$ or $\mathcal{X}_{free}$ is the complement of the obstacle space: $\mathcal{C}_{free} = \mathcal{C} \backslash \mathcal{C}_{obs}$ or $\mathcal{X}_{free} = \mathcal{X} \backslash \mathcal{X}_{obs}$.

The free space is generally an open set. One may want to be able to compute semi-free paths/ trajectories as well, which requires closing the set: $\text{cl}(\mathcal{C}_{free})$ or $\text{cl}(\mathcal{X}_{free})$.

4.1.2 Motion planning definitions

The terms motion, path and trajectory planning are often used interchangeably, but are in this work strictly defined. The following definitions are introduced for this purpose:

Path planning

Definition 4.1.5. In **path planning** a collision-free geometric curve $\tau : [0, 1] \rightarrow \mathcal{C}_{free}$ is sought from an initial point $\tau(0) = \mathbf{q}_I \in \mathcal{C}_{free}$ to a target point $\tau(1) = \mathbf{q}_G \in \mathcal{C}_{free}$.

This basic problem formulation only considering geometrical planning aspects is known as the *Piano mover's problem*, illustrated in Figure 4.1.

Trajectory planning

Definition 4.1.6. In **trajectory planning** time information is included along a path, and the velocity or acceleration along the path satisfies the differential constraints of the agent. In this type of planning, most often a trajectory $\tilde{x} : [0, T] \rightarrow \mathcal{X}_{free}$ is sought from an initial state $\tilde{x}(0) = \mathbf{x}_I \in \mathcal{X}_{free}$ to a target region $\tilde{x}(T) \in \mathcal{X}_G \subset \mathcal{X}_{free}$.

Trajectory planning is a type of motion planning under **differential constraints**. These constraints are a set of differential equations used to limit the velocities and in some cases accelerations of the system, representing mechanical limitations of the system [239]. Differential constraints may be formulated either implicitly, $g_i(\mathbf{q}, \dot{\mathbf{q}}) = 0$ or parametrically, $\dot{\mathbf{x}} = f(\mathbf{q}, \mathbf{u})$, where the latter is used more frequently due to its simplicity. The trajectory planning equivalent of the Piano mover's problem is known as the differentially-constrained mover's problem [241].

The two main trajectory planning approaches are a **coupled** or a **decoupled** approach (Figure 4.2) [239], although also hierarchical and reactive approaches may be considered [242]. The later two, however, require obtaining local information, i.e. local sensing, which is not useful in this study. In the *coupled* approach, also known as *direct planning*, a solution of the path and velocity/acceleration profile -satisfying the system's kinodynamic constraints- is searched simultaneously and directly in the state space $\mathcal{X}$ or state-time space $\mathcal{XT}$ [239]. In some studies [243], this approach is referred to trajectory planning itself, but this term is reserved for planning under differential constraints in general. In a *decoupled* or *decomposition* approach, a trajectory is generated in a multi-step approach separating spatial and temporal planning. This approach usually consists of some of the following steps:

- Computing a collision-free path (path planning): $\tau : [0, 1] \rightarrow \mathcal{C}_{free}$;
- Transforming the path such that it satisfies differential constraints: $\sigma \colon [0, 1] \rightarrow \mathcal{S}$;
- Reparameterising the trajectory with a *timing function* or *time scaling*, $s \colon [0, T] \rightarrow [0, 1]$, to deal with a possible time-changing environment. The convolution of the path and time scaling, $\sigma \circ s$, gives the time-parameterised path in configuration space: $\sigma(s(t)) : [0, T] \rightarrow \mathcal{C}_{free}$. Now fulfilling the differential constraints for all time t, the state trajectory is denoted as $\tilde{x}(t)$;

Various ways to combine these individual modules exist [239]. Especially in more recent approaches, trajectory optimisation is performed directly over seed paths that have been obtained with a different motion planning algorithm.

Motion planning

Definition 4.1.7. In this work, **motion planning** (MP) encompasses both path planning as well as trajectory planning.

4.1.3 Computational or operational criteria of motion planning algorithms

Important computational and operational properties of motion planning algorithms are formalised in the following definitions [241, 244, 245]. The used symbols in these formulations correspond to those defined for trajectory planning, but the definitions hold for path planning as well when $\tilde{x}$ and $\mathcal{X}$ are replaced with τ and $\mathcal{C}$.

Optimality

Definition 4.1.8. Optimal motion planning concerns finding a feasible plan that is optimised out of a set of plans Σ in accordance to some monotonic, bounded criterion $C : \Sigma_{\mathcal{X}_{feasible}} \rightarrow \mathbb{R}_{\geq 0}$ in addition to arriving at the goal state in finite time: $C(\tilde{x}^*) = \underset{\tilde{x} \in \Sigma_{\mathcal{X}_{feasible}}}{\arg\min}\ C(\tilde{x})$ [246]. Here, the asterisk character * is used to optimality.

Optimality may be **global** or **local**, depending on whether a global or local minimum of the cost function is found. A weaker definition of optimality is that of **asymptotic optimality**, which

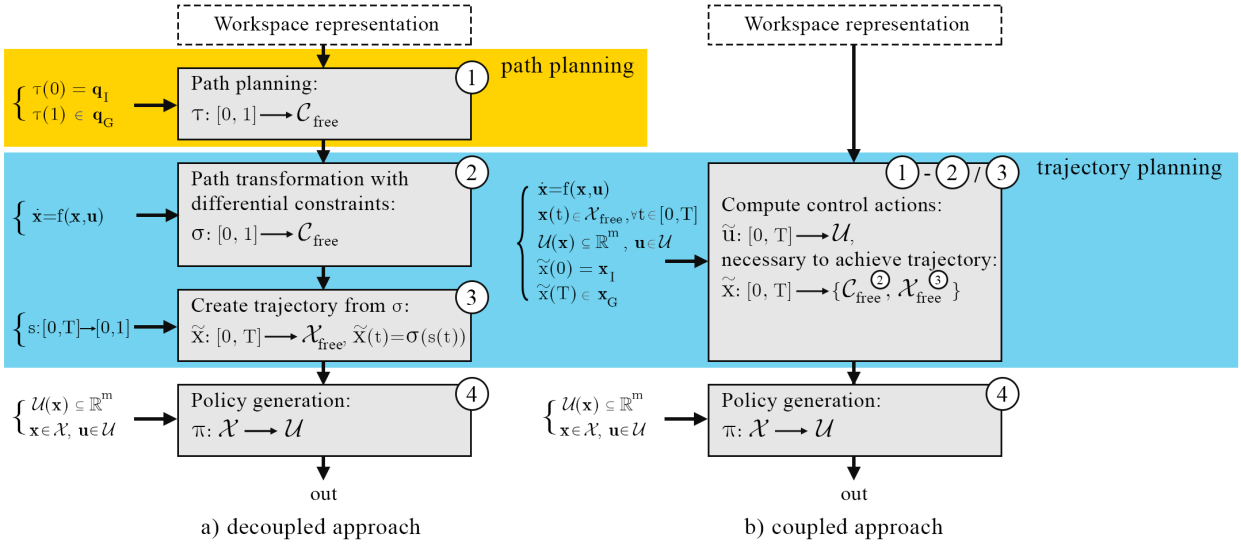

Figure 4.2: Schematic examples of a: (a) decoupled approach, and (b) coupled approach, where the first two (planning in $\mathcal{C}_{free}$) or three (planning in $\mathcal{X}_{free}$) modules of the decoupled approach are combined. Note that this scheme only presents example representations, for example in a path-constrained trajectory planning approach, such as described in Chapter 14 in LaValle (2006) [239], the second and third modules of the decoupled approach are combined. In this case, the time scaling function $s(t)$ is substituted in the equations of motion, i.e. differential constraints, such that the control actions may be obtained. Within motion planning, a distinction is made in this work in path planning (in gold) and trajectory planning (in blue) approaches.

states that the algorithm converges to the optimal solution after infinite time or iterations. Consider a criterion $C : \Sigma_{\mathcal{X}_{feasible}} \rightarrow \mathbb{R}_{\geq 0}$, which is 0 if the trajectory is optimal: $C(\tilde{x}^*) = 0$. The algorithm is assumed to converge to a minimum cost trajectory $\tilde{x}_n$ at iteration n, such that the limit $\lim_{n\rightarrow\infty}(C(\tilde{x}_n))$ exists. Then asymptotic optimality can be defined as [246]: $\mathbb{P}\left(\{\lim_{n\rightarrow\infty}(\sup C(\tilde{x}_n) = C(\tilde{x}^*))\}\right) = 1$. For a plan to be **feasible** in trajectory planning, the planned motion must satisfy the differential constraints, other constraints such as starting in the initial point and finish in the target region in finite time, and lie entirely in $\mathcal{X}_{free}$: $\Sigma_{\mathcal{X}_{feasible}} = \Sigma_{\mathcal{X}_{free}} \cap \Sigma_{\mathcal{X}_{start-goal}} \cap \Sigma_{\mathcal{X}_{steer}}$ [247]. For path planning, $\Sigma_{\mathcal{X}_{feasible}} = \Sigma_{\mathcal{X}_{free}} \cap \Sigma_{\mathcal{X}_{start-goal}}$.

Completeness

Definition 4.1.9. If the algorithm is able in finite time or iterations to find a solution if a feasible solution exists, i.e. $\Sigma_{\mathcal{X}_{feasible}} \neq \emptyset$, or report failure otherwise, this is known as **completeness**.

Many motion planners sacrifice completeness for the weaker notions of: (i) **probabilistic completeness**: the probability that a feasible solution is found if one exists approaches 1 if infinite time is allowed, or (ii) **resolution completeness**: a feasible solution is found if one exists if the resolution is increased beyond some (unknown) level. Resolution completeness is a deterministic property and hence stronger than probabilistic completeness which is a stochastic property. Both properties however do not imply that the planner is able to return failure when no solution exists and hence may run for infinite time. Note that completeness and optimality are intimately related; a necessary precondition for finding an optimal trajectory is that a solution is found if one exists.

Computational complexity

Definition 4.1.10. The **computational complexity** of an algorithm is the running time of that algorithm and is generally, when not indicated otherwise, characterised with an upper bound or worst-case complexity $O(\cdot)$.

This big-O notation $O(f(N))$ with function $f(N)$ indicates that this upper bound on the run time is at most $c \cdot f(N)$ for an input $N > k$ where c and k are finite constants. The input N may be the dimension, number of samples, resolution size, etc. Additionally, computational complexity of MP problems may be classified in P, NP, PSPACE and EXPTIME of which definitions can be found in Chapter 6 in LaValle (2006) [239]. For example, computing optimal (shortest) paths in a 3D environment was shown to be NP-hard [239].

Dimension scalability

Definition 4.1.11. Dimensional scalability is in this study defined as an ordinal variable indicating how the complexity or difficulty of implementation of an algorithm increases with an increase in the dimension of the problem (e.g. of the workspace or the amount of obstacles).

An algorithm is said to have a *'low'* dimensional scalability in this thesis if the algorithm scales exponentially in worst-case computational complexity with an increase in the dimension, if certain formulations have not been implemented previously in higher dimensions (e.g. a 3D workspace), or if the algorithm cannot be extended to higher dimensions. Contrarily, the algorithm is said to possess *'high'* dimensional scalability if an algorithm has a low additional computational cost associated to an increase in the dimension of the problem, and has been implemented or is extendable to higher dimensions. *'Medium'* scalability is assigned to algorithms combining aspects of both other categories.

Anytime

Definition 4.1.12. An algorithm is said to be **anytime** if it is efficiently able to find a feasible solution, of which the quality is iteratively improved.

The *anytime* property is desirable as a valid solution is generated even when the process is interrupted.

Soundness

Definition 4.1.13. Soundness is an property which ensures that the planner returns a feasible solution allowing for guaranteed successful traversal despite uncertainty being present.

Probabilistic soundness is a weaker property, where the planner guarantees safety of the motion up to a probability threshold.

Topologically informed

Definition 4.1.14. A planner is in this work said to be **topologically informed** if it uses topological information of the workspace to guide the planning.

Consider two topological spaces X and Y and continuous maps between these two spaces $f, g \colon X \to Y$. These functions are then called **homotopic** if $f \cong g$, if there exists a continuous function $h \colon X \times [0,1] \to Y$ satisfying $h(x,0) = f(x)$ and $h(x,1) = g(x)$ for all $x \in X$. Informally, two

functions are *homotopic* if one can be deformed continuously into the other without intersecting infeasible regions [248]. **Homology** is closely related to homotopy, and despite subtle differences may be used as a practical analogue [248].

4.2 The use of motion planning for BT needle channel planning

4.2.1 Previous work in needle channel planning algorithms

Three articles have discussed the development of needle channel planning algorithms for patient-tailored BT applicators [88–90], all using variations of standard MP algorithms. Garg et al. developed a rapidly-exploring random tree (RRT) algorithm capable of sequentially planning collision-free curvature-constrained channels in $SE(3)$ from a priori determined target points back to the entry region (Figure 4.3a) [88]. After a needle channel was planned, this was set as an obstacle in the remaining process. Target points were determined from the set of linear segments that maximised dose coverage of the discretised tumour volume in a pencil-packing problem.

Duan et al. formulated a constrained, non-convex optimisation problem and used a trajectory optimisation algorithm (TrajOpt) for locally optimising discretised curvature-constrained needle channel sections in $SE(3)$ from naïve straight line initialisation or perturbed versions of previous solutions [90]. The objective function considered both trajectory length and twist minimisation. In comparison with the RRT algorithm by Garg et al. [88], the trajectory optimisation procedure resulted in a higher success rate in generating feasible plans, whereas trajectory length and twist are decreased. However, this planner is only able to: (i) generate locally -and not globally- optimal trajectories, (ii) generate plans that are highly dependent, e.g. homotopy class-bound (Figure 4.3c and 4.3d), on the seed path used for warm-starting the optimisation [249, 250], (iii) generate trajectories with a stop-and-turn strategy that results in a non-continuous torsion, and (iv) simultaneously plan three needle channels at maximum due to the computation time required.

Patil et al. proposed a two-stage planning algorithm for simultaneously computing multiple curvature and torsion-constrained ensembles of channels called ribbons in $SE(3)$ (Figure 4.3b) [89]. To initialise the algorithm by generating feasible ribbon candidates, a RRT algorithm is used. These candidates are then locally optimised using sequential quadratic programming, based on cumulative torsion and twist. By warm-starting the optimisation with RRT-generated paths rather than naïve seed paths, although the planner is computationally expensive in comparison with RRT, trajectories can more likely be found that have minimum/zero torsion and twist. Ribbons could additionally improve the coverage of the plans, as more channels could be generated in close proximity of each other than in the case of single-channel arrangements. However, the planner is: (i) unable to find feasible solutions in narrow passages, and (ii) only able to return suboptimal / locally optimal trajectories that are highly dependent on the quality and the homotopy class of the solutions returned by the RRT (Figure 4.3c and 4.3d).

Although these algorithms have a great potential for planning needle channels in BT, some improvements must be done in order to incorporate these into practice. In all of these algorithms, straight dwell segments generated based on tumour coverage are used as a starting point, not taking into account OAR dose constraints or the possibility of positioning dwell locations along curved trajectories. Moreover, the simplified kinematic model used only takes into account the minimum radius of curvature, whereas due to the complex bending of the trajectories needle mechanics models may be required. Lastly, in the case of an uncertain environment where obstacle, i.e. OAR, position or volume might be altered, these algorithms could potentially plan

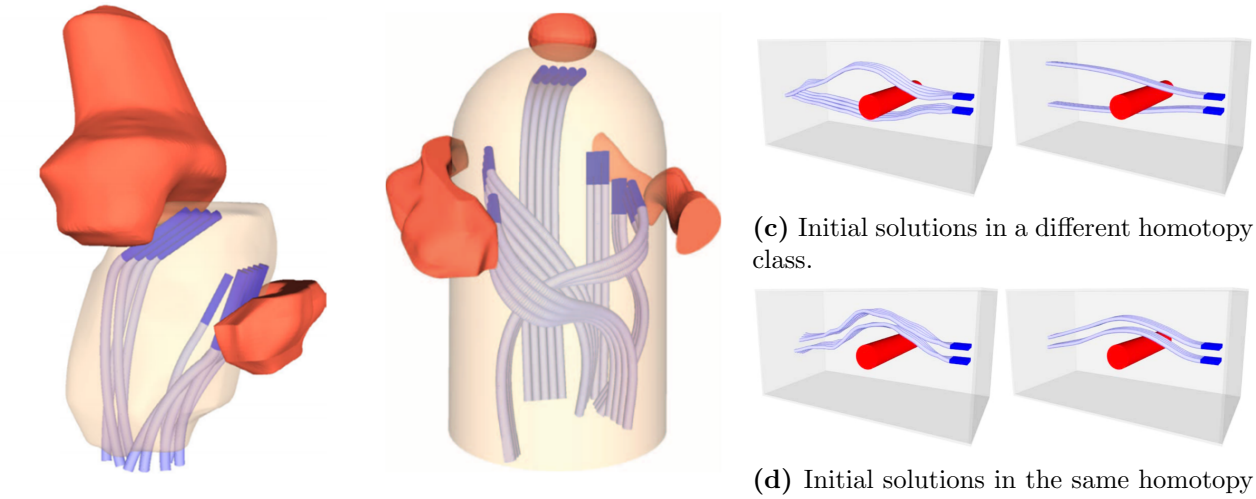

(a) Garg et al. [88].

(b) Patil et al. [89].

(c) Initial solutions in a different homotopy class.

(d) Initial solutions in the same homotopy class.

Figure 4.3: Previous needle channel planners for personalised intracavitary BT applicators depicted by: (a) Garg et al. [88], and (b) Patil et al. [89]. In (c) it is shown that when the initial path generated by RRT is in a different homotopy class, trajectory optimisation is able to compute an optimal path whereas this is not possible when the initial solution is in the same homotopy class (figure adapted from Ref. [89]). Target volumes are coloured in peach, channels are in violet, dwell segments containing multiple dwell points are coloured in dark blue, and obstacles are marked in red.

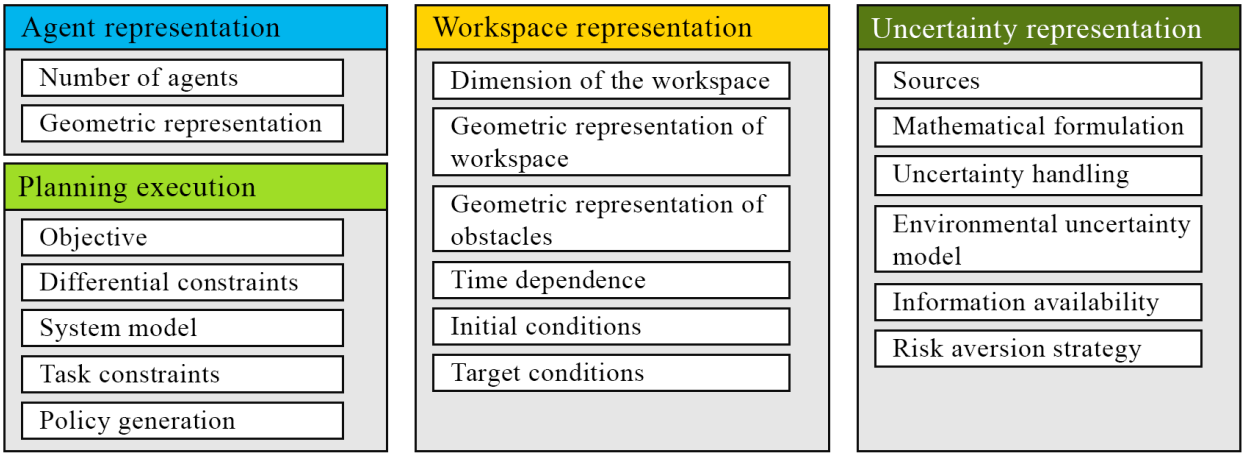

Figure 4.4: Taxonomy for decomposing a motion planning problem into a list of practical considerations.

appropriate dwell locations along the curved trajectories. First, the trajectories returned by these planners may become unusable as dwell locations along these trajectories could exceed OAR dose constraints. Moreover, as these planners are often homotopy-bound, these planners could fail to produce solutions in the narrow environment cluttered with needle channels under uncertainty [251–254]. Moreover, especially plans that are optimised, e.g. with respect to shortest length, can be highly sensitive to changes in the environment [255]. Therefore, in this chapter aspects of motion planning relevant to BT needle channel planning in an uncertain environment are elaborated and the BT needle channel planning problem under uncertainty is formulated.

4.2.2 Decomposing a motion planning problem

Motion planning problems may be decomposed into simple building blocks as is done in MP planning libraries. However, this refractoring approach remains on an abstract level, which is not

comprehensible to a layman. In a previous (unpublished) literature review, motion planning algorithms were dissected based on a simple taxonomy shown in Figure 4.4, based on more tangible practical considerations [240]. This taxonomy is an adaptation of the WRIT taxonomy [256], replacing the component 'information' for 'uncertainty representation' in order to stress the importance of taking into account uncertainty in planning.

4.3 Formulation of the BT needle channel planning problem under uncertainty

BT treatment planning in which the dose distribution is optimised can be formulated as a mathematical optimisation problem [257]. In this section, therefore, the previous clinical notions are converted into mathematical concepts and organised using the taxonomy for motion planning in Figure 4.4. For consistency, when concerning robust MP the notation is used as introduced in the works by Luders et al. [258, 259], whereas the notation by Patil et al. is used for needle planning aspects [89]. Nevertheless, the problem formulation in this chapter is described in general terms and is therefore applicable to and solvable by multiple types of MP algorithms.

4.3.1 Agent representation

Number of agents

For the BT needle channel planning problem multiple needle trajectories must be planned, which can be either simultaneously or sequentially. Simultaneous computation of multiple needle trajectories has been previously described [89, 90, 260]. Although this strategy improves the likelihood of finding feasible and optimal trajectories it is computationally intensive. Sequential planning, where after completion a computed trajectory is subsequently considered as an obstacle and added to the set $\mathcal{X}_m$, is simple and sufficient for this thesis. The state of the needle tip is denoted as $\mathbf{x}_t^i$ for $i = 1, ..., n_x$ needle channels.

Geometric representation

A typically used ^{192}Ir source for HDR-BT can be approximated by a cylinder with a diameter of 0.9 mm, and length $L = 5$ mm (Figure 1.3b). A corresponding plastic BT catheter (6F Pro-Guide sharp needle, Elekta, Stockholm, Sweden) has an outer diameter of 2.0 mm, such that the minimum channel width is set at $w = 2.6$ mm. The length of the source is used to limit the maximum step size $\bar{\lambda} = L = 5$ mm, which also corresponds with the commonly used intervals between dwell points in BT.

Considering that obstacle regions, i.e. OARs, are not necessarily occupying the stay-in region of the source positions, the physical geometry of the BT source is only important for avoiding collision with other needle channels. Of more relevance to the needle channel planning problem is the spatial dose distribution of the BT sources, which has been briefly described along the TG-43 formalism in Subsection 1.2.2. From the dose rate per fraction $\dot{d}(r, \theta)$ in Eq. 1.5, conventionally the total dose per fraction from a set of dwell points along catheter i to a calculation point p_d (with polar coordinates $[p_r, p_\theta]$) in treatment planning software is obtained via:

$$d_{p_d} = \sum_{i=1}^{n_x} \sum_{z_p^i=1}^{n_d^i} \dot{d}_{z_p}^{\,i}(p_r, p_\theta) \cdot t_{z_p^i} \tag{4.1}$$

where, d_{p_d} denotes the total dose at point p_d, $z_p^i = 1, ..., n_d^i$ indicates a dwell point and $t_{z_p^i}$ the corresponding dwell time. However, incorporating such a model already in the motion planning stage adds a high computational complexity and is out of scope for this thesis. For that reason, simplifications of this dose distribution model and DVH-based optimisation are required. First, the dwell time can be fixed to a constant value in the motion planning phase, which places equal importance on each of the dwell points. A consequence of this assumption is for example that dwell positions for which conventionally the dwell time would be set to zero, i.e. positions that are distant from the tumour and likely proximal to OARs, are conservatively placed to avoid exceeding OAR dose constraints. Contrarily, possibly more dwell positions or needles may be placed in the tumour region than required to obtain sufficient dosimetric coverage [108], which would normally be resolved by increasing the dwell time. Such issues may be resolved by adding constraints on the active length of the needle paths. Moreover, the dose distribution in Eq. 1.5 is simplified to a rotational symmetric distribution. This is performed by replacing the geometry function $G_L(r, \theta)$ in Eq. 1.6 by $G_P(r, \theta) = 1/r^2$, and substituting in the 1D anisotropy function $\Phi_{an}(r)$ for the 2D anisotropy function $F(r, \theta)$ [24]. The circular isodose, d_r, at a radius r from the centre of an individual dwell source can then be computed via:

$$d_r = \dot{d}(r) \cdot t_{z_p} = S_K \cdot \Lambda \cdot \frac{G_L(r, \theta_0)}{G_L(r_0, \theta_0)} \cdot g_L(r) \cdot \Phi_{an} \cdot t_{z_p} \tag{4.2}$$

where,

$$\Phi_{an}(r) = \frac{\int_0^\pi \dot{d}(r, \theta) \sin(\theta)\, d\theta}{2\dot{d}(r, \theta_0)} \tag{4.3}$$

and the other parameters are as previously specified. Data for the 1D anisotropy function is scarce, and therefore $\Phi_{an}(r)$ is coarsely estimated from Figure 5 in the article by Sabariego et al. [261]. Motion planning algorithms can leverage this simplification to a spherical symmetric BT dose distribution in several ways. First, the orientation of the agent is no longer of importance for the collision detection algorithm, speeding up the computation. Moreover, the spherical distribution is convex, opposed to the anisotropic distribution which is non-convex, implying that expressions for the intersection with or distance to other convex shapes are in some cases available in closed form. Lastly, this allows for a reduction of the computational complexity by a priori 'inflating' obstacles with a specified radius of the dose distribution, i.e. isodose constraint lines on OARs, for example using Minkowski addition [244], or tightening state constraints [262]. The radius corresponding to a certain dosimetric constraint of an OAR, d_C, is henceforth denoted as $r_{D,j} = \{r \mid d_r = d_C\}$. This dosimetric constraint is expressed as the maximum dose that may be received per dwell point, which can be justified as the total dose is a linear sum of doses from individual dwell points (Eq. 4.1).

4.3.2 Workspace representation

Dimension of the workspace

3D image-guided BT is the current standard of practice and therefore needle trajectories must be planned in a three-dimensional environment. However, in this thesis a simplified two-dimensional problem is treated. Since the geometric uncertainty of OARs is likely smallest in the lateral direction (Section 3.3), the problem is restricted to the sagittal plane. Nevertheless, the mathematics and concepts in planning in this thesis can to a certain extent directly carry over to the three-dimensional case, and for several other instances the required modifications for higher dimensional spaces are mentioned briefly.

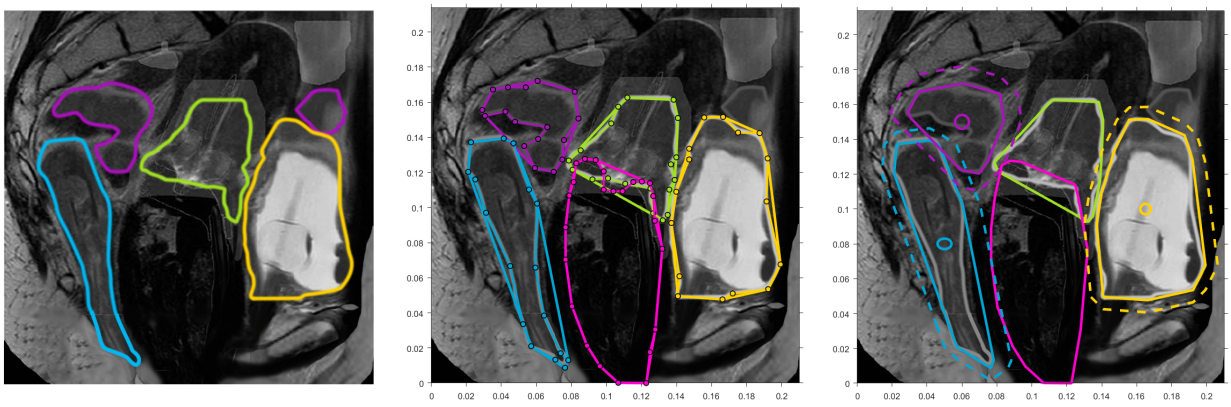

(a) Segmented contours. **(b)** Convexification of structures. **(c)** Addition of uncertainty.

Figure 4.5: Steps in the definition of the workspace. (a) segmented contours, (b) polygonal representation and convexification of structures using MATLAB Script A.1.9, and (c) addition of probabilistic uncertainty (ellipses) or bounded uncertainty (dotted lines). Regions of interest are: target volume (bright green —), bladder (gold —), rectum (blue —), sigmoid (purple —), and stay-in region (pink —). Figure adapted from Ref. [48]. The original image is extrapolated in order to visualise the entry region; the anatomy of the OARs, except for the rectum which is extended slightly as this was cut off on the original image, and target volume is left unaltered.

Geometric representation of workspace / obstacles

Prior to treatment, the clinical target volume and OARs are delineated as structure sets, which can be exported in Digital Imaging and Communications in Medicine (DICOM) RT format[1] containing point-lists per region of interest (ROI). Structures can then be extracted and the data transformed via a convex hull algorithm into three-dimensional volumes, i.e. convex polyhedra, if desired. Such a convex formulation is often required for computational tractability associated with solving the optimisation problem. In the 2D problem treated in this thesis, the data points of the structure set lying on the sagittal plane must be extracted per structure and used for interpolation between imaging slices to obtain closed curves. The extracted intersection curve on the sagittal plane is preferably convex and a simplification of the complex outline, to limit the amount of computation required for motion planning algorithms, despite not being anatomically accurate. If the structure is a convex polytope in $\mathbb{R}^3$, the intersection curve in $\mathbb{R}^2$ is also convex. However, ROIs in BT are not necessarily convex and therefore a simple MATLAB algorithm capable of converting ROIs from DICOM-RT files into simplified convex shapes in the sagittal plane is presented in Script A.1.8. The result of this operation is a set of closed convex polygons conservatively bounding the structures.

An alternative, when only two-dimensional images are available and not DICOM-RT files, is to trace the outlines of structures and to create a convex hull around these outlines for OARs or other anatomical regions. This is the method used in this work and can be seen in Figure 4.5. From this polygonal representation, conversions to any of the representations used for MP described by Hwang and Ahuja are possible [263]. The boundary of the potential volume which may be reached by the intracavitary catheters is arbitrarily drawn -roughly indicating the vaginal cavity- in Figure 4.5b in pink, and defines the stay-in region: $\mathcal{I} \subset \mathbb{R}^n$ [264]. This set can be defined as the conjunction of linear inequality constraints (Figure 4.6a):

[1]DICOM RT files are those which have a SOP class defined by the unique identifier (UID) 1.2.840.10008.5.1.4.1.1.481.3.

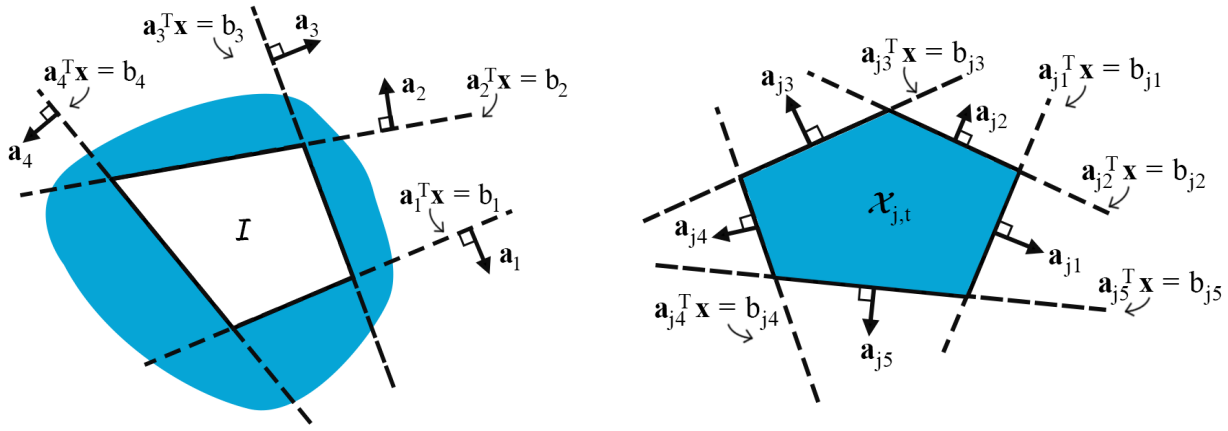

(a) Convex polytopic stay-in region $\mathcal{I}$, represented by a conjunction of linear inequalities. The agent must avoid the blue region.

(b) Convex polytopic obstacle region $\mathcal{X}_{j,t}$, represented by a disjunction of linear inequalities. The agent must avoid the blue region.

Figure 4.6: Representation of the stay-in region and an obstacle using linear inequalities. Figure adapted from Ref. [264].

$$\mathcal{I} = \{\mathbf{x}_t^i \mid A_0\mathbf{x}_t^i \leq \mathbf{b}_0\} \qquad \forall t \in \mathbb{Z}_{0,T}, \forall i \in \mathbb{Z}_{1,n_x} \tag{4.4}$$

$$\mathcal{I} = \bigwedge_{k=1}^{n_I} \mathbf{a}_k^T\mathbf{x}_t^i \leq b_k \qquad \forall t \in \mathbb{Z}_{0,T}, \forall i \in \mathbb{Z}_{1,n_x} \tag{4.5}$$

Organs at risk are considered as obstacles as these must be avoided by the catheters directly as well as by the high isodose lines irradiating from the sources. These are denoted as $\mathcal{X}_{j,t} \subset \mathbb{R}^n, \forall j \in \mathbb{Z}_{1,n_o}$ for n_o convex polytopic obstacles. The subscript $_t$ is used to indicate their possible time dependence. It follows that the jth polytopic obstacle can be defined through the conjunction of n_j linear inequalities (Figure 4.6b) [265]:

$$\mathcal{X}_{j,t} = \{\mathbf{x}_t^i \mid A_j\mathbf{x}_t^i \leq \mathbf{b}_{jt}\} \qquad \forall t \in \mathbb{Z}_{0,T}, \forall i \in \mathbb{Z}_{1,n_x} \tag{4.6}$$

$$\mathcal{X}_{j,t} = \bigwedge_{k=1}^{n_j} \mathbf{a}_{jk}^T\mathbf{x}_t^i \leq b_{jk} \qquad \forall t \in \mathbb{Z}_{0,T}, \forall i \in \mathbb{Z}_{1,n_x} \tag{4.7}$$

As the needles must avoid collision with each of the n_o obstacles, this can be represented by the following disjunction:

$$\bigvee_{k=1}^{n_j} \mathbf{a}_{jk}^T\mathbf{x}_t^i \geq b_{jk} \qquad \forall t \in \mathbb{Z}_{0,T}, \forall j \in \mathbb{Z}_{1,n_o}, \forall i \in \mathbb{Z}_{1,n_x} \tag{4.8}$$

The coefficients b_{jk} can be used to tighten the state constraints, and include the dose constraint radius $r_{D,j}$ to ensure sufficient distance to OARs.

Time dependence

A static environment is assumed due to the lack of detailed information on intra-fraction motion. For this reason, the subscript $_t$ is dropped for the obstacle regions. With the advances in real-time imaging used in BT and the possibility for 4D (compliant) BT applicators, it may be of interest to introduce time-dependency of the environment in a later stage.

Initial and target considerations

Previous BT needle channel planners first compute straight dwell segments, for example by solving a pencil packing problem to cover a discretised tumour region, consisting of dwell points at 5 mm intervals [88–90]. Using these dwell segments as starting poses, these planners then compute a trajectory back to the entry region $\mathcal{E}$ of the implant $\mathcal{I}$ as this is less constrained [88]. Similarly, in related fields, such as inspection planning, the problem is separated into two sub-problems [266]: (1) a coverage planning problem, such as the art-gallery problem, where points are established that sufficiently cover a region, and (2) a motion planning problem where one or multiple agents must visit or approach the found points, such as a travelling or covering salesman problem. Ideally, these two steps would be integrated into a single integrated planning problem where both sufficient tumour coverage and OAR avoidance is assured. However, as both the coverage and motion planning problems are in general cases NP-hard, and this is further complicated by considering multiple non-holonomic agents under environmental uncertainty in this work, solving an integrated problem is typically only tractable through approximate techniques. Several planning algorithms are able to solve integrated problems similar to the one considered in this thesis [266–268], but only consider some of the aforementioned aspects relevant to the BT needle channel problem. Hence, a two-stage approach is used in this work similar to that by Garg et al. [88], where from the coverage planning stage a set of fixed starting poses at the end of straight dwell segments in the target region $\mathbf{x}_0^i \in \mathcal{T}$ is specified. From these poses, robust curvature-constrained trajectories are planned towards the entry region which is reached at final time T, i.e. $\mathbf{x}_T^i \in \mathcal{E}$. Several assumptions are therefore made:

- For simplicity it is assumed that the entire stay-in region for the curvature-constrained trajectory planning is contained within the implant, and the set $\mathcal{I}$ also marks the boundaries of the implant;
- The straight dwell sections are therefore reached interstitially, without any tissue deflections and in a direction tangentially from exiting the implant;
- As the coverage from the interstitial needles may not be sufficient for the CTV_{HR}, additionally dwell points in the implant are present;
- In order to generate feasible trajectories in the second stage, the planner in the first stage must account for worst-case realisations of OAR movement;
- It is assumed that the geometry obtained by optimising spatial coverage of the tumour corresponds with the geometry required for an optimal dosimetric plan; e.g. hot or cold spots within the target region are not accounted for;
- The dwell time of interstitial dwell positions is generally around 10-20% of the total dwell times in IC/IS applicators, such that most of the dose is applied via the tandem and ring/ovoids [51, 269]. However, in the current implementation, a tandem is not necessarily present, and therefore to assure sufficient dose in the target region equal dwell times are assumed in interstitial and intracavitary region;
- This entire process is decoupled from dwell time optimisation, and instead dwell time is set as a constant.

The first problem is therefore to minimise the amount of straight skew dwell segments required to sufficiently cover the tumour region, but simultaneously conservatively avoid OARs. The needle planning by integer program (NPIP) algorithm by Siauw et al. is for this reason slightly modified and transformed to a two-dimensional case [270]. The first step is to generate a candidate set of dwell segments $\mathcal{N}$. In NPIP an entry and target region are defined on two parallel planes in 3D space and skew lines are randomly generated between points on these planes, and are truncated

such that the last dwell point is inside of the tumour region. In this work however, the baseline of the convexified polygonal tumour region is chosen as this 'entry region', and a candidate set of lines is generated from points on the contour of the tumour region (see Figure 4.8). To avoid discretisation issues points are randomly sampled on these contour lines with probability proportional to the length of these contours.

The second step is to find a set of dwell segments $\mathcal{S} \subset \mathcal{N}_{free}$, which is comprised of individual dwell segments $s_i \in \mathcal{N}_{free}$, that: (i) sufficiently cover the target region, (ii) are feasible, i.e. non-intersecting and not colliding with OAR worst-case realisations at least at the boundary of the implant, (iii) minimises the amount of dwell segments required, and (iv) conforms to constraints on the angle at the baseline. In order to assess the coverage of a set of dwell segments, the definition of coverage is first formalised. The convex polygonal tumour region is divided in evenly spaced points $\tau_q \in \mathcal{T}$ using a uniform grid. Assuming a spherical dose distribution, such as given in Eq. 4.2, a dwell point $z_p^i \in s_i$ is said to cover the tumour point τ_q if the latter lies within a ball of radius ϵ centred at z_p^i. Therefore, an individual dwell segment s_i covers τ_q, if: $\exists z_p^i \in s_i : \|z_p^i - \tau_q\|_2 \leq \epsilon$. Here, ϵ is referred to as the dose coverage radius, and is an important parameter to assure dose conformity. In the work by Siauw et al. ϵ is set between 25 and 50% of the radius of an equivalent sphere encapsulating the prostate volume in 5% increments, where $\epsilon =$ 35 or 40% enabled dosimetric constraints to be met for all tested patients [270]. Similarly, in this study the effect of varying the dose coverage radius is investigated. The dwell times $t_{z_p^i}$ can then be adjusted to accordingly set the isodose radius equal to the coverage radius.

It is desirable if a point in the tumour region can be covered by at least one dwell point, an assumption which neglects hot spots. The indices, q, of the tumour points that can be covered by a dwell segment can be expressed as:

$$I(\epsilon) = \{q \mid \exists s_i \in \mathcal{N}_{free} : \|z_p^i - \tau_q\|_2 \leq \epsilon, z_p^i \in s_i\} \tag{4.9}$$

This index function ideally includes all points of the gridded tumour region, but is used in case that some points are not reachable by any dwell segment. The set of dwell segments that covers a specific tumour point q is denoted as:

$$M_q(\epsilon) = \{i : \|z_p - \tau_q\|_2 \leq \epsilon, z_p \in s_i\} \tag{4.10}$$

The second aspect of the coverage problem is to constrain any intersection of multiple dwell segments, which is done by defining the set $\mathcal{Y}$ as all the pair of segments (s_i, s_o) which are within a distance of a multiple of w (channel diameter) of each other and formulating a restriction that only one of the pair can be chosen. To restrict exceeding OAR dose constraints, a convex hull around OARs with worst-case uncertainty is computed and intersection of the segment with a circle of radius $r_{D,j}$, corresponding to the OAR isodose constraint, is checked only at the intersection of the dwell segment with the intracavitary implant. The set $\mathcal{Z}$ defines the segments s_i that are in collision with one of the n_j OAR boundaries or segments that have a too steep angle at the baseline, and limits the segments that may be selected: $\mathcal{N}_{free} = \mathcal{N} - \mathcal{Z}$, with $-$ denoting set subtraction. This implies that at any other position in $\mathcal{T}$ the OAR dose constraints may be sacrificed to ensure sufficient target coverage. Lastly, the goal is to minimise the amount of dwell segments in the set $\mathcal{S}$, which is the objective function of the binary integer problem (BIP). The binary variable $x_i \in \{0, 1\}$ is used to indicate whether a segment is selected in the set $\mathcal{S}$:

$$x_i = \begin{cases} 1 & \text{if } x_i \text{ is selected} \\ 0 & \text{else} \end{cases} \tag{4.11}$$

The resulting BIP is shown in Subsection 4.3.5.

4.3.3 Uncertainty Representation

Sources

In literature commonly a division of uncertainty in motion planning problems is made in: (i) uncertainty in configuration sensing, (ii) uncertainty in configuration predictability, (iii) environment sensing, and (iv) environment predictability [271, 272]. To avoid confusion in how information of the environment is obtained, the term 'sensing' is replaced by knowledge instead. The former two are sometimes jointly referred to as internal uncertainty and the latter two as external uncertainty [259]. Intra-fraction uncertainty is an example of uncertainty in environmental knowledge. To the best of the author's knowledge, for needle trajectory planning this type of uncertainty has not been considered previously. Contrarily, numerous articles have described needle planning under uncertainty in configuration knowledge and predictability, in particular to complex needle/tissue interactions and uncertainty in the position of the needle from sensing modalities [273–275]. Although the extension to uncertainty in configuration knowledge is generally quite simple for standardised problems, i.e. Gaussian uncertainty and linear time-invariant systems, this type of uncertainty is not considered in this work due to the limited clinical impact of configuration uncertainties in BT (e.g. source position, strength, etc.).

Mathematical formulation

Uncertainty in MP can be classified in non-deterministic and probabilistic uncertainty [239], and similarly robustness can be interpreted in a non-deterministic or probabilistic sense. Equivalent are the terms of bounded uncertainty and probabilistic uncertainty [259], and the concepts of worst-case robust optimisation and stochastic programming as for example used in radiotherapy planning [105]. In case of the former type, no probability distribution is required, but rather a bounded uncertainty set is specified in which feasibility is guaranteed for all realisations. The benefit of such an approach is that no underlying probability distribution must be known and that this may take on any shape. Moreover, the use of non-deterministic uncertainty avoids the complexity of computing multi-dimensional probability integrals, which makes probabilistic uncertainty problems in many cases computationally intractable. However, this usually leads to conservative solutions or in the worst case rules out finding any feasible solution. Probabilistic approaches compute and optimise the likelihood or expectation of feasibility and ensure that this does not exceed a pre-set threshold. Such a method is particularly useful as it allows for sophisticated analysis of the conservatism versus the success rate of generating feasible paths [276]. Moreover, in several cases, probability distributions can better or more naturally describe the uncertainty than set boundaries or are readily available, e.g. as provided by (extended) Kalman filters [277]. As both methods have distinct benefits, it was decided to implement and review both for BT needle channel planning in this thesis.

Uncertainty handling

The uncertainty handling method is of great importance on several performance guarantees, which commonly involves a trade-off between feasibility and soundness on one hand, and computational tractability and scalability to more complex situations on the other. Motion planning algorithms may handle probabilistic uncertainty analytically or use approximation techniques, such as (Monte Carlo) sampling or numeric integration [278]. Similarly, for set-bounded uncertainty, analytical results may be possible, but also tractable reformulations/approximations have been proposed [279]. Although analytic techniques are preferred for the BT problem due to their performance guarantees, approximate techniques are more flexible and generally computationally faster.

Environmental uncertainty model

Uncertainty in the environment can be modelled implicitly or explicitly [239]. In this thesis, a static environment is assumed, with explicitly defined spatial and geometric uncertainty of organs at risk corresponding with the analyses in Chapter 3. Several conclusions may be drawn from this analysis and translated into modelling:

- Volumetric changes of OARs are likely to be limited when protocols are strictly adhered. Therefore, the shape of obstacles $\mathcal{X}_j$ is assumed to be constant;
- Rotational movement of OARs is constrained and has limited impact, and hence only translational movement needs to be modelled;
- Movement of OARs is likely independent and is therefore modelled as uncorrelated;
- No specific motion patterns are observed and therefore the translational movement of OARs may be modelled to be stochastic, i.e. Gaussian with equal eigenvalues of the covariance matrix, or bounded with equal values in all directions;
- Variation of the sigmoid is greater than that of the bladder and rectum;
- Expansion of the rectum in the anteroposterior direction may be stochastically modelled by increasing the eigenvalue of the corresponding eigenvector, or non-deterministically by increasing the bound in the anterior direction;

OARs are therefore modelled as obstacles with an uncertain position, but known shape and orientation, leveraging the framework provided in the articles by Luders et al. [259, 265]:

$$\mathcal{X}_j = \mathcal{X}_{j,0} + \mathbf{c}_j \qquad \forall j \in \mathbb{Z}_{1,n_o} \tag{4.12}$$

where, the + operator is used to denote a set translation which is represented by $\mathbf{c}_j \in \mathbb{R}^n$ as follows:

$$\begin{cases} \mathbf{c}_j \sim \mathcal{N}(0, P_{c_j}) & \forall j \in \mathbb{Z}_{1,n_o} \quad \text{(probabilistic formulation)} \\ \mathbf{c}_j \in S_j & \forall j \in \mathbb{Z}_{1,n_o} \quad \text{(bounded formulation)} \end{cases} \tag{4.13}$$

In the probabilistic formulation, the distribution of the translation is therefore a zero-mean Gaussian with covariance matrix $\Sigma_j = P_{c_j}$. For the bounded uncertainty formulation, the translation is contained in a set, of which there are several possibilities. For example, as used in the bounded uncertainty formulation by Luders and How, the (convex) polytopic set S_j, with worst-case realisations is written as the conjunction of linear inequalities: $S_j = \{\mathbf{c}_j \mid E_j \mathbf{c}_j \leq \mathbf{f}_j\}$ [259]. Alternatively, the bounded formulation may be based on the popular moment-based ambiguity sets. These methods -similar to probabilistic approaches- require a mean and covariance of the uncertainty, but from an unknown underlying distribution. Collision avoidance constraints are enforced under the worst-case distribution drawn from the ambiguity set $\mathcal{W}$ [280]. In this case the following formulation would be used:

$$\mathbf{c}_j \sim W_j^c \in \mathcal{W}_j^c \qquad \forall j \in \mathbb{Z}_{1,n_o} \qquad \text{(bounded moment-based formulation)} \tag{4.14}$$

For non-deterministic planning approaches the bounded set S_j may be any type of uncertainty set, e.g. a funnel or reachable set, and is deliberately not elaborated further in this section in order to limit the loss of generality.

With the specification of the environmental uncertainty, the disjunction in Eq. 4.8 can now be expressed via:

$$\bigvee_{k=1}^{n_j} \mathbf{a}_{jk}^T \mathbf{x}_t^i \geq b_{jk} \iff \bigvee_{k=1}^{n_j} \mathbf{a}_{jk}^T \mathbf{x}_t^i \geq \mathbf{a}_{jk}^T \mathbf{C}_{jk} + r_{D,j} \qquad \forall t \in \mathbb{Z}_{0,T}, \forall j \in \mathbb{Z}_{1,n_o}, \forall i \in \mathbb{Z}_{1,n_x} \tag{4.15}$$

where, $\mathbf{C}_{jk} = \hat{\mathbf{c}}_{jk} + \mathbf{c}_j$. In this formulation, $\hat{\mathbf{c}}_{jk}$ is a point on the kth constraint line of obstacle j when no uncertainty is present. $r_{D,j}$ is the radius of the isodose constraint line for the jth OAR. Conforming the findings in the literature review, the following parameters are coarsely estimated:

$$P_{c_{\text{bladder}}} = \begin{bmatrix} 9 & 0 \\ 0 & 9 \end{bmatrix} \text{ mm}^2; \quad P_{c_{\text{rectum}}} = \begin{bmatrix} 16 & 0 \\ 0 & 9 \end{bmatrix} \text{ mm}^2; \quad P_{c_{\text{sigmoid}}} = \begin{bmatrix} 16 & 0 \\ 0 & 16 \end{bmatrix} \text{ mm}^2; \tag{4.16}$$

$$\mathbf{f}_{\text{x,y,bladder}} = \mathbf{f}_{\text{y,rectum}} \in [-6,\ 6] \text{ mm}; \mathbf{f}_{\text{x,rectum}} = \in [-6,\ 8] \text{ mm}; \mathbf{f}_{\text{x,y,sigmoid}} \in [-8,\ 8] \text{ mm}; \tag{4.17}$$

Here, $\mathbf{f}_j$ is used to describe the bounded displacement interval and subscripts $_{x,y}$ are used to indicate the direction of displacement. An illustration of the probabilistic and bounded uncertainty scenario is shown in Figure 4.5c.

Information availability

Information on the environment is obtained in the pre-planning imaging session and imaging sessions prior to treatment delivery, such that motion planning is performed 'offline' with an invariable information set.

Risk aversion strategy

Decision-making under uncertainty has been studied in numerous fields, in which utility functions have been commonly used. With regard to motion planning, the notions from utility theory may be lend (e.g. see Ref. [281]), and risk-aversion approaches may be divided in absolute and relative risk approaches. With slight abuse of the definitions in utility theory, absolute risk aversion methods are defined as approaches that guarantee absolute safety with no concessions; for example, the agent must remain in a bounded set at all time. Relative risk aversion methods on the other hand are defined as to allow for a certain risk, most often expressed via a threshold Δ, or as to minimise the risk via an optimisation approach along with other variables. Therefore, this often concerns calculating and constraining the collision probability function. Examples of both risk aversion strategies are respectively:

$$\begin{cases} \mathbf{x}_t^i \notin \mathcal{X}_j, & \forall \mathbf{c}_j \in S_j & \text{(absolute risk aversion)} \\ \mathbb{P}(\mathbf{x}_t^i \notin \mathcal{X}_j) \geq 1 - \Delta, & \forall \mathbf{c}_j \sim \mathcal{N}(0, P_{c_j}) & \text{(relative risk aversion)} \end{cases} \tag{4.18}$$

That the absolute risk aversion and relative risk aversion approach in this example lend themselves to bounded uncertainty and probabilistic uncertainty formulations, then known as chance constraints, respectively is not coincidental. However, relative risk aversion has many manifestations with different gradations, and therefore such a binary representation does not necessarily have to be the case. For example, even within the category of relative risk aversion, absolute safety may be guaranteed -but up to a threshold- whether other approaches only consider the likelihood of collision. In a moment-based formulation the relative risk aversion strategy is common. For the BT needle channel planning problem, no preference for one of the two approaches in particular exists.

4.3.4 Planning execution

Objective

Criteria as used in the objective function of existing needle planning algorithms have included: (i) path length or duration [90, 282, 283], (ii) clearance to obstacles [90, 282–284], (iii) curvature and torsion (corresponding to the required bending energy) [89, 90, 283, 284], and (iv) likelihood of collision or cost of traversal through a cost map or weighted regions [284]. In robust treatment planning optimisation of brachytherapy, coverage (e.g. V_{100}), dose conformity (e.g. $|d - d_C|$), and variation in conformity (e.g. SD($|d - d_C|$)) have been incorporated previously in the objective

function [100, 106, 108]. The objective function evaluated per needle channel is preferably a linear user-weighted function of these aspects in the BT needle channel problem:

$$\min_{\mathcal{U}^i} \quad C(\mathcal{U}^i, \mathcal{X}^i, \mathcal{E}^i, \alpha) = \min_{\mathcal{U}^i} \quad \sum_{l=1}^{n_c} \left(\alpha_l \cdot \left[f_l(\mathbf{x}_T^i, \mathcal{E}^i) + \sum_{t=0}^{T^i-1} f_l(\mathbf{u}_t^i, \mathbf{x}_t^i) \right] \right) \tag{4.19}$$

where, α_l is a user-defined weight ($\alpha_l \geq 0$) corresponding to cost function $f_l(\mathbf{u}_t^i, \mathbf{x}_t^i, \mathcal{E}^i)$. The latter may for example represent: (i) trajectory length ($f_l = \delta \cdot v_{x,t}^i$), (ii) curvature ($f_l = \kappa_t^i$), or (iii) accumulated risk ($f_l = \Delta_t^i$). If the cost function contains stochastic components, the performance of the system can be judged based upon the expected value instead: $\mathbb{E}(C(\mathcal{U}^i, \mathcal{X}^i, \mathcal{E}^i, \alpha))$. Specific MP algorithms may place requirements on the objective function, such convexity, monotonicity, (Lipschitz) continuity, and additivity to guarantee certain performance criteria. No such requirements are however formulated on the objective function at this stage.

Differential constraints

BT needle channel planning algorithms insofar have directly implemented kinematics-based models used for steerable needles, assuming that in a channel the needle can be forced to behave similarly. These models typically incorporate non-holonomic constraints on the needle motion, limiting movement and rotations to and around the tangential direction. In a planar case, this corresponds to analogies of a Dubins' or Reeds-Shepp's car, which are curvature-constrained shortest trajectory models [285]. In a 3D environment steerable needle algorithms often use the analogy of planning curvature-constrained trajectories for unmanned aerial vehicles (UAVs), which is a natural extension of Dubins' car in 3D [286]. Non-holonomic constraints, however, can make finding optimal solutions complex, as this requires solving two-point boundary value problems (BVPs) for the steering function from one state to another [239]. As an alternative interpolation or approximation techniques may be used to post-process rectilinear paths, avoiding the complexity of accounting for differential constraints during planning, but these methods sacrifice several performance guarantees such as completeness and generally are inefficient. For that reason, incorporating non-holonomic constraints directly during planning is considered in this work.

System model

Consider the two-dimensional variant of the non-holonomic unicycle model commonly used for steerable needles as described in Webster III et al. [287]. It is assumed that these equations hold for smooth motion of channelled needles as well. These kinematic equations can be written as:

$$\dot{x}(t) = v(t)\cos(\theta(t)) \tag{4.20a}$$

$$\dot{y}(t) = v(t)\sin(\theta(t)) \tag{4.20b}$$

$$\dot{\theta}(t) = \omega(t) \tag{4.20c}$$

Here, $x(t), y(t) \in \mathbb{R}^2$ indicate the needle tip position, $\theta(t)$ is the heading, and $v(t)$ and $\omega(t)$ denote the longitudinal velocity and rate of change of the heading respectively (Figure 4.7a). These are also the control inputs of the needle: $\mathbf{u}(t) = [v(t), \omega(t)]^T$. However, the use of generalised coordinates -especially in higher dimensions- is prone to singularities, and hence for steerable needles coordinate-free representations are often used. The configuration of a unicycle-type system can be represented as an element of the Lie group $SE(n)$. The rigid transformation between the stationary world frame an a body-fixed frame oriented according to the Frenet–Serret frame -i.e. a pose in n-dimensional Euclidean space with the x-axis pointing in the direction of motion- is described with the following transformation:

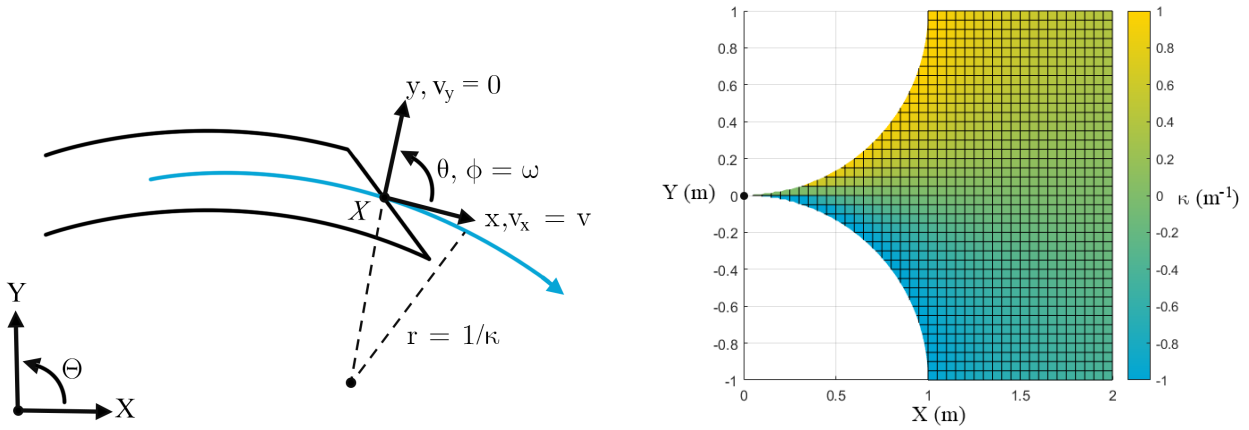

(a) Needle kinematic according to the unicycle model. Figure adapted from Ref. [287].

(b) Reachable region when initial location $\mathbf{p}_0 = [0,0]^T$, initial heading $\theta = 0$, and $-1 \leq \kappa \leq 1$.

Figure 4.7: Unicycle model as used to model needle kinematics. The MATLAB script for this model provided in script A.1.10.

$$X_t = \begin{bmatrix} R_t & \tilde{\mathbf{p}}_t \\ \mathbf{0} & 1 \end{bmatrix} \in SE(n) \tag{4.21}$$

where, $R_t \in SO(n)$ denotes the $n \times n$ rotation matrix, and $\tilde{\mathbf{p}}_t \in \mathbb{R}^n$ the translation vector between the two frames. For convenience, to indicate time-dependence the parenthesis notation is dropped and subscripts are used. For the description of Lie groups and algebra and their use in higher dimensional workspaces, the reader is referred to Murray et al. [288]. For the two-dimensional case, $n = 2$, Eq. 4.21 simply reduces to $\tilde{\mathbf{p}}_t = [\tilde{x}_t, \tilde{y}_t]^T$, and a rotation of θ:

$$X_t = \begin{bmatrix} \cos(\theta_t) & -\sin(\theta_t) & \tilde{x}_t \\ \sin(\theta_t) & \cos(\theta_t) & \tilde{y}_t \\ 0 & 0 & 1 \end{bmatrix} \in SE(2) \tag{4.22}$$

The pose of a needle propagates on SE(2) with the following left-invariant kinematics:

$$\dot{X}_t = X_t \hat{\xi}_t \tag{4.23}$$

where, $\hat{\xi}_t \in \mathfrak{se}(2)$ represents a velocity twist of the rigid body and is an element of the Lie algebra $\mathfrak{se}(2)$. The hat (or wedge) operator is used to map this velocity vector $\xi_t = (v_{x,t}, v_{y,t}, \phi_t)^T$ into its corresponding skew-symmetric matrix:

$$\hat{\xi}_t = \begin{bmatrix} \hat{\phi}_t & \mathbf{v}_t \\ \mathbf{0} & 0 \end{bmatrix} = \begin{bmatrix} 0 & -\phi_t & v_{x,t} \\ \phi_t & 0 & v_{y,t} \\ 0 & 0 & 1 \end{bmatrix} \tag{4.24}$$

For $\hat{\xi}_t$ constant for a duration δ, Eq. 4.23, this is simply an ordinary differential equation (ODE) with solution:

$$X_{t+\delta} = X_t \exp(\delta \hat{\xi}_t) \tag{4.25}$$

The exponential map, $\exp : \mathfrak{se}(2) \mapsto SE(2)$, is then well-defined, surjective, and of the closed form [289]:

$$\exp(\delta \hat{\xi}_t) = \delta \mathrm{e}^{\hat{\xi}_t} = \delta \begin{bmatrix} e^{\hat{\phi}_t} & V_2 \mathbf{v}_t \\ \mathbf{0} & 1 \end{bmatrix} \tag{4.26}$$

where,

$$e^{\hat{\phi}_t} = \begin{bmatrix} \cos(\phi_t) & -\sin(\phi_t) \\ \sin(\phi_t) & \cos(\phi_t) \end{bmatrix}, \quad V_2 = I_2 + \frac{1-\cos(\phi_t)}{\phi_t^2}\hat{\phi}_t + \frac{\phi_t - \sin(\phi_t)}{\phi_t^3}\hat{\phi}_t^2 \tag{4.27}$$

which follows from writing out the Taylor series expansion. Expanding Eq. 4.26 further:

$$\mathrm{e}^{\delta\hat{\xi}_t} = \delta \begin{bmatrix} \cos(\phi_t) & -\sin(\phi_t) & \frac{v_{x,t}}{\phi_t}\sin(\phi_t) - \frac{v_{y,t}}{\phi_t}(1-\cos(\phi_t)) \\ \sin(\phi_t) & \cos(\phi_t) & \frac{v_{y,t}}{\phi_t}\sin(\phi_t) + \frac{v_{x,t}}{\phi_t}(1-\cos(\phi_t)) \\ 0 & 0 & 1 \end{bmatrix} \tag{4.28}$$

Observing the kinematic equations of the unicycle in Eq. 4.20, the following substitutions can be done: (i) $v_{x,t} = v_t$, $v_{y,t} = 0$ (preventing sideways displacement), (ii) $\mathbf{p}_t = \mathbf{0}^T$ (the tip is at the origin at t), and (iii) $\phi_t = \omega_t = \kappa_t v_t$ (where κ_t is the curvature). For the pose of the needle after time δ and control input $\mathbf{u}_t$ therefore a fully analytic expression exists after combining Eq. 4.25 and Eq. 4.28. This pose can be converted back to the generalised coordinates $\mathbf{x}_t = (x_t, y_t, \theta_t)$ by noting that the two upper right entries mark the position and the angle of rotation is obtained by taking the inverse tangent of the two upper left entries (see Eq. 4.22). Formally, this is denoted via:

$$\mathbf{x}_{t+\delta} = (\log(X_{t+\delta}))^{\vee} \tag{4.29}$$

making use of the log-map, $\log : SE(2) \mapsto \mathfrak{se}(2)$, and vee-operator ($^{\vee}$) (inverse action of the wedge-operator). The control inputs become: $\mathbf{u}_t = [v_t, \kappa_t]^T$, where $v_t \in [0, 1]$ and $\kappa = \{\mathbb{R} \mid \kappa_t \neq 0\}$. One problem occurs when the degenerative case of $\kappa_t = 0$, a fully straight motion, is encountered, and for that reason a small perturbation to κ_t is in that case applied [89]. To limit the distance travelled per time step δ one may simply set a constant velocity v_t and step duration δ. The reachable region of a needle according to this model is shown in Figure 4.7b.

The curvature constraint of the needle channels is dependent on the geometrical and mechanical properties of the BT source and catheter, for which a value of $\bar{\kappa} = 1.0$ cm^{-1} has been used previously based on the geometry of the source [88–90]. This is similar to the curvature limits for the source and cables as reported for various afterloaders, which is around 1.3-1.5 cm ($\bar{\kappa} = 0.66 - 0.76$ cm^{-1}). However, in the research by Laan et al. a minimum radius of 35 mm, corresponding to a curvature of $\bar{\kappa} = 0.28$ cm^{-1}, was found to be practically attainable for interstitial needles based on insertion force analysis [48]. Although it is in this work assumed that the sources are contained within the implant and therefore higher curvatures may be achieved, the practical limit to the curvature as reported by Laan and colleagues is used as a first estimate.

Task constraints

The simple curvature-constrained kinematic model as previously introduced is not able to model more complex needle behaviour, especially in the case of multiple bends with non-constant radii of curvature in succession, which in tissue requires mechanics-based models [290]. As in BT implants the needles are forced through the channels, accounting for mechanical properties of the needle may be of greater importance, but this investigation is left for future work. Additionally, interstitial deflections of the catheters after exiting the implant are not considered in this work. Other types of constraints to include may for example be related to the visibility of catheters on the used imaging modality, or sparing of healthy tissues that are not segmented, all of which are not further explored.

Policy generation

For trajectory planning of non-holonomic systems it is common to use open-loop prediction, where control $\mathbf{u}_t^i$ is selected from discretisation or sampling of the control set $\mathcal{U}^i$ or one-step optimisation

[291]. Feedback is especially of importance under uncertainty in configuration knowledge or predictability to limit the covariance of the system [258]. As deterministic system kinematics are used in this thesis, closed-loop planning is therefore not of relevance.

4.3.5 Problem definition

The BT needle channel planning problem under uncertainty can heuristically be defined as the problem of computing multiple feasible, non-intersecting curvature-constrained channels under probabilistic uncertainty or bounded uncertainty of the environment such that the dose to the tumour is sufficient, and dose to the OARs and other trajectory costs are minimised. The starting point of this problem is target coverage planning, where the number of straight dwell segments is minimised whilst assuring sufficient coverage of the tumour. Problem (1.A) shows the BIP that is adapted from Siauw et al. [270]. The output of this problem is a set of dwell segments that are used as starting poses for computing the needle channels. The second part of this problem can therefore be mathematically described as either one of the two standard optimisation programs: (i) combining a bounded uncertainty formulation with an absolute risk aversion strategy in Problem (2.A), and (ii) probabilistic uncertainty formulation with a relative risk aversion strategy in Problem (2.B).

The following inputs are provided in order to solve the coverage problem or the optimal control problems:

- A physical description of the needles: width w, and length L;
- A fixed dwell time t_{z_p} for all dwell locations, based on the coverage radius ϵ to sufficiently cover the target region and fulfil dosimetric constraints;
- A set of dose constraints for each of the three OARs (bladder, rectum and sigmoid): d_C;
- Polygonal description of the stay-in region $\mathcal{I}$ for the intracavitary needles;
- Convex polygonal description of the OARs $\mathcal{X}_j$, along with a covariance matrix P_{c_j}, or bounded set S_j to describe translation uncertainty;
- Convex polygonal description of the target region $\mathcal{T}$, along with a discretised representation in tumour points τ_q and selected baseline;
- A candidate set of possible interstitial dwell segments $\mathcal{N}$ in tumour region $\mathcal{T}$ extending to the baseline;
- A description of the entry region $\mathcal{E}$ which represents the goal region of needle channels;
- A set of user-defined weights for the objective function α, and a user-set allowable risk parameter Δ if a probabilistic uncertainty formulation is used;
- A set of allowable control inputs $\mathcal{U}$, limited by constraints on the curvature $\bar{\kappa}$ and velocity $\bar{v}_t$;

A schematic illustration of the two problems is given in Figure 4.8 and Figure 4.9.

Problem (1.A): Target coverage planning problem

$$\min_{x_i} \quad \sum_i x_i \tag{4.30a}$$

$$\text{s.t.} \quad \sum_{i \in M_q(\epsilon)} x_i \geq 1 \qquad \forall q \in I(\epsilon) \tag{4.30b}$$

$$x_i + x_o \leq 1 \quad \forall (i,o) \in \mathcal{Y} \tag{4.30c}$$

$$x_i \in \{0,1\} \quad \forall i \tag{4.30d}$$

Problem (2.A): Bounded uncertainty needle channel planning with absolute risk aversion

$$\min_{\mathcal{U}^i} \quad \sum_{l=1}^{n_c} \left(\alpha_l \cdot \left[f_l(\mathbf{x}_T^i, \mathcal{E}^i) + \sum_{t=0}^{T^i-1} f_l(\mathbf{u}_t^i, \mathbf{x}_t^i) \right] \right) \tag{4.31a}$$

$$\text{s.t.} \quad \mathbf{x}_{t+1}^i = \left(\log \left(\hat{\mathbf{x}}_t^i \exp(\delta \hat{\xi}_t^i) \right) \right)^\vee, \quad \forall t \in \mathbb{Z}_{0,T}, \forall i \in \mathbb{Z}_{1,n_x} \tag{4.31b}$$

$$\xi_t^i = f(\mathbf{u}_i^t)$$

$$\mathbf{x}_0^i \in \mathcal{T}, \quad \mathbf{x}_T^i \in \mathcal{E}^i \qquad \forall t \in \mathbb{Z}_{0,T}, \forall i \in \mathbb{Z}_{1,n_x} \tag{4.31c}$$

$$\mathbf{u}_t^i \in \mathcal{U}^i \qquad \forall t \in \mathbb{Z}_{0,T}, \forall i \in \mathbb{Z}_{1,n_x} \tag{4.31d}$$

$$\mathbf{x}_t^i \in \mathcal{I} \qquad \forall t \in \mathbb{Z}_{0,T}, \forall i \in \mathbb{Z}_{1,n_x} \tag{4.31e}$$

$$\mathbf{x}_t^i \notin \mathcal{X}_m \qquad \forall t \in \mathbb{Z}_{0,T}, \forall i, m \in \mathbb{Z}_{1,n_x}, i \neq m \tag{4.31f}$$

$$\mathbf{x}_t^i \notin \mathcal{X}_j \qquad \forall \mathbf{c}_j \in S_j, \forall t \in \mathbb{Z}_{0,T}, \forall j \in \mathbb{Z}_{1,n_o}, \forall i \in \mathbb{Z}_{1,n_x} \tag{4.31g}$$

$$\mathcal{X}_j = \mathcal{X}_{j,0} + \mathbf{c}_j \qquad \forall \mathbf{c}_j \in S_j, \forall j \in \mathbb{Z}_{1,n_o} \tag{4.31h}$$

Problem (2.B): Probabilistic uncertainty needle channel planning with relative risk aversion

$$\min_{\mathcal{U}^i} \quad \sum_{l=1}^{n_c} \left(\alpha_l \cdot \left[f_l(\mathbf{x}_T^i, \mathcal{E}^i) + \sum_{t=0}^{T^i-1} f_l(\mathbf{u}_t^i, \mathbf{x}_t^i) \right] \right) \tag{4.32a}$$

$$\text{s.t.} \quad \mathbf{x}_{t+1}^i = \left(\log \left(\hat{\mathbf{x}}_t^i \exp(\delta \hat{\xi}_t^i) \right) \right)^\vee, \quad \forall t \in \mathbb{Z}_{0,T}, \forall i \in \mathbb{Z}_{1,n_x} \tag{4.32b}$$

$$\xi_t^i = f(\mathbf{u}_i^t)$$

$$\mathbf{x}_0^i \in \mathcal{T}, \quad \mathbf{x}_T^i \in \mathcal{E}^i \qquad \forall t \in \mathbb{Z}_{0,T}, \forall i \in \mathbb{Z}_{1,n_x} \tag{4.32c}$$

$$\mathbf{u}_t^i \in \mathcal{U}^i \qquad \forall t \in \mathbb{Z}_{0,T}, \forall i \in \mathbb{Z}_{1,n_x} \tag{4.32d}$$

$$\mathbf{x}_t^i \in \mathcal{I} \qquad \forall t \in \mathbb{Z}_{0,T}, \forall i \in \mathbb{Z}_{1,n_x} \tag{4.32e}$$

$$\mathbf{x}_t^i \notin \mathcal{X}_m \qquad \forall t \in \mathbb{Z}_{0,T}, \forall i, m \in \mathbb{Z}_{1,n_x}, i \neq m \tag{4.32f}$$

$$\mathbb{P}(\mathbf{x}_t^i \notin \mathcal{X}_j) \geq 1 - \Delta \qquad \forall \mathbf{c}_j \sim \mathcal{N}(0, P_{c_j}), \forall t \in \mathbb{Z}_{0,T}, \forall j \in \mathbb{Z}_{1,n_o}, \forall i \in \mathbb{Z}_{1,n_x} \tag{4.32g}$$

$$\mathcal{X}_j = \mathcal{X}_{j,0} + \mathbf{c}_j \qquad \forall \mathbf{c}_j \sim \mathcal{N}(0, P_{c_j}), \forall j \in \mathbb{Z}_{1,n_o} \tag{4.32h}$$

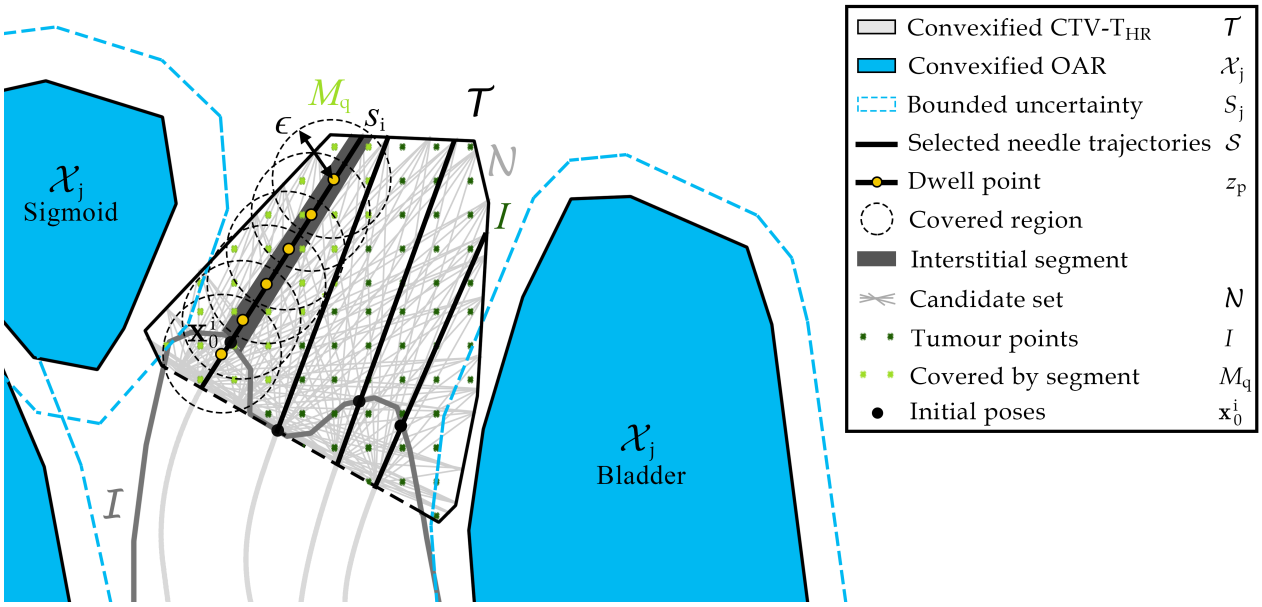

Figure 4.8: Schematic two-dimensional illustration of the target coverage planning problem as considered in this study. The number of straight interstitial dwell segments selected from a candidate set must be minimised, whilst providing sufficient coverage of the tumour region and adhering to other constraints.

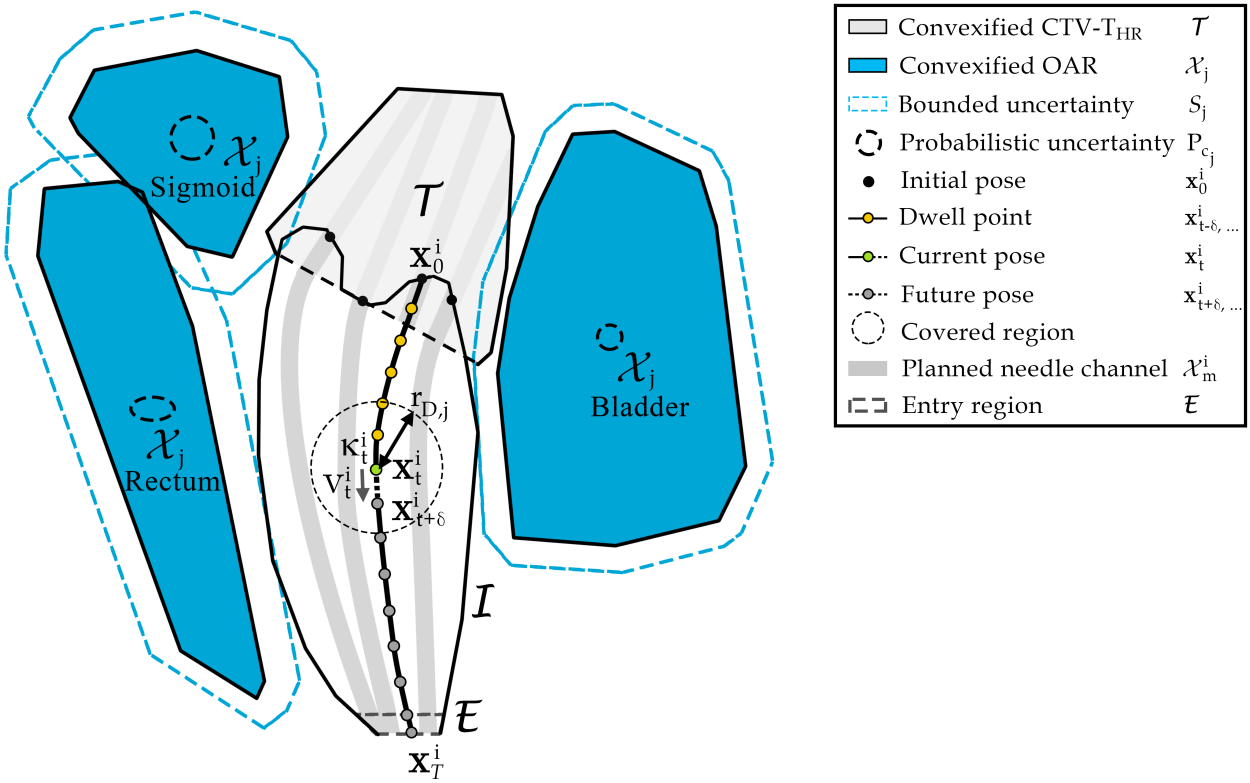

Figure 4.9: Schematic two-dimensional illustration of the needle trajectory planning problem under uncertainty as considered in this study. Trajectories are planned from fixed starting poses towards the entry region, minimising a cost function and adhering to other constraints. The obstacles are modelled as either having probabilistic or bounded spatial uncertainty.

Part II
Development of a tool for aiding the decision-making process between motion planning algorithms

In this part, a tool termed motion-planning quality function deployment (MP-QFD) is developed in order to aid the selection process between motion planning classes and to establish an algorithm which is able to provide solutions to the mathematically formulated BT needle channel planning problem in the previous chapter. First, a conventional approach in selecting a motion planning algorithm is discussed. Next, quality function deployment is introduced as a decision-making tool between alternatives and methodological issues are discussed. The step-by-step implementation of a simple extension to this approach, MP-QFD, is then described for the BT needle channel planning problem. This is used as a guideline and validation for the selection of a robust motion planning class.

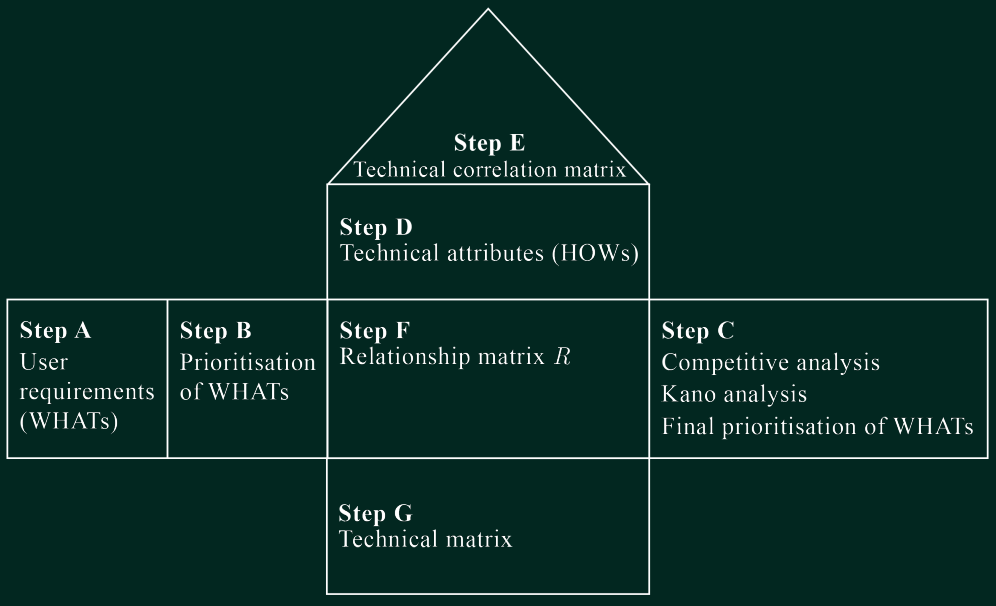

Illustration: Schematic illustration of the tool used for the selection between motion planning classes

5. Development of a tool for the selection of motion planning algorithms

5.1 Selection of robust motion planning algorithms

5.1.1 Algorithm classes

Motion planning (MP) may involve the planning of a collision-free: (i) path, i.e. where the only constraints are geometrical, or (ii) trajectory, i.e. where the system additionally obeys differential constraints, as has been described in Section 4.1. Assuming that in almost any case kinematically infeasible paths can be transformed such that these become traversable for systems with differential constraints, both path and trajectory planning algorithms are of interest for this thesis. In numerous surveys and textbooks MP techniques in a deterministic environment have been classified and reviewed [239, 241, 263, 292–295]. Contrarily, little work has been done in reviewing MP methods under uncertainty [272, 296, 297]. Dadkhah and colleagues provide a useful overview of MP methods under uncertainty [272], but only consider trajectory planning techniques. Moreover, their section on planning under uncertainty in environment knowledge is mainly focused on partially known or unknown dynamic environments which is mostly applicable to vehicles with on-board sensing. For that reason, in a previous review of literature, a taxonomy has been developed for both robust path and trajectory planning approaches under uncertainty in environment knowledge [240]. The robust motion planning classes in this taxonomy share similar computational and operational properties (see Subsection 4.1.3), and have similar forms of implementation (Figure 4.4). From the 37 reviewed studies in this literature study, the MP algorithms were categorised in 14 classes of which impressions are shown in Figure 5.1. A brief description of the working mechanisms of these MP classes is given in Appendix A.5. A reader familiar with MP may observe that these classes of planners acting under environmental uncertainty are similar to that of their counterparts in deterministic environments, indicating that the extension to robust planning can be relatively straightforward.

5.1.2 Previous work in aiding selection of MP algorithms

Little work has been devoted into aiding the decision-making process of selecting a MP algorithm from the myriad of options available given a heuristic problem description and a set of user requirements. Especially for non-software engineers for whom motion planning may be of interest in a practical application, selection may be a difficult process. The barrier for implementation by novice end users is increasingly lowered with the development and increased use of planning libraries and tools, such as Open Motion Planning Library (OMPL) [298], and MoveIt! [299]. Motion planning libraries may in some cases give indications on what algorithms to select. For example, benchmark tests may indicate which motion planner performs best on similar problems of interest [300]. Although helpful, the number of motion planners of which results are available in benchmark tests is still limited. Contrarily, an opposing movement may also be distinguished in which MP algorithms are first developed and applications are thereafter sought, i.e. technology push. For example, the effectiveness of TrajOpt was illustrated through application to various example motion planning problems, including needle steering and BT needle channel planning [286].

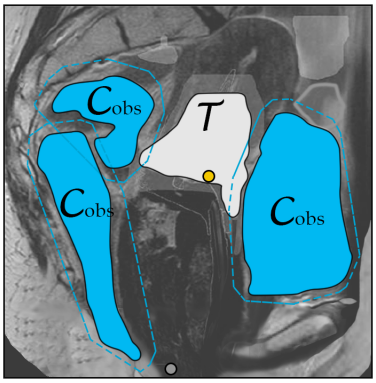

(a) Image from MRI-scan

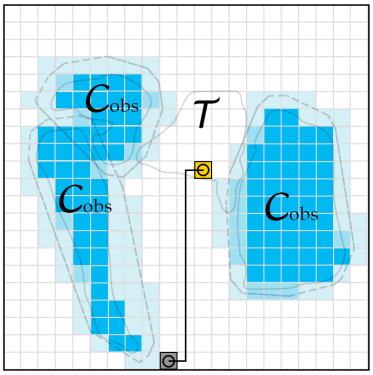

(b) Approximate cell decomposition

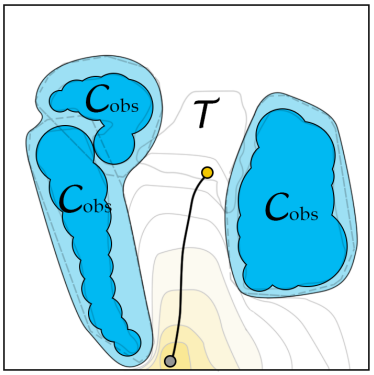

(c) Potential-based methods

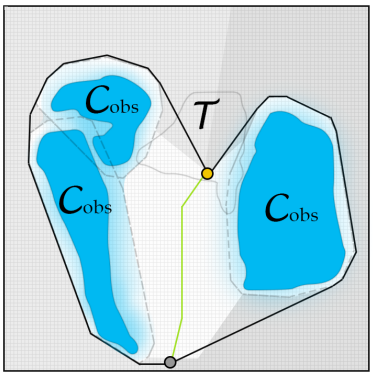

(d) Topology-based methods

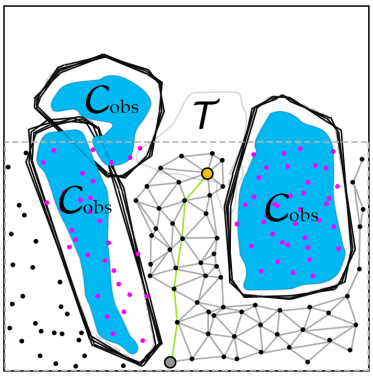

(e) Probabilistic roadmap

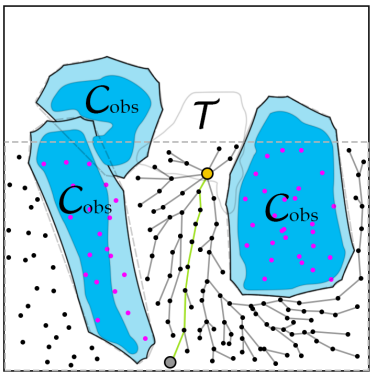

(f) Rapidly-exploring random trees

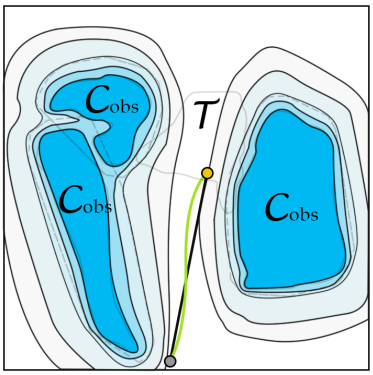

(g) Stochastic continuous-time optimisation

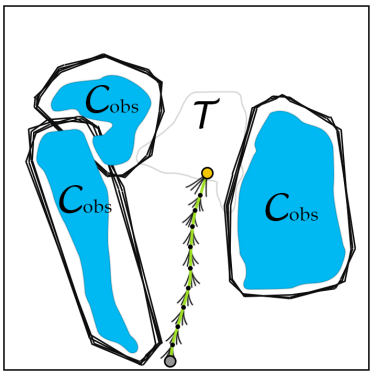

(h) Stochastic optimal control

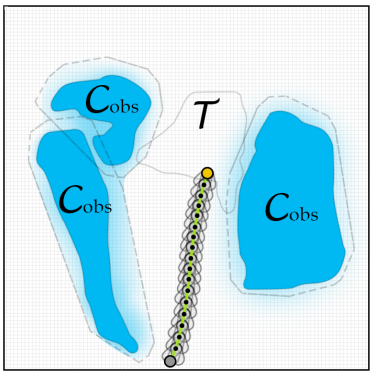

(i) Backward stochastic reachability

Figure 5.1: Schematic 2D impressions of the solutions to the needle channel planning problem in BT produced by classes of motion planners as distinguished in a previous review [240]. The gold dot (●) marks the starting location in the tumour region $\mathcal{T}$ of the planned motion, and the grey dot (●) the target location inside the entry region $\mathcal{E}$. OARs (bladder, rectum and sigmoid) are represented as obstacle regions ($\mathcal{C}_{obs}$), with various types of uncertainty representations. Illustrations (b)-(f) concern path planning classes, (g)-(j) coupled trajectory planning classes. Brief descriptions of the algorithm classes are given in Appendix A.5. Continues on next page.

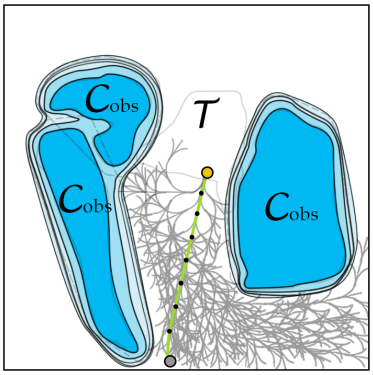

(j) Reachability tree

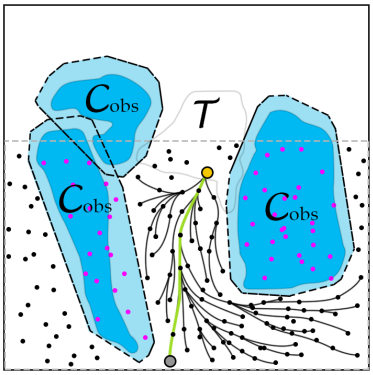

(k) Incremental sampling with chance constraints

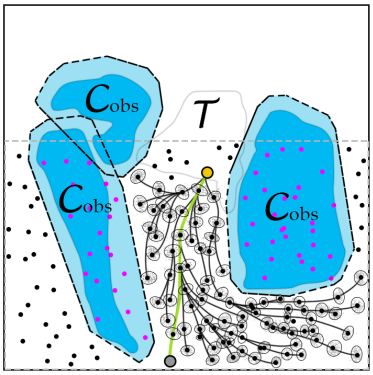

(l) Incremental sampling with particle expansion

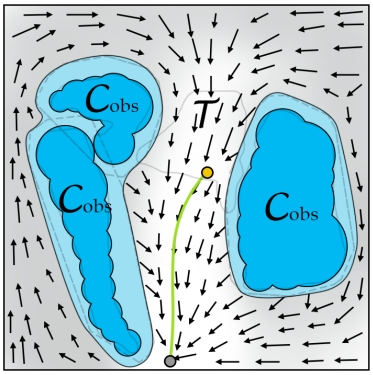

(m) Virtual potential field

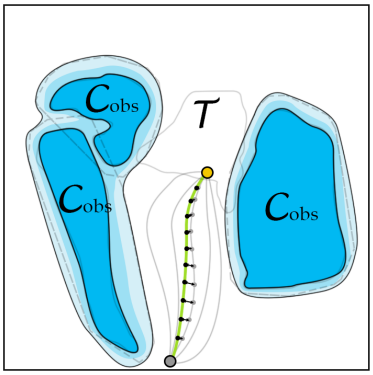

(n) Warm-started trajectory optimisation

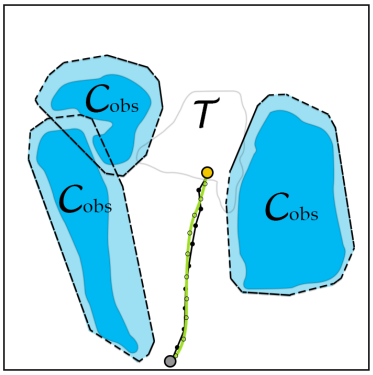

(o) Plan and transform

Figure 5.1: *(continued)* Schematic 2D impressions of the solutions to the needle channel planning problem in BT produced by classes of motion planners as distinguished in a previous review [240]. The gold dot (●) marks the starting location in the tumour region $\mathcal{T}$ of the planned motion, and the grey dot (●) the target location inside the entry region $\mathcal{E}$. OARs (bladder, rectum and sigmoid) are represented as obstacle regions ($\mathcal{C}_{obs}$), with various types of uncertainty representations. Illustrations (j)-(o) concern coupled trajectory planning classes, and (n)-(o) decoupled trajectory planning classes. Brief descriptions of the algorithm classes are given in Appendix A.5.

In general, the process of selecting a motion planner is based on a set of requirements, which usually are performance criteria. Coenen formulated a set of performance requirements that can serve as a guideline for selecting a suitable motion planner [292]. Lunenburg and colleagues present a series of flowcharts that aid in the selection of a combination of motion planners [301]. However, in both of these cases a practitioner unaware of the implications of algorithm properties may not be able to find a suitable planner. For example, such an inexperienced practitioner may not a priori know whether a single or multi-query approach would be more appropriate, what the consequences are of completeness, or whether a heuristic is possibly available. In other words, technical parameters of these algorithms do not directly coincide with the users' requirements. Furthermore, such a straightforward scheme may (incorrectly) suggest that an ideal algorithm class or solution is in any case available, whereas in reality multiple algorithms, or none, may be able to produce appropriate solutions. Therefore, a need exists for an approach that aids the selection process of MP algorithms.

5.2 Quality Function Deployment

5.2.1 An introduction and methodological evaluation of QFD

The problem of selecting an alternative based on a set of requirements is known as a multi-criteria decision-making (MCDM) problem, for which numerous potentially viable methods exist [302]. However, in several of these methods a focus on the demands of the user is lacking. Therefore, it is turned to the related fields of axiomatic design (AD) and quality function deployment (QFD) [303], where user-based requirements are central and are related via some kind of transformation to technical attributes. Quality Function Deployment, for which many guides have been written [304, 305], is a methodology for the development of products with a focus on achieving customer satisfaction by better conforming to the users' requirements. Moreover, it serves as a platform for communication between designers, engineers, market researchers and all other involved in product planning. Although QFD is not necessarily a decision-making tool between alternatives itself, it has been implemented as one or combined with other MCDM techniques successfully in numerous works in various fields [306–310]. QFD has also been successfully introduced for non-tangible products such as in the software engineering domain [311, 312]. The use of QFD for software selection on the other hand is a novelty. In order to select between motion planning classes, motion planning QFD (or MP-QFD) is in this chapter introduced.

Quality function deployment in its essence is a multi-phase process, which is driven by the customer demands -known as the voice of the customer (VOC)- at each of the product development stages [313]. The central component throughout these phases is a matrix diagram relating the objectives (WHATs) and responses (HOWs) of the product. In the often used four-phase QFD model, the first of these four matrix 'houses', is known as the house of quality (HOQ). Although following matrix houses continue to emphasise the voice of the customer, the fundamental significance of the HOQ means that it is often used as a standalone method for product development [313, 314]. The house of quality (Figure 5.2) is elaborated in the next subsections[1] and links user requirements to technical attributes to provide a prioritisation of these technical attributes. For a more in depth discussion of the house of quality, the reader is referred to Appendix A.6.

(A) User requirements

The first step in QFD -after identification and selection of a representative sample of customers or users- is the definition of user requirements. The collection of user requirements may be through surveys, individual interviews, focus groups among others. These user requirements are descriptions of the needs, wants and expectations to be fulfilled by the product and usually are expressed in the user's own words [315]. Processing and clustering can be difficult, as there is a risk of losing the original meaning of the VOC [305, 313, 316]. To facilitate analysis and further processing, individual user requirements may be structured in clusters, via methods such as affinity diagrams or hierarchical cluster analysis [305, 313, 315]. The result is generally an ordered list of 5-10 primary user requirements, which are denoted here as W_i for $i \in \mathbb{Z}_{1,I}$ and I the amount of user requirements.

(B) Prioritisation of user requirements

The next phase involves the prioritisation of user requirements, which aims at establishing the importance of individual requirements. This step is of major importance, since this directly affects the product development and eventually its success [317]. Many methods have been developed for

[1] The symbols used in this chapter differ in their expression from previous chapters and an overview of the relevant nomenclature is given in Section 0.3.

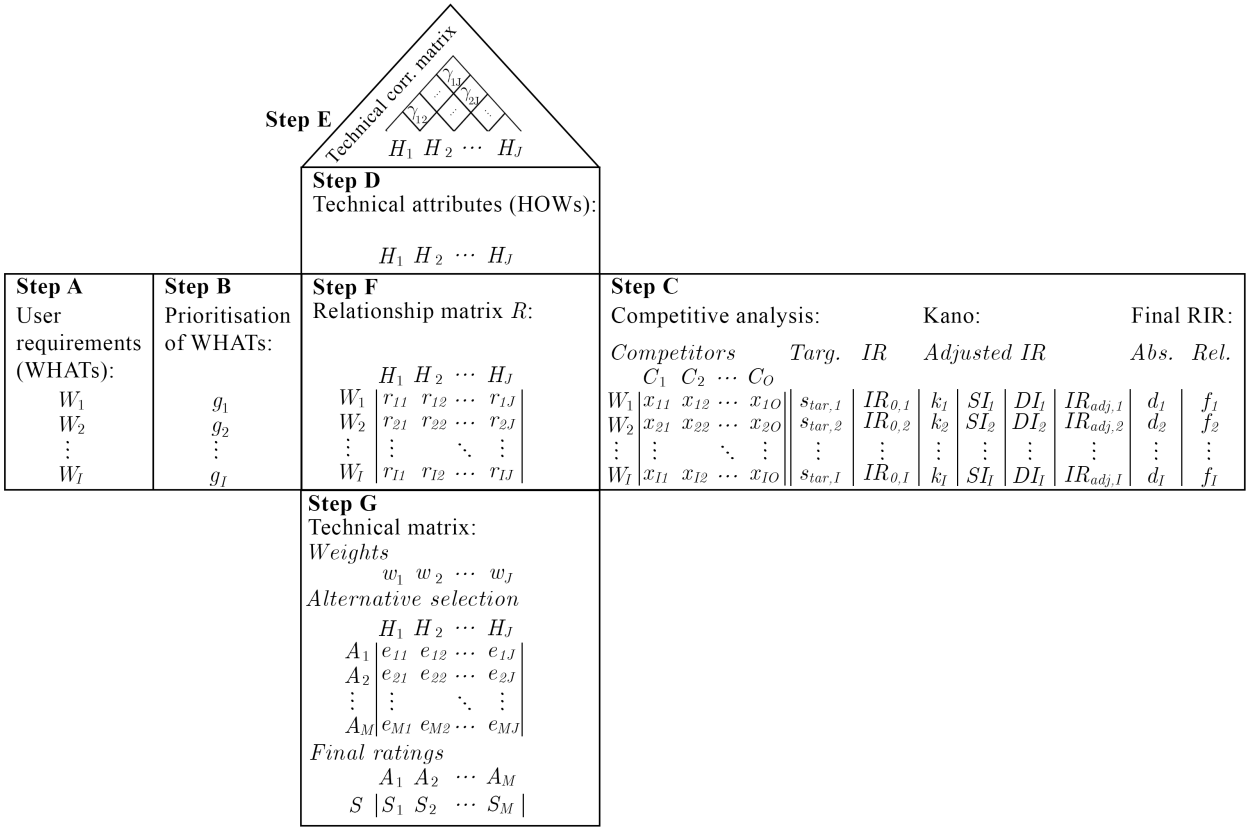

Figure 5.2: General quantitative model of a house of quality (HOQ) used as a selection method between alternatives. The relevant nomenclature is given in Section 0.3.

the purpose of defining relative importance ratings (RIRs), including [317–319]: (i) point direct scoring (PDS), (ii) analytic hierarchy process (AHP), (iii) analytic network process (ANP), (iv) outranking methods, (v) Kano's model, and (vi) preference ordering. Moreover, as the assessment of the importance of user requirements by individuals may be imprecise, incomplete or uncertain, many more complicated prioritisation techniques have been developed, such as: (vii) fuzzy variants [320], (viii) rough set based methods [321], (ix) preference graph [319], and (x) generalised Yager's method [318]. Additionally, the user sample may be heterogeneous, in which case a hierarchical importance ranking of users may be included [318, 321]. There is no gold standard among these methods, for a brief discussion see also Appendix A.6. In this study, the relative importance rating of a user requirement, g_i, is established from the average (or median) of responses on a self-stated importance questionnaire (PDS):

$$g_i = \sum_{k=1}^{K} g_{ik}/K \tag{5.1}$$

In this method, users are asked to indicate the importance ratings of WHATs on an ordinal response scale. This requires little user effort, does not require a large sample size and is simple to analyse. The raw importance weighting may possibly be normalised, i.e. $\sum_{i=1}^{I} g_i = 1$. In general for QFD, the user requirements must be independent from each other [322], which is an assumption that must be a priori validated.

(C) Competitive analysis and final importance ratings

In the third step a competitive analysis is performed, where the performance of a company's product is evaluated on the user requirements against competitors' similar products [313]. This enables the company to set strategic goals and create a value proposition. The information for this step is usually acquired by asking users to rate the performance in terms of satisfaction of the products by company and competitors per WHAT [316]. A company may then decide on a strategy to set goals per user requirement such as to improve, hold or copy its product's performance against that of competitors [313]. One obvious problem arises in the case when competitors are non-existent, when targets are not initially obvious or when it may not be possible to rate the satisfaction in using the product, such as in the case of developing new products [312, 322–324].

Methods that have been developed to determine competitive priority ratings, such as the improvement ratio (IR), sales point and entropy method, generally assume a linear or one-dimensional relation between performance on a user requirement and perceived satisfaction by the user [319]. However, this assumption neglects that users may perceive the importance of certain user requirements in a different way; i.e. as evidenced by Kano this relation may be non-linear or multi-dimensional [325]. In the Kano model, user requirements may be classified as: (i) type B; basic or must-be attributes, (ii) type O; one-dimensional attributes, and (iii) type A; attractive or excitement attributes [325]. Detailed descriptions of these categories have been given in Matzler and Hinterhuber [326]. Several modifications have been proposed to the original classification, including the addition of: (iv) type I; indifferent attributes, (v) type R; reverse attributes and (vi) type Q; questionable attributes (Figure 5.3a) [327]. Such a classification of user requirements into Kano categories is not a static one, where specifically attractive attributes may become one-dimensional and eventually basic over time [328]. Other modifications have therefore been introduced, with a possibly increased accuracy in establishing the importance of improving user requirements, but at the cost of complicating the original model. For an overview of some of these modifications see the work by Shahin et al. [329].

For the classification into Kano categories, usually a questionnaire is administered in a face-to-face interview containing a functional and dysfunctional question per user requirement [327]. The standard form of these two questions is performance-based, e.g.: 'If the performance of the product on this user requirement is good, how would you feel?', and 'If the performance of the product on this user requirement is poor, how would you feel?'. The respondents should then indicate their answers on a five-level scale. From the answers to the functional and dysfunctional questions for a user requirement the corresponding Kano category can be obtained using an evaluation table (Figure 5.3b). Some alternatives have been proposed for classifying user requirements in Kano's categories of which a concise overview is given in Appendix A.6.

Several publications have described integration of Kano's model in QFD (for a brief overview see Appendix A.6, or the book chapter by Violante et al. [330]). One convenient way that avoids the use of the mode statistic to classify requirements in Kano's categories, is the use of satisfaction and dissatisfaction indices. These indicate how the fulfillment or provision of a requirement would influence user satisfaction or dissatisfaction and would better preserve information on the distribution of answers [327]:

$$SI_i = \frac{A_i + O_i}{A_i + O_i + B_i + I_i} \quad ; \quad DI_i = -\frac{B_i + O_i}{A_i + O_i + B_i + I_i} \tag{5.2}$$

Here, SI_i and DI_i denote the satisfaction and dissatisfaction indices, and the other parameters are

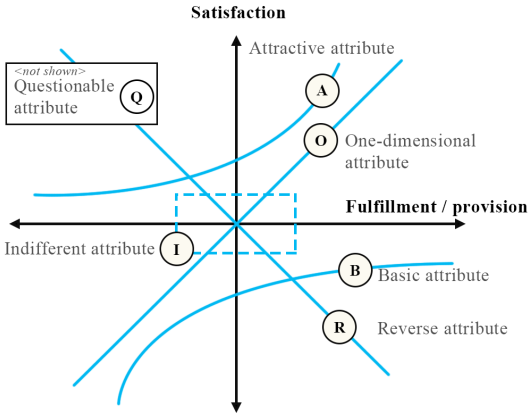

(a) Schematic illustration of Kano's model.

		Dysfunctional				
Functional	Answers →	*Like*	*Must-be*	*Neutral*	*Live with*	*Dislike*
	Like	Questionable	Attractive	Attractive	Attractive	One-dimensional
	Must-be	Reverse	Indifferent	Indifferent	Indifferent	Basic
	Neutral	Reverse	Indifferent	Indifferent	Indifferent	Basic
	Live with	Reverse	Indifferent	Indifferent	Indifferent	Basic
	Dislike	Reverse	Reverse	Reverse	Reverse	Questionable

(b) Kano's evaluation table.

Figure 5.3: Illustrations of the categories and the classification method in Kano's model [325]. Brief descriptions of the Kano categories: **Attractive** = provides satisfaction if fulfilled but absence does not cause dissatisfaction; **One-dimensional** = results in satisfaction when fulfilled and dissatisfaction when not fulfilled; **Basic** = is taken for granted when fulfilled and causes dissatisfaction when not fulfilled; **Indifferent** = satisfaction is not influenced by fulfillment; **Reverse** = results in dissatisfaction when fulfilled and satisfaction when not fulfilled; **Questionable** = stems from contradiction in answers.

the counts of the Kano attributes. One may then directly integrate these indices in QFD to compute the RIRs of user requirements [323], or couple these to the outcome of the competitive analysis, e.g. to compute an adjusted improvement ratio $IR_{adj,i}$ [324]. The absolute final importance d_i is then calculated by multiplying the raw importance g_i from Eq. 5.1 for a user requirement with the adjusted improvement ratio in (e.g. in Eq. A.25) [324]:

$$d_i = g_i \cdot IR_{adj,i} \tag{5.3}$$

The overall user satisfaction can then be modelled as a linear additive value function [322]:

$$S = \sum_{i=1}^{I} d_i y_i \tag{5.4}$$

Here, y_i is the degree of fulfillment of the ith user requirement.

(D) Technical attributes

Technical attributes, or HOWs, are objective measures of the product's technical requirements, characteristics or parameters which are known as design specifications, substitute quality characteristics or engineering characteristics (ECs) [313]. As these are specified by the manufacturer or designer, these are said to express the voice of the engineer (VOE). A common way of establishing these technical attributes is by performing cause-and-effect relations between the HOWs and WHATs, which is a complex operation that requires knowledge of the developed product and experience in how this brings satisfaction to users. Similar to the process of establishing user requirements, it is common to establish a hierarchy of primary, secondary and tertiary ECs, where the primary ECs are the first-order causes for the WHATs. The jth technical attribute, where $j \in \mathbb{Z}_{1,J}$, is denoted by H_j and its degree of attainment by e_j. According to conventional QFD theory, each EC should be defined as having a unit and a direction of improvement; i.e. these must be measurable [313]. However, the value of an EC, e_j, may not be in all cases be a continuous and unbounded variable, but is possibly discrete and bounded [331, 332], or must even be derived from a qualitative expression. This does not necessarily limit the

applicability of QFD theory and can in many cases straightforwardly be implemented. For example, one may set e_j as an indicator variable which is 1 if the feature is provided or at a certain threshold in performance, and 0 otherwise. However, one must be aware that such methods typically act on a different scale level than the preferred ratio scale for quantitative analysis.

(E) Technical correlation matrix

The technical correlation matrix captures the inter-relations between HOWs and their magnitude and is placed in the 'roof' of the HOQ [313]. The technical correlation matrix allows the designer to trade-off the attainment of technical attributes and thereby allocate the budget in improving the attainment of HOWs. These inter-correlations are denoted as γ_{lj}, capturing the correlation between the lth and jth technical attribute. Usually, the magnitude of the correlation is expressed from qualitative reasoning in the HOQ on a five-point ordinal scale, ranging from strongly negative to positive, or using the same scale as used in the relationship matrix. These are then converted to a numerical scale such that these can be used quantitatively. Some work has been devoted in automating this procedure by detecting similarities between HOWs and how they influence WHATs in the relationship matrix [333]. This is however out of scope for this thesis, and it is assumed that the correlations can be established from qualitative reasoning.

(F) Relationship matrix

The relationship matrix is the main element of the HOQ, containing the degree of relationship between WHATs and HOWs and therefore indicates how technical attributes affect the satisfaction of user requirements. Traditionally, and still the most common approach, the relations are obtained by expert consensus and rely mostly on experiences and in some cases on statistical analysis [305]. The relationship value between WHAT W_i and HOW H_j is usually expressed in a semi-quantitative manner through a correlation coefficient r_{ij}:

$$R = \begin{array}{c} \\ W_1 \\ W_2 \\ \vdots \\ W_I \end{array} \begin{array}{c} \begin{array}{cccc} H_1 & H_2 & \cdots & H_J \end{array} \\ \begin{bmatrix} r_{11} & r_{12} & \cdots & r_{1J} \\ r_{21} & r_{22} & \cdots & r_{2J} \\ \vdots & \vdots & \ddots & \vdots \\ r_{I1} & r_{I2} & \cdots & r_{IJ} \end{bmatrix}_{I \times J} \end{array} \tag{5.5}$$

The correlation coefficient r_{ij} couples the degree of attainment of a user requirement and the corresponding technical attributes according to a linear additive relation:

$$y_i = \sum_{j=1}^{J} r_{ij} e_j \tag{5.6}$$

One may link the overall satisfaction S as a function of the fulfillment of technical attributes e_j by substituting Eq. 5.6 into Eq. 5.4 or A.26. In the general QFD approach, for this the importance weights of user requirements are translated into prioritising technical attributes via a method known as the independent scoring method (ISM) [322]:

$$w_j = \sum_{i=1}^{I} d_i r_{ij} \tag{5.7}$$

Here, w_j is the weight given to the prioritisation of the jth technical attribute, which is a linear additive function of the importance of user requirements (e.g. see Eq. 5.3) and the (normalised) correlation coefficients r_{ij}. The overall satisfaction may then be found via (combining Eq. 5.4, 5.6, and 5.7) [322]:

$$S = \sum_{i=1}^{I} d_i y_i = \sum_{i=1}^{I} \sum_{j=1}^{J} d_i r_{ij} e_j = \sum_{j=1}^{J} w_j e_j \tag{5.8}$$

The technical attributes with the highest weights w_j would therefore increase satisfaction the most at constant effort, and should therefore possibly receive most of the focus in the product development. The relationship coefficient r_{ij} is typically defined as one of four levels (on an ordinal scale): strong (◎), medium (○), weak (△), or nonexistent (<blank>). Commonly suggested weights are: {9,3,1,0}, {5,3,1,0}, or {4,2,1,0} for strong, medium, weak or no relations respectively. A general recommendation is that these weights should be non-negative. Several considerations must be taken into account when establishing this relationship matrix, which are highlighted in Appendix A.6 (see also the work by van de Poel [322]), and can be summarised under:

- Introducing the possibility of negative and non-constant weights;
- Correcting for the amount of relations between WHATs and HOWs through normalisation and for correlations between HOWs;
- Scaling of relationship coefficients and avoiding rank reversal;
- Establishing these relationships for novel products, in the case of incomplete or uncertain information, or by an inexperienced practitioner.

The general message in any of the quantitative approaches to establish the priority ratings from the relationship matrix in QFD is that calculated weights w_j are determined based on subjective or arbitrary choices, are inevitably flawed by assumptions in the methodology and hence may lead to questionable outcomes [314, 334]. Correctness of an order of product alternatives that is determined based on these weights cannot be guaranteed and drawing direct conclusions on orderings should therefore be avoided. The quantitative approach to QFD can still be a powerful tool as it allows for incorporating more information than just conceptual mapping. A qualitative approach has the benefits of making the process less subjective and more intuitive [335], but this lacks the flexibility of accounting for factors such as Kano's categories, competitive analysis or correlations between technical attributes. An example of such an approach, is the ordinal approach by Francheschini et al. [335]. In this method, technical attributes are prioritised according to the function [335]:

$$w_j'' = \min_{i \in \mathbb{Z}_{1,I}} \left(\max \left\{ \text{neg}(g_i), r_{ij}'' \right\} \right) \tag{5.9}$$

Here, g_i and r_{ij}'' are defined on an ordinal level scale and neg$(\cdot)$ is the negation operator [335]. To further refine the ordering the following indicator function is proposed [335]:

$$T_j = \dim \left(W_i \mid r_{ij}'' > w_j'' \right) \tag{5.10}$$

In this indicator function the technical attributes with a stronger relation to user requirements receive a higher scoring of T_j, which are argued to be of greater importance.

(G) Technical matrix

Technical matrix in conventional QFD

The technical matrix has several different manifestations depending on the purpose of the QFD approach. In conventional QFD, the technical matrix determines the final prioritisation of technical attributes. The inputs in this matrix are the relative weights w_j of the technical attributes, most often inferred from the ISM in Eq. 5.7. The second step may be to perform a technical competitive analysis, where products of the competitors are benchmarked against the company's own product on their technical performance [313]. Based on this analysis, typically performance targets, sales points, constraints on the budget, and probability factors are set [313].

These enable calculation of a final importance weighting of technical attributes that guides the following phases of product development. One of the main problems in this technical matrix is that it is not directly clear how one can set targets in a logical and unequivocal way. Firstly, target values are usually set based on experience and intuition of the design team and can therefore be subjective and non-optimal. Moreover, the problem is that e_j is typically defined on a quotient scale and therefore becomes independent of the absolute values; e.g. an improvement of e_j from 0.6 to 1.0 or 0.4 to 0.8 has the same effect on the modelled user satisfaction S in Eq. 5.8 [322]. It is for these reasons not uncommon that companies terminate the house of quality after establishing the relative weights w_j.

Technical matrix in QFD-based selection approaches
The technical matrix serves a slightly different role in QFD-based selection methods. Considering a set of alternatives $A = (A_1, ...A_M)$, a decision matrix may be established in which the levels of attainment per technical attribute e_{mj} are graded for alternative A_m and preferably normalised:

$$E = \begin{array}{c} \\ A_1 \\ A_2 \\ \vdots \\ A_M \end{array} \begin{array}{c} \begin{array}{cccc} H_1 & H_2 & \cdots & H_J \end{array} \\ \begin{bmatrix} e_{11} & e_{12} & \cdots & e_{1J} \\ e_{21} & e_{22} & \cdots & e_{2J} \\ \vdots & \vdots & \ddots & \vdots \\ e_{M1} & e_{M2} & \cdots & e_{MJ} \end{bmatrix}_{M \times J} \end{array} \tag{5.11}$$

The simplest approach is to neglect the technical competitive analysis, use a point direct scoring method to establish the levels of attainment e_{mj}, and directly compute an overall score for each of the alternatives [306]. Overall user satisfaction (Eq. 5.8) may preferably be used as the overall score for consistency and to keep the approach user-centred, but any type of function may be implemented. Other QFD-based selection approaches typically integrate MCDM methods, such as AHP or ANP, with QFD to rate alternatives after a technical competitive analysis [310].

In an ordinal QFD approach, after having obtained an importance ordering of technical attributes, one must use an ordinal method to obtain a ranking of the alternatives. There are many multi-criteria decision making methods that use ordinal ranking of alternatives per criterion and convert this to cardinal data such as Borda count or pairwise comparisons [336]. One interesting strictly ordinal approach is MCDM-ORCA by Mazurek which also allows for an ordinal ranking of criteria [337]. The technical attributes are assumed to be (weakly) ordered according to their importance as follows: $H_1 \succ H_2 \succ ...H_J$, but may be tied. Per criterion the alternatives are ranked from the one achieving the highest attainment to the one with worst attainment. This method is based on index vectors; the first being the binary index vector:

$$\mathbb{U}_{A_m,A_n} = (u_1, ..., u_J) \tag{5.12}$$

Where, $u_j = 1$ if $e_{mj} > e_{nj}$, $u_j = 0.5$ if $e_{mj} = e_{nj}$, and $u_j = 0$ otherwise. The second type of index vector is the cumulative index vector and its counterpart:

$$\mathbb{H}_{A_m,A_n} = (h_1, ..., h_J), \quad \mathbb{H}_{A_n,A_m} = (h'_1, ..., h'_J) \tag{5.13}$$

Where, $\mathbb{H}_{A_m,A_n} = (u_1, \sum_{j=1}^{2} u_j, ..., \sum_{j=1}^{J} u_j)$. An alternative A_m is then said to dominate A_n, $A_m \succ A_n$, iff $h_j \geq h'_j \quad \forall j \in \mathbb{Z}_{1,J}$ and at least one of the inequality relations is strict. For more details, the reader is referred to the paper by Mazurek [337]. The main advantage of this approach is that it does not require any numerical judgements, and therefore is convenient in the case of technical attributes that are not directly measurable. Additionally, the approach does not violate

some of Arrow's impossibility theorem conditions, such as independence of irrelevant alternatives, which other similar methods do. Disadvantages of this method include that it may be indecisive and produce irrational outcomes as it does not rely on counts. For example, if alternative A_1 only performs better than alternative A_2 on the most important technical attribute H_1, but performs worse on every other attribute $H_2, ..., H_J$, the method is indecisive. An alternative approach would be to implement the ordinal method used for establishing a relationship matrix by Franceschini et al. [335]. In this case, the HOWs represent the decision criteria and are used to obtain an ordering alternatives. This can be done by replacing g_i and r''_{ij} in Eq. 5.9 by T''_j and e_{mj} respectively.

Recommendations for QFD-based selection approaches

In Appendix A.6 and in previous sections, some of the methodological issues with QFD in general and some alternative approaches have been discussed. It is important to note that some of these methodological flaws and particular the ones that stem from Arrow's impossibility theorem are subject to frequent discussion and highly dependent on the assumptions of the used QFD model. Moreover, despite methodological issues, these methods may still be useful as long as information is carefully processed and conclusions are derived from consensus based on experience, intuition and common sense along with the results of QFD. Two options to use QFD in a meaningful and viable way as a selection method can to the author's opinion be distinguished based on the rules and recommendations by Burke et al. [334]:

- **A quantitative ratio scale based approach**. One may try to select an option from a set of user requirements, technical attributes and alternatives by:
  - (i) Ensuring that the raw importance ratings g_i or -if applicable- final importance ratings d_i are expressed on a ratio scale (otherwise an interval scale), and checking unimodality and independence of user requirements;
  - (ii) Establishing a set of measurable technical attributes and expressing correlations between technical attributes γ_{lj} on a ratio scale;
  - (iii) Expressing the relationship coefficients r_{ij} between user requirements and technical attributes on a reasonable ratio scale;
  - (iv) Normalising the coefficients r_{ij} (preferably according to Eq. A.29 and not via Wassermann normalisation) and checking whether irrational rank reversals occur;
  - (v) Selecting an appropriate satisfaction model; proposed are Eq. 5.4 or Eq. A.26, combined with or without Kano's model or competitive analysis;
  - (vi) Expressing attainment of the technical attributes e_j for different alternatives A_m on a ratio or interval scale;
  - (vii) Calculating the predicted overall satisfaction or score for each of the alternatives;
  - (viii) Testing different relationship scales, such as {9,3,1,0}, {5,3,1,0} or {4,2,1,0}, for rank reversals;
  - (ix) Interpreting the satisfaction or overall scores as guidelines in conjunction with experience and common sense to make a decision.

- **A qualitative ordinal scale based approach**. One may try to select an option from a set of user requirements, technical attributes and alternatives by:
  - (i) Expressing the raw importance ratings g_i or -if applicable- final importance ratings d_i on an ordinal scale;
  - (ii) Establishing a set of measurable technical attributes;
  - (iii) Expressing the relationship coefficients r_{ij} between user requirements and technical attributes preferably on the same level ordinal scale;

(iv) Calculating the weights and importance ordering of the technical attributes via an ordinal method, e.g. from Eq. 5.9 and 5.10;
(v) Expressing a rank ordering of the alternatives A_m or scoring on an ordinal scale per technical attribute;
(vi) Using an ordinal technique, such as MCDM-ORCA, to obtain dominance relations for each pair of alternatives (Eq. 5.12 and 5.13) and extract a rank ordering of alternatives based on the rank ordering per technical attribute;
(vii) Interpreting these final rankings as guidelines in conjunction with experience and common sense to make a decision.

In general, for the development of novel products the qualitative ordinal scale based approach is the recommended option as has been argued previously. For improving existing products, the analysis would benefit from taking into account more complex information and a quantitative approach would be the preferred option.

5.3 Description and step-by-step application of MP-QFD

In this section, motion-planning QFD (MP-QFD) is introduced as a new method for motion planning class selection. A pilot study was performed to establish the relative importance ratings of user requirements for the selection and development of brachytherapy needle channel planning software. This section is written in the form of a step-by-step case example in order to guide readers through this process. In this case example, the selection of a suitable robust MP class for solving the BT needle channel planning problem is treated. A qualitative ordinal approach is selected, since this concerns a novel product with no current competitors. Additionally, technical attributes and user satisfaction are not directly measurable or verifiable in software engineering applications [312].

5.3.1 Formulation and prioritisation of user requirements

The first step in the MP-QFD method is the formulation of a set of user requirements. Although ideally these are collected through surveys or individual interviews, in this example the set of user requirements (Table 5.1) is derived from a review of literature [338, 339], technical reports and brochures of radiotherapy planning software. No further division in primary, secondary or tertiary requirements has been made as the list of requirements is concise enough for analysis. In order to prioritise these requirements, a pilot study was carried out. This study was approved by the Human Research Ethics Committee (HREC) of the TU Delft. Nine specialists in radiotherapy (5 radiation therapists, 3 medical physicists, and 1 radiation oncologist) from the Erasmus University Medical Center (Rotterdam, The Netherlands) were asked to participate in this study and written consent was obtained. The mean experience of the participants in their current function was 14 years (±7.5 years). A digital questionnaire, consisting of twenty-two questions, was developed in which participants were asked to:

- Indicate the importance ratings of the software requirements according to a common self-stated importance questionnaire (point direct scoring method);
- Assign these requirements into Kano categories via direct classification.

The full questionnaire was written in Dutch and is shown in Appendix A.7. Prior to these two parts, a brief introduction was given to ensure that the respondents were made aware of robust motion planning software for BT. For the self-stated importance questionnaire, the participants had to rate the importance of the provision of user requirements on a seven-point Likert scale with labels ranging from "(1) very unimportant" to "(7) very important". This format has been

Table 5.1: User requirements for the BT needle channel planning problem.

WHAT	Brief description	Elaborate description
W_1	Robust placement with respect to tumour	The MP guarantees robust optimal placement of sources with respect to tumour even in the case of anatomic changes
W_2	Robust placement with respect to OARs	The MP guarantees robust optimal placement of sources with respect to OARs even in the case of anatomic changes
W_3	Three-dimensional visualisation	The MP is able to visualise and position source locations in three-dimensions
W_4	Real-time adaptability	The MP is able to perform modifications in source locations and obtain results in real-time
W_5	Manual indication of waypoints	The MP is able to manually define waypoints as a starting/routing point for needle channel optimisation
W_6	Computational time	The MP requires brief computation time for source placement calculations
W_7	Resolution of anatomy and trajectories	The MP implements a high resolution of the anatomy and trajectories for visualisation and planning
W_8	Success rate in generating channels	The MP is able to generate plans with a high success rate
W_9	Reproducibility of the generated channels	The MP is able to generate channels that can be accurately reached by the afterloader in a 3D-printed applicator
W_{10}	Robust assessment of the risk levels	The MP is able to accurately estimate the risks of exceeding dose constraints even in the case of anatomic changes

commonly recommended [340], and can both be reviewed as an ordinal or interval scale method (the former being the preferred option). The results of this questionnaire are shown in Table 5.2. 'Reproducibility of the generated channels' (W_9) was generally thought to be the most important user requirement, followed by the 'success rate in generating channels' (W_8) and 'real-time adaptability' (W_4) / 'robust placement with respect to tumour' (W_1). The majority of the participants moreover indicated that the time for generating the catheter trajectories should be within an order of magnitude of seconds (data not shown). As can be seen in Table 5.2, the overall median score of the questionnaire was 6 (corresponding to "important"), and respondents' answers ranged from "(4) neutral" to "(7) very important". A median importance rating of "6" for all user requirements was found, except for the attributes 'manual indication of waypoints' (W_5, "(5) moderately important") and 'reproducibility of the generated channels' (W_9, "(7) very important"). Along with the comments by participants, these findings may indicate that all of the items in the questionnaire were deemed important for BT software. However, due to the high median scores the questionnaire's internal consistency was checked via Cronbach's α, assuming that the scale can be interpreted as an interval scale. Cronbach's α was evaluated to be $\alpha = -0.14$, which indicates that the reliability of the results is questionable.

A direct classification technique was used in this pilot study to establish Kano's categories [341], where respondents were briefly instructed in Kano's model and then asked to select appropriate Kano's categories. Both formal and informal descriptions of these categories in Dutch were given to ensure that participants would understand the model. The results of this questionnaire are shown in Table 5.3. Most of the respondents classified the requirements as must-be attributes, and according

Table 5.2: Results of the prioritisation of the user requirements in Table 5.1 for the BT needle channel planning problem by the nine respondents.

Frequencies	W_1	W_2	W_3	W_4	W_5	W_6	W_7	W_8	W_9	W_{10}
(7) Very important	3	3	1	4	0	2	0	4	7	2
(6) Important	5	3	5	2	4	6	5	5	1	4
(5) Moderately important	0	3	1	3	1	0	3	0	1	2
(4) Neutral	1	0	2	0	4	1	1	0	0	1
Statistics	W_1	W_2	W_3	W_4	W_5	W_6	W_7	W_8	W_9	W_{10}
Median	6	6	6	6	5	6	6	6	7	6
Mean	6.11	6.00	5.56	6.11	5.00	6.00	5.44	6.44	6.67	5.78
Variance	0.77	0.67	0.91	0.77	0.89	0.67	0.47	0.25	0.44	0.84

Overall statistics	**Value**	**Consistency**	**Value**
Overall median score	6	Sum of item variances	6.67
Overall mean score	5.91	Variance of total scores	5.88
		Cronbach's α	-0.15

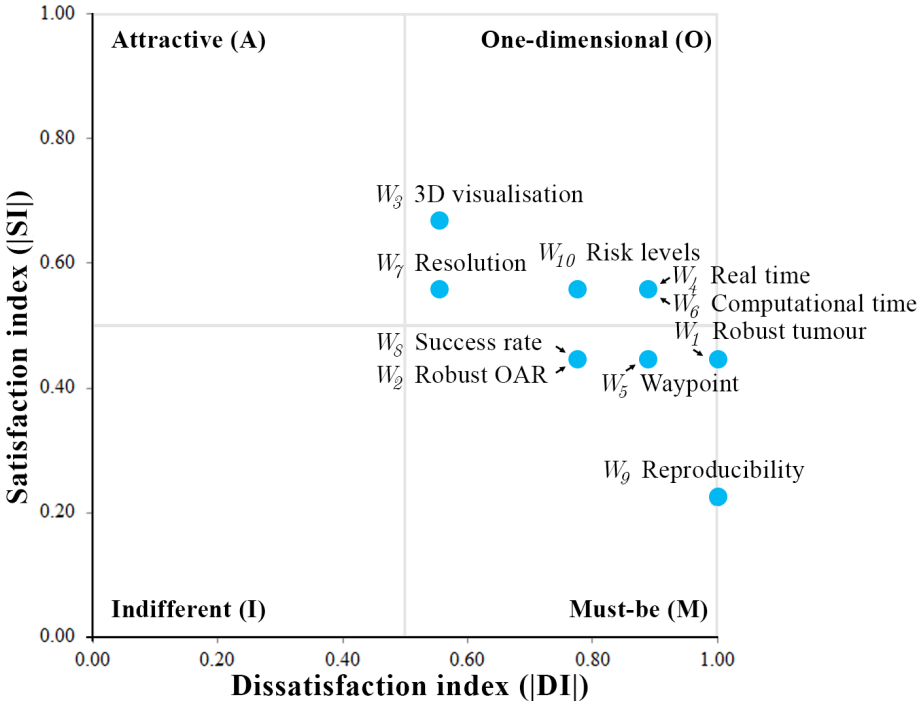

Figure 5.4: Absolute dissatisfaction-satisfaction $(|DI|, |SI|)$ plot of the user requirements in the case example.

to the statistical mode only two of the qualities were classified as attractive attributes (with one partially attractive, partially must-be), and two as one-dimensional attributes (both partially must-be, partially one-dimensional). Similarly, from the $(|DI|, |SI|)$-plot in Figure 5.4 it can be seen that all of the requirements fall in the quadrants of one-dimensional and must-be qualities. The inter-rater reliability was assessed using Krippendorff's α [342], which was calculated to be $\alpha = 0.12$. This indicates a low reliability, as a value of 0.8 is generally recommended. Therefore, equal importance ratings are henceforth assumed for the user requirements.

Table 5.3: Results of the Kano's questionnaire in which respondents where asked to directly classify the user requirements in Table 5.1 for the BT needle channel planning problem in Kano categories.

Frequencies	W_1	W_2	W_3	W_4	W_5	W_6	W_7	W_8	W_9	W_{10}
A. Attractive	0	2	4	1	1	1	4	2	0	2
M. Must-be	5	5	3	4	5	4	4	5	7	4
O. One-dimensional	4	2	2	4	3	4	1	2	2	3
I. Indifferent	0	0	0	0	0	0	0	0	0	0
Statistics	W_1	W_2	W_3	W_4	W_5	W_6	W_7	W_8	W_9	W_{10}
Mode	M	M	A	M/O	M	M/O	A/M	M	M	M
SI	0.44	0.44	0.67	0.56	0.44	0.56	0.56	0.44	0.22	0.56
DI	-1.00	-0.78	-0.56	-0.89	-0.89	-0.89	-0.56	-0.78	-1.00	-0.78
Overall statistics	**Value**									
Mode	M									
Krippendorff's α	0.12									

5.3.2 Formulation of technical attributes and technical correlations

For MP-QFD, a list of technical attributes must be composed that are characteristics of MP algorithms and able to realise the user requirements. Logically, this includes a set of computational or operational criteria of motion planning algorithms (see Subsection 4.1.3). Additionally, one may select more tangible technical attributes, for example commonly used parameters from benchmark studies -e.g. time, success rate, or path length- that are integrated in motion planning libraries. However, as not all the MP classes that are considered as alternatives in this study are represented in these libraries, this is not yet feasible. Instead, practical aspects that must be considered for the implementation of a MP algorithm (see Figure 4.4) to conform to the problem at hand are added to the list of technical attributes. In this example only the categories and not the individual practical considerations are included in the list of technical attributes:

- *Agent representation*: How able are algorithms in the MP class to handle multiple agents simultaneously?
- *Workspace representation*: How able are algorithms in the MP class to deal with three-dimensional obstacles and operate in a narrow cluttered environment?
- *Uncertainty representation*: How able are algorithms in the MP class to accurately handle spatial uncertainty of obstacles?
- *Planning execution*: How flexible are algorithms in the MP class to include (differential) constraints or different cost functions?

The attainment of these technical attributes is made measurable for a MP alternative by investigating implementations in literature. For example, it can be verified whether approximate cell decomposition techniques have been associated with multi-agent systems, and accordingly a rating can be assigned. In such an approach, it would be most appropriate to use a simple ordinal scale (e.g. 'applicable', 'partially applicable', and 'not applicable').

Correlations between technical attributes cannot directly be accounted for using the ordinal method. However, it is still useful to set up such a technical correlation matrix, since it can potentially benefit analysis. The strength of the correlations among HOWs is coarsely estimated on the same seven-level ordinal scale as is introduced for the relationship matrix.

Table 5.4: Correspondence map between raw importance ratings g_i and relationship coefficients r_{ij}, expressed on a 7-level ordinal scale. Adapted from Ref. [335]

Scale level	Linguistic interpretation of g_i	Importance value	Linguistic interpretation of r_{ij}	Symbol
L_1	Very unimportant	1	No relationship	<blank>
L_2	Unimportant	2	Weak relationship	△
L_3	Moderately unimportant	3	Moderately weak relationship	◬
L_4	Neutral	4	Medium relationship	□
L_5	Moderately important	5	Moderately strong relationship	⧈
L_6	Important	6	Strong relationship	○
L_7	Very important	7	Very strong relationship	◎

5.3.3 Generation of relationship matrix

For the ordinal scale approach by Fransceschini et al. [335], first a correspondence map (Table 5.4) is constructed on a seven-level ordinal scale as was used for the prioritisation of user requirements. This relationship matrix is established by the author of this thesis and the transformed relationship matrix using the correspondence map is illustrated in Table 5.5.

5.3.4 Ranking of a set of alternatives

For the selection of an option from a set of alternatives using the MCDM-ORCA method, one of the inputs is an importance ordering of technical alternatives. The weights and T-indicators are first calculated via Eq. 5.9 and 5.10 respectively. For example, one would obtain the weight w_1'' of technical attribute H_1 from Table 5.5 in the following manner [335]:

$$
\begin{aligned}
w_1'' &= \min_{i=1\ldots10} \left(\max\left\{\text{neg}(g_i), r_{i1}''\right\}\right) \\
&= \min\big(\max\left\{\text{neg}(g_1), r_{11}''\right\}, \max\left\{\text{neg}(g_2), r_{21}''\right\}, \max\left\{\text{neg}(g_3), r_{31}''\right\}, \max\left\{\text{neg}(g_4), r_{41}''\right\}, \\
&\qquad \max\left\{\text{neg}(g_5), r_{51}''\right\}, \max\left\{\text{neg}(g_6), r_{61}''\right\}, \max\left\{\text{neg}(g_7), r_{71}''\right\}, \\
&\qquad \max\left\{\text{neg}(g_8), r_{81}''\right\}, \max\left\{\text{neg}(g_9), r_{91}''\right\}, \max\left\{\text{neg}(g_{10}), r_{10,1}''\right\}\big) \\
&= \min\big(\max\left\{L_2, L_6\right\}, \max\left\{L_2, L_6\right\}, \max\left\{L_2, L_1\right\}, \max\left\{L_2, L_2\right\}, \max\left\{L_2, L_4\right\}, \\
&\qquad \max\left\{L_2, L_2\right\}, \max\left\{L_2, L_1\right\}, \max\left\{L_2, L_1\right\}, \max\left\{L_2, L_4\right\}, \max\left\{L_2, L_1\right\}\big) \\
&= \min\big(L_6, L_6, L_2, L_2, L_4, L_2, L_2, L_2, L_4, L_2\big) = L_2
\end{aligned}
$$

When calculating these weights for the case example, the same importance rating was found for for all attributes: $w_j'' = 2, \quad \forall j \in \mathbb{Z}_{1,10}$, i.e. $H_1 \approx H_2 \approx \ldots H_{10}$. The T-indicator to differentiate between the ECs for the first technical attribute H_1 is computed as follows (Eq. 5.10):

$$T_1 = \dim\left(W_i \mid r_{i1}'' > w_1''\right) = \dim\left(\{W_1, W_2, W_5, W_9\}\right) = 4$$

This establishes the following importance ordering of technical attributes:

$$(H_3 \approx H_{11}) \succ (H_1 \approx H_{10}) \succ (H_2 \approx H_6 \approx H_7 \approx H_8) \succ (H_4 \approx H_5 \approx H_9)$$

Having established an importance ordering of the technical attributes, all the alternatives must be ranked for each of the technical attributes. Since the selected list of technical attributes based on performance criteria ($\{H_1, \ldots H_7\}$ is valid, operational and practicable for any type of MP class or

Table 5.5: Transformed relationship matrix based on the seven-level ordinal scale correspondence map for the BT needle channel planning problem.

	Technical attributes (HOWs) →		Optimality	Completeness	Comp. complexity	Dim. Scalability	Anytime	Soundness	Topologically informed	Agent repr.	Workspace repr.	Uncertainty repr.	Planning execution
			Performance criteria							Practical aspects			
	User requirements (WHATs) ↓	g_i	H_1	H_2	H_3	H_4	H_5	H_6	H_7	H_8	H_9	H_{10}	H_{11}
W_1	Robust placement with respect to tumour	L_6	L_6	L_2	L_1	L_1	L_1	L_2	L_4	L_4	L_2	L_6	L_4
W_2	Robust placement with respect to OARs	L_6	L_6	L_2	L_1	L_1	L_1	L_4	L_6	L_6	L_2	L_6	L_4
W_3	Three-dimensional visualisation	L_6	L_1	L_1	L_4	L_6	L_1	L_1	L_1	L_1	L_6	L_1	L_1
W_4	Real-time adaptability	L_6	L_2	L_4	L_6	L_1	L_6	L_1	L_1	L_1	L_1	L_1	L_1
W_5	Manual indication of waypoints	L_6	L_4	L_2	L_1	L_1	L_1	L_1	L_1	L_1	L_2	L_1	L_1
W_6	Computational time	L_6	L_2	L_4	L_7	L_2	L_4	L_2	L_1	L_4	L_2	L_4	L_4
W_7	Resolution of anatomy and trajectories	L_6	L_1	L_1	L_4	L_4	L_1	L_1	L_1	L_1	L_6	L_1	L_4
W_8	Success rate in generating channels	L_6	L_1	L_6	L_2	L_1	L_1	L_4	L_4	L_2	L_1	L_2	L_2
W_9	Reproducibility of the generated channels	L_6	L_4	L_1	L_4	L_2	L_1	L_2	L_1	L_2	L_1	L_1	L_7
W_{10}	Robust assessment of the risk levels	L_6	L_1	L_1	L_2	L_1	L_1	L_6	L_2	L_1	L_2	L_7	L_1

Table 5.6: Ranking of a set of robust trajectory planning classes. Ties are allowed between alternatives. The numbers in the table represent the rank of an alternative (lowest number indicates the highest rank).

	Technical attributes (HOWs) →	Optimality	Completeness	Comp. complexity	Dim. Scalability	Anytime	Soundness	Topologically informed	Agent repr.	Workspace repr.	Uncertainty repr.	Planning execution
		Performance criteria							Practical aspects			
	Trajectory planning alternatives ↓	H_1	H_2	H_3	H_4	H_5	H_6	H_7	H_8	H_9	H_{10}	H_{11}
A_1	Stochastic continuous-time optimisation	2	4	4	2	1	2	2	2	1	2	2
A_2	Stochastic optimal control	3	2	3	2	2	1	2	1	1	1	1
A_3	Backward stochastic reachability	3	2	5	3	2	2	2	2	2	2	1
A_4	Reachability tree	4	2	3	3	2	2	2	3	3	2	1
A_5	Incremental sampling with chance constraints	3	3	2	1	1	1	2	1	1	1	1
A_6	Incremental sampling with particle expansion	4	4	2	1	1	1	2	1	1	2	1
A_7	Virtual potential field	5	1	1	1	2	2	2	1	3	3	1
A_8	Warm-started trajectory optimisations	1	4	4	2	1	2	1	2	2	2	1
A_9	Plan and transform	5	4	1	2	2	2	2	3	2	3	3

algorithm, and not only the robust motion planners considered in this thesis, such a decision matrix only needs to be established once and can then be applied to various MP problems. The measurability of technical attributes based on practical aspects ($\{H_8, \dots H_{11}\}$) has been discussed previously and may be more problem-dependent. The author of this thesis established weak orderings for the performance per criterion of the robust path and trajectory planning approaches under uncertainty in environment knowledge. The ranking for trajectory planning approaches is for illustration purposes shown in Table 5.6.

Using the ranking of alternatives and importance ordering of the criteria, the binary and cumulative index vector are computed. For example, for the pairwise comparison of alternatives A_1 and A_2 in the case example, one would compute via Eq. 5.12 and Table 5.6:

$$\mathbb{U}_{A_1,A_2} = \begin{array}{c} \begin{matrix} H_1 & H_2 & H_3 & H_4 & H_5 & H_6 & H_7 & H_8 & H_9 & H_{10} & H_{11} \end{matrix} \\ \begin{pmatrix} 1 & 0 & 0 & 0.5 & 1 & 0 & 0.5 & 0 & 0.5 & 0 & 0 \end{pmatrix} \end{array}$$

Subsequently, from the importance ordering of technical attributes, one could sum these scores and derive the index vector:

$$\mathbb{U}_{A_1,A_2} = \begin{array}{c} \begin{matrix} H_{3,11} & H_{1,10} & H_{2,6,7,8} & H_{4,5,9} \end{matrix} \\ \begin{pmatrix} 0 & 1 & 0.5 & 2 \end{pmatrix} \end{array}$$

Next, the cumulative index vector and its counterpart are derived according to Eq. 5.13. For the pairwise comparison of alternatives A_1 and A_2 these are:

$$\mathbb{H}_{A_1,A_2} = \begin{array}{c} \begin{matrix} H_{3,11} & H_{1,10} & H_{2,6,7,8} & H_{4,5,9} \end{matrix} \\ \begin{pmatrix} 0 & 1 & 1.5 & 3.5 \end{pmatrix} \end{array}, \quad \mathbb{H}_{A_2,A_1} = \begin{array}{c} \begin{matrix} H_{3,11} & H_{1,10} & H_{2,6,7,8} & H_{4,5,9} \end{matrix} \\ \begin{pmatrix} 2 & 3 & 6.5 & 7.5 \end{pmatrix} \end{array}$$

Since each entry h_j in $\mathbb{H}_{A_1,A_2}$ is less or equal than h'_j in $\mathbb{H}_{A_1,A_2}$ and at least one of these inequalities is strict, alternative A_2 is said to dominate A_1: $A_2 \succ A_1$. Performing such pairwise comparisons for each of the possible combinations of trajectory planning classes gave the following set of ordering equations:

$$A_5 \succ A_2 \succ A_8 \succ A_1 \succ A_3 \succ A_9; \qquad A_5 \succ A_2 \succ A_4 \succ A_9$$

$$A_5 \succ A_6 \succ A_8 \succ A_1 \succ A_3 \succ A_9; \qquad A_6 \succ A_4; \qquad A_7 \succ A_1 \succ A_9$$

As can be seen from these equations, due to the incomparability of some of the alternatives (especially A_4, A_6, A_7), a definite ranking cannot be established. From this information, one could already for example obtain that alternative A_5 is generally ranked best (although A_7 might be better) and $A_1 \succ A_3 \succ A_9$ are ranked worst. Nevertheless, a final overall ranking may be estimated based on the possible combinations that can be constructed whilst obeying these ranking constraints. A total of 44 different rankings remain possible in this case example. If one desires to establish a more 'definite' ranking, Borda count can be used to obtain which ranking is the most persistent [336]. For the case example, using Borda count would result in the following preference ordering:

$$A_5 \succ (A_2 \approx A_6) \succ A_7 \succ A_8 \succ A_4 \succ A_1 \succ A_3 \succ A_9$$

5.3.5 Selection of a motion planning class

The full house of quality of MP-QFD associated with the case example is illustrated in Figure 5.5. From the previous analyses the following rankings of trajectory and path planning classes could be respectively obtained:

$$\begin{cases} A_5 \succ (A_2 \approx A_6) \succ A_7 \succ A_8 \succ A_4 \succ A_1 \succ A_3 \succ A_9 & \text{Trajectory planning} \\ (A_2 \approx A_5) \succ A_1 \succ A_3 \succ A_4 & \text{Path planning} \end{cases}$$

This implies that the three highest performing robust trajectory planning classes for the BT needle channel planning problem according to MP-QFD analysis are:

- Incremental sampling approaches with analytic chance constraints (A_5);
- Incremental sampling approaches with particle expansion (A_6);
- Stochastic optimal control (A_2).

The three highest performing robust path planning classes are:

- Potential-based methods (A_2);
- Rapidly-exploring random trees (A_5);
- Approximate cell decomposition (A_1).

From the house of quality in Figure 5.5, one may also visually infer which classes of robust motion planners are most suitable for this problem. The first step in such an approach is selecting the 'depth' of analysis; for example one could only look at strong relations for simplicity. When users prioritise the user requirement 'robust optimal placement with respect to the tumour' (W_1), the central part of the diagram shows that one must regard motion planners that rank high on the criteria optimality (H_1), i.e. methods that are (asymptotically) optimal, and uncertainty representation (H_{10}), i.e. methods that are capable of analytically handling spatial uncertainty. As such, when next observing the technical (alternative ranking) matrix, the selected trajectory planning approaches could be warm-started trajectory optimisation (A_8) and stochastic continuous-time optimisation (A_1)[2]. Additionally, one could use the technical correlation matrix to further differentiate between alternatives. For example, one could obtain that uncertainty representation (H_{10}) is strongly linked to soundness (H_6) in the roof of the matrix. However as both warm-started trajectory optimisation and stochastic continuous-time optimisation are generally not able to generate sound trajectories, i.e. rank equally on soundness, in this case this does not allow for further differentiation. Now proceeding with such an approach for the most important user requirements one could quickly derive a set of applicable motion planning classes.

[2]Warm-started trajectory optimisation (A_8) is from the set of alternatives best able to generate (globally) optimal trajectories (H_1) and ranks second regarding uncertainty representation (H_{10}). Stochastic continuous-time optimisation (A_1) ranks second on both of these technical attributes.

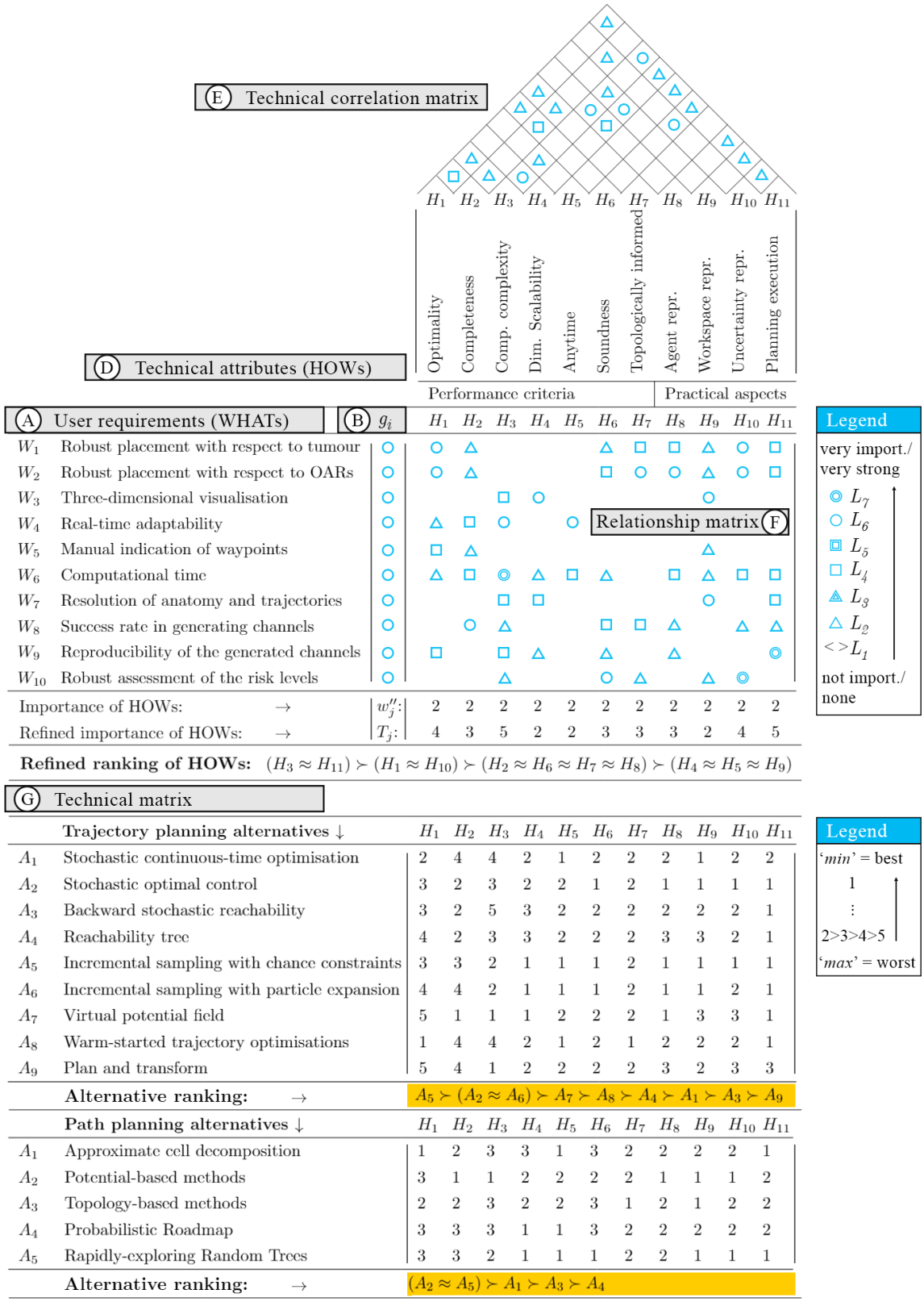

Figure 5.5: House of quality of MP-QFD for the case example of selecting a robust MP class suited for the BT needle channel planning problem.

5.4 Discussion and future work

The conceptual MP-QFD approach proposed in this chapter can be a useful tool in aiding the selection of a motion planning class, and has been successfully applied for developing brachytherapy software using the results from a pilot study. However, the results of this pilot study should be re-evaluated in a future study. A negative Cronbach's α was calculated for the questionnaire aiming to establish the prioritisation of user requirements. This indicates that the variance between respondents is low in comparison with the variation in individual respondents' answers. Several factors were hypothesised to explain this finding. First, the participants in this study were possibly not familiar with robust planning software[3] and may have experienced difficulties in understanding the formulated user requirements for a non-existing product. Moreover, the importance ratings of requirements may be conflicted by several biases, including a concavity bias as only requirements are included that are known to be of importance to users of the software [343], and response style bias. Furthermore, the negative Cronbach's α is possibly a consequence of the small number of participants included in this pilot study [344]. Indeed, simple power calculations with reasonable requirements ($1 - \beta = 0.8, a = 0.05, c = 0$) indicate that around twenty participants would be required for $\alpha = 0.7$ (acceptable consistency), but this is heavily dependent on the value of c and the planning value of α in this analysis [345]. The reliability of the labelled seven-point Likert scale used in this pilot study has moreover been criticised in some works. For example, this type of Likert scale may trouble the interval assumption, and the use of labels can perhaps influence the participants' understanding of the reference level for each item [340, 346]. Furthermore, rather than that the Likert scale ranges from 'not important' to 'very important', the negative connotation associated with the word 'unimportant' may have influenced the participants' choices. For future studies, preference ordering techniques in an ordinal approach are recommended over direct scoring methods. These would perhaps be more natural to the respondent and would enforce respondents to differentiate between the importance of user requirements. Moreover, for quantitative QFD it would be more consistent to not use a Likert scale (interval) in value assessment, but instead to use a ratio scale approach. For example, ratio scale pairwise comparison methods (e.g. AHP) would partially avoid such inconsistencies [334], although this form of judgement may not be natural or convenient for respondents [318].

Kano's categories were in this study established through direct classification to further differentiate between user requirements. Surprisingly, the respondents classified most of the user requirements as must-be attributes. This finding was unexpected since most of the respondents were likely not aware of the existence of (robust) automatic needle channel planning software nor its capabilities. These findings may additionally hint that direct classification through a digital questionnaire is not a suitable approach for Kano's model, as proper understanding by the respondents of user requirements and the product at hand as well as that of Kano's model cannot be validated as well as in a face-to-face interview which is the recommended procedure [347]. Understanding of Kano's model has been noted to be essential for a direct classification approach [341, 348]. In this study, the inter-rater reliability assessed using Krippendorff's α was low. In the study by Witell et al. it was shown that direct classification responses led to greater frequency of attributes in the one-dimensional quadrant opposed to other Kano classification methods, similarly to what is observed in this study [348]. Moreover, users are usually not aware of the satisfaction that attractive attributes will generate, and hence do not classify these as such [348]. As the vast majority of reviewed attributes was classified as must-be attributes and the statistical

[3]The data of this study does not directly support such a conclusion, but some respondents indicated that they were unfamiliar with the use of 'robust' in this context.

mode was not found to be appropriate for other attributes, differentiation into Kano categories does not make sense and hence the proposed model described by Wang and Ji could not be accurately applied to this data [349]. Respondents clearly considered all criteria to be very important. Both tests indicated that ratings were too close together to produce a reliable ranking. Therefore, equal importance ratings were assigned to all criteria.

Rather than the user-centred approach which MP-QFD generally aims to be, this implied that the ranking of technical attributes (HOWs) was obtained based solely on the strength and the number of relations in the relationship matrix for a technical attribute. This may give false impressions, e.g. in the example a technical attribute with many moderately weak relations scores higher than one with only a few strong relations. With the resulting importance ratings, technical attributes were ranked. However, although a seven-point ordinal scale was used for this purpose, only four levels in the importance ordering of technical were obtained. This flattening effect occurs naturally with the ordinal method used [335], but is strengthened as all raw importance ratings g_i are set to be of equal weight in the case example. For example, one would obtain the following ranking if $g_5 = L_5$, $g_9 = L_7$ and $g_i = L_6$ otherwise (which are the median importance ratings that were found in the pilot study): $(H_3 \approx H_{11}) \succ H_1 \succ (H_6 \approx H_8) \succ H_4 \succ H_9 \succ H_2 \succ H_{10} \succ H_7 \succ H_5$. The effect of this rating on the outcome ranking of alternatives was not investigated.

The MP-QFD approach has several advantages over conventional selection techniques. First, the approach has a strong user focus opposed to previous guidelines to select motion planning algorithms, which enables the selection of an alternative that potentially maximises user satisfaction. Second, the approach systematically establishes and conveniently illustrates the relations between user requirements and product parameters, which stimulates communication between users of the product and engineers, and can be established from collaborative effort. Furthermore, QFD is a flexible approach, which allows the addition of several modules such as Kano's model, (technical) competitive analysis, correlations between WHATs and HOWs, and fuzzy classification, all of which have been briefly discussed in this work. Owing to its simple structure, QFD is suited for implementation in a software application. For the selection of motion planning software, integration with planning libraries seems to be a logical step for future work. Lastly, after being established, the tool enables users to set the depth of analysis, e.g. as to prioritise alternatives based only the important user requirements.

There are however some inherent drawbacks in the methodology presented. The main drawback of the presented approach is that although MP-QFD was introduced for knowledge alleviation of a practitioner interested in motion planning, establishing the relationship matrix may still be complex. Both a practitioner inexperienced in motion planning but familiar with the user requirements, i.e. the medical specialist in this case example, or a practitioner experienced in motion planning but unfamiliar to the requirements of the eventual users, i.e. a software engineer, may struggle to accurately assess these relations themselves. Fuzzy theory (introduced in Appendix A.6) may aid in capturing uncertainty in decision-making and therefore would be of interest to include in an ordinal QFD approach in future work. For example for this purpose, an interesting integration into QFD would be ordinal-based intuitionistic membership grades [350]. Additionally, it is envisioned that MP-QFD as a communicative tool may bring both the communities of software engineers and practitioners desiring to implement MP together to find an effective solution by collaboratively establishing the relationship matrix and providing inputs. This is in line with the widely cited purpose of QFD: "quality function deployment focuses and coordinates skills within an organization..." [351].

Moreover, a user expecting a definite outcome of the tool may be disappointed in finding out that the tool only gives guidelines for the selection of alternatives. Despite that the ratings of alternatives in a quantitative approach may suggest a definite ranking, these ratings are the result of assumptions, subjectivity and arbitrariness. In a qualitative approach, the presence of incomparable relations results in the possibility of not being able to derive a definite ranking for all alternatives, as instead a set of rankings is given. The outcome does not say anything about the 'distance' between alternatives. A method to enable a final ranking of all alternatives in the qualitative approach has its own disadvantages. For example, the proposed Borda count is not a Condorcet method, and also violates the independence of irrelevant alternatives condition from Arrow's impossibility theorem [322, 336]. To illustrate the violation of Arrowian principles, one may drop alternative A_7. In this case, one would obtain that the order of all alternatives remains the same, with the exception that $A_8 \approx A_4$. Nonetheless, the algorithm was quite robust in this case example to such changes due to the generally relatively large differences between the counts of the evaluated alternatives. In future work, aggregating these rankings in a way that does not require cardinal data would be of interest. Lastly, one must note that QFD is an inherent simplification of reality. Alleviating assumptions of QFD, for example through Kano's model, market segmentation or demand modelling [322], could be an interesting subject of research in the further development of MP-QFD.

5.5 Conclusion

In this chapter, motion-planning QFD (MP-QFD) has been developed in order to aid the selection process of motion planning algorithms. This tool is an extension of QFD and similar to previously developed QFD-based selection approaches. Both a full quantitative and qualitative approach have been introduced and discussed, and a case example where the latter is implemented is provided. The main novelties of this work in contrast to previous QFD-based selection approaches is that a fully ordinal selection method has been proposed by combining the previous works by Franceschini et al. [335], and Mazurek [337]. This qualitative ordinal method is able to overcome several problems, such as the promotion of ordinal data into cardinal, interval or ratio data which violates conditions of Arrow's impossibility theorem. Moreover, as (technical) competitive analyses are left out, subjectivity and arbitrariness are minimised and the method can be more rightfully applied to the development of novel products.

The medical specialists that participated in this study indicated in the questionnaire and their comments that the most important user requirements for the software are reproducibility of the generated channels (W_9), success rate in generating the channels (W_8), and real-time adaptability (W_4). This substantiates the author's preferred choice for the selection of an incremental sampling approach with chance constraints (A_5), for which the mathematical formulation of the BT needle channel problem in the previous chapter is ideal. Therefore, in the next part of this thesis, chance constrained RRT is further developed and applied to the BT problem.

Part III
Robust brachytherapy needle channel planning under uncertainty

In this part, robust motion planning algorithms are proposed and implemented for solving the BT needle channel planning problem under uncertainty. Sampling-based motion planners were in the previous part found to possess the most favourable characteristics for solving this problem. Therefore, variants in this class of motion planners are introduced in Chapter 6. The main contribution of this chapter is the development of bounded uncertainty and probabilistic variants of sampling-based planners suitable for the trajectory planning of non-holonomic agents. In Chapter 7, first the coverage planning problem is solved to compute the optimal configuration of interstitial dwell segments for a simulated two-dimensional patient case. The resulting configuration is evaluated using dose-based optimisation and compared with standard treatment modalities. These configurations are then used to initialise trajectory planning. Three types of motion planners are implemented and evaluated for brachytherapy needle channel planning subject to probabilistic and bounded uncertainty.

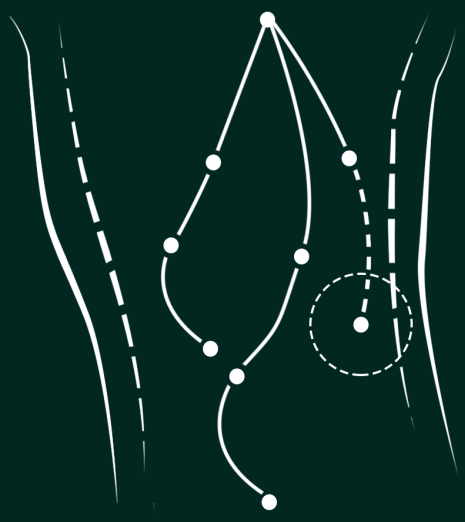

Illustration: Schematic illustration of chance constrained planning for a non-holonomic agent

6. Implementation of robust motion planning algorithms

6.1 An introduction in sampling-based planers

The concept of sampling-based planners has long been used for both path and trajectory planning [297]. These approaches avoid the explicit construction of feasible regions by instead probing the configuration or state space with sampled points to construct the connectivity of C_{free} or $\mathcal{X}_{free}$ [239]. A collection detection module separates the geometric model of the workspace and the motion planner (Figure 6.1). By building upon an implicit representation of the workspace independent of the actual geometric models, the complexity of deterministic motion planning is avoided. Any sampling-based motion planner can be decomposed into a set of primitives [239, 297]:

- **Sampling**: Through a sampling technique the configuration or state space is sampled. Several choices can be made here, including whether the sampling is performed: (i) deterministically or randomly, and (ii) uniformly or non-uniformly;
- **Metric**: A cost metric must be defined on the configuration or state space, which returns a cost between two configurations or states. Although such a metric is often simple to define for path planning, e.g. distance, in state space this becomes more difficult;
- **Nearest Neighbour**: To find the 'closest' point to the sampled point, a nearest neighbour or selection algorithm is required;
- **Steering function**: In order to connect the two configurations or states, a steering function must be computed for the system. Whereas in path planning this may simply be a straight line, for systems with differential constraints this may require solving a two-point boundary value problem (BVP);
- **Collision detection**: Collision detection typically using a Boolean function involves determination not only whether a configuration or state lies in the free space, but also whether the path or trajectory in between is in free space.

For a general overview of sampling-based motion planners see the review by Elbanhawi et al. [297]. Sampling-based planning may separate pre-processing of the workspace to generate an interconnected graph and then implement a graph search algorithm in a multi-query approach, or integrate exploration of the configuration or state space with path/trajectory searching in a single-query approach [239]. The two most well-known examples of these sampling-based planning methods are the multi-query probabilistic roadmap (PRM) approach [352], and the single-query rapidly exploring random tree (RRT) approach [353]. The ability of RRT approaches to effectively incorporate differential constraints by construction at low computational complexity makes this class of algorithms ideal for the BT needle channel planning problem formulated in Subsection 4.3.5.

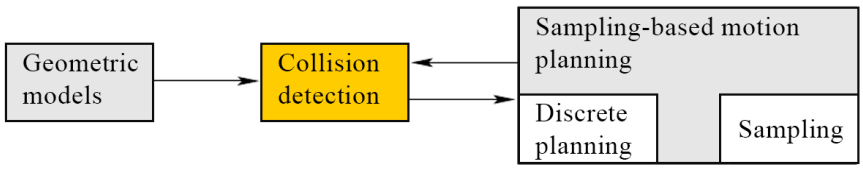

Figure 6.1: General model for sampling-based motion planning, where a collision detection model separates the workspace representation from the motion planning algorithm. Figure adapted from Ref. [239].

6.1.1 Basic rapidly-exploring random tree

Possibly the most commonly known and implemented sampling-based algorithm class in recent history is that of rapidly exploring dense trees (RDTs), of which most work has been focused on the subgroup of rapidly-exploring random trees (RRTs), originally developed by LaValle [353]. The former is a generalisation which may use deterministic or random sampling, whereas the latter subgroup is characterised by using a random sampling strategy. As previous research has predominantly focused on random sampling strategies, this thesis is limited to rapidly-exploring random trees. In RRTs, a unidirectional search tree is generated by randomly sampling the configuration or state space and interconnecting these configurations or states with a tree-like structure until the goal region is reached [239]. Although initially intended for kinodynamic planning [353], RRTs have acquired a huge popularity not only for trajectory planning, but also for path planning due to the simplicity and efficiency of the approach. Pseudocode of the basic RRT algorithm for path planning is shown in Algorithm 1. In Figure 6.2a and 6.2b the functioning of the algorithm is illustrated (see MATLAB Script A.1.11 for a working example).

Let us denote the graph or tree generated by RRT as $G = (V, E)$, comprised of the set of vertices $\mathbf{v} \in V$ and edges $\mathbf{e} \in E$ and follow the notation by Karaman and Frazzoli [354]. Moreover, denote initial and target configurations by $\mathbf{q}_I$ and $\mathbf{q}_G$ respectively. In the first step, using the function `Sample`, a sample $\mathbf{q}_{samp}$ is randomly drawn from the configuration space $\mathcal{C}$ or the free configuration space $\mathcal{C}_{free}$. If this configuration is feasible, i.e. does not lie in $\mathcal{C}_{obs}$, the `Extend` procedure is called which consists of the following steps. Firstly, the nearest neighbour $\mathbf{q}_{near}$ to this sampled configuration is sought in the already established tree G using the function `Nearest` based on the distance metric (line 5 in Algorithm 1). Typically in path planning this concerns an Euclidean distance metric, i.e. $\texttt{Nearest}(G, \mathbf{q}_{samp}) = \arg\min_{\mathbf{v} \in V} \|\mathbf{q}_{samp} - \mathbf{v}\|$. Next, the algorithm tries to connect the two configurations directly by using the `Steer` procedure. This returns a configuration $\mathbf{q}_{new}$ that is mathematically 'closer', based on the cost metric, to $\mathbf{q}_{samp}$ than $\mathbf{q}_{near}$ (line 6). This new node $\mathbf{q}_{new}$ is set: (i) equal to the sampled configuration, $\mathbf{q}_{samp}$, if this configuration is directly reachable, (ii) at a specified distance from $\mathbf{q}_{near}$ along the edge connecting these two configurations, or (iii) at another feasible location on this edge. This is followed by feasibility checks of both the resulting edge and vertex through the procedure `Collision_free` (line 7), which is a Boolean function returning `TRUE` if no collision is detected. The goal configuration $\mathbf{q}_G$ may be included as a sampled node periodically, to check whether a feasible connection between the start and goal configuration is possible. If the goal configuration has been reached successfully (line 10), the vertices and edges are appended to the tree G and the process is terminated. The algorithm is also terminated when exceeding a maximum number of iterations K.

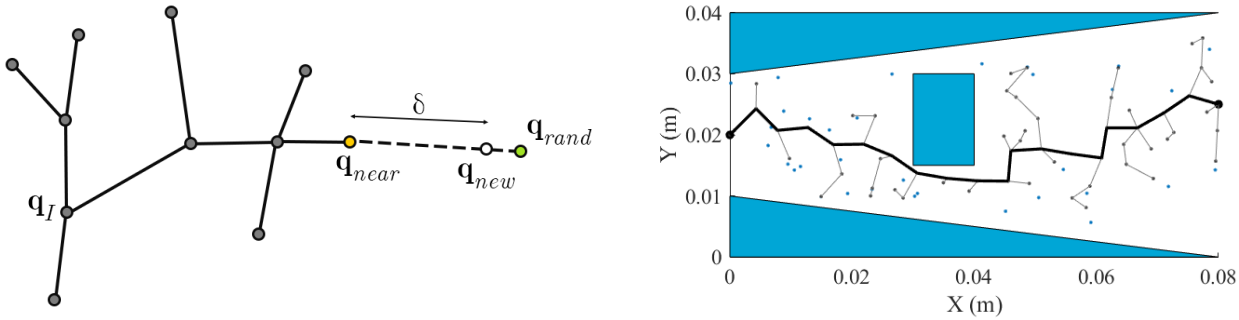

(a) Illustration of the basic RRT `Extend` procedure.

(b) Basic RRT in a standard environment.

Figure 6.2: Illustrations of the tree expansion and path finding of the basic RRT algorithm outlined in Algorithm 1. In MATLAB Script A.1.11, the code is provided to generate figure (b).

Algorithm 1: Basic RRT algorithm [353]

```
1  V ← q_I; E ← ∅; k ← 0;
2  for k = 1 to K do
3  |  G ← (V, E);
4  |  q_samp ← Sample() ;
5  |  q_near ← Nearest(G, q_samp);
6  |  q_new ← Steer(q_near, q_samp)
7  |  if Collision_free(q_near, q_new) then
8  |  |  V ← V ∪ {q_new};
9  |  |  E ← E ∪ {q_near, q_new};
10 |  |  if q_new = q_G then
11 |  |  |  G ← (V, E) ;
12 |  |  |  return G
13 |  |  else
14 |  |  |  continue;
15 |  |  end
16 |  end
17 end
18 return failure
```

Probabilistic completeness was shown to be guaranteed for the basic RRT algorithm [355]. Due to its ability to handle systems with complex dynamics and high-dimensional environments with low added complexity, it has been widely applied in such environments and for (nonlinear) systems with differential constraints, such as non-holonomic systems. To enhance the properties of basic RRT, many different modifications to the vanilla algorithm have been proposed.

6.1.2 Asymptotically optimal rapidly-exploring random tree

As can also be observed in Figure 6.2b, the basic RRT algorithm lacks optimality; in fact, it has been shown to almost surely converge to a sub-optimal solution [354]. Therefore, several modifications have been proposed to achieve asymptotic optimality. RRT* is the most well-known asymptotically optimal variant of RRT [354]. Its operation is two-fold. First, it links a newly generated vertex, $\mathbf{q}_{new}$, to the vertex in its neighbourhood that ensures that $\mathbf{q}_{new}$ is reached with minimum accumulated cost. Additionally, this algorithm rewires segments in the tree in favour of paths of lower cost branching from $\mathbf{q}_{new}$. The pseudocode of RRT* is shown in Algorithm 2.

The first rather subtle difference for RRT* in comparison with RRT is that the `Nearest`-procedure is used to compute a configuration termed $\mathbf{q}_{nearest}$, opposed to $\mathbf{q}_{near}$. Although the configuration $\mathbf{q}_{near}$ identified typically based on a distance metric may be 'closest' to the newly added node $\mathbf{q}_{new}$, this does not imply that this point ensures the lowest accumulated cost to $\mathbf{q}_{new}$. Instead, a node in the neighbourhood of $\mathbf{q}_{new}$ is sought that incurs this lowest cumulative cost according to a different cost metric (Figure 6.3). First, the set of vertices in the neighbourhood of $\mathbf{q}_{new}$ are found using the `Near` procedure (line 9 in Algorithm 2). This set is defined as all vertices in the current unidirectional graph $G = (V, E)$ that lie within a closed ball of variable radius $r_{|V|}$, which is a function of the number of nodes $|V|$, and is centred at $\mathbf{q}_{new}$:

$$Q_{near} = \left\{ V' \subseteq V \;\middle|\; \mathbf{v} \in V, \mathrm{norm}(\mathbf{v} - \mathbf{q}_{new}) < r_{|V|} = \min \left\{ \left(\frac{\gamma}{\xi_d} \frac{\log(|V|)}{|V|} \right)^{1/d}, \delta_x \right\} \right\} \tag{6.1}$$

Algorithm 2: RRT* algorithm [354]

```
1  V ← q_I; E ← ∅; k ← 0;
2  for k = 1 to K do
3      G ← (V, E);
4      q_samp ← Sample() ;
5      q_nearest ← Nearest(G, q_samp);
6      q_new ← Steer(q_nearest, q_samp)
7      if Collision_free(q_nearest, q_new) then
8          q_min ← q_nearest;
9          Q_near ← Near(G, q_new, |V|);
10         for all q_near ∈ Q_near do
11             if Collision_free(q_near, q_new) then
12                 C' ← Cost(q_near)+ C(q_near, q_new);
13                 if C' < Cost(q_new) then
14                     q_min ← q_near;
15                 end
16             end
17         end
18         V ← V ∪ {q_new};
19         E ← E ∪ {q_min, q_new};
20         for all q_near ∈ Q_near \ {q_min} do
21             if Collision_free(q_new, q_near) and Cost(q_near) > Cost(q_new) +
                C(q_new, q_near) then
22                 q_parent ← Parent(q_near);
23                 E ← E \ {q_parent, q_near};
24                 E ← E ∪ {q_new, q_near};
25             end
26         end
27     end
28 end
29 return G
```

Here, δ_x is a predefined maximum radius based on the step size in the `Steer`-procedure ($\delta_x = \delta \cdot \bar{v}_t$) , d is the dimension of the planning space, ξ_d the volume of the unit ball in dimension d, and γ a constant for which $\gamma > 2^d(1 + 1/d)\mu(\mathcal{C}_{free})$, where $\mu(\mathcal{C}_{free})$ is used to denote the volume of the free space. From this formulation one may observe that the radius decreases with the number of vertices in the tree with factor $\log(|V|)/|V|$. This rate of decrease in the radius is linked to the reduction of dispersion when uniformly sampling with a sampling-based planner. Effectively, the planner ensures that each iteration a number of connections proportional to $\log(|V|)$ are attempted [246]. Now define $\texttt{Cost}(\mathbf{q})$ as the total accumulated cost for reaching $\mathbf{q}$, and $\texttt{C}(\mathbf{q}_i, \mathbf{q}_j)$ the cost of traversing the edge between $\mathbf{q}_i$ and $\mathbf{q}_j$. In lines 10-17 using these procedures, a feasible connection between a node $\mathbf{q}_{near}$ in set Q_{near} and $\mathbf{q}_{new}$ is sought that reaches $\mathbf{q}_{new}$ with a lower cost than $\mathbf{q}_{nearest}$. In line 18 the new configuration is added to the list of vertices, and in line 19 the edge connecting $\mathbf{q}_{min}$ and $\mathbf{q}_{new}$ is added to the list of edges.

In the second step of RRT* (lines 20-26) minimum-cost connections from $\mathbf{q}_{new}$ to vertices in the set Q_{near} are attempted. The procedure $\texttt{Parent}(\mathbf{q})$ finds the parent of the node $\mathbf{q}$. When a

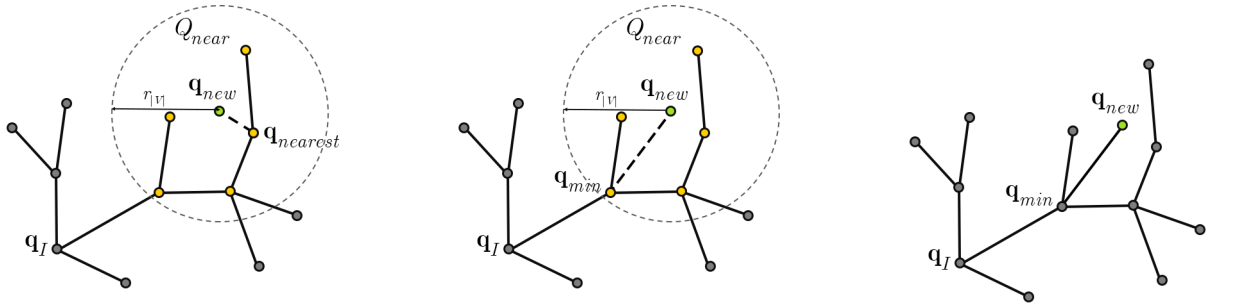

(a) Identifying Q_{near} using `Near`. **(b)** Finding minimum cost path. **(c)** Connecting the new edge.

Figure 6.3: Illustrations of RRT* trying to connect $\mathbf{q}_{new}$ to the existing tree along a minimum cost path.

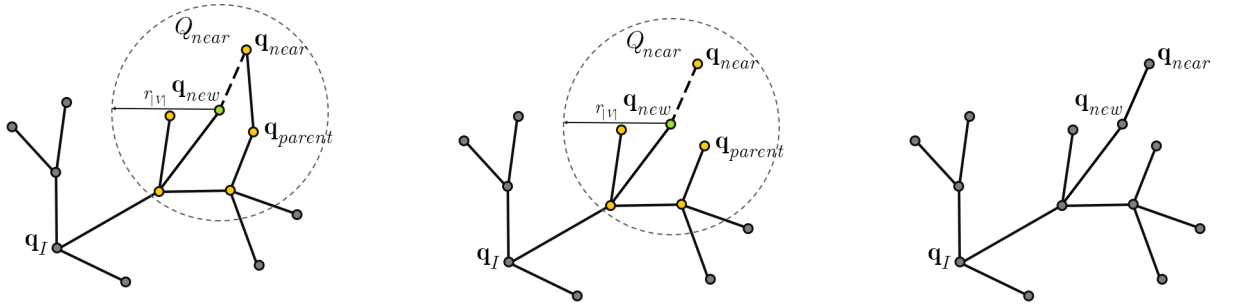

(a) Finding minimum cost path. **(b)** Removing old edge. **(c)** Connecting the new edge.

Figure 6.4: Illustrations of RRT* rewiring the tree by branching from $\mathbf{q}_{new}$ and replacing redundant edges.

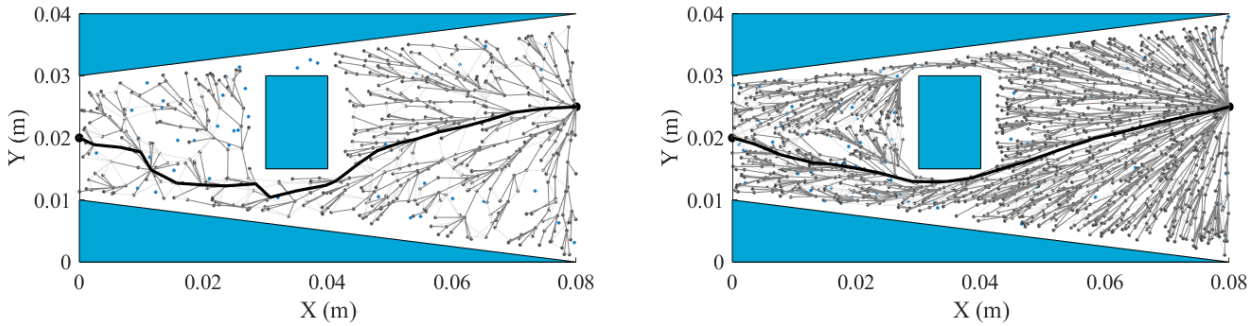

(a) RRT* in a standard environment with $K = 1000$. **(b)** RRT* in a standard environment with $K = 3{,}000$.

Figure 6.5: Illustrations of path finding using the RRT* algorithm outlined in Algorithm 2. In `MATLAB` Script A.1.11, the code is provided to generate these figures.

feasible lower-cost path has been found from $\mathbf{q}_{new}$ to any of the vertices in $\mathbf{q}_{near} \in Q_{near}$, the current edge connecting $\mathbf{q}_{near}$ and its parent is deleted (line 23) to maintain the acyclic graph structure, and the new edge connecting $\mathbf{q}_{new}$ and $\mathbf{q}_{near}$ is added (line 24), see also Figure 6.4. In Figure 6.5 a demonstration of RRT* is shown (based on `MATLAB` Script A.1.11).

Opposed to RRT, asymptotic optimality is guaranteed for the RRT* algorithm, which comes at the expense of per-iteration computational complexity that is within a constant factor [354]. However, the convergence of this algorithm may still be slow, especially in the case of high-dimensional or constrained systems. For systems with differential constraints, finding an optimal solution may require solving a two-point boundary value problem (BVP). This can be computationally intricate and for many kinodynamic systems no analytical solutions exist [356, 357].

6.2 RRT variants for MP of non-holonomic systems

Over the next subsections, a brief overview and illustrations are given of strategies and heuristics to enhance the performance of RRT and RRT*-based algorithms. The focus of this overview is on RRT variants suitable for robust MP of non-holonomic systems in an uncertain environment, such as the channeled BT needle. Therefore, the focus is shifted from configuration space towards state space and the corresponding notation is used (see Section 4.1) when applicable.

6.2.1 Sampling strategies

The standard sampling strategy for RRT is a random one, where samples are drawn from a uniform spatial distribution [358]. Such a scheme allows the planner to explore the free space through a property known as Voronoi bias and attempts to reduce the dispersion [359]. However, uniform sampling may waste computational time on non-viable regions. It has been an ongoing debate whether non-uniform sampling may be beneficial in increasing the convergence of the algorithm [297]. Two types of non-uniform sampling include importance sampling and adaptive sampling [360]. In importance sampling strategies the sampling scheme remains fixed during planning, opposed to adaptive sampling strategies where this scheme is altered based on changes encountered in the planning. Goal biasing, in which expansion of the tree towards the target point or region is promoted, is one of the most common forms of importance sampling [358]. A similar strategy is to try to connect the existing tree greedily to the target point or region. Although this is not necessarily a sampling strategy, this scheme is generally recommended in order to increase convergence as long as randomisation can be maintained [297]. Other typically used importance sampling strategies include: (i) obstacle-biased sampling, e.g. medial axis (away from obstacles) or boundary and Gaussian (around obstacles) bias, (ii) region-based sampling, e.g. heuristically-guided bias (in the low-cost direction), (iii) narrow-region sampling, e.g. bridge test (mid-way bias in a narrow tunnel region), (iv) path-biased sampling, e.g path-biasing (based on previously planned paths), and (v) their equivalents for uncertain environments [297, 358, 361, 362]. An interesting path-biasing approach is used in RRT*-Smart, where an optimised path is established by interconnecting directly visible nodes once a path is found [363]. This optimised path is then used to define bias points for intelligent sampling as to increase the rate of convergence of RRT*.

Adaptive sampling has been implemented especially for algorithms that aim to achieve asymptotic optimality through rewiring, such as RRT*, or algorithms dealing with dynamical systems. As an example of the former, in order to increase the rate of convergence one may actively reduce the search space during the planning [358]. In Informed RRT*, after an initial solution has been found, the sampling is focused on an ellipsoidal domain generated around this initial solution [362]. The size of this sampling domain, i.e. ellipsoid, is reduced upon improving the solution. However, due to its difficulty in scaling to higher dimensions and reliance on RRT*, this sampling technique may not be applicable for the planning of non-holonomic systems. Other informed sampling based variants such as BIT*, which instead of decreasing the sampling domain gradually increases this domain, may improve on its performance [364]. For systems with differential constraints, a modified adaptive sampling strategy is used in Reachability-Guided RRT (RG-RRT) [365]. This algorithm limits the set of nodes that need to be evaluated for the nearest-neighbour pairing to the nodes from which the sample is actually reachable. A sampled node is then only added to the tree if it is closer to the nearest point in the reachable set than to the nearest node in the tree. By confining this search to a small region of the configuration space and maintaining a sparse tree structure, the rate of convergence is increased.

In the case of a holonomic agent, which is constrained to move in a straight line, exploration of the search space can be made more efficient by growing a tree from the target configuration or state as well, known as bi-directional RRT [239]. However, attempting to connect these trees for a differentially constrained system requires solving the two-point BVP [297], and therefore for these systems growing a unidirectional RRT is usually more appropriate.

Sampling may be performed in state space $\mathcal{X}$ for trajectory planning, i.e. as to directly sample a needle pose. However Patil et al. argue that for non-holonomic systems such as a steerable needle it works better in practice to sample in Euclidean space, $\mathbb{R}^n$, instead [89].

6.2.2 Metric

The selection of an accurate metric is a difficult process, but of utmost importance for the appropriateness of the solutions and performance of the algorithm [366]. For holonomic systems, typically the weighted Euclidean distance metric is used. For non-holonomic systems, the Euclidean distance metric may be misleading as nodes that are physically closest based on Euclidean distance may actually be inconvenient to reach [366]. On the other hand, calculating the actual cost-to-go for these systems may be too computationally intensive, especially since the metric function is frequently evaluated. For steerable needles with non-holonomic constraints, the following reachability-guided distance measure has been proposed to define nearest neighbours (see also Figure 4.7) [367]:

$$\rho = \begin{cases} (\theta_{t+\delta} - \theta_t)/\kappa_t, & \text{if } \kappa_t = \{\mathbb{R} \mid |\kappa_t| < \bar{\kappa}, \kappa_t \neq 0\} \\ \infty, & \text{else} \end{cases} \tag{6.2}$$

The reasoning behind this metric, similar to that of RG-RRT, is to only evaluate nearest neighbours from which the sampled node is reachable. During the step of duration δ the curvature of the trajectory is assumed to remain constant. As the sampling for a non-holonomic agent is preferably done in Euclidean space, conversion from a stationary world frame to the body-fixed Frenet–Serret frame is required to evaluate κ_t and $\theta_{t+\delta}$ from a sampled point. This expression can be solved fully analytically.

In order to evaluate the quality of a motion of the non-holonomic agent in an adverse environment, an appropriate cost functional $f(\cdot)$ must be constructed. An admissible cost-functional for evaluating the quality of a path or trajectory in an asymptotically optimal approach must be a function that maps a configuration or state into a non-negative real number and satisfies monotonicity, additivity and Lipschitz continuity [262]. Denote the accumulated cost of motion from the start to a certain state or node $\mathbf{x}^i_{t_N}$ at time t_N for the ith agent as [262]:

$$C[\mathbf{x}^i_{t_N}] = \sum_{t=0}^{t_N} f(\mathbf{u}^i_t, \mathbf{x}^i_t) \tag{6.3}$$

This function up to state $\mathbf{x}^i_{t_N}$ may be recursively constructed as follows:

$$C[\mathbf{x}^i_{t_N}] = C[\mathbf{x}^i_{t_N-\delta}] + f(\mathbf{u}^i_{t_N-\delta}, \mathbf{x}^i_{t_N-\delta}) \tag{6.4}$$

Here, $C[\mathbf{x}^i_{t_N-\delta}]$ denotes the accumulated cost of the parent state of $\mathbf{x}^i_{t_N}$, and $f(\mathbf{u}^i_{t_N-\delta}, \mathbf{x}^i_{t_N-\delta})$ the cost for applying control action $\mathbf{u}^i_{t_N-\delta}$ when at state $\mathbf{x}^i_{t_N-\delta}$.

6.2.3 Nearest neighbour

Establishing the nearest neighbours can be a computational bottleneck in RRT variants or other sampling-based MP algorithms [368]. Selection of the nearest neighbour can be done through establishing the node in the existing tree that is 'closest' to the sampled point according to the reachability-guided distance measure in Eq. 6.2. However, in a brute force approach this requires checking all the neighbours, a procedure taking $O(cN)$ time for N nodes where c is the constant finite time used for the distance computation [354]. Sub-linear nearest neighbour algorithms have been introduced [354], such as k-d trees, which are potentially able to reduce this worst-case complexity to $O(c\log(N))$, with c a constant. However, these may scale exponentially with the dimension of the workspace [354], and may be more expensive than the naive algorithm when bounding boxes must be computed around reachability sets [357]. Approximate nearest neighbour algorithms are computationally cheaper, but may limit exploration of the search space and have not been implemented with reachability-guided distance metrics.

Another option is not to select a single nearest neighbour, but instead allow the algorithm to seek connections with the k-nearest neighbours in the `Nearest` procedure, and search from these parent vertices the optimal one to branch from. The drawback of such an approach is computational overhead [297]. The k-nearest neighbours algorithm may also be used for the `Near` procedure in RRT* instead of the radius-based formulation in Eq. 6.1. To achieve asymptotic optimality, k, a positive integer, is defined as a function of the cardinality of the list of vertices V [246]. This means that Q_{near} is of the order $O(k_{RRG}\log(|V|))$, where k_{RRG} is a constant, such that the same amount of calls are made to the local steering method and collision checker [369]. Alleviating this complexity by trading asymptotic optimality for near asymptotic optimality has been proposed [369].

6.2.4 Steering function

For a non-holonomic system, computing the steering function between two states requires solving a two-point Boundary Value Problem (BVP). For many differential-constrained systems finding an optimal trajectory is not trivial and closed-form solutions are only available for specific systems [356, 357]. For example, Kinodynamic RRT* has been proposed for systems with differential constraints and preserves asymptotic optimality guarantees [357], but this is only suitable for systems with linearised dynamics. Similarly, LQR-RRT* relies on locally linearising the system's dynamics [370]. Some other works construct an approximate steering function, which inevitably lead to non-optimal solutions as the rewiring operation of RRT* cannot be directly implemented. A common approach for non-holonomic steerable needles is to first determine from which near states $\mathbf{x}_{near}$ the sampled point $\mathbf{x}_{samp}$ is reachable. Then, the control inputs $\mathbf{u} = [v_t, \kappa]^T$ are (randomly) sampled and it is establish which of these controls -when applied from a near state $\mathbf{x}_{near}$- leads to a state closest, i.e. in terms of Euclidean distance, to $\mathbf{x}_{samp}$ [89]. Opposed to random sampling, selection from a fixed set has also been suggested [371]. Jeon et al. use a shooting method in combination with a bisection algorithm to determine the control input that brings the new state in proximity of the sampled node [356]. However, this approach may also be computationally cumbersome.

The main problem when approximating the steering function arises with the rewire operation, which a vital step in RRT* in order to achieve asymptotic optimality. The discrepancy between the final state of the steering procedure executed from $\mathbf{x}_{new}$ and the near state $\mathbf{x}_{near}$ affects all child vertices of $\mathbf{x}_{near}$ which may become infeasible (Figure 6.6a). In this case, the simplest solution is to delete all the children nodes from a node $\mathbf{x}_{near}$ when a lower cost trajectory to this node is found

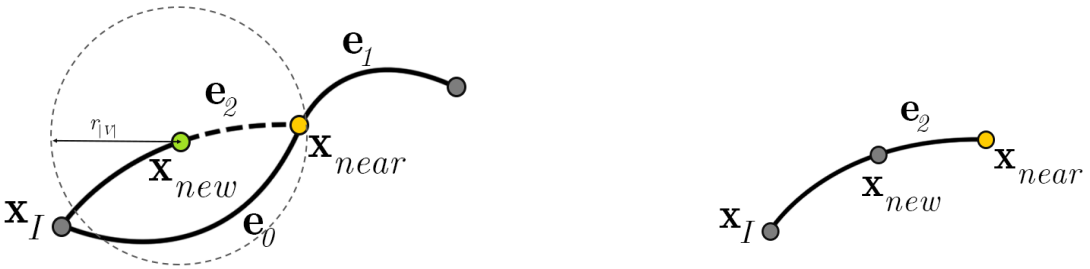

(a) $\mathbf{x}_{near}$ can be reached with a lower cost from $\mathbf{x}_{new}$ than from $\mathbf{e}_0$. When connecting $\mathbf{e}_2$, $\mathbf{e}_1$ is no longer kinematically feasible.

(b) The edge $\mathbf{e}_1$ is deleted and the tree is rewired with $\mathbf{e}_2$.

Figure 6.6: Illustration of the problem with rewiring when using an approximate steering function. Computational time is wasted by discarding previously computed feasible trajectories. Figure adapted from Ref. [372].

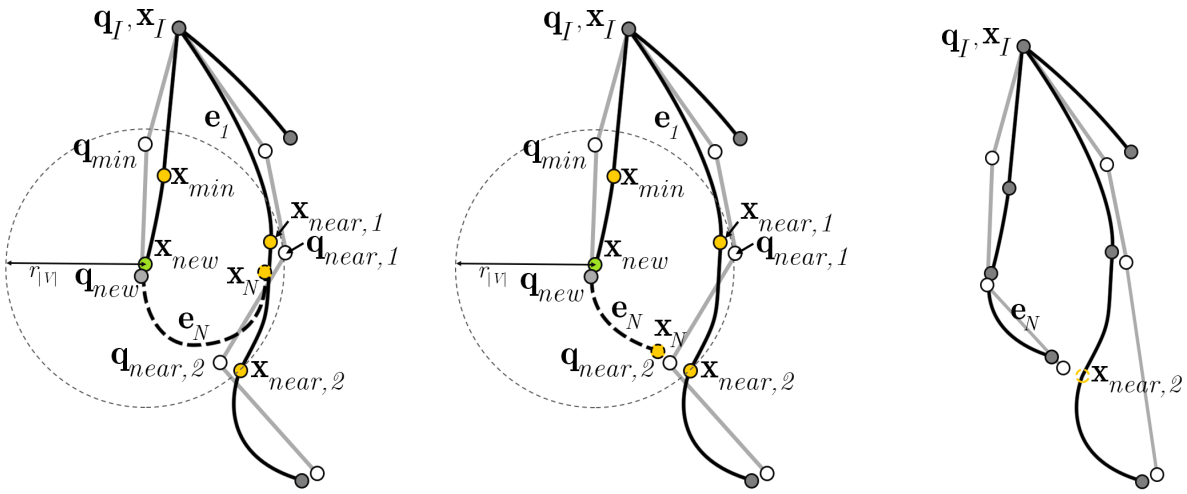

(a) Cost of $\mathbf{x}_{near,1}$ is lower than $\mathbf{x}_N$; reconnection not performed.

(b) Cost of $\mathbf{x}_N$ is lower than $\mathbf{x}_{near,2}$; reconnection is performed.

(c) Connecting the new edge and removing old node $\mathbf{x}_{near,2}$.

Figure 6.7: Illustrations of the reconnect procedure in DT-RRT. (a) The planner first tries to connect $\mathbf{q}_{new}$ and $\mathbf{q}_{near,1}$, but the accumulated cost of reaching $\mathbf{x}_{new}$ and $\mathbf{x}_N$ from $\mathbf{x}_{new}$ is higher than the cost to $\mathbf{x}_{near,1}$. The planner moves onto the next point in $\mathbf{Q}_{near}$. (b) The cost of reaching $\mathbf{x}_N$ is lower than that of $\mathbf{x}_{near,2}$ and therefore in (c) $\mathbf{x}_{near,2}$ is removed from the state tree and the workspace tree is reconnected.

(Figure 6.6b). However, by deleting all child nodes computational time is wasted. Instead, one may store the controls used for reaching these children nodes and re-propagate these when a lower cost solution to $\mathbf{x}_{near}$ is found [356]. However, this may sacrifice soundness of trajectories. In the dual-tree RRT (DT-RRT) approach by Moon et al., both a workspace and a state space tree are stored [372]. When a node $\mathbf{x}_{near}$ can be reached with lower accumulated cost, instead of deleting the children nodes and the edge connecting these, only $\mathbf{x}_{near}$ is removed from the list of vertices and the child edges and vertices are retained (Figure 6.7). It was shown that this reconnect procedure results in trajectories of higher quality at a slight increase in computational complexity. One other benefit of this approach is that trajectories are retained, which is convenient for multi-agent planning and for exploring the search space. A variant of this algorithm known as DT-RRT* uses a double-tree structure in which extension and optimisation procedures are separated [373]. However, this relies on solving BVPs via clothoid fitting.

6.2.5 Collision detection

The collision detection module plays an essential role in RRT and its variants as it allows to not establish an explicit representation of the environment (see Figure 6.1). Collision detection is one of the main computational bottlenecks in sampling-based motion planning, perhaps constituting up to 90% of the total planning time complexity [297], although its influence is traded off for nearest neighbour searching for an increasing number of samples in the search space [368]. For that reason, other strategies than naive collision checking, i.e. incremental checking at a specified interval, have been proposed to reduce the complexity. Lazy strategies, to only call upon collision detection after having established a path or trajectory, or to delay collision checking until these are likely encountered, may drastically decrease the computational time of the algorithm [374]. This type of strategies especially works well when infeasible configurations or states are not frequently encountered and when trajectory discretisation is sufficiently fine. For complex agent and environment models a two-phase strategy may be used: (i) the broad phase, where collision detection is performed using simple conservative bounding boxes, and (ii) the narrow phase, in which a more accurate representation for collision checking is required [239]. Continuous-time safety, i.e. also in between discretised time steps, may be guaranteed through swept volumes and computing the signed distance field [286]. In the narrow phase however, continuous-time collision checking requires approximately twice as many function evaluations.

To reduce the computational complexity for a single collision check, the complexity of objects such as the agent or obstacles may be reduced by computing bounding volume hierarchies (BVH). Common forms include bounding sphere, axis-aligned bounding box, oriented bounding box, convex hull and swept sphere volume methods [239, 368, 374]. These methods differ in their accuracy in reproducing the object and complexity in which collisions/intersections can be evaluated.

For systems with differential constraints, predicting whether collisions would likely occur when propagating the system after partial planning is useful. Conservative approximations of inevitable collision states (ICS), which are states that regardless of the selected control inputs end up in collision, have been used to prune trajectories in RRT [375]. However, such formulations are usually more applicable to kinodynamic planning, which include accelerations, over kinematic non-holonomic planning [371].

6.3 RRT and reconnect-tree RRT for non-holonomic systems

6.3.1 Implementation of RRT for non-holonomic systems with unicycle kinematics

In this section, a RRT variant is described that is suitable for trajectory planning of a non-holonomic unicycle model. State propagation is modelled in this RRT variant using Lie group theory on $SE(2)$, as described in Equation 4.3.4, and is similar to the work by Patil et al. on $SE(3)$ [89][1]. Extension to a higher order space, e.g. $SE(3)$, is therefore trivial. The pseudocode of this variant is shown in Algorithm 3.

Let us denote workspace points $\mathbf{p}_t$ by their Euclidean coordinates $[\mathrm{X}_t, \mathrm{Y}_t]^T$. States, $\mathbf{x}_t$, are expressed in generalised coordinates $[x_t, y_t, \theta_t]^T$. Allowed control inputs for the system are denoted

[1] Note that Patil et al. describe the state of the agent in $X_t \in SE(3)$. In this work, planning is not actually performed on $SE(2)$; i.e. the state of the agent $\mathbf{x}_t$ is described in generalised coordinates. For state propagation, (i) the state $\mathbf{x}_t$ is mapped to $SE(2)$, $X_t = \hat{\mathbf{x}}_t$, (ii) control inputs are applied for a constant duration δ and $X_{t+\delta}$ is computed, and (iii) the result is mapped back to generalised coordinates $\mathbf{x}_{t+\delta}$.

Algorithm 3: $SE(2)$-RRT for non-holonomic systems with unicycle kinematics (adapted from Ref. [89])

```
1  XV ← x_I; XE ← ∅; k ← 0;
2  for k = 1 to K do
3  |   XG ← (XV, XE);
4  |   p_samp ← Sample_free() ;
5  |   U_samp ← ∅; C_samp ← ∅; ;
6  |   for x_t ∈ XV do
7  |   |   [U_samp, C_samp] ← [U_samp, C_samp] ∪ Reachable(x_t, p_samp);
8  |   end
9  |   [u_near, x_near] ← Nearest_reachable(U_samp, XV, C_samp);
10 |   x_new ← Steer_control(u_near, x_near);
11 |   X_steps ← Intermediate_states(u_near, x_near, x_new);
12 |   if Motion_free(X_steps) then
13 |   |   XV ← XV ∪ {x_new};
14 |   |   XE ← XE ∪ X_steps;
15 |   |   if x_new ∈ X_G then
16 |   |   |   XG ← (XV, XE) ;
17 |   |   |   return XG
18 |   |   else
19 |   |   |   continue;
20 |   |   end
21 |   end
22 end
23 return failure
```

by $\mathbf{u} = [v_t, \kappa_t]^T$, with control limits $v_t \in [0, \bar{v}_t]$ and $\kappa_t = \{\mathbb{R} \mid |\kappa_t| < \bar{\kappa}, \kappa \neq 0\}$. Only a state tree $XG = (XV, XE)$ is in this algorithm constructed. First, a collision-free configuration $\mathbf{p}_{samp}$ is sampled in Euclidean space $\mathbb{R}^2$ (line 4)[2]. This sampling is performed uniformly with the procedure `Sample_free` (line 4). The only form of biasing used in this procedure is that on average in one of every hundred iterations an attempt to greedily connect the existing tree to the target point is performed, as is recommended [239]. Reachability-guided sampling could potentially speed up the search [282, 365], but is not yet used in this work. After a sample has been generated, this is followed by a conservative collision check as the orientation of the agent is not yet determined. The nearest neighbour $\mathbf{x}_{near}$ is then determined by checking whether $\mathbf{p}_{samp}$ is reachable from previous states in the graph $XG = (XV, XE)$ through the operations `Reachable` and `Nearest_reachable`. The procedure `Reachable` computes the controls $\mathbf{u} = [v_t, \kappa_t]^T$ to reach $\mathbf{p}_{samp}$ from $\mathbf{x}_{near} \in XV$, and assigns infinite costs to invalid control inputs (line 7). `Nearest_reachable` filters the nearest node based on the distance along the curve (line 9). This brute force approach results in evaluating the `Reachable` procedure $O(N)$ times per iteration. It would be more computationally efficient to for example approximate and store reachable states for each $\mathbf{x}_t \in XV$ as to limit the amount of function calls to `Reachable` [365]. This, however, relies on the existence of a simple geometric shape that could approximate the reachable region of a state.

[2] In $SE(3)$ sampling would be performed in $\mathbb{R}^3$ for workspace points $\mathbf{q}_t = [\mathrm{X}_t, \mathrm{Y}_t, \mathrm{Z}_t]^T$. The state would be denoted as $\mathbf{x}_t = [x_t, y_t, z_t, \theta_t, \phi_t, \psi_t]^T$. Control inputs are $\mathbf{u} = [v_t, \kappa_t, \tau_t]^T$

In order to compute the controls $\mathbf{u} = [v_t, \kappa_t]^T$ analytically, it may be observed that the two upper right entries in pose $X_{t+\delta}$ in Eq. 4.25 denote the positional displacements $\tilde{\mathbf{p}}_t = [\tilde{x}_t, \tilde{y}_t]^T = [\mathrm{X}_{t+\delta} - x_t, \mathrm{Y}_{t+\delta} - y_t]^T$ in $\mathbb{R}^2$ as a function of the control inputs $\mathbf{u}$. The origin of state $\mathbf{x}_t$ is defined at the needle tip which means that the displacement is given by: $\tilde{\mathbf{p}}_t = \mathbf{p}_{t+\delta}$. This yields the following analytical results (assuming all variables are real numbers):

$$\kappa_t = \frac{(2\mathrm{Y}_{t+\delta} \cdot \cos(\theta_t) - 2\mathrm{X}_{t+\delta} \cdot \sin(\theta_t))}{(\mathrm{X}_{t+\delta}^2 + \mathrm{Y}_{t+\delta}^2)}; \tag{6.5}$$

$$v_t = \frac{\big((\mathrm{X}_{t+\delta}\sin(\theta) + \mathrm{Y}_{t+\delta}\cos(\theta))(\mathrm{X}_{t+\delta}^2 + \mathrm{Y}_{t+\delta}^2)\big)}{\big(2\delta(\mathrm{Y}_{t+\delta}^2\cos(\theta)^2 - \mathrm{X}_{t+\delta}^2\sin(\theta)^2)\big)} \cdot (\tan^{-1}(\sin(2\theta) \cdot (\mathrm{Y}_{t+\delta}^2 - \mathrm{X}_{t+\delta}^2) + 2\mathrm{X}_{t+\delta}\mathrm{Y}_{t+\delta}\cos(2\theta), \\ 2\mathrm{X}_{t+\delta}\mathrm{Y}_{t+\delta}\sin(2\theta) + \cos(2\theta)(\mathrm{X}_{t+\delta} - \mathrm{Y}_{t+\delta})(\mathrm{X}_{t+\delta} + \mathrm{Y}_{t+\delta}))) \tag{6.6}$$

In the degenerate case of $\kappa = 0$, a small perturbation of $1E^{-5}$ is applied [89]. Multiplying v_t with duration δ results in an expression for the traversed distance λ_t along the tangent direction of the needle that is solely based on inputs $\mathrm{X}_{t+\delta} = p_{samp,x}$, $\mathrm{Y}_{t+\delta} = p_{samp,y}$, and the initial heading θ_t. From the states in the tree that do not require exceeding control limits to reach $\mathbf{p}_{samp}$, i.e. from which $\mathbf{p}_{samp}$ is reachable, the state $\mathbf{x}_{near}$ that uses the smallest step size λ_t is sought. Additionally, the associated control input $\mathbf{u}_{near}$ is stored.

For the steering procedure, Patil et al. sample random controls and determine which set of controls gets nearest with the Euclidean distance metric [89]. However, as this set of controls is readily available from the operator `Reachable`, these can directly be applied from $\mathbf{x}_{near}$ to obtain a new state $\mathbf{x}_{new}$ through the procedure `Steer_control`. Using sampling to obtain controls could still be a beneficial approach, which has been previously implemented by the author. In this case, defining $\mathbf{x}_{near}$ should not be done based on an Euclidean metric. Rather, another evaluation of `Reachable` and `Nearest_reachable` may be required to more accurately reflect the cost-to-go, which can become costly.

To detect whether the trajectory connecting $\mathbf{x}_{near}$ and $\mathbf{x}_{new}$ is feasible, incremental checking is performed by first discretising this trajectory through the procedure `Intermediate_states`, resulting in a set of states X_{steps} (line 11). The resolution of this discretisation is determined based on the smallest dimension of the agent. Then, collision checking is performed per state in the set X_{steps}. Although it was established that approximation of the shape of the agent and the use of a point-in-polygon (PIP) problem solver was computationally efficient for this problem, an exact polygon-polygon intersection algorithm could viably be used at the cost of a slight increase in planning time. Only if all of the states are determined to be collision-free using `Motion_free` (line 12), the state $\mathbf{x}_{new}$ is added to the list of vertices (line 13) and the edge containing all the intermediate steps to the list of edges (line 14). Although one could choose to add the intermediate states as well to the tree, when using a sufficiently small maximum step length this was not deemed necessary in this approach. In Figure 6.8 two demonstrations of RRT for non-holonomic systems in $SE(2)$ are shown (based on `MATLAB` Script A.1.13).

6.3.2 Implementation of a reconnect-tree variant of RRT for non-holonomic systems with unicycle kinematics

The standard RRT algorithm is only able to plan feasible motions, and cannot assure high-quality solutions. Asymptotically optimal sampling-based motion planning may be computationally

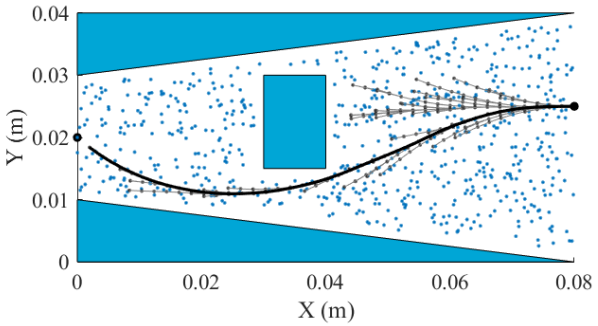

(a) RRT $SE(2)$ in a standard environment with $\bar{\kappa} = 30\ \mathrm{m}^{-1}$ and $\delta = 0.01$ s.

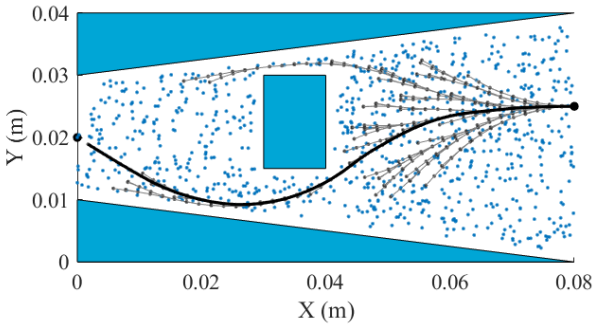

(b) RRT $SE(2)$ in a standard environment with $\bar{\kappa} = 40\ \mathrm{m}^{-1}$ and $\delta = 0.01$ s.

Figure 6.8: Illustrations of two trajectory planning solutions for a non-holonomic system with unicycle kinematics using the RRT $SE(2)$ algorithm outlined in Algorithm 3. In MATLAB Script A.1.13, the code is provided to generate these figures.

intricate for non-holonomic systems. In this work a different approach is therefore used to plan the motion of a non-holonomic system, based on the reconnect-tree procedure of DT-RRT. In DT-RRT, sampling and nearest neighbour search are performed in Euclidean space from the workspace tree [372]. Feasibility of the trajectory and kinematic and dynamic constraints are then considered using the state tree. The idea of DT-RRT to maintain two separate trees is particularly attractive for systems of which approximate steering functions are available; i.e. where the states do not directly reside with planned configurations. However, for the motion planning of systems with unicycle kinematics on $SE(2)$ or $SE(3)$ an analytic solution for reaching a sampled point from a state is available. In this work only the state graph $XG = (XV, XE)$ is retained, of which its members are data structures e.g. containing the pose, cost-to-reach, and children and parent vertices/edges. The ideas of sampling in Euclidean space and finding the nearest neighbour based on a reachability-guided search by Patil et al. [89, 367], establishing the minimum-cost trajectory from a set of near states in RRT* [354], and the reconnect-tree procedure from DT-RRT [372], are therefore leveraged in this work. The pseudocode of this algorithm is given in Algorithm 4.

First, similar to the RRT variant previously described for non-holonomic systems, a point $\mathbf{p}_{samp}$ is sampled in Euclidean space $\mathbb{R}^2$ (line 4), and the nearest reachable state $\mathbf{x}_{nearest}$ is determined based on the reachable distance metric (lines 5-9). Then, the system is steered towards $\mathbf{x}_{nearest}$ such that state $\mathbf{x}_{new}$ is obtained (line 10). The connection between $\mathbf{x}_{nearest}$ and $\mathbf{x}_{new}$ is not necessarily that of minimum cost. The cost functional $f(\cdot)$ proposed for this type of algorithm is a linear user-weighted additive function, $f(\mathbf{u}_t^i, \mathbf{x}_t^i) = \sum_{l=1}^{n_c} \left[\alpha_l \cdot f_l(\mathbf{u}_t^i, \mathbf{x}_t^i, \mathcal{E}^i)\right]$, which is composed of components for trajectory length and curvature and is constructed using Eq. 6.4:

$$f(\mathbf{u}_t^i, \mathbf{x}_t^i) = \alpha_D \cdot \delta v_t^i + \alpha_\kappa \cdot \delta \kappa_t^i \tag{6.7}$$

Length and curvature both act to minimise the control effort of the non-holonomic system. In order to assure asymptotic convergence towards the optimum cost, the cost function must first be monotonic [354]. Let us denote the concatenation of two trajectories $\tilde{x}_1$ and $\tilde{x}_2$ as $\tilde{x}_1 \mid \tilde{x}_2$ [262]. For monotonicity it must be shown that $C(\tilde{x}_1) \leq C(\tilde{x}_1 \mid \tilde{x}_2)$. Although weights $\alpha_D, \alpha_\kappa \geq 0$ and parameters $\delta, v_t^i \geq 0$, the curvature κ_t, however, is not non-negative and hence $f(\mathbf{u}_t^i, \mathbf{x}_t^i) \geq 0$ is not monotonic. Moreover, the cost must be Lipschitz continuous, which is shown for a similar cost function formulation by Luders et al. [262]. However, Lipschitz continuity is not assured for κ_t which is modelled as a piecewise function to avoid degenerate case of $\kappa_t = 0$. Therefore, the cost

Algorithm 4: Reconnect-tree RRT for non-holonomic systems with unicycle kinematics

$XV \leftarrow \mathbf{x}_I$; $XE \leftarrow \emptyset$; $k \leftarrow 0$;
for $k = 1$ **to** K **do**
  $XG \leftarrow (XV, XE)$;
  $\mathbf{p}_{samp} \leftarrow$ `Sample_free()` ;
  $U_{samp} \leftarrow \emptyset$; $C_{samp} \leftarrow \emptyset$; ;
  for $\mathbf{x}_t \in XV$ **do**
    $[U_{samp}, C_{samp}] \leftarrow [U_{samp}, C_{samp}] \cup$ `Reachable`$(\mathbf{x}_t, \mathbf{p}_{samp})$;
  end
  $[\mathbf{u}_{nearest}, \mathbf{x}_{nearest}] \leftarrow$ `Nearest_reachable`(U_{samp}, XV, C_{samp});
  $\mathbf{x}_{new} \leftarrow$ `Steer_control`$(\mathbf{u}_{nearest}, \mathbf{x}_{nearest})$;
  $X_{steps} \leftarrow$ `Intermediate_states`$(\mathbf{u}_{nearest}, \mathbf{x}_{nearest}, \mathbf{x}_{new})$;
  if `Motion_free`(X_{steps}) **then**
    $\mathbf{x}_{min} \leftarrow \mathbf{x}_{nearest}$;
    $X_{min,steps} \leftarrow X_{steps}$;
    $X_{near} \leftarrow$ `Near`$(XG, \mathbf{x}_{new}, |XV|)$;
    for all $\mathbf{x}_{near} \in X_{near}$ **do**
      $[\mathbf{u}_{near}, c_{near}] \leftarrow$ `Reachable`$(\mathbf{x}_{near}, \mathbf{x}^*_{new})$;
      $\mathbf{x}_{new,cand} \leftarrow$ `Steer_to_state`$(\mathbf{u}_{near}, \mathbf{x}_{near})$;
      $C' \leftarrow$ `Cost`$(\mathbf{x}_{near})+c_{near}$;
      if $C' <$ `Cost`$(\mathbf{x}_{new})$ **then**
        $X_{near,steps} \leftarrow$ `Intermediate_states`$(\mathbf{u}_{near}, \mathbf{x}_{near}, \mathbf{x}_{new,cand})$;
        if `Motion_free`$(X_{near,steps})$ **then**
          $\mathbf{x}_{min} \leftarrow \mathbf{x}_{near}$; $\mathbf{x}_{new} \leftarrow \mathbf{x}_{new,cand}$;
          $X_{min,steps} \leftarrow X_{near,steps}$;
        end
      end
    end
    $XV \leftarrow XV \cup \{\mathbf{x}_{new}\}$;
    $XE \leftarrow XE \cup X_{min,steps}$;
    for all $\mathbf{x}_{near} \in X_{near} \setminus \{\mathbf{x}_{min}\}$ **do**
      $[\mathbf{u}_{new}, c_{new}] \leftarrow$ `Reachable`$(\mathbf{x}_{new}, \mathbf{x}^*_{near})$;
      $\mathbf{x}_{new,near} \leftarrow$ `Steer_to_state`$(\mathbf{u}_{new}, \mathbf{x}_{new})$;
      $C'' \leftarrow$ `Cost`$(\mathbf{x}_{new})+c_{new}$;
      if $C'' <$ `Cost`$(\mathbf{x}_{near})$ **then**
        $X_{new,steps} \leftarrow$ `Intermediate_states`$(\mathbf{u}_{new}, \mathbf{x}_{new}, \mathbf{x}_{near})$;
        if `Motion_free`$(X_{new,steps})$ **then**
          $\mathbf{x}_{parent} \leftarrow$ `Parent`$(\mathbf{x}_{near})$; $X_{children} \leftarrow$ `Child`$(\mathbf{x}_{near})$;
          `Parent`$(X_{children}) \leftarrow \mathbf{x}_{parent}$;
          $XV \leftarrow XV \setminus \{\mathbf{x}_{near}\} \cup \{\mathbf{x}_{new,near}\}$;
          $XE \leftarrow XE \cup X_{new,steps}$;
        end
      end
    end
  end
end

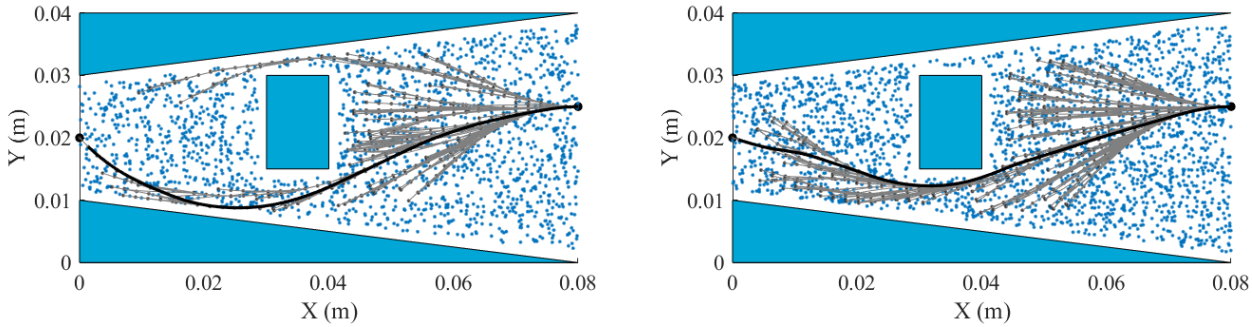

(a) $SE(2)$ reconnect-tree RRT variant in a standard environment with $K = 3{,}000$, $\kappa = 40$ m^{-1} and $\delta = 0.01$ s.

(b) $SE(2)$ reconnect-tree variant in a standard environment with $K = 4000$, $\kappa = 40$ m^{-1} and $\delta = 0.01$ s.

Figure 6.9: Illustrations of two trajectory planning solutions for a non-holonomic system with unicycle kinematics using the DT-RRT variant outlined in Algorithm 4. In MATLAB Script A.1.14, the code is provided to generate these figures.

function in Eq. 6.7 is not well-behaved, and only the trajectory length is at this stage included in the per-time step cost metric. If the trajectory between $\mathbf{x}_{nearest}$ and $\mathbf{x}_{new}$ as discretised in X_{steps} is feasible, the minimum-cost trajectory to $\mathbf{x}_{new}$ is sought from existing nodes in the tree $\mathbf{X}_{near}$ (lines 16-27). First, the set of nearest nodes X_{near} is determined through the use of Eq. 6.1 (line 15). From all states in this set, the procedure `Reachable` is used to determine the controls and cost to reach the candidate new state $\mathbf{x}_{new,cand}$ (line 17). The asterisk (*) is used here to mark the conversion of the state $\mathbf{x}$ to a point in Euclidean space $\mathbf{p}$. These controls are then used in the steering procedure `Steer_to_state` (line 18), which contrary to `Steer_control` is not limited by the maximum step size allowed. $\mathbf{x}_{new,cand}$ has the same coordinates in Euclidean space as $\mathbf{x}_{new}$, but a different pose. When the cost of reaching $\mathbf{x}_{new,cand}$ is lower than the current cost of reaching $\mathbf{x}_{new}$, and this new trajectory is feasible, the candidate state is set as the current state $\mathbf{x}_{new,cand} = \mathbf{x}_{new}$. This procedure is repeated for all states in the set X_{near}.

The procedure to reconnect the tree upon having established a new state in this thesis is based on the reconnect-tree scheme in DT-RRT [372], which is a variant of the rewire-procedure in RRT*. First, the controls and cost-to-reach are computed for all the trajectories between the newly generated state $\mathbf{x}_{new}$ and remaining states in its neighbourhood $\mathbf{x}_{near} \in X_{near} \setminus \{\mathbf{x}_{min}\}$ (line 31). The system is then steered towards $\mathbf{x}_{new}$ and the new pose $\mathbf{x}_{new,near}$ is obtained. If the cost to reach $\mathbf{x}_{new,near}$ from $\mathbf{x}_{new}$ is lower than the current cost of $\mathbf{x}_{near}$ and the trajectory is feasible, then the parent and possible children states of $\mathbf{x}_{near}$ are determined (line 37). If applicable, the parent of the children state(s) is changed to $\mathbf{x}_{parent}$ and the node $\mathbf{x}_{near}$ is replaced by $\mathbf{x}_{new,near}$ in the list of states. Lastly, the trajectory between $\mathbf{x}_{new}$ and $\mathbf{x}_{new,near}$ is added to the list of edges. In this approach, the trajectory between $\mathbf{x}_{new}$ and $\mathbf{x}_{near}$ is not deleted and children states are retained even when a trajectory of lower cost is found, similar to DT-RRT [372]. In Figure 6.9 this RRT variant is illustrated for a non-holonomic system with unicycle kinematics in a standard environment (based on MATLAB Script A.1.14).

6.4 Bounded uncertainty RRT

Bounded uncertainty RRT, BU-RRT*, is an asymptotically optimal sampling-based planner which can guarantee absolute feasibility for systems with linear dynamics subject to bounded noise, uncertainty in configuration knowledge, and/or environment knowledge [259]. This algorithm was shown to be probabilistically complete under mild assumptions. Through the use of

trajectory-wise constraint checking, BU-RRT* is able to plan trajectories in real time with similar complexity to the conventional RRT algorithm. The formulation here is analogous to the framework presented in Section 4.3 and a heavy simplification of the work by Luders and How [259]. Only uncertainty in environmental knowledge is considered. In this case, the bounded uncertainty formulation by Luders and How boils down to expanding obstacles with the bounded uncertainty through the Minkowski sum $\mathcal{X}_j \oplus S_j$ [259]. Nevertheless, the bounded uncertainty framework is still briefly introduced here as it allows for incorporating different uncertainty sources if desired for future work. Obstacles of known geometry with a bounded uncertain placement can be expressed as:

$$\mathcal{X}_j = \mathcal{X}_{j,0} + \mathbf{c}_j \qquad \forall j \in \mathbb{Z}_{1,n_o} \tag{6.8a}$$

$$\mathbf{c}_j \in S_j \qquad \forall j \in \mathbb{Z}_{1,n_o} \tag{6.8b}$$

Here, S_j is a convex polytopic set which is a conjunction of linear inequalities: $S_j = \{\mathbf{c}_j \mid E_j\mathbf{c}_j \leq \mathbf{f}_j\}$[3]. It has been previously shown (Eq. 4.15) that these obstacle collision avoidance constraints can equivalently be formulated via the following disjunction:

$$\bigvee_{k=1}^{n_j} \mathbf{a}_{jk}^T \mathbf{x}_t^i \geq \mathbf{a}_{jk}^T \mathbf{C}_{jk} + r \qquad \forall t \in \mathbb{Z}_{0,T}, \forall j \in \mathbb{Z}_{1,n_o}, \forall i \in \mathbb{Z}_{1,n_x} \tag{6.9}$$

Here, $\mathbf{C}_{jk} = \hat{\mathbf{c}}_{jk} + \mathbf{c}_j$, with $\hat{\mathbf{c}}_{jk}$ a point on the kth constraint line of the jth obstacle, $\mathbf{c}_j \in S$ the bounded displacement, and r the radius of the agent. To assure robust feasibility, for each individual collision avoidance constraint with bounded uncertainty it satisfies to take the tightest possible bound on the uncertainty. Introducing the deterministic tightening parameter, $\eta_j^c = \max_{\mathbf{c}_j \in S_j}(\mathbf{a}_{jk}^T \mathbf{c}_j)$, one may establish:

$$\bigvee_{k=1}^{n_j} \max\left(\mathbf{a}_{jk}^T \mathbf{C}_{jk} + r\right) = \bigvee_{k=1}^{n_j} \mathbf{a}_{jk}^T \hat{\mathbf{c}}_{jk} + r + \max\left(\mathbf{a}_{jk}^T \mathbf{c}_j\right) = \bigvee_{k=1}^{n_j} \mathbf{a}_{jk}^T \hat{\mathbf{c}}_{jk} + r + \eta_j^c \tag{6.10}$$

As this tightening is time and control input invariant, the constraint tightening parameter η_j^c can be offline, i.e. a priori, computed. A similar strategy would be used to include uncertainty from other sources. For example, one could include state and time-independent uncertainty in configuration knowledge by denoting the agent's position as $\mathbf{x}_t^i = \hat{\mathbf{x}}_t^i + \tilde{\mathbf{x}}_0^i$, where $\tilde{\mathbf{x}}_0^i \in S_x$. Next, the deterministic tightening parameter becomes: $\eta_j^x = \min_{\tilde{\mathbf{x}}_0^i \in S_x} \mathbf{a}_{jk}^T \tilde{\mathbf{x}}_0^i$, which is in this case subtracted on the right hand side from Eq. 6.9. Including state-dependent uncertainty sources for the non-linear non-holonomic system in this formulation requires linearisation of the system's kinodynamics for predicting the propagation of uncertainty. The robust collision avoidance constraints for a problem with only bounded uncertainty in environmental knowledge can be described as one of the following equivalent relations:

$$\mathbf{x}_t^i \notin \mathcal{X}_j \iff \neg(A_j \mathbf{x}_t^i \leq \mathbf{b}_j) \iff \bigvee_{k=1}^{n_j} \mathbf{a}_{jk}^T \mathbf{x}_t^i \geq \mathbf{a}_{jk}^T \hat{\mathbf{c}}_{jk} + r + \eta_j^c \tag{6.11}$$

To enforce the robustness constraints, BU-RRT* checks a generated sequence between two states for feasibility via the procedure `Robustly_feasible` [259]. Algorithm 4 therefore only requires slight modifications to lines 12, 22 and 36 for implementation with bounded uncertainty to check whether the generated intermediate states X_{steps} are robustly feasible.

[3] If the bounded uncertainty set is non-convex, as long as this set can be written as the union of polytopic sets it can still be used [259].

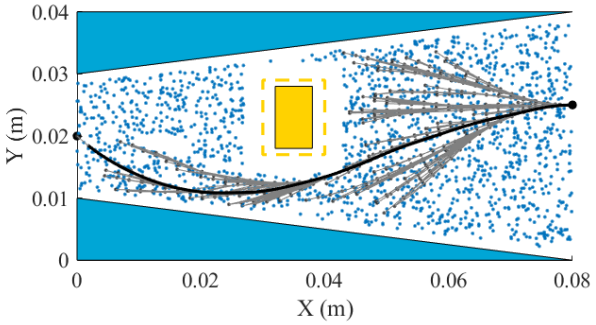

(a) Bounded uncertainty $SE(2)$ reconnect-tree RRT variant in a standard environment with $K = 3{,}000$, $\kappa = 40$ m^{-1}, and $\delta = 0.01$ s.

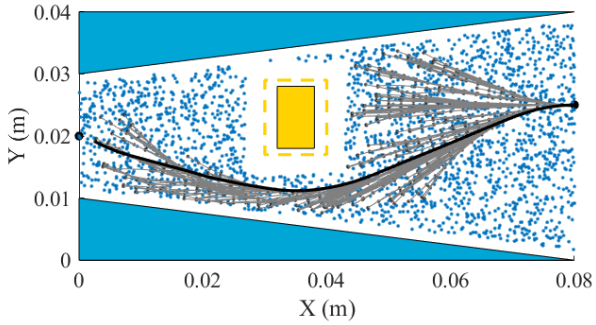

(b) Bounded uncertainty $SE(2)$ reconnect-tree RRT variant in a standard environment with $K = 4000$, $\kappa = 40$ m^{-1}, and $\delta = 0.01$ s.

Figure 6.10: Illustrations of two trajectory planning solutions for a non-holonomic system with unicycle kinematics where one obstacle has bounded position uncertainty. In MATLAB Script A.1.15, the code is provided to generate these figures.

Consider the scenario where the agent is rectangular-shaped ($w = 2.5$ mm and $L = 5$ mm) and must avoid collision with an uncertain obstacle that has a bounded displacement. A conservative bounding sphere with $r = 3$ mm is therefore constructed around the agent and orientations of the agent are neglected. The obstacle in the centre of the workspace is defined through the following set of (deterministic) parameters:

$$A_1 = \begin{bmatrix} 1 & 0 \\ -1 & 0 \\ 0 & 1 \\ 0 & -1 \end{bmatrix}, \quad \hat{\mathbf{b}}_1 = \begin{bmatrix} 38 \\ -32 \\ 28 \\ -18 \end{bmatrix} \text{ mm}, \quad \hat{\mathbf{c}}_{11} = \begin{bmatrix} 38 \\ 18 \end{bmatrix}^T, \hat{\mathbf{c}}_{12} = \begin{bmatrix} 32 \\ 28 \end{bmatrix}^T, \hat{\mathbf{c}}_{13} = \begin{bmatrix} 32 \\ 28 \end{bmatrix}^T, \hat{\mathbf{c}}_{14} = \begin{bmatrix} 38 \\ 18 \end{bmatrix}^T \text{ mm}$$

Moreover, this obstacle has a positional uncertainty which is captured by:

$$E_1 = \begin{bmatrix} 1 & 0 \\ -1 & 0 \\ 0 & 1 \\ 0 & -1 \end{bmatrix}, \quad \mathbf{f}_1 = \begin{bmatrix} 2 \\ 2 \\ 1 \\ 1 \end{bmatrix} \text{ mm}$$

In the worst case, the displacement $\mathbf{c}_1$ is equal to $[-2,-1]^T$, $[-2,1]^T$, $[2,-1]^T$ or $[2,-1]^T$ mm, in which case η_1^c is equal to $\mathbf{f}_1$. To account for obstacles with bounded uncertainty the dual-tree inspired RRT variant is slightly modified and implemented in MATLAB Script A.1.15. Figure 6.10a and 6.10b show the lowest cost trajectory returned by this algorithm for the non-holonomic system with unicycle kinematics. The objective function in this example is solely based on minimising the trajectory length.

6.5 Analytical chance constrained RRT

Characterising the uncertainty in a probabilistic approach may have several advantages over a set-bounded approach. Foremost, the specification of the probability of constraint violation allows the user to trade conservatism of the motion planning algorithm against a conflicting measure of performance or feasibility of the generated trajectories. One convenient way of capturing this relation is through the use of chance constraints [258]. These chance constraints directly specify the allowed probability of constraint violation. Chance constrained programming has been commonly applied to robust model predictive control (MPC) [376]. Chance constraints may be

joint, i.e. spanning over a larger planning horizon, or individual [376]. Unfortunately, the evaluation of joint chance constraints requires the computation of an integral over a known multivariate (Gaussian) distribution [264]. Two ways of handling joint chance constraints are: (i) analytical methods, such as ellipsoidal relaxation, or techniques revolving around Boole's inequality, or (ii) sampling methods, such as the scenario approach, convex bounding method, mixed-integer linear programming [376, 377]. Sampling techniques only approximate the chance constraints or the underlying probability distribution and can therefore never give guarantees on the feasibility [264]. Moreover, these methods are typically overly conservative and have a moderate computational complexity [377]. Instead, analytical methods can give (probabilistic) soundness guarantees at low computational cost. However, these methods also typically introduce conservativeness and are only applicable under mild restrictions, such as the assumption that the probability distributions are Gaussian. An approach that only introduces minor over-conservativeness and has a low computational complexity has been introduced by Blackmore et al. for MPC [264]. This work proposes to decompose joint chance constraints into a sequence of individual chance constraints, which can be evaluated accurately as univariate probability distributions, and to upper bound these using Boole's inequality. Then, the resulting linear chance constraints may be exactly converted to deterministic constraints, which can be used in a motion planning algorithm. Blackmore's chance constraint formulation has been extended to RRT and to include both time-step-wise and path-wise chance constraints by Luders et al. [258]. Chance constrained RRT, known as CC-RRT, and its asymptotically optimal variant CC-RRT*, have both shown to be capable of producing probabilistically feasible paths in real-time, under the assumption of Gaussian uncertainty [258, 262]. This framework is simplified and introduced for a non-holonomic system with uncertainty in environment knowledge only.

In this thesis, in a probabilistic uncertainty scenario the obstacles are modelled as convex polytopic sets with uncertain translation following a Gaussian distribution:

$$\mathcal{X}_j = \mathcal{X}_{j,0} + \mathbf{c}_j \qquad \forall j \in \mathbb{Z}_{1,n_o} \tag{6.12a}$$

$$\mathbf{c}_j \sim \mathcal{N}(0, P_{c_j}) \qquad \forall j \in \mathbb{Z}_{1,n_o} \tag{6.12b}$$

Consider the desire to limit the probability of collision with any of the obstacles of the entire sequence of states to at most Δ, i.e. $\mathbb{P}(\mathbf{x}_t^i \notin \mathcal{X}_j) \geq 1 - \Delta$. Then via Boole's bound it can be shown that it is sufficient to limit the probability of each collision event O_j to Δ/n_o, where n_o is the amount of obstacles [276]:

$$\mathbb{P}(\text{collision}) = \mathbb{P}(O_1 \cup O_2 \cup \dots O_{n_o}) \leq \sum_{j=1}^{n_o} (\mathbb{P}(O_j)) = \sum_{j=1}^{n_o} (\Delta/n_o) = \Delta \tag{6.13}$$

Regarding the linear collision constraints for defining an obstacle region $\mathcal{X}_j$ in Eq. 4.6, a collision only occurs when all linear inequalities in the conjunction are satisfied. Therefore, the probability of a collision for the jth obstacle can be written as [258]:

$$\mathbb{P}(O_j) = \mathbb{P}\left(\bigwedge_{k=1}^{n_j} \mathbf{a}_{jk}^T \left(\mathbf{x}_t^i - \mathbf{C}_{jk}\right) - r < 0\right) \leq \mathbb{P}\left(\mathbf{a}_{jk}^T \left(\mathbf{x}_t^i - \mathbf{C}_{jk}\right) - r < 0\right) \tag{6.14}$$

The right hand side of this equation provides an upper bound on the probability of collision which reflects that for any two events A and B, the probability of both occurring is always less than or equal to the individual probabilities: $\mathbb{P}(A \wedge B) \leq \mathbb{P}(A)$, $\mathbb{P}(A \wedge B) \leq \mathbb{P}(B)$ [264]. To ensure that no collision occurs with a particular obstacle, it is sufficient to guarantee that the constraint violation for one of the linear constraints of that obstacle is less than or equal to the probability Δ/n_o:

$$\bigvee_{k=1}^{n_j} \mathbb{P}\left(\mathbf{a}_{jk}^T\left(\mathbf{x}_t^i - \mathbf{C}_{jk}\right) - r < 0\right) \leq \Delta / n_o \tag{6.15}$$

Now assuming that $\mathbf{C}_{jk}$ follows a Gaussian distribution, this probabilistic chance constraint may be converted into a tightened deterministic constraint. Blackmore et al. therefore consider a change of variable to the single-variate random variable V [264]. This variable V represents the distance between the agent and the obstacle and can therefore for this work be computed as follows [258]:

$$V = \mathbf{a}_{jk}^T\left(\mathbf{x}_t^i - \mathbf{C}_{jk}\right) - r \tag{6.16}$$

Where,

$$\hat{v} = \mathbb{E}[V] = \mathbf{a}_{jk}^T\left(\mathbf{x}_t^i - \hat{\mathbf{C}}_{jk}\right) - r = \mathbf{a}_{jk}^T\left(\mathbf{x}_t^i - \hat{\mathbf{c}}_{jk}\right) - r \tag{6.17a}$$

$$\begin{aligned} P_v &= \sqrt{(\mathbb{E}[(V-\hat{v})(V-\hat{v})^T])} = \sqrt{\left(\mathbb{E}\left[(\mathbf{a}_{jk}^T(\mathbf{C}_{jk} - \hat{\mathbf{c}}_{jk}))(\mathbf{a}_{jk}^T(\mathbf{C}_{jk} - \hat{\mathbf{c}}_{jk}))^T\right]\right)} \\ &= \sqrt{\left(\mathbf{a}_{jk}^T\left(\mathbb{E}\left[(\mathbf{C}_{jk} - \mathbb{E}[\mathbf{C}_{jk}])(\mathbf{C}_{jk} - \mathbb{E}[\mathbf{C}_{jk}])^T\right]\right)\mathbf{a}_{jk}\right)} = \sqrt{\left(\mathbf{a}_{jk}^T P_{c_j}\mathbf{a}_{jk}\right)} \end{aligned} \tag{6.17b}$$

Note that uncertainty in the state knowledge can easily be incorporated in this formulation by considering that $\mathbf{x}_t^i$ follows a Gaussian distribution as well. The chance constraint in Eq. 6.15 is therefore equivalent to the chance constraint $\bigvee_{k=1}^{n_j} \mathbb{P}(V < 0) \leq \Delta / n_o$ and can be converted to the following equivalent deterministic constraint [264]:

$$\bigvee_{k=1}^{n_j} \mathbb{P}(V < 0) \leq \Delta / n_o \iff \hat{v} \geq \sqrt{2} P_v \operatorname{erf}^{-1}(1 - 2\Delta / n_o) \tag{6.18}$$

For a more elaborate description see the work by Luders et al. [258]. The constraint in Eq. 6.15 is then probabilistically satisfied if the following constraint holds true:

$$\bigvee_{k=1}^{n_j} \mathbf{a}_{jk}^T\left(\mathbf{x}_t^i - \hat{\mathbf{C}}_{jk}\right) - r \geq \bar{b}_{kj} \equiv \sqrt{2} P_v \operatorname{erf}^{-1}(1 - 2\Delta / n_o) \tag{6.19}$$

Here, erf^{-1} is the inverse error function. The variable $\bar{b}_{kj}$ represents the amount of deterministic constraint tightening such that probabilistic feasibility is attained [258]. This constant can be a priori computed and provides an upper bound to the collision probability for all obstacles.

However, using sampling-based approaches a more accurate, i.e. less conservative, bound can be computed online for each time step and the joint trajectory by, instead of allocating a fixed amount of risk for each chance constraint, using a risk allocation technique for each constraint [258]. Luders et al. have shown that the probability of constraint satisfaction for the kth chance constraint of the jth obstacle using the left hand side of Eq. 6.14 and the described change of variable can be formulated as:

$$\Delta_{jkt} = \frac{1}{2}\left(1 - \operatorname{erf}\left[\frac{\mathbf{a}_{jk}^T\left(\mathbf{x}_t^i - \hat{\mathbf{c}}_{jk}\right) - r}{\sqrt{2\mathbf{a}_{jk}^T P_{c_j}\mathbf{a}_{jk}}}\right]\right) \tag{6.20}$$

Proceeding analogous to the formulation by Luders and colleagues, only the most stringent constraint of the set of linear constraints for an obstacle has to be considered to upper bound the probability of collision (right hand side of Eq. 6.14) [258]:

$$\mathbb{P}(O_j) \leq \Delta_{jt} = \min_{j \in \mathbb{Z}_{1,n_o}} \Delta_{jkt} \tag{6.21}$$

Now considering all obstacles, it follows from Boole's inequality that for time step t the probability of collision can be bounded as follows:

$$\mathbb{P}(\text{collision}) \leq \sum_{j=1}^{n_o} (\min_{j \in \mathbb{Z}_{1,n_o}} \Delta_{jkt}) = \Delta_t \tag{6.22}$$

Here, Δ_t is an individual constraint value which provides an upper bound to the likelihood of collision at a certain time step. Additionally, the joint chance constraint for the entire trajectory can simply be found by summing the individual constraints over time:

$$\Delta = \sum_{t=0}^{t_N} \Delta_t \tag{6.23}$$

The constraints in Eq. 6.22 and 6.23 can be limited by user-specified risk parameters ψ_s and ψ_p respectively as follows:

$$\begin{cases} \Delta_t & \leq 1 - \psi_s & \text{stepwise probabilistic feasibility constraint} \\ \Delta & \leq 1 - \psi_p & \text{trajectory-wise probabilistic feasibility constraint} \end{cases} \tag{6.24}$$

The extension from RRT to chance constrained RRT variants including probabilistic feasibility checking is straightforward. Only lines 12, 22 and 36 of the pseudocode in Algorithm 4 need to be modified. The procedure `Motion_free` is modified to include probabilistic feasibility checking by evaluating the constraints in Eq. 6.24. Rather than pre-computing these constraints offline as is possible for the fixed bound in Eq. 6.19, the computation of these chance constraints must be performed online. The cost function for the ith agent may next to path duration include the accumulated probability of collision as follows:

$$f(\mathbf{u}_t^i, \mathbf{x}_t^i) = \alpha_D \cdot \delta v_t^i + \alpha_\Delta \cdot \delta \Delta_t^i \tag{6.25}$$

This type of function was shown to be admissible for asymptotically optimal motion planners, as it is monotonic, additive and Lipschitz continuous [262]. A similar scenario as used to introduce the bounded uncertainty RRT variant has been created to illustrate chance constrained trajectory planning for a non-holonomic agent using a variant of CC-RRT. The central obstacle's positional uncertainty can now be described through the covariance matrix:

$$P_{c_1} = \begin{bmatrix} 4 & 0 \\ 0 & 1 \end{bmatrix} \text{ mm}^2$$

In `MATLAB` Script A.1.16 the code to generate probabilistically feasible trajectories with the dual-tree inspired RRT variant is given. Two solutions that are returned by this script for different risk parameters are shown in Figure 6.11a and 6.11b.

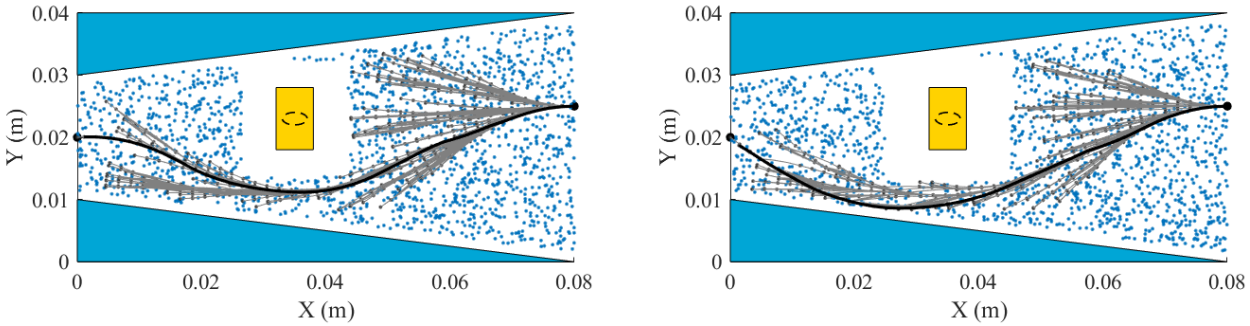

(a) Chance constrained $SE(2)$ reconnect-tree RRT variant in a standard environment with $K = 3{,}000$, $\kappa = 40$ m^{-1}, $\delta = 0.01$ s, $\psi_s = 0.8$ and $\psi_p = 0.6$.

(b) Chance constrained $SE(2)$ reconnect-tree RRT variant in a standard environment with $K = 3{,}000$, $\kappa = 40$ m^{-1}, $\delta = 0.01$ s, $\psi_s = 0.98$ and $\psi_p = 0.8$.

Figure 6.11: Illustrations of two trajectory planning solutions for a non-holonomic system with unicycle kinematics where one obstacle has Gaussian position uncertainty. In `MATLAB` Script A.1.16, the code is provided to generate these figures.

7. Robust brachytherapy needle channel planning

7.1 Inverse dose planning

The primary objective of this thesis is to generate robust needle channel solutions which ensure that dose constraints are obeyed despite geometric variations of OARs. A two-stage approach is proposed for the robust planning of needle channels for cervical cancer BT applicators. In Chapter 4, the target coverage planning problem (Problem 1.A) and bounded and probabilistic uncertainty needle channel planning problem (Problems 2.A and 2.B) have been formulated. For solving these problems, variants of the NPIP algorithm (under the header 'Initial and target considerations'), BU-RRT (Section 6.4), and CC-RRT (Section 6.5) have been introduced respectively. These solutions, however, simplify the main objective of this thesis by considering fixed dwell times. In order to evaluate whether the generated interstitial dwell segments and intracavitary channels present viable dwell positions for meeting the dose objectives, a dose optimisation method is required which is described in this section.

7.1.1 Dose-based treatment optimisation

In dose-based optimisation a dose interval is prescribed to dose calculation points of each tissue type and penalty costs are associated to exceeding this interval. Dose-based optimisation is therefore different from dose-volume based optimisation where DVH statistics are used to assess the quality of treatment plans. Although dose-volume based optimisation uses more clinically relevant constraints, this is more computationally intricate [105], and not appropriate for the two-dimensional simulation considered in this thesis. A common model used for dose-based optimisation in treatment planning is Inverse Planning by Simulated Annealing (IPSA), which has been converted to a linear programming (LP) problem by Alterovitz et al. [378]. This is the algorithm used for treatment planning in this thesis due to this convenience. This algorithm revolves around the assumption that the penalty cost function can be described by a piecewise linear function (see Figure 7.1). This penalty at a dose calculation point p_d belonging to anatomical structure a can then be represented by:

$$w_{ap_d} = \begin{cases} -M_a^{\min}(d_{ap_d} - d_s^{\min}) & \text{if } d_{ap_d} \leq d_a^{\min} \\ M_a^{\max}(d_{ap_d} - d_a^{\max}) & \text{if } d_{ap_d} \geq d_a^{\max} \\ 0 & \text{if } d_a^{\min} < d_{ap_d} d_a^{\max} \end{cases} \tag{7.1}$$

Here, d_{ap_d} is the total dose to the calculation point per fraction (calculated from summing the dose rates in Eq. 1.5 multiplied with dwell time), dose constraints $d_a^{\min}$ and $d_a^{\max}$, and penalty weights $M_a^{\min}$ and $M_a^{\max}$. However, this composite function is non-linear. To obtain a linear program, these penalty functions can be cast in the following linear constraints:

$$\begin{cases} c_{ap_d} \geq -M_a^{\min}(d_{ap_d} - d_a^{\min}) \\ c_{ap_d} \geq M_a^{\max}(d_{ap_d} - d_a^{\max}) \\ c_{ap_d} \geq 0 \end{cases} \tag{7.2}$$

The goal of the dose optimisation is to minimise the sum of all the penalty costs, weighted by the number of dose calculation points m_a in the structure a. The mathematical formulation of this linear dose optimisation problem is then the following [378]:

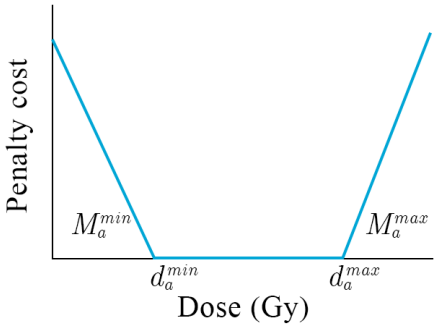

Figure 7.1: Linear penalty function as typically used for dose-based optimisation. Figure adapted from Ref. [105].

Problem (0.A): Linear dose optimisation problem

$$\min_{c_{ap_d},\, t_{z_p^i}} \quad \sum_{a=1}^{n_a} \sum_{p_d=1}^{m_a} \frac{c_{ap_d}}{m_a} \tag{7.3a}$$

$$\text{s.t.} \quad c_{ap_d} + \sum_{i=1}^{n_x} \sum_{z_p^i=1}^{n_d^i} M_a^{\min} \dot{d}_{z_p}^{\,i}(p_d) \cdot t_{z_p^i} \geq M_a^{\min} d_a^{\min} \quad \forall a \in \mathbb{Z}_{1,n_a},\ p_d \in \mathbb{Z}_{1,m_a} \tag{7.3b}$$

$$c_{ap_d} - \sum_{i=1}^{n_x} \sum_{z_p^i=1}^{n_d^i} M_a^{\max} \dot{d}_{z_p}^{\,i}(p_d) \cdot t_{z_p^i} \geq -M_a^{\max} d_a^{\max} \quad \forall a \in \mathbb{Z}_{1,n_a},\ p_d \in \mathbb{Z}_{1,m_a} \tag{7.3c}$$

$$c_{ap_d} \geq 0 \quad \forall a \in \mathbb{Z}_{1,n_a},\ p_d \in \mathbb{Z}_{1,m_a} \tag{7.3d}$$

$$t_{z_p^i} \geq 0 \quad \forall z_p^i \in \mathbb{Z}_{1,n_d^i} \tag{7.3e}$$

To restrict the dwell time differences between two adjacent dwell positions, one could opt for incorporating dwell time modulation restriction (DTMR). However, DTMR was shown to not be beneficial in the treatment optimisation of some prostate cancer patients [379]. For an overview of alternative dose optimisation models for HDR brachytherapy the reader is referred to De Boeck et al. [257].

7.1.2 Dose parameter estimation

In the inverse planning algorithm as described by Alterovitz et al. penalty functions for the target volume and critical organs are considered [378]. In accordance with the IPSA framework, these authors divided dose calculation points in two categories: (1) volume and (2) surface. To meet the minimum dose constraints for the target volume, in this study a prescription dose of 7 Gy is assigned to the target volume and surface. Dosimetric constraints for the OARs were in this study initially defined using surface dose calculation points on the bladder, rectum and sigmoid with similar parameters as used by Guthier et al. [380]. Empirically, several modifications to these parameters for the dose-based optimisation were determined. Contrary to the article by Guthier et al., the vagina is not considered as part of the target volume as no vaginal cancer was present in the selected patient case, nor is it considered as an OAR. Moreover, the penalty weight associated with OAR surface dose calculation points is lowered in comparison with the weight associated to the target region to reflect that meeting target dose constraints is to an extent more important than exceeding OAR dose constraints. Since the modelled dose distribution of the BT source is not

Table 7.1: Parameters used for the linear penalty cost functions based on common planning aims [50].

	Minimum dose $d_a^{\min}$ (Gy)	Minimum dose weight $M_a^{\min}$	Maximum dose $d_a^{\max}$ (Gy)	Maximum dose weight $M_a^{\max}$
CTV_{HR} (volume)	7	100	-	-
CTV_{HR} (surface)	7	100	-	-
Bladder (surface)	-	-	6.0	20
Rectum (surface)	-	-	3.7	20
Sigmoid (surface)	-	-	4.3	20

directly capped, the maximum dose for target volume or surface points is not defined. Lastly, the criteria were further refined to reflect recent evidence regarding planning dose constraints [50]. The resulting penalty weights and dose constraints are shown in Table 7.1.

7.1.3 Method evaluation

The linear inverse planning algorithm used for dose-based optimisation in this thesis has been implemented in `MATLAB` R2020a, and is given in Script A.1.17. The linear programming problem is solved using the built-in `linprog` function in `MATLAB` using the default `dual-simplex` algorithm. The dose contribution of a dwell position to a dose calculation point is calculated using the AAPM TG-43 formalism for a mHDR-v2 source model (see Subsection 1.2.2). As a two-dimensional planning case is considered, rather than calculating the dose-volume parameters, the selected dosimetric indices for the CTV_{HR} are the $D_{98\%}$, $D_{90\%}$, $D_{50\%}$ and $A_{100\%}$. Here, $D_{A\%}$ indicates the minimum absorbed dose by at least $A\%$ of the dose calculation points, and $A_{D\%}$ indicates the percentage of dose calculation points covered by at least $D\%$ of the prescribed dose. For the OARs, the selected dosimetric indices capture the relative amount of dose calculation points that is covered by the maximum doses allowed to the structure; $A_{6\text{ Gy}}$, $A_{3.7\text{ Gy}}$ and $A_{4.3\text{ Gy}}$ for the bladder, rectum and sigmoid respectively (see Table 7.1). Additionally, for the considered OARs the $D_{10\%}$ and $D_{2\%}$ are reported as a substitute for the conventionally used D_{2cm^3} and $D_{0.1cm^3}$. Generated plans are moreover compared on the objective function value, the number of active dwell positions, and mean, maximum and total dwell times.

7.2 Coverage planning

The starting point for the second stage, that of robust curvature-constrained intracavitary BT needle channel planning, is provided by a coverage planning algorithm. This algorithm must compute the minimal set of straight interstitial dwell segments that sufficiently cover the tumour, are feasible, do not intersect, and adhere to pose constraints. The binary integer program as formulated by Siauw et al. for prostate brachytherapy [270], which is mathematically formulated in Problem (1.A), is therefore adapted. In this section, an implementation of this method is described in detail. The solutions generated by this approach from varying input parameters were both quantitatively and qualitatively evaluated through the coverage optimisation and subsequent dose optimisation.

7.2.1 Materials and methods

Patient data set

The contours on T2-weighted sagittal MRI of the vaginal vault, target volume (CTV_{HR}) and OARs (bladder, rectum and sigmoid) of a single cervical cancer patient described in the study by Laan et al. [48], were traced manually, appropriately scaled and convexified (Figure 4.5). This data concerned a gynaecological cancer patient with a tumour involving the lateral parametrium

(Stage IIIB). The patient was originally treated using a tandem and ring applicator with both parallel and oblique needles. These interstitial needles were mainly required to extend the prescription isodose to cover the target region in the coronal and axial planes. In the considered sagittal image slice, the planned dose distribution in the study by Laan et al. led to sufficient target coverage, but overexposure of OARs [48]. Therefore, the considered sagittal data set was thought to be sufficiently challenging for this case study.

As the rectum was cut off in the original image, the image was manipulated using Photoshop CC 2018 (Adobe, San Jose, CA, USA). The rectum was manually extended to create a closed shape, whereas other structures were left unaltered. The entry zone for the dwell segments was chosen to be the base line of the convexified tumour region. Bounded uncertainty contours were added to the bladder, rectum and sigmoid based on the estimated bounded displacement interval in Eq. 4.17.

Candidate set generation

The candidate set of dwell segments $\mathcal{N}$ was generated by sampling a point on the entry region and a point on one of the contour lines of the target region and then connecting these two points with straight line segments. Since the CTV_{HR} is convexified, all these segments are contained within the target region. To avoid discretisation issues and to generate a different needle candidate set in each iteration, the points on the contour lines were randomly sampled with a probability made proportional to the length of the contour lines. For each line segment, the angle with the base line and the distance at the base line to the convex hull around OARs indicating worst-case uncertainty was computed and stored. The generated candidate interstitial dwell segment set consisted in each iteration of approximately 9,000 segments, which was found to generate consistent results.

Dwell segment selection

From the candidate set of dwell segments, first all the straight line segments that had an angle of more then 10° deviating from the normal of the base line were excluded. This angle is similar to that used for oblique needles in hybrid IC/IS applicators. As the bounded uncertainty contours of the sigmoid and bladder overlap with the target volume in the simplified scenario treated in this thesis, exceeding the dose constraints of OARs with worst-case positional uncertainty is unavoidable. To allow feasible intracavitary channel solutions to be generated by the motion planning algorithms in the case of worst-case uncertainty, only all the segments that were less than coverage radius ϵ away from the bounded uncertainty contours of OARs at the base line were discarded. Note that this constraint was less restrictive than the constraint proposed under the header 'Initial and target considerations', where the segments had to be at least dose constraint radius $r_{D,j}$ away from the bounded uncertainty contours of OARs at the intersection of the segment and implant. However, the latter was overly conservative for larger dwell times and therefore resulted in frequently infeasibility of the integer program. Addition of the newly formulated distance constraints came at the expense of the amount of points that were coverable by the feasible set of dwell segments. The resulting set of feasible dwell segments is termed $\mathcal{N}_{free}$ and consisted consistently of around 1,000 to 1,500 segments.

To evaluate the coverage of the feasible dwell segment set, the tumour region was uniformly discretised in points $\tau_q \in \mathcal{T}$ spaced 2.5 mm apart. Using Eq. 4.9 the indices of coverable points, $I(\epsilon)$, were extracted. The relative amount of dose calculation points in the target region that could be covered by $\mathcal{N}_{free}$ was experimentally evaluated to rarely drop below 95% of the total amount of dose calculation points. Tumour points that could not be covered with the constant radius ϵ were located at the anterior and posterior sides of the convexified tumour region, proximal to the sigmoid and bladder. With the subsequent dose planning, this issue could be in

the majority of cases resolved resulting in good spatial coverage of the target. The set of dwell segments that cover a single point in the target region with index q, $M_q(\epsilon)$, could then be extracted. Linear constraints were added to ensure that each point could be covered by at least one dwell segment. As this assumption could result in hot spots, an upper limit to the number of dwell segments covering a point was first implemented as well. Since this did not improve the solution quality and rather led to more frequent occurrence of infeasible linear programs, these constraints were later removed.

Collision between two interstitial dwell segments was conservatively defined to occur when these segments were closer than two times the channel width w. A matrix was constructed indicating the pairs of segments that are in collision. Constraints were added such that only one of the dwell segments in a collision set could be extracted.

The objective of the optimisation was to minimise the number of dwell segments in set $\mathcal{S}$. The reason for this was two-fold. First, this reduces the risk of mechanically caused tissue damage and possible serious complications. Secondly, as the planning is executed in a two-dimensional case, a greater number of dwell segments reduces the space available for the motion planning of the intracavitary needle channels and hence reduces the likelihood that feasible solutions are found in trajectory planning.

Method evaluation

The `MATLAB` R2020a code for coverage planning is given in Script A.1.18. All the calculations were performed on a mobile workstation with a 2.4GHz Intel i7-4700MQ processor with 8 GB of memory. The binary integer programming problem was solved using the built-in `intlinprog` function in `MATLAB`. The dose coverage radius ϵ was selected to range between 15% and 40% with 5% increments of the radius of the circle minimally encapsulating the target region, similar as had been described by Siauw et al. [270]. The latter was calculated using the `MATLAB` function `ExactMinBoundCircle` [381]. For values of ϵ smaller than 15% in many cases no feasible solution was found, whereas for values of ϵ greater than 40% dose constraints of multiple OARs were in any case exceeded. For the specified patient case the coverage planning problem was solved five times per value of ϵ. Adding the constraints generally took around 40 s, whereas solving the integer programming problem took around 3 s. For each planning instance the following parameters were recorded: (i) the number of dwell segments n_x, (ii) the ratio of coverable points to the total number of calculation points in the target region, (iii) whether failure of the solver occurred, and (iv) the dosimetric indices described in 7.1.3 calculated using the dose-based optimisation algorithm. Dose optimisation was performed for the convexified (conservative) structures, except for the target volume. Similarly, dosimetric indices were calculated for the convexified structures with exception of the indices for the tumour volume. All dose calculation points, i.e. surface and volume points, were spaced 2.5 mm apart. Dwell points were constructed along the dwell segments with a step size of 5 mm.

The dose conformity of the skew interstitial dwell segments that could possibly be reached through the 3D-printed intracavitary applicator was moreover compared with that of three current treatment modalities: (i) a conventional tandem/ring applicator, (ii) a hybrid tandem/ring applicator with parallel needles, and (iii) a hybrid tandem/ring applicator with oblique needles at 20°. These applicators were coarsely manually reconstructed based on the sagittal MRI provided in the study by Laan et al. [48]. For these applicators, the tandem length, ring diameter and needle insertion depth were assumed to be 6.0, 3.0, and 5.0 cm respectively. Dwell points were reconstructed along the tandem and needles with a step size of 5 mm.

7.2.2 Results

Coverage planning

Results of the coverage planning and sequential dose-based optimisation for various dose coverage radii are shown in Table 7.2. The coverage planning algorithm was in the majority of instances able to converge to an optimal solution. Infeasibility of a solution of the integer program was more likely to occur at smaller values of dose coverage radius ϵ, whereas from values of $\epsilon = 30\%$ up to 40% in all cases a feasible solution was found. The occurrence of infeasibility was linked to collisions at the entry region between dwell segments. After dwell segment coverage planning or the generation of dwell points for standard applicators, the dose-based optimisation algorithm was in all instances able to compute the optimal solution. For all feasible instances, the coverage planning returned dwell segments that could potentially deliver the prescribed dose to on average 99% calculation points of the target region in the simulated patient case. OAR dose constraints were exceeded in only 0.3% of the dose calculation points. SDs of the coverage quality and dosimetric indices for the generated plans were generally small, indicating that the selection of dwell segments from randomly generated candidate sets $\mathcal{N}$ produced consistent results.

With increasing dose coverage radius ϵ, the number of interstitial dwell segments required to sufficiently cover the target region decreased. The number of (active) dwell points decreased correspondingly such that the mean, maximum and total dwell times had to be increased in the dose optimisation to guarantee high dose conformity. Whereas for 42 active dwell points in 7 dwell segments the mean dwell time was only 4.7 s, this increased up to 38.4±3.4 s for 11 dwell points in 3 dwell segments. Accordingly, the decrease in the number of interstitial segments associated with larger values of ϵ resulted in exceeding OAR dose constraints. Ideally, the values of A_D for the OARs would be close to zero, indicating that dose constraints $d_a^{\max}$ are not exceeded. When optimising the dwell times for the set of three interstitial dwell segments the resulting dose distribution exceeded the allowable doses in calculation points of the bladder (up to only 0.1% of the points) and sigmoid (up to 1.5% of the points). In coverage planning solutions with more dwell segments, i.e. generated with smaller ϵ, OAR dose constraints were rarely exceeded. For the target volume, ideally the $A_{100\%}$ value would be 100%, indicating that the 100% isodose line (7 Gy) would cover all dose calculation points in the CTV_{HR}. For values of $\epsilon = 30\%$ and higher an almost ideal tumour coverage was achieved for all instances. Realistic dwell times that led to plans meeting most dose constraints were obtained for solutions with five ($\epsilon = 20\%$) and four ($\epsilon = 25\%$ or 30%) dwell segments.

In Figure 7.2b-7.2e representative isodose contour plots from the dose optimisation for various solutions of the coverage planning algorithm are shown. For larger values of ϵ, it can be observed that to compensate for the smaller amount of interstitial dwell segments the dwell times of the active positions are increased. Although this ensures that coverage of the target region by the prescription isodose contour of 7 Gy is sufficient, this results in areas where OARs and normal tissues are likely overexposed. In solutions containing a larger amount of dwell segments the prescription isodose contour of 7 Gy approximates the shape of the target region better. Small areas of underexposure in the tumour region, i.e. where doses are lower than 7 Gy, are the result of discretisation artifacts. Configurations with four dwell segments (Figure 7.2d), as obtained for $\epsilon \approx$ 25-30%, seem to generate dose distributions sufficiently covering the tumour, including involvement in the lateral parametrium, whilst not exceeding OAR dose constraints. Moreover, opposed to configurations with a larger amount of dwell segments, this solution limits physical trauma to the tissue.

Table 7.2: Results of the dose coverage algorithm and dosimetric evaluation for varying dose coverage radii. Continuous variables are expressed with the mean ± SD, and discrete variables with the median. For $\epsilon = 15\%$ and $\epsilon = 20\%$, the coverage planning algorithm successfully converged to a feasible solution in only 1 out of 5 instances such that no standard deviations could be reported.

Coverage planning	Skew line interstitial dwell segments						Current modalities		
Coverage radius →	$\epsilon = 15\%$	$\epsilon = 20\%$	$\epsilon = 25\%$	$\epsilon = 30\%$	$\epsilon = 35\%$	$\epsilon = 40\%$	T/R	T/R + par.	T/R + obl.
Number of segments	7	5	4	4	3	3	1	3	5
Coverable points (%)	98.3 ± [-]	97.8 ± [-]	97.6 ± 0.0	97.7 ± 0.0	97.5 ± 0.0	97.7 ± 0.0	-	-	-
Feasibility	1/5	1/5	3/5	5/5	5/5	5/5	-	-	-
Dose planning	Skew line interstitial dwell segments						Current modalities		
Coverage radius →	$\epsilon = 15\%$	$\epsilon = 20\%$	$\epsilon = 25\%$	$\epsilon = 30\%$	$\epsilon = 35\%$	$\epsilon = 40\%$	T/R	T/R + par.	T/R + obl.
Objective value	0.00 ± [-]	0.00 ± [-]	0.15 ± 0.04	0.38 ± 0.03	0.80 ± 0.15	1.30 ± 0.08	3.12 ± 0.00	0.53 ± 0.00	0.01 ± 0.00
Active dwell positions (Total)	42 (72)	24 (53)	17 (43)	19 (44)	12 (34)	11 (36)	3 (13)	16 (33)	25 (55)
Mean dwell time (s)	4.7 ± [-]	10.0 ± [-]	17.6 ± 2.3	18.3 ± 1.9	31.7 ± 2.4	38.4 ± 3.4	189.7 ± 0.0	28.7 ± 0.0	16.4 ± 0.0
Maximum dwell time (s)	43.9 ± [-]	63.3 ± [-]	80.9 ± 13.9	92.1 ± 8.0	139.4 ± 6.6	162.8 ± 5.3	291.1 ± 0.0	247.6 ± 0.0	186.5 ± 0.0
Total dwell time (s)	199.0 ± [-]	240.2 ± [-]	300.5 ± 4.4	332.9 ± 7.8	397.3 ± 11.8	434.3 ± 3.6	569.1 ± 0.0	459.3 ± 0.0	410.2 ± 0.0
CTV_{HR}									
$D_{98\%}$ (Gy)	7.0 ± [-]	7.0 ± [-]	7.0 ± 0.0	7.1 ± 0.0	7.1 ± 0.0	7.2 ± 0.2	7.8 ± 0.0	7.0 ± 0.0	7.0 ± 0.0
$D_{90\%}$ (Gy)	7.2 ± [-]	7.3 ± [-]	7.6 ± 0.1	7.6 ± 0.1	7.6 ± 0.1	7.7 ± 0.1	9.3 ± 0.0	7.9 ± 0.0	7.3 ± 0.0
$D_{50\%}$ (Gy)	9.9 ± [-]	9.9 ± [-]	10.8 ± 0.0	10.9 ± 0.2	11.6 ± 0.2	12.0 ± 0.2	15.4 ± 0.0	12.5 ± 0.0	9.5 ± 0.0
$A_{100\%}$ (%)	96.2 ± [-]	97.1 ± [-]	98.9 ± 1.0	99.5 ± 0.2	99.6 ± 0.1	99.8 ± 0.2	100.0 ± 0.0	98.7 ± 0.0	98.4 ± 0.0
Bladder									
$D_{10\%}$ (Gy)	1.9 ± [-]	2.2 ± [-]	2.6 ± 0.1	2.8 ± 0.1	3.1 ± 0.1	3.2 ± 0.0	3.8 ± 0.0	3.5 ± 0.0	3.0 ± 0.0
$D_{2\%}$ (Gy)	3.2 ± [-]	3.8 ± [-]	4.3 ± 0.1	4.5 ± 0.1	4.7 ± 0.1	4.8 ± 0.0	5.4 ± 0.0	5.0 ± 0.0	4.7 ± 0.0
$A_{6\ \mathrm{Gy}}$ (%)	0.0 ± [-]	0.0 ± [-]	0.0 ± 0.0	0.0 ± 0.0	0.0 ± 0.0	0.1 ± 0.0	0.9 ± 0.0	0.2 ± 0.0	0.0 ± 0.0
Rectum									
$D_{10\%}$ (Gy)	0.6 ± [-]	0.8 ± [-]	1.0 ± 0.0	1.1 ± 0.0	1.3 ± 0.0	1.5 ± 0.0	1.5 ± 0.0	1.5 ± 0.0	1.3 ± 0.0
$D_{2\%}$ (Gy)	0.8 ± [-]	1.0 ± [-]	1.2 ± 0.0	1.4 ± 0.0	1.7 ± 0.1	1.9 ± 0.0	1.9 ± 0.0	1.8 ± 0.0	1.6 ± 0.0
$A_{3.7\ \mathrm{Gy}}$ (%)	0.0 ± [-]	0.0 ± [-]	0.0 ± 0.0	0.0 ± 0.0	0.0 ± 0.0	0.0 ± 0.0	0.0 ± 0.0	0.0 ± 0.0	0.0 ± 0.0
Sigmoid									
$D_{10\%}$ (Gy)	2.0 ± [-]	2.2 ± [-]	2.5 ± 0.0	2.7 ± 0.0	2.9 ± 0.1	3.1 ± 0.0	3.5 ± 0.0	2.7 ± 0.0	2.4 ± 0.0
$D_{2\%}$ (Gy)	3.1 ± [-]	3.1 ± [-]	3.5 ± 0.0	3.7 ± 0.0	4.0 ± 0.1	4.1 ± 0.0	4.2 ± 0.0	3.6 ± 0.0	3.1 ± 0.0
$A_{4.3\ \mathrm{Gy}}$ (%)	0.0 ± [-]	0.0 ± [-]	0.3 ± 0.0	0.3 ± 0.0	1.0 ± 0.2	1.5 ± 0.2	1.7 ± 0.0	0.3 ± 0.0	0.0 ± 0.0

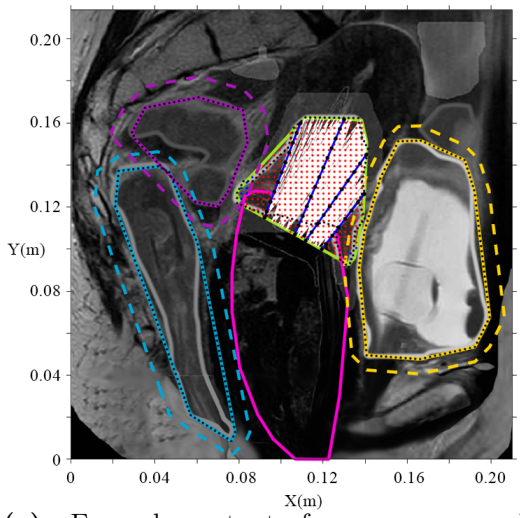

(a) Example output from coverage planning algorithm for $\epsilon = 30\%$.

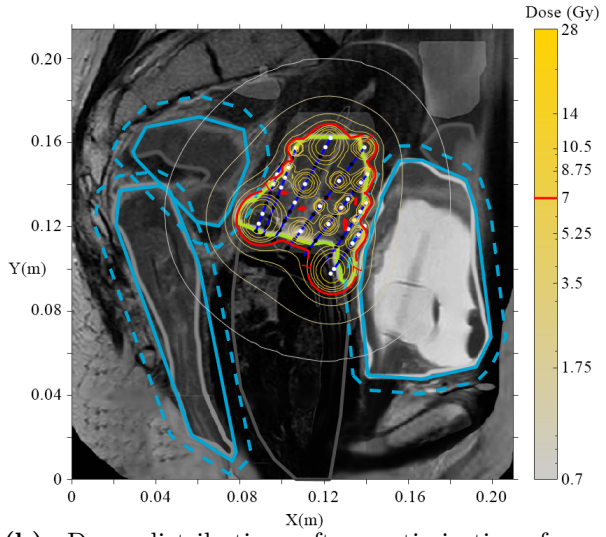

(b) Dose distribution after optimisation for a solution with 7 dwell segments ($\epsilon = 15\%$).

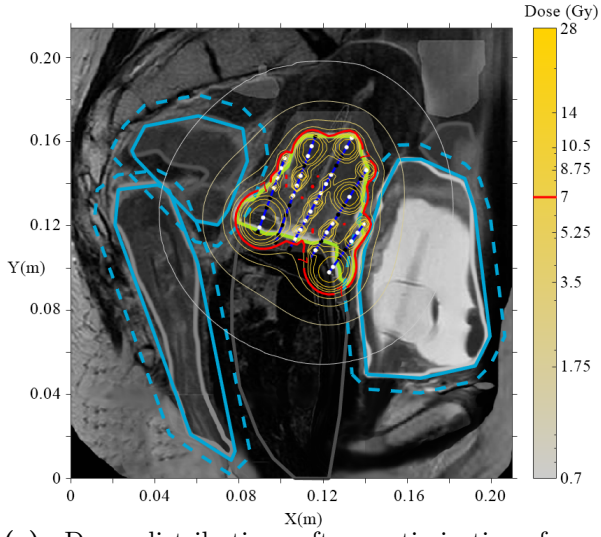

(c) Dose distribution after optimisation for a solution with 5 dwell segments ($\epsilon = 20\%$).

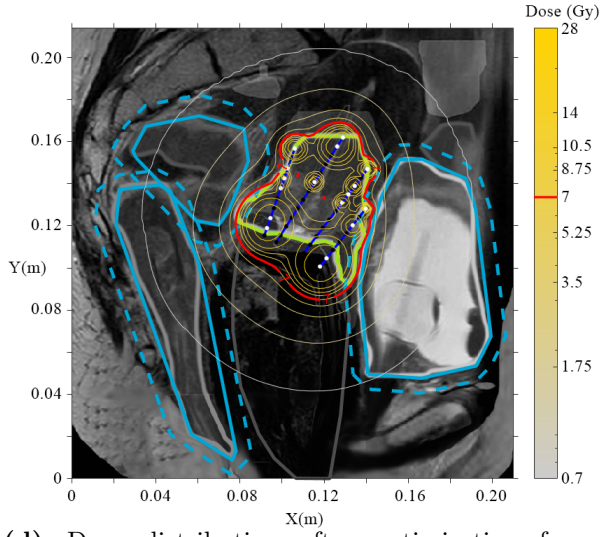

(d) Dose distribution after optimisation for a solution with 4 dwell segments ($\epsilon = 30\%$).

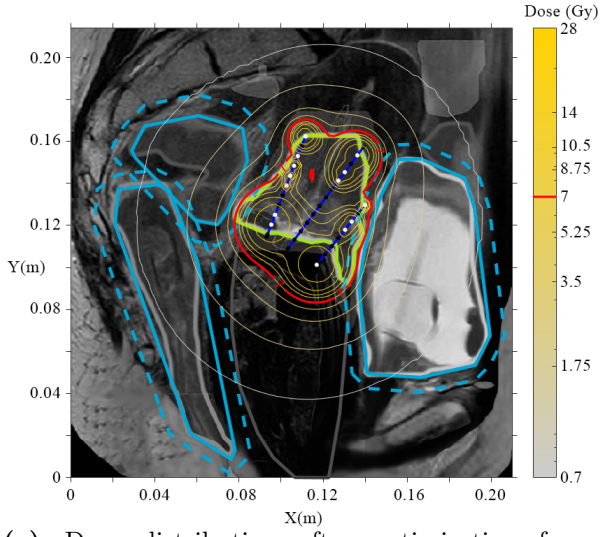

(e) Dose distribution after optimisation for a solution with 3 dwell segments ($\epsilon = 40\%$).

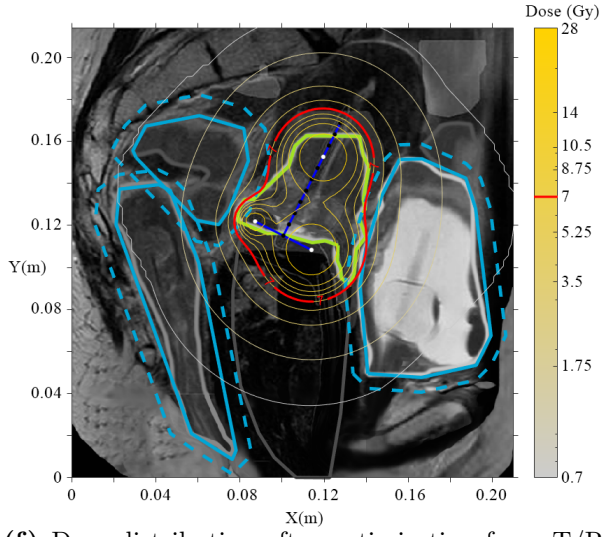

(f) Dose distribution after optimisation for a T/R applicator.

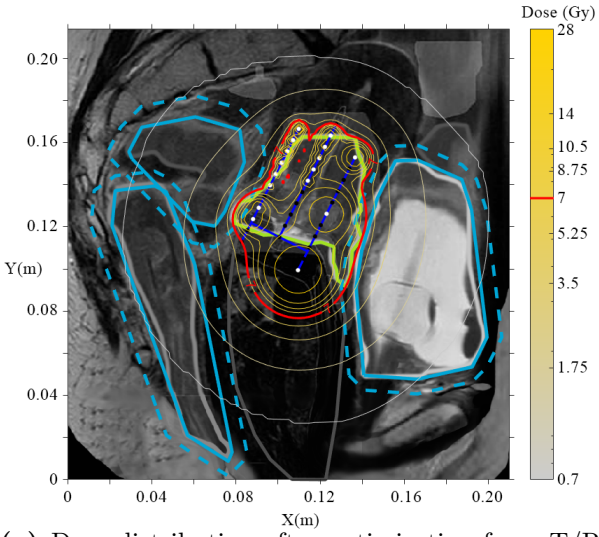

(g) Dose distribution after optimisation for a T/R applicator with parallel interstitial needles.

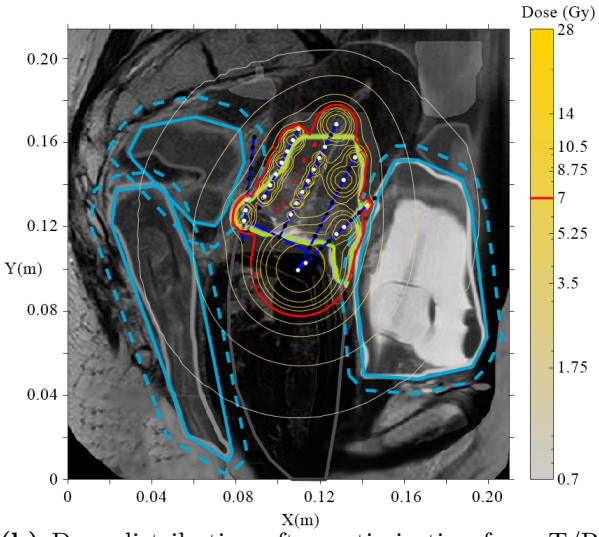

(h) Dose distribution after optimisation for a T/R applicator with both parallel and oblique interstitial needles.

Figure 7.2: Illustrations of the dose distributions calculated via the dose-based optimisation for an optimal set of interstitial dwell segments returned by the coverage planning algorithm for a single patient case.

An example output of the coverage planning algorithm for a dose coverage radius of $\epsilon = 30\%$ is illustrated in (a). In (a) shown are: target volume (bright green —), bladder (gold —), rectum (blue —), sigmoid (purple —), stay-in region (pink —), tumour coverage points (small red dots •), dwell segments (dark blue —), dwell points (black dots ●), and surface calculation points (small black dots •).

Contour plots of the computed dose distributions for coverage planning solutions with 7 to 3 interstitial dwell segments with varying radii ϵ are shown in (b)-(e). Contour plots of the optimised dose distributions for common current treatment modalities are shown (f)-(h). In (b)-(h) shown are: target volume (bright green —), OARs (blue —), dwell segments (dark blue —), inactive dwell points (black dots ●), active dwell points (white dots ○), isodose contours ( ), and prescription isodose line (7 Gy, red —).

Standard treatment modalities

For the standard treatment modalities, the dose-based optimisation converged in each iteration to a single solution. Table 7.2 and Figure 7.2f - 7.2h demonstrate the limitations of applicators with a standard configuration in the simulated patient case, as the dose must be escalated to cover the lateral extension of the tumour. For a standard tandem and ring applicator (T/R), the dose-based optimisation indicated that the highest dose conformity could be achieved with only three active dwell points with a mean dwell time of almost 190 s. However, in this case, dosimetric constraints of the bladder and sigmoid were exceeded in small partial volumes of these organs. Additionally, in this plan hot spots in and near the tumour region were present, overdosing proximal normal tissue. For a hybrid T/R applicator with two interstitial needles parallel to the tandem a higher dose conformity was achieved, i.e. lower value of the objective function. However, to cover the lateral

extension of the CTV_{HR}, the simulated maximum dwell time in the ring of the applicator (on the right) was on average 247.6±0.0 s. For the simulated hybrid T/R applicator with both parallel and oblique needles, the dose optimisation returned a solution in which OAR dose constraints were not exceeded, but tumour coverage was still not optimal; $A_{100\%} = 98.4\pm0.0\%$. Additionally, the dwell times of positions near the ring of the applicator proximal to the bladder remained high; i.e. a maximum dwell time of almost 186.5±0.0 s for a dwell position in one of the needles was computed. Nevertheless, as indicated by an almost zero value for the objective function the simulated dose distribution for the T/R applicator with both parallel and oblique needles achieved a high dose conformity. This was similar to that of dose distributions generated for solutions of the coverage planning algorithm with small coverage radii.

7.2.3 Discussion

In this section, an algorithm was presented and evaluated for computing a dwell segment configuration that achieves a high dose conformity even in challenging tumours based on the NPIP algorithm [270]. In this algorithm, the set of dwell segments minimally required to cover the tumour region is selected from a candidate set of dwell segments. The algorithm was shown to converge to a configuration of dwell segments that could achieve a high dose conformity in the majority of instances for a rather challenging simulated patient case. Opposed to standard applicators with fixed angles and dwell positions, these skew dwell segments have the potential to create plans with less hot spots and increased target coverage.

Performance of the algorithm was shown to depend on a single dose coverage parameter ϵ. For smaller values of ϵ, solutions were often not feasible. Dosimetric constraints were more frequently exceeded for larger values of ϵ. To both meet dosimetric constraints and minimise the number of required dwell segments for the simulated patient case, the dose coverage radius would ideally be set equal to around 25-30% of the radius of the minimally enclosing sphere of the tumour region. Values of ϵ of 35 or 40% yielded plans that met dosimetric constraints in the study Siauw et al. [270], which would lead to hot spots in OARs in the investigated patient case. Values of 25-30% resulted in a configuration with four straight line dwell segments. Interestingly, one of these dwell segments is then placed similarly to a central tandem, which has been noted to be crucial to prevent underdosage of the cervical region [66]. Figure 7.2 and the values of $A_{100\%}$ in Table 7.2 both indicate that underdosage of the tumour region could possibly occur. However, this was likely an artefact of discretisation and could therefore be resolved by using a finer grid. In the simulated case for configurations with four dwell segments only the dose constraints of the sigmoid were exceeded. It must be noted that in this case study, OARs were conservatively represented with a convex hull and therefore the actual dose in these organs would be less. Moreover, when using dose-volume based optimisation, such as IPIP [382], or the LDV model by Gorissen et al. [105], opposed to dose-based optimisation the conformity of the treatment plan may be improved. No constraints were included in the coverage planning algorithm to prevent hot spots in the cervical region. One could for example provide an upper bound to Eq. 4.30b, but this caused frequent infeasibility of the integer program and did not improve the solution quality.

Planning was in this thesis performed for a two-dimensional case, only in the sagittal plane. The lateral extension of the tumour present in the simulated patient case was therefore not represented accurately and could in most cases sufficiently be covered. The benefits of skew line optimisation of interstitial needles may be more conveniently illustrated for patients with invasion of the parametria on a (mid-)coronal image or by using three-dimensional planning and imaging. The algorithm could simply be extended to higher dimensions as has been done by Siauw et al. [270].

This would, however, drastically increase the overall computation time, which mainly depends on the size of the candidate set influencing time spent on collision checking and the number of dose calculation points that influences time for dose optimisation. The use of a more efficient collision checking algorithm or strategy would therefore be recommended. For example, as collisions are not likely to occur in an optimal configuration in a three-dimensional case, one could use a lazy strategy and only check whether collisions occur after an optimal configuration has been successfully generated. Moreover, rather than that the candidate set is generated randomly, informed sampling may be used to strategically position segments. In a three-dimensional case, the resulting isodose curves would likely be more smooth and dwell times would be less heterogeneous than the presently found results.

Siauw et al. have demonstrated for 18 prostate cancer patients that NPIP is able to generate clinically feasible plans [270], but have not compared these plans with those generated for standard applicators. It was in this section shown that higher dose conformity could be achieved using the coverage planning algorithm than with conventionally used applicators in a rather challenging simulated patient case. Previous computer models have shown that with the most advanced applicators, the planning aim isodose can potentially cover the target region for almost any patient case [70, 84]. From Figure 7.2h it can however be seen that even when using both parallel and oblique needles, standard applicators remain ill-adapted for tumours with parametrial extension. Although the tumour coverage was near-optimal and dose constraints of OARs were not exceeded for the T/R applicator with parallel and oblique needles in the patient case, dwell times were generally higher and more heterogeneous. Plans with large dwell time variations come at a risk of overdosing normal tissues and are more susceptible to uncertainty, e.g. intra-fraction changes [379]. Potentially, dose homogeneity could be improved through dwell-time modulation restriction or implementing dwell times in the objective of the dose-based optimisation, but no effective methods for this purpose exist as of yet [379]. Since only one patient case was considered in this thesis, comparisons between conventional applicators and configurations generated with the coverage planning algorithm must be re-investigated for a larger number of patients.

In the proposed two-stage approach, the intersections of the generated straight line dwell segments -extending to the base line of the convexified tumour region- with the vaginal cavity serve as the initial points for trajectory planning (Figure 4.9). It is therefore implicitly assumed that the curved channels, at least partially, coincide with these straight dwell segments. For trajectory planning in a bounded uncertainty scenario, to guarantee that a robustly feasible trajectory can be found, these points of intersection must be at least dose constraint radius $r_{D,j}$ away from the convex bounded uncertainty contours and the corresponding segments must be diverging from these contours. In this section, the only constraint implemented to position dwell segments away from OARs in coverage planning was a minimum distance constraint at the baseline of the convexified tumour region. Therefore, the coverage planning algorithm must be modified to provide initial conditions for needle trajectory planning subject to bounded uncertainty.

7.3 Needle trajectory planning under uncertainty

The problem of computing robust curvature-constrained intracavitary BT needle channels has been mathematically described in Problems (2.A) and (2.B) for scenarios with bounded uncertainty and probabilistic uncertainty in the position of OARs respectively. The algorithm must compute multiple feasible, non-intersecting curvature-constrained needle channels from the interstitial dwell segments towards an entry region maintaining sufficient distance to OARs. Dwell positions may be positioned along both the combined interstitial segments and intracavitary needle channels. In

this section, two robust motion planning algorithms are implemented and evaluated against the performance of an algorithm not taking into account uncertainty.

7.3.1 Materials and methods

Modified coverage planning algorithm

In the previous section it was established that for the patient case a dose coverage radius ϵ of 25-30% could generate configurations with four segments that yield plans with high conformity. In order to guarantee that the set of dwell segments could feasibly be reached, even by motion planners taking into account worst-case positional uncertainty of the OARs, two constraints were added. First, the intersection points of dwell segments with the vaginal cavity contours in the feasible candidate set $\mathcal{N}_{free}$ were constrained to be at least dose constraint radius $r_{D,j}$ from the bounded uncertainty contours. Secondly, dwell segments were only included in the candidate set $\mathcal{N}_{free}$ when, from the intersection points onwards, these diverged from the bounded uncertainty contours. To generate initial poses for the planning of intracavitary channels, $\mathbf{x}_0^i$, the coverage planning algorithm was run five times. The dose coverage radius was lowered to $\epsilon = 20\%$, which was empirically established to generate high quality solutions consisting of four dwell segments. A single configuration was selected from the generated alternatives, which achieved a high dose conformity and resulted in the lowest average dwell time. One of the dwell segments in this configuration was substituted for a central tandem to prevent tumour underdosage. This scenario is henceforth referred to as the **conservative OAR sparing** scenario (CO).

Achieving adequate target coverage is generally the most important criterion in brachytherapy. Therefore, the previously mentioned stringent robust feasibility conditions were for another scenario substituted with constraints that ensure that the segments are at least radius $r_{D,j}$ from the OAR contours. The dose coverage radius was set to $\epsilon = 25\%$, the coverage planning algorithm was iterated five times, and one configuration was selected. A central dwell segment was replaced with a 6 cm tandem. For this planning instance, all points in the convexified tumour region were coverable. Additionally, none of the OAR dose constraints were exceeded in dose-based optimisation. However, the resulting configuration of skew line dwell segments could only be used for nominal trajectory planners or trajectory planners assuming probabilistic uncertainty. This scenario is henceforth referred to as the **nominal planning** scenario (NP).

Problem formulation

The formulation of the needle trajectory planning problem under uncertainty is briefly described here, summarising Section 4.3 and using the taxonomy in Figure 4.4.

Agent representation

Two different shapes were considered for the agent. For physical collision checking with other needle channels or OARs, the BT source was modelled as a rectangle with length $L = 5$ mm and a width of 0.9 mm, corresponding to a channel width $w = 2.6$ mm. In order to prevent hot spots in OARs, the agent was represented as a circle with its radius depending on OAR dose constraints. For the CO scenario, the dose coverage radius ϵ was set equal to 20% of the minimally enclosing sphere around the target region, i.e. $\epsilon = 7.8$ mm. Using data of the mHDR-v2 source and the TG-43 formalism, this was associated with a dwell time of approximately 34 s. Accordingly, dose radii for the bladder, rectum and sigmoid were computed to be $r_{D,\text{bladder}} = 8.4$ mm (corresponding to the radius enclosing the 6 Gy isodose line), $r_{D,\text{rectum}} = 10.8$ mm (for 3.7 Gy), and $r_{D,\text{sigmoid}} = 10.0$ mm (for 4.3 Gy) respectively.

For the NP scenario, the dose coverage radius ϵ was set equal to 25%, equivalent to 9.7 mm. The corresponding dwell time and dose radii were computed to be 53 s, $r_{D,\text{bladder}} = 10.5$ mm, $r_{D,\text{rectum}} = 13.4$ mm, and $r_{D,\text{sigmoid}} = 12.4$ mm respectively.

Workspace representation
The aforementioned data set of a single cervical cancer patient was used to generate the planning environment. The boundaries of the vaginal cavity defined the stay-in region $\mathcal{I}$, constraining the sampling space. The OARs were convexified and represented through a set of inequality constraints. The initial states for the CO scenario, which resulted from the modified coverage planning algorithm, were given by:

$$\mathbf{x}^1_{0,\text{CO}} = \begin{bmatrix} 124.6\text{ mm} \\ 113.5\text{ mm} \\ 4.0337\text{ rad} \end{bmatrix} \quad \mathbf{x}^2_{0,\text{CO}} = \begin{bmatrix} 111.3\text{ mm} \\ 113.8\text{ mm} \\ 4.1328\text{ rad} \end{bmatrix} \quad \mathbf{x}^3_{0,\text{CO}} = \begin{bmatrix} 100.0\text{ mm} \\ 114.0\text{ mm} \\ 4.2432\text{ rad} \end{bmatrix} \quad \mathbf{x}^4_{0,\text{CO}} = \begin{bmatrix} 95.9\text{ mm} \\ 124.4\text{ mm} \\ 4.3723\text{ rad} \end{bmatrix}$$

Here, the third dwell segment served as a central tandem. For the NP scenario, the following initial states were obtained from coverage planning:

$$\mathbf{x}^1_{0,\text{NP}} = \begin{bmatrix} 126.7\text{ mm} \\ 109.6\text{ mm} \\ 4.1500\text{ rad} \end{bmatrix} \quad \mathbf{x}^2_{0,\text{NP}} = \begin{bmatrix} 119.4\text{ mm} \\ 115.9\text{ mm} \\ 4.0947\text{ rad} \end{bmatrix} \quad \mathbf{x}^3_{0,\text{NP}} = \begin{bmatrix} 100.0\text{ mm} \\ 114.0\text{ mm} \\ 4.2432\text{ rad} \end{bmatrix} \quad \mathbf{x}^4_{0,\text{NP}} = \begin{bmatrix} 93.1\text{ mm} \\ 126.5\text{ mm} \\ 4.2364\text{ rad} \end{bmatrix}$$

For each individual dwell segment, a goal region centre $\mathbf{x}^i_T$ was specified in the entry region $\mathcal{E}$ with a tolerance of 2.5 mm:

$$\mathbf{x}^1_T = \begin{bmatrix} 122.6\text{ mm} \\ 0.0\text{ mm} \\ [-]\text{ rad} \end{bmatrix} \quad \mathbf{x}^2_T = \begin{bmatrix} 117.3\text{ mm} \\ 0.0\text{ mm} \\ [-]\text{ rad} \end{bmatrix} \quad \mathbf{x}^3_T = \begin{bmatrix} 112.0\text{ mm} \\ 0.0\text{ mm} \\ [-]\text{ rad} \end{bmatrix} \quad \mathbf{x}^4_T = \begin{bmatrix} 106.7\text{ mm} \\ 0.0\text{ mm} \\ [-]\text{ rad} \end{bmatrix}$$

No constraints on the orientation of the final state in this entry region were specified.

Uncertainty representation
For the motion planning instances that considered bounded uncertainty, the displacements of the bladder, rectum and sigmoid were constrained within the intervals in Eq. 4.17. In the case of probabilistic uncertainty, the centres of the OARs were distributed according to the covariance matrices in Eq. 4.16. Bounded uncertainty contours coincided roughly with the 95% confidence intervals over the Gaussian distributed obstacle faces. Due to this simplified representation of organ motion and deformations, the target region and uncertainty manifestation could overlap.

Planning execution
The objective functions used in the cases of deterministic planning and planning under bounded uncertainty represented the trajectory length, by setting $f(\mathbf{u}^i_t, \mathbf{x}^i_t) = \delta v^i_t$. For the probabilistic uncertainty scheme, the cost function in Eq. 6.25 was used with $\alpha_D = 1$, $\alpha_\Delta = 5$. Constraints were imposed on the curvature $\bar{\kappa} = 0.028\text{ mm}^{-1}$ and maximum step size $\bar{\lambda} = 5$ mm, i.e. $\delta = 0.05$ s and $\bar{v}_t = 100$ mm/s.

Method evaluation
Three of the discussed algorithms capable of planning trajectories for non-holonomic systems were compared on their performance in the simulated patient case. The following planning variants were selected for the two scenarios:

Conservative OAR sparing scenario (CO)

- Nominal reconnect-tree RRT, rt-RRT, described in Subsection 6.3.2;
- The bounded uncertainty variant of reconnect-tree RRT, BU-rt-RRT, described in Section 6.4;
- The chance constrained variant of reconnect-tree RRT with medium tolerated risk levels: $\psi_s = 0.8$ and $\psi_p = 0.6$, CC-rt-RRT (med.), described in Section 6.5;
- The chance constrained variant of reconnect-tree RRT with low tolerated risk levels: $\psi_s = 0.99$ and $\psi_p = 0.95$, CC-rt-RRT (low).

Nominal planning scenario (NP)

- Nominal reconnect-tree RRT, abbreviated as rt-RRT, described in Subsection 6.3.2;
- The chance constrained variant of reconnect-tree RRT with medium tolerated risk levels: $\psi_s = 0.8$ and $\psi_p = 0.6$, CC-rt-RRT (med.).

These planners were programmed in `MATLAB` R2020a. For each of the scenarios and instances, the planner was run five times with 3,000 iterations. All simulations were performed on a mobile workstation with a 2.4 GHz Intel i7-4700MQ processor with 8 GB of memory. To increase the rate of convergence, the target region centre $\mathbf{x}_T^i$ was included as a sample on average in five out of hundred iterations. Trajectories were planned sequentially, starting with the initial pose nearest to the entry region and continuing in increasing order of distance to the entry region. This strategy was shown to minimally obstruct the generation of subsequent trajectories [89]. After a trajectory was successfully constructed, poses along the trajectory were extracted and a new obstacle was created from the union of these poses.

The planning instances were evaluated on their: (i) total trajectory length, (ii) maximum risk per step and accumulated risk by considering that the OARs are distributed with probabilistic uncertainty, (iii) total runtime, and (iv) failure rate. Shortest curvature-constrained trajectories between two states without obstacles are Dubins' curves [239]. If the terminal angle of the second state is not constrained, this is known as a 'relaxed' Dubins' curve [383], for which simple analytic solutions are available [384]. Assuming that the optimal solution for each trajectory is of type 'LS' and providing an upper bound on the curvature, then the optimal length can be found from optimisation. Therefore, the computed trajectory lengths were compared with relaxed Dubins' shortest curves of which the length is optimised using `fmincon` in `MATLAB`. The goal tolerance was subtracted from this length. The total runtime was defined as the time from initialisation of the motion planner to returning the lowest-cost trajectory for all four initial conditions. Intracavitary dwell positions were spaced at regular intervals of 5 mm along the generated trajectories, by using the `MATLAB` functions `arclength` and `interparc` [385, 386], and performing spline interpolation. For the purpose of coarsely evaluating the risk of the generated trajectories, at each of the dwell positions along the trajectory the probability of exceeding dose contours was computed using Eq. 6.20. After the generation of these trajectories, dose-based optimisation was performed. The dose distribution was optimised for the combined intracavitary and interstitial dwell segments in a deterministic scenario using the dose-based optimisation algorithm introduced in this chapter. Only the five intracavitary dwell positions per needle channel that were most proximal to the tumour region were considered for dose-based optimisation. Dosimetric indices and outcome parameters mentioned in Subsection 7.1.3 were determined for the relevant structures. Additionally, dosimetric indices and outcome parameters were computed for a worst-case scenario where dwell times were maintained and the dose calculation points were regularly positioned within the bounded uncertainty contours at a 2.5 mm interval.

7.3.2 Results

Trajectory planning simulation

All of the implemented motion planning algorithms were able to construct feasible trajectories from an initial condition to the goal region in the case study. In Table 7.3 the properties of the planners and solution trajectories are shown for both coverage planning scenarios. Figure 7.3 and 7.4 show representative solution trajectories for the selected planners.

Conservative OAR sparing scenario (CO)

Visual inspection of Figure 7.3a-7.3d indicated that all planners were able to generate similar near-shortest length trajectories for the non-holonomic agent in the CO scenario. Shortest trajectory lengths using Dubins' theory for the four intracavitary segments were calculated to be respectively 113.4, 113.2, 113.4, and 122.9 mm. The mean lengths of the trajectories returned by the motion planners were within 2% of these theoretical lengths. No differences were found between the trajectory lengths generated with any of the planning approaches in this scenario. Similarly, no differences between the solution trajectories' maximum stepwise risk or accumulated risks were observed, despite the addition of robust feasibility constraints in the bounded uncertainty and chance constrained approaches. In BU-rt-RRT (Figure 7.3b), the sampling domain was directly constrained by obstacles that were 'inflated' with the dose constraint radius and bounded uncertainty. The resulting feasible space, however, contained the set of Dubins' shortest curves which could therefore be found. Addition of probabilistic feasibility constraints and incorporation of a risk-based objective in CC-rt-RRT (Figure 7.3c and 7.3d) did not alter the

Table 7.3: Trajectory planning results for the selected motion planners in the simulated patient case for two coverage planning scenarios. Each planner was run 5 times for 3,000 iterations. Variables are expressed with the mean ± SD. Abbreviations: Max. = maximum, Acc. = accumulated.

	Conservative OAR sparing				**Nominal planning**	
	rt-RRT	BU-rt-RRT	CC-rt-RRT (med.)	CC-rt-RRT (low)	rt-RRT	CC-rt-RRT (med.)
Total length (mm)	467.4 ± 0.6	468.7 ± 1.3	468.0 ± 0.7	467.3 ± 0.9	469.3 ± 1.0	470.0 ± 1.3
Length $\tilde{x}^1$ (mm)	114.0 ± 0.5	114.2 ± 0.2	114.4 ± 0.6	114.3 ± 0.5	109.6 ± 0.8	110.2 ± 0.9
Length $\tilde{x}^2$ (mm)	114.2 ± 0.4	114.6 ± 0.3	114.8 ± 0.8	114.6 ± 0.2	117.1 ± 0.7	117.3 ± 0.6
Length $\tilde{x}^3$ (mm)	114.5 ± 0.3	114.9 ± 0.9	114.4 ± 0.8	114.5 ± 0.4	114.1 ± 0.4	114.2 ± 0.5
Length $\tilde{x}^4$ (mm)	124.6 ± 0.2	125.0 ± 09	124.4 ± 0.5	124.0 ± 0.3	128.6 ± 0.1	128.8 ± 0.4
Max. risk ($\cdot 10^{-3}$)	6.5 ± 0.0	6.5 ± 0.0	6.5 ± 0.0	6.5 ± 0.0	198.9 ± 0.0	198.9 ± 0.0
Acc. risk ($\cdot 10^{-3}$)	15.3 ± 1.0	15.0 ± 0.2	15.4 ± 0.9	16.0 ± 1.3	786.6 ± 15.0	659.3 ± 1.3
Acc. risk $\tilde{x}^1$ ($\cdot 10^{-3}$)	7.7 ± 1.0	7.4 ± 0.2	7.9 ± 0.9	8.5 ± 1.2	457.6 ± 15.8	332.2 ± 1.1
Acc. risk $\tilde{x}^2$ ($\cdot 10^{-3}$)	0.0 ± 0.0	0.0 ± 0.0	0.0 ± 0.0	0.0 ± 0.0	0.1 ± 0.0	0.1 ± 0.0
Acc. risk $\tilde{x}^3$ ($\cdot 10^{-3}$)	0.0 ± 0.0	0.0 ± 0.0	0.0 ± 0.0	0.0 ± 0.0	0.1 ± 0.0	0.1 ± 0.0
Acc. risk $\tilde{x}^4$ ($\cdot 10^{-3}$)	7.6 ± 0.1	7.6 ± 0.0	7.5 ± 0.0	7.5 ± 0.1	328.7 ± 1.3	326.8 ± 2.4
Total runtime (s)	249.4 ± 12.0	196.7 ± 9.1	1120 ± 80.3	840.6 ± 51.8	262.0 ± 0.8	836.5 ± 81.9
Runtime $\tilde{x}^1$ (s)	64.1 ± 6.8	53.6 ± 4.7	132.6 ± 19.1	95.7 ± 5.7	62.8 ± 4.2	92.6 ± 14.4
Runtime $\tilde{x}^2$ (s)	62.8 ± 3.1	48.6 ± 0.9	200.7 ± 4.1	152.6 ± 14.3	70.6 ± 3.3	166.5 ± 7.9
Runtime $\tilde{x}^3$ (s)	61.7 ± 4.7	44.8 ± 3.4	295.2 ± 22.8	155.4 ± 9.3	63.2 ± 4.2	259.5 ± 28.8
Runtime $\tilde{x}^4$ (s)	60.8 ± 2.1	49.7 ± 6.1	492.0 ± 47.7	436.8 ± 41.0	65.3 ± 7.3	317.9 ± 41.0
Failure rate	0/5	2/5	2/5	2/5	1/5	2/5

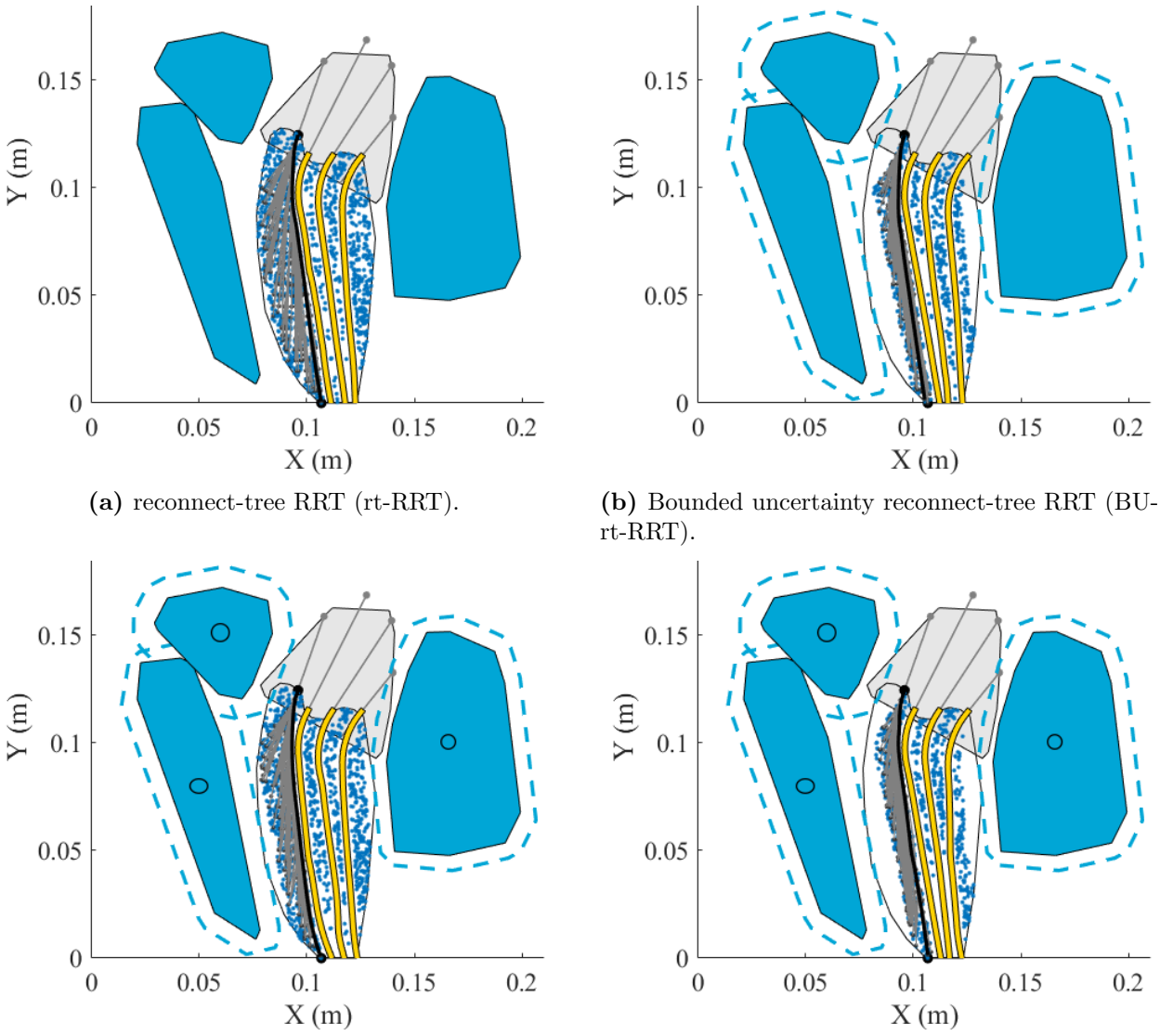

(a) reconnect-tree RRT (rt-RRT).

(b) Bounded uncertainty reconnect-tree RRT (BU-rt-RRT).

(c) Chance constrained reconnect-tree RRT with $\psi_s = 0.8$ and $\psi_p = 0.6$ (CC-rt-RRT (med.)).

(d) Chance constrained reconnect-tree RRT with $\psi_s = 0.99$ and $\psi_p = 0.95$ (CC-rt-RRT (low)).

Figure 7.3: Representative trajectory planning solutions for the BT needle channel planning problem under uncertainty in the conservative OAR sparing scenario (CO). Shown are the: convexified CTV_{HR} (grey), OARs (blue), and previously planned needle channels (gold). Uncertainty is indicated with dotted lines (bounded uncertainty), or ellipses (probabilistic uncertainty).

behaviour of trajectory planning in the simulated patient case. Despite that lowering the tolerated risk levels led to an increasingly constrained sampling space, the theoretical shortest trajectories remained feasible for the evaluated instances. The fourth initial condition, $\mathbf{x}^4_{0,\text{CO}}$, was associated with the maximum stepwise risk level for all planners due to its location proximal to the sigmoid. Nevertheless, this maximum risk level for a single step was below the lowest tolerated risk in the chance constrained approaches, i.e. $1 - \psi_s = 0.01$. The accumulated risks of exceeding OARs dose constraints were found to be roughly similar for the first and fourth trajectory, that were respectively in proximity to the bladder and sigmoid. Accumulated risk levels were in any case lower than the specified joint tolerated risk levels. Probabilistic feasibility was therefore for every generated trajectory maintained.

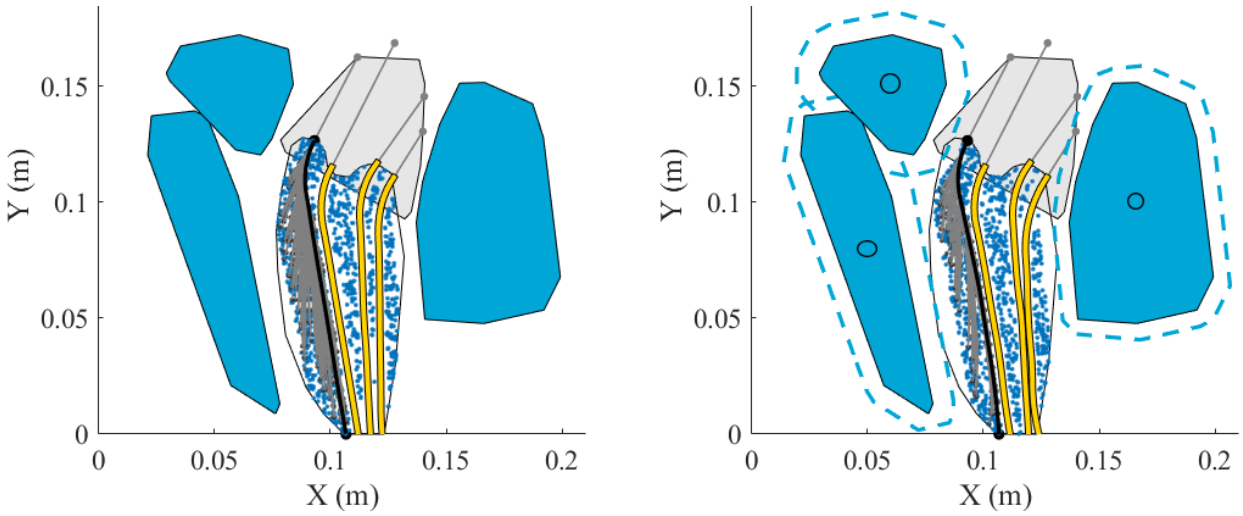

(a) reconnect-tree RRT (rt-RRT).

(b) Chance constrained reconnect-tree RRT with $\psi_s = 0.80$ and $\psi_p = 0.60$ (CC-rt-RRT (med.)).

Figure 7.4: Representative trajectory planning solutions for the BT needle channel planning problem under uncertainty for the nominal planning scenario (NP). Shown are the: convexified CTV_{HR} (grey), OARs (blue), and previously planned needle channels (gold). Uncertainty is indicated with dotted lines (bounded uncertainty), or ellipses (probabilistic uncertainty).

Total computation times for the generation of the four trajectories were different between all of the planning variants. BU-rt-RRT was generally the fastest, followed by rt-RRT, and CC-rt-RRT with low and medium tolerated risk levels. Whereas for nominal rt-RRT and BU-rt-RRT the computational times were relatively constant over the computation of individual trajectories, these drastically increased for CC-rt-RRT approaches. For example, whereas computation of the first trajectory took on average 95.7 ± 5.7 s, this increased to 436.8 ± 41.0 s for the fourth trajectory in CC-rt-RRT with low tolerated risk. Further analysis on the distribution of the running time for the programmed planners showed that in the chance constrained variants the minimum-cost and reconnect procedures scaled almost exponentially in time complexity with the number of needles. In other evaluated approaches, most of the computation time was spent on collision checking of the agent with OARs. Failure of the planner to find feasible trajectories occurred for the robust motion planners in 2/5 instances. Planning typically failed for the trajectory generated last, i.e. the trajectory generated from the starting pose furthest from the entry region and passing the sigmoid.

Nominal planning scenario (NP)

In the nominal planning scenario dwell segments were considered that achieved full spatial coverage of the target, whilst not exceeding the maximum tolerable stepwise risk at the initial states for trajectory planning. Similar to the conservative OAR sparing scenario, in the nominal planning scenario the rt-RRT and CC-rt-RRT algorithms generated near-shortest length trajectories that deviated at most 2% from theoretical lengths (Figure 7.4a and 7.4b). No differences in the trajectory lengths between the planners were observed. However, in this scenario, the accumulated risk for both planning approaches differed. Comparing Figure 7.4a and 7.4b it can be observed that, to maintain probabilistic feasibility, the chance constrained approach selected trajectories that were more distant to OARs than those generated with the rt-RRT approach. Whereas CC-rt-RRT generated trajectories that did not violate the specified joint chance constraints, i.e. $\Delta \leq 1 -$

$\psi_p = 0.40$, the standard rt-RRT algorithm yielded trajectories exceeding these limits (Table 7.3). In particular, note that proximal to the bladder, i.e. the rightmost obstacle, rt-RRT seemed to select trajectories of shortest length. Contrarily, near the bladder, CC-rt-RRT appeared to identify trajectories with greater curvature as to avoid the corresponding probabilistic uncertainty region. The resulting needle trajectories with CC-rt-RRT are slightly S-shaped, opposed to the concatenated circular arc and straight line segments generated with rt-RRT.

Dose-based evaluation

Results of the dose-based optimisation for the combined generated skew-line dwell segments and intracavitary needle channels are shown in Appendix A.8. The main findings are discussed here.

Conservative OAR sparing scenario (CO)
The intracavitary needle trajectories generated by the four motion planning variants in the CO scenario were almost identical near the target region. Therefore, the optimised dose distributions for the combined interstitial segments and intracavitary needle trajectories yielded virtually the same dosimetric indices (Table A.4). Generally, the set of generated shortest-length intracavitary channels enabled high dose constraint satisfaction as was indicated by the small value of the objective function. The CTV_{HR} $A_{100\%}$ was on average $99.1 \pm 0.1\%$ indicating near-optimal target coverage. Only in at most 0.7% of the calculation points in the sigmoid the optimised dose distribution exceeded the allowable doses; for other OARs the dose constraints were respected in all dose calculation points. The main contribution to the dose distribution came from dwell points in the tandem or interstitial segments. Roughly one-third of the total dwell time, 357.9 ± 0.66 s, was linked to dwell positions in the intracavitary curved channels, i.e. 113.4 ± 0.9 s. These dwell times optimised for the nominal contours were maintained, and the dosimetric indices were re-evaluated for worst-case positional uncertainty of OARs. No differences were found in the dosimetric indices of OARs subject to worst-case uncertainty between the set of trajectories generated by the four planning variants. Under the simplified worst-case assumption, the average $D_{2\%}$ of the bladder, rectum and sigmoid were respectively 8.0 ± 0.0 Gy, 2.1 ± 0.0 Gy and 8.1 ± 0.0 Gy. For the bladder and sigmoid the dose constraints were exceeded in $4.2 \pm 0.0\%$ and $8.5 \pm 0.0\%$ of the dose calculation points respectively, regardless of the planning method.

Nominal planning scenario (NP)
The trajectories generated by rt-RRT or CC-rt-RRT with medium risk toleration for the NP scenario yielded treatment plans of higher quality for nominal structures than those generated for the conservative OAR sparing scenario, i.e. $E = 0.03 \pm 0.00$ vs $E = 0.59 \pm 0.00$. Target coverage was adequate for the set of trajectories generated using rt-RRT or CC-rt-RRT. None of the dose constraints in individual calculation points of OARs were exceeded for sets of trajectories generated by either one of the two motion planners. In the trajectories resulting from the CC-rt-RRT approach the mean, maximum, and total dwell times, of dwell points in the intracavitary channels were on average higher than those obtained for the rt-RRT approach: 25.3 ± 0.0, 44.6 ± 0.2, and 75.9 ± 0.1 s respectively versus 17.4 ± 0.0, 36.7 ± 0.3, and 69.5 ± 0.2 s. The total dwell time of all active positions for rt-RRT and CC-rt-RRT instances remained similar, i.e. 292.0 ± 0.3 s and 297.6 ± 0.1 s. From visual inspection of Figure 7.5a and 7.5b, it seems that dose escalation in intracavitary dwell points near the bladder was required to cover the tumour extension in the chance constrained approach. Subsequently, dosimetric indices for both approaches in the nominal scenario or in a scenario assuming worst-case uncertainty were similar.

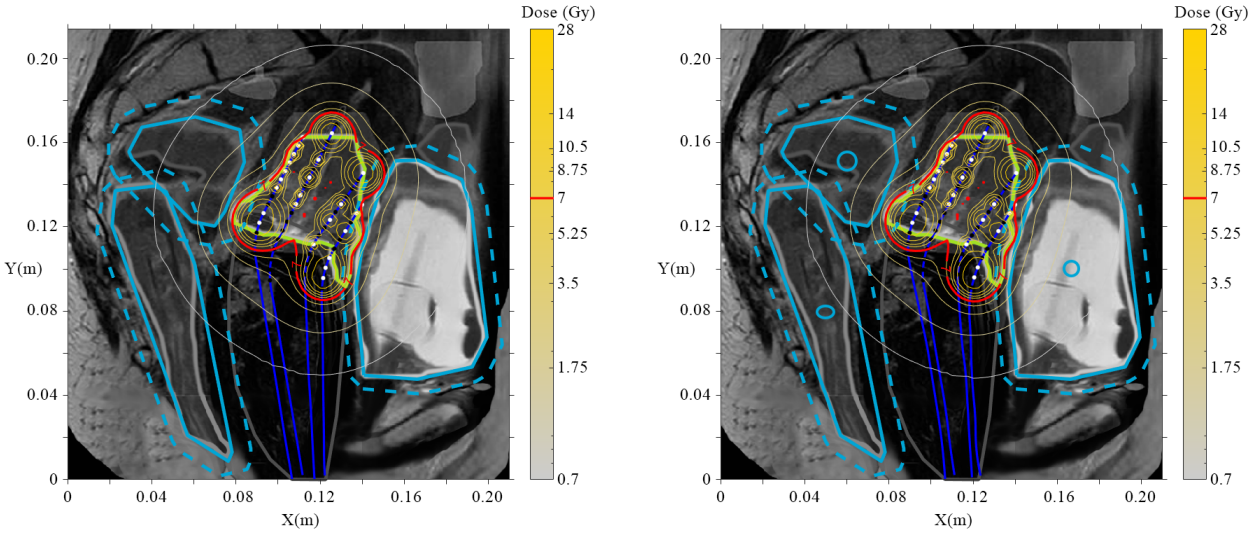

(a) reconnect-tree RRT (rt-RRT).

(b) Chance constrained reconnect-tree RRT with $\psi_s = 0.80$ and $\psi_p = 0.60$ (CC-rt-RRT (med.)).

Figure 7.5: Illustrations of the dose distributions calculated via the dose-based optimisation for combined interstitial dwell segments and intracavitary needle trajectories in the nominal planning scenario for a single patient case. An overview of the used symbols is given in Figure 7.2.

7.3.3 Discussion

This section presented the first implementation of robust MP algorithms for brachytherapy needle channel planning subject to uncertainty. A two-stage approach was proposed, where motion planning was initialised with the optimal set of straight-line interstitial dwell segments given by a coverage planning algorithm in either a conservative or nominal scenario. Curvature-constrained needle trajectories were planned sequentially from these initial poses towards an entry region with minimal trajectory length and/or risk. Two variants of rapidly-exploring random trees (RRTs), a sampling-based MP algorithm, were introduced that are able to compute non-intersecting curvature-constrained channels in the presence of bounded or probabilistic, i.e. Gaussian distributed, uncertainty. Performance of these algorithms on computational and operational criteria was evaluated against that of a nominal sampling-based MP algorithm in a single patient case study. Furthermore, dosimetric indices and other characteristics of the optimised treatment plans generated for the combined interstitial and intracavitary trajectories were compared for nominal and worst-case uncertainty contours of OARs.

General implementation of (robust) motion planning variants for BT

Previous sampling-based motion planning algorithms for computing intracavitary channels in brachytherapy applicators have similarly focused on the generation of curvature-constrained trajectories from straight dwell segments towards an entry region [88–90]. In the work by Patil et al. simultaneous trajectory optimisation of multiple needle trajectories was performed to generate locally optimal trajectories from RRT initialisation [89]. The latter is computationally intensive and relies on the quality and the homotopy class of the solutions returned by the RRT algorithm. Contrary to this two-stage approach, asymptotically optimal RRT variants for nonholonomic systems may be used to directly compute optimal trajectories, but require solving two-point BVPs. In this thesis, rt-RRT was introduced, based on the reconnect-tree procedure of the DT-RRT algorithm [372], and on the use of sampling in Euclidean space and reachability-guided search as suggested by Patil et al. [89]. This algorithm was shown to be able to efficiently

construct high quality trajectories approaching the theoretical optimum for a non-holonomic agent. Additionally, this algorithm maintains Voronoi bias to explore different homotopy classes. However, rt-RRT is not guaranteed to asymptotically converge to a globally (near-)optimal solution. RRT variants with asymptotic near-optimality guarantees, such as LBT-RRT or SST [369], may therefore be implemented in future work.

In previous sampling-based MP algorithms for BT needle channel planning the possibility of positioning dwell locations along the curved trajectories was not taken into account. As an introduction to an integrated approach where coverage planning and trajectory planning are combined, this work proposed simplifications to account for OAR dose constraints during trajectory planning. Dwell times were kept fixed over the entire trajectory, which leads to conservatism of the intracavitary trajectories. In this case study this was not necessarily detrimental for the planning results as the OARs were sufficiently distant from the theoretically shortest trajectories. Integrating approximate dwell time planning with trajectory planning to efficiently predict dwell times may reduce this conservatism for other instances. Moreover, previous BT needle channel planning algorithms neglect the presence of uncertainty in the environment. The bounded uncertainty and analytical chance constrained framework that was introduced for RRT by Luders et al. [258, 259], was leveraged in this thesis. The formulated BU-rt-RRT and CC-rt-RRT algorithms were able to generate guaranteed or probabilistically feasible trajectories by construction in presence of spatial uncertainty of OARs. However, both of these approaches are often overly conservative. To reduce conservatism, Patil et al. have therefore proposed an analytical approach in which probability distributions are truncated by assuming inter-dependence with collision probabilities of previous states [278]. Similar ideas can be used here to speed up the probabilistic feasibility checking. Of particular interest are also chance constrained approaches for moment-based ambiguity sets [280], since it is unclear whether spatial uncertainty of OARs can be accurately described by Gaussian distributions. One of the main qualities of the implemented bounded uncertainty or chance constrained framework for motion planning is that it can be extended to include different forms of uncertainty, e.g. in configuration knowledge. This may allow the addition of uncertainties in configuration knowledge such as source strength or source positioning.

In this thesis sequential planning of trajectories was considered. However, failure to generate trajectories occurred frequently, i.e. around 2/5 instances, in the narrow cluttered environment posed by the BT needle channel planning problem. Especially the construction of a feasible trajectory for the agent considered last proved to be difficult. To avoid ordering issues and to guarantee optimality of all trajectories, rt-RRT and robust variants must be made applicable for multi-agent systems. Postlethwaite and Kothari proposed a 'reactive' coordination strategy to sequentially resolve conflicts in a decentralised multi-agent chance constrained RRT approach [387]. To obtain a combined optimal solution for multiple cooperating agents and to preserve feasibility guarantees, however, it is of particular interest to extend the risk allocation concept to multi-agent systems and to implement an efficient decentralised optimisation approach for sampling-based motion planners [388].

Planning scenario and outcomes

In this section two planning scenarios were created to evaluate the motion planning variants. In the conservative OAR sparing scenario, no differences in trajectory length or risk between the trajectories generated by the motion planning variants were observed. Initial states for the trajectory planning were positioned at guaranteed feasible locations. Additionally, the initial

heading angles were constrained such that each trajectory initially diverged from the bounded uncertainty contours. These conservative assumptions ensured that the near-shortest length trajectories generally avoided infeasible regions or regions of higher uncertainty. All planning variants were therefore able to generate near-shortest length trajectories in this scenario with low maximum and accumulated risks, comparable to the optimal relaxed Dubins' curves. Accordingly, no differences were found in the treatment planning parameters or dosimetric indices of optimised dose distributions for these planning variants.

Of greater interest is the nominal planning scenario in which rt-RRT and CC-rt-RRT were implemented. It was shown in the patient case study that CC-rt-RRT was able to reduce trajectories' maximum and accumulated risk to below an a priori specified threshold. In particular, this approach generated trajectories that maintained larger distance to OARs. However, by accounting for spatial uncertainty of OARs, the dwell positions along these trajectories were also positioned less favourably to the extension of the target region in the simulated patient case. In the subsequent dose-based optimisation, this was associated with increased dwell times in the intracavitary channels to cover the tumour region sufficiently. Therefore, dosimetric indices for nominal contours were not improved in comparison with the treatment plans generated for trajectories computed with rt-RRT. In the robust treatment optimisation approach by Balvert et al., it has been similarly described that in some patients the target coverage reduced when accounting for uncertainty of the rectum contours [100]. This issue may be potentially resolved by including the accumulated negation probability of a state covering the target region in the objective function, which would serve as a counterpart to the probabilistic OAR avoidance component. Moreover, in this thesis only a simplified case study was considered using a sagittal image of a single patient case. Robust brachytherapy needle channel planning must be re-evaluated for three-dimensional treatment planning and a greater number of patients.

Implementation in clinical practice

Robust planning of needle channels for personalised applicators may have great potential to improve dose conformity of BT treatment. In the previous section it was shown that coverage planning of straight interstitial segments may enable treatment plans with higher dose conformity than for those generated in conventional applicators. The addition of dwell points in the curved intracavitary channels further improves this dose conformity. Although this thesis considered two-dimensional planning only, the extension to a three-dimensional case is trivial for the coverage planning and the nominal rt-RRT algorithms. The implementation of chance constrained programming for a three-dimensional environment is more complicated on the other hand. Even though the formulated polytopic representation of obstacles allows analytical chance constraints to still be used in a 3D environment, the computational complexity required to enable accurate OAR representation may make other representations, e.g. ellipsoidal obstacles, potentially more viable.

The runtime of the currently implemented RRT variants in the two-dimensional planning case in this thesis was too slow for clinical implementation. In the pilot study to determine the relative importance of user requirements (Section 5.3), RT specialists indicated that the time for generating the catheter trajectories should be on a seconds time scale. Especially for the CC-rt-RRT the convergence to a high quality solution in the currently described implementations of the motion planners was much slower (Table 7.3). However, this speed may be improved. Even with online deterministic parameter tightening, the original implementation of CC-RRT by Luders et al. was almost ten times faster per node [258]. The main computational bottleneck in the current implementation was the needle-needle collision checking, of which the time complexity

may be reduced by computing bounding volume hierarchies. Additionally, lazy collision checking strategies, reachability-guided sampling, and approximate nearest neighbour search (see Section 6.2) may all be implemented to reduce planning time. Lastly, the implementation in MATLAB, as it is an interpreter, may be less efficient than in alternatives.

Reproducibility of the generated channels was considered to be the most important property of the motion planning software in the user study in Section 5.3. In this thesis, similar to previous works, it has been assumed that a catheter that is forced through an intracavitary applicator channel behaves similar to a steerable needle, and can therefore be modelled as a unicycle-type system. However, this assumption must be validated, especially for channels with multiple bends in succession. Although in this section trajectories were generated that were composed of at most three segments, needle channel planning in a three-dimensional case may concern multiple complex bends with non-constant radii [89]. Mechanics-based models may be used to improve the accuracy of modelling catheter behaviour in channels. This may especially be useful for 3D-printed applicators in which material surface properties may increase friction, and thereby introduce positioning errors [48, 389]. For 3D-printed brachytherapy mould designs with 3.5 mm channel diameters, the reproducibility of 6F BT catheters was assessed to be on average 0.5 mm from CT rescanning [389]. This geometric uncertainty is similar to that of conventional afterloaders [205], and therefore does not limit applicability. Alternatively, needle trajectories may be represented with Gaussian state uncertainty in the chance constrained framework, or via Gaussian processes which naturally provide a concept of uncertainty [390, 391].

8. Conclusions and future work

Patient-tailored BT applicators can offer several advantages over conventional BT applicators in the treatment of locally advanced cervical cancer. However, automated needle channel planning required for these applicators is currently not capable of handling the spatial uncertainty that is posed by this complex planning environment. Uncertainty in BT treatment has been shown to significantly impact the delivered dose of both the target region and OARs and subsequently the occurrence of normal tissue complications. To account for these uncertainties, this study introduces the paradigm of robust patient-tailored applicator development in brachytherapy. Both the freedom of source placement that 3D-printed applicators allow and the principle of robust treatment optimisation are leveraged in this thesis to develop robust needle channel planning software for patient-tailored applicators. This thesis provides a theoretical framework for the development of robust planning software, which is possibly able to lead to treatment plans with greater dose conformity in future patient case series.

The first aim of this study was to provide an updated overview of dosimetric uncertainty components, estimate their clinical impact on brachytherapy for cervical cancer, and accordingly make a case for the implementation of robust planning software. Contouring uncertainty was established to be the largest individual contributor to dosimetric uncertainty of the primary tumour volume ($SD = 9.5\%,\ k = 1$). However, when it is assured that a high dose (>85 Gy EQD2) is delivered to the target region, the predicted occurrence of local control is rather robust against the reviewed uncertainties (<1.0% decrease). Inter and intra-fraction uncertainty were shown to be the main contributors to the delivered dose to OARs, increasing the delivered dose potentially up to $4.0 \pm 20\%$ ($k = 1$). These may realistically increase the occurrence of moderate to severe tissue morbidity of the bladder or rectum by respectively 1.5 and 3.7%. In the case of suboptimal dose conformity, the predicted occurrences increased up to 2.0 and 9.0% respectively. Contrarily to inter-fraction uncertainty which can be largely resolved through repeated imaging acquisition and treatment planning, intra-fraction uncertainty is almost inherent to treatment. Therefore, in this thesis geometric intra-fraction uncertainty was further investigated, converted into probabilistic and bounded uncertainty representations and cast into a motion planning (MP) problem. The formulation used in this thesis enables different forms of BT uncertainty to be represented in future work. As OAR motion patterns were ill-defined in literature and therefore had to be heavily simplified in this thesis, future studies could moreover focus on characterising critical structure movement in patient cohorts and individual patients.

This thesis secondly aimed to aid the decision-making process for the selection of a MP class from a set of alternatives given on a trivial problem formulation and a set of user requirements. The main contribution of this work was the development of a fully ordinal selection method, in a tool termed MP-QFD, which does not rely on arbitrary promotion of ordinal data, and minimises the subjectivity and arbitrariness conventionally associated with decision-making tools. The efficacy of this tool was illustrated for the BT needle channel planning problem. Using the results from a pilot study among nine medical specialists, the outcomes of this tool substantiated the preferred choice for an incremental sampling-based MP algorithm. Future work could potentially focus on integrating this tool in web-based applications and evaluating its role in the facilitation of cross-disciplinary collaboration between software engineers and end users.

Third and foremost, this thesis aimed to develop, implement and evaluate robust sampling-based algorithms for the BT needle channel planning problem under uncertainty. A two-stage approach was proposed consisting of coverage planning and robust trajectory planning. The main contributions of this part were the development of sampling-based MP variants capable of guaranteeing (probabilistic) feasibility of the trajectories generated for non-holonomic agents in environments subject to uncertainty. In a two-dimensional simulated patient case, it was shown that these planners were able to generate near-optimal needle channels that (probabilistically) guaranteed not exceeding OAR dose constraints. Subsequent dose-based optimisation showed that the dwell positions from combined coverage planning and (robust) trajectory planning could theoretically yield treatment plans with improved dose conformity over those generated for conventional applicators. Due to modelling assumptions, robust motion planning did not result in improved dose conformity over the nominal motion planning approach in a worst-case scenario. Future work should first validate the assumption that catheters that are forced through intracavitary applicator channel can be accurately modelled as a unicycle-type system. Moreover, the trajectory and coverage planning algorithms should be extended to include three-dimensional planning cases and runtimes should be improved for clinical implementation. Lastly, whether robust needle channel planning is able to improve the dose conformity in cervical cancer brachytherapy subject to uncertainty must be validated in a patient case series.

Bibliography

[1] Bray, F., Ferlay, J., Soerjomataram, I., Siegel, R. L., Torre, L. A., and Jemal, A. Global cancer statistics 2018: GLOBOCAN estimates of incidence and mortality worldwide for 36 cancers in 185 countries. *CA: A Cancer Journal for Clinicians*, 68(6):394–424, 2018.

[2] Franco, E. L., Duarte-Franco, E., and Ferenczy, A. Cervical cancer: epidemiology, prevention and the role of human papillomavirus infection. *Cmaj*, 164(7):1017–25, 2001.

[3] Cuzick, J., Arbyn, M., Sankaranarayanan, R., Tsu, V., Ronco, G., Mayrand, M. H., Dillner, J., and Meijer, C. J. Overview of Human Papillomavirus-Based and Other Novel Options for Cervical Cancer Screening in Developed and Developing Countries. *Vaccine*, 26:K29–K41, 2008.

[4] Kim, J. J., Brisson, M., Edmunds, W. J., and Goldie, S. J. Modeling Cervical Cancer Prevention in Developed Countries. *Vaccine*, 26:K76–K86, 2008.

[5] Levenback, C. F. Treatment of Early Cervical Cancer. In *Gynecologic Cancer*, chapter 9, pages 87–101. Springer, New York, NY, 2006.

[6] Barbera, L. and Thomas, G. Management of Early and Locally Advanced Cervical Cancer. *Seminars in Oncology*, 36(2):155–169, 2009.

[7] International Commission on Radiation Units and Measurements. *Report 89: Prescribing, Recording, and Reporting Brachytherapy for Cancer of the Cervix*, volume 13. Oxford University Press, 2016.

[8] Banerjee, R. and Kamrava, M. Brachytherapy in the treatment of cervical cancer: A review. *International Journal of Women's Health*, 6(1):555–564, 2014.

[9] Tanderup, K., Eifel, P. J., Yashar, C. M., Pötter, R., and Grigsby, P. W. Curative radiation therapy for locally advanced cervical cancer: Brachytherapy is NOT optional. *International Journal of Radiation Oncology Biology Physics*, 88(3):537–539, 2014.

[10] Viswanathan, A. N. and Thomadsen, B. American Brachytherapy Society consensus guidelines for locally advanced carcinoma of the cervix. Part I: General principles. *Brachytherapy*, 11 (1):33–46, 2012.

[11] Cibula, D., Pötter, R., Planchamp, F., Avall-Lundqvist, E., Fischerova, D., Haie Meder, C., Köhler, C., Landoni, F., Lax, S., Lindegaard, J. C., Mahantshetty, U., Mathevet, P., McCluggage, W. G., McCormack, M., Naik, R., Nout, R., Pignata, S., Ponce, J., Querleu, D., Raspagliesi, F., Rodolakis, A., Tamussino, K., Wimberger, P., and Raspollini, M. R. The European Society of Gynaecological Oncology/European Society for Radiotherapy and

Oncology/European Society of Pathology Guidelines for the Management of Patients With Cervical Cancer. *International Journal of Gynecological Cancer*, 28(4):641–655, 2018.

[12] Haie-Meder, C., Pötter, R., Van Limbergen, E., Briot, E., De Brabandere, M., Dimopoulos, J., Dumas, I., Hellebust, T. P., Kirisits, C., Lang, S., Muschitz, S., Nevinson, J., Nulens, A., Petrow, P., and Wachter-Gerstner, N. Recommendations from Gynaecological (GYN) GEC-ESTRO Working Group (I): Concepts and terms in 3D image based 3D treatment planning in cervix cancer brachytherapy with emphasis on MRI assessment of GTV and CTV. *Radiotherapy and Oncology*, 74(3):235–245, 2005.

[13] International Commission of Radiation Units and Measurements (ICRU). ICRU report no. 38: Dose and volume specification for reporting intracavitary therapy in gynecology. Technical report, ICRU, Bethesda, Maryland, 1985.

[14] Nag, S., Chao, C., Erickson, B., Fowler, J., Gupta, N., Martinez, A., and Thomadsen, B. The American Brachytherapy Society recommendations for low-dose-rate brachytherapy for carcinoma of the cervix. *International Journal of Radiation Oncology Biology Physics*, 52(1): 33–48, 2002.

[15] Uyeda, M., Friedrich, F., and Pellizzon, A. C. A. High dose rate (HDR) brachytherapy in gynecologic cancer regression: a review of the literature. *Applied Cancer Research*, 38(1):1–5, 2018.

[16] Stewart, A. J. and Viswanathan, A. N. Current controversies in high-dose-rate versus low-dose-rate brachytherapy for cervical cancer. *Cancer*, 107(5):908–915, 2006.

[17] Lee, L. J., Das, I. J., Higgins, S. A., Jhingran, A., Small, W., Thomadsen, B., Viswanathan, A. N., Wolfson, A., and Eifel, P. American Brachytherapy Society consensus guidelines for locally advanced carcinoma of the cervix. Part III: Low-dose-rate and pulsed-dose-rate brachytherapy. *Brachytherapy*, 11(1):53–57, 1 2012.

[18] Sadozye, A. H. and Reed, N. A review of recent developments in image-guided radiation therapy in cervix cancer. *Current Oncology Reports*, 14(6):519–526, 2012.

[19] Tanderup, K., Georg, D., Pötter, R., Kirisits, C., Grau, C., and Lindegaard, J. C. Adaptive Management of Cervical Cancer Radiotherapy. *Seminars in radiation oncology*, 20(2):121–129, 2010.

[20] Stewart, A. J. and Bentzen, S. M. Radiobiological aspects of brachytherapy in the era of 3-dimensional imaging. In Viswanathan, A. N., Kirisits, C., Erickson, B., and Pötter, R., editors, *Gynecologic Radiation Therapy*, pages 131–142. Springer, Berlin, Heidelberg., 2011.

[21] Lang, S., Nulens, A., Briot, E., Kirisits, C., De Brabandere, M., Dumas, I., Dimopoulos, J., Petrow, P., Georg, D., Van Limbergen, E., Haie-Meder, C., and Pötter, R. Intercomparison of treatment concepts for MR image assisted brachytherapy of cervical carcinoma based on GYN GEC-ESTRO recommendations. *Radiotherapy and Oncology*, 78(2):185–193, 2006.

[22] Pötter, R., Haie-Meder, C., Van Limbergen, E., Barillot, I., De Brabandere, M., Dimopoulos, J., Dumas, I., Erickson, B., Lang, S., Nulens, A., Petrow, P., Rownd, J., and Kirisits, C. Recommendations from gynaecological (GYN) GEC ESTRO working group (II): concepts and terms in 3D image-based treatment planning in cervix cancer brachytherapy—3D dose volume parameters and aspects of 3D image-based anatomy, radiation physics, radiobiology. *Radiotherapy and Oncology*, 78(1):67–77, 2006.

[23] Drzymala, R. E., Mohan, R., Brewster, L., Chu, J., Goitein, M., Harms, W., and Urie, M. Dose-volume histograms. *International Journal of Radiation Oncology, Biology, Physics*, 21 (1):71–78, 1991.

[24] Rivard, M. J., Venselaar, J. L., and Beaulieu, L. The evolution of brachytherapy treatment planning. *Medical Physics*, 36(6):2136–2153, 2009.

[25] DeWerd, L. A., Ibbott, G. S., Meigooni, A. S., Mitch, M. G., Rivard, M. J., Stump, K. E., Thomadsen, B. R., and Venselaar, J. L. A dosimetric uncertainty analysis for photon-emitting brachytherapy sources: Report of AAPM Task Group No. 138 and GEC-ESTRO. *Medical Physics*, 38(2):782–801, 2011.

[26] ESTRO. Ir-192 HDR sources, 2020. URL https://www.estro.org/About/ESTRO-Organisation-Structure/Committees/GEC-ESTRO-Committee/GEC-ESTRO-BRAPHYQS/Ir-192-HDR.

[27] Pötter, R., Dimopoulos, J., Georg, P., Lang, S., Waldhäusl, C., Wachter-Gerstner, N., Weitmann, H., Reinthaller, A., Knocke, T. H., Wachter, S., and Kirisits, C. Clinical impact of MRI assisted dose volume adaptation and dose escalation in brachytherapy of locally advanced cervix cancer. *Radiotherapy and Oncology*, 83(2):148–155, 2007.

[28] Pötter, R., Georg, P., Dimopoulos, J. C., Grimm, M., Berger, D., Nesvacil, N., Georg, D., Schmid, M. P., Reinthaller, A., Sturdza, A., and Kirisits, C. Clinical outcome of protocol based image (MRI) guided adaptive brachytherapy combined with 3D conformal radiotherapy with or without chemotherapy in patients with locally advanced cervical cancer. *Radiotherapy and Oncology*, 100(1):116–123, 2011.

[29] Sturdza, A., Pötter, R., Fokdal, L. U., Haie-Meder, C., Tan, L. T., Mazeron, R., Petric, P., Šegedin, B., Jurgenliemk-Schulz, I. M., Nomden, C., Gillham, C., McArdle, O., Van Limbergen, E., Janssen, H., Hoskin, P., Lowe, G., Tharavichitkul, E., Villafranca, E., Mahantshetty, U., Georg, P., Kirchheiner, K., Kirisits, C., Tanderup, K., and Lindegaard, J. C. Image guided brachytherapy in locally advanced cervical cancer: Improved pelvic control and survival in RetroEMBRACE, a multicenter cohort study. *Radiotherapy and Oncology*, 120(3):428–433, 2016.

[30] Fokdal, L., Pötter, R., Kirchheiner, K., Lindegaard, J. C., Jensen, N. B. K., Kirisits, C., Chargari, C., Mahantshetty, U., Jürgenliemk-Schulz, I. M., Segedin, B., Hoskin, P., and Tanderup, K. Physician assessed and patient reported urinary morbidity after radio-chemotherapy and image guided adaptive brachytherapy for locally advanced cervical cancer. *Radiotherapy and Oncology*, 127(3):423–430, 2018.

[31] van Leeuwen, C. M., Oei, A. L., Crezee, J., Bel, A., Franken, N. A., Stalpers, L. J., and Kok, H. P. The alfa and beta of tumours: A review of parameters of the linear-quadratic model, derived from clinical radiotherapy studies. *Radiation Oncology*, 13(1):1–11, 2018.

[32] Bentzen, S. M. Dose-response relationships in radiotherapy. In Joiner, M. C. and van der Kogel, A., editors, *Basic clinical radiobiology*, chapter 5, pages 56–66. Hodder Arnold, London, UK, 2009.

[33] Jones, B. and Dale, R. G. The reduction of tumour control with increasing overall time: Mathematical considerations. *British Journal of Radiology*, 69(825):830–838, 1996.

[34] Jones, B. and Dale, R. G. Mathematical models of tumour and normal tissue response. *Acta Oncologica*, 38(7):883–893, 1999.

[35] IAEA. Accuracy Requirements and Uncertainties in Radiotherapy. Technical report, IAEA, Vienna, 2016.

[36] Okunieff, P., Morgan, D., Niemierko, A., and Suit, H. D. Radiation dose-response of human tumors. *International Journal of Radiation Oncology, Biology, Physics*, 32(4):1227–1237, 1995.

[37] Bentzen, S. M. and Tucker, S. L. Quantifying the position and steepness of radiation dose-response curves. *International Journal of Radiation Biology*, 71(5):531–542, 1997.

[38] Nesvacil, N., Tanderup, K., Lindegaard, J. C., Pötter, R., and Kirisits, C. Can reduction of uncertainties in cervix cancer brachytherapy potentially improve clinical outcome? *Radiotherapy and Oncology*, 120(3):390–396, 2016.

[39] Tanderup, K., Nielsen, S. K., Nyvang, G. B., Pedersen, E. M., Røhl, L., Aagaard, T., Fokdal, L., and Lindegaard, J. C. From point A to the sculpted pear: MR image guidance significantly improves tumour dose and sparing of organs at risk in brachytherapy of cervical cancer. *Radiotherapy and Oncology*, 94(2):173–180, 2010.

[40] Srivastava, A. and Datta, N. R. Brachytherapy in cancer cervix: Time to move ahead from point A? *World J Clin Oncol*, 5(4):764–777, 2014.

[41] Vinod, S. K., Caldwell, K., Lau, A., and Fowler, A. R. A comparison of ICRU point doses and volumetric doses of organs at risk (OARs) in brachytherapy for cervical cancer. *Journal of Medical Imaging and Radiation Oncology*, 55(3):304–310, 2011.

[42] Mazeron, R., Kamsu Kom, L., Rivin del Campo, E., Dumas, I., Farha, G., Champoudry, J., Chargari, C., Martinetti, F., Lefkopoulos, D., and Haie-Meder, C. Comparison between the ICRU rectal point and modern volumetric parameters in brachytherapy for locally advanced cervical cancer. *Cancer/Radiothérapie*, 18(3):177–182, 2014.

[43] Dimopoulos, J. C., Lang, S., Kirisits, C., Fidarova, E. F., Berger, D., Georg, P., Dörr, W., and Pötter, R. Dose-Volume Histogram Parameters and Local Tumor Control in Magnetic Resonance Image-Guided Cervical Cancer Brachytherapy. *International Journal of Radiation Oncology Biology Physics*, 75(1):56–63, 2009.

[44] Dimopoulos, J. C., Pötter, R., Lang, S., Fidarova, E., Georg, P., Dörr, W., and Kirisits, C. Dose-effect relationship for local control of cervical cancer by magnetic resonance image-guided brachytherapy. *Radiotherapy and Oncology*, 93(2):311–315, 2009.

[45] Pötter, R., Kirisits, C., Fidarova, E. F., Dimopoulos, J. C., Berger, D., Tanderup, K., and Lindegaard, J. C. Present status and future of high-precision image guided adaptive brachytherapy for cervix carcinoma. *Acta Oncologica*, 47(7):1325–1336, 2008.

[46] Schmid, M. P., Kirisits, C., Nesvacil, N., Dimopoulos, J. C., Berger, D., and Pötter, R. Local recurrences in cervical cancer patients in the setting of image-guided brachytherapy: A comparison of spatial dose distribution within a matched-pair analysis. *Radiotherapy and Oncology*, 100(3):468–472, 2011.

[47] Gill, B. S., Kim, H., Houser, C. J., Kelley, J. L., Sukumvanich, P., Edwards, R. P., Comerci, J. T., Olawaiye, A. B., Huang, M., Courtney-Brooks, M., and Beriwal, S. MRI-guided high-dose-rate intracavitary brachytherapy for treatment of cervical cancer: The university of Pittsburgh experience. *International Journal of Radiation Oncology Biology Physics*, 91(3): 540–547, 2015.

[48] Laan, R. C., Nout, R. A., Dankelman, J., and van de Berg, N. J. MRI-driven design of customised 3D printed gynaecological brachytherapy applicators with curved needle channels. *3D Printing in Medicine*, 5(1), 2019.

[49] Kim, R. Y., Shen, S., and Duan, J. Image-based three-dimensional treatment planning of intracavitary brachytherapy for cancer of the cervix: Dose-volume histograms of the bladder, rectum, sigmoid colon, and small bowel. *Brachytherapy*, 6(3):187–194, 2007.

[50] Pötter, R., Tanderup, K., Kirisits, C., de Leeuw, A., Kirchheiner, K., Nout, R., Tan, L. T., Haie-Meder, C., Mahantshetty, U., Segedin, B., Hoskin, P., Bruheim, K., Rai, B., Huang, F., Van Limbergen, E., Schmid, M., Nesvacil, N., Sturdza, A., Fokdal, L., Jensen, N. B. K., Georg, D., Assenholt, M., Seppenwoolde, Y., Nomden, C., Fortin, I., Chopra, S., van der Heide, U., Rumpold, T., Lindegaard, J. C., and Jürgenliemk-Schulz, I. The EMBRACE II study: The outcome and prospect of two decades of evolution within the GEC-ESTRO GYN working group and the EMBRACE studies. *Clinical and Translational Radiation Oncology*, 9:48–60, 2018.

[51] Nomden, C. N., De Leeuw, A. A., Moerland, M. A., Roesink, J. M., Tersteeg, R. J., and Jürgenliemk-Schulz, I. M. Clinical use of the Utrecht applicator for combined intracavitary/ interstitial brachytherapy treatment in locally advanced cervical cancer. *International Journal of Radiation Oncology Biology Physics*, 82(4):1424–1430, 2012.

[52] Castelnau-Marchand, P., Chargari, C., Maroun, P., Dumas, I., Del Campo, E. R., Cao, K., Petit, C., Martinetti, F., Tafo-Guemnie, A., Lefkopoulos, D., Morice, P., Haie-Meder, C., and Mazeron, R. Clinical outcomes of definitive chemoradiation followed by intracavitary pulsed-dose rate image-guided adaptive brachytherapy in locally advanced cervical cancer. *Gynecologic Oncology*, 139(2):288–294, 2015.

[53] Kang, H. C., Shin, K. H., Park, S. Y., and Kim, J. Y. 3D CT-based high-dose-rate brachytherapy for cervical cancer: Clinical impact on late rectal bleeding and local control. *Radiotherapy and Oncology*, 97(3):507–513, 2010.

[54] Ohno, T., Noda, S. E., Okonogi, N., Murata, K., Shibuya, K., Kiyohara, H., Tamaki, T., Ando, K., Oike, T., Ohkubo, Y., Wakatsuki, M., Saitoh, J. I., and Nakano, T. In-room computed tomography-based brachytherapy for uterine cervical cancer: Results of a 5-year retrospective study. *Journal of Radiation Research*, 58(4):543–551, 2017.

[55] Ribeiro, I., Janssen, H., De Brabandere, M., Nulens, A., De Bal, D., Vergote, I., and Van Limbergen, E. Long term experience with 3D image guided brachytherapy and clinical outcome in cervical cancer patients. *Radiotherapy and Oncology*, 120(3):447–454, 2016.

[56] Lindegaard, J. C., Fokdal, L. U., Nielsen, S. K., Juul-Christensen, J., and Tanderup, K. MRI-guided adaptive radiotherapy in locally advanced cervical cancer from a Nordic perspective. *Acta Oncologica*, 52(7):1510–1519, 2013.

[57] Charra-Brunaud, C., Harter, V., Delannes, M., Haie-Meder, C., Quetin, P., Kerr, C., Castelain, B., Thomas, L., and Peiffert, D. Impact of 3D image-based PDR brachytherapy on outcome of patients treated for cervix carcinoma in France: Results of the French STIC prospective study. *Radiotherapy and Oncology*, 103(3):305–313, 2012.

[58] Derks, K., Steenhuijsen, J. L., Van Den Berg, H. A., Houterman, S., Cnossen, J., Van Haaren, P., and De Jaeger, K. Impact of brachytherapy technique (2D versus 3D) on outcome following radiotherapy of cervical cancer. *Journal of Contemporary Brachytherapy*, 10(1):17–25, 2018.

[59] Schmid, M. P., Fidarova, E., Pötter, R., Petric, P., Bauer, V., Woehs, V., Georg, P., Kirchheiner, K., Berger, D., Kirisits, C., Dörr, W., and Dimopoulos, J. C. Magnetic resonance imaging for assessment of parametrial tumour spread and regression patterns in adaptive cervix cancer radiotherapy. *Acta Oncologica*, 52(7):1384–1390, 2013.

[60] Jastaniyah, N., Yoshida, K., Tanderup, K., Lindegaard, J. C., Sturdza, A., Kirisits, C., Šegedin, B., Mahantshetty, U., Rai, B., Jürgenliemk-Schulz, I. M., Haie-Meder, C., Banerjee, S., and Pötter, R. A volumetric analysis of GTVD and CTVHR as defined by the GEC ESTRO recommendations in FIGO stage IIB and IIIB cervical cancer patients treated with IGABT in a prospective multicentric trial (EMBRACE). *Radiotherapy and Oncology*, 120(3): 404–411, 2016.

[61] Villafranca, E., Navarrete, P., Sola, A., Muruzabal, J. C., Aguirre, S., Ostiz, S., Sanchez, C., Guarch, R., Lainez, N., and Barrado, M. Image-guided brachytherapy in cervical cancer: Experience in the Complejo Hospitalario de Navarra. *Reports of Practical Oncology and Radiotherapy*, 23(6):510–516, 2018.

[62] Tiwari, R., Narayanan, G. S., Jayakumar, V., Narayanan, S., Vishwanathan, B., Mandal, S. K., Babu, S., Ramya, V., and George, D. The promise of image-guided brachytherapy of better clinical outcomes in treatment of cervical cancer: Does it deliver? An Indian scenario. *Gynecologic Oncology*, 150(3):420–425, 2018.

[63] Rijkmans, E. C., Nout, R. A., Rutten, I. H., Ketelaars, M., Neelis, K. J., Laman, M. S., Coen, V. L., Gaarenstroom, K. N., Kroep, J. R., and Creutzberg, C. L. Improved survival of patients with cervical cancer treated with image-guided brachytherapy compared with conventional brachytherapy. *Gynecologic Oncology*, 135(2):231–238, 2014.

[64] Kirchheiner, K., Nout, R. A., Tanderup, K., Lindegaard, J. C., Westerveld, H., Haie-Meder, C., Petrič, P., Mahantshetty, U., Dörr, W., and Pötter, R. Manifestation pattern of early-late vaginal morbidity after definitive radiation (Chemo)therapy and image-guided adaptive brachytherapy for locally advanced cervical cancer: An analysis from the embrace study. *International Journal of Radiation Oncology Biology Physics*, 89(1):88–95, 2014.

[65] Kirchheiner, K., Pötter, R., Tanderup, K., Lindegaard, J. C., Haie-Meder, C., Petrič, P., Mahantshetty, U., Jürgenliemk-Schulz, I. M., Rai, B., Cooper, R., Dörr, W., Nout, R. A., Fokdal, L., Van Der Steen Banasik, E., Dumas, I., Chargari, C., Van Limbergen, E., Segedin, B., Hudej, R., Erickson, B., Hoskin, P., Lowe, G., Swamidas, J., Shrivastava, S. K., De Leeuw, A., Lutgens, L. C., Hadjiev, J., Bownes, P., Sundset, M., Bruheim, K., Hellebust, T. P., Huang, F., Menon, G., Villafranca, E., Oinam, A. S., Tan, L. T., Bachand, F., Jacobson, G., Anttila, M., and Pieters, B. Health-Related Quality of Life in Locally Advanced Cervical Cancer Patients after Definitive Chemoradiation Therapy Including Image Guided Adaptive

Brachytherapy: An Analysis from the EMBRACE Study. *International Journal of Radiation Oncology Biology Physics*, 94(5):1088–1098, 2016.

[66] Hsu, I. C. J., Speight, J., Hai, J., Vigneault, E., Phillips, T., and Pouliot, J. A comparison between tandem and ovoids and interstitial gynecologic template brachytherapy dosimetry using a hypothetical computer model. *International Journal of Radiation Oncology Biology Physics*, 52(2):538–543, 2002.

[67] Bansal, A. K., Semwal, M. K., Sharma, D. N., Thulkar, S., Julka, P. K., and Rath, G. K. A patient-based dosimetric study of intracavitary and interstitial brachytherapy in advanced stage carcinoma of the cervix. *Journal of Applied Clinical Medical Physics*, 15(3):63–70, 2014.

[68] Rangarajan, R. Incidence of Suboptimal Applicator Placement and the Resulting Dosimetric Impact in Image-Based Intracavitary Brachytherapy. *Journal of Medical Physics*, 43(3):168–172, 2018.

[69] Ma, J. K., Mourad, W. F., Allbright, R., Packianathan, S., Harrell, L. M., Chinchar, E., Nguyen, A., and Vijayakumar, S. Short-term clinical outcome and dosimetric comparison of tandem and ring versus tandem and ovoids intracavitary applicators. *Journal of Contemporary Brachytherapy*, 7(3):218–223, 2015.

[70] Rogelj, P. and Barakovic, M. Cervix Cancer Spatial Modelling for Brachytherapy Applicator Analysis. *Informatica*, 39:261–269, 2015.

[71] Elekta. Brachytherapy Applicators and Accessoiries. Technical report, 2017.

[72] Bansal, I., Panda, D., Rathi, A., Anand, A., and Bansal, A. Rationale, indications, techniques and applications of interstitial brachytherapy for carcinoma cervix. *Asian Journal of Oncology*, 02(02):069–078, 2016.

[73] Nomden, C. N. *Radiotherapy of advanced cervical cancer: Impact of MRI guidance on brachytherapy*. PhD thesis, Utrecht University, 2015.

[74] Mendez, L. C., Weiss, Y., D'Souza, D., Ravi, A., Barbera, L., and Leung, E. Three-dimensional-guided perineal-based interstitial brachytherapy in cervical cancer: A systematic review of technique, local control and toxicities. *Radiotherapy and Oncology*, 123(2):312–318, 2017.

[75] Yoshida, K., Yamazaki, H., Kotsuma, T., Takenaka, T., Ueda, M. M., Miyake, S., Tsujimoto, Y., Masui, K., Yoshioka, Y., Sumida, I., Uesugi, Y., Shimbo, T., Yoshikawa, N., Yoshioka, H., Tanaka, E., and Narumi, Y. Simulation analysis of optimized brachytherapy for uterine cervical cancer: Can we select the best brachytherapy modality depending on tumor size? *Brachytherapy*, 15(1):57–64, 2016.

[76] Mikami, M., Yoshida, K., Takenaka, T., Yamazaki, H., Kotsuma, T., Yoshida, M., Aramoto, K., Yamada, S., Ban, C., Tanaka, E., and Honda, K. Daily computed tomography measurement of needle applicator displacement during high-dose-rate interstitial brachytherapy for previously untreated uterine cervical cancer. *Brachytherapy*, 10(4):318–324, 2011.

[77] Damato, A. L., Cormack, R. A., and Viswanathan, A. N. Characterization of implant displacement and deformation in gynecologic interstitial brachytherapy. *Brachytherapy*, 13 (1):100–109, 2014.

[78] Fokdal, L., Sturdza, A., Mazeron, R., Haie-Meder, C., Tan, L. T., Gillham, C., Šegedin, B., Jürgenliemk-Schultz, I., Kirisits, C., Hoskin, P., Pötter, R., Lindegaard, J. C., and Tanderup, K. Image guided adaptive brachytherapy with combined intracavitary and interstitial technique improves the therapeutic ratio in locally advanced cervical cancer: Analysis from the retroEMBRACE study. *Radiotherapy and Oncology*, 120(3):434–440, 2016.

[79] Kirisits, C., Lang, S., Dimopoulos, J., Berger, D., Georg, D., and Pötter, R. The Vienna applicator for combined intracavitary and interstitial brachytherapy of cervical cancer: Design, application, treatment planning, and dosimetric results. *International Journal of Radiation Oncology Biology Physics*, 65(2):624–630, 2006.

[80] Berger, D., Pötter, R., Dimopoulos, J. C., and Kirisits, C. New Vienna Applicator Design for Distal Parametrial Disease in Cervical Cancer. *Brachytherapy*, 9(2010):S51–S52, 2010.

[81] Walter, F., Maih, C., Sch, L., Well, J., Burges, A., Ertl-wagner, B., Mahner, S., Belka, C., Gallwas, J., and Corradini, S. Combined intracavitary and interstitial brachytherapy of cervical cancer using the novel hybrid applicator Venezia : Clinical feasibility and initial results. *Brachytherapy*, 17(5):775–781, 2018.

[82] Fokdal, L., Tanderup, K., Hokland, S. B., Røhl, L., Pedersen, E. M., Nielsen, S. K., Paludan, M., and Lindegaard, J. C. Clinical feasibility of combined intracavitary/interstitial brachytherapy in locally advanced cervical cancer employing MRI with a tandem/ring applicator in situ and virtual preplanning of the interstitial component. *Radiotherapy and Oncology*, 107(1):63–68, 2013.

[83] Mahantshetty, U., Sturdza, A., Naga CH, P., Berger, D., Fortin, I., Motisi, L., Schmid, M. P., Aravindakshan, D., Ghadi, Y., Swamidas, J. V., Chopra, S., Gurram, L., Nesvacil, N., Kirisits, C., and Pötter, R. Vienna-II ring applicator for distal parametrial/pelvic wall disease in cervical cancer brachytherapy: An experience from two institutions: Clinical feasibility and outcome. *Radiotherapy and Oncology*, 141:123–129, 2019.

[84] Petric, P., Hudej, R., Rogelj, P., Lindegaard, J., Tanderup, K., Kirisits, C., Berger, D., Dimopoulos, J., and Pötter, R. 54 oral: Frequency-Distribution Mapping of HR-CTV in Locally Advanced Cervix Cancer: A New Tool for Development of Novel Brachytherapy Techniques. *Radiotherapy and Oncology*, 91:S18–S19, 2009.

[85] Serban, M., Kirisits, C., de Leeuw, A., Pötter, R., Jürgenliemk-Schulz, I., Nesvacil, N., Swamidas, J., Hudej, R., Lowe, G., Hellebust, T. P., Menon, G., Oinam, A., Bownes, P., Oosterveld, B., De Brabandere, M., Koedooder, K., Langeland Marthinsen, A. B., Whitney, D., Lindegaard, J., and Tanderup, K. Ring Versus Ovoids and Intracavitary Versus Intracavitary-Interstitial Applicators in Cervical Cancer Brachytherapy: Results From the EMBRACE I Study. *International Journal of Radiation Oncology Biology Physics*, 2020.

[86] Magné, N., Chargari, C., SanFilippo, N., Messai, T., Gerbaulet, A., and Haie-Meder Christine, C. Technical aspects and perspectives of the vaginal mold applicator for brachytherapy of gynecologic malignancies. *Brachytherapy*, 9(3):274–277, 2010.

[87] Wiebe, E., Easton, H., Thomas, G., Barbera, L., D'Alimonte, L., and Ravi, A. Customized vaginal vault brachytherapy with computed tomography imaging-derived applicator prototyping. *Brachytherapy*, 14(3):380–384, 2015.

[88] Garg, A., Patil, S., Siauw, T., Cunha, J. A. M., Hsu, I. C., Abbeel, P., Pouliot, J., and Goldberg, K. An algorithm for computing customized 3D printed implants with curvature constrained channels for enhancing intracavitary brachytherapy radiation delivery. In *IEEE International Conference on Automation Science and Engineering*, number August 2013, pages 466–473. IEEE, 2013.

[89] Patil, S., Pan, J., Abbeel, P., and Goldberg, K. Planning Curvature and Torsion Constrained Ribbons in 3D with Application to Intracavitary Brachytherapy. *IEEE Transactions on Automation Science and Engineering*, 12(4):1332–1345, 2015.

[90] Duan, Y., Patil, S., Schulman, J., Goldberg, K., and Abbeel, P. Planning locally optimal, curvature-constrained Trajectories in 3D using sequential convex optimization. In *Proceedings - IEEE International Conference on Robotics and Automation*, pages 5889–5895. IEEE, 2014.

[91] Sethi, R., Cunha, A., Mellis, K., Siauw, T., Diederich, C., Pouliot, J., and Hsu, I. C. Clinical applications of custom-made vaginal cylinders constructed using three-dimensional printing technology. *Journal of Contemporary Brachytherapy*, 8(3):208–214, 2016.

[92] Zhao, Z., Tang, X., Mao, Z., and Zhao, H. The design of an individualized cylindrical vaginal applicator with oblique guide holes using 3D modeling and printing technologies. *Journal of Contemporary Brachytherapy*, 11(5):479–487, 2019.

[93] Zhang, D., Yang, Z., Shan, J., Zhou, Z., and Wang, W. Individualized and inverse optimized needle configuration for combined intracavitary-interstitial brachytherapy in locally advanced cervical cancer. *Journal of Cancer Research and Therapeutics*, 15(7):1589–1596, 2019.

[94] Lindegaard, J. C., Madsen, M. L., Traberg, A., Meisner, B., Nielsen, S. K., Tanderup, K., Spejlborg, H., Fokdal, L. U., and Nørrevang, O. Individualised 3D printed vaginal template for MRI guided brachytherapy in locally advanced cervical cancer. *Radiotherapy and Oncology*, 118(1):173–175, 2016.

[95] Logar, H. B. Z., Hudej, R., and Šegedin, B. Development and assessment of 3D-printed individual applicators in gynecological MRI-guided brachytherapy. *Journal of Contemporary Brachytherapy*, 11(2):128–136, 2019.

[96] Skinner, L., Niedermayr, T., Fahimian, B., Prionas, N., Perl, J., and Kidd, E. Directionally Modulated Ir-192 Brachytherapy Using Simple 3D Printed Shielded Applicators. *Brachytherapy*, 18(3):S91–S92, 2019.

[97] Yuan, X., Zhang, Y., Cui, M., Miao, J., Gao, L., Hu, J., Tian, D., and You, J. Dosimetry comparison between a 3D printed minimally invasive guidance template and free implantation in the brachytherapy treatment of postoperative recurrent cervical carcinoma. *Cancer Management and Research*, 11:5013–5018, 2019.

[98] Kirisits, C., Rivard, M. J., Baltas, D., Ballester, F., De Brabandere, M., Van Der Laarse, R., Niatsetski, Y., Papagiannis, P., Hellebust, T. P., Perez-Calatayud, J., Tanderup, K., Venselaar, J. L., and Siebert, F. A. Review of clinical brachytherapy uncertainties: Analysis guidelines of GEC-ESTRO and the AAPM. *Radiotherapy and Oncology*, 110(1):199–212, 2014.

[99] Tanderup, K., Nesvacil, N., Pötter, R., and Kirisits, C. Uncertainties in image guided adaptive cervix cancer brachytherapy: Impact on planning and prescription. *Radiotherapy and Oncology*, 107(1):1–5, 2013.

[100] Balvert, M., Den Hertog, D., and Hoffmann, A. L. Robust optimization of dose-volume metrics for prostate HDR-brachytherapy incorporating target and oar volume delineation uncertainties. *INFORMS Journal on Computing*, 31(1):100–114, 2019.

[101] Van Herk, M. Errors and Margins in Radiotherapy. *Seminars in Radiation Oncology*, 14(1): 52–64, 2004.

[102] Yartsev, S. and Bauman, G. Target margins in radiotherapy of prostate cancer. *British Journal of Radiology*, 89(1067):1–12, 2016.

[103] Ahmad, R., Bondar, L., Voet, P., Mens, J. W., Quint, S., Dhawtal, G., Heijmen, B., and Hoogeman, M. A margin-of-the-day online adaptive intensity-modulated radiotherapy strategy for cervical cancer provides superior treatment accuracy compared to clinically recommended margins: A dosimetric evaluation. *Acta Oncologica*, 52(7):1430–1436, 2013.

[104] Bohoslavsky, R., Witte, M. G., Janssen, T. M., and Van Herk, M. Probabilistic objective functions for margin-less IMRT planning. *Physics in Medicine and Biology*, 58(11):3563–3580, 2013.

[105] Gorissen, B. L., Den Hertog, D., and Hoffmann, A. L. Mixed integer programming improves comprehensibility and plan quality in inverse optimization of prostate HDR brachytherapy. *Physics in Medicine and Biology*, 58(4):1041–1057, 2013.

[106] Jo, B., Park, K., Kim, K. H., Shin, D., Lim, Y. K., Jeong, J. H., Lee, S. B., Kim, H.-j., and Kim, H. Robust Optimization to Reduce Dose Delivery Uncertainty by Potential Applicator Displacements for a Cervix Brachytherapy. 2020.

[107] Van der Meer, M. C., Pieters, B. R., Niatsetski, Y., Alderliesten, T., Bel, A., and Bosman, P. A. N. Better and Faster Catheter Position Optimization in HDR Brachytherapy for Prostate Cancer using Multi-Objective Real-Valued GOMEA. In *Proceedings of the Genetic and Evolutionary Computation Conference*, pages 1387–1394, 2018.

[108] Van der Meer, M. C., Bel, A., Niatsetski, Y., Alderliesten, T., Pieters, B. R., and Bosman, P. A. N. Robust Evolutionary Bi-objective Optimization for Prostate Cancer Treatment with High-Dose-Rate Brachytherapy. In *International Conference on Parallel Problem Solving from Nature*, pages 441–453. Springer, 2020.

[109] Jo, B., Park, K., Kim, K. H., Shin, D., Lim, Y. K., Jeong, J. H., Lee, S. B., Kim, H.-j., and Kim, H. Robust Optimization to Reduce Dose Delivery Uncertainty by Potential Applicator Displacements for a Cervix Brachytherapy. 2020.

[110] Petric, P., Hudej, R., Al-Hammadi, N., and Segedin, B. Virtual modelling of novel applicator prototypes for cervical cancer brachytherapy. *Radiology and Oncology*, 50(4):433–441, 2016.

[111] Nesvacil, N., Tanderup, K., Hellebust, T. P., De Leeuw, A., Lang, S., Mohamed, S., Jamema, S. V., Anderson, C., Pötter, R., and Kirisits, C. A multicentre comparison of the dosimetric impact of inter- and intra-fractional anatomical variations in fractionated cervix cancer brachytherapy. *Radiotherapy and Oncology*, 107(1):20–25, 2013.

[112] Dimopoulos, J. C., Schirl, G., Baldinger, A., Helbich, T. H., and Pötter, R. MRI assessment of cervical cancer for adaptive radiotherapy. *Strahlentherapie und Onkologie*, 185(5):282–287, 2009.

[113] van Dyk, S., Kondalsamy-Chennakesavan, S., Schneider, M., Bernshaw, D., and Narayan, K. Assessing changes to the brachytherapy target for cervical cancer using a single MRI and serial ultrasound. *Brachytherapy*, 14(6):889–897, 2015.

[114] Gerbaulet, A., Pötter, R., and Haie-Meder, C. Cervix cancer. In Gerbaulet, A., Pötter, R., Mazeron, J., Meertens, H., and Van Limbergen, E., editors, *The GEC ESTRO Handbook of Brachytherapy*, pages 301–363. ACCO, Leuven, Belgium, 2002.

[115] Van Dyk, J., Battista, J. J., and Baumann, G. S. Accuracy and Uncertainty Considerations in Modern Radiation Oncology. In Van Dyk, J., editor, *The modern Technology of radiation oncology*, volume 3, chapter 11, pages 362–412. Medical Physics Pub Corp Madison, 2011.

[116] Nag, S., Dobelbower, R., Glasgow, G., Gustafson, G., Syed, N., Thomadsen, B., and Williamson, J. F. Inter-society standards for the performance of brachytherapy: A joint report from ABS, ACMP and ACRO. *Critical Reviews in Oncology/Hematology*, 48(1):1–17, 2003.

[117] Nath, R., Rivard, M. J., DeWerd, L. A., Dezarn, W. A., Heaton II, H. T., Ibbott, G. S., Meigooni, A. S., Ouhib, Z., Rusch, T. W., and Siebert, F.-A. Guidelines by the AAPM and GEC-ESTRO on the use of innovative brachytherapy devices and applications: Report of Task Group 167. *Medical Physics*, 43(6):3178–3205, 2016.

[118] Hartmann, G. H. Accuracy Strategies in Radiotherapy. In Lemoigne, Y. and Caner, A., editors, *Radiotherapy and Brachytherapy*, chapter 2, pages 11–28. Springer Science+Business Media, LLC, 2009.

[119] Tanderup, K., Hellebust, T. P., Lang, S., Granfeldt, J., Pötter, R., Lindegaard, J. C., and Kirisits, C. Consequences of random and systematic reconstruction uncertainties in 3D image based brachytherapy in cervical cancer. *Radiotherapy and Oncology*, 89(2):156–163, 2008.

[120] Oinam, A. S., Tomar, P., Patel, F. D., Singh, L., Rai, B., and Bahl, A. CT and MR image fusion of tandem and ring applicator using rigid registration in intracavitary brachytherapy planning. *Journal of Applied Clinical Medical Physics*, 15(2):191–204, 2014.

[121] Van Herk, M., Remeijer, P., Rasch, C., and Lebesque, J. V. The probability of correct target dosage: dose-population histograms for deriving treatment margins in radiotherapy. *International Journal of Radiation Oncology Biology Physics*, 47(4):1121–1135, 2000.

[122] Yan, D., Lockman, D., Martinez, A., Wong, J., Brabbins, D., Vicini, F., Liang, J., and Kestin, L. Computed Tomography Guided Management of Interfractional Patient Variation. *Seminars in radiation oncology*, 15(3):168–179, 2005.

[123] Van Herk, M., Witte, M., and Remeijer, P. Performance of patient specific margins derived using a Bayesian statistical method. *IFMBE Proceedings*, 25(1):769–771, 2009.

[124] Sonke, J.-J. and Van Herk, M. Errors, Margins, Localization, and Correction. In Timmerman, R. and Xing, L., editors, *Image-Guided and Adaptive Radiation Therapy*, chapter 3, pages 41–54. Lippincott Williams and Wilkins, 2010.

[125] Korreman, S., Rasch, C., McNair, H., Verellen, D., Oelfke, U., Maingon, P., Mijnheer, B., and Khoo, V. The European Society of Therapeutic Radiology and Oncology-European Institute of Radiotherapy (ESTRO-EIR) report on 3D CT-based in-room image guidance systems: A practical and technical review and guide. *Radiotherapy and Oncology*, 94(2):129–144, 2010.

[126] Hellebust, T. P., Dale, E., Skjønsberg, A., and Olsen, D. R. Inter fraction variations in rectum and bladder volumes and dose distributions during high dose rate brachytherapy treatment of the uterine cervix investigated by repetitive CT-examinations. *Radiotherapy and Oncology*, 60(3):273–280, 2001.

[127] Davidson, M. T., Yuen, J., D'Souza, D. P., and Batchelar, D. L. Image-guided cervix high-dose-rate brachytherapy treatment planning: Does custom computed tomography planning for each insertion provide better conformal avoidance of organs at risk? *Brachytherapy*, 7(1): 37–42, 2008.

[128] Mohamed, S., Nielsen, S. K., Fokdal, L. U., Pedersen, E. M., Lindegaard, J. C., and Tanderup, K. Feasibility of applying a single treatment plan for both fractions in PDR image guided brachytherapy in cervix cancer. *Radiotherapy and Oncology*, 107(1):32–38, 2013.

[129] Lang, S., Nesvacil, N., Kirisits, C., Georg, P., Dimopoulos, J. C., Federico, M., and Pötter, R. Uncertainty analysis for 3D image-based cervix cancer brachytherapy by repetitive MR imaging: Assessment of DVH-variations between two HDR fractions within one applicator insertion and their clinical relevance. *Radiotherapy and Oncology*, 107(1):26–31, 2013.

[130] Njeh, C. F. Tumor delineation: The weakest link in the search for accuracy in radiotherapy. *Journal of medical physics/Association of Medical Physicists of India*, 33(4):136–140, 2008.

[131] Seravalli, E., Van Haaren, P. M., Van Der Toorn, P. P., and Hurkmans, C. W. A comprehensive evaluation of treatment accuracy, including end-to-end tests and clinical data, applied to intracranial stereotactic radiotherapy. *Radiotherapy and Oncology*, 116(1):131–138, 2015.

[132] Dimopoulos, J. C., Kirisits, C., Petric, P., Georg, P., Lang, S., Berger, D., and Pötter, R. The Vienna applicator for combined intracavitary and interstitial brachytherapy of cervical cancer: Clinical feasibility and preliminary results. *International Journal of Radiation Oncology Biology Physics*, 66(1):83–90, 2006.

[133] Karlsson, L., Thunberg, P., With, A., Mordhorst, L. B., and Persliden, J. 3D image-based adapted high-dose-rate brachytherapy in cervical cancer with and without interstitial needles: Measurement of applicator shift between imaging and dose delivery. *Journal of Contemporary Brachytherapy*, 9(1):52–58, 2017.

[134] Tornero-López, A. M. and Guirado, D. Radiobiological considerations in combining doses from external beam radiotherapy and brachytherapy for cervical cancer. *Reports of Practical Oncology and Radiotherapy*, 23(6):562–573, 2018.

[135] Burman, C., Kutcher, G. J., Emami, B., and Goitein, M. Fitting of normal tissue tolerance data to an analytic function. *International Journal of Radiation Oncology, Biology, Physics*, 21(1):123–135, 1991.

[136] Cozzi, L., Dinshaw, K. A., Shrivastava, S. K., Mahantshetty, U., Engineer, R., Deshpande, D. D., Jamema, S. V., Vanetti, E., Clivio, A., Nicolini, G., and Fogliata, A. A treatment planning study comparing volumetric arc modulation with RapidArc and fixed field IMRT for cervix uteri radiotherapy. *Radiotherapy and Oncology*, 89(2):180–191, 2008.

[137] Dale, E., Hellebust, T. P., Skjønsberg, A., Høgberg, T., and Olsen, D. R. Modeling normal tissue complication probability from repetitive computed tomography scans during fractionated high-dose-rate brachytherapy and external beam radiotherapy of the uterine cervix. *International Journal of Radiation Oncology Biology Physics*, 47(4):963–971, 2000.

[138] Georg, P., Lang, S., Dimopoulos, J. C., Dörr, W., Sturdza, A. E., Berger, D., Georg, D., Kirisits, C., and Pötter, R. Dose-volume histogram parameters and late side effects in magnetic resonance image-guided adaptive cervical cancer brachytherapy. *International Journal of Radiation Oncology Biology Physics*, 79(2):356–362, 2011.

[139] Bahena, J. H., Martinez, A., Yan, D., Mele, E., Edmunson, G., Brown, D., Hardy, M., Brabbins, D. S., and Gustafson, G. High-Dose Rate Cervix Applicator. *Int. J. Radiation Oncology Biol. Phys*, 41(1):13–19, 1998.

[140] Kim, R. Y., Meyer, J. T., Spencer, S. A., Meredith, R. F., Jennelle, R. L. S., and Salter, M. M. Major geometric variations between intracavitary applications in carcinoma of the cervix: high dose rate vs. low dose rate. *International Journal of Radiation Oncology Biology Physics*, 35(5):1035–1038, 1996.

[141] Hoskin, P. J., Cook, M., Bouscale, D., and Cansdale, J. Changes in applicator position with fractionated high dose rate gynaecological brachytherapy. *Radiotherapy and Oncology*, 40(1): 59–62, 1996.

[142] Kim, Y., Meredith, R. F., Meyer, T., Salter, M., and Spencer, A. Therapeutic Applications in Cancer ofthe Cervix : and Types. *Radiology*, 195(2):419–422, 1995.

[143] Ebruli, C., Demiral, N., Çetingöz, R., Eyiler, F., and Kınay, M. The variability of applicator position among high dose rate intracavitary brachytherapy applications in cervical cancer patients treated with ring & tandem applicators. *Tumori Journal*, 93(5):432–438, 2007.

[144] Datta, N. R., Kumar, S., Das, K. J. M., Pandey, C. M., Halder, S., and Ayyagari, S. Variations of intracavitary applicator geometry during multiple HDR brachytherapy insertions in carcinoma cervix and its influence on reporting as per ICRU report 38. *Radiotherapy and Oncology*, 60(1):15–24, 2001.

[145] Jamema, S. V., Mahantshetty, U., Tanderup, K., Malvankar, D., Sharma, S., Engineer, R., Chopra, S., Shrivastava, S. K., and Deshpande, D. D. Inter-application variation of dose and spatial location of D2cm3 volumes of OARs during MR image based cervix brachytherapy. *Radiotherapy and Oncology*, 107(1):58–62, 2013.

[146] Corn, B. W., Hanlon, A. L., Pajak, T. F., Owen, J., and Hanks, G. E. Technically accurate intracavitary insertions improve pelvic control and survival among patients with locally advanced carcinoma of the uterine cervix. *Gynecologic Oncology*, 53(3):294–300, 1994.

[147] Kissel, M., Silva, M., Lequesne, J., Grellard, J.-m., Barraux, V., Lerouge, D., Lecornu, M., Haie-meder, C., Chargari, C., and Thariat, J. Impact of suboptimal tandem implantation on local control and complications in intracavitary brachytherapy for cervix cancer. *Brachytherapy*, 18(6):753–762, 2019.

[148] Viswanathan, A., Moughan, J., Small, W., Levenback, C., Iyer, R., Hymes, S., Dicker, A., Miller, B., Erickson, B., and Gaffney, D. Quality of Cervical Cancer Brachytherapy Implantation in RTOG Prospective Trials. *International Journal of Radiation Oncology Biology Physics*, 75(3):S86–S87, 2009.

[149] Rigaud, B., Klopp, A., Vedam, S., Venkatesan, A., Taku, N., Simon, A., Haigron, P., De Crevoisier, R., Brock, K. K., and Cazoulat, G. Deformable image registration for dose mapping between external beam radiotherapy and brachytherapy images of cervical cancer. *Physics in Medicine and Biology*, 64(11), 2019.

[150] Schindel, J., Zhang, W., Bhatia, S. K., Sun, W., and Kim, Y. Dosimetric impacts of applicator displacements and applicator reconstruction-uncertainties on 3D image-guided brachytherapy for cervical cancer. *Journal of Contemporary Brachytherapy*, 5(4):250–257, 2013.

[151] Gerstzen, K., Faul, C., King, G., Mogus, R., Sonnik, D., and Kalend, A. High dose rate tandem and ring applicator movement with patient transfer from simulation to treatment. *Journal of Brachytherapy International*, 14:15–20, 1998.

[152] Kim, Y., Huang, Y., Chesnut, D., Sangster, N., and Oldham, A. Applicator displacements due to additional scan for 3D image guided brachytherapy for cervical cancer. *Radiotherapy and Oncology*, 99:S257–S258, 2011.

[153] Andrew, M., Kim, Y., Ginader, T., Smith, B. J., Sun, W., and Wang, D. Reduction of applicator displacement in MR/CT-guided cervical cancer HDR brachytherapy by the use of patient hover transport system. *Journal of Contemporary Brachytherapy*, 10(1):85–90, 2018.

[154] Balsdon, A., Timotin, E., Hunter, R., and Diamond, K. Stability of Intracavitary Applicator Placement for HDR Brachytherapy of Cervix Cancer. *Journal of Medical Imaging and Radiation Sciences*, 50(3):441–448, 2019.

[155] Tanderup, K., Viswanathan, A. N., Kirisits, C., and Frank, S. J. Magnetic Resonance Image Guided Brachytherapy. *Seminars in Radiation Oncology*, 24(3):181–191, 2014.

[156] Richart, J., Carmona-Meseguer, V., García-Martínez, T., Herreros, A., Otal, A., Pellejero, S., Tornero-López, A., and Pérez-Calatayud, J. Review of strategies for MRI based reconstruction of endocavitary and interstitial applicators in brachytherapy of cervical cancer. *Reports of Practical Oncology and Radiotherapy*, 23(6):547–561, 2018.

[157] Berger, D., Dimopoulos, J., Pötter, R., and Kirisits, C. Direct reconstruction of the Vienna applicator on MR images. *Radiotherapy and Oncology*, 93(2):347–351, 2009.

[158] Kirisits, C., Federico, M., Nkiwane, K., Fidarova, E., Jürgenliemk-Schulz, I., de Leeuw, A., Lindegaard, J., Pötter, R., and Tanderup, K. Quality assurance in MR image guided adaptive brachytherapy for cervical cancer: Final results of the EMBRACE study dummy run. *Radiotherapy and Oncology*, 117(3):548–554, 2015.

[159] Haack, S., Nielsen, S. K., Lindegaard, J. C., Gelineck, J., and Tanderup, K. Applicator reconstruction in MRI 3D image-based dose planning of brachytherapy for cervical cancer. *Radiotherapy and Oncology*, 91(2):187–193, 2009.

[160] Petit, S., Wielopolski, P., Rijnsdorp, R., Mens, J. W., and Kolkman-Deurloo, I. K. MR guided applicator reconstruction for brachytherapy of cervical cancer using the novel titanium Rotterdam applicator. *Radiotherapy and Oncology*, 107(1):88–92, 2013.

[161] Hrinivich, W. T., Morcos, M., Viswanathan, A., and Lee, J. Automatic tandem and ring reconstruction using MRI for cervical cancer brachytherapy. *Medical Physics*, 46(10):4324–4332, 2019.

[162] Kim, Y., Modrick, J. M., Pennington, E. C., and Kim, Y. Commissioning of a 3D image-based treatment planning system for high-dose-rate brachytherapy of cervical cancer. *Journal of Applied Clinical Medical Physics*, 17(2):405–426, 2016.

[163] Kim, Y., Muruganandham, M., Modrick, J. M., and Bayouth, J. E. Evaluation of artifacts and distortions of titanium applicators on 3.0-tesla MRI: Feasibility of titanium applicators in MRI-guided brachytherapy for gynecological cancer. *International Journal of Radiation Oncology Biology Physics*, 80(3):947–955, 2011.

[164] van Heerden, L. E., Gurney-Champion, O. J., van Kesteren, Z., Houweling, A. C., Koedooder, C., Rasch, C. R., Pieters, B. R., and Bel, A. Quantification of image distortions on the Utrecht interstitial CT/MR brachytherapy applicator at 3T MRI. *Brachytherapy*, 15(1):118–126, 2016.

[165] Petrič, P., Hudej, R., Rogelj, P., Blas, M., Tanderup, K., Fidarova, E., Kirisits, C., Berger, D., Dimopoulos, J. C. A., Pötter, R., and Hellebust, T. P. Uncertainties of target volume delineation in MRI guided adaptive brachytherapy of cervix cancer: A multi-institutional study. *Radiotherapy and Oncology*, 107(1):6–12, 2013.

[166] Hellebust, T. P., Tanderup, K., Lervåg, C., Fidarova, E., Berger, D., Malinen, E., Pötter, R., and Petrič, P. Dosimetric impact of interobserver variability in MRI-based delineation for cervical cancer brachytherapy. *Radiotherapy and Oncology*, 107(1):13–19, 2013.

[167] Viswanathan, A. N., Erickson, B., Gaffney, D. K., Beriwal, S., Bhatia, S. K., Lee Burnett, O., D'Souza, D. P., Patil, N., Haddock, M. G., Jhingran, A., Jones, E. L., Kunos, C. A., Lee, L. J., Lin, L. L., Mayr, N. A., Petersen, I., Petric, P., Portelance, L., Small, W., Strauss, J. B., Townamchai, K., Wolfson, A. H., Yashar, C. M., and Bosch, W. Comparison and consensus guidelines for delineation of clinical target volume for CT- and MR-based brachytherapy in locally advanced cervical cancer. *International Journal of Radiation Oncology Biology Physics*, 90(2):320–328, 2014.

[168] Vinod, S. K., Lim, K., Bell, L., Veera, J., Ohanessian, L., Juresic, E., Borok, N., Chan, P., Chee, R., Do, V., Govindarajulu, G., Sridharan, S., Johnson, C., Moses, D., Van Dyk, S., and Holloway, L. High-risk CTV delineation for cervix brachytherapy: Application of GEC-ESTRO guidelines in Australia and New Zealand. *Journal of Medical Imaging and Radiation Oncology*, 61(1):133–140, 2017.

[169] Duane, F. K., Langan, B., Gillham, C., Walsh, L., Rangaswamy, G., Lyons, C., Dunne, M., Walker, C., and McArdle, O. Impact of delineation uncertainties on dose to organs at risk in CT-guided intracavitary brachytherapy. *Brachytherapy*, 13(2):210–218, 2014.

[170] Van der Meer, M. C., Bosman, P. A. N., Pieters, B. R., Niatsetski, Y., Van Wieringen, N., Alderliesten, T., and Bel, A. Sensitivity of dose-volume indices to computation settings in high-dose-rate prostate brachytherapy treatment plan evaluation. *Journal of Applied Clinical Medical Physics*, 20(4):66–74, 2019.

[171] Otani, Y., Shimamoto, S., Sumida, I., Takahashi, Y., Tani, S., Oshima, T., Onosaka, S., Isohashi, F., Tamari, K., and Ogawa, K. Impact of different Ir-192 source models on dose calculations in high-dose-rate brachytherapy. *Physics and Imaging in Radiation Oncology*, 7 (July):23–26, 2018.

[172] Nelms, B., Stambaugh, C., Hunt, D., Tonner, B., Zhang, G., and Feygelman, V. Methods, software and datasets to verify DVH calculations against analytical values: Twenty years late(r). *Medical Physics*, 42(8):4435–4448, 2015.

[173] Kanani, A., Owrangi, A. M., and Mosleh-shirazi, M. A. Physica Medica Comprehensive methodology for commissioning modern 3D-image-based treatment planning systems for high dose rate gynaecological brachytherapy : A review. *Physica Medica*, 77(March):21–29, 2020.

[174] Kirisits, C., Siebert, F. A., Baltas, D., De Brabandere, M., Hellebust, T. P., Berger, D., and Venselaar, J. Accuracy of volume and DVH parameters determined with different brachytherapy treatment planning systems. *Radiotherapy and Oncology*, 84(3):290–297, 2007.

[175] Gossman, M. S. Addendum to brachytherapy dose-volume histogram commissioning with multiple planning systems. *Journal of Applied Clinical Medical Physics*, 17(3):502–505, 2016.

[176] Mikell, J. K., Klopp, A. H., Gonzalez, G. M., Kisling, K. D., Price, M. J., Berner, P. A., Eifel, P. J., and Mourtada, F. Impact of heterogeneity-based dose calculation using a deterministic grid-based boltzmann equation solver for intracavitary brachytherapy. *International Journal of Radiation Oncology Biology Physics*, 83(3):e417–e422, 2012.

[177] Mikell, J. K., Klopp, A. H., Price, M., and Mourtada, F. Commissioning of a grid-based Boltzmann solver for cervical cancer brachytherapy treatment planning with shielded colpostats. *Brachytherapy*, 12(6):645–653, 2013.

[178] Hofbauer, J., Kirisits, C., Resch, A., Xu, Y., Sturdza, A., Pötter, R., and Nesvacil, N. Impact of heterogeneity-corrected dose calculation using a grid-based Boltzmann solver on breast and cervix cancer brachytherapy. *Journal of Contemporary Brachytherapy*, 8(2):143–149, 2016.

[179] Jacob, D., Lamberto, M., DeSouza Lawrence, L., and Mourtada, F. Clinical transition to model-based dose calculation algorithm: A retrospective analysis of high-dose-rate tandem and ring brachytherapy of the cervix. *Brachytherapy*, 16(3):624–629, 2017.

[180] Sinnatamby, M., Nagarajan, V., Reddy, K. S., Karunanidhi, G., and Singhavajala, V. Comparison of image-based three-dimensional treatment planning using AcurosTM BV and AAPM TG-43 algorithm for intracavitary brachytherapy of carcinoma cervix. *Journal of Radiotherapy in Practice*, 15(3):254–262, 2016.

[181] Abe, K., Kadoya, N., Sato, S., Hashimoto, S., Nakajima, Y., Miyasaka, Y., Ito, K., Umezawa, R., Yamamoto, T., Takahashi, N., Takeda, K., and Jingu, K. Impact of a commercially available model-based dose calculation algorithm on treatment planning of high-dose-rate brachytherapy in patients with cervical cancer. *Journal of Radiation Research*, 59(2):198–206, 2018.

[182] Beaulieu, L., Carlsson Tedgren, , Carrier, J. F., Davis, S. D., Mourtada, F., Rivard, M. J., Thomson, R. M., Verhaegen, F., Wareing, T. A., and Williamson, J. F. Report of the Task Group 186 on model-based dose calculation methods in brachytherapy beyond the TG-43 formalism: Current status and recommendations for clinical implementation. *Medical Physics*, 39(10):6208–6236, 2012.

[183] Andersen, E. S., Noe, K. , Sørenson, T. S., Nielsen, S. K., Fokdal, L., Paludan, M., Lindegaard, J. C., and Tanderup, K. Simple DVH parameter addition as compared to deformable registration for bladder dose accumulation in cervix cancer brachytherapy. *Radiotherapy and Oncology*, 107(1):52–57, 2013.

[184] van Heerden, L. E., Houweling, A. C., Koedooder, K., van Kesteren, Z., van Wieringen, N., Rasch, C. R., Pieters, B. R., and Bel, A. Structure-based deformable image registration:

Added value for dose accumulation of external beam radiotherapy and brachytherapy in cervical cancer. *Radiotherapy and Oncology*, 123(2):319–324, 2017.

[185] Kobayashi, K., Murakami, N., Wakita, A., Nakamura, S., Okamoto, H., Umezawa, R., Takahashi, K., Inaba, K., Igaki, H., Ito, Y., Shigematsu, N., and Itami, J. Dosimetric variations due to interfraction organ deformation in cervical cancer brachytherapy. *Radiotherapy and Oncology*, 117(3):555–558, 2015.

[186] Gelover, E., Katherine, C., Mart, C., Sun, W., and Kim, Y. Patient's specific integration of OAR doses (D2 cc) from EBRT and 3D image-guided brachytherapy for cervical cancer. *Journal of Applied Clinical Medical Physics*, 19(2):83–92, 2018.

[187] Abe, T., Tamaki, T., Makino, S., Ebara, T., Hirai, R., Miyaura, K., Kumazaki, Y., Ohno, T., Shikama, N., Nakano, T., and Kato, S. Assessing cumulative dose distributions in combined radiotherapy for cervical cancer using deformable image registration with pre-imaging preparations. *Radiation Oncology*, 9(1):1–8, 2014.

[188] Jamema, S. V., Mahantshetty, U., Andersen, E., Noe, K. T., Sørensen, T. S., Kallehauge, J. F., Shrivastava, S. K., Deshpande, D. D., and Tanderup, K. Uncertainties of deformable image registration for dose accumulation of high-dose regions in bladder and rectum in locally advanced cervical cancer. *Brachytherapy*, 14(6):953–962, 2015.

[189] Jamema, S., Kirisits, C., De Brabandere, M., Hellebust, T. P., Siebert, F. A., and Tanderup, K. Image registration, contour propagation and dose accumulation of external beam and brachytherapy in gynecological radiotherapy. *Radiotherapy and Oncology*, 143:1–11, 2020.

[190] Tanderup, K., Christensen, J. J., Granfeldt, J., and Lindegaard, J. C. Geometric stability of intracavitary pulsed dose rate brachytherapy monitored by in vivo rectal dosimetry. *Radiotherapy and Oncology*, 79(1):87–93, 2006.

[191] Cooper, R., Brearley, E., Hurmuz, P., Musunuru, H. B., Richardson, C., Swift, S., Orton, J., and Bownes, P. Assessment of uterus position as a surrogate for high-risk clinical target volume with respect to the applicator position for multiple fractions of brachytherapy in cervical cancer. *Archives of Gynecology and Obstetrics*, 290(6):1201–1205, 2014.

[192] Cengiz, M., Gürdalli, S., Selek, U., Yildiz, F., Saglam, Y., Özyar, E., and Atahan, I. L. Effect of Bladder Distension on Dose Distribution of Intracavitary Brachytherapy for Cervical Cancer: Three-Dimensional Computed Tomography Plan Evaluation. *International Journal of Radiation Oncology Biology Physics*, 70(2):464–468, 2008.

[193] Lim, J., Durbin-Johnson, B., Valicenti, R., Mathai, M., Stern, R., and Mayadev, J. The impact of maximum rectal distension and tandem angle on rectal dose in 3D planned gynecologic high-dose-rate brachytherapy for locally advanced cervical cancer. *International Journal of Gynecological Cancer*, 23(6):1078–1083, 2014.

[194] Sheybani, A., Tennapel, M. J., Sun, W., Kim, Y., and Rockey, W. M. Dose-Volume Effect of Bladder and Rectal Filling during Intracavitary High-Dose-Rate Brachytherapy. *Brachytherapy*, 12(2013):S27, 2013.

[195] Patra, N. B., Manir, K. S., Basu, S., Goswami, J., Kabasi, A. K., Rp, D., Sarkar, S. K., and Card, D. Effect of bladder distension on dosimetry of organs at risk in computer tomography based planning of high-dose-rate intracavitary brachytherapy for cervical cancer. *Journal of contemporary brachytherapy*, 5(1):3–9, 2013.

[196] Talluri, A. K., Alluri, K. R., Gudipudi, D. K., Ahamed, S., Sresty, M. M., and Reddy, A. Y. Study of positional dependence of dose to bladder, pelvic wall and rectal points in High-Dose-Rate Brachytherapy in cervical cancer patients. *Journal of Medical Physics*, 38(4):178–184, 2013.

[197] Rai, B., Patel, F. D., Chakraborty, S., Kapoor, R., Sharma, S. C., Kumaravelu, S., Raghukumar, P., and Aprem, A. S. Bladder-rectum spacer balloon versus vaginal gauze packing in high dose rate brachytherapy in cervical cancer: A randomised study (Part II). *Clinical Oncology*, 27(12):713–719, 2015.

[198] Chakraborty, S., Patel, F. D., Patil, V. M., Oinam, A. S., and Sharma, S. C. Magnitude and Implications of Interfraction Variations in Organ Doses during High Dose Rate Brachytherapy of Cervix Cancer: A CT Based Planning Study. *ISRN Oncology*, 2014(1):1–7, 2014.

[199] Ju, S. G., Huh, S. J., Shin, J. S., Park, W., Nam, H., Bae, S., Oh, D., Hong, C. S., Kim, J. S., Han, Y., and Choi, D. H. Different effects of bladder distention on point A-based and 3D-conformal intracavitary brachytherapy planning for cervical cancer. *Journal of Radiation Research*, 54(2):349–356, 2013.

[200] Mahantshetty, U., Shetty, S., Majumder, D., Adurkar, P., Swamidas, J., Engineer, R., Chopra, S., and Shrivastava, S. Optimal bladder filling during high-dose-rate intracavitary brachytherapy for cervical cancer: A dosimetric study. *Journal of Contemporary Brachytherapy*, 9(2):112–117, 2017.

[201] Mazeron, R., Champoudry, J., Gilmore, J., Dumas, I., Goulart, J., Oberlander, A. S., Rivin del Campo, E., Diallo, I., Lefkopoulos, D., and Haie-Meder, C. Intrafractional organs movement in three-dimensional image-guided adaptive pulsed-dose-rate cervical cancer brachytherapy: Assessment and dosimetric impact. *Brachytherapy*, 14(2):260–266, 2015.

[202] Simha, V., Patel, F. D., Sharma, S. C., Rai, B., Oinam, A. S., Krishnatry, R., and Dhanireddy, B. Evaluation of intrafraction motion of the organs at risk in image-based brachytherapy of cervical cancer. *Brachytherapy*, 13(6):562–567, 2014.

[203] Nomden, C. N., De Leeuw, A. A., Roesink, J. M., Tersteeg, R. J., Westerveld, H., and Jürgenliemk-Schulz, I. M. Intra-fraction uncertainties of MRI guided brachytherapy in patients with cervical cancer. *Radiotherapy and Oncology*, 112(2):217–220, 2014.

[204] Miyasaka, Y., Kadoya, N., Ito, K., Umezawa, R., Kubozono, M., Yamamoto, T., Nakajima, Y., Saito, M., Takayama, Y., Nemoto, K., Iwai, T., and Jingu, K. Quantitative analysis of intra-fractional variation in CT-based image guided brachytherapy for cervical cancer patients. *Physica Medica*, 73(March):164–172, 2020.

[205] Elfrink, R. J., Kolkman-Deurloo, I. K. K., Van Kleffens, H. J., Rijnders, A., Schaeken, B., Aalbers, T. H., Dries, W. J., and Venselaar, J. L. Determination of the accuracy of implant reconstruction and dose delivery in brachytherapy in The Netherlands and Belgium. *Radiotherapy and Oncology*, 59(3):297–306, 2001.

[206] Bellezzo, M., Baeza, J. A., Voncken, R., Reniers, B., Verhaegen, F., and Fonseca, G. P. Mechanical evaluation of the Bravos afterloader system for HDR brachytherapy. *Brachytherapy*, 18(6):852–862, 2019.

[207] Awunor, O. A., Dixon, B., and Walker, C. Direct reconstruction and associated uncertainties of 192Ir source dwell positions in ring applicators using gafchromic film in the treatment planning of HDR brachytherapy cervix patients. *Physics in Medicine and Biology*, 58(10): 3207–3225, 2013.

[208] Humer, I., Kirisits, C., Berger, D., Trnková, P., Pötter, R., and Nesvacil, N. Improved source path localisation in ring applicators and the clinical impact for gynecological brachytherapy. *Journal of Contemporary Brachytherapy*, 7(3):239–243, 2015.

[209] Onoe, T., Nose, T., Yamashita, H., Yoshioka, M., Toshiyasu, T., Kozuka, T., Oguchi, M., and Nakagawa, K. High-dose-rate interstitial brachytherapy for gynecologic malignancies–dosimetric changes during treatment period. *Journal of radiation research*, 54(4):663–670, 2013.

[210] Morgia, M., Cuartero, J., Walsh, L., Jezioranski, J., Keeler, K., Xie, J., Massey, C., Williamson, D., Cho, Y. B., Oh, S., Fyles, A., and Milosevic, M. Tumor and normal tissue dosimetry changes during MR-guided pulsed-dose-rate (PDR) brachytherapy for cervical cancer. *Radiotherapy and Oncology*, 107(1):46–51, 2013.

[211] Dolezel, M., Ph, D., Odrazka, K., Ph, D., Zizka, J., Ph, D., Vanasek, J., Ph, D., Kohlova, T., Kroulik, T., Sc, M., Spitzer, D., Ph, D., Ryska, P., Tichy, M., Kostal, M., Ph, D., Jalcova, L., and Sc, B. MRI-based Preplanning Using CT and MRI Data Fusion in Patients With Cervical Cancer Treated With 3D-based Brachytherapy : Feasibility and Accuracy Study. *Radiation Oncology Biology*, 84(1):146–152, 2012.

[212] Sun, W., Bhatia, S. K., Jacobson, G. M., Flynn, R. T., and Kim, Y. Target volume changes through high-dose-rate brachytherapy for cervical cancer when evaluated on high resolution (3.0 Tesla) magnetic resonance imaging. *Practical Radiation Oncology*, 2(4):e101–e106, 2012.

[213] Kharofa, J., Morrow, N., Kelly, T., Rownd, J., Paulson, E., Rader, J., Uyar, D., Bradley, W., and Erickson, B. 3-T MRI-based adaptive brachytherapy for cervix cancer : Treatment technique and initial clinical outcomes. *Brachytherapy*, 13(4):319–325, 2014.

[214] Anderson, C., Lowe, G., Wills, R., Inchley, D., Beenstock, V., Bryant, L., Chapman, C., and Hoskin, P. J. Critical structure movement in cervix brachytherapy. *Radiotherapy and Oncology*, 107(1):39–45, 2013.

[215] Niemierko, A. and Goitein, M. Modeling of normal tissue response to radiation: The critical volume model. *International Journal of Radiation Oncology, Biology, Physics*, 25(1):135–145, 1993.

[216] Jackson, A., Kutcher, G. J., and Yorke, E. D. Probability of radiation-induced complications for normal tissues with parallel architecture subject to nonuniform irradiation. *Medical Physics*, 20(3):613–625, 1993.

[217] Carlone, M. C., Warkentin, B., Stavrev, P., and Fallone, B. G. Fundamental form of a population TCP model in the limit of large heterogeneity. *Medical Physics*, 33(6):1634–1642, 2006.

[218] Jadon, R., Pembroke, C. A., Hanna, C. L., Palaniappan, N., Evans, M., Cleves, A. E., and Staffurth, J. A Systematic Review of Organ Motion and Image-guided Strategies in External Beam Radiotherapy for Cervical Cancer. *Clinical Oncology*, 26(4):185–196, 2014.

[219] Reniers, B., Janssens, G., Orban de Xivry, J., Landry, G., and Verhaegen, F. Dose distribution for gynecological brachytherapy with dose accumulation between insertions: Feasibility study. *Brachytherapy*, 15(4):504–513, 2016.

[220] Gordon, J., Weiss, E., Abayomi, O., Siebers, J. V., and Dogan, N. The effect of uterine motion and uterine margins on target and normal tissue doses in intensity modulated radiation therapy of cervical cancer. *Physics in Medicine and Biology*, 56(10):2887–2901, 2011.

[221] Vásquez Osorio, E. M., Kolkman-Deurloo, I. K. K., Schuring-Pereira, M., Zolnay, A., Heijmen, B. J., and Hoogeman, M. S. Improving anatomical mapping of complexly deformed anatomy for external beam radiotherapy and brachytherapy dose accumulation in cervical cancer. *Medical Physics*, 42(1):206–220, 2015.

[222] Liao, Y., Dandekar, V., Chu, J. C., Turian, J., Bernard, D., and Kiel, K. Reporting small bowel dose in cervix cancer high-dose-rate brachytherapy. *Medical Dosimetry*, 41(1):28–33, 2016.

[223] Chapman, C. H., Polan, D., Vineberg, K., Jolly, S., Maturen, K. E., Brock, K. K., and Prisciandaro, J. I. Deformable image registration–based contour propagation yields clinically acceptable plans for MRI-based cervical cancer brachytherapy planning. *Brachytherapy*, 17 (2):360–367, 2018.

[224] Garipağaoğlu, M., Tuncl, N., Köseoğlu, F. G., Gülkesen, H., Kizildağ, A. , Toy, A., and Dalmaz, M. G. Geometric and dosimetric variations of ICRU bladder and rectum reference points in vaginal cuff brachytherapy using ovoids. *International Journal of Radiation Oncology Biology Physics*, 58(5):1607–1615, 2004.

[225] Grigsby, P. W., Georgiou, A., W, J. F., and Perez, C. A. Anatomic variation of gynecologic brachytherapy prescription points. *International Journal of Radiation Oncology, Biology, Physics*, 27(3):725–729, 1993.

[226] Oku, Y., Arimura, H., Nguyen, T. T. T., Hiraki, Y., Toyota, M., Saigo, Y., Yoshiura, T., and Hirata, H. Investigation of whether in-room CT-based adaptive intracavitary brachytherapy for uterine cervical cancer is robust against interfractional location variations of organs and/or applicators. *Journal of Radiation Research*, 57(6):677–683, 2016.

[227] Marosevic, G., Ljuca, D., Osmic, H., Fazlic, S., and Arsovski, O. Inter-application displacement of brachytherapy dose received by the bladder and rectum of the patients with inoperable cervical cancer. *Radiology and oncology*, 48(2):203–209, 2014.

[228] Elhanafy, O. A., Das, R. K., Paliwal, B. R., Migahed, M. D., Sakr, H. A., and Elleithy, M. Anatomic variation of prescription points and treatment volume with fractionated high-dose rate gynecological brachytherapy. *Journal of applied clinical medical physics / American College of Medical Physics*, 3(1):1–5, 2002.

[229] Kim, R. Y., Dragovic, A. F., Whitley, A. C., and Shen, S. Image-guided brachytherapy for cervical cancer: Analysis of D2cc hot spot in three-dimensional and anatomic factors affecting D2cc hot spot inorgans at risk. *Brachytherapy*, 13(2):203–209, 2014.

[230] Mazeron, R., Castelnau-Marchand, P., Dumas, I., Del Campo, E. R., Kom, L. K., Martinetti, F., Farha, G., Tailleur, A., Morice, P., Chargari, C., Lefkopoulos, D., and Haie-Meder, C. Impact of treatment time and dose escalation on local control in locally advanced cervical

cancer treated by chemoradiation and image-guided pulsed-dose rate adaptive brachytherapy. *Radiotherapy and Oncology*, 114(2):257–263, 2015.

[231] Phillips, J., Yaparpalvi, R., Mehta, K., Kuo, H., Desai, S., Tang, J., and Kalnicki, S. An Analysis of the Effect of Intrafraction Organ Motion on Gynecological High-Dose-Rate Brachytherapy Treatment. *International Journal of Radiation Oncology Biology Physics*, 96 (2):E307, 2016.

[232] De Leeuw, A. Image guided brachytherapy: HDR treatments in the MR room, 2014.

[233] Söhn, M., Sobotta, B., and Alber, M. Dosimetric treatment course simulation based on a statistical model of deformable organ motion. *Physics in Medicine and Biology*, 57(12): 3693–3709, 2012.

[234] Budiarto, E., Keijzer, M., Storchi, P. R., Hoogeman, M. S., Bondar, L., Mutanga, T. F., De Boer, H. C., and Heemink, A. W. A population-based model to describe geometrical uncertainties in radiotherapy: Applied to prostate cases. *Physics in Medicine and Biology*, 56 (4):1045–1061, 2011.

[235] Rios, R., De Crevoisier, R., Ospina, J. D., Commandeur, F., Lafond, C., Simon, A., Haigron, P., Espinosa, J., and Acosta, O. Population model of bladder motion and deformation based on dominant eigenmodes and mixed-effects models in prostate cancer radiotherapy. *Medical Image Analysis*, 38:133–149, 2017.

[236] Rigaud, B., Simon, A., Gobeli, M., Leseur, J., Duvergé, L., Williaume, D., Castelli, J., Lafond, C., Acosta, O., Haigron, P., and De Crevoisier, R. Statistical Shape Model to Generate a Planning Library for Cervical Adaptive Radiotherapy. *IEEE Transactions on Medical Imaging*, 38(2):406–416, 2019.

[237] Tilly, D., Van De Schoot, A. J., Grusell, E., Bel, A., and Ahnesjö, A. Dose coverage calculation using a statistical shape model - Applied to cervical cancer radiotherapy. *Physics in Medicine and Biology*, 62(10):4140–4159, 2017.

[238] Rigaud, B., Cazoulat, G., Vedam, S., Venkatesan, A. M., Peterson, C. B., Taku, N., Klopp, A. H., and Brock, K. K. Modeling Complex Deformations of the Sigmoid Colon Between External Beam Radiation Therapy and Brachytherapy Images of Cervical Cancer. *Radiation Oncology Biology*, 106(5):1084–1094, 2020.

[239] LaValle, S. M. *Planning Algorithms*. Cambridge University Press, 2006.

[240] Straathof, R. Risk-aware motion planning in adverse environments under spatial uncertainty: a systematic review and application to brachytherapy needle channel planning. Technical report, TU Delft, Faculty of Mechanical, Maritime and Materials Engineering, Delft, 2020.

[241] Goerzen, C., Kong, Z., and Mettler, B. A survey of motion planning algorithms from the perspective of autonomous UAV guidance. *Journal of Intelligent and Robotic Systems: Theory and Applications*, 57(1-4):65–100, 2010.

[242] Lunenburg, J. *Context-aware design and motion planning for autonomous service robots*. PhD thesis, TU Eindhoven, 2015.

[243] Kim, Y. and Kim, B. K. Time-Optimal Trajectory Planning Based on Dynamics for Differential-Wheeled Mobile Robots with a Geometric Corridor. *IEEE Transactions on Industrial Electronics*, 64(7):5502–5512, 2017.

[244] Hacohen, S., Shoval, S., and Shvalb, N. Probability Navigation Function for Stochastic Static Environments. *International Journal of Control, Automation and Systems*, 17(8):2097–2113, 8 2019.

[245] Bollino, K. P. and Lewis, L. R. Collision-free multi-UAV optimal path planning and cooperative control for tactical applications. *AIAA Guidance, Navigation and Control Conference and Exhibit*, 2008.

[246] Karaman, S. and Frazzoli, E. Sampling-based algorithms for optimal motion planning. *International Journal of Robotics Research*, 30(7):846–894, 2011.

[247] Gammell, J. D., Strub, M. P., and Sep, R. O. A Survey of Asymptotically Optimal Sampling-based Motion Planning Methods. *Annual Review of Control, Robotics, and Autonomous Systems*, 4:1–25, 2021.

[248] Bhattacharya, S. *Topological and geometric techniques in graph search-based robot planning*. PhD thesis, University of Pennsylvania, 2012.

[249] Petrović, L. Motion planning in high-dimensional spaces. *arXiv*, 2018. URL https://arxiv.org/pdf/1806.07457.pdf.

[250] Dai, S. *Probabilistic Motion Planning and Optimization Incorporating Chance Constraints*. PhD thesis, Massachusetts Institute of Technology, 2018.

[251] Bhardwaj, M., Boots, B., and Mukadam, M. Differentiable Gaussian Process Motion Planning. *arXiv*, 2, 2019. URL https://arxiv.org/pdf/1907.09591.pdf.

[252] Bhattacharya, S. and Likhachev, M. Search-Based Path Planning with Homotopy Class Constraints. In *Twenty-Fourth AAAI Conference on Artificial Intelligence*, pages 1230–1237, 2010.

[253] Yu, H., Lu, W., and Liu, D. A unified closed-loop motion planning approach for an I-AUV in cluttered environment with localization uncertainty. *Proceedings - IEEE International Conference on Robotics and Automation*, 2019-May:4646–4652, 2019.

[254] Kolur, K., Chintalapudi, S., Boots, B., and Mukadam, M. Online Motion Planning Over Multiple Homotopy Classes with Gaussian Process Inference. *arXiv*, 2019. URL https://arxiv.org/pdf/1908.00641.pdf.

[255] Alterovitz, R., Simeon, T., Goldberg, K., Alterovitz, R., Simeon, T., Goldberg, K., Stochastic, T., Roadmap, M., Alterovitz, R., and Goldberg, K. The Stochastic Motion Roadmap : A Sampling Uncertainty. *Robotics: Science and Systems*, 2007.

[256] Masehian, E. The Role of Motion Planning in Robotics. *Applied Mechanics and Materials*, 811:311–317, 2015.

[257] De Boeck, L., Beliën, J., and Egyed, W. Dose optimization in high-dose-rate brachytherapy: A literature review of quantitative models from 1990 to 2010. *Operations Research for Health Care*, 3(2):80–90, 2014.

[258] Luders, B. D., Kothari, M., and How, J. P. Chance constrained RRT for probabilistic robustness to environmental uncertainty. *AIAA Guidance, Navigation, and Control Conference*, pages 0–21, 2010.

[259] Luders, B. D. and How, J. P. An Optimizing Sampling-based Motion Planner with Guaranteed Robustness to Bounded Uncertainty. In *2014 American Control Conference (ACC)*, pages 771–777, 2014.

[260] Xu, J., Duindam, V., Alterovitz, R., Pouliot, J., Cunha, J. A. M., Hsu, I. C., and Goldberg, K. Planning fireworks trajectories for steerable medical needles to reduce patient trauma. *2009 IEEE/RSJ International Conference on Intelligent Robots and Systems, IROS 2009*, pages 4517–4522, 2009.

[261] Sabariego, M. P., Porras, I., and Lallena, A. M. On the shape of the Task Group 43 anisotropy factor for linear brachytherapy sources at short distances. *Brachytherapy*, 13(4):424–429, 2014.

[262] Luders, B. D., Karaman, S., and How, J. P. Robust sampling-based motion planning with asymptotic optimality guarantees. In *AIAA Guidance, Navigation, and Control (GNC) Conference*, pages 1–25, 2013.

[263] Hwang, Y. K. and Ahuja, N. Gross Motion Planning — A Survey. *ACM Computing Surveys (CSUR)*, 24(3):219–291, 1992.

[264] Blackmore, L., Ono, M., and Williams, B. C. Chance-constrained optimal path planning with obstacles. *IEEE Transactions on Robotics*, 27(6):1080–1094, 2011.

[265] Luders, B. D., Kothari, M., and How, J. P. Chance constrained RRT for probabilistic robustness to environmental uncertainty. In *AIAA Guidance, Navigation, and Control Conference*, 2010.

[266] Papadopoulos, G., Kurniawati, H., and Patrikalakis, N. M. Asymptotically Optimal Inspection Planning using Systems with Differential Constraints. In *2013 IEEE International Conference on Robotics and Automation (ICRA)*, pages 4126–4133, Karlsruhe, Germany, 2013. IEEE.

[267] Guo, Y. and Balakrishnan, M. Complete coverage control for nonholonomic mobile robots in dynamic environments. *Proceedings - IEEE International Conference on Robotics and Automation*, 2006(May):1704–1709, 2006.

[268] Araujo, J. F., Sujit, P. B., and Sousa, J. B. Multiple UAV area decomposition and coverage. In *2013 IEEE symposium on computational intelligence for security and defense applications (CISDA)*, pages 30–37. IEEE, 2013.

[269] Viswanathan, A. N., Beriwal, S., Santos, J. F. D. L., Demanes, D. J., Gaffney, D., Hansen, J., Jones, E., Kirisits, C., Thomadsen, B., and Erickson, B. American Brachytherapy Society consensus guidelines for locally advanced carcinoma of the cervix. Part II: High-dose-rate brachytherapy. *Brachytherapy*, 11(1):47–52, 2012.

[270] Siauw, T., Cunha, A., Goldberg, K., and Pouliot, J. NPIP: A skew line needle configuration optimization system for HDR brachytherapy. *Medical Physics*, 39(July):4339–4346, 2012.

[271] LaValle, S. M. and Sharma, R. On Motion Planning in Changing, Partially Predictable Environments. *The International Journal of Robotics Research*, 16(6):775–805, 1997.

[272] Dadkhah, N. and Mettler, B. Survey of motion planning literature in the presence of uncertainty: Considerations for UAV guidance. *Journal of Intelligent and Robotic Systems: Theory and Applications*, 65(1-4):233–246, 2012.

[273] Alterovitz, R., Branicky, M., and Goldberg, K. Motion planning under uncertainty for image-guided medical needle steering. *International Journal of Robotics Research*, 27(11-12):1361–1374, 2008.

[274] Van Den Berg, J., Patil, S., Alterovitz, R., Abbeel, P., and Goldberg, K. LQG-based planning, sensing, and control of steerable needles. *Springer Tracts in Advanced Robotics*, 68(STAR): 373–389, 2010.

[275] Sun, W. and Alterovitz, R. Motion planning under uncertainty for medical needle steering using optimization in belief space. In *IEEE International Conference on Intelligent Robots and Systems*, pages 1775–1781. IEEE, 2014.

[276] Kothari, M. and Postlethwaite, I. A probabilistically robust path planning algorithm for UAVs using rapidly-exploring random trees. *Journal of Intelligent and Robotic Systems: Theory and Applications*, 71(2):231–253, 2013.

[277] Blackmore, L. A probabilistic particle control approach to optimal, robust predictive control. In *Collection of Technical Papers - AIAA Guidance, Navigation, and Control Conference 2006*, volume 3, pages 1866–1880, 2006.

[278] Patil, S. and Alterovitz, R. Estimating Probability of Collision for Safe Motion Planning under Gaussian Motion and Sensing Uncertainty. In *2012 IEEE International Conference on Robotics and Automation (pp. 3238-3244).*, pages 3238–3244. IEEE, 2012.

[279] Lu, M. and Shen, Z. J. M. A Review of Robust Operations Management under Model Uncertainty. *Production and Operations Management*, 0(0):1–17, 2020.

[280] Summers, T. Distributionally Robust Sampling-Based Motion Planning Under Uncertainty. In *2018 IEEE/RSJ International Conference on Intelligent Robots and Systems (IROS)*, IEEE International Conference on Intelligent Robots and Systems, pages 6518–6523, 2018.

[281] Chaves, S. M., Walls, J. M., Galceran, E., and Eustice, R. M. Risk aversion in belief-space planning under measurement acquisition uncertainty. *IEEE International Conference on Intelligent Robots and Systems*, 2015-Decem:2079–2086, 2015.

[282] Patil, S. and Alterovitz, R. Interactive motion planning for steerable needles in 3D environments with obstacles. *2010 3rd IEEE RAS and EMBS International Conference on Biomedical Robotics and Biomechatronics, BioRob 2010*, pages 893–899, 2010.

[283] Favaro, A., Cerri, L., Galvan, S., Baena, F. R. Y., and De Momi, E. Automatic Optimized 3D Path Planner for Steerable Catheters with Heuristic Search and Uncertainty Tolerance. *Proceedings - IEEE International Conference on Robotics and Automation*, pages 9–16, 2018.

[284] Caborni, C., Ko, S. Y., De Momi, E., Ferrigno, G., and Y Baena, F. R. Risk-based path planning for a steerable flexible probe for neurosurgical intervention. In *Proceedings of the IEEE RAS and EMBS International Conference on Biomedical Robotics and Biomechatronics*, number June, pages 866–871, 2012.

[285] Alterovitz, R., Branicky, M., and Goldberg, K. Constant-curvature motion planning under uncertainty with applications in image-guided medical needle steering. *Springer Tracts in Advanced Robotics*, 47:319–334, 2008.

[286] Schulman, J., Duan, Y., Ho, J., Lee, A., Awwal, I., Bradlow, H., Pan, J., Patil, S., Goldberg, K., and Abbeel, P. Motion planning with sequential convex optimization and convex collision checking. *International Journal of Robotics Research*, 33(9):1251–1270, 2014.

[287] Webster, R. J., Kim, J. S., Cowan, N. J., Chirikjian, G. S., and Okamura, A. M. Nonholonomic modeling of needle steering. *International Journal of Robotics Research*, 25(5-6):509–525, 2006.

[288] Murray, R. M., Li, Z., and Shankar Sastry, S. *A mathematical introduction to robotic manipulation*. CRC Press, 1994.

[289] Blanco, J. A tutorial on se (3) transformation parameterizations and on-manifold optimization. Technical Report 3, University of Malaga, Malaga, 2013.

[290] Roesthuis, R. J., Abayazid, M., and Misra, S. Mechanics-based model for predicting in-plane needle deflection with multiple bends. *Proceedings of the IEEE RAS and EMBS International Conference on Biomedical Robotics and Biomechatronics*, pages 69–74, 2012.

[291] Luders, B. D., Karaman, S., Frazzoli, E., and How, J. P. Bounds on tracking error using closed-loop rapidly-exploring random trees. In *Proceedings of the 2010 American Control Conference, ACC 2010*, pages 5406–5412. IEEE, 2010.

[292] Coenen, S. *Motion Planning for Mobile Robots - A Guide*. PhD thesis, Eindhoven University ofTechnology, 2012.

[293] Latombe, J.-C. *Robot Motion Models*. Springer Science+Business Media, LLC, New York, NY, 2nd edition, 1991.

[294] Yang, L., Qi, J., Song, D., Xiao, J., Han, J., and Xia, Y. Survey of Robot 3D Path Planning Algorithms. *Journal of Control Science and Engineering*, 2016.

[295] Souissi, O. Path Planning : A 2013 Survey. In *Proceedings of 2013 International Conference on Industrial Engineering and Systems Management (IESM)*, number January, pages 1–8, Rabat, Morocco, 2013. IEEE-IESM.

[296] Shin, H. and Chae, J. A performance review of collision-free path planning algorithms. *Electronics (Switzerland)*, 9(2), 2020.

[297] Elbanhawi, M. and Simic, M. Sampling-based robot motion planning: A review. *IEEE Access*, 2(July):56–77, 2014.

[298] Şucan, I. A., Moll, M., and Kavraki, L. The open motion planning library. *IEEE Robotics and Automation Magazine*, 19(4):72–82, 2012.

[299] Chitta, S., Sucan, I., and Cousins, S. MoveIt! *IEEE Robotics and Automation Magazine*, 19 (1):18–19, 2012.

[300] Moll, M., Sucan, I. A., and Kavraki, L. E. Benchmarking Motion Planning Algorithms: An Extensible Infrastructure for Analysis and Visualization. *IEEE Robotics and Automation Magazine*, 22(3):96–102, 2015.

[301] Lunenburg, J., Coenen, S., Naus, G., van de Molengraft, M., and Steinbuch, M. Motion Planning for Mobile Robots: A Method for the Selection of a Combination of Motion-Planning Algorithms. *IEEE Robotics & Automation Magazine*, 23(4):107–117, 2016.

[302] Velasquez, M. and Hester, P. An analysis of multi-criteria decision making methods. *International Journal of Operations Research*, 10(2):56–66, 2013.

[303] Silverstein, D., DeCarlo, N., and Slocum, M. *INsourcing Innovation*. Auerbach publications, 2008.

[304] Roozenburg, N. F. M. and Eekels, J. *Productontwerpen structuur en methoden*. Lemma, 1998.

[305] Franceschini, F. *Advanced quality function deployment*. CRC Press, 2002.

[306] Prasad, K. and Chakraborty, S. A quality function deployment-based model for materials selection. *Materials and Design*, 49:525–535, 2013.

[307] Dursun, M. and Karsak, E. E. A QFD-based fuzzy MCDM approach for supplier selection. *Applied Mathematical Modelling*, 37(8):5864–5875, 2013.

[308] Bevilacqua, M., Ciarapica, F. E., and Giacchetta, G. A fuzzy-QFD approach to supplier selection. *Journal of Purchasing and Supply Management*, 12(1):14–27, 2006.

[309] Liu, H. T. Product design and selection using fuzzy QFD and fuzzy MCDM approaches. *Applied Mathematical Modelling*, 35(1):482–496, 2011.

[310] Bhattacharya, A., Sarkar, B., and Mukherjee, S. K. Integrating AHP with QFD for robot selection under requirement perspective. *International Journal of Production Research*, 43 (17):3671–3685, 2005.

[311] Herzwurm, G. and Schockert, S. The leading edge in QFD for software and electronic business. *International Journal of Quality and Reliability Management*, 20(1):36–55, 2003.

[312] Karlsson, J. Managing software requirements using quality function deployment. *Software Quality Journal*, 6(4):311–326, 1997.

[313] Chan, L.-k. and Wu, M.-l. Quality Function Deployment: A Comprehensive Review of Its Concepts and Methods. *Quality Engineering*, 15(1):23–35, 2002.

[314] Olewnik, A. and Lewis, K. Limitations of the house of quality to provide quantitative design information. *International Journal of Quality and Reliability Management*, 25(2):125–146, 2008.

[315] Griffin, A. and Hauser, J. R. The Voice of the Customer. *Marketing Science*, 12(1):1–27, 1993.

[316] Chan, L. K. and Wu, M. L. A systematic approach to quality function deployment with a full illustrative example. *Omega*, 33(2):119–139, 2005.

[317] Li, Y. L., Chin, K. S., and Luo, X. G. Determining the final priority ratings of customer requirements in product planning by MDBM and BSC. *Expert Systems with Applications*, 39 (1):1243–1255, 2012.

[318] Franceschini, F., Maisano, D., and Mastrogiacomo, L. Customer requirement prioritization on QFD: a new proposal based on the generalized Yager's algorithm. *Research in Engineering Design*, 26(2):171–187, 2015.

[319] Nahm, Y. E., Ishikawa, H., and Inoue, M. New rating methods to prioritize customer requirements in QFD with incomplete customer preferences. *International Journal of Advanced Manufacturing Technology*, 65(9-12):1587–1604, 2013.

[320] Kwong, C. K., Ye, Y., Chen, Y., and Choy, K. L. A novel fuzzy group decision-making approach to prioritising engineering characteristics in QFD under uncertainties. *International Journal of Production Research*, 49(19):5801–5820, 2011.

[321] Zheng, P., Xu, X., and Xie, S. Q. A weighted interval rough number based method to determine relative importance ratings of customer requirements in QFD product planning. *Journal of Intelligent Manufacturing*, 30(1):3–16, 2019.

[322] Van De Poel, I. Methodological problems in QFD and directions for future development. *Research in Engineering Design*, 18(1):21–36, 2007.

[323] Tontini, G. Integrating the Kano Model and QFD for Designing New Products Integrating the Kano Model and QFD for Designing New Products. *Total Quality Management*, 18(6): 599–612, 2007.

[324] Chaudha, A., Jain, R., Singh, A. R., and Mishra, P. K. Integration of Kano's Model into quality function deployment (QFD). *The International Journal of Advanced Manufacturing Technology*, 53:689–698, 2011.

[325] Kano, N. Attractive quality and must-be quality. *Hinshitsu (Quality, The Journal of Japanese Society for Quality Control)*, 14:39–48, 1984.

[326] Matzler, K. and Hinterhuber, H. H. How to make product development projects more successful by integrating Kano' s model of customer satisfaction into quality function deployment. *Technovation*, 18(1):25–38, 1998.

[327] Berger, C., Blauth, R., and Boger, D. Kano's methods for understanding customer-defined quality. *Center for Quality Management Journal*, 2(4):3–36, 1993.

[328] Shen, X. X., Tan, K. C., and Xie, M. An integrated approach to innovative product development using Kano's model and QFD. *European Journal of Innovation Management*, 3 (2):91–99, 2000.

[329] Shahin, A., Pourhamidi, M., Antony, J., and Park, S. H. Typology of Kano models: A critical review of literature and proposition of a revised model. *International Journal of Quality and Reliability Management*, 30(3):341–358, 2013.

[330] Violante, M. G., Vezzetti, E., and Nonis, F. The Kano Model in the Development of Customer Oriented Products. In Kahraman, C. and Cebi, S., editors, *Customer Oriented Product Design*, pages 187–214. Springer, 2020.

[331] Delice, E. K. and Güngör, Z. A new mixed integer linear programming model for product development using quality function deployment. *Computers & Industrial Engineering*, 57(3): 906–912, 2009.

[332] Ji, P., Jin, J., Wang, T., and Chen, Y. Quantification and integration of Kano' s model into QFD for optimising product design. *International Journal of Production Research*, 52(21): 6335–6348, 2014.

[333] Franceschini, F. and Rossetto, S. Quality function deployment: How to improve its use. *Total Quality Management*, 9(6):491–500, 1998.

[334] Burke, E., Kloeber, J. M., and Deckro, R. F. Using and abusing QFD scores. *Quality Engineering*, 15(1):9–21, 2002.

[335] Franceschini, F., Galetto, M., Maisano, D., and Mastrogiacomo, L. Ordinal aggregation operators to support the engineering characteristic prioritization in QFD. *The International Journal of Advanced Manufacturing Technology*, 91:4069–4080, 2017.

[336] Dym, C. L., Wood, W. H., and Scott, M. J. Rank ordering engineering designs: Pairwise comparison charts and Borda counts. *Research in Engineering Design*, 13(4):236–242, 2002.

[337] Mazurek, J. A new model for multiple criteria decision making with ordinal rankings of criteria and alternatives. *International Journal of Economics and Statistics*, 2:75–82, 2014.

[338] Zhang, L., Hub, M., Mang, S., Thieke, C., Nix, O., Karger, C. P., and Floca, R. O. Software for quantitative analysis of radiotherapy: Overview, requirement analysis and design solutions. *Computer Methods and Programs in Biomedicine*, 110(3):528–537, 2013.

[339] Vorwerk, H., Zink, K., Wagner, D. M., and Engenhart-Cabillic, R. Making the right software choice for clinically used equipment in radiation oncology. *Radiation Oncology*, 9(1):1–8, 2014.

[340] Weijters, B., Cabooter, E., and Schillewaert, N. The effect of rating scale format on response styles: The number of response categories and response category labels. *International Journal of Research in Marketing*, 27(3):236–247, 2010.

[341] Mikulić, J. and Prebežac, D. A critical review of techniques for classifying quality attributes in the Kano model. *Managing Service Quality*, 21(1):46–66, 2011.

[342] Hayes, A. F., Krippendorff, K., Hayes, A. F., and Krippendorff, K. Answering the Call for a Standard Reliability Measure for Coding Data. *Communication Methods and Measures*, 1(1): 77–89, 2007.

[343] Gustafsson, A. and Johnson, M. D. Determining Attribute Importance in a Service Satisfaction Model. *Journal of Service Research*, 7(2):124–141, 2004.

[344] Helms, J. E., Henze, K. T., Sass, T. L., and Mifsud, V. A. Treating Cronbach's Alpha Reliability Coefficients as Data in Counseling Research. *The Counseling Psychologist*, 34(5): 630–660, 2006.

[345] Bonett, D. G. Sample size requirements for testing and estimating coefficient alpha. *Journal of Educational and Behavioral Statistics*, 27(4):335–340, 2002.

[346] Greenleaf, E. A. Improving Rating Scale Measures by Detecting and Correcting Bias Components in Some Response Styles. *Journal of Marketing Research*, 29(2):176, 1992.

[347] Matzler, K., Fuchs, M., and Schubert, A. K. Employee satisfaction: Does Kano's model apply? *Total Quality Management and Business Excellence*, 15(9-10):1179–1198, 2004.

[348] Witell, L. and Löfgren, M. Classification of quality attributes. *Managing Service Quality*, 17 (1):54–73, 2007.

[349] Wang, T. and Ji, P. Understanding customer needs through quantitative analysis of Kano's model. *International Journal of Quality and Reliability Management*, 27(2):173–184, 2010.

[350] Yager, R. R. Multicriteria Decision Making With Ordinal / Linguistic Intuitionistic Fuzzy Sets For Mobile Apps. *IEEE Transactions on Fuzzy Systems*, 24(3):590–599, 2016.

[351] Hauser, J. R. and Clausing, D. The house of quality. *Harvard Business Review*, 66(3):63–73, 1988.

[352] Kavraki, L. E., Švestka, P., Latombe, J. C., and Overmars, M. H. Probabilistic roadmaps for path planning in high-dimensional configuration spaces. *IEEE Transactions on Robotics and Automation*, 12(4):566–580, 1996.

[353] LaValle, S. M. Rapidly-Exploring Random Trees: A New Tool for Path Planning. Technical report, Computer Science Department, Iowa State University, 1998.

[354] Karaman, S. and Frazzoli, E. Incremental Sampling-based Algorithms for Optimal Motion Planning. *Robotics Science and Systems VI*, 104(2):1–20, 2010.

[355] Kuffner, J. J. and Lavalle, S. M. RRT-Connect : An Efficient Approach to Single-Query Path Planning. In *Proceedings of the 2000 IEEE International Conference on Robotics & Automation*, number April, pages 995–1001, San Francisco, CA, 2000.

[356] Jeon, J. H., Karaman, S., and Frazzoli, E. Anytime Computation of Time-Optimal Off-Road Vehicle Maneuvers using the RRT. In *50th IEEE Conference on Decision and Control and European Control Conference (CDC-ECC)*, pages 3276–3282, Orlando, Fl, 2011. IEEE.

[357] Webb, D. J. and Berg, J. v. d. Kinodynamic RRT*: Optimal Motion Planning for Systems with Linear Differential Constraints. *arXiv preprint*, pages 1–8, 2012. URL http://arxiv.org/abs/1205.5088.

[358] Véras, L. G. D. O., Medeiros, F. L. L., and Guimarães, L. N. F. Systematic Literature Review of Sampling Process in Rapidly-Exploring Random Trees. *IEEE Access*, 7:50933–50953, 2019.

[359] Lindemann, S. R. and La Valle, S. M. Incrementally reducing dispersion by increasing voronoi bias in RRTs. *Proceedings - IEEE International Conference on Robotics and Automation*, 2004 (4):3251–3257, 2004.

[360] Lindemann, S. R. and LaValle, S. M. Current issues in sampling-based motion planning. In *Robotics research. The eleventh international symposium*, pages 36–54. Springer, 2005.

[361] Missiuro, P. E. and Roy, N. Adapting probabilistic roadmaps to handle uncertain maps. *Proceedings - IEEE International Conference on Robotics and Automation*, 2006(May):1261–1267, 2006.

[362] Gammell, J. D., Srinivasa, S. S., and Barfoot, T. D. Informed RRT: Optimal sampling-based path planning focused via direct sampling of an admissible ellipsoidal heuristic. In *IEEE International Conference on Intelligent Robots and Systems*, pages 2997–3004. IEEE, 2014.

[363] Islam, F., Nasir, J., Malik, U., Ayaz, Y., and Hasan, O. RRT*-Smart: Rapid convergence implementation of RRT* towards optimal solution. In *2012 IEEE International Conference on Mechatronics and Automation, ICMA 2012*, pages 1651–1656. IEEE, 2012.

[364] Gammell, J. D., Srinivasa, S. S., and Barfoot, T. D. Batch Informed Trees (BIT*): Sampling-based Optimal Planning via the Heuristically Guided Search of Implicit Random Geometric Graphs. In *2015 IEEE International Conference on Robotics and Automation (ICRA) Washington State Convention Center*, pages 3067–3074, Seattle, Washington, 2015. IEEE.

[365] Shkolnik, A., Walter, M., and Tedrake, R. Reachability-guided sampling for planning under differential constraints. *Proceedings - IEEE International Conference on Robotics and Automation*, pages 2859–2865, 2009.

[366] LaValle, S. M. From Dynamic Programming to RRTs: Algorithmic Design of Feasible Trajectories. In Bicchi, A., Prattichizzo, D., and Christensen, H. I., editors, *Control Problems in Robotics*, pages 19–37. Springer, 2003.

[367] Patil, S., Burgner, J., Webster, R. J., and Alterovitz, R. Needle steering in 3-D Via rapid replanning. *IEEE Transactions on Robotics*, 30(4):853–864, 2014.

[368] Kleinbort, M., Salzman, O., and Halperin, D. Collision detection or nearest-neighbor search? On the computational bottleneck in sampling-based motion planning. In Goldberg, K., Abbeel, P., Bekris, K., and Miller, L., editors, *Algorithmic Foundations of Robotics XII*, pages 624–639. Springer, 2020.

[369] Salzman, O. and Halperin, D. Asymptotically Near-Optimal RRT for Fast, High-Quality Motion Planning. *IEEE Transactions on Robotics*, 32(3):473–483, 2016.

[370] Perez, A., Jr, R. P., Konidaris, G., Kaelbling, L., and Lozano-perez, T. LQR-RRT : Optimal Sampling-Based Motion Planning with Automatically Derived Extension Heuristics. In *2012 IEEE International Conference on Robotics and Automation*, pages 2537–2542, Saint Paul, Minnesota, 2012. IEEE.

[371] LaValle, S. M. and Kuffner, J. J. Randomized kinodynamic planning. *The International Journal of Robotics Research*, 20(55):378–400, 2001.

[372] Moon, C. B. and Chung, W. Kinodynamic planner dual-tree RRT (DT-RRT) for two-wheeled mobile robots using the rapidly exploring random tree. *IEEE Transactions on Industrial Electronics*, 62(2):1080–1090, 2015.

[373] Chen, L., Shan, Y., Tian, W., Li, B., and Cao, D. A Fast and Efficient Double-Tree RRT-Like Sampling-Based Planner Applying on Mobile Robotic Systems. *IEEE/ASME Transactions on mechatronics*, 23(6):2568–2578, 2018.

[374] Sánchez, G. and Latombe, J.-c. Checking in PRM Planning: Application to Multi-Robot. *The International Journal of Robotics Research*, 21(1):5–26, 2002.

[375] Petti, S. and Fraichard, T. Safe motion planning in dynamic environments. In *2005 IEEE/RSJ International Conference on Intelligent Robots and Systems, IROS*, pages 2210–2215. IEEE, 2005.

[376] Farina, M., Giulioni, L., and Scattolini, R. Stochastic linear Model Predictive Control with chance constraints - A review. *Journal of Process Control*, 44:53–67, 2016.

[377] Vitus, M. P., Zhou, Z., and Tomlin, C. J. Stochastic Control With Uncertain Parameters via Chance Constrained Control. *IEEE Transactions on Automatic Control*, 61(10):2892–2905, 10 2016.

[378] Alterovitz, R., Lessard, E., Pouliot, J., Hsu, I. C. J., O'Brien, J. F., and Goldberg, K. Optimization of HDR brachytherapy dose distributions using linear programming with penalty costs. *Medical Physics*, 33(11):4012–4019, 2006.

[379] Balvert, M., Gorissen, B. L., Den Hertog, D., and Hoffmann, A. L. Dwell time modulation restrictions do not necessarily improve treatment plan quality for prostate HDR brachytherapy. *Physics in Medicine and Biology*, 60(2):537–548, 2015.

[380] Guthier, C. V., Damato, A. L., Viswanathan, A. N., Hesser, J. W., and Cormack, R. A. A fast multitarget inverse treatment planning strategy optimizing dosimetric measures for high-dose-rate (HDR) brachytherapy:. *Medical Physics*, 44(9):4452–4462, 2017.

[381] Semechko, A. Exact minimum bounding spheres and circles, 2020. URL https://nl.mathworks.com/matlabcentral/fileexchange/48725-exact-minimum-bounding-spheres-and-circles.

[382] Siauw, T., Cunha, A., Atamtürk, A., Hsu, I. C., Pouliot, J., and Goldberg, K. IPIP: A new approach to inverse planning for HDR brachytherapy by directly optimizing dosimetric indices. *Medical Physics*, 38(7):4045–4051, 2011.

[383] Meyer, Y., Isaiah, P., and Shima, T. On Dubins paths to intercept a moving target. *Automatica*, 53:256–263, 2015.

[384] Bui, X.-N. and Boissonnat, J.-D. Accessibility region for a car that only moves forwards along optimal paths. Technical report, INRIA France, 1994.

[385] D'Errico, J. interparc, 2012. URL https://nl.mathworks.com/matlabcentral/fileexchange/34874-interparc.

[386] D'Errico, J. arclength, 2012. URL https://nl.mathworks.com/matlabcentral/fileexchange/34871-arclength.

[387] Postlethwaite, I. and Kothari, M. Multi-agent motion planning for nonlinear Gaussian systems. *International Journal of Control*, 86(11):2075–2089, 2013.

[388] Ono, M. and Williams, B. C. Decentralized Chance-Constrained Finite-Horizon Optimal Control for Multi-Agent Systems. In *49th IEEE Conference on Decision and Control*, pages 138–145. IEEE, 2010.

[389] Harris, B. D., Nilsson, S., and Poole, C. M. A feasibility study for using ABS plastic and a low-cost 3D printer for patient-specific brachytherapy mould design. *Australasian Physical & Engineering Sciences in Medicine*, 38(3):399–412, 2015.

[390] Mukadam, M., Dong, J., Yan, X., Dellaert, F., and Boots, B. Continuous-time Gaussian process motion planning via probabilistic inference. *arXiv*, 2018. URL https://arxiv.org/pdf/1707.07383.pdf.

[391] Francis, G., Ott, L., and Ramos, F. Stochastic functional gradient for motion planning in continuous occupancy maps. In *Proceedings - IEEE International Conference on Robotics and Automation*, pages 3778–3785, 2017.

[392] Vemprala, S. 2D/3D RRT* algorithm, 2017. URL https://nl.mathworks.com/matlabcentral/fileexchange/60993-2d-3d-rrt-algorithm.

[393] Agarwal, S. Belief Space Motion Planning using iLQG, 2017. URL https://nl.mathworks.com/matlabcentral/fileexchange/61139-belief-space-motion-planning-using-ilqg?s_tid=prof_contriblnk.

[394] McMahon, S. J. The linear quadratic model: Usage, interpretation and challenges. *Physics in Medicine and Biology*, 64(1), 2019.

[395] Joiner, M. C. and Bentzen, S. M. Fractionation: the linear-quadratic approach. In Joiner, M. C. and van der Kogel, A., editors, *Basic clinical radiobiology*, chapter 8, pages 102–119. Hodder Arnold, London, UK, 2009.

[396] Yuta, S., Otsuka, S., Hiromitsu, I., Sugie, C., Ogino, H., and Tomita, N. Radiobiological Evaluation of the Radiation Dose as Used in High-precision Radiotherapy: Effect of Prolonged Delivery Time and Applicability of the Linear-quadratic Model. *Journal of Radiation Research*, 53(1):1–9, 2012.

[397] Dale, R. G., Coles, I. P., Deehan, C., and O'Donoghue, J. A. Calculation of integrated biological response in brachytherapy. *International Journal of Radiation Oncology Biology Physics*, 38(3):633–642, 1997.

[398] Dale, R. G. and Coles, I. P. Allowance for the radiobiological effects of dose gradients in gynaecological applications. *Radiotherapy and Oncology*, 60(June):7, 2001.

[399] Armpilia, C., Dale, R. G., Sandilos, P., and Vlachos, L. Radiobiological modelling of dose-gradient effects in low dose rate, high dose rate and pulsed brachytherapy. *Physics in Medicine and Biology*, 51(17):4399–4411, 2006.

[400] Niemierko, A. Reporting and analyzing dose distributions: A concept of equivalent uniform dose. *Medical Physics*, 24(1):103–110, 1997.

[401] Fields, E. C., Melvani, R., Hajdok, G., D'Souza, D., Jones, B., Stuhr, K., Diot, Q., Fisher, C. M., Mukhopadhyay, N., and Todor, D. A Multi-institution, Retrospective Analysis of Cervix Intracavitary Brachytherapy Treatments. Part 1: Is EQD2 Good Enough for Reporting Radiobiological Effects? *International Journal of Radiation Oncology Biology Physics*, 99(1): 219–226, 2017.

[402] Fields, E., Waters, M., Melvani, R., Mukhopadhyay, N., and Todor, D. Understanding Outcome Beyond EQD2 in Tandem and Ovoid Cervical Cancer Brachytherapy Treatments. *International Journal of Radiation Oncology Biology Physics*, 99(2):E291, 2017.

[403] De Leeuw, A. A. C., Van De Kamer, J. B., Moerland, M. A., Philippens, M. E. P., and Jürgenliemk-schulz, I.-m. The effect of alternative biological modelling parameters (a/b and half time of repair T1/2) on reported EQD2 values in the treatment of advanced cervical cancer. *Radiotherapy and Oncology*, 101(2):337–342, 2011.

[404] Bentzen, S. M. and Joiner, M. C. The linear-quadratic approach in clinical practice. In Joiner, M. C. and van der Kogel, A., editors, *Basic clinical radiobiology*, chapter 9, pages 120–133. Hodder Arnold, London, UK, 2009.

[405] Chow, B., Warkentin, B., and Menon, G. Radiobiological dose calculation parameters for cervix cancer brachytherapy: A systematic review. *Brachytherapy*, 18(4):546–558, 2019.

[406] Fiorino, C., Briganti, A., and Cozzarini, C. Re: Mark K. Buyyounouski. Radiobiological Modeling and the Study of Hypofractionated Radiotherapy for Prostate Cancer. *European Urology*, 67(3):56–57, 2015.

[407] Nahum, A. E. The Radiobiology of Hypofractionation. *Clinical Oncology*, 27(5):260–269, 2015.

[408] Datta, N. R., Rajkumar, A., and Basu, R. Variations in clinical estimates of tumor volume regression parameters and time factor during external radiotherapy in cancer cervix: Does it mimic the linear-quadratic model of cell survival? *Indian Journal of Cancer*, 42(2):70–77, 2005.

[409] Tanderup, K., Fokdal, L. U., Sturdza, A., Haie-Meder, C., Mazeron, R., van Limbergen, E., Jürgenliemk-Schulz, I., Petric, P., Hoskin, P., Dörr, W., Bentzen, S. M., Kirisits, C., Lindegaard, J. C., and Pötter, R. Effect of tumor dose, volume and overall treatment time on local control after radiochemotherapy including MRI guided brachytherapy of locally advanced cervical cancer. *Radiotherapy and Oncology*, 120(3):441–446, 2016.

[410] Holschneider, C. H., Petereit, D. G., Chu, C., Hsu, I. C., Ioffe, Y. J., Klopp, A. H., Pothuri, B., Chen, L. m., and Yashar, C. Brachytherapy: A critical component of primary radiation therapy for cervical cancer: From the Society of Gynecologic Oncology (SGO) and the American Brachytherapy Society (ABS). *Brachytherapy*, 18(2):123–132, 2019.

[411] Fowler, J. F. The linear-quadratic formula and progress in fractionated radiotherapy. *The British Journal of Radiology*, 62(August):679–694, 1989.

[412] Suwinski, R., Wzietek, I., Tarnawski, R., Namysl-Kaletka, A., Kryj, M., Chmielarz, A., and Wydmanski, J. Moderately Low Alpha/Beta Ratio for Rectal Cancer May Best Explain the Outcome of Three Fractionation Schedules of Preoperative Radiotherapy. *International Journal of Radiation Oncology Biology Physics*, 69(3):793–799, 2007.

[413] Eifel, P. J. and Thames, H. D. Has the influence of treatment duration on local control of carcinoma of the cervix been defined? *International Journal of Radiation Oncology, Biology, Physics*, 32(5):1527–1529, 1995.

[414] Marks, L. B., Yorke, E. D., Jackson, A., Ten Haken, R. K., Constine, L. S., Eisbruch, A., Bentzen, S. M., Nam, J., and Deasy, J. O. The Use of Normal Tissue Complication Probability (NTCP) Models in the Clinic. *International Journal of Radiation Oncology Biology Physics*, 76(3):10–19, 2010.

[415] Berger, D., Dimopoulos, J., Georg, P., Georg, D., Pötter, R., and Kirisits, C. Uncertainties in Assesment of the Vaginal Dose for Intracavitary Brachytherapy of Cervical Cancer using a Tandem-ring Applicator. *International Journal of Radiation Oncology Biology Physics*, 67 (5):1451–1459, 2007.

[416] Dörr, W. and van der Kogel, A. J. The volume effect in radiotherapy. In Joiner, M. C. and van der Kogel, A., editors, *Basic Clinical Radiobiology*, chapter 14, pages 191–206. Hodder Arnold, London, UK, 2009.

[417] Moiseenko, V., Song, W. Y., Mell, L. K., and Bhandare, N. A comparison of dose-response characteristics of four NTCP models using outcomes of radiation-induced optic neuropathy and retinopathy. *Radiation Oncology*, 6(1):61, 2011.

[418] Plataniotis, G. A. and Dale, R. G. Use of Concept of Chemotherapy-Equivalent Biologically Effective Dose to Provide Quantitative Evaluation of Contribution of Chemotherapy to Local Tumor Control in Chemoradiotherapy Cervical Cancer Trials. *International Journal of Radiation Oncology Biology Physics*, 72(5):1538–1543, 2008.

[419] Webb, S. and Nahum, A. E. A model for calculating tumour control probability in radiotherapy including the effects of inhomogeneous distributions of dose and clonogenic cell density To. *Physics in Medicine and Biology*, 38:653–666, 1993.

[420] Lyman, J. T. Complication Probability as Assessed from Dose-Volume Histograms. *Radiation Research*, 104(2):13–19, 1985.

[421] Kong, F. M. S., Pan, C., Eisbruch, A., and Haken, R. K. Physical Models and Simpler Dosimetric Descriptors of Radiation Late Toxicity. *Seminars in Radiation Oncology*, 17(2): 108–120, 2007.

[422] Kutcher, G. J. and Burman, C. Calculation of complication probability factors for non-uniform normal tissue irradiation: The effective volume method. *International Journal of Radiation Oncology Biology Physics*, 16(6):1623–1630, 1989.

[423] Luxton, G., Keall, P. J., and King, C. R. A new formula for normal tissue complication probability (NTCP) as a function of equivalent uniform dose (EUD). *Physics in Medicine and Biology*, 53(1):23–36, 2008.

[424] Mohan, R., Mageras, G. S., Baldwin, B., Brewster, L. J., Kutcher, G. J., Leibel, S., Burman, C. M., and Ling, C. C. Clinically relevant optimization of 3D conformal treatments. *Medical Physics*, 19(4):933–944, 1992.

[425] Niemierko, A. A generalized concept of equivalent uniform dose (EUD). *Medical Physics1*, 26 (6):1100, 1999.

[426] Oinam, A. S., Singh, L., Shukla, A., Ghoshal, S., Kapoor, R., and Sharma, S. C. Dose volume histogram analysis and comparison of different radiobiological models using in-house developed software. *Journal of Medical Physics*, 36(4):220–229, 2011.

[427] Cremonesi, M., Botta, F., Ferrari, M., Strigari, L., Bonomo, G., Orsi, F., and Orecchia, R. The radiation biology of radioembolization. In Pasciak, A. S., McKinney, J. M., and Bradley, Y. C., editors, *Handbook of Radioembolization: Physics, Biology, Nuclear Medicine, and Imaging*, chapter 8, pages 167–195. CRC Press, 2016.

[428] Cozzi, L., Buffa, F. M., and Fogliata, A. Comparative analysis of dose volume histogram reduction algorithms for normal tissue complication probability calculations. *Acta Oncologica*, 39(2):165–171, 2000.

[429] Källman, P., Ågren, A., and Brahme, A. Tumour and normal tissue responses to fractionated non-uniform dose delivery. *International journal of radiation biology*, 62(2):249–262, 1992.

[430] Yorke, E. D. and Ellen, D. Modeling the effects of inhomogeneous dose distributions in normal tissues. *Seminars in Radiation Oncology*, 11(3):197–209, 2001.

[431] Giacomo, P. News from the BIPM. *Metrologia*, 17:69–74, 1981.

[432] Joint Committee For Guides In Metrology (JCGM). Evaluation of measurement data — Guide to the expression of uncertainty in measurement. Technical Report September, 2010.

[433] Taylor, Barry N and Kuyatt, C. E. NIST Technical Note 1297 Guidelines for Evaluating and Expressing the Uncertainty of NIST Measurement Results. *Technology*, 1994.

[434] Standardization, I. O. f. Uncertainty of Measurement–Part 3: Guide to the expression of Uncertainty in Measurement"(GUM: 1995). Technical report, ISO, 2008.

[435] Taylor, A. and Powell, M. E. An assessment of interfractional uterine and cervical motion: Implications for radiotherapy target volume definition in gynaecological cancer. *Radiotherapy and Oncology*, 88(2):250–257, 2008.

[436] Farrance, I. and Frenkel, R. Uncertainty of Measurement : A Review of the Rules for Calculating Uncertainty Components through Functional Relationships. *The Clinical Biochemist Reviews*, 33(2):49–75, 2012.

[437] Royal College of Radiologists, Institute of Physics and Engineering in Medicine, and Society and College of Radiographers. On target: ensuring geometric accuracy in radiotherapy. Technical report, The Royal College of Radiologists London, 2008.

[438] Keall, P. J., Siebers, J. V., Jeraj, R., and Mohan, R. The effect of dose calculation uncertainty on the evaluation of radiotherapy plans. *Medical Physics*, 27(3):478–484, 2000.

[439] Selvaraj, J., Uzan, J., Baker, C., and Nahum, A. Loss of local control due to tumor displacement as a function of margin size, dose-response slope, and number of fractions. *Medical Physics*, 40(4):1–11, 2013.

[440] Moiseenko, V., Battista, J., and Van Dyk, J. Normal tissue complication probabilities: dependence on choice of biological model and dose-volume histogram reduction scheme. *International Journal of Radiation Oncology Biology Physics*, 46(4):983–993, 2000.

[441] Gay, H. A. and Niemierko, A. A free program for calculating EUD-based NTCP and TCP in external beam radiotherapy. *Physica Medica*, 23(3-4):115–125, 2007.

[442] Emami, B., Lyman, J., Brown, A., Coia, L., Goitein, M., Munzenrider, J. E., Shank, B., Solin, L. J., and Wesson, M. Tolerance of normal tissue to therapeutic irradiation. *International Journal of Radiation Oncology Biology Physics*, 21(1):109–122, 1991.

[443] Svolos, P., Tsougos, I., Kyrgias, G., Kappas, C., and Theodorou, K. On the use of published radiobiological parameters and the evaluation of NTCP models regarding lung pneumonitis in clinical breast radiotherapy. *Australasian Physical and Engineering Sciences in Medicine*, 34(1):69–81, 2011.

[444] Chi, A., Gao, M., Sinacore, J., Nguyen, N. P., Vali, F., and Albuquerque, K. Single Versus Customized Treatment Planning for Image-guided High-Dose-Rate Brachytherapy for Cervical Cancer: Dosimetric Comparison and Predicting Factor for Organs at Risk Overdose With Single Plan Approach. *International Journal of Radiation Oncology Biology Physics*, 75(1): 309–314, 2009.

[445] Holloway, C. L., Racine, M. L., Cormack, R. A., O'Farrell, D. A., and Viswanathan, A. N. Sigmoid dose using 3D imaging in cervical-cancer brachytherapy. *Radiotherapy and Oncology*, 93(2):307–310, 2009.

[446] Thomadsen, B. R., Shahabi, S., Stitt, J. A., Buchler, D., Fowler, J., Paliwal, B. R., and T.J., K. High dose rate intracavitary brachytherapy for carcinoma of the cervix: the Madison system: II. Procedural and physical considerations. *International Journal of Radiation Oncology, Biology, Physics*, 24(2):349–357, 1992.

[447] Patel, R. B., Gururajachar, J. M., and Revathy, T. Implications of bladder volume on target coverage and dose to critical structures during high dose rate intracavitary brachytherapy for cervical cancer: A dosimetric study. *Journal of Cancer Research and Therapeutics*, 15(6): 1207–1211, 2019.

[448] Stewart, A. J., Cormack, R. A., Lee, H., Xiong, L., Hansen, J. L., O'Farrell, D. A., and Viswanathan, A. N. Prospective Clinical Trial of Bladder Filling and Three-Dimensional Dosimetry in High-Dose-Rate Vaginal Cuff Brachytherapy. *International Journal of Radiation Oncology Biology Physics*, 72(3):843–848, 2008.

[449] Hung, J., Shen, S., De Los Santos, J. F., and Kim, R. Y. Image-based 3D treatment planning for vaginal cylinder brachytherapy: Dosimetric effects of bladder filling on organs at risk. *International Journal of Radiation Oncology Biology Physics*, 83(3):980–985, 2012.

[450] Elfes, A. Using occupancy grids for mobile robot perception and navigation. *Computer*, 22 (6):46–57, 1989.

[451] Khatib, O. Real-Time Obstacle Avoidance for Manipulators and Mobile Robots. *The International Journal of Robotics Research*, 5(1):396–404, 1986.

[452] Bhattacharya, S., Ghrist, R., and Kumar, V. Persistent Homology for Path Planning in Uncertain Environments. *IEEE Transactions on Robotics*, 31(3):578–590, 2015.

[453] Axelrod, B., Kaelbling, L. P., and Lozano-Pérez, T. Provably safe robot navigation with obstacle uncertainty. *International Journal of Robotics Research*, 37(13-14):1760–1774, 2018.

[454] Francis, G., Ott, L., and Ramos, F. Fast stochastic functional path planning in occupancy maps. *Proceedings - IEEE International Conference on Robotics and Automation*, 2019-May: 929–935, 2019.

[455] Qin, S. J. and Badgwell, T. A. Process Control Dynamic. *Control Engineering Practice*, 11: 733–764, 2003.

[456] Summers, S., Kamgarpour, M., Tomlin, C., and Lygeros, J. A stochastic reach-avoid problem with random obstacles. *HSCC'11 - Proceedings of the 2011 ACM/SIGBED Hybrid Systems: Computation and Control*, pages 251–260, 2011.

[457] Lenz, D., Rickert, M., and Knoll, A. Heuristic search in belief space for motion planning under uncertainties. *IEEE International Conference on Intelligent Robots and Systems*, 2015-Decem: 2659–2665, 2015.

[458] Melchior, N. A. and Simmons, R. Particle RRT for path planning with uncertainty. In *Proceedings - IEEE International Conference on Robotics and Automation*, pages 1617–1624, 2007.

[459] Masoud, A. A. Motion planning with gamma-harmonic potential fields. *IEEE Transactions on Aerospace and Electronic Systems*, 48(4):2786–2801, 2012.

[460] Merkt, W., Ivan, V., and Vijayakumar, S. Continuous-Time Collision Avoidance for Trajectory Optimization in Dynamic Environments. In *IEEE International Conference on Intelligent Robots and Systems*, pages 7248–7255, 2019.

[461] González-Arribas, D., Soler, M., Sanjurjo-Rivo, M., Kamgarpour, M., and Simarro, J. Robust aircraft trajectory planning under uncertain convective environments with optimal control and rapidly developing thunderstorms. *Aerospace Science and Technology*, 89:445–459, 2019.

[462] Jacobs, J. F., Poel, I. V. D., and Osseweijer, P. Clarifying the debate on selection methods for engineering: Arrow's impossibility theorem, design performances, and information basis. *Research in Engineering Design*, 25(1):3–10, 2014.

[463] Franceschini, F. and Rupil, A. Rating scales and prioritization in QFD. *International Journal of Quality & Reliability Management*, 16(1):85–97, 1999.

[464] Chen, L.-H. and Chen, C.-N. Normalisation models for prioritising design requirements for quality function deployment processes. *International Journal ofProduction Research*, 52(2): 299–313, 2014.

[465] Song, H. A critical review of Kano's wording and its impact on attribute classification: A case study of smartphone in Korea. *Total Quality Management and Business Excellence*, 29 (1-2):1–28, 2018.

[466] Kim, M.-H., Song, H., and Park, Y. T. Comparing the Questionnaires for Classifying Quality Attributes in the Kano Model. *Journal of the Korean society for quality management*, 41(2): 209–220, 2013.

[467] Song, H. and Park, Y. T. Wordings of the Kano Model's Questionnaire. *Journal of the Korean society for quality management*, 40(4):453–466, 2012.

[468] Tan, K. C. and Shen, X. X. Integrating Kano's model in the planning matrix of quality function deployment. *Total Quality Management*, 11(8):1141–1151, 2000.

[469] Nahm, Y. E. A novel approach to prioritize customer requirements in QFD based on customer satisfaction function for customer-oriented product design. *Journal of Mechanical Science and Technology*, 27(12):3765–3777, 2013.

[470] Chaudhuri, A. and Bhattacharyya, M. A combined QFD and integer programming framework to determine attribute levels for conjoint study. *International Journal of Production Research*, 47(23):6633–6649, 2009.

[471] Wasserman, G. S. On how to prioritize design requirements during the qfd planning process. *IIE Transactions (Institute of Industrial Engineers)*, 25(3):59–65, 1993.

[472] Raharjo, H. On normalizing the relationship matrix in quality function deployment. *International Journal of Quality and Reliability Management*, 30(6):647–661, 2013.

[473] Olewnik, A. T. and Lewis, K. On Validating Engineering Design Decision Support Tools. *Concurrent Engineering*, 13(2):111–122, 2005.

[474] Chen, Y., Fung, R. Y., and Tang, J. Rating technical attributes in fuzzy QFD by integrating fuzzy weighted average method and fuzzy expected value operator. *European Journal of Operational Research*, 174(3):1553–1566, 2006.

[475] Chen, L. H. and Weng, M. C. An evaluation approach to engineering design in QFD processes using fuzzy goal programming models. *European Journal of Operational Research*, 172(1):230–248, 2006.

[476] Klir, G. J. and Yuan, B. *Fuzzy sets and fuzzy logic: Theory and applications*. Prentice Hall PTR, Upper Saddle River, NJ, 1995.

[477] Ko, W. C. and Chen, L. H. An approach of new product planning using quality function deployment and fuzzy linear programming model. *International Journal of Production Research*, 52(6):1728–1743, 2014.

A. Appendices

A.1 MATLAB scripts

A.1.1 Script accompanying Figure 1.3

```
%% MATLAB - Line source distribution (mHDR-v2)
% Robin Straathof (2020)
clc
clear all
close all

% Data from mHDR-v2
%   Download online; save as 'mHDR_v2.xlsx'
%   Save g_l and F_l data in two separate sheets
global L theta_0 r_0
S_K         = 40820;    % Air-kerma strength: U
Lambda      = 1.109;    % Dose-rate constant: cm-2
L           = 0.35;     % Active length: cm
theta_0     = pi/2;     % Reference angle: rad
r_0         = 1;        % Reference distance: cm
diam        = 0.09;     % Source diameter: cm
l           = 0.5;      % Source length: cm

data_gl     = readmatrix('mHDR_v2.xlsx','Sheet','g_l');
data_Fl     = readmatrix('mHDR_v2.xlsx','Sheet','F_l');
theta_Fl    = data_Fl(2:end,1)./180*pi;
r_Fl        = data_Fl(1,2:end);
val_Fl      = data_Fl(2:end,2:end);

% Compute relevant functions
G_l0        = G_l(r_0,theta_0);
r_vec       = linspace(0.3,10,98); % offset from centre due to errors
theta_vec   = linspace(0,pi,101);

for i = 1:(length(r_vec))
    r = r_vec(i);
    g_l = interp1(data_gl(:,1),data_gl(:,2),r);             % linearly interpolate
    for j = 1:(length(theta_vec))
        theta = theta_vec(j);
        F_l   = interp2(r_Fl,theta_Fl,val_Fl,r,theta);      % linearly interpolate
        G_lp(i,j)   = G_l(r,theta);
        d_rate(i,j) = d(S_K,Lambda,G_lp(i,j),G_l0,g_l,F_l); % cGy/hour
    end
end

% Plot result
[t,r] = meshgrid(theta_vec,r_vec./100);
[x,y] = pol2cart(t,r);

figure(1)
surf(x,y,d_rate);
xlabel('X (m)'), ylabel('Y (m)')
```

```
hold on
surf(x,-y,d_rate);
colormap([linspace(0.8,1,256)',linspace(0.8,210/255,256)',linspace(0.8,0,256)'])
colorbar
set(gca,'ColorScale','log')

figure(2)
contour(x,y,d_rate,10)
xlim([-0.02 0.02])
ylim([-0.02 0.02])
xlabel('X (m)'), ylabel('Y (m)')
hold on
rectangle('Position',[-l/200 -diam/200 l/100 diam/100],'FaceColor', 'k') % source
contour(x,-y,d_rate,10)
colormap([linspace(0.8,1,256)',linspace(0.8,210/255,256)',linspace(0.8,0,256)'])
colorbar
set(gca,'ColorScale','log')

%% Functions
% Geometry function
function G_l_out = G_l(r,theta)
global L

beta = atan2(r*cos(theta)+L/2, r*sin(theta))- atan2(r*cos(theta)-L/2, r*sin(theta));
if theta == 0 || theta == pi
    G_l_out = 1/(r^2-L^2/4);
else
    G_l_out = beta/(L*r*sin(theta));
end

end

% Absorbed dose calculation
function d_out = d(S_K,Lambda,G_lp,G_l0,g_l,F_l)
d_out       = S_K*Lambda*G_lp/G_l0*g_l*F_l;
end
```

A.1.2 Script accompanying Figure A.1a

```
%% MATLAB - D90 EQD2 vs TCP
% Robin Straathof (2020)
clc
clear all
close all

% Symbolic variables
syms alpha_B beta_B N_B d_B G_B   % subscript `B' denotes BT
syms alpha_E beta_E N_E d_E G_E   % subscript `E' denotes EBRT
syms R x
syms gamma_50 TCD_50 D

%% Computation of (equivalent) Biologically effective dose (BED_(eq))
% Formulas BED and BED_eq for spherical dose (see Dale et al. (1997))
BED_B     =  N_B*d_B*(1+G_B*d_B/(alpha_B/beta_B));
BED_E     =  N_E*d_E*(1+G_E*d_E/(alpha_E/beta_E));
f         =  exp(-alpha_B*N_B*d_B*(R/x)^2-beta_B*G_B*N_B*d_B^2*(R/x)^4);
BED_eq_B  = -1/alpha_B*log(3/R^3*vpaintegral(x^2*f,x,0,R));

%% Computation of EQD2_(eq) for BT+EBRT
% Formulas as derived with the method in ICRU 89 (2016)
EQD2    =  BED_B/((2*G_B)/(alpha_B/beta_B)+1)   + BED_E/((2*G_E)/(alpha_E/beta_E)+1);
EQD2_eq =  BED_eq_B/((2*G_B)/(alpha_B/beta_B)+1)+ BED_E/((2*G_E)/(alpha_E/beta_E)+1);

%% Logistic TCP model
% Formula for the logistic TCP model
TCP       =  1/(1+exp(4*gamma_50*(1-D/TCD_50)));
TCP_EQD2  =  subs(TCP,D,EQD2);
TCP_EQD2_eq  =  subs(TCP,D,EQD2_eq);

%% Plot
% Variable declaration
alpha_B = 0.35; beta_B = 0.35/10; N_B = 4;  G_B = 1; R = 0.02; d_B = 5;
alpha_E = 0.35; beta_E = 0.35/10; N_E = 25; G_E = 1; d_E = 1.8;

TCP_EQD2     = subs(TCP_EQD2,{gamma_50,TCD_50},{0.47,36.0});
% From Nesvacil et al. (2016)
TCP_EQD2_eq  = subs(TCP_EQD2_eq,{gamma_50,TCD_50},{0.48,39.4});
% Estimated parameters

% Generate plot
for i = 1:61
    TCP_EQD2_vec(i)    = eval(TCP_EQD2);     EQD2_vec(i)     = eval(EQD2);
    TCP_EQD2_eq_vec(i) = eval(TCP_EQD2_eq);  EQD2_eq_vec(i)  = eval(EQD2_eq);
    d_B                = d_B + 0.1;
end

% Plot results
figure('Name','Figure 2a','NumberTitle','off')
plot(EQD2_vec,TCP_EQD2_vec,'LineWidth',3,'color',[0 166/255 214/255])
hold on
plot(EQD2_vec,TCP_EQD2_eq_vec,'LineWidth',3,'color',[1 210/255 0])
set(gca,'FontName', 'Times New Roman','xlim',[65 120],'ylim',[0.85 1],...
'FontSize',18,'LineWidth',1.5)
xlabel('BT + EBRT {\it D}_{90} CTV_{HR} (EQD2_{\alpha/\beta = 10Gy})');ylabel('TCP')
h=legend({'EQD2','EQD2_{eq}'},'location','northwest');
```

A.1.3 Script accompanying Figure A.1b

```
%% MATLAB - D2cm3 EQD2 vs NTCP
% Robin Straathof (2020)
clc
clear all
close all

% Symbolic variables
syms alpha_B beta_B N_B d_B G_B   % subscript `B' denotes BT
syms alpha_E beta_E N_E d_E G_E   % subscript `E' denotes EBRT
syms R x
syms gamma_50 TCD_50 D

%% Computation of (equivalent) Biologically effective dose (BED_(eq))
% Formulas BED and BED_eq for spherical dose (see Dale et al. (1997))
BED_B     =  N_B*d_B*(1+G_B*d_B/(alpha_B/beta_B));
BED_E     =  N_E*d_E*(1+G_E*d_E/(alpha_E/beta_E));
f         =  exp(-alpha_B*N_B*d_B*(R/x)^2-beta_B*G_B*N_B*d_B^2*(R/x)^4);
BED_eq_B  = -1/alpha_B*log(3/R^3*vpaintegral(x^2*f,x,0,R));

%% Computation of EQD2_(eq) for BT+EBRT
% Formulas as derived with method in ICRU 89 (2016)
EQD2    =  BED_B/((2*G_B)/(alpha_B/beta_B)+1)   + BED_E/((2*G_E)/(alpha_E/beta_E)+1);
EQD2_eq =  BED_eq_B/((2*G_B)/(alpha_B/beta_B)+1)+ BED_E/((2*G_E)/(alpha_E/beta_E)+1);

%% Logistic NTCP model
% Formula for the logistic NTCP model
NTCP      =  1/(1+exp(4*gamma_50*(1-D/TCD_50)));
NTCP_EQD2 =  subs(NTCP,D,EQD2);
NTCP_EQD2_eq  =  subs(NTCP,D,EQD2_eq);

%% Plot
% Variable declaration
alpha_B = 0.35; beta_B = 0.35/10; N_B = 4;  G_B = 1; R = 0.02; d_B = 2;
alpha_E = 0.35; beta_E = 0.35/10; N_E = 25; G_E = 1; d_E = 1.8;

NTCP_EQD2    = subs(NTCP_EQD2,{gamma_50,TCD_50},{2.0,110});
% From Nesvacil et al. (2016)
NTCP_EQD2_eq = subs(NTCP_EQD2_eq,{gamma_50,TCD_50},{2.05,118});
% Estimated parameters

% Generate plot
for i = 1:61
    NTCP_EQD2_vec(i)    = eval(NTCP_EQD2);     EQD2_vec(i)    = eval(EQD2);
    NTCP_EQD2_eq_vec(i) = eval(NTCP_EQD2_eq);  EQD2_eq_vec(i) = eval(EQD2_eq);
    d_B                 = d_B + 0.1;
end

% Plot results
figure('Name','Figure 2b','NumberTitle','off')
plot(EQD2_vec,NTCP_EQD2_vec,'LineWidth',3,'color',[0 166/255 214/255])
hold on
plot(EQD2_vec,NTCP_EQD2_eq_vec,'LineWidth',3,'color',[1 210/255 0])
set(gca,'FontName', 'Times New Roman','xlim',[55 85],'ylim',[0 0.2],...
'FontSize',18,'LineWidth',1.5)
xlabel('BT + EBRT {\it D}_{2cm^3} OAR (EQD2_{\alpha/\beta = 3Gy})');ylabel('NTCP')
h=legend({'EQD2','EQD2_{eq}'},'location','northwest');
```

A.1.4 Script accompanying Figure A.2 and Figure A.3

```
%% MATLAB - D2cm3 EQD2 vs NTCP
% Robin Straathof (2020)
clc
clear all
close all

% Symbolic variables
syms TD_50 V_eff_vec D_ref y V_i D_i m n

%% Probit NTCP model
% Variable declaration
m_blad = 0.11; n_blad = 0.5; TD_blad_50 = 80;       % data from Burman et al. (1991)
m_rect = 0.15; n_rect = 0.12; TD_rect_50 = 80;      % data from Burman et al. (1991)
ax_int = 0:1:100;

% Input cumulative DVH data (1)
v_blad    = [1 1 1 1 1 1 0.8 0.35 0.1 0.04 0.01];
EQD2_blad = [0 10 20 30 40 50 60 70 80 90 100];

% Input cumulative DVH data (2)
v_rect  = [1 1 1 1 0.5 0.15 0.1 0.08 0.02 0.01 0];

% Generate smooth cumulative DVH diagrams from fitting data
fun_blad  = @(z_blad,EQD2_blad) 1./(1+exp((EQD2_blad-z_blad(2))*z_blad(1)));
z_blad    = lsqcurvefit(fun_blad,[0.1,50],EQD2_blad,v_blad);
DVH_blad_cm     = [ax_int;fun_blad(z_blad,ax_int)];
[l_blad,L_blad] = size(DVH_blad_cm);

z_rect    = lsqcurvefit(fun_blad,[0.1,50],EQD2_blad,v_rect);
DVH_rect_cm     = [ax_int;fun_blad(z_rect,ax_int)];

% Generate differential DVH (see Gay and Niemierko (2007))
DVH_blad  = DVH_blad_cm;
for i = 2:1:L_blad
    DVH_blad(1,i-1) = DVH_blad(1,i-1)+(DVH_blad(1,i)-DVH_blad(1,i-1))/2;
    DVH_blad(2,i-1) =(DVH_blad(2,i-1)-DVH_blad(2,i));
end

DVH_rect  = DVH_rect_cm;
for i = 2:1:L_blad
    DVH_rect(1,i-1) = DVH_rect(1,i-1)+(DVH_rect(1,i)-DVH_rect(1,i-1))/2;
    DVH_rect(2,i-1) =(DVH_rect(2,i-1)-DVH_rect(2,i));
end

%% Reduced DVH diagrams and NTCP curve
% Reduced DVH diagram with KB reduction algorithm (Kutcher and Burman (1989))
% Generate the NTCP curves
D_ref_blad = max(DVH_blad(1,:));
for i = 1:1:L_blad
    D_blad_i          = DVH_blad(1,i);
    v_blad_i          = DVH_blad(2,i);
    v_eff_blad_vec(i) = v_blad_i*(D_blad_i/D_ref_blad)^(1/n_blad);
    v_eff_blad        = sum(v_eff_blad_vec);
end
```

```
D_ref_rect = max(DVH_rect(1,:));
for j = 1:1:L_blad
    D_rect_j           = DVH_rect(1,j);
    v_rect_j           = DVH_rect(2,j);
    v_eff_rect_vec(j)  = v_rect_j*(D_rect_j/D_ref_rect)^(1/n_rect);
    v_eff_rect         = sum(v_eff_rect_vec);
end

% Formula for the probit NTCP model by Lyman (1985) for the effective volume
TDV_blad_eff_50  = TD_blad_50/(v_eff_blad^n_blad);
t_blad_eff       = (D_ref_blad-TDV_blad_eff_50)/(m_blad*TDV_blad_eff_50);
NTCP_blad_eff    = eval(1/sqrt(2*pi)*vpaintegral(exp(-y^2/2),y,-100,t_blad_eff))

TDV_rect_eff_50  = TD_rect_50/(v_eff_rect^n_rect);
t_rect_eff       = (D_ref_rect-TDV_rect_eff_50)/(m_rect*TDV_rect_eff_50);
NTCP_rect_eff    = eval(1/sqrt(2*pi)*vpaintegral(exp(-y^2/2),y,-100,t_rect_eff))

% Generate NTCP plot data
for i = 1:1:L_blad
    TDV_blad_50  = TD_blad_50/(1^n_blad);
    t_blad       = (DVH_blad(1,i)-TDV_blad_50)/(m_blad*TDV_blad_50);
    NTCP_blad(i) = eval(1/sqrt(2*pi)*vpaintegral(exp(-y^2/2),y,-100,t_blad));
end

for j = 1:1:L_blad
    TDV_rect_50  = TD_rect_50/(1^n_rect);
    t_rect       = (DVH_rect(1,j)-TDV_rect_50)/(m_rect*TDV_rect_50);
    NTCP_rect(j) = eval(1/sqrt(2*pi)*vpaintegral(exp(-y^2/2),y,-100,t_rect));
end

% Calculate dose corresponding to NTCP
D_blad_NTCP      = interp1(NTCP_blad,DVH_blad_cm(1,:),NTCP_blad_eff)
D_blad_50        = interp1(DVH_blad_cm(2,:),DVH_blad_cm(1,:),0.5)
NTCP_blad_D_50   = interp1(DVH_blad_cm(1,:),NTCP_blad,D_blad_50)

D_rect_NTCP      = interp1(NTCP_rect,DVH_rect_cm(1,:),NTCP_rect_eff)
D_rect_50        = interp1(DVH_rect_cm(2,:),DVH_rect_cm(1,:),0.5)
NTCP_rect_D_50   = interp1(DVH_rect_cm(1,:),NTCP_rect,D_rect_50)

%% Plot
% Plot results
% DVHs
figure('Name','Figure 3a','NumberTitle','off')
plot(EQD2_blad,v_blad,'ko','Markerfacecolor','k')
hold on
plot(DVH_blad_cm(1,:),DVH_blad_cm(2,:),'LineWidth',3,'color',[0 166/255 214/255])
set(gca,'FontName', 'Times New Roman','xlim',[0 100],'ylim',[0 1],...
'FontSize',18,'LineWidth',1.5)
xlabel('BT + EBRT {\it D} Bladder (EQD2_{\alpha/\beta = 3Gy})');
ylabel('Volume {\it v} (%)');
```

```
figure('Name','Figure 3b','NumberTitle','off')
plot(EQD2_blad,v_rect,'ko','Markerfacecolor','k')
hold on
plot(DVH_rect_cm(1,:),DVH_rect_cm(2,:),'LineWidth',3,'color',[0 166/255 214/255])
set(gca,'FontName', 'Times New Roman','xlim',[0 100],'ylim',[0 1],...
'FontSize',18,'LineWidth',1.5)
xlabel('BT + EBRT {\it D} Rectum (EQD2_{\alpha/\beta = 3Gy})');
ylabel('Volume {\it v} (%)');

% NTCP-EQD2 graphs
figure('Name','Figure 4a','NumberTitle','off')
plot(DVH_blad_cm(1,:),NTCP_blad(1,:),'LineWidth',3,'color',[0 166/255 214/255])
hold on
plot(D_blad_NTCP,NTCP_blad_eff,'ko','MarkerSize',14,'LineWidth',2)
set(gca,'FontName', 'Times New Roman','xlim',[0 100],'ylim',[0 1],...
'FontSize',14,'LineWidth',1.5)
xlabel('BT + EBRT {\it D} Bladder (EQD2_{\alpha/\beta = 3Gy})');ylabel('NTCP')
h=legend({'NTCP','NTCP_{eff}'},'location','northwest');

figure('Name','Figure 4b','NumberTitle','off')
plot(DVH_rect_cm(1,:),NTCP_rect(1,:),'LineWidth',3,'color',[0 166/255 214/255])
hold on
plot(D_rect_NTCP,NTCP_rect_eff,'ko','MarkerSize',14,'LineWidth',2)
set(gca,'FontName', 'Times New Roman','xlim',[0 100],'ylim',[0 1],...
'FontSize',14,'LineWidth',1.5)
xlabel('BT + EBRT {\it D} Rectum (EQD2_{\alpha/\beta = 3Gy})');ylabel('NTCP')
h=legend({'NTCP','NTCP_{eff}'},'location','northwest');
```

A.1.5 Script accompanying Figure 2.1 and Table 2.1

```
%% MATLAB - Error calculations
% Robin Straathof (2020)
clc
clear all
close all

% Patient data
Pat_1   = [ 2  3 ;  3  3 ;  2  2 ;  3  2];
Pat_2   = [ 1  0 ;  2  0 ;  0  2 ; -1  1];
Pat_3   = [-2 -3 ; -2 -2 ; -1 -3 ; -2 -2];

% Mean and SD of patients
Mean_1x = mean(Pat_1(:,1));  SD_1x = std(Pat_1(:,1));
Mean_1y = mean(Pat_1(:,2));  SD_1y = std(Pat_1(:,2));
Mean_2x = mean(Pat_2(:,1));  SD_2x = std(Pat_2(:,1));
Mean_2y = mean(Pat_2(:,2));  SD_2y = std(Pat_2(:,2));
Mean_3x = mean(Pat_3(:,1));  SD_3x = std(Pat_3(:,1));
Mean_3y = mean(Pat_3(:,2));  SD_3y = std(Pat_3(:,2));

% Statistics
Mx      = mean([Mean_1x,Mean_2x,Mean_3x]);          % Group systematic error
My      = mean([Mean_1y,Mean_2y,Mean_3y]);          % Group systematic error
Sx      = std([Mean_1x,Mean_2x,Mean_3x]);           % SD of systematic error
Sy      = std([Mean_1y,Mean_2y,Mean_3y]);           % SD of systematic error
RMSx    = rms([SD_1x,SD_2x,SD_3x]);                 % Group random error
RMSy    = rms([SD_1y,SD_2y,SD_3y]);                 % Group random error
SDSDx   = std([SD_1x,SD_2x,SD_3x]);                 % Spread of random error
SDSDy   = std([SD_1y,SD_2y,SD_3y]);                 % Spread of random error
R_x     = std([Pat_1(:,1);Pat_2(:,1);Pat_3(:,1)])   % Random error total
R_y     = std([Pat_1(:,2);Pat_2(:,2);Pat_3(:,2)])   % Random error total

% Generate circles for plotting later
[cSD_1x,cSD_1y] = circle(Mean_1x,Mean_1y,sqrt(SD_1x^2+SD_1y^2));
[cSD_2x,cSD_2y] = circle(Mean_2x,Mean_2y,sqrt(SD_2x^2+SD_2y^2));
[cSD_3x,cSD_3y] = circle(Mean_3x,Mean_3y,sqrt(SD_3x^2+SD_3y^2));
[cSD_x,cSD_y]   = circle(Mx,My,sqrt(Sx^2+Sy^2));
[RSD_x,RSD_y]   = circle(Mx,My,sqrt(R_x^2+R_y^2));
[SDSD_x,SDSD_y]   = circle(Mx,My,sqrt(R_x^2+R_y^2));

%% Tables
t = array2table([Pat_1,Pat_2,Pat_3;,...
    Mean_1x Mean_1y Mean_2x Mean_2y Mean_3x Mean_3y;,...
    SD_1x SD_1y SD_2x SD_2y SD_3x SD_3y],...
    'RowNames',{'Fraction 1' 'Fraction 2' 'Fraction 3' 'Fraction 4' 'Mean' 'SD' },...
    'VariableNames',{'Pat_1x' 'Pat_1y' 'Pat_2x' 'Pat_2y' 'Pat_3x' 'Pat_3y'})

s = array2table([Mx My; Sx Sy; RMSx RMSy; SDSDx SDSDy],...
    'RowNames',{'M' 'S' 'RMS' 'SDSD'},...
    'VariableNames',{'x' 'y'})

%% Figure as illustration
figure('Name','Figure 4','NumberTitle','off')
x_ax =linspace(-10,10) ;
y_ax =linspace(0,0) ;
plot(x_ax,y_ax,'k-','LineWidth',1.5) ;
```

```
hold on
grid on
axis equal
plot(y_ax,x_ax,'k-','LineWidth',1.5);

% Plot statistics
plot(cSD_1x,cSD_1y,'LineWidth',2,'color',[0 166/255 214/255]);
plot(cSD_2x,cSD_2y,'LineWidth',2,'color',[1 210/255 0]);
plot(cSD_3x,cSD_3y,'LineWidth',2,'color',[88/255 128/255 10/255]);
plot(cSD_x,cSD_y,'LineWidth',2,'color','k');
plot(RSD_x,RSD_y,'LineWidth',2,'color',[0.8 0.8 0.8]);

plot(Pat_1(:,1),Pat_1(:,2),'ko','Markerfacecolor',[0 166/255 214/255],...
'MarkerSize',10,'LineWidth',2);
plot(Pat_2(:,1),Pat_2(:,2),'ko','Markerfacecolor',[1 210/255 0],...
'MarkerSize',10,'LineWidth',2);
plot(Pat_3(:,1),Pat_3(:,2),'ko','Markerfacecolor',[88/255 128/255 10/255],...
'MarkerSize',10,'LineWidth',2);

plot(Mean_1x,Mean_1y,'ko','Markerfacecolor',[0 166/255 214/255],...
'MarkerSize',14,'LineWidth',2);
plot(Mean_2x,Mean_2y,'ko','Markerfacecolor',[1 210/255 0],...
'MarkerSize',14,'LineWidth',2);
plot(Mean_3x,Mean_3y,'ko','Markerfacecolor',[88/255 128/255 10/255],...
'MarkerSize',14,'LineWidth',2);

plot(Mx,My,'ko','Markerfacecolor','k','MarkerSize',16,'LineWidth',2);
xlabel('Error x (mm)');ylabel('Error y (mm)')
set(gca,'FontName', 'Times New Roman','xlim',[-4 4],'ylim',[-4 4],...
'FontSize',18,'LineWidth',1.5)
```

A.1.6 Script accompanying Table 2.3 and Figure 2.10b

In order to model the tissue morbidity of organs at risk, the parameters `gamma_50`, `TCD_50`, `alpha_B/beta_B` and `D_90` must be changed to the appropriate values.

```
%% MATLAB - CTVHR D90 EQD2 vs TCP under dosimetric uncertainty
% Robin Straathof (2020)
clc
clear all
close all

% Symbolic variables
syms alpha_B beta_B N_B d_B G_B     % subscript `B' denotes BT
syms alpha_E beta_E N_E d_E G_E     % subscript `E' denotes EBRT
syms gamma_50 TCD_50 D

%% Computation of Biologically equivalent dose (BED)
% Formula BED
BED_B       =  N_B*d_B*(1+G_B*d_B/(alpha_B/beta_B));
BED_E       =  N_E*d_E*(1+G_E*d_E/(alpha_E/beta_E));

%% Computation of equieffective dose at 2 Gy fractions (EQD2) for BT+EBRT
EQD2        =  BED_B/((2*G_B)/(alpha_B/beta_B)+1)+BED_E/((2*G_E)/(alpha_E/beta_E)+1);

%% Variables
% Variable declaration
alpha_B     = 0.35; beta_B = 0.35/10; N_B = 4;  G_B = 1;
alpha_E     = 0.35; beta_E = 0.35/10; N_E = 25; G_E = 1; d_E = 1.8;

gamma_50    = 0.47;     % Parameters from Nesvacil et al. (2016)
TCD_50      = 36.0;     % Parameters from Nesvacil et al. (2016)

% Dosimetric variables
M_p_sys     = 0.0;      % Group mean systematic error for systematic effects (in %)
sigma_p_sys = 0.0;      % Overall random error for systematic effects (in %)
M_p_ran     = 0.0;      % Group mean systematic error for random effects (in %)
sigma_p_ran = 0.0;      % Overall random error for random effects (in %)

%% Simulation of dose-effect relation with uncertainty
% Generate TCP data
N_pat = 1000;

% Planning-aim dose and TCP
d_B   = linspace(0,12,61);
EQD2_plan(1,:)  =  eval(EQD2);
TCP_plan(1,:)   =  1./(1+exp(4*gamma_50*(1-EQD2_plan(1,:)./TCD_50)));

for k = 1:N_pat         % Number of patients
    % Delivered dose and TCP
    for i = 1:2         % Number of insertions
        % Calculate systematic impact
        Delta_sys(2*(i-1)+1,:)     = normrnd(M_p_sys*d_B/100,sigma_p_sys*d_B/100);
        Delta_sys(2*i,:)           = Delta_sys(2*(i-1)+1,:);
        for j = 1:2     % Number of fractions
            % Calculate random impact
            Delta_ran(j+2*(i-1),:) = normrnd(M_p_ran*d_B/100,sigma_p_ran*d_B/100);
        end
    end
```

```
    for l = 1:length(d_B)
        % Delivered dose
        d_B_tilde(:,l)  = d_B(:,l) + Delta_sys(:,l) + Delta_ran(:,l);
        % BED from delivered dose
        BED_B_tilde(:,l)=  sum(d_B_tilde(:,l).*(1+G_B*d_B_tilde(:,l) ...
        ./(alpha_B/beta_B)));

        % EQD2 from delivered dose
        EQD2_tilde(:,l) =  eval(BED_B_tilde(:,l)/((2*G_B)/(alpha_B/beta_B)+1) + ...
        BED_E/((2*G_E)/(alpha_E/beta_E)+1));

        % Formula for the logistic TCP model
        TCP_tilde(:,l)  =  1/(1+exp(4*gamma_50*(1-EQD2_tilde(:,l)/TCD_50)));

        % Compute occurrence of events: '1' is no event, '2' is event occurring
        LC_tilde(:,l)   =  randsample(2,1,true,[1-TCP_tilde(:,l) TCP_tilde(:,l)]);
        LC_plan(:,l)    =  randsample(2,1,true,[1-TCP_plan(:,l) TCP_plan(:,l)]);
    end

    % Store variables in matrices
    TCP_tilde_mat(k,:)  =  TCP_tilde;
    EQD2_tilde_mat(k,:) =  EQD2_tilde;
    LC_tilde_mat(k,:)   =  LC_tilde;
    LC_plan_mat(k,:)    =  LC_plan;

    % Reset vectors
    TCP_tilde           = 0;
    EQD2_tilde          = 0;
    k     % counter
end

% Set '0' is no event, '1' is event
LC_tilde_mat(LC_tilde_mat==1)       = 0;
LC_tilde_mat(LC_tilde_mat==2)       = 1;
LC_plan_mat(LC_plan_mat==1)         = 0;
LC_plan_mat(LC_plan_mat==2)         = 1;

%% Generate new curves
% Logistic regression between events and EQD2
for k = 1:N_pat
    EQD2_data             = EQD2_plan;
    X_logit               = mnrfit(EQD2_data,categorical(LC_tilde_mat(k,:)),...
    'model','nominal');
    TCP_pred              = mnrval(X_logit,linspace(0,120,120)',...
    'model','nominal');
    if isempty(TCP_pred)  == false
      TCP_pred_vec(k,:)   = TCP_pred(:,2)';
    end

    X_logit_2             = mnrfit(EQD2_data,categorical(LC_plan_mat(k,:)),...
    'model','nominal');
    TCP_pred_2            = mnrval(X_logit_2,linspace(0,120,120)',...
    'model','nominal');
    if isempty(TCP_pred_2)== false
      TCP_pred_2_vec(k,:) = TCP_pred_2(:,2)';
    end
end
```

```
% Compute average models
TCP_pred_vec(~any(TCP_pred_vec,2), : ) = [];
TCP_tilde_avg           = mean(TCP_pred_vec);
TCP_tilde_SD            = std(TCP_pred_vec);

TCP_pred_2_vec(~any(TCP_pred_2_vec,2), : ) = [];
TCP_plan_avg            = mean(TCP_pred_2_vec);
TCP_plan_SD             = std(TCP_pred_2_vec);

%% Plot results
% Plot results
figure('Name','Figure 1.10','NumberTitle','off')

% Without uncertainty
plot(linspace(0,120,120),TCP_plan_avg,'LineWidth',3,'color',[0 166/255 214/255])
hold on
plot(linspace(0,120,120),TCP_plan_avg-TCP_plan_SD,'--','LineWidth',3,...
'color',[0.8 0.8 0.8],'HandleVisibility','off')
plot(linspace(0,120,120),TCP_plan_avg+TCP_plan_SD,'--','LineWidth',3,...
'color',[0.8 0.8 0.8])

% With uncertainty
plot(linspace(0,120,120),TCP_tilde_avg,'LineWidth',3,'color',[1 210/255 0])
plot(linspace(0,120,120),TCP_tilde_avg-TCP_tilde_SD,'LineWidth',3,...
'color',[0.8 0.8 0.8],'HandleVisibility','off')
plot(linspace(0,120,120),TCP_tilde_avg+TCP_tilde_SD,'LineWidth',3,...
'color',[0.8 0.8 0.8])
set(gca,'FontName', 'Times New Roman','xlim',[70 120],'ylim',[0.85 1.0],...
'FontSize',18,'LineWidth',1.5)
xlabel('BT + EBRT {\it D}_{90} CTV_{HR} (EQD2_{\alpha/\beta = 10Gy})');ylabel('TCP')
h=legend({'No uncertainty','SD (without uncertainty)',...
'Inter-fraction uncertainty','SD (with uncertainty)'},'location','northwest');

% Calculate clinical impact at planning-aim dose level
D_90     = 90;                                      % Planning-aim dose level
val_TCP  = TCP_tilde_avg(:,D_90)
err_TCP  = TCP_tilde_avg(:,D_90)-TCP_plan_avg(:,D_90)
SD_TCP   = TCP_tilde_SD(:,D_90)
```

A.1.7 Script accompanying Figure 2.9

In order to model the impact of other uncertainty components, the type of uncertainty must be changed for the first **for**-loop.

```
%% MATLAB - Impact of dosimetric uncertainty type
% Robin Straathof (2020)
clc
clear all
close all

% Symbolic variables
syms alpha_B beta_B N_B d_B G_B     % subscript `B' denotes BT
syms alpha_E beta_E N_E d_E G_E     % subscript `E' denotes EBRT
syms gamma_50 TCD_50 D

%% Computation of Biologically equivalent dose (BED)
% Formula BED
BED_B       =  N_B*d_B*(1+G_B*d_B/(alpha_B/beta_B));
BED_E       =  N_E*d_E*(1+G_E*d_E/(alpha_E/beta_E));

%% Computation of equieffective dose at 2 Gy fractions (EQD2) for BT+EBRT
EQD2        =  BED_B/((2*G_B)/(alpha_B/beta_B)+1)+BED_E/((2*G_E)/(alpha_E/beta_E)+1);

%% Variables
% Variable declaration
alpha_B     = 0.35; beta_B = 0.35/10; N_B = 4;  G_B = 1;
alpha_E     = 0.35; beta_E = 0.35/10; N_E = 25; G_E = 1; d_E = 1.8;

gamma_50    = 0.47;     % Parameters from Nesvacil et al. (2016)
TCD_50      = 36.0;     % Parameters from Nesvacil et al. (2016)

% Generate TCP data
N_pat = 200;

% Planning-aim dose and TCP
d_B   = linspace(0,12,61);
EQD2_plan(1,:)  =  eval(EQD2);
TCP_plan(1,:)   =  1./(1+exp(4*gamma_50*(1-EQD2_plan(1,:)./TCD_50)));

% Dosimetric variables
M_p_sys     = 0;        % Group mean systematic error for systematic effects (in %)
sigma_p_sys = 0;        % Overall random error for systematic effects (in %)
M_p_ran     = 0;        % Group mean systematic error for random effects (in %)
sigma_p_ran = 0;        % Overall random error for random effects (in %)
q = 1;
for M_p_sys = -12:4:12  % Select M_p_sys / sigma_p_sys / M_p_ran / sigma_p_ran
for k = 1:N_pat         % Number of patients
    % Delivered dose and TCP
    for i = 1:2         % Number of insertions
        % Calculate systematic impact
        Delta_sys(2*(i-1)+1,:)     = normrnd(M_p_sys*d_B/100,sigma_p_sys*d_B/100);
        Delta_sys(2*i,:)           = Delta_sys(2*(i-1)+1,:);
        for j = 1:2     % Number of fractions
            % Calculate random impact
            Delta_ran(j+2*(i-1),:) = normrnd(M_p_ran*d_B/100,sigma_p_ran*d_B/100);
        end
    end
```

```
    for l = 1:length(d_B)
        % Delivered dose
        d_B_tilde(:,l)  = d_B(:,l) + Delta_sys(:,l) + Delta_ran(:,l);

        % BED from delivered dose
        BED_B_tilde(:,l)=  sum(d_B_tilde(:,l).*(1+G_B*d_B_tilde(:,l) ...
        ./(alpha_B/beta_B)));

        % EQD2 from delivered dose
        EQD2_tilde(:,l) =  eval(BED_B_tilde(:,l)/((2*G_B)/(alpha_B/beta_B)+1) + ...
        BED_E/((2*G_E)/(alpha_E/beta_E)+1));

        % Formula for the logistic TCP model
        TCP_tilde(:,l)  =  1/(1+exp(4*gamma_50*(1-EQD2_tilde(:,l)/TCD_50)));

        % Compute occurrence of events: '1' is no event, '2' is event occurring
        LC_tilde(:,l)   =  randsample(2,1,true,[1-TCP_tilde(:,l) TCP_tilde(:,l)]);
        LC_plan(:,l)    =  randsample(2,1,true,[1-TCP_plan(:,l) TCP_plan(:,l)]);
    end

    % Store variables in matrices
    TCP_tilde_mat(k,:)  =  TCP_tilde;
    EQD2_tilde_mat(k,:) =  EQD2_tilde;
    LC_tilde_mat(k,:)   =  LC_tilde;
    LC_plan_mat(k,:)    =  LC_plan;

    % Reset vectors
    TCP_tilde           = 0;
    EQD2_tilde          = 0;
    k
end

% Set '0' is no event, '1' is event for clarity
LC_tilde_mat(LC_tilde_mat==1)       = 0;
LC_tilde_mat(LC_tilde_mat==2)       = 1;
LC_plan_mat(LC_plan_mat==1)         = 0;
LC_plan_mat(LC_plan_mat==2)         = 1;

% Logistic regression between events and EQD2
for k = 1:N_pat
    EQD2_data             = EQD2_plan;
    X_logit               = mnrfit(EQD2_data,categorical(LC_tilde_mat(k,:)),...
    'model','nominal');
    TCP_pred              = mnrval(X_logit,linspace(0,120,120)',...
    'model','nominal');
    if isempty(TCP_pred)  == false
      TCP_pred_vec(k,:)   = TCP_pred(:,2)';
    end

    X_logit_2             = mnrfit(EQD2_data,categorical(LC_plan_mat(k,:)),...
    'model','nominal');
    TCP_pred_2            = mnrval(X_logit_2,linspace(0,120,120)',...
    'model','nominal');
    if isempty(TCP_pred_2)== false
      TCP_pred_2_vec(k,:) = TCP_pred_2(:,2)';
    end
end
```

```
% Compute average models
TCP_pred_vec(~any(TCP_pred_vec,2), : ) = [];
TCP_tilde_avg(q,:)      = mean(TCP_pred_vec);
TCP_tilde_SD(q,:)       = std(TCP_pred_vec);

TCP_pred_2_vec(~any(TCP_pred_2_vec,2), : ) = [];
TCP_plan_avg(q,:)       = mean(TCP_pred_2_vec);
q = q+1
end

%% Plot results
% Plot results
figure('Name','Figure 1.9','NumberTitle','off')
for z = 1:(q-1)
    plot(linspace(0,120,120),TCP_tilde_avg(z,:),'LineWidth',6,...
    'color',[1-(z-1)*0.07 210/255-(z-1)*0.07 (z-1)*0.07])
    hold on
end
plot(linspace(0,120,120),TCP_plan_avg(2,:),'LineWidth',6,...
'color',[0 166/255 214/255])
set(gca,'FontName', 'Times New Roman','xlim',[0 120],'ylim',[0 1.0],...
'FontSize',40,'LineWidth',1.5)
xlabel('BT + EBRT dose (EQD2)');ylabel('Event probability')
h=legend({'M_p = -12%','M_p = -8%','M_p = -4%','M_p = 0%',...
'M_p = 4%', 'M_p = 8%','M_p = 12%','No uncertainty'},'location','northwest');
```

A.1.8 Script for converting DICOM-RT into 2D convex shapes in the sagittal plane

```
%% MATLAB - DICOM-RT to sagittal contours
% Robin Straathof (2020)
clc
clear all
close all

% Load DICOM-RT structure and plot contours
info = dicominfo('rtstruct.dcm');
contour = dicomContours(info);
figure(1)
plotContour(contour)

for i = 1:size(contour.ROIs,1)
    points_a = [NaN,NaN];
    points_p = [NaN,NaN];
    for j = 1:1:size(contour.ROIs.ContourData{i,1},1)
        data = contour.ROIs.ContourData{i,1}{j};
        X = data(:,1);
        Y = data(:,2);
        Z = data(1,3);

        % Find intersection points with sagittal plane
        [x0,y0] = intersections(X,Y,[0 0],[-1000 1000]);
        % 'intersections' function by Douglas M. Schwarz
        % Version: 2.0, 25 May 2017
        % https://nl.mathworks.com/matlabcentral/fileexchange/
        % 11837-fast-and-robust-curve-intersections
        points_a = [points_a; y0(1) Z];
        points_p = [points_p; y0(2) Z];
    end
    points_ROI{i} = [points_a;flip(points_p);points_a(2,:)];
    points_ROI{i} = rmmissing(points_ROI{i});
    [k,av] = convhull(points_ROI{i})

    % Plot result
    figure(i+1)
    plot(points_ROI{i}(:,1),points_ROI{i}(:,2),'k-');
    hold on
    plot(points_ROI{i}(k,1),points_ROI{i}(k,2),'LineWidth',2,'color',[1 210/255 0])
end
```

A.1.9 Script accompanying Figure 4.5

```
%% MATLAB - Trace sagittal MRI to compute convex shapes
% Robin Straathof (2020)
clc
clear all
close all

% Load sagittal MR image
MR = imread('Delineation_extended.png');
MR = rgb2gray(MR);

% Scale image to real-world size
x_Limits = [0.000 0.210];
y_Limits = [0.000 0.214];
RMR      = imref2d(size(MR),x_Limits,y_Limits);

% Plot MR image
figure(1)
imshow(flipud(MR),RMR);
axis xy;

% Select CVT_HR
msgbox('Trace CTV_HR', 'WindowStyle', 'modal');
ctv      = drawpolygon('FaceAlpha',0);
ctv.Color = [161/255 225/255 36/255];
ctv_coord = ctv.Position;
ctv_conv  = convhull(ctv_coord);
ctv_coord = ctv_coord(ctv_conv,:);
hold on
plot(ctv_coord(:,1),ctv_coord(:,2),'LineWidth',3,'color',ctv.Color)

% Select vaginal cavity
msgbox('Trace vaginal cavity', 'WindowStyle', 'modal');
cav       = drawpolygon('FaceAlpha',0);
cav.Color = [1 0 207/255];
cav_coord = cav.Position;
cav_conv  = convhull(cav_coord);
cav_coord = cav_coord(cav_conv,:);
hold on
plot(cav_coord(:,1),cav_coord(:,2),'LineWidth',3,'color',cav.Color)

% Select bladder
msgbox('Trace bladder', 'WindowStyle', 'modal');
blad       = drawpolygon('FaceAlpha',0);
blad.Color = [1 210/255 0];
blad_coord = blad.Position;
blad_conv  = convhull(blad_coord);
blad_coord = blad_coord(blad_conv,:);
hold on
plot(blad_coord(:,1),blad_coord(:,2),'LineWidth',3,'color',blad.Color)

% Select rectum
msgbox('Trace rectum', 'WindowStyle', 'modal');
rect       = drawpolygon('FaceAlpha',0);
rect.Color = [0 166/255 214/255];
rect_coord = rect.Position;
rect_conv  = convhull(rect_coord);
rect_coord = rect_coord(rect_conv,:);
```

```
hold on
plot(rect_coord(:,1),rect_coord(:,2),'LineWidth',3,'color',rect.Color)

% Select sigmoid
msgbox('Trace sigmoid', 'WindowStyle', 'modal');
sigm       = drawpolygon('FaceAlpha',0);
sigm.Color = [168/255 22/255 184/255];
sigm_coord = sigm.Position;
sigm_conv  = convhull(sigm_coord);
sigm_coord = sigm_coord(sigm_conv,:);
hold on
plot(sigm_coord(:,1),sigm_coord(:,2),'LineWidth',3,'color',sigm.Color)

% Save data
disp('Done')
save('structures_2.mat','ctv_coord','cav_coord','blad_coord','rect_coord',...
'sigm_coord')
```

A.1.10 Script accompanying Figure 4.7b

```
%% MATLAB - Computing reachable region (partially using Maple (2015))
% Robin Straathof (2020)
clc
clear all
syms d_t phi v_x v_y
syms theta x y kappa
syms X Y

% Lie group and algebra equations
X_t  = [cos(theta), -sin(theta), x;
        sin(theta),  cos(theta), y;
        0         ,           0, 1];
e_v  = [cos(d_t*phi),-sin(d_t*phi),v_x/phi*sin(d_t*phi)-v_y/phi*(1-cos(d_t*phi));
            sin(d_t*phi), cos(d_t*phi),v_y/phi*sin(d_t*phi)+v_x/phi*(1-cos(d_t*phi));
            0       ,        0,                                          1];

X_td = X_t*e_v;

% Unicycle kinematics
x     = 0;
y     = 0;
v_y   = 0;
theta = 0;
phi   = kappa*v_x;
d_t   = 1;
X_td  = eval(X_td);

% Solve for known positions (done using Maple (2015))
% sol = solve(X_td(1,3)==X,X_td(2,3)==Y)
kappa = (2*cos(theta)*Y-2*X*sin(theta))/(X^2+Y^2);
v_x   = (1/2)*(X*sin(theta)+cos(theta)*Y)*(X^2+Y^2)*atan2(-(2*(sin(theta)*...
cos(theta)*X^2-sin(theta)*cos(theta)*Y^2-2*cos(theta)^2*X*Y+X*Y))/(X^2+Y^2),...
(4*cos(theta)*X*Y*sin(theta)+2*cos(theta)^2*X^2-2*cos(theta)^2*Y^2-X^2+Y^2)/...
(X^2+Y^2))/(d_t*(cos(theta)^2*X^2+cos(theta)^2*Y^2-X^2));

[X,Y] = meshgrid(0:0.05:2,-1:0.05:1);
g     = surf(X,Y,eval(kappa));
axis equal
xlabel('X'); ylabel('Y');
caxis([-1 1]);
colormap([linspace(0,1,256)',linspace(166/255,210/255,256)',...
linspace(214/255,0,256)'])
h = colorbar;
i = ylabel(h, '\kappa','Fontsize',18,'VerticalAlignment','middle');
set(i,'rotation',0);
zlim([-1 1]);
view(0,90);
```

A.1.11 Script for basic RRT algorithm (accompanying Figure 6.2b)

This MATLAB script consists of multiple components. The main file is 'RRT_basic.m'. Other files need to be stored in the same folder in order to work properly. Classes are defined for each of the primitives, which are in turn part of superclasses that may be used for property inheritance (not used in this thesis). These codes are based on the previous MATLAB scripts by Vemprala [392], and Agarwal [393].

Main file - save as: 'RRT_basic.m'

```
%%%%%%%%%%%%%%%%%%%%%%%%%%%%%%%%%%%%%%%%%%%%%%%%%%%%%%%%%%%%%%%%
%% MATLAB -  Basic RRT
% Robin Straathof (2020)
% Based on: - Sai Vemprala (2017)
%           - Saurav Agarwal (2017)
%%%%%%%%%%%%%%%%%%%%%%%%%%%%%%%%%%%%%%%%%%%%%%%%%%%%%%%%%%%%%%%%

function RRT_basic
% Add subfolders to path
addpath(genpath(pwd));

clear variables
clc;
close all;

%% Load example problem
% Workspace representation
map.bounds       = [0.00 0.00 0.08 0.08 0.00;...
                    0.00 0.04 0.04 0.00 0.00];
map.obstacles{1} = [0.00 0.00 0.08 0.00;...
                    0.03 0.04 0.04 0.03];
map.obstacles{2} = [0.00 0.00 0.08 0.00;...
                    0.00 0.01 0.00 0.00];
map.obstacles{3} = [0.03 0.04 0.04 0.03 0.03;...
                    0.015 0.015 0.03 0.03 0.015];
map.start1       = [0.08; 0.025];
map.target       = [0.00; 0.02];

global Tol
Tol              = 1E-3;   % [m]; target region width tolerance

qI_1             = map.start1;
qG_1             = map.target;

% Agent representation
global agent_width agent_length
agent_width      = 2.5E-3; % [m]; agent width
agent_length     = 5.0E-3; % [m]; agent length

% Planning execution
global N_Nodes delay
N_Nodes          = 2000;   % [ ]; maximum number of nodes
delay            = 0.02;   % [s]; delay for animation
SampBias         = 0.01;   % [ ]; bias towards goal region
delta            = 5.0E-3; % [m]; maximum step size
```

```
%% Initialise sampling-based primitives
% Sampling
Sample          = RandUni_Sampler(map,SampBias);  % Random uniform sampler
% Metric
Metric          = Euc_CostFunction;               % Euclidean cost function
% Nearest Neighbour
Nearest         = Euc_NearNeighbour;              % Euclidean nearest neighbour
% Steering function
Steer           = Path_MotionModel(delta);        % Straight line towards new sample
% Collision detection
Conf_free       = @(q) isConfValid(q,map);        % Configuration validity checker
Motion_free     = Samp_MotionChecker(delta);      % Sampled motion validity checker


%% Run motion planner
% Create plan for a single agent
planner_RRT   = RRT(map,Sample,Metric,Nearest,Steer,Conf_free,Motion_free);
Sol_Path      = planner_RRT.plan(qI_1,qG_1);
```

Motion Planning algorithm - save as: 'RRT.m'

```
%%%%%%%%%%%%%%%%%%%%%%%%%%%%%%%%%%%%%%%%%%%%%%%%%%%%%%%%%%%%
% Basic RRT algorithm
% Original codes by Agarwal (2017) and Vemprala (2017)

% G:        Contains vertices and edges.
% V:        Contains list of all explored nodes. Each node contains its
%           pose, cost to reach, its parent and index.
% E:        Contains list of all explored edges. Each edge contains its
%           two nodes, cost and indices of the nodes.

% Brief description of algorithm:
% 1. Sample a node q_rand.
% 2. Find the closest node q_near from explored nodes to branch out from, towards
%    q_rand.
% 3. Steer from q_near towards q_rand to obtain q_new
% 4. Check whether the nodes and edges are feasible
% 5. Add configuration and path to tree;
% 6. Continue until maximum number of nodes is reached or goal is hit.

classdef RRT < handle
    properties
        Map           = [];
        Sampler       = [];
        CostFunction  = [];
        NearNeighbour = [];
        MotionModel   = [];
        ConfValidityChecker   = [];
        MotionValidityChecker = [];
    end

    methods
        % Input Motion Planner Primitives
        function obj = RRT(map,Sample,Metric,Nearest,Steer,Conf_free,Motion_free)
            %obj@Planner_Class(); % Only when superclass 'Planner_Class' is defined
```

```
        obj.Map                   = map;
        obj.Sampler               = Sample;
        obj.CostFunction          = Metric;
        obj.NearNeighbour         = Nearest;
        obj.MotionModel           = Steer;
        obj.ConfValidityChecker   = Conf_free;
        obj.MotionValidityChecker = Motion_free;
    end

    % Main path planning function
    function [Sol_Path] = plan(obj,qI_i,qG_i)

        % Workspace definition
        global Tol

        x_max = max(obj.Map.bounds(1,:)); % x-limits
        y_max = max(obj.Map.bounds(2,:)); % y-limits

        q_start.pose     = qI_i; q_start.cost = 0; q_start.parent = 0;
        q_start.index    = 1;    q_target.pose = qG_i;

        % Plot workspace
        figh = figure;
        axis([0 x_max 0 y_max])
        obj.drawObstacles(figh);
        set(gca,'FontName', 'Times New Roman','FontSize',14)
        hold on
        plot(q_start.pose(1),q_start.pose(2),'.k','MarkerSize',20)
        plot(q_target.pose(1),q_target.pose(2),'.k','MarkerSize',20)
        axis equal
        xlim([0 x_max]); ylim([0 y_max]);
        xlabel('X (m)'); ylabel('Y (m)');

        % Planning Execution
        global N_Nodes delay
        Sol_Path = [];

        % Start of algorithm
        V(1)              = q_start;
        E(1).line         = []; E(1).cost = 0; E(1).n1 = 0; E(1).n2 = 0;

        for k = 1:1:N_Nodes
            G.V = V; G.E = E;  % add vertices and edges to tree

            % 1. Sample a node q_rand
            q_rand_cand = obj.Sampler.sample();
            if obj.ConfValidityChecker(q_rand_cand) % only sample valid points
                q_rand = q_rand_cand;
                line(q_rand(1), q_rand(2),'Marker','.','Color', [0 0.45 0.74]);
            else
                continue
            end

            % 2. Find the closest node q_near from explored nodes
            q_near      = obj.NearNeighbour.nearest(G,q_rand,obj.CostFunction);

            % 3. Steer from q_near towards q_rand
            q_new       = obj.MotionModel.steer(q_near,q_rand);
```

```
                % 4. Check whether the nodes and edges are feasible
                if obj.MotionValidityChecker.collision_free(q_near.pose,...
                q_new.pose,obj.ConfValidityChecker)
                    q_new.index = length(V)+1;

                    % 5. Add configuration and path to tree;
                    V           = [V q_new];    % append to vertices
                    line(q_new.pose(1),q_new.pose(2),'Marker','.',...
                    'Color', [0.2 0.2 0.2]);

                    E_new.line  = [q_near.pose,q_new.pose];
                    E_new.cost  = q_new.cost-q_near.cost;
                    E_new.n1    = q_near.index;
                    E_new.n2    = q_new.index;
                    E           = [E E_new];    % append to edges
                    line(E_new.line(1,:), E_new.line(2,:),'Color',[0.5 0.5 0.5]);

                    % 6. Continue until target is reached
                    if norm(q_target.pose-q_new.pose,2) < Tol && k <= N_Nodes
                        G.V = V; G.E = E;

                        q_end = q_new;
                        while q_end.parent ~= 0
                            ix = q_end.parent;
                            line([q_end.pose(1),V(ix).pose(1)], [q_end.pose(2),...
                            V(ix).pose(2)], 'Color', 'k', 'LineWidth', 2);
                            q_end = V(ix);
                            Sol_Path = [Sol_Path q_end.pose];
                        end

                        Sol_Path = fliplr(Sol_Path);
                        return;
                    end
                end
                pause(delay);
            end

            if k == N_Nodes && isempty(Sol_Path)
                disp("No solution found");
                return;
            end
        end

        % Utility functions
        function drawObstacles(obj,h)
            % Input:
            % h: figure handle

            obstacles = obj.Map.obstacles;
            figure(h)
            hold on
            for i = 1:length(obstacles)
                obs = obstacles{i};
                fill(obs(1,:),obs(2,:),[0 166/255 214/255]);
            end
        end
    end
end
```

Sampling - save as: 'RandUni_Sampler.m'

```
%%%%%%%%%%%%%%%%%%%%%%%%%%%%%%%%%%%%%%%%
% Random uniform sampler
% Input:
            % map:  map of workspace
classdef RandUni_Sampler < handle
    properties
        GoalBias  = [];
        map       = [];
    end
    methods
        function obj = RandUni_Sampler(map,bias)
            %obj@Sampler;      % Only when superclass 'Sampler' is defined
            obj.map       = map;
            obj.GoalBias  = bias;
        end
        function [q_rand] = sample(obj)
            x_max  = max(obj.map.bounds(1,:));   % x-limits
            y_max  = max(obj.map.bounds(2,:));   % y-limits
            if rand < obj.GoalBias               % with probability of GoalBias
                q_rand = obj.map.target;                  % target point
            else
                q_rand = [rand(1)*x_max;rand(1)*y_max];    % random point
            end
        end
    end
end
```

Metric - save as: 'Euc_CostFunction.m'

```
%%%%%%%%%%%%%%%%%%%%%%%%%%%%%%%%%%%%%%%%
% Euclidean distance metric function
% Input:
            % qi,qj:  two configurations
classdef Euc_CostFunction < handle
    properties
    end
    methods
        function obj = Euc_CostFunction
            %obj@CostFunction;  % Only when superclass 'CostFunction' is defined
        end
        function [cost] = metric(obj,qi,qj)
            cost = norm(qi-qj,2); % Euclidean distance in 2D
        end
    end
end
```

Nearest Neighbour - save as: 'Euc_NearNeighbour.m'

```
%%%%%%%%%%%%%%%%%%%%%%%%%%%%%%%%%%%%%%%%
% Nearest neighbour using Euclidean distance function
% Input:
            % q:            configuration
            % G:            current tree
            % CostFunction: metric
```

```
classdef Euc_NearNeighbour < handle
    properties
    end
    methods
        function obj = Euc_NearNeighbour
            %obj@NearNeighbour;  % Only when superclass 'NearNeighbour' is defined
        end

        function [q_near] = nearest(obj,G,q,CostFunction)
            V    = G.V; N = length(V); v = zeros(2,N); cost = zeros(1,N);

            % Determine distance from all vertices to q_rand
            for i=1:N
                v(:,i)    = V(i).pose;
                cost(1,i) = CostFunction.metric(v(:,i),q);
            end

            % Determine nearest vertex
            [val, idx] = min(cost);
            q_near     = V(idx);
        end
    end
end
```

Steering Function - save as: 'Path_MotionModel.m'

```
%%%%%%%%%%%%%%%%%%%%%%%%%%%%%%%%%%%%
% Motion Model of a straight path system
% Input:
            % q_near:  near configuration
            % q_rand:  sampled configuration

classdef Path_MotionModel < handle
    properties
        delta = [];
    end
    methods
        function obj = Path_MotionModel(delta)
            %obj@MotionModel;      % Only when superclass 'MotionModel' is defined
            obj.delta       = delta;
        end
        function [q_new] = steer(obj,q_near,q_rand)
            dist = norm(q_near.pose-q_rand,2);
            if dist < obj.delta
                q_new.pose   = q_rand;
                q_new.cost   = q_near.cost + dist;
                q_new.parent = q_near.index;
            else
                q_new.pose   = q_near.pose + obj.delta*(q_rand-q_near.pose)/...
                norm(q_rand-q_near.pose,2);
                q_new.cost   = q_near.cost + obj.delta;
                q_new.parent = q_near.index;
            end
        end
    end
end
```

Configuration validity checker - save as: 'isConfValid.m'

```
function bool = isConfValid(q, map)
%%%%%%%%%%%%%%%%%%%%%%%%%%%%%%%%%%%%%%%%%%%%%%%%
% Function that calculates whether the configuration is in collision
% Input:
%   q:    agent state
%   map:  obstacle map

% Agent parameters
global agent_width agent_length
w = agent_width; l = agent_length;
N = 5;                    % discretisation level
lpts_x = reshape(repmat(linspace(-l/2,l/2,N),N,1),1,[]);
lpts_y = reshape(repmat(linspace(-w/2,w/2,N)',1,N),1,[]);

for i =1:N^2
    agent(:,i) = [q(1);q(2)] + [lpts_x(i);lpts_y(i)];
end

% Check collision using inpolygon
for i=1:length(map.obstacles)
    obs = map.obstacles{i};
    collided = inpolygon(agent(1,:),agent(2,:),obs(1,:),obs(2,:));
    if any(collided)
        bool = false;     % when in collision
        return;
    end
end
bool = true;              % when not in collision
end
```

Motion validity checker - save as: 'Samp_MotionChecker.m'

```
%%%%%%%%%%%%%%%%%%%%%%%%%%%%%%%%%%%%%%%%
% Sampled motion validity checker
% Input:
            % q_near:  near configuration
            % q_new:   new configuration

classdef Samp_MotionChecker < handle
    properties
        delta = [];
    end
    methods
        function obj = Samp_MotionChecker(delta)
            %obj@MotionChecker;   % Only when superclass 'MotionChecker' is defined
            obj.delta       = delta;
        end
        function [bool] = collision_free(obj,q_near,q_new,ConfValidityChecker)
            global agent_length
            steps = ceil(norm((q_new-q_near),2)/ min(obj.delta,agent_length));
            % number of collision checks
            p_x = linspace(q_near(1),q_new(1),steps);
            p_y = linspace(q_near(2),q_new(2),steps);
```

```
            bool = true;
            for i = 1:size(p_x,2)
                if ConfValidityChecker([p_x(i);p_y(i)]) == 0 % i.e. in collision
                    bool = false;
                end
            end
        end
    end
end
```

A.1.12 Script for RRT* (accompanying Figure 6.5)

This MATLAB script consists of multiple components that are similar to that of the basic RRT algorithm. The main file is 'RRT_Star_basic.m'. The actual motion planning algorithm is given in 'RRT_Star.m'. Other files need to be copied from Appendix A.1.11 and stored in the same folder in order to work properly. These codes are based on the previous MATLAB scripts by Vemprala [392], and Agarwal [393].

Main file - save as: 'RRT_Star_basic.m'

```
%%%%%%%%%%%%%%%%%%%%%%%%%%%%%%%%%%%%%%%%%%%%%%%%%%%%%%%%%%%%
%% MATLAB -  RRT*
% Robin Straathof (2020)
% Based on: - Sai Vemprala (2017)
%           - Saurav Agarwal (2017)
%%%%%%%%%%%%%%%%%%%%%%%%%%%%%%%%%%%%%%%%%%%%%%%%%%%%%%%%%%%%

function RRT_Star_basic
% Add subfolders to path
addpath(genpath(pwd));

clear variables
clc;
close all;

%% Load example workspace
% Workspace representation
map.bounds       = [0.00 0.00 0.08 0.08 0.00;...
                    0.00 0.04 0.04 0.00 0.00];
map.obstacles{1} = [0.00 0.00 0.08 0.00;...
                    0.03 0.04 0.04 0.03];
map.obstacles{2} = [0.00 0.00 0.08 0.00;...
                    0.00 0.01 0.00 0.00];
map.obstacles{3} = [0.03 0.04 0.04 0.03 0.03;...
                    0.015 0.015 0.03 0.03 0.015];
map.start1       = [0.08; 0.025];
map.target       = [0.00; 0.02];

global Tol
Tol              = 1E-3;   % [m]; target region width tolerance

qI_1             = map.start1;
qG_1             = map.target;

% Agent representation
global agent_width agent_length
agent_width      = 2.5E-3; % [m]; agent width
agent_length     = 5.0E-3; % [m]; agent length

% Planning execution
global N_Nodes delay delta
N_Nodes          = 3000;   % [ ]; maximum number of nodes
delay            = 0.0001; % [s]; delay for animation
SampBias         = 0.01;   % [ ]; bias towards goal region
delta            = 5.0E-3; % [m]; maximum step size
```

```
%% Initialise sampling-based primitives
% Sampling
Sample          = RandUni_Sampler(map,SampBias);  % Random uniform sampler
% Metric
Metric          = Euc_CostFunction;               % Euclidean cost function
% Nearest Neighbour
Nearest         = Euc_NearNeighbour;              % Euclidean nearest neighbour
% Steering function
Steer           = Path_MotionModel(delta);        % Straight line towards new sample
% Collision detection
Conf_free       = @(q) isConfValid(q,map);        % Configuration validity checker
Motion_free     = Samp_MotionChecker(delta);      % Sampled motion validity checker

%% Run motion planner
% Create plan for a single agent
planner_RRT_Star    = RRT_Star(map,Sample,Metric,Nearest,Steer,Conf_free,Motion_free);
Sol_Path            = planner_RRT_Star.plan(qI_1,qG_1);
```

Motion Planning algorithm - save as: 'RRT_Star.m'

```
%%%%%%%%%%%%%%%%%%%%%%%%%%%%%%%%%%%%%%%%%%%%%%%%%%%%%%%%%%%%%%%%
% RRT* algorithm
% Original codes by Agarwal (2017) and Vemprala (2017)

% G:        Contains vertices and edges.
% V:        Contains list of all explored nodes. Each node contains its
%           pose, cost to reach, its parent and index.
% E:        Contains list of all explored edges. Each edge contains its
%           two nodes, cost and indices of the nodes.

% Brief description of algorithm:
% 1. Sample a node q_rand.
% 2. Find the closest node q_nearest from explored nodes to branch out from, towards
%    q_rand.
% 3. Steer from q_nearest towards q_rand to obtain q_new
% 4. Check whether the nodes and edges are feasible
% 5. Find q_min that gives the minimum cost path towards q_new
% 6. Rewire the tree from q_new
% 7. After maximum number of nodes is reached, find least cost path

classdef RRT_Star < handle
    properties
        Map           = [];
        Sampler       = [];
        CostFunction  = [];
        NearNeighbour = [];
        MotionModel   = [];
        ConfValidityChecker   = [];
        MotionValidityChecker = [];
    end

        methods
        % Input Motion Planner Primitives
       function obj = RRT_Star(map,Sample,Metric,Nearest,Steer,Conf_free,Motion_free)
            %obj@Planner_Class(); % Only when superclass 'Planner_Class' is defined
```

```
        obj.Map                   = map;
        obj.Sampler               = Sample;
        obj.CostFunction          = Metric;
        obj.NearNeighbour         = Nearest;
        obj.MotionModel           = Steer;
        obj.ConfValidityChecker   = Conf_free;
        obj.MotionValidityChecker = Motion_free;
    end

    % Main path planning function
    function [Sol_Path] = plan(obj,qI_i,qG_i)

        % Workspace definition
        global Tol

        x_max = max(obj.Map.bounds(1,:)); % x-limits
        y_max = max(obj.Map.bounds(2,:)); % y-limits

        q_start.pose     = qI_i;
        q_start.cost     = 0;
        q_start.parent   = 0;
        q_start.index    = 1;
        q_target.pose    = qG_i;

        % Plot workspace
        figh = figure;
        axis([0 x_max 0 y_max])
        obj.drawObstacles(figh);
        set(gca,'FontName', 'Times New Roman','FontSize',14)
        hold on
        plot(q_start.pose(1),q_start.pose(2),'.k','MarkerSize',20)
        plot(q_target.pose(1),q_target.pose(2),'.k','MarkerSize',20)
        axis equal
        xlim([0 x_max])
        ylim([0 y_max])
        xlabel('X (m)'); ylabel('Y (m)');

        % Planning Execution
        global N_Nodes delay delta
        Sol_Path = [];

        % Start of algorithm
        V(1)             = q_start;
        E(1).line        = []; E(1).cost = 0; E(1).n1 = 0; E(1).n2 = 0;

        for k = 1:1:N_Nodes
            G.V = V; G.E = E;  % add vertices and edges to tree

            % 1. Sample a node q_rand
            q_rand_cand = obj.Sampler.sample();
            if obj.ConfValidityChecker(q_rand_cand) % only sample valid points
                q_rand = q_rand_cand;
                line(q_rand(1), q_rand(2),'Marker','.','Color', [0 0.45 0.74]);
            else
                continue
            end
```

```
% 2. Find the closest node q_nearest from explored nodes
q_nearest   = obj.NearNeighbour.nearest(G,q_rand,obj.CostFunction);

% 3. Steer from q_near towards q_rand
q_new       = obj.MotionModel.steer(q_nearest,q_rand);

% 4. Check whether the nodes and edges are feasible
if obj.MotionValidityChecker.collision_free(q_nearest.pose,...
q_new.pose,obj.ConfValidityChecker)

    % 5. Find q_min that gives the minimum cost path towards q_new
    q_min          = q_nearest;
    [Q_near,Q_idx] = obj.Near(G,q_new,length(V),delta);
    % establish nodes in neighbourhood of q_new
    if not(isempty(Q_near))
        Q_N     = length(Q_near);
        C_new   = q_new.cost;
        for j   = 1:1:Q_N
            q_near = Q_near(j);
            if obj.MotionValidityChecker.collision_free(...
            q_near.pose,q_new.pose,obj.ConfValidityChecker)
                C_acc = q_near.cost + obj.CostFunction.metric(...
                q_near.pose,q_new.pose);
                if C_acc < C_new
                    q_min        = q_near;
                    q_new.cost   = C_acc;
                    q_new.parent = q_min.index;
                    C_new        = C_acc;
                end
            end
        end
    end
    q_new.index  = length(V)+1;

    % 6. Rewire the tree from q_new
    if not(isempty(Q_near))
        Q_idx(q_min.index) = 0;
        Q_near_rew         = V(Q_idx);
        if not(isempty(Q_near_rew))
            Q_N_rew = length(Q_near_rew);
            for l   = 1:1:Q_N_rew
                q_near = Q_near_rew(l);
                C_new_rew = obj.CostFunction.metric(...
                q_new.pose,q_near.pose);
                if q_near.cost > q_new.cost + C_new_rew
                    if obj.MotionValidityChecker.collision_free(...
                    q_new.pose,q_near.pose,obj.ConfValidityChecker)
                        % Delete old edge and update references
                        q_parent = V(q_near.parent);
                        E([E.n1] == q_parent.index & [E.n2] == ...
                        q_near.index) =[]; % remove redundant edge
                        V(q_near.index).parent = q_new.index;
                        V(q_near.index).cost   = q_new.cost + ...
                        C_new_rew;
```

```
                                % Create new edge
                                E_new_rew.line = [q_new.pose,q_near.pose];
                                E_new_rew.cost = C_new_rew;
                                E_new_rew.n1   = q_new.index;
                                E_new_rew.n2   = q_near.index;
                                E = [E E_new_rew];       % append to edges
                            end
                        end
                    end
                end
            end

            % Add new vertex and line to list of vertices and edges
            V           = [V q_new];    % append to vertices
            line(q_new.pose(1),q_new.pose(2),'Marker','.',...
            'Color', [0.2 0.2 0.2]);

            E_new.line  = [q_min.pose,q_new.pose];
            E_new.cost  = q_new.cost-q_min.cost;
            E_new.n1    = q_min.index;
            E_new.n2    = q_new.index;
            E           = [E E_new];    % append to edges
            line(E_new.line(1,:), E_new.line(2,:),...
            'Color',[0.9 0.9 0.9]);
        end
        pause(delay);
    end

% 7. After maximum number of nodes is reached, find least cost path
G.V = V; G.E = E;

% Plot edges graph
for p = 2:length(E)
    line(E(p).line(1,:),E(p).line(2,:),'Color',[0.5 0.5 0.5])
end

% Compute distances to target point
V_n    = length(V);
dist_m = zeros(1,V_n);
for m = 1:1:V_n
    dist_m(m) = norm(q_target.pose-V(m).pose,2);
end
[cost_path,idx] = min(dist_m); % find node closest to target
```

```
            q_end = V(idx);                % iterate backwards
            while q_end.parent ~= 0
                ix = q_end.parent;
                line([q_end.pose(1),V(ix).pose(1)],[q_end.pose(2),V(ix).pose(2)],...
                'Color', 'k', 'LineWidth', 2);
                q_end = V(ix);
                Sol_Path = [Sol_Path q_end.pose];
            end

            Sol_Path = fliplr(Sol_Path);
            return;
        end

        % Utility functions
        function drawObstacles(obj,h)
            % Input:
            % h: figure handle

            obstacles = obj.Map.obstacles;
            figure(h)
            hold on;
            for i = 1:length(obstacles)
                obs = obstacles{i};
                fill(obs(1,:),obs(2,:),[0 166/255 214/255]);
            end
        end

        function [Q_near,Q_near_idx] = Near(obj,G,q_new,V_card,delta)
        % Input:
            % G:         current tree
            % q_new:     new point
            % V_card:    cardinality of the list of vertices

            % Parameters for RRT*
            ksi_d  = pi;                % volume of unit ball in R2
            mu     = max(obj.Map.bounds(1,:))*max(obj.Map.bounds(2,:));
            % conservative area approx. of C_free
            gamma  = 2^2*(1+1/2)*mu;    % constant
            eta    = delta;             % step size
            r      = min((gamma/ksi_d*log(V_card)/V_card)^(1/2),eta);

            % Nodes in neighbourhood
            V      = G.V;
            dist   = zeros(1,V_card);
            for i  = 1:1:V_card
                dist(i) = norm(V(i).pose-q_new.pose,2);
            end
            Q_near_idx  = dist < r;
            if sum(Q_near_idx)>0
                Q_near = V(Q_near_idx);
                return;
            end
            Q_near = [];
        end
    end
end
```

A.1.13 Script for RRT in SE(2) algorithm (accompanying Figure 6.8)

This MATLAB script consists of multiple components. The main file is 'RRT_SE2_main.m'. All other files need to be stored in the same folder in order to work properly. 'RandUni_Sampler.m' must be obtained from Appendix A.1.11. Classes are defined for each of the primitives, which are in turn part of superclasses that may be used for property inheritance (not used in this thesis). These codes are based on the previous MATLAB scripts by Vemprala [392], and Agarwal [393].

Main file - save as: 'RRT_SE2_main.m'

```
%%%%%%%%%%%%%%%%%%%%%%%%%%%%%%%%%%%%%%%%%%%%%%%%%%%%%%%%%%%%%%%%%%%%%%%%%%%%%%%%
%% MATLAB -  RRT SE(2)
% Robin Straathof (2020)
% Based on: - Sai Vemprala (2017)
%           - Saurav Agarwal (2017)
%%%%%%%%%%%%%%%%%%%%%%%%%%%%%%%%%%%%%%%%%%%%%%%%%%%%%%%%%%%%%%%%%%%%%%%%%%%%%%%%

function RRT_SE2_main
% Add subfolders to path
addpath(genpath(pwd));

clear variables
clc;
close all;

%% Load example workspace
% Workspace representation
map.bounds       = [0.00 0.00 0.08 0.08 0.00;...
                    0.00 0.04 0.04 0.00 0.00];
map.obstacles{1} = polyshape([0.00 0.00 0.08],[0.03 0.04 0.04]);
map.obstacles{2} = polyshape([0.00 0.00 0.08],[0.00 0.01 0.00]);
map.obstacles{3} = polyshape([0.03 0.04 0.04 0.03],[0.015 0.015 0.03 0.03]);
map.start1       = [0.08; 0.025; pi];
map.target       = [0.00; 0.02];

global Tol
Tol              = 3E-3;        % [m]; target region width tolerance

xI_1             = map.start1;
xG_1             = map.target;

% Agent representation
w                = 2.5E-3;      % [m]; agent width
l                = 5.0E-3;      % [m]; agent length
max_dim          = sqrt((w/2)^2+(l/2)^2);
agent.rep        = polyshape([0 0 l l],[0 w w 0]);
agent.cons       = polyshape([0 0 max_dim max_dim],[0 max_dim max_dim 0]);
agent.width      = w;
agent.length     = l;

% Planning execution
global N_Nodes delay kappa_max v_max
N_Nodes          = 3000;        % [ ];    maximum number of nodes
delay            = 0.0001;      % [s];    delay for animation
kappa_max        = 40;          % [m-1];  curvature constraint
v_max            = 0.2;         % [ms-1]; velocity constraint
```

```
SampBias          = 0.01;        % [ ];    bias towards goal region
delta             = 0.01;        % [s];    time step
l_max             = v_max*delta; % [m];    step size
lc_max            = min(w,l);    % [m];    collision step size

%% Initialise sampling-based primitives
% Sampling
Sample             = RandUni_Sampler(map,SampBias);       % Random uniform sampler
% Metric
Metric             = Reach_CostFunction(delta); % Reachability-guided cost function
% Nearest Neighbour
Nearest_reachable = Reach_NearNeighbour;  % Reachability-guided nearest neighbour

% Steering function
Steer              = SE2_MotionModel(delta,l_max,lc_max); % Nonholonomic system
% Collision detection
State_free         = @(x) isStateValid(x,map,agent);  % State validity checker
Motion_free        = Samp_MotionChecker;      % Sampled motion validity checker

%% Run motion planner
% Create plan for a single agent
planner_RRT_SE2    = RRT_SE2(map,Sample,Metric,Nearest_reachable,Steer,...
State_free,Motion_free);
Sol_Traj           = planner_RRT_SE2.plan(xI_1,xG_1);
```

Motion Planning algorithm - save as: ‘`RRT_SE2.m`’

```
%%%%%%%%%%%%%%%%%%%%%%%%%%%%%%%%%%%%%%%%%%%%%%%%%%%%
% RRT algorithm for nonholonomic systems in SE(2)
% Original codes by Agarwal (2017) and Vemprala (2017)

% XG:       Contains vertices and edges.
% XV:       Contains list of all explored states. Each node contains its
%           pose, cost to reach, its parent and index.
% XE:       Contains list of all explored edges. Each edge contains its
%           two nodes.

% Brief description of algorithm:
% 1. Pick a random point p_rand and check collision.
% 2. Determine from which x_near in the list of explored states p_rand is
% reachable
% 3. Find the closest state x_near and associated control from this set
% 4. Steer from x_near towards p_rand to obtain x_new and the set of intermediate
% states
% 5. Check whether the intermediate states are feasible
% 6. Add configuration and path to tree;
% 7. Continue until maximum number of nodes is reached or goal is hit.

classdef RRT_SE2 < handle
    properties
        Map           = [];
        Sampler       = [];
        CostFunction  = [];
        NearNeighbour = [];
```

```
        MotionModel   = [];
        StateValidityChecker  = [];
        MotionValidityChecker = [];
    end

    methods
       % Input Motion Planner Primitives
       function obj = RRT_SE2(map,Sample,Metric,Nearest,Steer,State_free,Motion_free)
            %obj@Planner_Class(); % Only when superclass 'Planner_Class' is defined
            obj.Map                   = map;
            obj.Sampler               = Sample;
            obj.CostFunction          = Metric;
            obj.NearNeighbour         = Nearest;
            obj.MotionModel           = Steer;
            obj.StateValidityChecker  = State_free;
            obj.MotionValidityChecker = Motion_free;
        end

        % Main path planning function
        function [Sol_Traj] = plan(obj,xI_i,xG_i)

            % Workspace definition
            global Tol

            x_max = max(obj.Map.bounds(1,:)); % x-limits
            y_max = max(obj.Map.bounds(2,:)); % y-limits

            x_start.pose     = xI_i;
            x_start.cost     = 0;
            x_start.parent   = 0;
            x_start.index    = 1;
            x_target.pose    = xG_i;

            % Plot workspace
            figh = figure;
            axis([0 x_max 0 y_max])
            obj.drawObstacles(figh);
            set(gca,'FontName', 'Times New Roman','FontSize',14)
            hold on
            plot(x_start.pose(1),x_start.pose(2),'.k','MarkerSize',20)
            plot(x_target.pose(1),x_target.pose(2),'.k','MarkerSize',20)
            axis equal
            xlim([0 x_max])
            ylim([0 y_max])
            xlabel('X (m)'); ylabel('Y (m)');

            % Planning Execution
            global N_Nodes delay kappa_max
            Ctrl_lim = kappa_max;
            Sol_Traj = [];
```

```
% Start of algorithm
XV(1)              = x_start;
XE(1).line         = [];
XE(1).cost         = 0;
XE(1).n1           = 0;
XE(1).n2           = 0;

for k = 1:1:N_Nodes
    XG.V = XV; XG.E = XE;  % add vertices and edges to tree
    % 1. Pick a node p_rand randomly and uniformly
    p_rand_cand = obj.Sampler.sample();
    if obj.StateValidityChecker(p_rand_cand) % only sample valid points
        p_rand  = p_rand_cand;
        line(p_rand(1), p_rand(2),'Marker','.','Color', [0 0.45 0.74]);
    else
        continue
    end

    % 2. Determine from which x_near in the list of explored states
    % p_rand is reachable
    N           = length(XG.V);
    U_rand      = zeros(2,N);
    C_rand      = zeros(1,N);
    for i = 1:N
        u_rand  = obj.MotionModel.reachable(XG.V(i).pose,p_rand);
        U_rand(:,i) = u_rand;
        C_rand(:,i) = obj.CostFunction.metric(u_rand,Ctrl_lim);
    end

    % 3. Find the closest state x_near and associated control
    [u_near,x_near,c_near] = obj.NearNeighbour.nearest_reachable(...
    U_rand,XG.V,C_rand);
    if isinf(c_near)
        continue
    end

    % 4. Steer from x_near towards p_rand to obtain x_new
    % and the set of intermediate states
    [x_new,X_steps] = obj.MotionModel.steer(u_near,x_near,c_near);

    % 5. Check whether the intermediate states are feasible
    if obj.MotionValidityChecker.motion_free(X_steps,...
    obj.StateValidityChecker)
        x_new.index = length(XV)+1;

        % 6. Add configuration and path to tree;
        XV          = [XV x_new];    % append to vertices
        line(x_new.pose(1),x_new.pose(2),'Marker',...
        '.','Color', [0.2 0.2 0.2]);

        XE_new.line  = X_steps;
        XE_new.cost  = x_new.cost-x_near.cost;
        XE_new.n1    = x_near.index;
        XE_new.n2    = x_new.index;
        XE           = [XE XE_new];   % append to edges
        line(XE_new.line(1,:), XE_new.line(2,:),'Color',[0.5 0.5 0.5]);
```

```
            % 7. Continue until maximum number of nodes is reached or goal is hit.
                    if norm(x_target.pose-x_new.pose(1:2),2) < Tol && k <= N_Nodes
                        XG.V = XV; XG.E = XE;

                        x_end = x_new;
                        while x_end.parent ~= 0
                            ix = x_end.parent;
                            line([x_end.pose(1),XV(ix).pose(1)],[x_end.pose(2),...
                            XV(ix).pose(2)], 'Color', 'k', 'LineWidth', 2);
                            x_end = XV(ix);
                            Sol_Traj = [Sol_Traj x_end.pose];
                        end

                        Sol_Traj = fliplr(Sol_Traj);
                        return;
                    end
                end
                pause(delay);
            end

            if k == N_Nodes && isempty(Sol_Traj)
                disp("No solution found");
                return;
            end
        end

        % Utility functions
        function drawObstacles(obj,h)
            % Draw obstacles in the world.
            % Input:
            % h: figure handle
            % obstacles: list of obstacle vertices

            obstacles = obj.Map.obstacles;
            figure(h)
            hold on;
            for i = 1:length(obstacles)
                obs = obstacles{i};
                plot(obs,'FaceColor',[0 166/255 214/255],'FaceAlpha',1);
            end
        end
    end
end
```

Metric - save as: 'Reach_CostFunction.m'

```
%%%%%%%%%%%%%%%%%%%%%%%%%%%%%%%%%%%%%%%
% Reachability based metric function
% Input:
            % u = control input
            % Ctrl_lim = control limits

classdef Reach_CostFunction < handle
    properties
```

```
        delta = [];
    end
    methods
        function obj = Reach_CostFunction(delta)
            %obj@CostFunction;  % Only when superclass 'CostFunction' is defined
            obj.delta       = delta;
        end
        function [c_rand] = metric(obj,u,Ctrl_lim)
            v_t         = u(1);
            kappa_t     = u(2);
            kappa_max   = Ctrl_lim;
            if kappa_t < kappa_max && kappa_t > -kappa_max && v_t > 0
                c_rand = v_t*obj.delta;
            else
                c_rand = inf;
            end
        end
    end
end
```

Nearest Neighbour - save as: 'Reach_NearNeighbour.m'

```
%%%%%%%%%%%%%%%%%%%%%%%%%%%%%%%%%%%%
% Nearest neighbour using reachable distance function
% Input:
            % U:   set of control actions
            % XV:  set of vertices in state tree
            % C:   distance metric

classdef Reach_NearNeighbour < handle
    properties
    end
    methods
        function obj = Reach_NearNeighbour
            %obj@NearNeighbour;  % Only when superclass 'NearNeighbour' is defined
        end

        function [u_near,x_near,c_near] = nearest_reachable(obj,U,XV,C)
            % Determine 'nearest' vertex
            [c_near, idx] = min(C);
            u_near        = U(:,idx);
            x_near        = XV(idx);
        end
    end
end
```

Steering Function - save as: 'SE2_MotionModel.m'

```
%%%%%%%%%%%%%%%%%%%%%%%%%%%%%%%%%%%%
% Motion Model of a nonholonomic system in SE(2)
% Input:
            % x_t:   starting pose
            % p_t:   end point
            % u_t:   control action
            % c_t:   associated cost
```

```
classdef SE2_MotionModel < handle
    properties
        delta  = [];
        l_max  = [];
        lc_max = [];
    end
    methods
        function obj = SE2_MotionModel(delta,l_max,lc_max)
            %obj@MotionModel;      % Only when superclass 'MotionModel' is defined
            obj.delta    = delta;
            obj.l_max    = l_max;
            obj.lc_max   = lc_max;
        end
        function [u_rand] = reachable(obj,x_t,p_t)
            x_tilde      = p_t(1)-x_t(1);
            y_tilde      = p_t(2)-x_t(2);
            theta        = x_t(3);

            % From SE(2) algebra
            kappa_t      = (2*y_tilde*cos(theta)-2*x_tilde*sin(theta))/...
            (x_tilde^2+y_tilde^2);  % curvature
            if isnan(kappa_t)
                kappa_t  = 1E-5;    % to avoid the degenerate case of kappa = 0;
            end
            v_t   = (1/2)*(x_tilde*sin(theta)+y_tilde*cos(theta))*...
            (x_tilde^2+y_tilde^2)*atan2((2*x_tilde*y_tilde*cos(2*theta)+...
            (y_tilde^2-x_tilde^2)*sin(2*theta)),((x_tilde-y_tilde)*...
            (x_tilde+y_tilde)*cos(2*theta)+2*x_tilde*y_tilde*sin(2*theta)))/...
                (obj.delta*(y_tilde^2*cos(theta)^2-x_tilde^2*sin(theta)^2));
            % analytic expression of tangential velocity

            u_rand       = [v_t;kappa_t];
        end

        function [x_new,X_steps] = steer(obj,u_t,x_t,c_t)
            % Compute x_new
            if c_t > obj.l_max
                v_t      = obj.l_max/obj.delta;
                c_t      = obj.l_max;
            else
                v_t      = u_t(1);
            end

            k_t          = u_t(2);
            theta        = x_t.pose(3);
            d_t          = obj.delta;
            X_t = [cos(theta)*cos(k_t*v_t*d_t)-sin(theta)*sin(k_t*v_t*d_t),...
                  -cos(theta)*sin(k_t*v_t*d_t)-sin(theta)*cos(k_t*v_t*d_t),...
                   (cos(theta)*sin(k_t*v_t*d_t)+sin(theta)*cos(k_t*v_t*d_t)-...
                   sin(theta))/k_t;...
                    sin(theta)*cos(k_t*v_t*d_t)+cos(theta)*sin(k_t*v_t*d_t),...
                    cos(theta)*cos(k_t*v_t*d_t)-sin(theta)*sin(k_t*v_t*d_t),...
                   (sin(theta)*sin(k_t*v_t*d_t)-cos(theta)*cos(k_t*v_t*d_t)+...
                   cos(theta))/k_t;...
                    0,0,1];
            x_new.pose   = [x_t.pose(1:2)+X_t(1:2,3);atan2(X_t(2,1),X_t(1,1))];
            x_new.cost   = x_t.cost+c_t;
            x_new.parent = x_t.index;
```

```
            % Compute X_steps (only poses are required for collision checking)
            n_s          = ceil(c_t/obj.lc_max)+1;  % amount of steps
            v_t_vec      = linspace(0,v_t,n_s);
            X_steps      = [x_t.pose,zeros(3,n_s-2),x_new.pose];
            for i = 2:(n_s-1)
                v_t     = v_t_vec(i);
                X_t = [cos(theta)*cos(k_t*v_t*d_t)-sin(theta)*sin(k_t*v_t*d_t),...
                 -cos(theta)*sin(k_t*v_t*d_t)-sin(theta)*cos(k_t*v_t*d_t),...
                 (cos(theta)*sin(k_t*v_t*d_t)+sin(theta)*cos(k_t*v_t*d_t)-...
                 sin(theta))/k_t;...
                  sin(theta)*cos(k_t*v_t*d_t)+cos(theta)*sin(k_t*v_t*d_t),...
                  cos(theta)*cos(k_t*v_t*d_t)-sin(theta)*sin(k_t*v_t*d_t),...
                 (sin(theta)*sin(k_t*v_t*d_t)-cos(theta)*cos(k_t*v_t*d_t)+...
                 cos(theta))/k_t;...
                 0,0,1];
                X_steps(1:3,i) = [x_t.pose(1:2)+X_t(1:2,3);atan2(X_t(2,1),X_t(1,1))];
            end
        end
    end
end
```

State validity checker - save as: 'isStateValid.m'

```
function bool = isStateValid(x, map,agent)
%%%%%%%%%%%%%%%%%%%%%%%%%%%%%%%%%%%%%%%%%%%%%%%%%%%
% Function that calculates whether the configuration is in collision
% Input:
%   x:     agent state
%   map:   obstacle map
%   agent: agent representation

% Agent representation
if length(x) == 2
    agent_poly  = agent.cons;
    max_dim     = sqrt((agent.length/2)^2+(agent.width/2)^2);
    x(3)        = 0;
    agent_state = translate(rotate(agent_poly,x(3)/pi*180,...
    [max_dim/2 max_dim/2]),[x(1)-max_dim/2 x(2)-max_dim/2]);
else
    agent_poly  = agent.rep;
    agent_state = translate(rotate(agent_poly,x(3)/pi*180,...
    [agent.length/2 agent.width/2]),[x(1)-agent.length/2 x(2)-agent.width/2]);
end

% Check collision using intersects
for i=1:length(map.obstacles)
    obs = map.obstacles{i};
    col = intersect([agent_state,obs]);
    if col.NumRegions>0
        bool = false;    % when in collision
        return;
    end
end
bool = true;            % when not in collision
end
```

Motion validity checker - save as: 'Samp_MotionChecker.m'

```
%%%%%%%%%%%%%%%%%%%%%%%%%%%%%%%%%%%%%%%%
% Sampled motion validity checker
% Input:
            % X_steps:  vector of intermediate steps

classdef Samp_MotionChecker < handle
    properties
    end
    methods
        function obj = Samp_MotionChecker()
            %obj@MotionChecker;   % Only when superclass 'MotionChecker' is defined
        end
        function [bool] = motion_free(obj,X_steps,StateValidityChecker)
            bool = true;
            for i = 2:size(X_steps,2)
                if StateValidityChecker(X_steps(:,i)) == 0
                    bool = false; % when one state is in collision
                end
            end
        end
    end
end
```

A.1.14 Script for reconnect-tree RRT variant (accompanying Figure 6.9)

This MATLAB script consists of multiple components. The main file is 'RRT_DT_SE2_main.m'. All other files need to be stored in the same folder in order to work properly. 'RandUni_Sampler.m' must be obtained from Appendix A.1.11, whereas 'isStateValid.m', 'Samp_MotionChecker.m', 'Reach_CostFunction.m', and 'Reach_NearNeighbour.m' can be obtained from Appendix A.1.13. Classes are defined for each of the primitives, which are in turn part of superclasses that may be used for property inheritance (not used in this thesis). These codes are based on the previous MATLAB scripts by Vemprala [392], and Agarwal [393].

Main file - save as: 'RRT_DT_SE2_main.m'

```
%%%%%%%%%%%%%%%%%%%%%%%%%%%%%%%%%%%%%%%%%%%%%%%%%%%%%%%%
%% MATLAB -  reconnect-tree based RRT for SE(2)
% Robin Straathof (2020)
% Based on: - Sai Vemprala (2017)
%           - Saurav Agarwal (2017)
%%%%%%%%%%%%%%%%%%%%%%%%%%%%%%%%%%%%%%%%%%%%%%%%%%%%%%%%

function RRT_DT_SE2_main
% Add subfolders to path
addpath(genpath(pwd));

clear variables
clc;
close all;

%% Load example workspace
% Workspace representation
map.bounds       = [0.00 0.00 0.08 0.08 0.00;...
                    0.00 0.04 0.04 0.00 0.00];
map.obstacles{1} = polyshape([0.00 0.00 0.08],[0.03 0.04 0.04]);
map.obstacles{2} = polyshape([0.00 0.00 0.08],[0.00 0.01 0.00]);
map.obstacles{3} = polyshape([0.03 0.04 0.04 0.03],[0.015 0.015 0.03 0.03]);
map.start1       = [0.08; 0.025; pi];
map.target       = [0.00; 0.02];

global Tol
Tol              = 3E-3;        % [m]; target region width tolerance

xI_1             = map.start1;
xG_1             = map.target;

% Agent representation
w                = 2.5E-3;      % [m]; agent width
l                = 5.0E-3;      % [m]; agent length
max_dim          = sqrt((w/2)^2+(l/2)^2);
agent.rep        = polyshape([0 0 l l],[0 w w 0]);
agent.cons       = polyshape([0 0 max_dim max_dim],[0 max_dim max_dim 0]);
agent.width      = w;
agent.length     = l;

% Planning execution
global N_Nodes delay kappa_max v_max delta
N_Nodes          = 3000;        % [ ];    maximum number of nodes
delay            = 0.0001;      % [s];    delay for animation
```

```
kappa_max        = 40;          % [m-1];  curvature constraint
v_max            = 0.2;         % [ms-1]; velocity constraint
SampBias         = 0.01;        % [ ];    bias towards goal region
delta            = 0.02;        % [s];    time step
l_max            = v_max*delta; % [m];    step size
lc_max           = min(w,l);    % [m];    collision step size

%% Initialise sampling-based primitives
% Sampling
Sample           = RandUni_Sampler(map,SampBias);       % Random uniform sampler
% Metric
Metric           = Reach_CostFunction(delta);
% Reachability-guided cost function
% Nearest Neighbour
Nearest_reachable = Reach_NearNeighbour;
% Reachability-guided nearest neighbour
% Steering function
Steer            = SE2_MotionModel(delta,l_max,lc_max); % Nonholonomic unicycle
% Collision detection
State_free       = @(x) isStateValid(x,map,agent);      % State validity checker
Motion_free      = Samp_MotionChecker;
% Sampled motion validity checker

%% Run motion planner
% Create plan for a single agent
planner_RRT_DT_SE2   = RRT_DT_SE2(map,Sample,Metric,Nearest_reachable,Steer,...
State_free,Motion_free);
Sol_Traj             = planner_RRT_DT_SE2.plan(xI_1,xG_1);
```

Motion Planning algorithm - save as: 'RRT_DT_SE2.m'

```
%%%%%%%%%%%%%%%%%%%%%%%%%%%%%%%%%%%%%%%%%%%%%%%%%%%%%%%%%%%%
% Dual-tree inspired RRT algorithm for nonholonomic systems in SE(2)
% Original codes by Agarwal (2017) and Vemprala (2017)

% XG:       Contains vertices and edges.
% XV:       Contains list of all explored states. Each node contains its
%           pose, cost to reach, its parent, children and index.
% XE:       Contains list of all explored edges. Each edge contains its
%           two nodes.

% Brief description of algorithm:
% 1. Pick a random point p_rand and check collision.
% 2. Determine from which x_near in the list of explored states p_rand is
% reachable
% 3. Find the closest state x_near and associated control from this set
% 4. Steer from x_near towards p_rand to obtain x_new and the set of intermediate
% states
% 5. Check whether the intermediate states are feasible
% 6. Find the near state x_near which reaches p_new with minimum cost
% 7. Determine whether other near states can be reached at lower cost from x_new
% 8. If trajectory connecting x_new and x_near is feasible, reconnect
% children states
% 9. After maximum number of nodes is reached, find least cost trajectory
```

```
classdef RRT_DT_SE2 < handle
    properties
        Map            = [];
        Sampler        = [];
        CostFunction   = [];
        NearNeighbour  = [];
        MotionModel    = [];
        StateValidityChecker  = [];
        MotionValidityChecker = [];
    end

    methods
        % Input Motion Planner Primitives
        function obj = RRT_DT_SE2(map,Sample,Metric,Nearest,Steer,State_free,...
        Motion_free)
            %obj@Planner_Class(); % Only when superclass 'Planner_Class' is defined
            obj.Map                   = map;
            obj.Sampler               = Sample;
            obj.CostFunction          = Metric;
            obj.NearNeighbour         = Nearest;
            obj.MotionModel           = Steer;
            obj.StateValidityChecker  = State_free;
            obj.MotionValidityChecker = Motion_free;
        end

        % Main path planning function
        function [Sol_Traj] = plan(obj,xI_i,xG_i)

            % Workspace definition
            global Tol

            x_max = max(obj.Map.bounds(1,:)); % x-limits
            y_max = max(obj.Map.bounds(2,:)); % y-limits

            x_start.pose     = xI_i;
            x_start.cost     = 0;
            x_start.parent   = 0;
            x_start.child    = NaN;
            x_start.index    = 1;
            x_target.pose    = xG_i;

            % Plot workspace
            figh = figure;
            axis([0 x_max 0 y_max])
            obj.drawObstacles(figh);
            set(gca,'FontName', 'Times New Roman','FontSize',14)
            hold on
            plot(x_start.pose(1),x_start.pose(2),'.k','MarkerSize',20)
            plot(x_target.pose(1),x_target.pose(2),'.k','MarkerSize',20)
            axis equal
            xlim([0 x_max])
            ylim([0 y_max])
            xlabel('X (m)'); ylabel('Y (m)');

            % Planning Execution
            global N_Nodes delay kappa_max delta
            Ctrl_lim = kappa_max;
            Sol_Traj = [];
```

```
% Start of algorithm
XV(1)              = x_start;
XE(1).line         = [];
XE(1).cost         = 0;
XE(1).n1           = 0;
XE(1).n2           = 1;

for k = 1:1:N_Nodes
    XG.V = XV; XG.E = XE;  % add vertices and edges to tree
    % 1. Pick a node p_rand randomly and uniformly
    p_rand_cand = obj.Sampler.sample();
    if obj.StateValidityChecker(p_rand_cand) % only sample valid points
        p_rand  = p_rand_cand;
        line(p_rand(1), p_rand(2),'Marker','.','Color', [0 0.45 0.74]);
    else
        continue
    end

    %2. Determine from which x_near in the list of explored
    % states p_rand is reachable
    N           = length(XG.V);
    U_rand      = zeros(2,N);
    C_rand      = zeros(1,N);
    for i = 1:N
        u_rand  = obj.MotionModel.reachable(XG.V(i).pose,p_rand);
        U_rand(:,i) = u_rand;
        C_rand(:,i) = obj.CostFunction.metric(u_rand,Ctrl_lim);
    end

    % 3. Find the closest state x_near and control from this set
    [u_nearest,x_nearest,c_nearest] = ...
    obj.NearNeighbour.nearest_reachable(U_rand,XG.V,C_rand);
    if isinf(c_nearest)
        continue
    end

    % 4. Steer from x_near towards p_rand to obtain x_new and the set
    % of intermediate states
    [x_new,X_steps] = obj.MotionModel.steer_control(u_nearest,...
    x_nearest,c_nearest);

    % 5. Check whether the intermediate states are feasible
    if obj.MotionValidityChecker.motion_free(X_steps,...
    obj.StateValidityChecker)

        % 6. Find the state x_near which reaches p_new with minimum cost
        x_min          = x_nearest;
        X_min_steps    = X_steps;
        [X_near,X_idx] = obj.Near(XG,x_new,length(XV),delta);
        if not(isempty(X_near))
            X_N        = length(X_near);
            C_new      = x_new.cost;
            for j      = 1:1:X_N
                x_near = X_near(j);
                u_near = obj.MotionModel.reachable(x_near.pose,...
                x_new.pose(1:2));
                c_near = obj.CostFunction.metric(u_near,Ctrl_lim);
                C_acc   = x_near.cost + c_near;
```

```
        if C_acc < C_new
            [x_new_cand,X_near_steps] = obj.MotionModel.steer_to_state(u_near,...
            x_near,c_near);
            if obj.MotionValidityChecker.motion_free(X_near_steps,...
            obj.StateValidityChecker)
                x_min         = x_near;
                x_new         = x_new_cand;
                X_min_steps   = X_near_steps;
                C_new         = C_acc;
            end
        end
    end
end
x_new.index = length(XV)+1;
XV(x_min.index).child = [XV(x_min.index).child x_new.index]; % make x_new a child

% 7. Determine whether other near states can be reached at lower cost from x_new
if not(isempty(X_near))
    X_idx(x_min.index) = 0;          % exclude x_min
    X_near_rew         = XV(X_idx);  % remaining near states
    if not(isempty(X_near_rew))
        X_N_rew = length(X_near_rew);
        for l   = 1:1:X_N_rew
            X_near_rew = XV(X_idx);
            x_near_2 = X_near_rew(l);
            u_new  = obj.MotionModel.reachable(x_new.pose,x_near_2.pose(1:2));
            c_new  = obj.CostFunction.metric(u_new,Ctrl_lim);
            C_acc_acc = x_new.cost + c_new;
            if C_acc_acc < x_near_2.cost
            [x_new_near,X_new_steps] = obj.MotionModel.steer_to_state(u_new,...
            x_new,c_new);

            % 8. If trajectory connecting x_new and x_near is feasible, reconnect
            % children states
            if obj.MotionValidityChecker.motion_free(X_new_steps,...
            obj.StateValidityChecker)
            x_parent    = XG.V(x_near_2.parent); % parent of near node
            ix          = x_near_2.index;        % index of near node
            x_new_near.index = ix;               % change index of connected state
                                                 % to that of near node
            XV(ix)      = x_new_near;            % replace x_near with x_new_near
            x_new.child = ix;                    % x_new_near is a child of x_new
            XV(x_parent.index).child([XG.V(x_parent.index).child] == ix) = NaN;
                                                 % delete child entry for parent

            XE_par_near = XE([XE.n1] == x_parent.index & [XE.n2] == ix);
            XE_par_near = XE_par_near(1);

            idx_child  = x_near_2.child;
            idx_child(isnan(idx_child)) = [];
            if ~isempty(idx_child)
                for o = 1:length(idx_child)
                    XE_near_chi = XE([XE.n1] == ix & [XE.n2] == idx_child(o));
                    XE_near_chi = XE_near_chi(1);
```

```
                    % Create line between parent and children
                    XE_par_chi.line  = [XE_par_near.line,XE_near_chi.line];
                    XE_par_chi.cost  = XE_par_near.cost + XE_near_chi.cost;
                    XE_par_chi.n1    = x_parent.index;
                    XE_par_chi.n2    = idx_child(o);
                    XE = [XE XE_par_chi];

                    % Change parent/child
                    XV(x_parent.index).child = [XV(x_parent.index).child ...
                    idx_child(o)];
                    XV(idx_child(o)).parent  = x_parent.index;
                end
            end

            % Create new edge
            XE_new_rew.line    = X_new_steps;
            XE_new_rew.cost    = c_new;
            XE_new_rew.n1      = x_new.index;
            XE_new_rew.n2      = ix;
            XE = [XE XE_new_rew];            % append to edges
        end
    end
  end
end
end

% Add new vertex and line to list of vertices and edges
XV          = [XV x_new];    % append to vertices
line(x_new.pose(1),x_new.pose(2),'Marker','.','Color', [0.2 0.2 0.2]);

XE_new.line  = X_min_steps;
XE_new.cost  = x_new.cost-x_min.cost;
XE_new.n1    = x_min.index;
XE_new.n2    = x_new.index;
XE           = [XE XE_new];    % append to edges
line(XE_new.line(1,:), XE_new.line(2,:),'Color',[0.5 0.5 0.5]);
end
pause(delay);
end

% 9. After maximum number of nodes is reached, find least cost trajectory
XG.V = XV; XG.E = XE;

% Plot edges graph
for p = 2:length(XE)
    line(XE(p).line(1,:),XE(p).line(2,:),'Color',[0.5 0.5 0.5])
end

% Compute distances to target point
XV_n    = length(XV);
dist_m  = zeros(1,XV_n);
ind     = [];
for m = 1:1:XV_n
    dist = norm(x_target.pose(1:2)-XV(m).pose(1:2),2);
```

```
    if dist < Tol
        dist_m(m) = dist;
        ind = [ind m];
    else
        dist_m(m) = inf;
    end
end
if min(dist_m) == inf
    disp('No solution found')
    return
else
    XV_target = XV(ind);
    % Find node with lowest cost to target
    [Traj_Cost,id] = min(arrayfun(@(x) min(x.cost), XV_target));
    idx = XV_target(id).index;
end

x_end = XV(idx);                % iterate backwards
while x_end.parent ~= 0
    ix_c = x_end.index;
    ix_p = x_end.parent;
    e_cp = XE([XE.n1] == ix_p & [XE.n2] == ix_c);
    line([e_cp.line(1,:)],[e_cp.line(2,:)], 'Color', 'k', 'LineWidth', 2);
    x_end = XV(ix_p);
    Sol_Traj = [Sol_Traj x_end.pose];
end

Sol_Traj = fliplr(Sol_Traj);
return;
end

% Utility functions
function drawObstacles(obj,h)
    % Draw obstacles in the world.
    % Input:
    % h: figure handle
    % obstacles: list of obstacle vertices

    obstacles = obj.Map.obstacles;
    figure(h)
    hold on;
    for i = 1:length(obstacles)
        obs = obstacles{i};
        plot(obs,'FaceColor',[0 166/255 214/255],'FaceAlpha',1);
    end
end

function [X_near,X_near_idx] = Near(obj,XG,x_new,XV_card,delta)
    % Input:
    % XG:        current tree
    % x_new:     new point
    % V_card:    cardinality of the list of vertices

    % Parameters for RRT*
    ksi_d  = pi;                % volume of unit ball in R2
    mu     = max(obj.Map.bounds(1,:))*max(obj.Map.bounds(2,:));
```

```
    % conservative area approx. of C_free
            gamma  = 2^2*(1+1/2)*mu;    % constant
            eta    = delta;             % step size
            r      = min((gamma/ksi_d*log(XV_card)/XV_card)^(1/2),eta);

            % Nodes in neighbourhood
            XV      = XG.V;
            dist   = zeros(1,XV_card);
            for i  = 1:1:XV_card
                dist(i) = norm(XV(i).pose(1:2)-x_new.pose(1:2),2);
            end
            X_near_idx  = dist < r;
            if sum(X_near_idx)>0
                X_near = XV(X_near_idx);
                return;
            end
            X_near = [];
        end
    end
end
```

Steering Function - save as: 'SE2_MotionModel.m'

```
%%%%%%%%%%%%%%%%%%%%%%%%%%%%%%%%%%%%%%
% Motion Model of a nonholonomic system in SE(2)
% Input:
            % x_t:   starting pose
            % p_t:   end point
            % u_t:   control action
            % c_t:   associated cost

classdef SE2_MotionModel < handle
    properties
        delta  = [];
        l_max  = [];
        lc_max = [];
    end
    methods
        function obj = SE2_MotionModel(delta,l_max,lc_max)
            %obj@MotionModel;      % Only when superclass 'MotionModel' is defined
            obj.delta    = delta;
            obj.l_max    = l_max;
            obj.lc_max   = lc_max;
        end
        function [u_rand] = reachable(obj,x_t,p_t)
            x_tilde      = p_t(1)-x_t(1);
            y_tilde      = p_t(2)-x_t(2);
            theta        = x_t(3);

            % From SE(2) algebra
            kappa_t      = (2*y_tilde*cos(theta)-2*x_tilde*sin(theta))/...
            (x_tilde^2+y_tilde^2);  % curvature
            if isnan(kappa_t)
                kappa_t  = 1E-5;    % to avoid the degenerate case of kappa = 0;
            end
```

```
        v_t   = (1/2)*(x_tilde*sin(theta)+y_tilde*cos(theta))*...
        (x_tilde^2+y_tilde^2)*atan2((2*x_tilde*y_tilde*cos(2*theta)+...
        (y_tilde^2-x_tilde^2)*sin(2*theta)),((x_tilde-y_tilde)*...
        (x_tilde+y_tilde)*cos(2*theta)+2*x_tilde*y_tilde*sin(2*theta)))/...
            (obj.delta*(y_tilde^2*cos(theta)^2-x_tilde^2*sin(theta)^2));
        % analytic expression of tangential velocity

        u_rand       = [v_t;kappa_t];
    end

    function [x_new,X_steps] = steer_control(obj,u_t,x_t,c_t)
        % Compute x_new
        if c_t > obj.l_max
            v_t      = obj.l_max/obj.delta;
            c_t      = obj.l_max;
        else
            v_t      = u_t(1);
        end

        k_t          = u_t(2);
        theta        = x_t.pose(3);
        d_t          = obj.delta;
        X_t = [cos(theta)*cos(k_t*v_t*d_t)-sin(theta)*sin(k_t*v_t*d_t),...
              -cos(theta)*sin(k_t*v_t*d_t)-sin(theta)*cos(k_t*v_t*d_t),...
              (cos(theta)*sin(k_t*v_t*d_t)+sin(theta)*cos(k_t*v_t*d_t)-...
              sin(theta))/k_t;...
               sin(theta)*cos(k_t*v_t*d_t)+cos(theta)*sin(k_t*v_t*d_t),...
               cos(theta)*cos(k_t*v_t*d_t)-sin(theta)*sin(k_t*v_t*d_t),...
              (sin(theta)*sin(k_t*v_t*d_t)-cos(theta)*cos(k_t*v_t*d_t)+...
              cos(theta))/k_t;...
               0,0,1];
        x_new.pose   = [x_t.pose(1:2)+X_t(1:2,3);atan2(X_t(2,1),X_t(1,1))];
        x_new.cost   = x_t.cost+c_t;
        x_new.parent = x_t.index;
        x_new.child  = NaN;

        % Compute X_steps (only poses are required for collision checking)
        n_s          = ceil(c_t/obj.lc_max)+1;  % amount of steps
        v_t_vec      = linspace(0,v_t,n_s);
        X_steps      = [x_t.pose,zeros(3,n_s-2),x_new.pose];
        for i = 2:(n_s-1)
             v_t     = v_t_vec(i);
             X_t = [cos(theta)*cos(k_t*v_t*d_t)-sin(theta)*sin(k_t*v_t*d_t),...
              -cos(theta)*sin(k_t*v_t*d_t)-sin(theta)*cos(k_t*v_t*d_t),...
              (cos(theta)*sin(k_t*v_t*d_t)+sin(theta)*cos(k_t*v_t*d_t)-...
              sin(theta))/k_t;...
               sin(theta)*cos(k_t*v_t*d_t)+cos(theta)*sin(k_t*v_t*d_t),...
               cos(theta)*cos(k_t*v_t*d_t)-sin(theta)*sin(k_t*v_t*d_t),...
              (sin(theta)*sin(k_t*v_t*d_t)-cos(theta)*cos(k_t*v_t*d_t)+...
              cos(theta))/k_t;...
               0,0,1];
            X_steps(1:3,i) = [x_t.pose(1:2)+X_t(1:2,3);atan2(X_t(2,1),X_t(1,1))];
        end
    end
```

```
        function [x_new,X_steps] = steer_to_state(obj,u_t,x_t,c_t)
            v_t          = u_t(1);
            k_t          = u_t(2);
            theta        = x_t.pose(3);
            d_t          = obj.delta;
            X_t = [cos(theta)*cos(k_t*v_t*d_t)-sin(theta)*sin(k_t*v_t*d_t),...
                  -cos(theta)*sin(k_t*v_t*d_t)-sin(theta)*cos(k_t*v_t*d_t),...
                  (cos(theta)*sin(k_t*v_t*d_t)+sin(theta)*cos(k_t*v_t*d_t)-...
                  sin(theta))/k_t;...
                   sin(theta)*cos(k_t*v_t*d_t)+cos(theta)*sin(k_t*v_t*d_t),...
                   cos(theta)*cos(k_t*v_t*d_t)-sin(theta)*sin(k_t*v_t*d_t),...
                  (sin(theta)*sin(k_t*v_t*d_t)-cos(theta)*cos(k_t*v_t*d_t)+...
                  cos(theta))/k_t;...
                   0,0,1];
            x_new.pose   = [x_t.pose(1:2)+X_t(1:2,3);atan2(X_t(2,1),X_t(1,1))];
            x_new.cost   = x_t.cost+c_t;
            x_new.parent = x_t.index;
            x_new.child  = NaN;

            % Compute X_steps (only poses are required for collision checking)
            n_s          = ceil(c_t/obj.lc_max)+1;  % amount of steps
            v_t_vec      = linspace(0,v_t,n_s);
            X_steps      = [x_t.pose,zeros(3,n_s-2),x_new.pose];
            for i = 2:(n_s-1)
                 v_t     = v_t_vec(i);
                 X_t = [cos(theta)*cos(k_t*v_t*d_t)-sin(theta)*sin(k_t*v_t*d_t),...
                  -cos(theta)*sin(k_t*v_t*d_t)-sin(theta)*cos(k_t*v_t*d_t),...
                  (cos(theta)*sin(k_t*v_t*d_t)+sin(theta)*cos(k_t*v_t*d_t)-...
                  sin(theta))/k_t;...
                   sin(theta)*cos(k_t*v_t*d_t)+cos(theta)*sin(k_t*v_t*d_t),...
                   cos(theta)*cos(k_t*v_t*d_t)-sin(theta)*sin(k_t*v_t*d_t),...
                  (sin(theta)*sin(k_t*v_t*d_t)-cos(theta)*cos(k_t*v_t*d_t)+...
                  cos(theta))/k_t;...
                   0,0,1];
                X_steps(1:3,i) = [x_t.pose(1:2)+X_t(1:2,3);atan2(X_t(2,1),X_t(1,1))];
            end
        end
    end
end
```

A.1.15 Script for bounded uncertainty reconnect-tree RRT in SE(2) (accompanying Figure 6.10)

This MATLAB script consists of multiple components. The main file is 'BU_RRT_DT_SE2_main.m'. All other files need to be stored in the same folder in order to work properly. 'RandUni_Sampler.m' can be obtained from Appendix A.1.11, 'Samp_MotionChecker.m', 'Reach_CostFunction.m', 'Reach_NearNeighbour.m' can be obtained from Appendix A.1.13, and 'SE2_MotionModel.m' can be obtained from Appendix A.1.14. The motion planning algorithm 'RRT_DT_SE2.m' from Appendix A.1.14 is renamed to 'BU_RRT_DT_SE2.m' and only the utility function 'drawObstacles' is changed to illustrate uncertainty bounds. Classes are defined for each of the primitives, which are in turn part of superclasses that may be used for property inheritance (not used in this thesis). These codes are based on the previous MATLAB scripts by Vemprala [392], and Agarwal [393].

Main file - save as: 'BU_RRT_DT_SE2_main.m'

```
%%%%%%%%%%%%%%%%%%%%%%%%%%%%%%%%%%%%%%%%%%%%%%%%%%%%%%%%
%% MATLAB -  Bounded uncertainty reconnect-tree based RRT for SE(2)
% Robin Straathof (2020)
% Based on: - Sai Vemprala (2017)
%           - Saurav Agarwal (2017)
%%%%%%%%%%%%%%%%%%%%%%%%%%%%%%%%%%%%%%%%%%%%%%%%%%%%%%%%

function BU_RRT_DT_SE2_main
% Add subfolders to path
addpath(genpath(pwd));

clear variables
clc;
close all;

%% Load example workspace
% Agent representation
w                = 2.5E-3;      % [m]; agent width
l                = 5.0E-3;      % [m]; agent length
r                = 3.0E-3;      % [m]; agent radius
max_dim          = sqrt((w/2)^2+(l/2)^2);
agent.rep        = polyshape([0 0 l l],[0 w w 0]);
agent.cons       = polyshape([0 0 max_dim max_dim],[0 max_dim max_dim 0]);
agent.width      = w;
agent.length     = l;
agent.radius     = r;

% Workspace representation
map.bounds       = [0.00 0.00 0.08 0.08 0.00;...
                    0.00 0.04 0.04 0.00 0.00];
map.start1       = [0.08; 0.025; pi];
map.target       = [0.00; 0.02];
xI_1             = map.start1;
xG_1             = map.target;

%   Deterministic obstacles
map.det_obstacles(1)       = polyshape([0.00 0.00 0.08],[0.03 0.04 0.04]);
map.det_obstacles(2)       = polyshape([0.00 0.00 0.08],[0.00 0.01 0.00]);

%   Uncertain obstacles
A_1              = [1 0;-1 0;0 1;0 -1]; % Uncertain obstacle normals
```

```
eta_1            = [2;2;1;1]*10^(-3);   % [m]; obstacle max displacement
c_hat_1          = [0.038 0.018; 0.032 0.028; 0.032 0.028; 0.038 0.018];
for i = 1:size(A_1,1)
    const_1(i,:) = A_1(i,:)*c_hat_1(i,:)'+r+eta_1(i,:);
end
map.unc_obstacles(1).shape = polyshape([0.032 0.038 0.038 0.032],...
[0.018 0.018 0.028 0.028]);
map.unc_obstacles(1).const = const_1;
map.unc_obstacles(1).A     = A_1;
map.unc_obstacles(1).eta   = eta_1;

% Planning execution
global N_Nodes delay kappa_max v_max delta Tol
Tol              = 3E-3;        % [m];    target region width tolerance
N_Nodes          = 3000;        % [ ];    maximum number of nodes
delay            = 0.0001;      % [s];    delay for animation
kappa_max        = 40;          % [m-1];  curvature constraint
v_max            = 0.2;         % [ms-1]; velocity constraint
SampBias         = 0.01;        % [ ];    bias towards goal region
delta            = 0.01;        % [s];    time step
l_max            = v_max*delta; % [m];    step size
lc_max           = min(w,l);    % [m];    collision step size

%% Initialise sampling-based primitives
% Sampling
Sample            = RandUni_Sampler(map,SampBias);       % Random uniform sampler
% Metric
Metric            = Reach_CostFunction(delta);
% Reachability-guided cost function
% Nearest Neighbour
Nearest_reachable = Reach_NearNeighbour;
% Reachability-guided nearest neighbour
% Steering function
Steer             = SE2_MotionModel(delta,l_max,lc_max); % Nonholonomic unicycle
% Collision detection
State_free        = @(x) isStateValid(x,map,agent);      % State validity checker
Motion_free       = Samp_MotionChecker;
% Sampled motion validity checker

%% Run motion planner
% Create plan for a single agent
planner_BU_RRT_DT_SE2   = BU_RRT_DT_SE2(map,Sample,Metric,Nearest_reachable,...
Steer,State_free,Motion_free);
Sol_Traj                = planner_BU_RRT_DT_SE2.plan(xI_1,xG_1);
```

Utility function in Motion Planning algorithm - (1) save 'RRT_DT_SE2.m' as 'BU_RRT_DT_SE2.m', (2) change all references from 'RRT_DT_SE2' to 'BU_RRT_DT_SE2.m', and (3) substitute the utility function 'drawObstacles' with the following function:

```
% Utility functions
    function drawObstacles(obj,h)
        % Input:
        % h: figure handle
        % obstacles: list of obstacle vertices
```

```
        det_obstacles = obj.Map.det_obstacles;
        unc_obstacles = obj.Map.unc_obstacles;
        figure(h)
        hold on;
        for i = 1:length(det_obstacles)
            obs = det_obstacles(i);
            plot(obs,'FaceColor',[0 166/255 214/255],'FaceAlpha',1);
        end
        for j = 1:length(unc_obstacles)
            obs     = unc_obstacles(j).shape;
            plot(obs,'FaceColor',[1 210/255 0],'FaceAlpha',1);
            obs_c   = obs.Vertices;
            obs_n_c = length(obs_c);
            e       = unc_obstacles(j).eta;
            obs_bu  = [obs_c;obs_c+repmat([e(1),e(3)],obs_n_c,1);...
            obs_c+repmat([e(1),-e(3)],obs_n_c,1);obs_c+repmat([-e(1),e(3)],...
            obs_n_c,1);obs_c+repmat([-e(1),-e(3)],obs_n_c,1)];
            obs_conv_bu  = convhull(obs_bu);
            obs_bu  = obs_bu(obs_conv_bu,:);
            plot(obs_bu(:,1),obs_bu(:,2),'--','LineWidth',2,'color',[1
            210/255 0])
        end
    end
```

State validity checker - save as: 'isStateValid.m'

```
function bool = isStateValid(x, map,agent)
%%%%%%%%%%%%%%%%%%%%%%%%%%%%%%%%%%%%%%%%%%%%%%%%
% Function that calculates whether the configuration is in collision
% Input:
%   x:     agent state
%   map:   obstacle map
%   agent: agent representation

% Agent representation
if length(x) == 2
    agent_poly  = agent.cons;
    max_dim     = sqrt((agent.length/2)^2+(agent.width/2)^2);
    x(3)        = 0;
    agent_state = translate(rotate(agent_poly,x(3)/pi*180,...
    [max_dim/2 max_dim/2]),[x(1)-max_dim/2 x(2)-max_dim/2]);
else
    agent_poly  = agent.rep;
    agent_state = translate(rotate(agent_poly,x(3)/pi*180,...
    [agent.length/2 agent.width/2]),[x(1)-agent.length/2 x(2)-agent.width/2]);
end

% Check collision using intersect
obstacles = [map.det_obstacles,map.unc_obstacles.shape];
for i=1:length(obstacles)
    obs = obstacles(i);
    col = intersect([agent_state,obs]);
```

```
if col.NumRegions>0
        bool = false;    % when in collision
        return;
    end
end
unc_obstacles = map.unc_obstacles;

% Check robust feasibility with linear constraints
for j=1:length(unc_obstacles)
    obs   = unc_obstacles(j);
    A     = obs.A;
    const = obs.const;
    for k = 1:size(A,1)
        if A(k,:)*x(1:2,1) < const(k)
            ind(k) = 0;
        else
            ind(k) = 1;
        end
    end
    if sum(ind)==0
        bool = false;    % when not robustly feasible
        return;
    end
end
bool = true;            % when not in collision
end
```

A.1.16 Script for a chance constrained reconnect-tree RRT variant in SE(2) (accompanying Figure 6.11)

This MATLAB script consists of multiple components. The main file is 'CC_RRT_DT_SE2_main.m'. All other files need to be stored in the same folder in order to work properly. 'RandUni_Sampler.m' can be obtained from Appendix A.1.11, 'Reach_NearNeighbour.m' can be obtained from Appendix A.1.13, and 'SE2_MotionModel.m' can be obtained from Appendix A.1.14. Classes are defined for each of the primitives, which are in turn part of superclasses that may be used for property inheritance (not used in this thesis). These codes are based on the previous MATLAB scripts by Vemprala [392], and Agarwal [393].

Main file - save as: 'CC_RRT_DT_SE2_main.m'

```
%%%%%%%%%%%%%%%%%%%%%%%%%%%%%%%%%%%%%%%%%%%%%%%%%%%%%%%%
%% MATLAB -  Chance constrained reconnect-tree based RRT for SE(2)
% Robin Straathof (2020)
% Based on: - Sai Vemprala (2017)
%           - Saurav Agarwal (2017)
%%%%%%%%%%%%%%%%%%%%%%%%%%%%%%%%%%%%%%%%%%%%%%%%%%%%%%%%

function CC_RRT_DT_SE2_main
% Add subfolders to path
addpath(genpath(pwd));

clear variables
clc;
close all;

%% Load example workspace
% Agent representation
w                = 2.5E-3;      % [m]; agent width
l                = 5.0E-3;      % [m]; agent length
r                = 3.0E-3;      % [m]; agent radius
max_dim          = sqrt((w/2)^2+(l/2)^2);
agent.rep        = polyshape([0 0 l l],[0 w w 0]);
agent.cons       = polyshape([0 0 max_dim max_dim],[0 max_dim max_dim 0]);
agent.width      = w;
agent.length     = l;
agent.radius     = r;

% Workspace representation
map.bounds       = [0.00 0.00 0.08 0.08 0.00;...
                    0.00 0.04 0.04 0.00 0.00];
map.start1       = [0.08; 0.025; pi];
map.target       = [0.00; 0.02];
xI_1             = map.start1;
xG_1             = map.target;

%   Deterministic obstacles
map.det_obstacles(1)       = polyshape([0.00 0.00 0.08],[0.03 0.04 0.04]);
map.det_obstacles(2)       = polyshape([0.00 0.00 0.08],[0.00 0.01 0.00]);

%   Uncertain obstacles
A_1              = [1 0;-1 0;0 1;0 -1]; % Uncertain obstacle normals
P_c1             = [4,0;0,1]*10^(-6);   % [m]; covariance matrix
c_hat_1          = [0.038 0.028; 0.032 0.018; 0.032 0.028; 0.038 0.018];
```

```
map.unc_obstacles(1).shape = polyshape([0.032 0.038 0.038 0.032],...
[0.018 0.018 0.028 0.028]);
map.unc_obstacles(1).A     = A_1;
map.unc_obstacles(1).P_c   = P_c1;
map.unc_obstacles(1).c_hat = c_hat_1;

% Planning execution
global N_Nodes delay kappa_max v_max delta Tol
Tol              = 3E-3;        % [m];    target region width tolerance
N_Nodes          = 3000;        % [ ];    maximum number of nodes
delay            = 0.0001;      % [s];    delay for animation
kappa_max        = 40;          % [m-1];  curvature constraint
v_max            = 0.2;         % [ms-1]; velocity constraint
SampBias         = 0.01;        % [ ];    bias towards goal region
delta            = 0.01;        % [s];    time step
l_max            = v_max*delta; % [m];    step size
lc_max           = min(w,l);    % [m];    collision step size
psi.s            = 0.98;        % [ ];    step-wise probability constraint
psi.p            = 0.8;         % [ ];    traj-wise probability constraint
alpha.D          = 1;           % [ ];    weight of trajectory duration
alpha.Delta      = 5;           % [ ];    weight of trajectory risk

%% Initialise sampling-based primitives
% Sampling
Sample            = RandUni_Sampler(map,SampBias);       % Random uniform sampler
% Metric
Metric            = Reach_CostFunction(delta,alpha);
% Reachability-guided cost function
% Nearest Neighbour
Nearest_reachable = Reach_NearNeighbour;
% Reachability-guided nearest neighbour
% Steering function
Steer             = SE2_MotionModel(delta,l_max,lc_max); % Nonholonomic unicycle
% Collision detection
State_free        = @(x,risk) isStateValid(x,risk,map,agent,psi);
% State validity checker
Motion_free       = Samp_MotionChecker;
% Sampled motion validity checker

%% Run motion planner
% Create plan for a single agent
planner_CC_RRT_DT_SE2   = CC_RRT_DT_SE2(map,Sample,Metric,Nearest_reachable,...
Steer,State_free,Motion_free);
Sol_Traj                = planner_CC_RRT_DT_SE2.plan(xI_1,xG_1);
```

Motion Planning algorithm - save as: 'CC_RRT_DT_SE2.m'

```
%%%%%%%%%%%%%%%%%%%%%%%%%%%%%%%%%%%%%%%%%%%%%%%%%%%%%%%%
% Chance constrained dual-tree inspired RRT algorithm for nonholonomic system
% Original codes by Agarwal (2017) and Vemprala (2017)

% XG:       Contains vertices and edges.
% XV:       Contains list of all explored states. Each node contains its
%           pose, cost to reach, its parent, children, index and per time-step risk.
% XE:       Contains list of all explored edges. Each edge contains its
%           two nodes.
```

```
% Brief description of algorithm:
% 1. Pick a random point p_rand and check collision.
% 2. Determine from which x_near in the list of explored states p_rand is
% reachable
% 3. Find the closest state x_near and associated control from this set
% 4. Steer from x_near towards p_rand to obtain x_new and the set of intermediate
% states
% 5. Check whether the intermediate states are probabilistically feasible
% 6. Find the near state x_near which reaches p_new with minimum cost
% 7. Determine whether other near states can be reached at lower cost from x_new
% 8. If trajectory connecting x_new and x_near is probabilistically feasible,
% reconnect children states
% 9. After maximum number of nodes is reached, find least cost trajectory

classdef CC_RRT_DT_SE2 < handle
    properties
        Map           = [];
        Sampler       = [];
        CostFunction  = [];
        NearNeighbour = [];
        MotionModel   = [];
        StateValidityChecker  = [];
        MotionValidityChecker = [];
    end

    methods
        % Input Motion Planner Primitives
        function obj = CC_RRT_DT_SE2(map,Sample,Metric,Nearest,...
        Steer,State_free,Motion_free)
            %obj@Planner_Class(); % Only when superclass 'Planner_Class' is defined
            obj.Map                   = map;
            obj.Sampler               = Sample;
            obj.CostFunction          = Metric;
            obj.NearNeighbour         = Nearest;
            obj.MotionModel           = Steer;
            obj.StateValidityChecker  = State_free;
            obj.MotionValidityChecker = Motion_free;
        end

        % Main path planning function
        function [Sol_Traj] = plan(obj,xI_i,xG_i)

            % Workspace definition
            global Tol

            x_max = max(obj.Map.bounds(1,:)); % x-limits
            y_max = max(obj.Map.bounds(2,:)); % y-limits

            x_start.pose     = xI_i;
            x_start.cost     = 0;
            x_start.parent   = 0;
            x_start.child    = NaN;
            x_start.index    = 1;
            x_start.risk     = 0;
            x_target.pose    = xG_i;
```

```
% Plot workspace
figh = figure;
axis([0 x_max 0 y_max])
obj.drawObstacles(figh);
set(gca,'FontName', 'Times New Roman','FontSize',14)
hold on
plot(x_start.pose(1),x_start.pose(2),'.k','MarkerSize',20)
plot(x_target.pose(1),x_target.pose(2),'.k','MarkerSize',20)
axis equal
xlim([0 x_max])
ylim([0 y_max])
xlabel('X (m)'); ylabel('Y (m)');

% Planning Execution
global N_Nodes delay kappa_max delta
Ctrl_lim = kappa_max;
Sol_Traj = [];

% Start of algorithm
XV(1)              = x_start;
XE(1).line         = [];
XE(1).cost         = 0;
XE(1).n1           = 0;
XE(1).n2           = 1;

for k = 1:1:N_Nodes
    XG.V = XV; XG.E = XE;  % add vertices and edges to tree
    % 1. Pick a node p_rand randomly and uniformly
    p_rand_cand = obj.Sampler.sample();
    if obj.StateValidityChecker(p_rand_cand,NaN) % sample valid points
        p_rand  = p_rand_cand;
        line(p_rand(1), p_rand(2),'Marker','.','Color', [0 0.45 0.74]);
    else
        continue
    end

    %2. Determine from which x_near in the list of explored states
    % p_rand is reachable
    N           = length(XG.V);
    U_rand      = zeros(2,N);
    C_rand      = zeros(1,N);
    for i = 1:N
        u_rand  = obj.MotionModel.reachable(XG.V(i).pose,p_rand);
        U_rand(:,i) = u_rand;
        C_rand(:,i) = obj.CostFunction.dist_metric(u_rand,Ctrl_lim);
    end

    % 3. Find the closest state x_near and control from this set
    [u_nearest,x_nearest,c_nearest] = ...
    obj.NearNeighbour.nearest_reachable(U_rand,XG.V,C_rand);
    if isinf(c_nearest)
        continue
    end

    % 4. Steer from x_near towards p_rand to obtain x_new
    % and the set of intermediate states
    [x_new,X_steps] = obj.MotionModel.steer_control(u_nearest,...
    x_nearest,c_nearest);
```

```
% 5. Check whether the intermediate states are feasible
[yesno,Delta_t] = obj.MotionValidityChecker.motion_free(X_steps,...
x_nearest.risk,obj.StateValidityChecker);
if yesno
    % 6. Find the near state x_near which reaches p_new with minimum cost
    x_new.cost     = x_nearest.cost+obj.CostFunction.cost_metric(c_nearest,Delta_t);
    x_new.risk     = x_nearest.risk + Delta_t;
    x_min          = x_nearest;
    X_min_steps    = X_steps;
    [X_near,X_idx] = obj.Near(XG,x_new,length(XV),delta); % nodes in neighbourhood
    if not(isempty(X_near))
        X_N        = length(X_near);
        C_new      = x_new.cost;
        for j      = 1:1:X_N
            x_near = X_near(j);
            u_near = obj.MotionModel.reachable(x_near.pose,x_new.pose(1:2));
            c_near = obj.CostFunction.dist_metric(u_near,Ctrl_lim);
            if c_near~=inf
             [x_new_cand,X_near_steps] = obj.MotionModel.steer_to_state(...
              u_near,x_near,c_near);
              [yesno_2,Delta_t_near]    = obj.MotionValidityChecker.motion_free(...
              X_near_steps,x_near.risk,obj.StateValidityChecker);
              C_acc  = x_near.cost+obj.CostFunction.cost_metric(c_near,Delta_t_near);
                if C_acc < C_new & yesno_2
                    x_min         = x_near;
                    x_new         = x_new_cand;
                    x_new.cost    = C_acc;
                    x_new.risk    = x_near.risk + Delta_t_near;
                    X_min_steps   = X_near_steps;
                    C_new         = C_acc;
                end
            end
        end
    end
    x_new.index = length(XV)+1;
    XV(x_min.index).child = [XV(x_min.index).child x_new.index]; % make x_new a child

    % 7. Determine whether other near states can be reached at lower cost from x_new
    if not(isempty(X_near))
        X_idx(x_min.index) = 0;          % exclude x_min
        X_near_rew         = XV(X_idx);  % remaining near states
        if not(isempty(X_near_rew))
            X_N_rew = length(X_near_rew);
            for l   = 1:1:X_N_rew
                X_near_rew = XV(X_idx);
                x_near_2 = X_near_rew(l);
                u_new  = obj.MotionModel.reachable(x_new.pose,x_near_2.pose(1:2));
                c_new  = obj.CostFunction.dist_metric(u_new,Ctrl_lim);
                if c_new ~= inf
                    [x_new_near,X_new_steps] = obj.MotionModel.steer_to_state(...
                    u_new,x_new,c_new);
                    % 8. If trajectory connecting x_new and x_near is feasible,
                    % reconnect children states
                    [yesno_3,Delta_t_new]   = ...
                    obj.MotionValidityChecker.motion_free(X_new_steps,...
                    x_new.risk,obj.StateValidityChecker);
```

```
    C_acc_acc = x_new.cost + obj.CostFunction.cost_metric(c_new,Delta_t_new);
    if C_acc_acc < x_near_2.cost & yesno_3
    x_new_near.cost = C_acc_acc;
    x_new_near.risk = x_new.risk + Delta_t_new;
    x_parent    = XG.V(x_near_2.parent); % parent of near node
    ix          = x_near_2.index;        % index of near node
    x_new_near.index = ix;               % change index of new connected state
                                         % to that of near node
    XV(ix)      = x_new_near;            % replace x_near with x_new_near in tree
    x_new.child = ix;                    % x_new_near is a child of x_new
    XV(x_parent.index).child([XG.V(x_parent.index).child] == ix) = NaN;
                                       % delete child entry for parent node

    XE_par_near = XE([XE.n1] == x_parent.index & [XE.n2] == ix);
    XE_par_near = XE_par_near(1);

    idx_child  = x_near_2.child;
    idx_child(isnan(idx_child)) = [];
    if ~isempty(idx_child)
        for o = 1:length(idx_child)
            XE_near_chi = XE([XE.n1] == ix & [XE.n2] == idx_child(o));
            XE_near_chi = XE_near_chi(1);

            % Create line between parent and children
            XE_par_chi.line  = [XE_par_near.line,XE_near_chi.line];
            XE_par_chi.cost  = XE_par_near.cost + XE_near_chi.cost;
            XE_par_chi.n1    = x_parent.index;
            XE_par_chi.n2    = idx_child(o);
            XE = [XE XE_par_chi];

            % Change parent/child
            XV(x_parent.index).child = [XV(x_parent.index).child idx_child(o)];
            XV(idx_child(o)).parent  = x_parent.index;
        end
    end

    % Create new edge
    XE_new_rew.line    = X_new_steps;
    XE_new_rew.cost    = c_new;
    XE_new_rew.n1      = x_new.index;
    XE_new_rew.n2      = ix;
    XE = [XE XE_new_rew];                          % append to edges
    end
end
end
end
end

% Add new vertex and line to list of vertices and edges
XV          = [XV x_new];    % append to vertices
line(x_new.pose(1),x_new.pose(2),'Marker','.','Color', [0.2 0.2 0.2]);

XE_new.line  = X_min_steps;
XE_new.cost  = x_new.cost-x_min.cost;
XE_new.n1    = x_min.index;
XE_new.n2    = x_new.index;
XE           = [XE XE_new];    % append to edges
```

```
line(XE_new.line(1,:), XE_new.line(2,:),'Color',[0.5 0.5 0.5]);
end
pause(delay);
end

% 9. After maximum number of nodes is reached, find least cost trajectory
XG.V = XV; XG.E = XE;

% Plot edges graph
for p = 2:length(XE)
    line(XE(p).line(1,:),XE(p).line(2,:),'Color',[0.5 0.5 0.5])
end

% Compute distances to target point
XV_n    = length(XV);
dist_m  = zeros(1,XV_n);
ind     = [];
for m = 1:1:XV_n
    dist = norm(x_target.pose(1:2)-XV(m).pose(1:2),2);
    if dist < Tol
        dist_m(m) = dist;
        ind = [ind m];
    else
        dist_m(m) = inf;
    end
end
if min(dist_m) == inf
    disp('No solution found')
    return
else
    XV_target = XV(ind);
    % Find node with lowest cost to target
    [Traj_Cost,id] = min(arrayfun(@(x) min(x.cost), XV_target));
    idx = XV_target(id).index;
end

x_end = XV(idx);                % iterate backwards
while x_end.parent ~= 0
    ix_c = x_end.index;
    ix_p = x_end.parent;
    e_cp = XE([XE.n1] == ix_p & [XE.n2] == ix_c);
    line([e_cp.line(1,:)],[e_cp.line(2,:)], 'Color', 'k', 'LineWidth', 2);
    x_end = XV(ix_p);
    Sol_Traj = [Sol_Traj x_end.pose];
end

Sol_Traj = fliplr(Sol_Traj);
return;
end

% Utility functions
function drawObstacles(obj,h)
    % Input:
    % h: figure handle
    % obstacles: list of obstacle vertices
```

```
    det_obstacles = obj.Map.det_obstacles;
    unc_obstacles = obj.Map.unc_obstacles;
    figure(h)
    hold on;
    for i = 1:length(det_obstacles)
        obs = det_obstacles(i);
        plot(obs,'FaceColor',[0 166/255 214/255],'FaceAlpha',1);
    end
    for j = 1:length(unc_obstacles)
        obs     = unc_obstacles(j).shape;
        plot(obs,'FaceColor',[1 210/255 0],'FaceAlpha',1);
        obs_c   = obs.Vertices;
        obs_x   = (max(obs_c(:,1))+min(obs_c(:,1)))/2;
        obs_y   = (max(obs_c(:,2))+min(obs_c(:,2)))/2;
        obs_P   = unc_obstacles.P_c;
        el_t    = linspace(0,2*pi) ;
        el_x    = sqrt(obs_P(1,1))*cos(el_t)+obs_x;
        el_y    = sqrt(obs_P(2,2))*sin(el_t)+obs_y;
        plot(el_x,el_y,'--','LineWidth',1,'color','k')
    end
end

function [X_near,X_near_idx] = Near(obj,XG,x_new,XV_card,delta)
    % Input:
    % XG:        current tree
    % x_new:     new point
    % V_card:    cardinality of the list of vertices

    % Parameters for RRT*
    ksi_d  = pi;                % volume of unit ball in R2
    mu     = max(obj.Map.bounds(1,:))*max(obj.Map.bounds(2,:));
    % conservative area approx. of C_free
    gamma  = 2^2*(1+1/2)*mu;    % constant
    eta    = delta;             % step size
    r      = min((gamma/ksi_d*log(XV_card)/XV_card)^(1/2),eta);

    % Nodes in neighbourhood
    XV      = XG.V;
    dist   = zeros(1,XV_card);
    for i  = 1:1:XV_card
        dist(i) = norm(XV(i).pose(1:2)-x_new.pose(1:2),2);
    end
    X_near_idx  = dist < r;
    if sum(X_near_idx)>0
        X_near = XV(X_near_idx);
        return;
    end
    X_near = [];
end
end
end
```

Metric - save as: 'Reach_CostFunction.m'

```
%%%%%%%%%%%%%%%%%%%%%%%%%%%%%%%%%%%%
% Reachability based metric function
% Input:
            % u = control input
            % Ctrl_lim = control limits
            % c_dist   = trajectory length
            % Delta_t  = step-wise risk

classdef Reach_CostFunction < handle
    properties
        delta = [];
        alpha = [];
    end
    methods
        function obj = Reach_CostFunction(delta,alpha)
            %obj@CostFunction;  % Only when superclass 'CostFunction' is defined
            obj.delta       = delta;
            obj.alpha       = alpha;
        end
        function [c_rand] = dist_metric(obj,u,Ctrl_lim)
            v_t         = u(1);
            kappa_t     = u(2);
            kappa_max   = Ctrl_lim;
            if kappa_t < kappa_max && kappa_t > -kappa_max && v_t > 0
                c_rand = v_t*obj.delta;
            else
                c_rand = inf;
            end
        end

        function [cost] = cost_metric(obj,c_dist,Delta_t)
            cost = obj.alpha.D*c_dist + obj.alpha.Delta*obj.delta*Delta_t;
        end
    end
end
```

State validity checker - save as: 'Reach_CostFunction.m'

```
function [bool,Delta_t] = isStateValid(x,risk, map,agent,psi)
    %%%%%%%%%%%%%%%%%%%%%%%%%%%%%%%%%%%%%%%%%%%%%%%%
    % Function that calculates whether the configuration is in collision
    % Input:
    %   x:     agent state
    %   risk:  accumulated risk
    %   map:   obstacle map
    %   agent: agent representation
    %   psi:   probabilistic feasibility constraint values

    % Agent representation
    if length(x) == 2
        agent_poly  = agent.cons;
        max_dim     = sqrt((agent.length/2)^2+(agent.width/2)^2);
        x(3)        = 0;
```

```
        agent_state = translate(rotate(agent_poly,x(3)/pi*180,...
                      [max_dim/2 max_dim/2]),[x(1)-max_dim/2 x(2)-max_dim/2]);
    else

        agent_poly  = agent.rep;
        agent_state = translate(rotate(agent_poly,x(3)/pi*180,...
        [agent.length/2 agent.width/2]),[x(1)-agent.length/2 x(2)-agent.width/2]);
    end

    % Check collision using intersect
    obstacles = [map.det_obstacles,map.unc_obstacles.shape];
    for i=1:length(obstacles)
        obs = obstacles(i);
        col = intersect([agent_state,obs]);
        if col.NumRegions>0
            bool    = false;    % when in collision
            Delta_t = 0;
            return;
        end
    end

    % Probabilistic feasibility checking
    unc_obstacles = map.unc_obstacles;
    Delta_jt = zeros(length(unc_obstacles),1);
    for j=1:length(unc_obstacles)
        obs   = unc_obstacles(j);
        A     = obs.A;
        P_c   = obs.P_c;
        c_hat = obs.c_hat;
        r     = agent.radius;
        Delta_jkt = zeros(size(A,1),1);
        for k = 1:size(A,1)
            Delta_jkt(k,:) = 1/2*(1-erf((A(k,:)*(x(1:2)-c_hat(k,:)')-r)/...
            (sqrt(2*A(k,:)*P_c*A(k,:)'))));
        end
        Delta_jt(j,:) = min(Delta_jkt);
    end
    Delta_t = sum(Delta_jt);

    if length(x) == 2  % when sampling a point the accumulated cost is not clear
        Delta = 0;
    else
        Delta = risk + Delta_t;
    end

    if Delta_t > 1-psi.s || Delta > 1-psi.p
        bool = false;    % when not robustly feasible
        return;
    end
    bool = true;            % when not in collision
end
```

Motion validity checker - save as: 'Samp_MotionChecker.m'

```
%%%%%%%%%%%%%%%%%%%%%%%%%%%%%%%%%%%%%%%%
% Sampled motion validity checker
% Input:
            % X_steps:  vector of intermediate steps

classdef Samp_MotionChecker < handle
    properties
    end
    methods
        function obj = Samp_MotionChecker()
            %obj@MotionChecker;   % Only when superclass 'MotionChecker' is defined
        end
        function [bool,Delta_t] = motion_free(obj,X_steps,risk,StateValidityChecker)
            bool = true;
            Delta_t_steps = zeros(size(X_steps,2),1);
            for i = 2:size(X_steps,2)
                [yesno,Delta_t_steps(i,1)] = StateValidityChecker(X_steps(:,i),risk);
                if  yesno == 0 % when one state is in collision
                    bool = false;
                end
            end
            Delta_t = max(Delta_t_steps);
        end
    end
end
```

A.1.17 Script for linear dose-based optimisation

In order to use this script, the user must provide (evenly spaced) dose calculation points for the tumour volume `[P_x_ctv,P_y_ctv]`, tumour surface `P_s_ctv`, and OAR surfaces `P_s_blad`, `P_s_rect`, and `P_s_sigm`. Additionally the user must provide dwell points `point_s`.

```
%% MATLAB dose-based optimisation
% (c) Robin Straathof 2020
% Based on algorithm by Alterovitz et al. (2006)
clc
close all
clear all

% Data from mHDR-v2
%   Download online; save as 'mHDRv2.xlsx'
%   Save gl and Fl data in two separate sheets
S_K         = 40820;    % Air-kerma strength: U
Lambda      = 1.109;    % Dose-rate constant: cm-2
L           = 0.35;     % Active length: cm
theta_0     = pi/2;     % Reference angle: rad
r_0         = 1;        % Reference distance: cm
diam        = 0.09;     % Source diameter: cm
l           = 0.5;      % Source length: cm

data_gl     = readmatrix('mHDR_v2.xlsx','Sheet','g_l');
data_Fl     = readmatrix('mHDR_v2.xlsx','Sheet','F_l');
data_phi_l  = readmatrix('mHDR_v2.xlsx','Sheet','phi_l');

% Compute relevant functions
G_l0        = G_l(r_0,theta_0,L);
x_s         = point_s(:,1)*100;
y_s         = point_s(:,2)*100;

% Structure data
%   Load in the following variables;
%   [P_x_ctv,P_y_ctv]:    [m_ctv_v X 2] volume data points CTV_HR
%   P_s_ctv           :    [m_ctv_s X 2] surface data points CTV_HR
%   P_s_blad          :    [m_blad X 2] data points bladder
%   P_s_rect          :    [m_rect X 2] data points rectum
%   P_s_sigm          :    [m_sigm X 2] data points sigmoid

% Dwell point data
%   Load in the following variables;
%   [point_s]:            [n_d X 2]    dwell points

% Optimisation variables
m_ctv_v     = length(P_x_ctv);
m_ctv_s     = length(P_s_ctv);
m_blad      = length(P_s_blad);
m_rect      = length(P_s_rect);
m_sigm      = length(P_s_sigm);

c_ctvvpd     = optimvar('c_ctvvpd',m_ctv_v);
c_ctvspd     = optimvar('c_ctvspd',m_ctv_s);
c_bladpd     = optimvar('c_bladpd',m_blad);
c_rectpd     = optimvar('c_rectpd',m_rect);
c_sigmpd     = optimvar('c_sigmpd',m_sigm);
t_zp         = optimvar('t_zp',length(point_s));
```

```
% Constraint variables [Example values!]
M_ctv_v_min  = 100; M_ctv_s_min  = 100; M_blad_max   = 20;
M_rect_max   = 20;  M_sigm_max   = 20;
d_ctv_v_min  = 7.0; d_ctv_s_min  = 7.0; d_blad_max   = 6.0;
d_rect_max   = 3.7; d_sigm_max   = 4.3;

% Optimisation problem
dwell_time = optimproblem;
dwell_time.Objective = sum(c_ctvvpd/m_ctv_v)+sum(c_ctvspd/m_ctv_s)+...
sum(c_bladpd/m_blad)+sum(c_rectpd/m_rect)+sum(c_sigmpd/m_sigm);

% Constraints CTV volume
dwell_time.Constraints.ctv_v_con_min = [];
for i = 1:m_ctv_v
    min_ctv_v_con = 0;
    for j = 1:length(point_s)
        d_ctv_vzp = dose_point(P_x_ctv(i)*100,P_y_ctv(i)*100,point_s(j,1)*100,...
        point_s(j,2)*100,data_gl,data_phi_l,theta_0,L,S_K,Lambda,G_l0);
        min_ctv_v_con = min_ctv_v_con+M_ctv_v_min*d_ctv_vzp*t_zp(j);
    end
    dwell_time.Constraints.ctv_v_con_min(i) = c_ctvvpd(i)+min_ctv_v_con>=...
    M_ctv_v_min*d_ctv_v_min;
end
dwell_time.Constraints.ctv_v_con_c = c_ctvvpd'>=0;

% Constraints CTV surface
dwell_time.Constraints.ctv_s_con_min = [];
for i = 1:m_ctv_s
    min_ctv_s_con = 0;
    for j = 1:length(point_s)
        d_ctv_szp = dose_point(P_s_ctv(i,1)*100,P_s_ctv(i,2)*100,point_s(j,1)*100,...
        point_s(j,2)*100,data_gl,data_phi_l,theta_0,L,S_K,Lambda,G_l0);
        min_ctv_s_con = min_ctv_s_con+M_ctv_s_min*d_ctv_szp*t_zp(j);
    end
    dwell_time.Constraints.ctv_s_con_min(i) = c_ctvspd(i)+min_ctv_s_con>=...
    M_ctv_s_min*d_ctv_s_min;
end
dwell_time.Constraints.ctv_s_con_c = c_ctvspd'>=0;

% Constraints bladder surface
dwell_time.Constraints.blad_con_max = [];
for i = 1:m_blad
    max_blad_con = 0;
    for j = 1:length(point_s)
      d_blad_zp = dose_point(P_s_blad(i,1)*100,P_s_blad(i,2)*100,point_s(j,1)*100,...
      point_s(j,2)*100,data_gl,data_phi_l,theta_0,L,S_K,Lambda,G_l0);
      max_blad_con = max_blad_con+M_blad_max*d_blad_zp*t_zp(j);
    end
    dwell_time.Constraints.blad_con_max(i) = c_bladpd(i)-max_blad_con>=...
    -M_blad_max*d_blad_max;
end
dwell_time.Constraints.blad_con_c = c_bladpd'>=0;

% Constraints rectum
dwell_time.Constraints.rect_con_max = [];
for i = 1:m_rect
```

```
    max_rect_con = 0;
    for j = 1:length(point_s)
      d_rect_zp = dose_point(P_s_rect(i,1)*100,P_s_rect(i,2)*100,point_s(j,1)*100,...
      point_s(j,2)*100,data_gl,data_phi_l,theta_0,L,S_K,Lambda,G_l0);
      max_rect_con = max_rect_con+M_rect_max*d_rect_zp*t_zp(j);
    end
    dwell_time.Constraints.rect_con_max(i) = c_rectpd(i)-max_rect_con>=...
    -M_rect_max*d_rect_max;
end
dwell_time.Constraints.rect_con_c = c_rectpd'>=0;

% Constraints sigmoid
dwell_time.Constraints.sigm_con_max = [];
for i = 1:m_sigm
    max_sigm_con = 0;
    for j = 1:length(point_s)
      d_sigm_zp = dose_point(P_s_sigm(i,1)*100,P_s_sigm(i,2)*100,point_s(j,1)*100,...
      point_s(j,2)*100,data_gl,data_phi_l,theta_0,L,S_K,Lambda,G_l0);
      max_sigm_con = max_sigm_con+M_sigm_max*d_sigm_zp*t_zp(j);
    end
    dwell_time.Constraints.sigm_con_max(i) = c_sigmpd(i)-max_sigm_con>=...
    -M_sigm_max*d_sigm_max;
end
dwell_time.Constraints.sigm_con_c = c_sigmpd'>=0;

% Dwell time constraint
dwell_time.Constraints.t_min = t_zp >=0;

% Solve problem
[sol,fval,exitflag,output,lambda] = solve(dwell_time);
d_t_sol = sol.t_zp;
ind_act = d_t_sol > 0;
zp_act  = point_s(ind_act,:);

% Output parameters
disp('Dose-based optimisation output:');
disp(['Objective value: ',num2str(fval)]);
disp(['Active dwell positions: ',num2str(length(zp_act)),' out of ',...
num2str(length(point_s))]);
disp(['Mean dwell time: ',num2str(mean(nonzeros(d_t_sol)))]);
disp(['Max dwell time: ',num2str(max(nonzeros(d_t_sol)))]);
disp(['Total dwell time: ',num2str(sum(nonzeros(d_t_sol)))]);

%% Dose evaluation
% Create grid
x_vec      = linspace(0,x_Limits(2)*100,(x_Limits(2)/g_size+1));
y_vec      = linspace(0,y_Limits(2)*100,(y_Limits(2)/g_size+1));

D_tot      = zeros(length(x_vec),length(y_vec));
for i = 1:length(x_vec)
    x_p = x_vec(i);

    for j = 1:length(y_vec)
        y_p = y_vec(j);

        for k = 1:length(x_s)
            r         = norm([x_p y_p]-[x_s(k) y_s(k)]);
            g_l       = interp1(data_gl(:,1),data_gl(:,2),r);
            phi_l     = interp1(data_phi_l(:,1),data_phi_l(:,2),r);
```

```
            G_lp      = G_l(r,theta_0,L);
            d_rate    = dose(S_K,Lambda,G_lp,G_l0,g_l,phi_l); % [cGy/hour]: dose rate
            d_p(k)    = d_rate/(3600*100)*d_t_sol(k);         % [Gy]: dose
        end
        d_p = sum(d_p,'omitnan');
        if d_p > 100                        % truncate dose
            d_p = 100;
        end
        D_tot(i,j) = d_p;                   % append dose to grid
    end
end
[x,y] = meshgrid(x_vec./100,y_vec./100); % grid in cm to m

% Extract dose distributions for each structure
ind_ctv    = inpolygon(x,y,P_s_ctv(:,1),P_s_ctv(:,2));
ind_blad   = inpolygon(x,y,P_s_blad(:,1),P_s_blad(:,2));
ind_rect   = inpolygon(x,y,P_s_rect(:,1),P_s_rect(:,2));
ind_sigm   = inpolygon(x,y,P_s_sigm(:,1),P_s_sigm(:,2));

D_ctv      = D_tot(ind_ctv');
D_blad     = D_tot(ind_blad');
D_rect     = D_tot(ind_rect');
D_sigm     = D_tot(ind_sigm');

% Establish dose parameters
% CTV-HR
N_ctv      = length(D_ctv);
disp('CTV-HR dosimetric indices:')
D_98_ctv   = min(maxk(D_ctv,ceil(0.98*N_ctv)))
D_90_ctv   = min(maxk(D_ctv,ceil(0.90*N_ctv)))
D_50_ctv   = min(maxk(D_ctv,ceil(0.50*N_ctv)))
A_100_ctv  = length(D_ctv(D_ctv > d_ctv_v_min))/N_ctv*100

% Bladder
N_blad     = length(D_blad);
disp('Bladder dosimetric indices:')
D_10_blad  = min(maxk(D_blad,ceil(0.1*N_blad)))
D_2_blad   = min(maxk(D_blad,ceil(0.02*N_blad)))
A_6Gy_blad = length(D_blad(D_blad > 6))/N_blad*100

% Rectum
N_rect     = length(D_rect);
disp('Rectum dosimetric indices:')
D_10_rect  = min(maxk(D_rect,ceil(0.1*N_rect)))
D_2_rect   = min(maxk(D_rect,ceil(0.02*N_rect)))
A_37Gy_rect= length(D_rect(D_rect > 3.7))/N_rect*100

% Sigmoid
N_sigm     = length(D_sigm);
disp('Sigmoid dosimetric indices:')
D_10_sigm  = min(maxk(D_sigm,ceil(0.1*N_sigm)))
D_2_sigm   = min(maxk(D_sigm,ceil(0.02*N_sigm)))
A_43Gy_sigm= length(D_sigm(D_sigm > 4.3))/N_sigm*100
```

```
%% Functions
% Geometry function
function G_l_out = G_l(r,theta,L)

beta = atan2(r*cos(theta)+L/2, r*sin(theta))- atan2(r*cos(theta)-L/2, r*sin(theta));
if theta == 0 || theta == pi
    G_l_out = 1/(r^2-L^2/4);
else
    G_l_out = beta/(L*r*sin(theta));
end

end

% Absorbed dose calculation
function d_out = dose(S_K,Lambda,G_lp,G_l0,g_l,phi_l)
d_out       = S_K*Lambda*G_lp/G_l0*g_l*phi_l;
end

% Dose point function
function d_ij = dose_point(x_i,y_i,x_s,y_s,data_gl,data_phi_l,theta_0,...
L,S_K,Lambda,G_l0)
        r         = norm([x_i y_i]-[x_s y_s]);
        if r>10
            r = 10;
        end
        g_l       = interp1(data_gl(:,1),data_gl(:,2),r);
        phi_l     = interp1(data_phi_l(:,1),data_phi_l(:,2),r);
        G_lp      = G_l(r,theta_0,L);
        d_rate    = dose(S_K,Lambda,G_lp,G_l0,g_l,phi_l);       % cGy/hour
        d_ij      = d_rate/(100*3600);                          % Gy/s
end
```

A.1.18 Script for coverage planning

In order to use this script, the user must provide coordinates of structures in the file `structures_BT.mat` generated with Script A.1.9 of a MR image (here called 'Delineation_extended.png'), the function `ExactMinBoundCircle` [381], and source data (here used is `mHDR_v2.xlsx` [26]). Note that this is only a minimal working example not including plotting. To evaluate the generated configuration of dwell segments, the dose-based optimisation in Script A.1.17 may be used.

```
%% MATLAB NPIP-inspired coverage planning
% (c) Robin Straathof 2020
clc
clf
close all
clear all

load('structures_BT.mat');
x_Limits   = [0.000 0.210];
y_Limits   = [0.000 0.214];

%% Generate dwell segment candidate set N_free
% Parameters
n        = 1000;                                % dwell segment density
d_int    = 5E-3;                                % [m]:   step size
g_size   = 2.5E-3;                              % [m]:   grid size
w        = 2.2E-3;                              % [m]:   channel width
max_a    = 80/180*pi;                           % [rad]: maximum angle
eps      = ExactMinBoundCircle(ctv_coord)*0.30; % [m]:   radius

% Select CTV_HR base
E     = ctv_coord(3:4,:);
n_e   = round(n*norm(E(1,:)-E(2,:)));
e_i   = E(1,:) + rand(n_e,1).*(E(2,:)-E(1,:));

% Initialisation
idx      = 1;
N.edge   = [NaN,NaN]; N.points = [NaN,NaN]; N.angle = [NaN]; N.idx = idx;
N_f.edge = [NaN,NaN]; N_f.points = [NaN,NaN]; N_f.angle = [NaN]; N_f.idx = idx;

for i  = 1:(size(ctv_coord,1)-1)
    if i == 3                           % base of tumour
        continue
    end

    C   = ctv_coord(i:(i+1),:);         % contour line of tumour
    n_c = round(n*norm(C(1,:)-C(2,:))); % number of points on contour length
    c_i = C(1,:) + rand(n_c,1).*(C(2,:)-C(1,:)); % random point on contour
    for j = 1:n_c
        c_p = c_i(j,:);
        for k = 1:n_e
            e_p   = e_i(k,:);           % base point
            idx   = idx+1;
            L     = floor(norm(e_p-c_p)/d_int)+1; % number of dwell points
            for l = 1:L
                z_p(l,:) = c_p + d_int*(e_p-c_p)/norm(e_p-c_p)*(l-1);
            end
```

```
            c_vec        = e_p-c_p;
            e_vec        = E(2,:)-E(1,:);
            ang          = acos(min(1,max(-1, c_vec(:).'*e_vec(:)/...
            (norm(c_vec)*norm(e_vec))));

            % Generate candidate set N
            N_new.edge   = [c_p;e_p];
            N_new.points = [z_p;e_p];
            N_new.angle  = ang;
            N_new.idx    = idx;
            N            = [N N_new];

            % Compute distance between worst-case bound of OARs and base point
            for m = 1:(size(blad_coord_bu,1)-1)
                b1       = blad_coord_bu(m,:);
                b2       = blad_coord_bu(m+1,:);

                d_b1b2   = norm(b1-b2);
                d_b1e    = norm(b1-e_p);
                d_b2e    = norm(b2-e_p);

                if dot(b1-b2,e_p-b2)*dot(b2-b1,e_p-b1)>=0
                    A        = [b1,1;b2,1;e_p,1];
                    dist_blad(m) = abs(det(A))/d_b1b2;
                else
                    dist_blad(m) = min(d_b1e, d_b2e);
                end
            end

            for o = 1:(size(sigm_coord_bu,1)-1)
                b3       = sigm_coord_bu(o,:);
                b4       = sigm_coord_bu(o+1,:);

                d_b3b4   = norm(b3-b4);
                d_b3e    = norm(b3-e_p);
                d_b4e    = norm(b4-e_p);

                if dot(b3-b4,e_p-b4)*dot(b4-b3,e_p-b3)>=0
                    B        = [b3,1;b4,1;e_p,1];
                    dist_sigm(o) = abs(det(B))/d_b3b4;
                else
                    dist_sigm(o) = min(d_b3e, d_b4e);
                end
            end

            % Extract segments that are feasible and where the angle with
            % base is within limits
            if min(dist_blad) > eps && min(dist_sigm) > eps && ...
            max_a < ang && ang < (pi-max_a)
                N_fnew.edge   = N_new.edge;
                N_fnew.points = N_new.points;
                N_fnew.angle  = N_new.angle;
                N_fnew.idx    = idx;
                N_f           = [N_f N_fnew];
            end
            z_p = [];
        end
    end
end
```

```
N_k = size(N_f,2);

%% Generate coverable points
% Regularly spaced points in tumour
x_1 = min(ctv_coord(:,1));
y_1 = min(ctv_coord(:,2));
x_2 = max(ctv_coord(:,1));
y_2 = max(ctv_coord(:,2));
n_x = ceil((x_2-x_1)/g_size);
n_y = ceil((y_2-y_1)/g_size);

[P_x,P_y] = meshgrid(linspace(x_1,x_1+n_x*g_size,n_x),...
linspace(y_1,y_1+n_y*g_size,n_y));
P_ind     = inpolygon(P_x,P_y,ctv_coord(:,1),ctv_coord(:,2));
P_x = P_x(P_ind);
P_y = P_y(P_ind);
line(P_x,P_y,'linestyle','none','marker','.','color','b')

% Coverable points
I_eps = zeros(length(P_x),1);
Q     = size(P_x,1);
for s_i = 1:N_k
    for p = 1:size(N_f(s_i).points,1)
        for q = 1:Q
            if I_eps(q) ~= 1
                if norm(N_f(s_i).points(p,:)-[P_x(q,1),P_y(q,1)])<eps
                    I_eps(q) = 1;
                end
            end
        end
    end
end

I_x = P_x(logical(I_eps));
I_y = P_y(logical(I_eps));
line(I_x,I_y,'linestyle','none','marker','.','color','r')

%% Linear integer programming
% Set of needles that cover tumour points
M_i = zeros(length(I_x),N_k);
for i = 1:length(I_x)
    for s_i = 1:N_k
        for p = 1:size(N_f(s_i).points,1)
            if norm(N_f(s_i).points(p,:)-[I_x(i,1),I_y(i,1)])<=eps
                M_i(i,s_i) = 1;
                continue
            end
        end
    end
end
M_iL = logical(M_i);
```

```
% Set of colliding needles
Y = zeros(size(N_f,2));
for k = 2:size(N_f,2)
    for j = k:size(N_f,2)
        if line_dist(N_f(k).edge(1,:),N_f(k).edge(2,:),...
        N_f(j).edge(1,:),N_f(j).edge(2,:))<2*w
            Y(k,j) = 1;
        end
    end
end
Y = logical(Y);

% Optimisation parameters
x = optimvar('x',N_k,'Type','integer','LowerBound',0,'UpperBound',1);
NPIP = optimproblem;
NPIP.Objective = sum(x);

% Coverage constraints
NPIP.Constraints.cov = [];
for i = 1:length(I_x)
    NPIP.Constraints.cov(i) = 1-sum(x(M_iL(i,:)),1) <= 0;
end

% Collision constraints
NPIP.Constraints.col = [];
for l = 1:N_k
    NPIP.Constraints.col(l) = sum(x(Y(l,:)))-1 <=0;
end

% Solution
NPIPln  = solve(NPIP);
sol_ind = find(NPIPln.x);
disp(['Coverable points: ',num2str(length(I_x)/length(I_eps)*100),' %']);
point_s = [];
for i = 1:length(sol_ind)
    point_s = [point_s; N_f(sol_ind(i)).points];
end

%% Generate dose evaluation points
% Regularly space points in CTV-HR volume
x_1_ctv = min(ctv_coord_nonc(:,1));
y_1_ctv = min(ctv_coord_nonc(:,2));
x_2_ctv = max(ctv_coord_nonc(:,1));
y_2_ctv = max(ctv_coord_nonc(:,2));
n_x_ctv = ceil((x_2_ctv-x_1_ctv)/g_size);
n_y_ctv = ceil((y_2_ctv-y_1_ctv)/g_size);

[P_x_ctv,P_y_ctv] = meshgrid(linspace(x_1_ctv,x_1_ctv+n_x_ctv*g_size,n_x_ctv),...
linspace(y_1_ctv,y_1_ctv+n_y_ctv*g_size,n_y_ctv));
P_ind_ctv     = inpolygon(P_x_ctv,P_y_ctv,ctv_coord_nonc(:,1),ctv_coord_nonc(:,2));
P_x_ctv = P_x_ctv(P_ind_ctv);
P_y_ctv = P_y_ctv(P_ind_ctv);

% Regularly space points along surface
P_s_ctv = [];
for i = 1:(length(ctv_coord_nonc)-1)
    n_ctv = ceil(norm(ctv_coord_nonc(i,:)-ctv_coord_nonc(i+1,:),2)/g_size)+1;
```

```
    L_ctv = [linspace(ctv_coord_nonc(i,1),ctv_coord_nonc(i+1,1),n_ctv).' ...
        linspace(ctv_coord_nonc(i,2),ctv_coord_nonc(i+1,2),n_ctv).'];
    P_s_ctv = [P_s_ctv; L_ctv];
end

% Regularly spaced points along the surface of OARs
% Bladder
P_s_blad = [];
for i = 1:(length(blad_coord)-1)
    n_blad = ceil(norm(blad_coord(i,:)-blad_coord(i+1,:),2)/g_size)+1;
    L_blad = [linspace(blad_coord(i,1),blad_coord(i+1,1),n_blad).' ...
        linspace(blad_coord(i,2),blad_coord(i+1,2),n_blad).'];
    P_s_blad = [P_s_blad; L_blad];
end

% Rectum
P_s_rect = [];
for i = 1:(length(rect_coord)-1)
    n_rect = ceil(norm(rect_coord(i,:)-rect_coord(i+1,:),2)/g_size)+1;
    L_rect = [linspace(rect_coord(i,1),rect_coord(i+1,1),n_rect).' ...
        linspace(rect_coord(i,2),rect_coord(i+1,2),n_rect).'];
    P_s_rect = [P_s_rect; L_rect];
end

% Sigmoid
P_s_sigm = [];
for i = 1:(length(sigm_coord)-1)
    n_sigm = ceil(norm(sigm_coord(i,:)-sigm_coord(i+1,:),2)/g_size)+1;
    L_sigm = [linspace(sigm_coord(i,1),sigm_coord(i+1,1),n_sigm).' ...
        linspace(sigm_coord(i,2),sigm_coord(i+1,2),n_sigm).'];
    P_s_sigm = [P_s_sigm; L_sigm];
end

% Insert linear dose-based optimisation script here

%% Functions
function dist = line_dist(a,b,c,d)
% Lines intersect
t = det([c'-a',d'-c'])/det([b'-a',d'-c']);
s = det([a'-c',b'-a'])/det([d'-c',b'-a']);

if 0<=t && t<=1 && 0<=s && s<=1 && det([d'-c',b'-a'])~=0
    dist = 0;
    return
end

% Lines do not intersect, may be parallel
d_ab  = norm(a-b);
d_ac  = norm(a-c);
d_ad  = norm(a-d);
d_bc  = norm(b-c);
d_bd  = norm(b-d);
d_cd  = norm(c-d);
```

```
% Line a to cd
if dot(c-d,a-d)*dot(d-c,a-c)>=0
    A       = [c,1;d,1;a,1]; dist_a  = abs(det(A))/d_cd;
else
    dist_a  = min(d_ac, d_ad);
end

% Line b to cd
if dot(c-d,b-d)*dot(d-c,b-c)>=0
    B       = [c,1;d,1;b,1]; dist_b  = abs(det(B))/d_cd;
else
    dist_b  = min(d_bc, d_bd);
end

% Line c to ab
if dot(a-b,c-b)*dot(b-a,c-a)>=0
    C       = [a,1;b,1;c,1]; dist_c  = abs(det(C))/d_ab;
else
    dist_c  = min(d_ac, d_bc);
end

% Line d to ab
if dot(a-b,d-b)*dot(b-a,d-a)>=0
    D       = [a,1;b,1;d,1]; dist_d  = abs(det(D))/d_ab;
else
    dist_d  = min(d_ad, d_bd);
end
dist = min([dist_a,dist_b,dist_c,dist_d]);
end

% Geometry function
function G_l_out = G_l(r,theta,L)
beta = atan2(r*cos(theta)+L/2, r*sin(theta))- atan2(r*cos(theta)-L/2, r*sin(theta));
if theta == 0 || theta == pi
    G_l_out = 1/(r^2-L^2/4);
else
    G_l_out = beta/(L*r*sin(theta));
end
end

% Absorbed dose calculation
function d_out = dose(S_K,Lambda,G_lp,G_l0,g_l,phi_l)
d_out       = S_K*Lambda*G_lp/G_l0*g_l*phi_l;
end

% Dose point function
function d_ij = dose_point(x_i,y_i,x_s,y_s,data_gl,data_phi_l,theta_0,L,...
S_K,Lambda,G_l0)
        r         = norm([x_i y_i]-[x_s y_s]);
        if r>10
            r = 10;
        end
        g_l       = interp1(data_gl(:,1),data_gl(:,2),r);
        phi_l     = interp1(data_phi_l(:,1),data_phi_l(:,2),r);
        G_lp      = G_l(r,theta_0,L);
        d_rate    = dose(S_K,Lambda,G_lp,G_l0,g_l,phi_l);       % cGy/hour
        d_ij      = d_rate/(100*3600);                          % Gy/s
end
```

A.2 A brief overview and discussion on dose and radiobiological concepts and models in brachytherapy

Biologically effective dose (BED)

The biologically effective dose (BED) formalism and other techniques transforming absorbed dose to equivalent or equieffective dose are typically based on the use of the linear quadratic (LQ) model. An excellent review on the history and ability of the LQ model to characterise radiation effects was recently published [394]. Some critique on this model includes: (i) that its validity is believed for delivered dose per fraction ranging between 0.5 Gy to 6 Gy, and may overestimate the effect at higher dosages [7, 20, 22, 394, 395][1], (ii) that radiosensitivity coefficients α and β can vary for different tumour histologies or tissue types [7, 20, 394, 395], and (iii) that it does not take into account the gradient of the dose in brachytherapy, such that the actual equivalent dose is underestimated with a factor of 1.15-1.30 [397–399]. Considering the latter, Dale et al. proposed to calculate the equivalent dose if a uniform dose distribution was to be generated from a non-uniform applicator dose distribution [397, 398], similar to the **equivalent uniform dose (EUD)** concept [400]. In the *'spherical model'*, it is assumed that the point dose falloff primarily follows an *inverse square law* [397–399], which is similar to the distribution most intracavitary brachytherapy applicators produce. Assuming a spherical model with radius R and prescribed dose at distance $r = R$ from the point source as well[2], the **equivalent BED**, BED_{eq}, for a non-uniform BT, e.g. tandem-ovoid, applicator, is found as follows (derivation in Ref. [397]):

$$\text{BED}_{eq,\alpha/\beta} = -\frac{1}{\alpha} \ln \left(\frac{3}{R^3} \int_0^R x^2 f(x) dx \right) \tag{A.1}$$

With, $f(x)$ derived for HDR-BT from Eq. 1.1:

$$f(x) = \exp \left(-\alpha N d \left(\frac{R}{x} \right)^2 - \beta G N d^2 \left(\frac{R}{x} \right)^4 \right) \tag{A.2}$$

Although this is a simple analytical formulation, i.e. with simplified geometry, its accuracy was established to be within 2% of doses derived with voxel-based approaches [399][3]. Nevertheless the accuracy of such a method was questioned recently [401]. The analytical method may perform poorly against voxel-by-voxel approaches, due to its inability to: (i) compensate for asymmetrical dose shapes, i.e. deviation from the pear dose shape, (ii) distinguish between plans for different applicators, and (iii) be robust against variability stemming from physician, or treatment planning aspects. Nevertheless, although the author acknowledges that **equivalent uniform BED (EUBED)** or **generalized biologically equivalent uniform dose (gBEUD)**[4] are more accurate metrics -especially for lower values of α-, and may possibly even predict clinical outcome more accurately [401, 402], for the purpose of illustration the BED (Eq. 1.1), and equivalent BED (Eq. A.1), are sufficient. It must be noted that in its latest report the ICRU does not promote the use of the equivalent BED, BED_{eq}, for organs at risk as it is clinically unproven, its influence on organ at risk dosage is limited and its parameters are uncertain [7].

[1] Interestingly, the dose used typically for HDR brachytherapy amounts to 7 Gy per fraction which implies that the calculated BED may overestimate the effect, but this is rarely questioned [134]. At higher dose rates, a change in the rate of repair might be observed as the result of overloading repair enzymes, which has led to the development of new models, e.g. LQL and gLQ in other fields of radiotherapy [396], at the expense of additional parameters and complexity. The LQ-model has insofar remained the standard approach due to its simplicity and its reproducibility of clinical observations [394].

[2] This means that the equivalent dose is independent of R, which drops out of the equation.

[3] The authors of this article refer to data by Dale and Coles [398], which the author of this thesis was not able to retrieve.

[4] gBEUD is an extension of gEUD, which is expressed in Eq. A.19, using the BED opposed to the absorbed dose.

Equieffective dose (EQDX)

The equieffective dose can be derived from the linear quadratic model in Eq. 1.1 by assigning the total dose given during treatment the product of the number of fractions and dose per fraction, $D = Nd$, and using subscripts $_1$ and $_2$ to denote the absorbed dose and equieffective dose respectively:

$$D_1\left(1+G_1\frac{d_1}{\alpha_1/\beta_1}\right) = \mathrm{EQDX}\left(1+G_2\frac{d_2}{\alpha_2/\beta_2}\right) \tag{A.3}$$

$$\mathrm{EQDX} = D_1\frac{(\alpha_2(G_1\beta_1 d_1+\alpha_1))}{(\alpha_1(G_2\beta_2 d_2+\alpha_2))} \tag{A.4}$$

Now: (i) assuming that all dose-related parameters do not change ($\alpha_1 = \alpha_2 = \alpha$, $\beta_1 = \beta_2 = \beta$, $G_1 = G_2 = G$), (ii) rewriting Eq. 1.1 such that $D_1 = \mathrm{BED}/[1 + (Gd)/(\alpha/\beta)]$, and (iii) defining $d_2 = 2$ Gy as to obtain the equivalent dose at 2 Gy reference fractions, the equations for $\mathrm{EQD2}_{\alpha/\beta}$ simply follows:

$$\mathrm{EQD2}_{\alpha/\beta} = \frac{\mathrm{BED}_{\alpha/\beta}}{\left(\frac{2G}{\alpha/\beta}+1\right)} \tag{A.5}$$

The EQD2 values from EBRT and brachytherapy may now be added for specific dose volumes or points. The addition of dose volume relations typically involves using a worst-case assumption that the volume receiving the highest dose, in the case of organs at risk, or the lowest dose, in the case of the tumour volume, remains at the same location throughout treatment [22], which is the subject of discussion under the header 'Treatment planning: DVH addition'. Other critique on the EQD2 model includes the aforementioned dependence [134, 403], and uncertainty in the estimated values of the radiosensitivity coefficients; sensitivity data for different organ and tissue types, and tumour histologies has been reviewed in several works [31, 404, 405]. For example, for the bladder a ratio of $\alpha/\beta = 0.4$ Gy was shown to produce the best fit with the incidence of severe urinary toxicity out of the three tested values (0.4, 3 and 5 Gy) in hypofractionated radiotherapy of prostate cancer [406]. Moreover, it must be emphasised that the α/β ratio is not constant during treatment [395]. For the tumour, in cervical cancer radiotherapy the radiosensitivity coefficient ratio may vary from $\alpha/\beta = 6$ Gy [407], to 21 Gy [405], similar to reports for other tumours with α/β = 7-20 Gy [7]. In the study by Datta et al. a value of $\alpha/\beta = 26$ Gy was found for cervical cancer patients in a LQ-model also incorporating treatment time [408].

Whether to include a *time factor* in the LQ-model for HDR brachytherapy has been questioned [134, 395]. As mentioned, the repair function G is commonly assumed to be equal to one for HDR-BT, indicating that complete sublethal damage repair occurs in between fractions [7]. However, it has been shown that longer treatment time, i.e. longer than 8 weeks or 55 days, requires additional dose to the tumour to achieve similar biological effects and is related subsequently to poorer local control and survival rates [409, 410]. This may be the result of accelerated cellular repopulation, which does not result in significant dose differences until several weeks after the onset of treatment, usually modelled with a 'kick-off time' T_k [134, 395, 405, 411]. As introduced by Fowler (1989), this means that the BED accounting for delayed proliferation may be written as (from eq (1.1)) [411]:

$$\mathrm{BED}_{\alpha/\beta}(t) = Nd\left(1+G\frac{d}{\alpha/\beta}\right) - \kappa(t-T_k) \tag{A.6}$$

With, $\kappa = \ln(2)/(\alpha T_p)$ the time factor, t the overall treatment time, and T_p the average doubling time of the cells [411]. With such a model, Tornero-López et al. were reasonably able to predict the additional dose required to compensate for the loss of local control as the effect of prolonged treatment duration [134]. However, there are several reasons for not including time factors in the

LQ-model. Firstly, the model introduces three additional parameters, which are difficult to estimate [411]. Moreover, inclusion of this time factor may alter the values of the other parameters in the model significantly; e.g. when including a time factor the estimated α/β value increased from 5.1 Gy to 11.1 Gy in the work by Suwinski et al.[412]. This implies that transition from the LQ-model which usually provides a good fit, to a new model including time factors requires new parameter estimation. Lastly, rather than that the loss of tumour control probability with increased duration is attributed to biological factors, one may argue that patients with less favourable prognoses generally have longer treatment times and hence reduced tumour control probability is caused by poor management [413]. However, after controlling for possible biases such as tumour volume and stage, Tanderup et al. still found treatment prolongation of one week correlated to equieffective dose differences of 5 Gy $\text{EQD2}_{\alpha/\beta=10}$ [409].

Dose-volume parameters

One main complication with interpreting and extracting parameters from DVHs is that these reduce the spatial dosimetric information into two-dimensional dose-volume relations [7, 23, 414], in order to be able to correlate biological effects or treatment outcomes between patients with the absorbed dose. However, in doing so, valuable information is lost. For example, DVHs cannot indicate where within a structure hot or cold spots are present [23]. In another example; an assymmetric dose distribution over a specified volume could result in a similar DVH as when computed for a symmetric dose distribution over the same volume [415]. Moreover, such a model does not discriminate between functional or structural organisation of different subregions [416], or their dose response [7]. This limits the predictive power of dose-effect relationships based on DVH parameters and means that the spatial distribution of the dose with respect to the topography must always be analysed for plan evaluation and final prescription [7].

Furthermore, the calculation of accumulated dose over succeeding EBRT and BT fractions, is more complex than simple DVH parameter addition. When adding DVH parameters, such as the $D_{98\%}$, it is assumed that the location of the concerning volume remains identical for each fraction [7, 22, 98]. For the target dose this leads to a *'worst-case assumption'* under the supposition that the relative position between applicator and tumour is fixed, whereas this term is inaccurate for organs and normal tissues [7].

Dose-response models

The *logistic* model in Eq. 1.9 for relating local tumour control to the radiation dose has been commonly used. However, one disadvantage of this model is that the value of TCP at zero dose is non-zero -although this rarely becomes an issue [35]- and for that purpose the *log-logistic* function may be used [37]:

$$\text{TCP} = \frac{1}{\left(1 + (\text{TCD}_{50}/D)^{(4\gamma_{50})}\right)} \tag{A.7}$$

Log-logistic formulations may however yield dose-response parameters that are different from those in other models [417], possibly as the log-logistic distribution is positively skewed. Note that rather than D, also the BED (Eq. 1.1) or EQD2 (Eq. 1.2) doses could be related to local control via this formulation. In addition, to account for dose gradients, one may incorporate the equivalent BED, BED_{eq} (Eq. A.1), or equivalent EQD2, EQD2_{eq}, in the TCP formulation as for example done in the study by Plataniotis et al. [418]. More complex, mechanistic models, such as Poisson models, take into account clonogenic tumour cell distribution [419], but this is out of scope for the models used in this thesis.

For modelling the NTCP, other than the logistic model, it is more common to use the **Lyman model** [420], which assumes a *power-law relation* between the *tolerance dose* and the irradiated volume fraction:

$$\mathrm{TD}(v) = \mathrm{TD}(1)/v^n \tag{A.8}$$

Here, $\mathrm{TD}(v)$ is the tolerance dose for a partial volume v, $\mathrm{TD}(1)$ is the tolerance dose for the full volume and n a fitted power law parameter used for describing the magnitude of the volume effect. The NTCP may then be determined via the integral of a normal distribution, as the cumulative distribution function for a normal distribution has a sigmoid shape, leading to the following *'probit'* model [420]:

$$\mathrm{NTCP}(D, v) = \frac{1}{\sqrt{2\pi}} \cdot \int_{-\infty}^{t} \{\exp\left(-x^2/2\right)\} dx \tag{A.9}$$

Where,

$$t = \frac{(D - \mathrm{TD}_{50}(v))}{(\sigma(v))} \tag{A.10}$$

$$\mathrm{TD}_{50}(v) = \mathrm{TD}_{50}(1)/v^n \tag{A.11}$$

In this expression, it is thus assumed that the complication probability as a function of the dose D and uniformly irradiated volume v follows a normal distribution characterised by the mean, $\mathrm{TD}_{50}(v)$, and standard deviation, $\sigma(v)$, which is approximated by $\sigma(v) = m \cdot \mathrm{TD}_{50}(v)$ [420]. Therefore, only three model parameters are required to calculate the NTCP of specific (partial) organ or tissue volumes: TD_{50}, n, and m. The latter parameter, m is related to the steepness of the dose-response curve [32]. Uniform irradiation however cannot be assumed, and therefore non-uniform information, generally obtained from a DVH, must be converted into a uniform dose to a (partial) volume [32]. This histogram reduction may involve an effective volume method irradiated to a reference dose or determining an equivalent uniform dose applied to the full volume [421]. The Kutcher–Burman (KB) reduction algorithm, using the Lyman model and collectively known as the **Lyman-Kutcher–Burman (LKB) model** is the most frequently used method for calculating the *effective fractional volume* [32, 422]. This LKB-model assumes that each irradiated fractional sub-volume v_i receiving dose D_i, leads to the same NTCP as an partial effective volume, $v_{\mathrm{eff},i}$, irradiated with a uniform reference dose D_{ref}:

$$v_{\mathrm{eff},i} = v_i \cdot \left(\frac{D_i}{D_{\mathrm{ref}}}\right)^{1/n} \tag{A.12}$$

These smaller effective volumes may then be summed, such that:

$$v_{\mathrm{eff}} = \sum_{i=1}^{j} v_{\mathrm{eff},i} \tag{A.13}$$

The reference dose, D_{ref}, may be selected arbitrarily as the NTCP is independent of this dose [423]. This volume reduction model may now be implemented in the Lyman model, by modifying Eq. A.10, such that:

$$t = \frac{(D_{\mathrm{ref}} - \mathrm{TD}_{50}(v_{\mathrm{eff}}))}{(m \cdot \mathrm{TD}_{50}(v_{\mathrm{eff}}))} \tag{A.14}$$

Similarly, one could also derive an *effective dose*, D_{eff} [424]:

$$D_{\mathrm{eff}} = \left(\sum_{i=1}^{j} v_i \cdot (D_i)^{1/n}\right)^n \tag{A.15}$$

$$t = \frac{(D_{\mathrm{eff}} - \mathrm{TD}_{50}(v))}{(m \cdot \mathrm{TD}_{50}(v))} \tag{A.16}$$

This is conceptually equivalent to the *EUD* (which uses $a = 1/n$) [425], and typically a probit-formulation:

$$\mathrm{EUD} = \left(\sum_{i=1}^{j} v_i \cdot (D_i)^a \right)^{1/a} \tag{A.17}$$

$$t = \frac{(\mathrm{EUD} - \mathrm{EUD}_{50}(v))}{(m \cdot \mathrm{EUD}_{50}(v))} \tag{A.18}$$

Or a log-logistic formulation [426]:

$$\mathrm{NTCP} = \frac{1}{\left(1 + (\mathrm{TD}_{50}/\mathrm{EUD})^{(4\gamma_{50})}\right)} \tag{A.19}$$

Note that in all of the above formulations, the dose D may be changed to BED (Eq. 1.1) or EQD2 (Eq. 1.2). The LKB model has a high sensitivity to small high-dose regions [427], which are present in the case of brachytherapy. Moreover, although the KB reduction and EUD formulation have shown to have less inconsistencies in their formulation than comparable models [428], still their predictive and comparative power is limited and their results therefore must be interpreted with caution [32]. Furthermore, the often used Burman NTCP model parameters, derived from data by Emami et al., have been developed for conventional radiotherapy [427], at the time of two-dimensional imaging and planning, and have to be re-evaluated for brachytherapy with more complex three-dimensional dose distributions. Lastly, one problem with the previous NTCP formulations is that these do not account for functional or structural organisation of different subregions, and for that reason the use of biophysically based models, such as the **relative seriality model**, is encouraged [416].

Definition A.2.1. Serial organs: *Serial organs* consist of a chain of functional units, where the function of the entire chain depends on the function of each of its links.

Definition A.2.2. Parallel organs: *Parallel organs* consist of individual functional units which function independently and are therefore only impacted when a number of units are inactivated.

For example, the rectum, sigmoid colon and bowel are considered as serial organs when regarding their role in transporting stool [7]. However, such a classification is in general difficult as some organs may exhibit serial-parallel behaviour [416]. Nevertheless, in the relative seriality model, serial or parallel behaviour is captured in the parameter s, with higher values of s indicating greater seriality [429]:

$$\mathrm{NTCP} = \left(1 - \prod_{i=1}^{j} [1 - P(D_i)^s]^{v_i} \right)^{1/s} \tag{A.20}$$

Here, $P(D_i)$ describes the response in each compartment via a model, e.g. logistic, Poisson or probit. For other NTCP methods and their considerations the reader is referred to more elaborate reviews [414, 430].

A.3 Terminology and modelling of uncertainty in brachytherapy

The evaluation and expression of uncertainties is most often performed based on documents by the Comité International des Poids et Mesures (CIPM) [431], Joint Committee for Guides in Metrology (JCGM) [432], U.S. National Institute of Standards and Technology (NIST) [433], among others. Regarding radiotherapy, the International Atomic Energy Agency (IAEA) has recently a issued a publication in accuracy issues and their management [35], with its definitions based upon the aforementioned documents. The latter is primarily used for the terminology in this work.

The following basic terms considering uncertainty are used throughout this thesis:

A.3.1 Uncertainty

Definition A.3.1. Uncertainty: *Uncertainty* expresses the dispersion of the values that are obtained for repeated measurements. The **overall** or **expanded uncertainty** is expressed as V, opposed to the conventional U, in order to avoid confusion with the symbol for the units of air-kerma strength used in radiotherapy [25, 98]. The uncertainty of a measurement result is commonly termed **standard uncertainty**, some suggesting the symbol u_i [25, 433].

Uncertainty or its components may be grouped into one of two categories according to the method used to estimate their numerical value:

- **Type A:** Those which are evaluated by applying statistical methods. For the ith type A component, the standard uncertainty is represented by the *standard deviation* (SD), s_i, which is the positive square root of the *statistically estimated variance* s_i^2;
- **Type B:** Those which are evaluated by any other type of means. For the jth type B component, the standard uncertainty is represented by the quantity u_j or *approximated variance* u_j^2.

The associated number of degrees of freedom for both type A and type B components is represented by ν. The distinction between type A and B components is merely for the purpose of convenience for discussion on quality of data, as both components are often treated in similar manner; i.e. uncertainty from either type is quantified by variances or standard deviations [434]. The distinction between type A and type B uncertainties is rarely used in recent brachytherapy literature [98], and not particularly useful for this work.

NOTE: Type A and type B uncertainties are sometimes referred to as *'random'* and *'systematic'* respectively, but such a simple correspondence is not always the case. Although the BIPM and NIST recommend avoiding the use of the term 'systematic uncertainty' altogether for this reason as the example below points out [431, 433], radiotherapy literature often uses the terms 'random' and 'systematic' to describe the effect of corresponding errors [35]. However, the term 'error' is sometimes discouraged in this context [25, 35], such that -recognising that this may be confusing- the terms 'random uncertainty' and 'systematic uncertainty' are still used throughout this work. These are subsequently, acknowledging possible confusions from the example below, defined as 'component of uncertainty arising from a *random effect*' or '[...] *systematic effect*' respectively [434, 435].

Example: It may be ambiguous to classify an uncertainty component itself as 'random' or 'systematic'. The contribution of uncertainty in one measurement stemming from a random error may become systematic if a new measurement is based on this previous uncertainty component. If one was to plan a treatment dose based on a single acquired image prior to treatment, with possible uncertainty due to random organ motion, during delivery this error may systematically be present in consecutive dose fractions. In this particular case, uncertainty in delivered dose would stem from both a random error, i.e. the random organ movement that is still present during treatment delivery itself, and a systematic error, i.e. as the imaged random position is used throughout the treatment fractions.

When assuming uncorrelated equally weighed components and sufficient degrees of freedom, the **combined standard uncertainty**, u_c, is obtained via the *law of propagation of uncertainty* what is commonly known as the *'root sum of squares'*, taking the root of the sum of components in quadrature, i.e. in its simplest form: $u_c = \sqrt{\sum_{i=1}^{I} s_i^2 + \sum_{j=1}^{J} u_j^2}$. Although usually uncorrelated components may be assumed for radiotherapy or in particular brachytherapy [98], typically for margin calculation in radiotherapy different weights are assigned to the combination of these uncertainty components [35].

The overall or expanded uncertainty, V, captures a confidence interval of the about the measurement result, y, within which the value of the measurand, Y, is confidently asserted to lie. This expanded uncertainty is derived by multiplying the combined standard uncertainty with a **coverage factor**, k, that defines the desired level of confidence, via:

$$V = ku_c \tag{A.21}$$

such that: $Y = y \pm V$ represents the interval of the measurand to the level of confidence specified by k. The conventional and recommended coverage factor used for brachytherapy reporting is $k = 2$, specifying approximately a 95% confidence interval in the case of an assumed normal distribution [99]. Nevertheless, such a factor should only be applied for the calculation of the combined uncertainty, and not for the individual components from the uncertainty budget.

Lastly, uncertainty may be expressed in: (i) an **absolute form**: $|u(y)|$, i.e. the magnitude of the difference between a measured and expected value, or commonly in, (ii) a **relative form**: $|u(y)/y|$, i.e. when the absolute error is divided by the magnitude of the expected value [436]. However, relative uncertainty must be carefully analysed in literature, as this ratio may involve different units, e.g. absorbed dose in Gy or EQD2 dose, or could for example be related to the total dose from combined treatment, solely the brachytherapy dose, or even the dose per fraction [98].

A.3.2 Error

Definition A.3.2. Error: An *error* is the discrepancy between a measured or calculated value and the expected, actual or true value.

Two types of errors may be distinguished:

- **Random error:** The *random error*, typically denoted ϵ, describes the fluctuation of the error around the true or accepted value. This type of error varies in both direction and magnitude and may be obtained by subtracting the mean of infinite measurements from the result of

a measurement. Typically it is assumed that this random error is Gaussian distributed; i.e. having a zero mean and being distributed according to variance σ_V^2;

- **Systematic error:** The *systematic error*, sometimes denoted b (derived from the term 'bias'[5]), is the difference between the mean of infinite measurements and the true value of the measurand. A systematic error is predictable in its direction and its magnitude is generally constant or proportional to the value of the measurand.

NOTE: The term *error* is **not** used here to denote a mistake or failure of an action.

Although random errors cannot directly be compensated for, these may be estimated by performing repeated measurements and their effect reduced through averaging over the number observations as their expected value is zero. However, for example in radiotherapy treatment the number of fractions is finite, and therefore the random error may not completely die out, but rather results in an error which is distributed with the standard deviation of the random errors divided by the square root of the number of fractions [98, 101]. It is difficult to detect systematic errors as the value of the measurand is unknown. Although the systematic effect may be quantified, a **correction** or **correction factor** is inherently uncertain and thus despite compensating for this effect when applied, the systematic error is not eliminated [434].

A **gross error** is an unacceptably large error, and therefore in the case of radiotherapy must be determined and corrected prior to treatment delivery [437]. Generally gross errors may be identified using image after treatment planning, but before treatment delivery. These will not be treated in this work.

A.3.3 Accuracy

Definition A.3.3. Accuracy: *Accuracy* is used to describe the closeness of agreement between a calculated or measured value and the true or accepted value.

Accuracy is a qualitative term resulting from the combination of systematic and random errors.

A.3.4 Precision

Definition A.3.4. Precision: *Precision* is used to describe the closeness or variability of replicate measurements of a measurand.

Therefore, precision does not require a true or accepted value of the measurand but is a concept related to the *repeatability* (or reproducibility)[6] of measurements. As it solely depends on random errors, precision may be quantified as a standard deviation accordingly.

A.3.5 Action level or maximum permissable error

Definition A.3.5. Action level or **maximum permissable error:** As described by the IAEA [35], the *action level* is a threshold value above which intervention should be undertaken. The *maximum permissable error* denotes a similar value level.

Often, the word *'tolerance'* is used to define the range of acceptability, but as this may conflict with 'action level' this is not used in this work [35].

[5] Although bias is used almost synonymously to systematic error, the latter term is recommended [433]. Bias may be used for expressing the magnitude of the systematic error.

[6] Some recommendations include both repeatability and reproducibility in the definition of precision [433].

A.3.6 Intra-fraction, inter-fraction, and inter-application variation

Definition A.3.6. Intra-fraction variation: *Intra-fraction variation* refers to the variation, e.g. in dose or treated volume, within the time span of imaging, planning and delivering a brachytherapy fraction [7].

Definition A.3.7. Inter-fraction variation: *Inter-fraction variation* refers to the variation, e.g. in dose or treated volume, between different fractions of brachytherapy, typically from a single imaging, planning and application session [7].

Definition A.3.8. Inter-application variation: *Inter-application variation* refers to the variation, e.g. in dose or treated volume, between applicator insertions [7].

This is also illustrated in Figure 1.2. The former two may also be regarded as *intra-application variation* as these occur within the same application. In literature, the used definitions of these terms may vary, e.g. depending on the treatment schedule and the measurement method, leading to ambiguities. For example, imaging may be performed directly before and after a treatment session, such that the intra-fraction variation in between these sessions can be established. However, with real-time imaging the variation occurring within a continuous period of irradiation solely may also be considered as intra-fraction variation.

A.3.7 Establishing models for estimating the effect of dosimetric uncertainty

The impact of dosimetric changes on the clinical outcome due to different types of uncertainty has been researched in several works for radiotherapy [35, 438–440], and brachytherapy [38]. In this subsection, some basic models to predict a clinical outcome from a prescribed dose without uncertainty are described. As to encourage readers to reproduce the figures, MATLAB (MATLAB R2020a, MathWorks, Natick, MA, USA) scripts are provided.

It was decided to use the logistic TCP model as described in Eq. 1.9 to estimate the impact of dosimetric differences on local control, based on the work by Nesvacil et al. [38]. A MATLAB code shown in Script A.1.2 is used for generating the equieffective dose - local control relationship, i.e. the effect of the D_{90} $\mathrm{EQD2}_{\alpha/\beta=10}$ of the high-risk clinical target volume on the TCP. The parameters used to generate Figure A.1a, $\gamma_{50} = 0.47$ and $D_{50} = 36.0$ Gy, were obtained from clinical data for image guided cervix cancer brachytherapy as described in the study by Nesvacil et al. [38]. In this work, it was assumed that the treatment schedule consists of 25 EBRT fractions of 1.8 Gy, and four BT fractions of varying prescribed dose. Considering dose uniformity, the $\mathrm{EQD2}_{eq,\alpha/\beta=10}$ derived from the BED_{eq} in Eq. A.1, could as well be used for generating a fit with the clinical data, but then with manually tweaked parameters $\gamma_{50} = 0.48$ and $D_{50} = 39.4$ Gy.

In order to model the impact of dosimetric differences on the NTCP of three organs at risk during cervical cancer brachytherapy treatment, Nesvacil et al. used the logistic model for generating the equieffective dose - tissue morbidity relationship, i.e. the effect of the D_{2cm^3} $\mathrm{EQD2}_{\alpha/\beta=3}$ of an organ at risk on the NTCP [38]. Their results, shown in Figure A.1b, were reproduced with MATLAB Script A.1.3 and parameters $\gamma_{50} = 2.0$ and $D_{50} = 110.0$ Gy (or $\gamma_{50} = 2.05$ and $D_{50} = 118.0$ Gy for $\mathrm{EQD2}_{eq,\alpha/\beta=3}$). The International Atomic Energy Agency (IAEA) considered a similar model to investigate the impact of uncertainties on simulated biological effects or outcome [35]. However, in these models it is assumed that a uniform dose is applied to the (partial) volume of the tumour or organ, whereas the dose distribution in brachytherapy is heterogeneous, and that

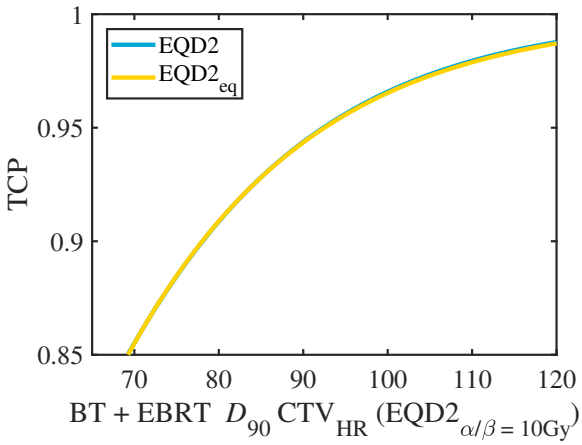

(a) Equieffective dose - local control relationship.

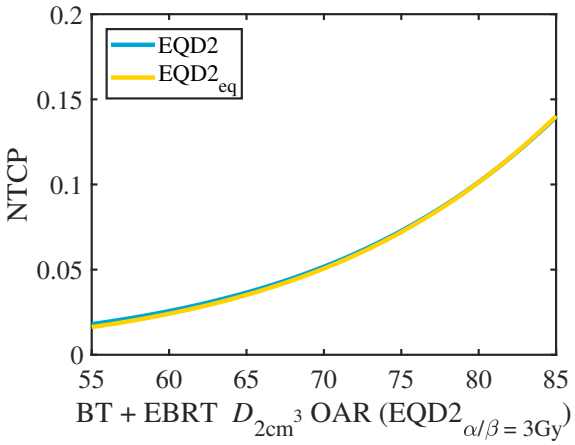

(b) Equieffective dose - tissue morbidity relationship.

Figure A.1: Simulation of the TCP and NTCP as a function of the equieffective dose via a logistic model (Eq. 1.9), as previously performed by Nesvacil et al. [38]. The MATLAB script for generating this figure is given in Script A.1.2.

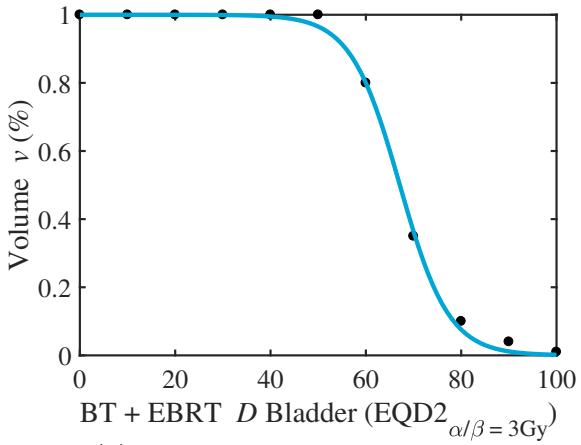

(a) Cumulative DVH of the bladder.

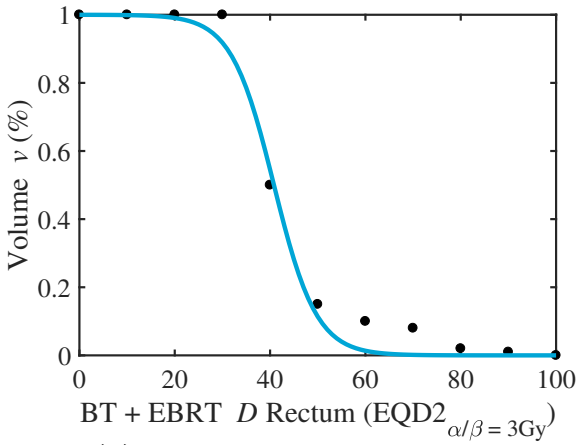

(b) Cumulative DVH of the rectum.

Figure A.2: Typical cumulative dose volume histograms of two organs at risk involved in cervical cancer brachytherapy, attained from a logistic (sigmoid curve) fit through sample dose-volume data pairs. The MATLAB script for generating this figure is given in Script A.1.4.

the irradiated tissue is homogeneous. The equivalent BED model, BED_{eq}, may be used to incorporate the effect of the brachytherapy dose gradient, but may require investigation of the organisational or functional structure of OAR tissue to determine the volume of integration [397].

To illustrate the effect of dose non-uniformity, the LKB-model (Eq. A.9 and A.14), or the EUD-formulation (Eq. A.19), may be used. Data pairs, $\{D_i, V_i\}$, of a cumulative DVH of a bladder were generated for a typical simulated dose-volume relation and a smooth sigmoidal-shaped function is fitted through these data points (Figure A.2a), see MATLAB Script A.1.4. The data are converted into a differential DVH, as described by Gay and Niemierko [441], and the effective volume V_{eff} is calculated. Using the effective volume, a NTCP of 8.2% was computed, via Eq. A.9, and using the parameters for the estimation of bladder tissue complication probability at fractions of 1.8 - 2.0 Gy by Burman et al. [135, 442]. This corresponds to a dose of 67.2 Gy in the NTCP-EQD2 relation plotted in Figure A.3a. Conventionally, when not accounting

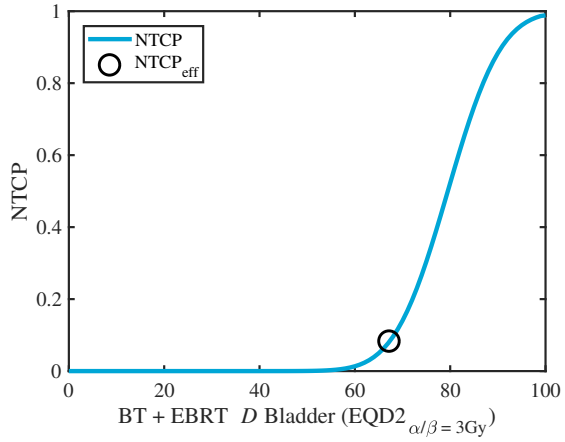

(a) Equieffective dose - tissue morbidity relationship of the bladder.

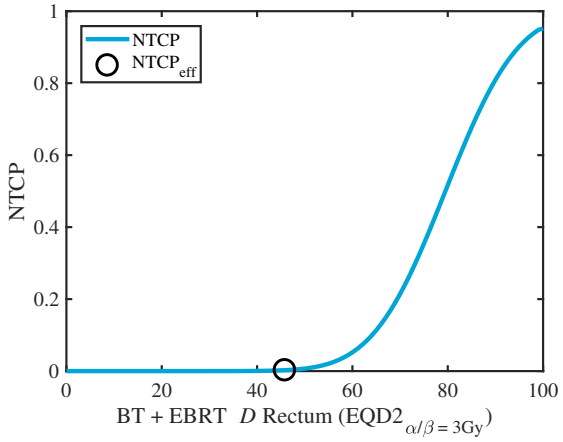

(b) Equieffective dose - tissue morbidity relationship of the rectum.

Figure A.3: Simulation of the NTCP as a function of the equieffective dose via the Lyman equation (Eq. A.9), and the point marking the NTCP for the effective volume (Eq. A.14) after KB reduction. The MATLAB script for generating this figure is given in Script A.1.4.

for the nonuniform dose distribution, one would likely take the average dose of the DVH in Figure A.2a, $D(50\%)$, which is 67.1 Gy, and corresponds to a NTCP of 8.0%, which is similar to the number found using the KB reduction scheme[7]. However, the larger the deviation of n from unity, where the equivalent uniform dose becomes the mean dose, and the more heterogeneously distributed the DVH becomes, the larger the inaccuracy. This is illustrated using the rectum as an example, which has $n = 0.12$ opposed to $n = 0.5$ for the bladder [135], and the sample DVH in Figure A.2b. This results in a NTCP of 0.25% with the effective volume computation, whereas taking the mean dose, $D(50\%) = 40.8$ Gy, would result in a NTCP of $6.4 \cdot 10^{-2}$ % (Figure A.3b). Therefore, one must be aware of the inaccuracies in using the models assuming dose uniformity.

A problem arises however when one desires to evaluate the impact of uncertainty in the dose per fraction of brachytherapy on the NTCP using an aforementioned DVH reduction scheme as expressing the total DVH as a function of the BT dose per fraction is complicated. An alternative approach is to manipulate a DVH curve at specific portions or its parameters based on uncertainty distributions, see for example Moiseenko et al. [440], and compute the impact of the distribution parameters on the NTCP after DVH reduction. However, it would still be difficult to relate these distribution parameters to uncertainty in BT fractions. In this thesis, hence it is opted for using the logistic NTCP and TCP model for illustration purposes as used in previous works, acknowledging that its accuracy is limited and that its outcomes must be carefully evaluated.

[7] Some studies in other types of cancer treatment have shown that the mean dose is able to predict the incidence of complications [443], which supports this practice.

A.4 Literature review on inter and intra-fraction geometric uncertainty

A.4.1 Inter-fraction uncertainty

Five studies describing inter-fraction volumetric changes and five studies describing positional changes of one or more OARs were identified. Table A.1 summarises the findings of these studies.

Table A.1: Overview of inter-fraction geometric uncertainty in cervical cancer BT literature

Volumetric change													
Ref.	***N***	**Modality**	**Imag.**	**Applic.**	**Time frame**	**Method**	**Protocol**	**Corr.**	**Structure**	**Statistic**	**Begin**	**End**	**Change**
[198]	44	HDR (fx = 2)	CT	TO	Weekly (2 app.)	Manual contour differences	Foley catheter	-	Bladder	Mean (±SD)	84.1 cm^3	78.2 cm^3	+30.6 (±38.1) cm^3
									Rectum	Mean (±SD)	43.2 cm^3	44.5 cm^3	+9.2 (±7.8) cm^3
[145]	27	HDR (fx = 2)	MR	TR	Weekly (2 app.)	Manual contour differences	Foley catheter	-	Bladder	Ind. Pat.	-	-	N.D.
							Bowel preparation		Rectum	Ind. Pat.	-	-	N.D.
									Sigmoid	Ind. Pat.	-	-	N.D.
[210]	43	PDR (3 days)	MR	IU	Daily (3 app.)	Manual contour differences	Bladder catheter	-	Bladder	Mean	-	-	N.D.
							Dietary requirements		Rectum	Mean	53.0 cm^3	65.0 cm^3 57.1 cm^3	N.D.**
[68]	85	HDR (fx = 2)	CT	TR/TO	Weekly (2 app.)	Manual contour differences	Foley catheter	-	Bladder	Median	-	-	+11 cm^3 (N:35%) −7 cm^3 (N:61%)
									Rectum	Median	-	-	+8.5 cm^3 (N:49%) −7 cm^3 (N:46%)
									Sigmoid	Median	-	-	+4 cm^3 (N:31%) −2cm^3 (N:64%)
[126]	11	HDR (fx = 3)	CT	TR (11) VC (2)	1-12 d. (3 app.)	Manual contour differences	Void prior to BT	BV - Dur.**	Bladder	CV_{mean}	-	-	44.1 %
									Rectum	CV_{mean}	-	-	23.3 %

Table A.1: *(continued)*

Positional change														
Ref.	***N***	**Modality**	**Imag.**	**Applic.**	**Time frame**	**Method**	**Protocol**	**Corr.**	**Structure**	**Statistic**	**A-P**	**S-I**	**R-L**	**Total**
[222]	7	HDR (fx = 4)	CT/MR	TR	? (2 app.)	RIR	Spasmolytic agent	-	Bladder $2cm^3$	Mean (±SD)	-	0.1 (±1.1) cm	-	1.1 (±0.6) cm
									Rectum $2cm^3$	Mean (±SD)	-	0.2 (±1.7) cm	-	1.6 (±1.3) cm
									Sigmoid $2cm^3$	Mean (±SD)	-	1.1 (±1.2) cm	-	2.0 (±1.6) cm
[223]	10	HDR (fx = 5)	CT/MR	TR	? (5 app.)	RIR DIR	Foley catheter	-	Bladder RIR / DIR	Mean MDA (±SD)	-	-	-	4.2 (±3.9) mm / 3.0 (±3.1) mm
									Rectum RIR / DIR	Mean MDA (±SD)	-	-	-	3.7 (±3.5) mm / 2.5 (±2.8) mm
									Sigmoid RIR / DIR	Mean MDA (±SD)	-	-	-	7.2 (±7.4) mm / 5.4 (±6.8) mm
[444]	10	HDR (fx = 5)	CT	TR (4) TO (6)	? (5 app.)	Axial CT diff.	Bladder filling	-	Bladder PW	Range PWD	-	-	-	[-0.85, 0.4] cm
[141]	15	HDR (fx = 2)	X-ray	TO	? (2 app.)	Lateral film diff.	None	-	Rectum AW	Median ARW	-	-	-	-10.5 mm
[445]	34	HDR (fx = 5)	CT	TR (17) TO (5) TC (2)	? (5 app.)	Axial CT diff.	Foley catheter	-	Sigmoid PP	CV_{mean}	-	-	-	40%

Denotations/abbreviations: ** = significance found. N.D.: No summarised data presented.

- *Study aspects:* N = number of patients; Imag. = imaging modality; Corr. = correlations; A-P = anterior-posterior; SI = superior-inferior; R-L = lateral.
- *Modality:* fx = fractions.
- *Applicator:* TR = tandem/ring; TO = tandem/ovoid; TC = tandem/cylinder; IU = intrauterine line; VC = vaginal cylinder.
- *Time frame:* app. = applications.
- *Method:* RIR = rigid registration; DIR = deformable image registration.
- *Correlations:* BV - Dur. = bladder volume - treatment duration.
- *Structure:* PW = posterior wall; AW = anterior wall; PP = proximal point.
- *Statistic:* Ind. Pat. = individual patients; CV = coefficient of variation; MDA = mean distance to agreement; PWD = posterior wall distance to applicator; ARW = anterior rectal wall distance to applicator.

A.4.2 Intra-fraction uncertainty

Three studies describing intra-fraction volumetric changes and four studies describing positional changes of one or more OARs were identified. Table A.2 summarises the findings of these studies.

Table A.2: Overview of intra-fraction geometric uncertainty in cervical cancer BT literature

Volumetric change

Ref.	*N*	Modality	Imag.	Applic.	Time frame	Method	Protocol	Corr.	Structure	Statistic	Begin	End	Change
[202]	50	HDR (fx = 4)	CT/MR	?	2 h.	Manual contour differences	Bladder filling	-	Bladder	Mean (±SD)	-	-	15.7 (±13.8) cm^3
									Rectum	Mean (±SD)	-	-	7.8 (±6.7) cm^3
									Sigmoid	Mean (±SD)	-	-	14.9 (±13.3) cm^3
[214]	21	HDR (fx = 2)	MR	TR	4.8 h.	Manual contour differences	Bladder catheter	Time - Mov.	Bladder	Mean (±SD)	60 (±33) cm^3	52 (±10) cm^3	|22.5| (±24.7) cm^3
								Time - Mov.	Rectum	Mean (±SD)	48 (±39) cm^3	56 (±42) cm^3	|20.0| (±20.8) cm^3
								Time - Mov.	Sigmoid	Mean (±SD)	130 (±113) cm^3	156 (±131) cm^3	|57.9| (±56.9) cm^3
[204]	15	HDR (fx = 3-5)	CT	TO	43 m.	Manual contour differences	Bladder filling	-	Bladder	Mean (±SD)	135.1 (±87.2) cm^3	214.8 (±161.1) cm^3	65.1 (±84.3) cm^3 **
									Rectum	Mean (±SD)	125 (±72.3) cm^3	113.7 (±61.8) cm^3	-5.9 (±19.0) cm^3 **

Positional change

Ref.	*N*	Modality	Imag.	Applic.	Time frame	Method	Protocol	Corr.	Structure	Statistic	A-P	S-I	R-L	Total
[201]	19	PDR (3 days)	MR/CT	VM	?	Manual contour differences	Bladder cath.	-	Bladder $\cap$ V_{10Gy}	Mean (±SD)	-	-	-	-1.1 (±4.0) cm^3
							Enema		Rectum $\cap$ V_{10Gy}	Mean (±SD)	-	-	-	2.1 (±3.3) cm^3
									Bowel $\cap$ V_{10Gy}	Mean (±SD)	-	-	-	-0.3 (±0.9) cm^3

Table A.2: *(continued)*

[204]	15	HDR (fx = 3-5)	CT	TO	43 m.	DIR	Bladder filling	Time - DVF	Bladder	Mean (±SD)	-2.3 (±2.9) mm	2.8 (±5.1) mm	-0.4 (±1.3) mm	-
									Rectum	Mean (±SD)	-1.5 (±2.4) mm	0.4 (±3.1) mm	0.1 (±1.1) mm	-
[190]	14	PDR (?)	-	TR	?	Rectal diode	Enema	-	Rectal wall	SD (±σ)	0.9 (±0.6) mm	1.2 (±0.7) mm	1.2 (±0.8) mm	-
[446]	10	HDR (fx = 1-3)	X-ray	TO	?	Lateral film differences	None	-	Bladder	Mean	-	-	-	2.5 mm

Denotations/abbreviations: ** = significance found. N.D.: No summarised data presented.

- *Study aspects:* N = number of patients; Imag. = imaging modality; Corr. = correlations; A-P = anterior-posterior; SI = superior-inferior; R-L = lateral.
- *Modality:* fx = fractions.
- *Applicator:* TR = tandem/ring; TO = tandem/ovoid; VM = vaginal mould.
- *Method:* DIR = deformable image registration.
- *Correlations:* Time - Mov. = treatment time - OAR movement; Time - DVF. = treatment time - mean deformation vector field distance.

A.4.3 Bladder distension

In order to illustrate the effects that bladder distension has on the movement of OARs, the results of five studies have been summarised in Table A.3. As can be seen, lateral displacements of all OARs are generally limited, whereas the bladder may push the sigmoid away in the superior and posterior directions. The rectum is likely less affected, but may move superiorly according to the presented findings.

Table A.3: Overview of BT literature investigating the influence of bladder distension

Positional change													
Ref.	***N***	**Modality**	**Imag.**	**Applic.**	**Method**	**Protocol**	**Corr.**	**Structure**	**Statistic**	**A-P**	**S-I**	**R-L**	**Total**
[200]	21	HDR (fx = 2-3)	CT	TR	Manual contour differences	Fill bladder with saline: 50 - 100 cm^3	-	Bladder 2cm^3	COV mean (±SD) 50 cm^3 / 100 cm^3	0.6 (±5.4) mm/ 1.3 (±6.3) mm	0.2 (±2.4) mm/ 1.1 (±4.7) mm	2.5 (±4.7) mm/ 1.0 (±2.6) mm	-
[447]	40	HDR (fx = 4)	CT	TO	Manual contour differences	Fill bladder with saline: 100 cm^3	-	Bladder PW	Mean dist. 0 cm^3 / 100 cm^3	0.19 cm / 0.26 cm*	-0.62 cm / -0.63 cm	0.04 cm / 0.08 cm	-
[448]	20	HDR (fx = 3)	CT	VC	Sagittal CT differences	Drink water: 950 cm^3	-	Bowel PP	Median dist. empty / full	-	-	-	5.8 / 11.6* mm

Table A.3: *(continued)*

[449]	12	HDR (fx = 2-5)	CT	VC	Sagittal CT differences	Fill bladder with water: 180 cm^3	-	Bowel PP	Mean dist. empty / full	-	-	-	0.72 / 0.92 cm

Denotations/abbreviations: ** = significance found. N.D.: No summarised data presented.

- *Study aspects:* N = number of patients; Imag. = imaging modality; Corr. = correlations; A-P = anterior-posterior; SI = superior-inferior; R-L = lateral.
- *Modality:* fx = fractions.
- *Applicator:* TR = tandem/ring; TO = tandem/ovoid; VC = vaginal cylinder.
- *Structure:* PW = posterior wall; PP = proximal point.
- *Statistic:* COV = centre of volume.

A.5 Description of robust motion planning algorithm classes

In this Appendix, brief descriptions of robust motion planner classes are given, that were distinguished in a previous literature review [240].

Path planning classes

Approximate cell decomposition

In approximate cell decomposition the free configuration space is represented with a set of non-overlapping cells with pre-specified shapes [293]. Rather than in exact cell decomposition, $\mathcal{C}_{free}$ is (conservatively) approximated. The decomposition of the workspace may be regular, such as a fixed-size grid, or adaptive, such as quadtree decomposition. Uncertainty of the environment is usually incorporated by indicating the probability of occupation within a cell, known as occupancy mapping [450]. In the second step, a non-directed connectivity graph is created which captures the adjacency between cells. This can then be searched by a graph search algorithm to find the least-cost path.

Potential-based methods

In potential-based methods, a potential field U consisting of attractive potential towards the goal region and repulsive potential to steer the system from obstacle regions is imposed over the free space $\mathcal{C}_{free}$ [451]. A force field, which is the gradient of the potential function $\mathbf{F}(\mathbf{q}) = -\nabla U(\mathbf{q})$, drives the system from start to goal such that an optimal path is found. However, this gradient descent may converge to local minima of the potential function. For that reason: (i) a potential field may be defined that is free of local minima and contains only one minimum located at the goal location, known as a navigation function [239], or (ii) a potential field method may be combined with a different MP approach in a so-called hybrid approach. Uncertainty may be incorporated in potential-based methods by directly assigning the strength of repulsive potential to the probability of collision, or by bounding the collision probability and assuring that the gradient steers the system from these bounds [244].

Topology-based methods

Concepts from topology have been used extensively in motion planning, such as retraction and cell decomposition. In these topology-based methods, topological information of the free space is extracted and embedded in a topological map. In an uncertain environment, represented by an occupancy map, topological information may be used to find the homotopy class which is most robust to uncertainty. This concept is known as persistent homology, and can be used to establish classes and paths belonging to these classes that are 'most safe' [452]. After reducing the workspace to a discrete representation, least cost paths may then be sought with a graph search algorithm.

Probabilistic roadmap

A probabilistic roadmap, commonly abbreviated as PRM, is a multi-query approach where a roadmap is constructed from nodes that are sampled in the configuration space [352]. In the learning phase, a sampled configuration $\mathbf{q}_{samp}$, which may be uniformly or non-uniformly sampled, is added to the roadmap's list of vertices if it is feasible. Nodes in the existing list of vertices are sought which may be connected to this sample, usually the nearest neighbour $\mathbf{q}_{near}$ is sought based on a Euclidean distance function. In the last step of the learning phase, if feasible, a connection is established between $\mathbf{q}_{samp}$ and $\mathbf{q}_{near}$ and added to the list of edges. In the query phase, a least-cost path is sought by adding the start and goal configurations to the roadmap and

using a graph search algorithm. Environmental uncertainty may for example be incorporated by adjusting the sampling distribution or by assigning the collision probabilities as weights in the graph.

Rapidly-exploring random trees

A rapidly-exploring random tree (RRT), belonging to the more general method rapidly-exploring dense trees (RDTs), is a single-query method in which the configuration space is explored implicitly with a tree-like structure [239]. A sample is drawn from the configuration space, $\mathbf{q}_{samp}$, and when feasible a nearest neighbour $\mathbf{q}_{near}$ is sought in the already established tree. A new node $\mathbf{q}_{new}$ is added along the edge connecting these two samples at a distance from the nearest node or at a feasible location on this edge, which is again followed by feasibility checks of both the resulting edge and node. The goal configuration may be included as a sampled node periodically to check whether a feasible connection between start and goal configuration is possible. An interesting approach for RRTs to account for environmental uncertainty is that of computing shadows, which are geometric equivalents of confidence intervals over uncertain obstacle faces [453].

Trajectory planning classes

Stochastic continuous-time optimisation

In trajectory optimisation approaches a naive, possibly infeasible, solution is locally optimised in accordance with a cost function $C(\tilde{x}(t))$ such that it obeys constraints. Typically, the problem or trajectory $\tilde{x}(t)$ is discretised in time. However, a finely discretised trajectory is required in order to assure feasibility, and it may not be possible to handle problems with many (non-differentiable) constraints [249, 390]. Continuous-time optimisation approaches can be computationally efficient and assure smooth trajectories. For this purpose, the trajectory is commonly represented using continuous-time interpolation methods, such as splines, or non-parametric representations, such as Gaussian processes. In order to incorporate uncertainty of the environment, planning typically is performed on occupancy maps, for which Hilbert maps are a viable continuous alternative [391, 454].

Stochastic optimal control

The problem of optimising the motion of a kinodynamic system through selecting a set of input controls, also known as an optimal control problem, is conventionally numerically solved using mathematical programming. This may involve the trajectory optimisation approaches such as discussed under the previous heading, whereas recent work focuses as well on numerical optimal control techniques over a finite horizon to make computations more tractable. In Model Predictive Control (MPC) or Receding Horizon Control (RHC), an open-loop control policy is designed over a finite time receding horizon and executed until the goal region is reached [241]. After execution of a policy, a filter is used to estimate the state and used to update the control problem in closed-loop fashion. Linear-Quadratic- Gaussian (LQG) control is another type of optimal control approach, but where a state estimator is combined with a Linear-Quadratic Regulator (LQR) and optisation is performed over a fixed size time window [455]. Uncertainty in these approaches is generally incorporated in the form of chance constraints, i.e. restricting the feasibility constraints to hold up to a certain probability limit.

Backward stochastic reachability

The optimal control problem may also be solved by introducing an expected cost-to-go or value function, known as Bellman's optimality equation, which can be iterated back in time to establish reachable sets from an initial state. The optimal control policy that maximises the cost is then

found using dynamic programming (DP). In order to include uncertainty of the environment in this problem, a so-called Discrete-Time Stochastic Hybrid System (DTSHS) is considered, and a Markov policy may be sought that maximises the probability of reaching a target set and avoiding the obstacle set, which is represented as a random closed set [456]. Since dynamic programming is computationally intensive, numerical methods are usually used to solve this problem.

Reachability tree

In reachability tree methods, the system is constrained to act according to motion primitives that are obtained by applying a control action from a discretised set of actions, which combine to form a lattice-like structure from an initial state. A graph search algorithm may then be used to find an optimal trajectory. This concept has also been extended in order to deal with uncertain environments. One example approach in this category plans in belief space, where a belief describes knowledge of the state distribution with a mean and covariance [457], which is a popular approach in motion planning under configuration knowledge uncertainty. The current belief state is expanded by performing all possible control actions and calculating the success probability, i.e. the probability of non-collision, of the resulting list of belief states. The lowest-cost trajectory to the goal is then established from the tree using a heuristic search algorithm.

Incremental sampling with analytic chance constraints

In incremental sampling-based algorithms, such as RRTs, a state is sampled from the environment $\mathbf{x}_{samp}$ and the nearest node in the existing tree $\mathbf{x}_{near}$ is identified for expansion using a distance or reachability-based metric. From this nearest node, the tree is expanded towards the sampled node by selecting the control input that brings the system in proximity of this sampled node. The resulting state $\mathbf{x}_{new}$, found by simulating the kinodynamics of the system, is added to the tree if this is in proximity to the sampled state and if it is feasible. In order to include environmental uncertainty, incremental sampling approaches have mainly focused on one of two techniques: chance constraints and particle expansion. The former is an analytical, slightly conservative approach usually involving the use of Boole's inequality to bound the probability of collision instead of having to evaluate a multivariate probability integral. However, such an approach is often bound to severe restrictions such as Gaussian uncertainty, convex constraints and linear dynamics.

Incremental sampling with particle expansion

A technique which may be used to approximate the probability integral without any conservatism is that of particle expansion, which uses particles to represent possible realisations of trajectories under uncertainty [458]. Clustering is used to combine these realisations back to nodes in the incremental sampling approach.

Virtual potential field

A navigation policy may be directly generated from a combined probability $P(\mathbf{x})$ and potential field $V(\mathbf{x})$, in an approach called gamma harmonic potential field planning [459]. This probability field $P(\mathbf{x})$ is a type of globally defined cost map, which may be based on collision probability, traversability, etc. The boundary conditions chosen determine how obstacles are avoided and are critical to generate a navigation potential, such that local minima are averted.

Warm-started trajectory optimisation

Warm-starting a trajectory optimisation approach aims at using a generated feasible solution from an inexpensive motion planning approach, such as: (i) to avoid getting 'trapped' in local minima,

(ii) to minimise the total computation time by offloading time to an exploration phase, and (iii) to allow for alleviating constraints from the optimisation problem [460]. Especially when multiple homotopy classes are present, warm-starting through an explorative planner may allow for increasing the likelihood that a globally optimum trajectory is found. An example for robust optimisation is shown in the work by González-Arribas and colleagues where randomised Legendre polynomials are used in an initialisation step to allow a globally optimal trajectory to be found during trajectory optimisation [461].

Plan and transform

Trajectories may simply be generated from paths by transforming kinematically infeasible sections in a decoupled approach such that these satisfy differential constraints of the system [239]. Common interpolation methods -such as clothoids, Dubins' curves, β-splines- may be used for this purpose, but also other local planning methods may compute a trajectory segment. The correctness of the solution depends on the initial solution provided by the path planner, and when no solution can be found with the plan and transform approach replanning by the path planner may be required.

A.6 Methodological problems and inaccuracies in QFD

In this Appendix, a small discussion of methodological problems an inaccuracies in QFD is given, mainly based on the article by van de Poel [322].

(B) Prioritisation of user requirements

Many methods have been developed for the purpose of defining relative importance ratings (RIRs), relying on different input data scales, assumptions on the crispness of users' answers and hierarchies of users. Some methods require promotion from a nominal or ordinal scale towards a ratio one, which may be methodologically inappropriate [318]. Another problem is a high complexity of many prioritisation techniques for the respondent, such as a pairwise comparison technique, which may lead to inconsistencies in answers. Moreover, many approaches such as preference ordering techniques require the translation of individual preference rankings into a collective ordering, which may violate conditions of Arrow's impossibility theorem [322].

In a point direct scoring method, if the resulting distribution of the relative importance rating is unimodal and assuming that the responses on this ordinal scale can be treated as interval data, the mean value can simply be extracted to establish the individual RIRs. In other cases the results may be re-investigated since these may indicate that different market segments were confronted [305]. Although one may correctly argue that a point direct scoring method lacks a common reference or starting level [318], promotes an ordinal scale to a cardinal one such that it violates Arrowian principles [318, 462], and that a preference ordering may be more natural to the respondent [463], this method is selected for its simplicity. The relative importance weights can be established via:

$$g_i = \sum_{k=1}^{K} g_{ik}/K \tag{A.22}$$

The user requirements must be independent from each other [322], but if this is not the case, one may try and incorporate correlations among these importance weights [464]:

$$g_i^{\text{norm}} = \frac{\left(\sum_{m=1}^{I} \beta_{im}\right) g_i}{\sum_{i=1}^{I} \left(\sum_{m=1}^{I} \beta_{im}\right) g_i} \tag{A.23}$$

Here, β_{im} denotes the correlation between the ith and mth user requirements.

(C) Competitive analysis and final importance ratings

Both the wording of the questions and the answer possibilities in Kano's model have been criticised frequently [465]. First, provision-based questions were suggested instead of performance-based questions to increase the reliability of answers [341], but concrete evidence is lacking to conclude whether provision-based questionnaires indeed have an increased reliability over performance-based methods. The five-level answer scale is moreover often falsely interpreted as a five-point ordinal scale by both respondents as well as researchers, and contains ambiguities and language association problems for which many modifications have been proposed [465]. Furthermore, several adaptations to the original evaluation table have been suggested [465]. Moreover, the questionnaire becomes lengthy and cumbersome in the case when many attributes are reviewed [347]. For this reason, the validity of alternative approaches such as three-point questionnaires, direct classification and dual-importance grid has been investigated [348]. Classification through direct questions seems to be a viable alternative to avoid having to use the

functional and dysfunctional question format [341, 348], although this requires a correct understanding of Kano's model by the respondents. Evidence on the reliability of this direct approach as a substitute for a five-level scale shows mixed results [348, 466, 467].

Many variants have been proposed to integrate Kano's model in QFD. Tan and Shen proposed to modify the improvement ratio $IR_{0,i}$ that is derived from the competitive analysis per user requirement i and represents the ratio between target and current satisfaction: $IR_{0,i} = s_{tar,i}/s_{0,i}$ [468]. As they argue that satisfaction s and performance p on a requirement may be related via a parameter k that represents Kano's category and constant c via: $s_i = cp_i^k$, the improvement ratio may then be adjusted to reflect Kano's category according to: $IR_{adj,i} = (IR_{0,i})^k$. Here, IR_{adj} and IR_0 are the adjusted and original improvement ratios respectively, and k is equal to '2', '1' or '1/2' for attractive, one-dimensional or basic requirements. However, a common critique is that these parameters are arbitrary and subjective [318, 469]. Moreover, the use of the mode statistic for classifying an attribute into a fixed Kano category with associated weight based on respondents' answers may not be appropriate [327]. For that reason, satisfaction and dissatisfaction indices were coined which would better preserve information on the distribution of answers and would indicate how the fulfillment or provision of a requirement would influence user satisfaction or dissatisfaction [327]:

$$SI_i = \frac{A_i + O_i}{A_i + O_i + B_i + I_i} \;\; ; \;\; DI_i = -\frac{B_i + O_i}{A_i + O_i + B_i + I_i} \tag{A.24}$$

Here, SI_i and DI_i denote the satisfaction and dissatisfaction indices, and the other parameters are the counts of the Kano attributes. Usually these indices are plotted on a two-dimensional $(|DI|, |SI|)$-plot where the quadrants indicate the Kano category [327]. Tontini directly integrated these indices in QFD to compute the relative importance of user requirements: $d_i = \max(|SI_i|, |DI_i|)$ [323]. However, this implies that two requirements from different Kano categories, but with the same maximum coefficient value, receive the same importance which seems odd. Therefore, Chaudha and colleagues coupled these indices to the improvement ratio by Tan and Shen via [324]:

$$IR_{adj,i} = (1 + \max(|SI_i|, |DI_i|))^k \cdot IR_{0,i} \tag{A.25}$$

The parameter k is chosen here as '0', '0.5', '1', and '1.5' for indifferent, basic, one-dimensional and attractive attributes respectively. These weights are arbitrary and may lead to a wrong focus [469]. For example the '0' score implies that one does not have to pay attention on improving the performance of indifferent requirements, which may become attractive attributes over time according to Kano's original theory. Moreover, the computation of an improvement ratio based on competitive analysis may not make sense in the case of novel products and are often subjective. An interesting approach to calculate the transformation function between satisfaction and fulfillment of the user requirement based on satisfaction and dissatisfaction indices has been developed by Wang and Ji [332, 349], which deviates from other approaches by not calculating the improvement ratio from a competitive analysis and instead using competitors' product performance as a constraint in a mathematical program. In this model it is assumed that the overall satisfaction of the user can be modelled via the following linear additive value function [332, 349]:

$$S' = \sum_{i=1}^{I} g_i s_i(y_i) \tag{A.26}$$

Observing Figure 5.3a, one may establish relations between satisfaction and the fulfillment of user requirements based on parameters a and b: $s_i(y_i) = a\phi(y_i) + b$. These parameters are derived by

assuming that the fulfillment level is a continuous variable ranging from 0 to 1, $y_i \in [0, 1]$, and that $\phi(y_i)$ is a linear or exponential function depending on the Kano category. The following satisfaction - user requirement relations are proposed by Wang and Ji [349]:

$$\begin{cases} s_i(y_i) = & \frac{SI_i - DI_i}{\mathrm{e}-1}\mathrm{e}^{y_i} - \frac{SI_i - \mathrm{e}DI_i}{\mathrm{e}-1} & \text{(attractive attribute)} \\ s_i(y_i) = & (SI_i - DI_i)y_i + DI_i & \text{(one-dimensional attribute)} \\ s_i(y_i) = & -\frac{\mathrm{e}(SI_i - DI_i)}{\mathrm{e}-1}\mathrm{e}^{-y_i} + \frac{\mathrm{e}SI_i - DI_i}{\mathrm{e}-1} & \text{(basic attribute)} \end{cases} \tag{A.27}$$

No such relation is proposed for indifferent requirements, which are therefore ignored in this analysis. Note that in the model in Eq. A.27, Kano's category is determined based on the statistic mode of the responses, which has been criticised previously [327]. Additionally, these satisfaction functions are monotonically increasing with increasing attainment, which may not be the actual case. Furthermore, one may question whether fulfillment of a user requirement is always a continuous variable and hence satisfaction can be modelled as a continuous function; i.e. many user requirements may be described better in a provision-based formulation rather than a performance-based formulation. Even so, this model is able to deal with discrete values of y_i without loss of accuracy. Lastly, although the idea of neglecting the competitive analysis is attractive, especially for novel products, simultaneously it loses the ability of setting 'company considerations' to discriminate between user requirements, such as sales points or target values [322]. Due to its simplicity and direct, i.e. explicit, association with users' satisfaction via Eq. A.26, and Kano's model, this model is particularly useful.

(F) Relationship matrix

Several considerations for the relationship matrix have been discussed in the sections below and are based on the paper by van de Poel [322].

Negative and non-constant relationship coefficients

Although traditionally for a certain technical parameter a direction is specified which is said to mark improvement satisfaction of a user requirement for increasing attainment, this has been criticised as it may conflict with improvement of other user requirements [322]. Indeed, whereas the weight of a car negatively affects fuel economy it may positively correlate to safety of the passengers [322]. Moreover, as an undesirable consequence of normalisation some of the relations may become negative [464]. One may simply solve these problems by only taking the absolute of the correlation values, but this rules out finding an optimal solution from the QFD and loses meaning of the outcome [322]. In some instances, through proper selection of negative/positive formulations or omitting technical attributes one may be able to find non-conflicting satisfaction functions, but this is not possible in all cases nor desirable. Another option is to allow for negative correlations, but this may divert the company from investing in possibly important HOWs that are levelled out and therefore entails additional analyses [470]. This is in many cases still the preferred approach. Additionally, r_{ij} is implicitly assumed to be constant for all levels of e_j whereas van de Poel indicates that this does not necessarily have to be the case and is not convenient [322]. An interesting solution may be to make r_{ij} dependent on the level of e_j, which has been previously incorporated in QFD [470]. The obvious problem is that establishing these additional magnitude-dependent relations may be a rather tedious process and in the general case impossible.

Normalisation of relationships and correlations

The importance of normalisation of the coefficients r_{ij} in QFD has been distinguished to avoid

artificial distortion of the outcome prioritisation of technical attributes [471]. The commonly used Wasserman's normalisation builds upon Lyman's normalisation and takes into account inter-correlation between the engineering characteristics via [471]:

$$r_{ij}^{\text{norm}} = \frac{\sum_{l=1}^{J} r_{il} \cdot \gamma_{lj}}{\sum_{j=1}^{J} \sum_{l=1}^{J} r_{il} \cdot \gamma_{jl}} \tag{A.28}$$

Here, γ_{lj} denotes the inter-correlation between the lth and jth engineering characteristic, and $\gamma_{lj} = \gamma_{jl}$. The model assumes that user requirements are independent. Interestingly, this computation may introduce artefacts such as introducing a relation between a WHAT and HOW when previously the relation intensity was null [464]. To ensure that WHATs and HOWs with a void relation remain orthogonal, i.e. uncorrelated, Chen and Chen therefore propose the following normalisation [464]:

$$r_{ij}^{\text{norm'}} = \frac{\left(\sum_{l=1}^{J} \gamma_{lj}\right) r_{ij}}{\sum_{j=1}^{J} \left(\sum_{l=1}^{J} \gamma_{lj}\right) r_{ij}} \tag{A.29}$$

In this formulation, one may observe that inter-correlation coefficients may strengthen or lessen the correlation coefficient r_{ij} and not involving other relations. However, this assumes that all inter-correlation coefficients are of equal importance and are not affected by the intensity of the corresponding relation between user requirement and technical parameter. Whereas this is possibly inaccurate, Eq. A.29 avoids the methodological problems of the Wasserman correlation and is therefore the preferred option.

Scaling of relationship coefficients and rank reversal

The main issues with the HOQ have to do with translating the importance weights of user requirements into prioritising technical attributes via a method that is known as the independent scoring method (ISM) [322]:

$$w_j = \sum_{i=1}^{I} d_i r_{ij} \tag{A.30}$$

Here, w_j is the weight given to the prioritisation of the jth technical parameter, which is a linear additive function of the importance of user requirements d_i and the (normalised) correlation coefficients r_{ij} or r_{ij}^{norm} from Eq. A.28. The overall satisfaction may then be found via (combining Eq. 5.4, 5.6, and 5.7) [322]:

$$S = \sum_{i=1}^{I} d_i y_i = \sum_{i=1}^{I} \sum_{j=1}^{J} d_i r_{ij}^{\text{norm}} e_j = \sum_{j=1}^{J} w_j e_j \tag{A.31}$$

The technical attributes with the highest weights w_j would therefore increase satisfaction the most at constant effort, and should therefore possibly receive most of the focus in the product development. The first step in this method is converting the ordinal scale of the correlation coefficients to a set of weights which is argued to be a ratio scale [322, 472]. The latter implies, roughly put, that one may state that a relation with weight '9' is three times as correlated one with weight '3'. However, Olewnik and Lewis have for example shown that the choice of the ratio scale, even when random or unreasonable scores are used, does not influence the prioritisation of technical attributes [314, 473]. One may interpret these findings in the sense that the outcomes of QFD are robust to the scale used, and perhaps argue that the arbitrariness of these weights from translating ordinal information to a ratio one is not critical for the methodological soundness [472]. In this light, it is commonly recommended that the validity of the outcome is checked by selecting different weights

and performing a sanity check [304]. However, more fundamentally, it may indicate that the ratio scale lacks the ability to model relationships between customer and technical attributes despite falsely giving such an impression [314]. It may seem that if one acknowledges that the resulting quantitative outcomes, i.e. weights of the customer requirements, are not the absolute truth and are susceptible to changes, one may be able to still draw some qualitative conclusions such as the ordering of the technical attributes. However, as will be illustrated, this is not possible with the general assumptions made in QFD. Another option is to abandon numerical relations altogether and instead define these on an ordinal scale level [335]. In the ordinal approach by Francheschini et al. technical attributes are prioritised according to the function [335]:

$$w''_j = \min_{i \in \mathbb{Z}_{1,I}} \left(\max \left\{ \text{neg}(g_i), r''_{ij} \right\} \right) \tag{A.32}$$

Here, g_i and r''_{ij} are defined on an ordinal level scale and $\text{neg}(\cdot)$ is the negation operator [335]. Although this enables calculation of an importance ordering of the technical attributes, the resulting weak ordering may be dissatisfying from the designer's point of view as it does not indicate target values. Moreover, the weights w''_j in Eq. A.32 -expressed on an ordinal scale- may be the same for different ECs due to flattening effects [335]. In this case, one can refine the ordering by using the following indicator function [335]:

$$T_j = \dim \left(W_i \mid r''_{ij} > w''_j \right) \tag{A.33}$$

In this indicator function the technical attributes with a stronger relation to user requirements receive a higher scoring of T_j, which are argued to be of greater importance. Note that this implies that the discriminatory power of the ranking using this method is thereby limited by the level of the ordinal scale, which in turn limits the amount of technical attributes that can be included in analysis. The resulting ranking of HOWs cannot be directly used with target setting approaches, for which another method is required (hybrid approach). Additionally, one may desire to capture the inter-relations between the technical attributes, but this generally requires the promotion of the ordinal scale to a cardinal one.

The main problem with the relationship matrix and its normalisation is the violation of the condition 'independence of irrelevant alternatives' in Arrow's impossibility theorem [322]. If one was to add or remove a technical parameter, this may affect the ordering of two different technical attributes, known as rank reversal. Partially this is caused by the promotion of ordinal information to numerical information, and hence one suggestion has been to maintain an ordinal scale level for the correlations [335], or possibly consider ratio information for measurements [462]. Van de Poel and colleagues however argue that both can not escape from Arrow's Impossibility Theorem [322, 462]. The effects of this theorem may be reduced by alleviating Eq. 5.6 [322], for example by converting the multi-criteria problem to a single criterion problem or by establishing a satisfaction relation for each individual user. However, to the best of the author's knowledge, no QFD approach has been developed that (partially) alleviate the consequences of Arrow's theorem in this manner. Rank reversal in QFD has also been observed without inclusion or exclusion of a technical parameter due to normalisation [472]. As Raharjo argues, rank reversal due to normalisation may not always be undesirable; contrarily, it may even be desirable by correcting for the artificial distortion when no normalisation has been applied [472]. A set of guidelines was proposed to whenever possible correct for rank reversal due to normalisation.

Establishing relationships for novel products or by inexperienced practitioners

A challenge in formulating the HOQ is the way of establishing relationships between user

requirements and technical attributes in the case of incomplete or inaccurate information such as in the early development process. Moreover, when the practitioner may be unfamiliar with either the WHATs or HOWs, e.g. a marketeer is aware of the WHATs but not of the HOWs and for an engineer vice versa, accurate assessment of the relationship matrix is difficult. Most of the research in this field has focused on applying fuzzy logic to QFD models, capturing these uncertain relationships in linguistic terms. One problem with this type of method is that this still relies on arbitrary conversion of nominal or ordinal data to numeric membership functions and violates Arrowian principles similar to general QFD approaches [322, 335]. For designers inexperienced with fuzzy theory, including membership functions may further increase the arbitrariness and subjectivity in the process. This similarly holds for related approaches such as rough set based methods. Nevertheless, fuzzy logic does provide a means for the inexperienced practitioner to assess the relationships between WHATs and HOWs in an understandable way. A brief account of fuzzy set theory is given here, but the reader is invited to explore other literature on this topic; e.g. see the work by Chen et al. or Chen and Weng for a general implementation of fuzzy set theory in QFD [474, 475], and the work by Dursun and Karsak or Liu for a fuzzy QFD-based selection method [307, 309].

A fuzzy set $\tilde{F} = (U, m)$ is a pairing of a set (known as universe of discourse) U, and membership function $m : U \to [0, 1]$. The grade of membership $m(x)$, where $x \in U$, indicates therefore the degree of belonging to the set. The membership function of fuzzy set $\tilde{F}$ is denoted as $\mu_{\tilde{F}}$, where $m = \mu_{\tilde{F}}$. A fuzzy number is a special type of (convex, normalised) fuzzy set where the universe of discourse is the real number line, i.e. $x \in U \subseteq \mathbb{R}$, and where the membership function is a (segmentally) continuous mapping to closed interval $[0, 1]$: $\tilde{F} = \{[x, \mu_{\tilde{F}}(x)], x \in \mathbb{R}\}$. A triangular fuzzy number can be described by the triplet of parameters (l, m, u), where $l \leq m \leq u$, which are the supports of the set $\tilde{M}$ and denote lower bound, mode, and upper bound respectively. The membership function of a triangular fuzzy number is the following piecewise function:

$$\mu_{\tilde{M}}(x) = \begin{cases} \frac{1}{m-l}x - \frac{l}{m-l} & x \in [l, m] \\ \frac{1}{m-u}x - \frac{u}{m-u} & x \in [m, u] \\ 0 & \text{otherwise} \end{cases} \tag{A.34}$$

Triangular fuzzy numbers are widely used as these are both simple to handle and interpret. A special type of triangular fuzzy number is that of a symmetric triangular fuzzy number, denoted by $\tilde{T}(l, u)$, which has the following membership function [316]:

$$\mu_{\tilde{T}}(x) = \begin{cases} 1 - \frac{|x-(u+l)/2|}{(u-l)/2} & x \in [l, u] \\ 0 & \text{otherwise} \end{cases} \tag{A.35}$$

Both types of fuzzy numbers have been often used in fuzzy QFD, but any form of membership function may be used. One important concept in fuzzy set theory is that of an α-cut, which is given a fuzzy set $\tilde{F}$ on set U and confidence degree $\alpha \in [0, 1]$, defined as [476]:

$$\tilde{F}_\alpha = \{x \mid \tilde{F}(x) \geq \alpha\} \tag{A.36}$$

For example, the triangular fuzzy number and symmetrical triangular fuzzy number may be characterised by the following α-cuts of the fuzzy sets:

$$\tilde{M}_\alpha = [(m - l)\alpha + l, (m - u)\alpha + u] \tag{A.37}$$

$$\tilde{S}_\alpha = [(u - l)\alpha/2 + l, (l - u)\alpha/2 + u] \tag{A.38}$$

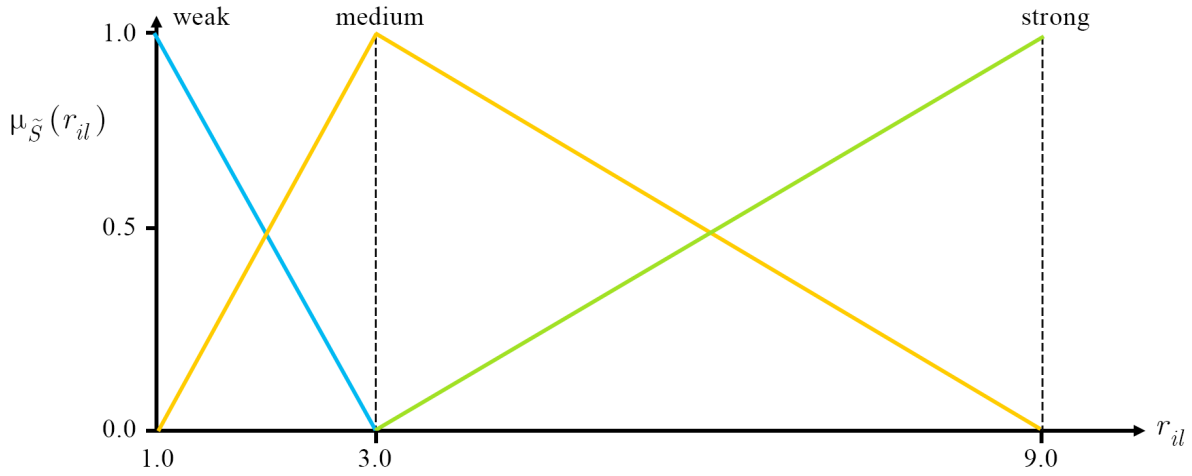

Figure A.4: Example of triangular membership functions of linguistic variables that can be used to express the strength of the relations between WHATs and HOWs in fuzzy QFD.

As can be observed, the α-cut procedure results in sets with a lower and upper bounds under confidence interval α. Extending this principle to QFD, in this brief account, the approach by Chen and Weng is taken as an example [475]. Starting from Wassermann's normalisation (Eq. A.28) -but one may freely use the normalisation by Chen and Chen (Eq. A.29)- one can define the following fuzzy numbers from their crisp counterparts:

$$\tilde{\mathcal{R}}_{ij}^{\text{norm}} = \frac{\sum_{l=1}^{J} \tilde{\mathcal{R}}_{il} \cdot \tilde{\mathcal{G}}_{lj}}{\sum_{j=1}^{J} \sum_{l=1}^{J} \tilde{\mathcal{R}}_{il} \cdot \tilde{\mathcal{G}}_{lj}} \tag{A.39a}$$

$$\tilde{\mathcal{R}}_{il} = \{[r_{il}, \mu_{\tilde{\mathcal{R}}_{il}}(r_{il})] \mid r_{il} \in \mathcal{R}_{il}\} \tag{A.39b}$$

$$\tilde{\mathcal{G}}_{lj} = \{[\gamma_{lj}, \mu_{\tilde{\mathcal{G}}_{lj}}(\gamma_{lj})] \mid \gamma_{lj} \in \mathcal{G}_{lj}\} \tag{A.39c}$$

For example, one may convert the linguistic relations 'strong', 'medium', and 'weak' between WHATs and HOWs to the triangular fuzzy numbers characterised by triplets (3,9,9), (1,3,9), and (1,1,3) respectively (Figure A.4). Using the α-cut on these numbers defines the following sets [475]:

$$(\mathcal{R}_{il})_\alpha = [(\mathcal{R}_{il})_\alpha^L, (\mathcal{R}_{il})_\alpha^U] = [\min_{r_{il}}\{r_{il} \in \mathcal{R}_{il} \mid \mu_{\tilde{\mathcal{R}}_{il}}(r_{il}) \geq \alpha\}, \max_{R_{il}}\{r_{il} \in \mathcal{R}_{il} \mid \mu_{\tilde{\mathcal{R}}_{il}}(r_{il}) \geq \alpha\}] \tag{A.40a}$$

$$(\mathcal{G}_{lj})_\alpha = [(\mathcal{G}_{lj})_\alpha^L, (\mathcal{G}_{lj})_\alpha^U] = [\min_{\gamma_{lj}}\{\gamma_{lj} \in \mathcal{G}_{lj} \mid \mu_{\tilde{\mathcal{G}}_{lj}}(\gamma_{lj}) \geq \alpha\}, \max_{\gamma_{lj}}\{\gamma_{lj} \in \mathcal{G}_{lj} \mid \mu_{\tilde{\mathcal{G}}_{lj}}(\gamma_{lj}) \geq \alpha\}] \tag{A.40b}$$

Here, superscripts ^{L} and ^{U} are used to denote the lower and upper bounds respectively. For example, when considering that the fuzzy number $\tilde{\mathcal{R}}_{il}$ is associated with linguistic variable 'strong' $\tilde{S}$ (see Figure A.4), then it has the triangular membership function:

$$\mu_{\tilde{S}}(r_{il}) = \begin{cases} \frac{1}{6} r_{il} - \frac{1}{2} & r_{il} \in [3, 9] \\ 0 & \text{otherwise} \end{cases} \tag{A.41}$$

The α-cuts of this membership function results in the following crisp set:

$$(\mathcal{R}_{il})_\alpha = [(\mathcal{R}_{il})_\alpha^L, (\mathcal{R}_{il})_\alpha^U] = [6\alpha + 3, 9] \tag{A.42}$$

In order to establish the fuzzy weighted average $\tilde{\mathcal{R}}_{ij}^{\text{norm}}$, the membership function is found based on Zadeh's extension principle [475]:

$$\mu_{\tilde{\mathcal{R}}_{ij}^{\text{norm}}}(r_{ij}^{\text{norm}}) = \sup_{r_{il},\gamma_{lj}} \min \left\{ \mu_{\tilde{\mathcal{R}}_{il}}(r_{il}), \mu_{\tilde{\mathcal{G}}_{lj}}(\gamma_{lj}) \mid r_{ij}^{\text{norm}} = \frac{\sum_{l=1}^{J} r_{il} \cdot \gamma_{lj}}{\sum_{j=1}^{J} \sum_{l=1}^{J} r_{il} \cdot \gamma_{jl}} \right\} \tag{A.43}$$

In constructing this membership function $\mu_{\tilde{\mathcal{R}}_{ij}^{\text{norm}}}$, one has several options. For example, one may use α-cuts to determine: (i) extreme bounds $(\mathcal{R}_{ij}^{\text{norm}})_{\alpha}^{L}$ and $(\mathcal{R}_{ij}^{\text{norm}})_{\alpha}^{U}$, (ii) more accurate bounds $m(\mathcal{R}_{ij}^{\text{norm}})_{\alpha}^{L}$ and $m(\mathcal{R}_{ij}^{\text{norm}})_{\alpha}^{U}$, or (iii) corrected bounds $({}^{*}\mathcal{R}_{ij}^{\text{norm}})_{\alpha}^{L}$ and $({}^{*}\mathcal{R}_{ij}^{\text{norm}})_{\alpha}^{U}$ (see Refs. [475, 477]). When using the independent scoring method (ISM) (Eq. A.30) and the importance weights of user requirements are numeric non-fuzzy variables, the importance weights of technical attributes are expressed via [477]:

$$(\mathcal{W}_j)_{\alpha} = [(\mathcal{W}_j)_{\alpha}^{L}, (\mathcal{W}_j)_{\alpha}^{U}] = \left[\frac{\sum_{i=1}^{I} d_i \cdot (\mathcal{R}_{ij}^{\text{norm}})_{\alpha}^{L}}{\sum_{i=1}^{I} d_i}, \frac{\sum_{i=1}^{I} d_i \cdot (\mathcal{R}_{ij}^{\text{norm}})_{\alpha}^{U}}{\sum_{i=1}^{I} d_i} \right] \tag{A.44}$$

These weights of the technical attributes may then be implemented in the technical matrix to select between a set of alternatives whilst keeping lower and upper bounds on the scoring. In the case of multiple fuzzy numbers, or more difficult functions -such as the satisfaction models treated in this thesis- these computations may become computationally intensive or require approximations. Nevertheless, it is for example most certainly possible to integrate non-linear models, such as Kano's model, in fuzzy QFD. Moreover, fuzzy models can well be used for the ordinal methods; in fact, the preference ranking equations in Eq. A.32 and Eq. A.33 are based on fuzzy sets. Approaches that incorporate non-crisp numbers or variables, such as the 2-tuple linguistic model, however, often transform the information from an ordinal scale into a cardinal one.

A.7 Questionnaire for determining relative importance ratings

WAARDE-BEPALING KWALITEITSKENMERKEN BRACHYTHERAPIE SOFTWARE

GEÏNFORMEERDE TOESTEMMING

Dank voor uw interesse in deelname aan dit onderzoek. Dit onderzoek maakt deel uit van een Master's thesis aan de afdeling BioMechanical Engineering van de TU Delft naar de ontwikkeling van software voor het automatiseren en optimaliseren van de positie-bepaling van stralingsbronnen voor brachytherapie van de cervix (zogeheten motion-planning software). Deze studie is een onderdeel van het ARCHITECT onderzoeksprogramma waarin - samen met de afdeling Radiotherapie van het Erasmus MC - 3D-geprinte patiënt-specifieke gynaecologische brachytherapie applicatoren ontwikkeld worden.

Het doel van dit onderzoek is het **vaststellen van de waarde van vooraf geselecteerde kwaliteitskenmerken** (specificaties) op de mate van tevredenheid in het gebruik van te ontwikkelen software. Uw antwoorden dragen bij aan de ontwikkeling van applicatoren met verbeterde positionering van stralingsbronnen met als resultaat een hogere dosis conformiteit en verminderde blootstelling van gezonde weefsels aan straling.

Dit onderzoek omvat een digitale vragenlijst bestaande uit 22 vragen en neemt ongeveer 20 minuten in beslag. Voorafgaand worden twee vragen gesteld om uw rol in de behandeling vast te stellen. De vragenlijst bestaat uit twee delen:

1. Om het belang van kwaliteitskenmerken aan te geven op uw mogelijke tevredenheid in het gebruik van deze software.
2. Om de kwaliteitskenmerken te categoriseren op hoe deze uw tevredenheid beïnvloeden.

Uw deelname aan dit onderzoek is vrijwillig. U kunt uw medewerking op elk moment stopzetten zonder opgave van reden en zonder verdere gevolgen.

Geen nadelen worden verwacht ten gevolge van uw deelname. Voor dit onderzoek wordt persoonlijke informatie verzameld: uw naam en e-mailadres (voor contact), uw specialisme en de tijdsduur dat u werkzaam bent in deze functie. Op de volgende wijzen worden risico's geminimaliseerd:

- Uw antwoorden worden anoniem en vertrouwelijk verwerkt.
- De resultaten van dit onderzoek worden enkel op groepsniveau geanalyseerd en gerapporteerd.
- De digitale dataset wordt bewaard in een veilige omgeving (TU Delft Project Drive), waartoe enkel Robin Straathof en Nick van de Berg middels een code toegang hebben.
- De inhoud van de drive wordt uiterlijk 10 jaar na voltooiing van de studie verwijderd.

Geanonimiseerde data worden online beschikbaar gemaakt als bijlage van de Master's thesis en kan gebruikt mogelijk worden voor toekomstige studies. U kunt contact opnemen met Robin Straathof om de verkregen geanonimiseerde data vooraf in te zien.

Bij aanvullende vragen of klachten naar aanleiding van dit onderzoek kunt u contact opnemen met:

Robin Straathof
Student Technische Universiteit Delft – Master Mechanical Engineering
Verantwoordelijk onderzoeker
Email: r.straathof@student.tudelft.nl

Onder supervisie van:
Dr.ir. Nick van de Berg, Dr.ir. Linda Wauben, Prof.dr. Remi Nout.

Klik in de selectievakjes om uw deelname te bevestigen **Ja**

Deelname in studie

Ik bevestig dat ik de informatie van de studie naar het bepalen van relatieve belangen van kwaliteitskenmerken heb gelezen. Tevens bevestig ik dat ik de kans heb gekregen om vragen over dit onderzoek te stellen en dat ik tevreden ben met de antwoorden en uitleg die ik heb ontvangen. ☐

Ik bevestig mijn deelname op vrijwillige basis aan dit onderzoek en begrijp dat ik te allen tijde ik vragen mag weigeren te beantwoorden en dat ik vrij ben om op elk moment deze vragenlijst te verlaten, zonder dat ik hiervoor een reden dien op te geven. ☐

Ik begrijp dat ik voor deze studie zelf en zonder overleg een online vragenlijst dien in te vullen, bestaande uit 22 vragen. ☐

Bevindingen van studie

Ik begrijp dat de resultaten van de studie geanonimiseerd verwerkt en gerapporteerd worden voor de Master's thesis van de verantwoordelijk onderzoeker. ☐

Ik begrijp dat persoonlijke informatie die mogelijk te herleiden valt tot mij, enkel bekend is bij de onderzoekers met toegang tot de volledige dataset (Robin Straathof en Nick van de Berg) en enkel op groepsniveau wordt geanalyseerd. ☐

Toestemming

Ik geef mijn toestemming voor deelname aan dit onderzoek. ☐

Naam van deelnemer:
Voornaam Achternaam

Ik bevestig dat de deelnemer zo goed mogelijk geïnformeerd is over het onderzoek. Ik verklaar mij bereid om aanvullende vragen over het onderzoek naar vermogen te beantwoorden.

Naam van onderzoeker:
Robin Straathof

VRAGENLIJST

Instructies voor het invullen van de vragenlijst

Voor het invullen van deze vragenlijst wil ik u vragen de volgende voorstelling te maken:

Binnen het ARCHITECT programma wensen wij patiënt-specifieke applicatoren te 3D-printen. In deze prints worden katheter-paden gedefinieerd in de vrije ruimte (intracavitair en interstitieel), aan de hand van de anatomie van de patiënt (MRI), zie onderstaand figuur. Dit is dus complexer dan de huidige situatie, waarbij in de planning gekozen kan worden uit een beperkt aantal gedefinieerde paden bepaald door de vaste geometrie van de applicator. Het intekenen van katheter-paden wordt volledig geautomatiseerd in de software, maar de resultaten kunnen (enigszins) worden aangepast. Tevens kunnen de paden zo gepland worden dat deze rekening houden met de mogelijke relatieve verplaatsing van omringende structuren. Na deze vormbepaling kan de applicator geïmporteerd worden in treatment planning software om een behandelingsplan te genereren.

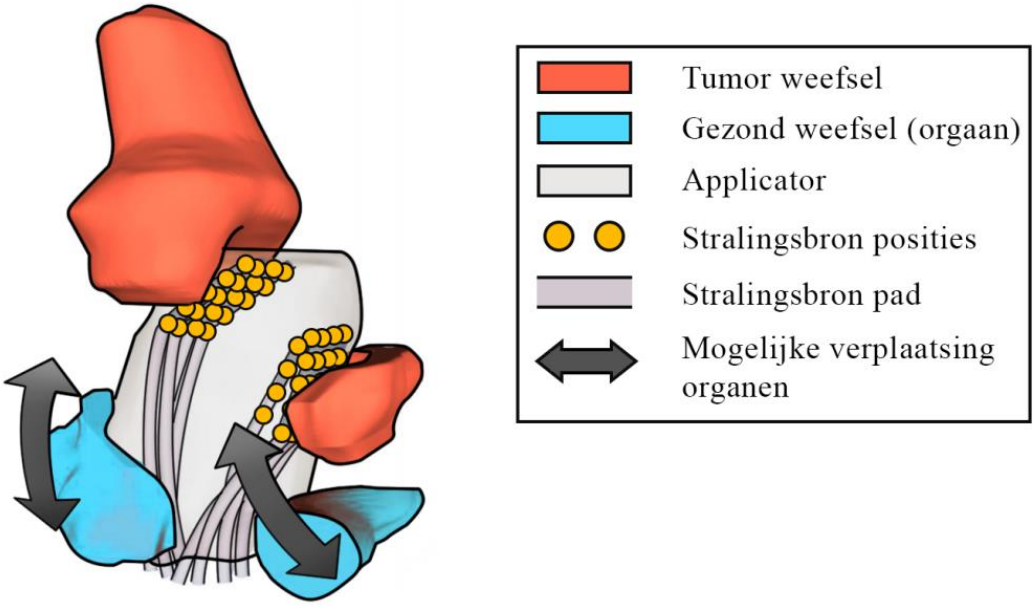

Figuur. De software kan paden te plannen zodoende dat de stralingsbronnen in nabijheid van het tumorweefsel worden gebracht.

De vragenlijst richt zich op de eerste fase: het genereren van paden voor stralingsbron locaties die gekozen kunnen worden in het behandelplan.

DEEL 0: ALGEMENE INFORMATIE

(1) Kunt u uw specialisme aangeven?

<Vul uw specialisme in>

Anders, namelijk -

(2) Hoe lang bent u werkzaam in uw huidige functie?

- < kies eenheid >

DEEL 1: BELANG VAN KWALITEITSKENMERKEN

Instructie
Kunt u per kwaliteitskenmerk aan geven hoe belangrijk voor u de inclusie of de mate van vervulling van dit kenmerk zou zijn voor de software?

(1) Hoe belangrijk is de mogelijkheid van de software om robuust optimale plaatsing van stralingsbronnen ten opzichte van de tumor te garanderen?
Toelichting: Robuust optimale plaatsing betekent dat de planner proximale plaatsing van stralingsbronnen bij de tumor garandeert, zelfs mochten er anatomische veranderingen gedurende de behandeling optreden. De software kan aannames maken voor de ideale oriëntatie van paden, zodat de kans op een hoge conformiteit zo groot mogelijk is.

<Selecteer hier uw antwoord>

(2) Hoe belangrijk is de mogelijkheid van de software om robuust optimale plaatsing van stralingsbronnen ten opzichte van de gezonde weefsels en structuren (organs at risk) te garanderen?
Toelichting: Robuust optimale plaatsing betekent dat de planner plaatsing van stralingsbronnen garandeert zodoende dat dosimetrische grenswaarden in omringende gezonde weefsels niet worden overschreden, zelfs mochten er anatomische veranderingen optreden gedurende de behandeling optreden. De software kan aannames maken voor de ideale oriëntatie van paden, zodat de kans op een hoge conformiteit zo groot mogelijk is.

<Selecteer hier uw antwoord>

(3) Hoe belangrijk is de mogelijkheid van de software om driedimensionale (3D) visualisatie en positie-bepaling van de stralingsbronnen uit te voeren?

<Selecteer hier uw antwoord>

(4) Hoe belangrijk is de mogelijkheid van de software om in reële tijd (real-time, binnen een tijdsbestek van enkele seconden) aanpassingen uit te voeren in katheter-paden en de resultaten hiervan te zien?

<Selecteer hier uw antwoord>

(5) Hoe belangrijk is de mogelijkheid van de software om de positie van stralingsbronnen als een startpunt voor de optimalisatie handmatig vast te leggen en te gebruiken als routepunt (waarlangs het katheter-pad moet volgen)?

<Selecteer hier uw antwoord>

(6) Hoe belangrijk is de mogelijkheid van de software om in een korte tijd de stralingsbron positie-bepaling uit te voeren?

<Selecteer hier uw antwoord>

(6.2) Wat vindt u een 'korte tijd' voor het plannen van een pad?
- < kies eenheid >

(7) Hoe belangrijk is de mogelijkheid van de software om visualisatie en planning met een hoge resolutie uit te voeren?
Toelichting: Bij een hogere resolutie wordt de anatomie realistischer weergegeven en zijn de paden ook accurater, maar het genereren van de paden kost meer tijd.

<Selecteer hier uw antwoord>

(8) Hoe belangrijk is de mogelijkheid van de software om met een lage kans op mislukking een succesvol plan te genereren?
Toelichting: Sommige softwareoplossingen voor het plannen van paden zijn niet per definitie succesvol (kunnen vastlopen zonder een optimaal pad te vinden). In dat geval dient opnieuw de software te worden gestart.

<Selecteer hier uw antwoord>

(9) Hoe belangrijk is de mogelijkheid van de software om paden te genereren, die reproduceerbaar gevolgd kunnen worden in de 3D-geprinte applicator door katheters aangestuurd via een afterloader?
Toelichting: Bijvoorbeeld scherpe bochten kunnen mogelijk niet nauwkeurig gevolgd worden.

<Selecteer hier uw antwoord>

(10) Hoe belangrijk is de mogelijkheid van de software om een inschatting te maken van de risiconiveaus op het overschrijden van grenswaarden voor gezonde weefsels (organs at risk) voor het gebruik van treatment planning software, zelfs mochten er anatomische veranderingen gedurende de behandeling optreden?

<Selecteer hier uw antwoord>

DEEL 2: INVLOED VAN KWALITEITSKENMERKEN OP TEVREDENHEID

Instructie
De invloed van de mate van vervulling of de aanwezigheid van een kwaliteitskenmerk op de tevredenheid kan verschillen per kwaliteitskenmerk. Een model om de tevredenheid ten gevolge van een kwaliteitskenmerk te categoriseren is Kano's model.

Dit model onderscheidt **vier typen kenmerken**:

Afk.	Kenmerk	Beschrijving formeel	Beschrijving informeel
A.	**Aantrekkelijk/ Wenselijk**	Een kwaliteitskenmerk dat voor een grotere mate van tevredenheid zorgt wanneer aanwezig, dan de mate van ontevredenheid wanneer deze niet aanwezig is	*Wordt niet verwacht, maar zorgt voor extra tevredenheid*
P.	**Prestatie/ Relevant**	Een kwaliteitskenmerk dat voor dezelfde mate van tevredenheid zorgt wanneer aanwezig, als de mate van ontevredenheid wanneer deze niet aanwezig is;	*Valt binnen de verwachting, zorgt wel voor tevredenheid*
B.	**Basis/ Noodzakelijk**	Een kwaliteitskenmerk dat voor een grote mate ontevredenheid zorgt wanneer dit niet aanwezig is, maar een lage mate van tevredenheid wanneer wel aanwezig;	*Moet minimaal aan worden voldaan*
O.	**Onverschillig/ Irrelevant**	Het maakt niet uit of het kwaliteitskenmerk aanwezig is.	*Niet relevant*

Kunt u per eerder beschreven kwaliteitskenmerk aangeven in welke categorie u dit kenmerk beschouwt?

Nr. Deel 1	**Kwaliteitskenmerk** (korte omschrijving, zie de volledige in deel 1)	**Categorie van tevredenheid**
(1)	Robuust optimale plaatsing ten opzichte van tumor	< selecteer categorie >
(2)	Robuust optimale plaatsing ten opzichte van organen	< selecteer categorie >
(3)	3D visualisatie en positie-bepaling	< selecteer categorie >
(4)	Aanpassingen in reële tijd (real-time)	< selecteer categorie >
(5)	Vastleggen positie van stralingsbronnen als routepunt	< selecteer categorie >
(6)	Tijdsduur van het plannen	< selecteer categorie >
(7)	Resolutie van structuren en paden	< selecteer categorie >
(8)	Kans op succesvol plan	< selecteer categorie >
(9)	Reproduceerbaar volgen van paden	< selecteer categorie >
(10)	Inschatting van risiconiveaus	< selecteer categorie >

Optioneel. Ruimte voor opmerkingen.

<Einde van vragenlijst>
Druk op de onderstaande knop om uw antwoorden op te slaan

Opslaan

A.8 Dose-based optimisation results of generated needle channels

Table A.4: Results of the dosimetric evaluation for the combined intracavitary trajectories and straight interstitial dwell segments in two coverage planning scenarios. Dose distributions are evaluated for regularly spaced dose calculation points in the nominal delineations of structures and within the worst-case uncertainty contours. Continuous variables are expressed with the mean ± SD, and discrete variables with the median. Abbreviations: DT = dwell time, DT IC = dwell time in intracavitary part.

		Conservative OAR sparing				**Nominal planning**	
		rt-RRT	BU-rt-RRT	CC-rt-RRT (med.)	CC-rt-RRT (low)	rt-RRT	CC-rt-RRT (med.)
Objective value		0.59 ± 0.00	0.59 ± 0.01	0.59 ± 0.00	0.59 ± 0.00	0.03 ± 0.00	0.03 ± 0.00
Active dwell positions (Total)		18 (61)	18 (61)	18 (61)	18 (61)	24 (59)	23 (59)
Mean DT (s)		19.9 ± 0.0	19.9 ± 0.0	19.9 ± 0.0	19.9 ± 0.1	12.0 ± 0.2	12.8 ± 0.3
Maximum DT (s)		96.2 ± 0.1	96.1 ± 0.2	95.4 ± 0.3	95.6 ± 0.5	63.3 ± 0.0	62.7 ± 0.1
Total DT (s)		357.7 ± 0.2	358.1 ± 0.6	357.8 ± 0.4	358.2 ± 1.0	292.0 ± 0.3	297.6 ± 0.1
Mean DT IC (s)		56.5 ± 0.2	56.8 ± 0.4	56.8 ± 0.3	57.0 ± 0.7	17.4 ± 0.0	25.3 ± 0.0
Maximum DT IC (s)		71.3 ± 0.2	71.5 ± 0.2	71.5 ± 0.3	71.6 ± 0.5	36.7 ± 0.3	44.6 ± 0.2
Total DT IC (s)		113.0 ± 0.3	113.5 ± 0.9	113.6 ± 0.7	114.0 ± 1.4	69.5 ± 0.2	75.9 ± 0.1
Nominal contours							
CTV_{HR}	$D_{98\%}$ (Gy)	7.1 ± 0.0	7.1 ± 0.0	7.1 ± 0.0	7.1 ± 0.0	7.0 ± 0.0	7.0 ± 0.0
	$D_{90\%}$ (Gy)	7.6 ± 0.0	7.7 ± 0.0	7.7 ± 0.0	7.7 ± 0.0	7.3 ± 0.0	7.3 ± 0.0
	$D_{50\%}$ (Gy)	11.4 ± 0.0	11.4 ± 0.0	11.4 ± 0.0	11.4 ± 0.0	10.4 ± 0.0	10.3 ± 0.0
	$A_{100\%}$ (%)	99.0 ± 0.1	99.1 ± 0.1	99.1 ± 0.1	99.0 ± 0.1	98.7 ± 0.1	98.4 ± 0.4
Bladder	$D_{10\%}$ (Gy)	2.9 ± 0.0	2.9 ± 0.0	2.9 ± 0.0	2.9 ± 0.0	2.8 ± 0.0	2.8 ± 0.0
	$D_{2\%}$ (Gy)	4.5 ± 0.0	4.5 ± 0.0	4.5 ± 0.0	4.5 ± 0.0	4.4 ± 0.0	4.4 ± 0.0
	$A_{6\ \mathrm{Gy}}$ (%)	0.0 ± 0.0	0.0 ± 0.0	0.0 ± 0.0	0.0 ± 0.0	0.0 ± 0.0	0.0 ± 0.0
Rectum	$D_{10\%}$ (Gy)	1.2 ± 0.0	1.2 ± 0.0	1.2 ± 0.0	1.2 ± 0.0	0.8 ± 0.0	0.9 ± 0.0
	$D_{2\%}$ (Gy)	1.6 ± 0.0	1.5 ± 0.0	1.5 ± 0.0	1.5 ± 0.0	1.1 ± 0.0	1.1 ± 0.0
	$A_{3.7\ \mathrm{Gy}}$ (%)	0.0 ± 0.0	0.0 ± 0.0	0.0 ± 0.0	0.0 ± 0.0	0.0 ± 0.0	0.0 ± 0.0
Sigmoid	$D_{10\%}$ (Gy)	2.9 ± 0.0	2.8 ± 0.0	2.8 ± 0.0	2.8 ± 0.0	2.4 ± 0.0	2.4 ± 0.0
	$D_{2\%}$ (Gy)	3.8 ± 0.0	3.8 ± 0.0	3.8 ± 0.0	3.8 ± 0.0	3.3 ± 0.0	3.4 ± 0.0
	$A_{4.3\ \mathrm{Gy}}$ (%)	0.7 ± 0.0	0.7 ± 0.0	0.7 ± 0.0	0.7 ± 0.0	0.0 ± 0.0	0.0 ± 0.0
Worst-case uncertainty							
Bladder	$D_{10\%}$ (Gy)	3.7 ± 0.0	3.7 ± 0.0	3.7 ± 0.0	3.7 ± 0.0	3.9 ± 0.0	3.9 ± 0.0
	$D_{2\%}$ (Gy)	8.0 ± 0.0	8.0 ± 0.0	8.0 ± 0.0	8.0 ± 0.0	8.9 ± 0.0	8.8 ± 0.0
	$A_{6\ \mathrm{Gy}}$ (%)	4.2 ± 0.0	4.2 ± 0.0	4.2 ± 0.0	4.2 ± 0.0	4.8 ± 0.0	4.8 ± 0.0
Rectum	$D_{10\%}$ (Gy)	1.5 ± 0.0	1.5 ± 0.0	1.5 ± 0.0	1.5 ± 0.0	1.1 ± 0.0	1.1 ± 0.0
	$D_{2\%}$ (Gy)	2.1 ± 0.0	2.1 ± 0.0	2.1 ± 0.0	2.1 ± 0.0	1.6 ± 0.0	1.6 ± 0.0
	$A_{3.7\ \mathrm{Gy}}$ (%)	0.0 ± 0.0	0.0 ± 0.0	0.0 ± 0.0	0.0 ± 0.0	0.0 ± 0.0	0.0 ± 0.0
Sigmoid	$D_{10\%}$ (Gy)	4.0 ± 0.0	4.0 ± 0.0	4.0 ± 0.0	4.0 ± 0.0	3.4 ± 0.0	3.5 ± 0.0
	$D_{2\%}$ (Gy)	8.1 ± 0.0	8.1 ± 0.0	8.1 ± 0.0	8.1 ± 0.0	8.2 ± 0.0	8.2 ± 0.0
	$A_{4.3\ \mathrm{Gy}}$ (%)	8.5 ± 0.0	8.5 ± 0.0	8.5 ± 0.0	8.5 ± 0.0	7.0 ± 0.0	7.0 ± 0.0